Ultrasound Strain and Photoacoustic Imaging Algorithms for Cardiac Health Assessment in Murine Models

By

Rashid Al Mukaddim

A dissertation submitted in partial fulfillment of
the requirements for the degree of

Doctor of Philosophy
(Electrical and Computer Engineering)

at the
UNIVERSITY OF WISCONSIN-MADISON
2021

Date of final oral examination: 06/23/2021

The dissertation is approved by the following members of the Final Oral Committee:

Tomy Varghese, Professor, Medical Physics

Carol Mitchell, Associate Professor, Medicine

William Sethares, Professor, Electrical and Computer Engineering

Dan Negrut, Professor, Mechanical Engineering

Acknowledgments

"My Lord, increase me in knowledge" – (Holy Quran, 20:114)

My PhD journey felt like a marathon with many ups and downs along the way. There were moments of joy and satisfaction along with moments of despair from failure. However, there were some people who always had my back throughout my entire journey and helped me make this dissertation a possibility. I would like to use this section as an opportunity to thank them and acknowledge their contributions.

I would like to start by thanking my PhD advisor, Prof. Tomy Varghese, for giving me the opportunity to work with him on ultrasound strain and photoacoustic imaging. He has been a constant source of encouragement and helped me navigate graduate school coursework and research. He was always open to have discussions about new research ideas and trusted me to pursue my own areas of interest. I have highly benefitted from his guidance on technical writing and research publication.

Next, I am thankful to Dr. Kaisar Alam for introducing to me to the world of ultrasound imaging and signal processing. He patiently taught me research methodologies and provided me with invaluable guidance when I was applying to graduate school to pursue doctoral research.

I would also like to thank my PhD thesis committee members Profs. William Sethares, Dan Negrut, and Carol Mitchell for their valuable inputs and suggestions on this dissertation. I was fortunate enough to learn basic and advanced concepts of image processing from Prof. William Sethares which helped me to solve several problems during my PhD. He gave me his valuable time to discuss my research problems and provide me with his advice. Prof. Dan Negrut taught me GPU

programming which has been extensively used throughout this dissertation. Prof. Carol Mitchell offered clinical insights and helped design the imaging protocol used during this dissertation. Her attention to details allowed us to acquire high quality data which were instrumental to the success for our *in vivo* experiments. Furthermore, her encouraging words acted as a positive momentum for my work. So, Thank you. I would also like to acknowledge Prof. Tim Hall for serving in my preliminary examination committee and providing constructive feedback on my initial research proposal. Additionally, I would like to thank Prof. James A. Zagzebski for teaching me the ultrasound lab course which substantiated my practical knowledge on ultrasound systems.

An *in vivo* longitudinal study with mice was designed as a part of this dissertation and many people played crucial roles for successful execution of it. I want to acknowledge Drs. Timothy Hacker and Rachel Taylor from Cardiovascular Physiology Research Core for acquiring the murine models and performing relevant surgical procedures. Specially, I have been benefited from the deep knowledge of Dr. Timothy Hacker on mice cardiac physiology and want to thank him for tolerating my naive inquiries about mouse heart. I want to specially mention Ashley Weichmann for her contribution for *in vivo* data collection. Our *in vivo* data collection faced several hurdles including but not limited to Covid-19 pandemic, broken laser, flooding from roof pipe leaks, interference from bio-safety cabinet but Ashley helped me tremendously to navigate all these and successfully finish data collection. I would also like to mention Dr. Melissa Graham, Thomas Pier, and Joe Hardin for their contribution in histopathological slide preparation and image interpretation.

Dr. Orhan Unal, Director of Medical Physics IT/IS/Scientific Computing deserves praise for always being responsive to solve my medical physics server related concerns. He had put together a GPU cluster during my PhD which had accelerated my data analysis significantly.

I was fortunate enough to have some amazing friends over the past five years. I am grateful to Dr. Catherine Steffel, Nafisah Islam, Dr. Md Abdul Kader Sagar, Michael Turney, and XiongMee Vang for being wonderful friends to me and for their constant support regarding my research work and other matters as well.

I am indebted to the past and present members of Ultrasound research group at UW-Madison: Dr. Chi Ma, Dr. Atul Ingle, Dr. Kayvan Samimi, Dr. Nirvedh Meshram, Dr. Catherine Steffel, Dr. Robert Pohlman, Michael Turney, Yurim Lee, Dr. Andrew Paul Santoso, Dr. Mohammadreza Kari, and Dr. Ivan Rosado-Mendez for their help, support, invaluable research inputs, and delightful companionship.

I am immensely grateful to my parents: Dr. Md. Nasir Uddin and Keswara Sultana, and my sister: Dr. Fatema Tuj Zohora for their unconditional love and support. My parents always prioritized my education over anything else which instilled within me the importance of hard-work and thus, I have come this far in my life. No matter what I do, I will not be able to repay their debts. I would also like to thank my father-in-law (Shakhawat Khan), mother-in-law (Afifa Malik) and sister-in-law (Shifa Khan) for treating me as their son and a brother.

And, most importantly I want to thank my amazing wife, Dr. Samia Khan, for always being there for me. I am grateful to her for allowing me to prioritize this work over our vacation plans; for patiently listening to me talk about my research; proofreading my manuscripts; and encouraging me to be my best self. But, above all, thank you Samia for always loving me and believing in me. I am very lucky to have you in my life.

– Rashid Al Mukaddim (06/06/2021)

Abstract

Coronary artery disease leading to myocardial infarction (MI) is the number one cause of mortality worldwide. MI is typically caused by prolonged durations of ischemia. Murine models of myocardial ischemia and infarction and ischemia-reperfusion (IR) play an instrumental role to gain mechanistic insights into cardiac remodeling post-MI. However, the success of these models depends on the availability of accurate and reproducible techniques for measuring cardiac physiology. The goal of this dissertation is to demonstrate a composite imaging framework combining two different modalities (cardiac strain and photoacoustic imaging) for *in vivo* assessment of functional and perfusion changes in the myocardium associated with MI and IR murine models non-invasively.

Cardiac strain imaging (CSI) is an ultrasound-based approach to estimate myocardial relative tissue elasticity by tracking cardiac deformation induced by the natural contraction and relaxation of the heart. CSI is now used for assessing global and regional myocardial function. Displacement estimation is an important processing step to ensure accuracy and precision of CSI-derived strain tensors. To this end, we developed a multi-level block matching algorithm with Bayesian regularization (BR) which imposes local spatial continuity during displacement estimation using Bayes theorem. Later, an adaptive BR scheme was developed which utilizes local input data statistics to perform optimal regularization. A spatiotemporal BR method was also developed to utilize temporal information for regularization. The results from a pre-clinical longitudinal study demonstrate the efficacy of the BR methods for estimating cardiac strain accurately along with correlation to histopathological findings.

There is an unmet clinical need for non-invasive imaging to efficiently study myocardial blood flow and perfusion. We propose to utilize PAI to generate parametric maps of blood oxygen saturation (sO_2) to quantify cardiac perfusion in murine models. We developed a myocardial sO_2 estimation method termed Oxygenation estimation using Physiological signal gating and Motion Compensation (OPMC). Novel adaptive beamforming and image processing algorithms such as spatiotemporal coherence weighting, photoacoustic sub-aperture processing and spatiotemporal singular value decomposition were developed for OPMC. Our results suggest that OPMC had better spatiotemporal resolution owing to elimination of high persistence and data collection at higher frame rate compared to a conventional approach.

Table of Contents

List of Figures

List of Tables

Chapter 1

Introduction and Research Question

Coronary heart disease (CHD) including myocardial infarction (MI) is the number one cause of mortality worldwide according to American Heart Association annual statistical update 2021 [1]. Virani *et al.* reported that roughly 13% of deaths in USA were caused by CHD with more than 360,000 deaths annually in 2018 [1]. According to data available from 2013, CHD was one of the most expensive conditions treated in US hospitals with an annual financial burden of $9.0 billion [1]. MI results from hypoxia in cardiac muscle cells leading to cell death, typically caused by prolonged duration of ischemia (from a diminished supply of blood) [2]. Myocardium undergoes a series of morphological changes (e.g., change in mass and geometry, scar formation) after MI known as cardiac remodeling [3]. Improved management strategies for patients after MI can be realized with better understanding of these changes [4].

Animal models of ischemia and infarction have been instrumental for gaining better insights on cardiac remodeling [4, 5]. In particular, murine models of CHD have been routinely utilized in pre-clinical research due to its similarity to human cardiovascular physiology and ease of genetic alteration [6]. The greatest advantage of the murine model is the availability of various relevant transgenic and knockout (KO) strains [7]. It allows us to gain mechanistic insights into pathogenesis of heart failure and disease progression and detect targets for pharmacological or molecular therapy [7] which is not feasible in clinical situations [8]. Additionally, these models are amenable choices to enable translation of novel treatments and therapeutic interventions such as stem cell therapy from laboratory to the clinic [9]. To understand the anatomical and physiological changes associated with these models, accurate and reproducible techniques for

measuring cardiac physiology in mice is of utmost importance [9]. In this regard, non-invasive cardiac imaging plays a pivotal role to meet the technological demand of studying mice cardiac physiology [6, 7] and is the focus of this dissertation.

1.1 Non-Invasive Imaging Tools to Study Cardiac Mechanics

The heart demonstrates complex left ventricular (LV) motion mechanics during a cardiac cycle while circulating blood and oxygen to the cardiovascular system consisting of arteries and veins [10, 11]. The LV demonstrates inward motion associated with myocardial wall thickening, the base moving towards the apex and ventricular twist due to the apex and base rotating in opposing directions [11, 12] during ventricular systole with reverse motion mechanics during diastole. In the event of myocardial ischemia and infarction, normal LV structure and function undergoes rapid changes such as loss of contractile tissue, bulging of infarcted area, LV wall dilation, enhanced myocardial stiffness and hyperkinesia of viable tissue [9, 13]. Assessment of cardiac function through non-invasive imaging can provide valuable information regarding LV mechanical changes associated with MI.

Echocardiography has been routinely used to assess myocardial function as it is cost-effective, fast, portable and provides high temporal resolution for real-time visualization of the heart in a clinical setting [14, 15]. Qualitative assessment of echocardiographic image sequences over several cardiac cycles (visual wall motion scoring and wall thickening evaluation) by expert clinicians have been used to quantify myocardial function [16]. However, the accuracy of these assessments is dependent on extensive training, expertise [17, 18] and suffers from inter-observer variability. Myocardial deformation imaging has therefore been utilized to obtain clinically valuable information based on an objective assessment of regional and global ventricular function [19]. Deformation imaging methods quantify myocardial function in terms of regional cardiac

displacement and strain, an unitless measure of the degree of deformation with respect to initial cardiac dimensions [20]. Deformation imaging in mice is typically done by deriving cardiac motion either using ultrasound echocardiography or by strain mapping via tagged magnetic resonance imaging (MRI) data such as displacement encoding via-simulated echo (DENSE), and spatial modulation of magnetization (SPAMM) [6, 9]. Tagged-MRI methods allow direct measurement of myocardial tissue properties, however, this method suffers from limitations such as low temporal resolution and not being real-time unlike echocardiography [6, 21]. On the other hand, cardiac strain imaging (CSI) utilizing two-dimensional (2-D), or three-dimensional (3-D) echocardiography data, has shown widespread applicability in both clinical and pre-clinical setups as it can be performed with data collected during a conventional echocardiographic examination [21-27]. In particular, CSI using ultrasound radiofrequency (RF) data (cardiac or myocardial elastography) is more sensitive to subtle myocardial motion abnormalities compared to conventional echocardiography and envelope-based speckle tracking [28-30]. However, accurate strain estimation in murine models poses unique challenges due their small size and rapid heart rate [31]. Higher heart rate results in increased RF signal decorrelation and additional out-of-plane scatterer motion due to complex 3-D cardiac deformation imaged in 2-D thus degrading the quality of CSI. Therefore, CSI is still being actively researched to address the above-mentioned challenges.

1.2 Myocardial Microcirculation and Role of Perfusion Imaging

Myocardial blood flow (MBF) is regulated by coronary circulation comprising an extensive network of arteries and arterioles penetrating the cardiac muscle tissue [32]. Oxygen supply and nutrient demand of cardiac tissue are met by MBF whose dysfunction leads to cardiac hypoxia and tissue necrosis [33]. Positron emission tomography (PET), single-photon positron emission

computed tomography (SPECT) and magnetic resonance imaging (MRI) are currently being employed for imaging MBF in humans with PET being the clinical reference standard [33]. However, the small size and rapid heart rate in the mouse heart poses significant challenges for myocardial perfusion imaging with these techniques [34, 35]. Application of these tools is difficult in murine models for financial (e.g., expense of a MR/PET scanner, requirement of cyclotron facilities to produce radionuclide [33]) and technical reasons (e.g., ionizing dose, poor spatial resolution of SPECT [33], low temporal resolution, long acquisition time) [34]. For example, blood oxygen level-dependent (BOLD) MRI imaging and first-pass MRI with intravenous bolus injection can quantitatively investigate MBF at the expense of relatively longer image acquisition time and technical challenges associated with bolus injection [9, 33]. Furthermore, these methods do not operate in real-time. A relatively low cost solution without the use of any ionizing radiation is myocardial contrast echocardiography (MCE) which has been used to evaluate myocardial perfusion and identify perfusion defects in ischemia models [36]. MCE involves intravenous injection of contrast agents (gas filled micro bubbles) to enhance the myocardial ultrasound B-mode images with higher spatial and temporal resolution than SPECT, PET and MRI [36]. However, performing MCE in a small animal model with a rapidly beating heart is quite demanding both in terms of surgical procedures and image acquisition with a high resolution scanner [37]. Therefore, there is an unmet need for a non-invasive imaging method to efficiently study MBF in murine models. We propose to utilize photoacoustic imaging (PAI) to generate parametric maps of blood oxygen saturation to assess perfusion of ischemic regions.

1.3 Specific Research Aims

The primary objective of this dissertation was to develop a unified imaging framework to study mechanical and perfusion changes in the myocardium due to myocardial infarction and

ischemia-reperfusion injury in murine models. Four specific aims were established to achieve the above-mentioned research objective.

Aim 1: Non-invasive quantification of myocardial oxygen saturation with Photoacoustic imaging. Non-invasive quantification of myocardial perfusion may be more definitive for indicating the extent of ischemia. We hypothesized that photoacoustic imaging (PAI) has the potential to be a non-invasive, non-ionizing and real time monitoring tool for studying perfusion changes in the myocardium due to ischemia.

Aim 2: Development of a complete strain estimation framework by incorporating Bayesian regularization-based hierarchical block matching algorithm with Lagrangian motion description and myocardial polar strain estimation. Cardiac elastography (CE) has been utilized to perform objective assessment of regional and global myocardial function [23, 27]. We hypothesized that application of Bayesian regularization techniques in CE will result in a robust and accurate strain estimation framework to study functional changes associated with ischemia.

Aim 3: Development of an adaptive Bayesian regularization algorithm for robust low and high strain estimation. Spatial variation of elasticity in the myocardium requires a strain estimation algorithm to be robust for both low and high strain field estimation. We hypothesized that adaptively varying the extent of regularization based on the quality of data (e.g., signal decorrelation) will allow estimation of both low and high strain fields in a robust manner.

Aim 4: Development of spatiotemporal Bayesian regularization-based motion estimation approach for invoking temporal consistency in cardiac elastography. Dynamically varying strain rates in the cardiac cine loops due to cardiac pulsation pose a fundamental challenge in CE. We hypothesized that spatiotemporal regularization-based motion estimation framework will be

more robust to tackle dynamically varying myocardial strain rates resulting in smoothly varying temporal strain curves.

1.4 Dissertation Outline

Chapter 2 presents a literature review on ultrasound elastography methods and relevant signal processing techniques for cardiac function assessments using strain imaging.

Chapter 03 introduces photoacoustic imaging (PAI) and provides a detailed literature review on solving acoustic (beamforming) and optical (oxygen saturation estimation) inverse problem related to PAI.

Chapter 04 proposes and validates a complete cardiac strain estimation pipeline incorporating Bayesian regularization-based hierarchical block matching algorithm, Lagrangian description of motion and myocardial polar strain estimation (*Aim 2*).

Chapter 05 presents an adaptive iterative Bayesian regularization framework based on local signal decorrelation levels derived from input RF data that adaptively varies the extent of regularization thus allowing estimation of both low and high strain fields in a robust manner (*Aim 3*).

Chapter 06 extends the Bayesian regularization algorithm into the temporal domain with an underlying assumption of smooth variation in velocity over a short span of time during tissue deformation and validates it using simulation and *in vivo* cardiac datasets (*Aim 4*).

Chapter 07 investigates dynamic frame skip and log compression of the correlation function in the context of improving Bayesian regularization for ultrasound strain imaging. (*Aim 2 and 3*).

Chapter 08 reports on the utilization of a commercially available dual-wavelength PAI solution to generate parametric maps of blood oxygen saturation that were overlaid on high resolution high-

frequency ultrasound images of the myocardium. Our results demonstrate that PAI is sensitive to changes in myocardial oxygenation associated with acute myocardial ischemia (*Aim 1*).

Chapter 09 proposes and validates a photoacoustic beamforming algorithm incorporating spatiotemporal information to tackle temporally varying incoherent clutter noise seen in cardiac PAI (*Aim 1*).

Chapter 10 presents photoacoustic image formation based on sub-aperture processing to optimally recover both coherent and diffuse photoacoustic (PA) signals while suppressing clutter and sidelobes (*Aim 1*).

Chapter 11 incorporates the developed photoacoustic sub-aperture processing (PSAP) method in Chapter 10 into a minimum variance (MV) beamformer to address sidelobe corruption while preserving resolution improvement obtained with MV.

Chapter 12 presents a spatiotemporal singular value decomposition (SVD) processing method to enhance myocardial signal specificity using ECG and respiratory signal (ECG-R) gating and *in vivo* cardiac murine PAI data beamformed with delay-and-sum (DAS) (*Aim 1*).

Chapter 13 demonstrates a physiological signal gated PAI technique with motion compensation to improve the sensitivity and resolution of myocardial oxygen saturation estimation *in vivo* (*Aim 1*).

Chapter 14 reports on a Lagrangian CSI framework incorporating Adaptive Bayesian Regularization (ABR-CSI) and investigate the feasibility of this method for longitudinal monitoring of cardiac remodeling in murine models of myocardial infarction and ischemia-reperfusion injury *in vivo* (*Aims 2 – 3*).

Chapter 15 summarizes the contribution of this dissertation and outlines future research directions.

Supplemental materials are presented in the Appendices.

List of References

[1] S. S. Virani, A. Alonso, H. J. Aparicio, E. J. Benjamin, M. S. Bittencourt, C. W. Callaway, *et al.*, "Heart Disease and Stroke Statistics-2021 Update: A Report From the American Heart Association," *Circulation,* vol. 143, pp. e254-e743, Feb 23 2021.

[2] K. Thygesen, J. S. Alpert, H. D. White, A. S. Jaffe, F. S. Apple, M. Galvani, *et al.*, "Universal definition of myocardial infarction: Kristian Thygesen, Joseph S. Alpert and Harvey D. White on behalf of the Joint ESC/ACCF/AHA/WHF Task Force for the Redefinition of Myocardial Infarction," *European heart journal,* vol. 28, pp. 2525-2538, 2007.

[3] P. S. Azevedo, B. F. Polegato, M. F. Minicucci, S. A. Paiva, and L. A. Zornoff, "Cardiac remodeling: concepts, clinical impact, pathophysiological mechanisms and pharmacologic treatment," *Arquivos brasileiros de cardiologia,* vol. 106, pp. 62-69, 2016.

[4] J. Mill, I. Stefanon, L. Dos Santos, and M. Baldo, "Remodeling in the ischemic heart: the stepwise progression for heart failure," *Braz J Med Biol Res,* vol. 44, pp. 890-898, 2011.

[5] R. D. Patten and M. R. Hall-Porter, "Small animal models of heart failure: development of novel therapies, past and present," *Circulation: Heart Failure,* vol. 2, pp. 138-144, 2009.

[6] C. K. Phoon and D. H. Turnbull, "Cardiovascular imaging in mice," *Current protocols in mouse biology,* vol. 6, pp. 15-38, 2016.

[7] R. D. Patten and M. R. Hall-Porter, "Small animal models of heart failure: development of novel therapies, past and present," *Circ Heart Fail,* vol. 2, pp. 138-44, Mar 2009.

[8] M. L. Lindsey, R. Bolli, J. M. Canty Jr, X.-J. Du, N. G. Frangogiannis, S. Frantz, *et al.*, "Guidelines for experimental models of myocardial ischemia and infarction," *American Journal of Physiology-Heart and Circulatory Physiology,* vol. 314, pp. H812-H838, 2018.

[9] M. L. Lindsey, Z. Kassiri, J. A. Virag, L. E. de Castro Brás, and M. Scherrer-Crosbie, "Guidelines for measuring cardiac physiology in mice," *American Journal of Physiology-Heart and Circulatory Physiology,* vol. 314, pp. H733-H752, 2018.

[10] National Heart Lung and Blood Institute. (May 30, 2021). *How the heart works*. Available: https://www.nhlbi.nih.gov/health-topics/how-heart-works

[11] M. Biswas, S. Sudhakar, N. C. Nanda, G. Buckberg, M. Pradhan, A. U. Roomi*, et al.*, "Two- and three-dimensional speckle tracking echocardiography: clinical applications and future directions," *Echocardiography,* vol. 30, pp. 88-105, Jan 2013.

[12] T. Helle-Valle, J. Crosby, T. Edvardsen, E. Lyseggen, B. H. Amundsen, H. J. Smith*, et al.*, "New noninvasive method for assessment of left ventricular rotation: speckle tracking echocardiography," *Circulation,* vol. 112, pp. 3149-56, Nov 15 2005.

[13] F. A. Flachskampf, M. Schmid, C. Rost, S. Achenbach, A. N. DeMaria, and W. G. Daniel, "Cardiac imaging after myocardial infarction," *European Heart Journal,* vol. 32, pp. 272-283, 2010.

[14] H. Chen and T. Varghese, "Three-dimensional canine heart model for cardiac elastography," *Medical physics,* vol. 37, pp. 5876-5886, 2010.

[15] C. Papadacci, E. A. Bunting, E. Y. Wan, P. Nauleau, and E. E. Konofagou, "3-D Myocardial ElastographyIn Vivo," *IEEE transactions on medical imaging,* vol. 36, pp. 618-627, 2017.

[16] C. Ma and T. Varghese, "Lagrangian displacement tracking using a polar grid between endocardial and epicardial contours for cardiac strain imaging," *Medical physics,* vol. 39, pp. 1779-1792, 2012.

[17] E. Picano, F. Lattanzi, A. Orlandini, C. Marini, and A. L'Abbate, "Stress echocardiography and the human factor: the importance of being expert," *Journal of the American College of Cardiology,* vol. 17, pp. 666-669, 1991.

[18] A. J. Teske, B. W. De Boeck, P. G. Melman, G. T. Sieswerda, P. A. Doevendans, and M. J. Cramer, "Echocardiographic quantification of myocardial function using tissue deformation imaging, a guide to image acquisition and analysis using tissue Doppler and speckle tracking," *Cardiovascular ultrasound,* vol. 5, p. 27, 2007.

[19] J.-U. Voigt, G. Pedrizzetti, P. Lysyansky, T. H. Marwick, H. Houle, R. Baumann*, et al.*, "Definitions for a common standard for 2-D speckle tracking echocardiography: consensus document of the EACVI/ASE/Industry Task Force to standardize deformation imaging," *European Heart Journal-Cardiovascular Imaging,* vol. 16, pp. 1-11, 2014.

[20] S. Mondillo, M. Galderisi, D. Mele, M. Cameli, V. S. Lomoriello, V. Zacà*, et al.*, "Speckle-tracking echocardiography: a new technique for assessing myocardial function," *J Ultrasound Med,* vol. 30, pp. 71-83, Jan 2011.

[21] M. S. Amzulescu, M. De Craene, H. Langet, A. Pasquet, D. Vancraeynest, A. C. Pouleur*, et al.*, "Myocardial strain imaging: review of general principles, validation, and sources of discrepancies," *Eur Heart J Cardiovasc Imaging,* vol. 20, pp. 605-619, Jun 1 2019.

[22] R. Lopata, M. M. Nillesen, C. Verrijp, S. Singh, M. Lammens, J. A. van der Laak*, et al.*, "Cardiac biplane strain imaging: initial in vivo experience," *Physics in Medicine & Biology,* vol. 55, p. 963, 2010.

[23] E. E. Konofagou, J. D'hooge, and J. Ophir, "Myocardial elastography—A feasibility study in vivo," *Ultrasound in medicine & biology,* vol. 28, pp. 475-482, 2002.

[24] J. D'hooge, "Principles and different techniques for speckle tracking," *Myocardial imaging tissue Doppler and speckle tracking,* pp. 17-25, 2007.

[25] J. D'hooge, A. Heimdal, F. Jamal, T. Kukulski, B. Bijnens, F. Rademakers*, et al.*, "Regional strain and strain rate measurements by cardiac ultrasound: principles, implementation and limitations," *European Journal of Echocardiography,* vol. 1, pp. 154-170, 2000.

[26] S. Langeland, J. D'hooge, T. Claessens, P. Claus, P. Verdonck, P. Suetens*, et al.*, "RF-based two-dimensional cardiac strain estimation: a validation study in a tissue-mimicking phantom," *IEEE transactions on ultrasonics, ferroelectrics, and frequency control,* vol. 51, pp. 1537-1546, 2004.

[27] T. Varghese, J. Zagzebski, P. Rahko, and C. Breburda, "Ultrasonic imaging of myocardial strain using cardiac elastography," *Ultrasonic imaging,* vol. 25, pp. 1-16, 2003.

[28] C. Ma and T. Varghese, "Comparison of cardiac displacement and strain imaging using ultrasound radiofrequency and envelope signals," *Ultrasonics,* vol. 53, pp. 782-792, 2013.

[29] R. G. Lopata, M. M. Nillesen, J. M. Thijssen, L. Kapusta, and C. L. de Korte, "Three-dimensional cardiac strain imaging in healthy children using RF-data," *Ultrasound in medicine & biology,* vol. 37, pp. 1399-1408, 2011.

[30] M. Orlowska, A. Ramalli, A. Petrescu, M. Cvijic, S. Bezy, P. Santos*, et al.*, "A Novel 2-D Speckle Tracking Method for High-Frame-Rate Echocardiography," *IEEE Trans Ultrason Ferroelectr Freq Control,* vol. 67, pp. 1764-1775, Sep 2020.

[31] A. Bhan, A. Sirker, J. Zhang, A. Protti, N. Catibog, W. Driver*, et al.*, "High-frequency speckle tracking echocardiography in the assessment of left ventricular function and remodeling after murine myocardial infarction," *American Journal of Physiology-Heart and Circulatory Physiology,* vol. 306, pp. H1371-H1383, 2014.

[32] M. Dewey, M. Siebes, M. Kachelrieß, K. F. Kofoed, P. Maurovich-Horvat, K. Nikolaou*, et al.*, "Clinical quantitative cardiac imaging for the assessment of myocardial ischaemia," *Nat Rev Cardiol,* vol. 17, pp. 427-450, Jul 2020.

[33] M. Verkaik, E. M. Van Poelgeest, R. F. Kwekkeboom, P. M. Ter Wee, C. E. Van Den Brom, M. G. Vervloet*, et al.*, "Myocardial contrast echocardiography in mice: technical and physiological aspects," *American Journal of Physiology-Heart and Circulatory Physiology,* vol. 314, pp. H381-H391, 2018.

[34] S. Gargiulo, A. Greco, M. Gramanzini, M. P. Petretta, A. Ferro, M. Larobina*, et al.*, "PET/CT imaging in mouse models of myocardial ischemia," *BioMed Research International,* vol. 2012, 2012.

[35] B. A. French, Y. Li, A. L. Klibanov, Z. Yang, and J. A. Hossack, "3-D perfusion mapping in post-infarct mice using myocardial contrast echocardiography," *Ultrasound in medicine & biology,* vol. 32, pp. 805-815, 2006.

[36] S. Gao, D. Ho, D. E. Vatner, and S. F. Vatner, "Echocardiography in mice," *Current protocols in mouse biology,* pp. 71-83, 2011.

[37] B. A. French, Y. Li, A. L. Klibanov, Z. Yang, and J. A. Hossack, "3-D perfusion mapping in post-infarct mice using myocardial contrast echocardiography," *Ultrasound in Medicine and Biology,* vol. 32, pp. 805-815, 2006.

Chapter 2

Ultrasound Elastography for Cardiac Health Assessment: A Literature Review

Objective quantification of myocardial function non-invasively has been a key area of interest in clinical cardiology [1]. Echocardiography has been routinely used to assess myocardial function as it is cost-effective, fast, portable and provides high temporal resolution for real-time visualization of heart in a clinical setting [2, 3]. Qualitative assessment of echocardiographic image sequences over several cardiac cycles (visual wall motion scoring and wall thickening evaluation) by expert clinicians have been used to quantify myocardial function [4]. However, the accuracy of these assessments is dependent on extensive training, expertise [1, 5] and suffers from inter-observer variability. Quantitative parameters such as left ventricular ejection fraction (LVEF) can also be derived from echocardiographic images to assess cardiac function. However, LVEF has been shown to have limited ability for risk prediction in heart failure patients with reports of preserved LVEF even in the event of heart failure [6]. To address these issues, cardiac deformation imaging has been developed and utilized to obtain clinically valuable information based on an objective assessment of regional and global ventricular function [7]. In this chapter, we review peer-reviewed literature related to technical developments and applications of cardiac deformation imaging performed based on ultrasound.

2.1 Strain and Strain Rate Imaging with Tissue Doppler Imaging (TDI)

Initial approaches to perform cardiac deformation imaging was based on tissue Doppler imaging (TDI) for strain rate and strain estimation. Strain rate (SR) measurements were typically

done based on the spatial velocity gradient by assessing at least two fixed points along the ultrasound (US) beam as shown below [8-10].

$$SR = \frac{v(r) - v(r + \Delta r)}{\Delta r} \tag{2.1}$$

where, v is the tissue Doppler velocity and Δr is the distance between interrogation points. Alternatively, SR was also measured using linear regression over multiple velocity estimates over a fixed distance [11]. Finally, strain was derived though temporal integration of these SR curves. Even though TDI derived strain measurements have been investigated for clinical applications [8, 12], they suffer from several limitations limiting clinical applicability [13]. First, these measurements are angle-dependent thus limited to measuring strain and strain rates from myocardial segments aligned only along the US beam [14-16]. Second, they were highly susceptible to signal contribution from the left ventricular blood pool and reverberation artifacts [15]. Third, TDI is intrinsically one-dimensional (1-D) while cardiac deformation is three-dimensional (3-D) in nature [16, 17]. Therefore, there was shift towards developing non-Doppler US based cardiac deformation approaches.

2.2 Ultrasound Elastography Approaches for Cardiac Deformation Estimation

2.2.1 Basic Principles of Ultrasound Elastography

Ultrasound elastography (UE) refers to signal processing methods to estimate tissue elasticity properties using US radiofrequency (RF) data from perturbed tissue [18-21]. Elastography was pioneered by the research group headed by Dr. Jonathan Ophir back in 1991 when they demonstrated the formation of two-dimensional (2-D) images of tissue elasticity (strain) by estimating inter-frame deformation between two consecutive RF frame under uniaxial compression [22]. Thirty years later, elastography is a well-researched technology being readily

available in clinical US machines (e.g., VirtualTouch^{TM} from Siemens [23], LOGIQ E9 from GE). Based on several innovations driven by researchers around the world, UE has widespread applications in clinical settings for assessing diagnostic information from organs such as the breast [24], liver [25], heart [26] and so on. Typically, UE is a three-step process. First, induction of tissue deformation and collection of RF data at pre- and post-deformation state. Second, tracking of induced displacements either using 2-D normalized cross-correlation (NCC) based block matching (BM) [27-29], phase-based estimators [30, 31] or cost function-based optimization methods [32-34]. Finally, strain estimation as a spatial gradient of tracked displacement [20, 22, 35].

Based on perturbation techniques to induce local tissue deformation, UE can be broadly categorized into two groups. The first group includes quasi-static elastography where a constant stress is applied (e.g., freehand compression with the imaging transducer) to induce tissue deformation [36, 37]. Varghese *et al.* [37] further classified quasi-static elastography into three categories based on the mechanical stimulus generating the quasi-static compression namely: (a) Steady state quasi-static excitation (e.g., known applied deformation) , (b) Steady state quasi-static low frequency excitation (e.g., free-hand perturbation [38]) and (c) Steady state quasi-static physiological excitation (e.g., deformation induced from cardiac muscle and cardiovascular sources [4, 39-41]). Note that, the stress (σ) and strain relationship (ε) can be described by Hooke's law in terms of Young's modulus (E) as shown below.

$$\sigma = E\varepsilon \tag{2.2}$$

However, in practice, the applied deformation is unknown thus quasi-static elastography provides a relative measurement of tissue elasticity. For further details, interested readers are referred to the following seminal review articles [21, 36, 37, 42, 43] and books [19, 44]. The second group of methods is termed as dynamic elastography, where continuous or transient mechanical vibration

induces dynamic tissue deformation. Examples include sonoelasticity imaging [45], acoustic radiation force impulse imaging (ARFI) [46], vibro-acoustography [47], shear wave elasticity imaging (SWEI) [48]. For further details, interested readers are referred to the following seminal review articles describing dynamic elastography [36, 49-51] and books [19, 44]. In the following section, we discuss both quasi-static and dynamic elastography in the context of cardiac elasticity imaging.

2.2.2 Cardiac Strain Imaging for Cardiac Deformation Quantification

Cardiac strain imaging (CSI) estimates myocardial tissue elasticity by processing US data corresponding to the natural contraction and relaxation of the myocardium [26, 41]. Widespread application of cardiac strain imaging in both human and animal studies has been reported in the literature [7]. Applications in human imaging [15] include detection of patients with coronary heart disease (CHD) [52], myocardial ischemia [53], monitoring cardiac radiofrequency ablation in human subjects *in vivo* [54] and dilated cardiomyopathies [55]. CSI has also been used in detection of myocardial infarction in murine models [56, 57] and assessment of response to cardiac therapy [58]. These wide ranges of applications were the driving force behind innovations and improvements in CSI. Accurately estimating underlying cardiac motion or displacement is critical for CSI. The myocardium exhibits complex 3-D motion patterns due to torsion, thickening across and contraction along fibers over a cardiac cycle [59]. This complex 3-D motion causes out-of-plane motion of scatterers when 2-D imaging is employed for CSI resulting in significant challenges for accurate strain quantification [60]. Improving the accuracy of cardiac displacement and strain estimation is one of the main goals of this dissertation. Therefore, related signal processing approaches to improve CSI have been reviewed in detail separately in **Section 2.3**.

2.2.3 Dynamic Elastography for Cardiac Stiffness Quantification

In this section, we summarize literature reports pertaining to the use of ARFI induced dynamic elastography methods for estimating myocardial stiffness. For a broader review of ARFI elastography methods, interested readers are referred to following review papers [49, 50].

2.2.3.1 Acoustic Radiation Force Impulse (ARFI) Imaging for Myocardial Stiffness Measurement

ARFI Imaging is a dynamic elastography technique using a transient excitation mechanism where internal tissue motion is induced using an impulsive focused acoustic radiation force (ARF) [44, 46, 61]. The magnitude of ARF (F) inducing the localized tissue defamation can be represented as follows.

$$F = \frac{2\alpha I}{c} \tag{2.3}$$

where, α, I and c represent acoustic absorption coefficient, local mean temporal intensity of acoustic beam and speed of sound, respectively. ARFI data acquisition starts by collecting "reference" data in single lateral location without any ARF excitation. Then, using the same US transducer, ARF excitation pulse or "pushing" pulse (pushing pulse with longer pulse length compared to conventional B-mode imaging pulses) is delivered to generate impulsive ARF and consequently induce localized tissue deformation. Finally, multiple diagnostic US pulses ("tracking" pulses) are used to collect post deformation data and induced tissue displacements are tracked typically using correlation-based estimators [30]. Similar pulse sequences are repeated across a lateral spatial extent to generate 2-D ARFI images which can provide qualitative maps of local tissue stiffness [44]. Several clinical applications of ARFI imaging are reviewed in the following papers [44, 62]. In this chapter, we review ARFI imaging in the context of cardiac health

and dynamics assessment. Fahey *et al.* [63] first demonstrated the use of ARFI to image myocardial radiofrequency ablation (RFA) of a beating heart in an open chest experimental setup. Authors demonstrated that ARFI could be used to visualize cardiac lesions formed in two sheep hearts by RFA and argued for the potential use of this method to monitor myocardial ischemia and infarction [63]. ECG-gating was employed to discard frames with motion artifacts resulting in a single ARFI image per heartbeat. Later, Hsu *et al.* [64] extended the technique for monitoring the dynamic variation of myocardial stiffness over a cardiac cycle using ARFI M-mode imaging. Experimentation involved imaging exposed canine hearts using linear array transducers and employed advanced beam sequencing and parallel-receive imaging [65] to collect data at a higher frame rate (40 Hz for ARFI M-mode imaging). Even though, ARFI induced displacements demonstrated cyclic variation over the cardiac cycle, fixed ROI placement for ARFI M-mode imaging could induce uncertainty in the results due to underlying cardiac motion. Recently, Kakkad *et al.* [66] investigated the *in vivo* feasibility of ARFI M-mode imaging using transthoracic RF data from 12 healthy human volunteers and found that the success rate of the proposed method in studying dynamic myocardial stiffness was somewhat limited (41 % of total 204 acquisitions). Authors limited their analysis to the intra-ventricular septum and collected data in both parasternal long and short axis views. ARFI images were quantitively studied by deriving parameters such as stiffness ratio, rates of relaxation and contraction and time constants of relaxation and contraction through analysis of the ARF-induced displacement profiles. These studies highlight potential challenges for using ARFI for *in vivo* cardiac imaging which stems from the fundamental physics behind ARFI imaging. First, ARF-induced displacements are directly related to the intensity of acoustic excitation pulse which might be absorbed by highly attenuating tissue layers such as muscle and connective tissue before reaching the myocardium. This is turn in will contribute

towards unsuccessful ARFI acquisition. Second, the ARFI analysis ROI was fixed in location and size based on the estimate of focal point of ARF pulse. However, the myocardium continuously moves and changes shape due to contraction and relaxation of the myocardium thus potentially leaving the ROI during data acquisition.

2.2.3.2 Shear Wave Elasticity Imaging (SWEI) for Myocardial Stiffness Assessment

Shear Wave Elasticity Imaging (SWEI) is a quantitative dynamic elastography technique pioneered by Sarvazyan *et al.* [48] based on shear waves generated by remote excitation using acoustic radiation force. Assuming linear, isotropic, semi-infinite medium, Sarvazyan demonstrated that the velocity of shear wave propagation (c_T) is related to shear modulus (μ) and medium density (ρ) in the following form.

$$c_T = \sqrt{\frac{\mu}{\rho}} \tag{2.4}$$

Myocardial tissue typically violates the required assumption, therefore c_T is typically used to measure myocardial stiffness [67-70]. One of the initial reports on the use of SWEI for myocardial stiffness assessment was by Bouchard *et al.* [67] where authors employed ARFI-induced SWEI to investigate the mechanical properties of left ventricular (LV) free wall at the mid-myocardium level. Experimentation involved a canine beating heart in an open chest setup with shear wave speed (c_T) measurements done at mid-diastole of cardiac cycle after ECG-gating. They reported on consistent beat-to-beat shear wave speed measurements (calculated using Lateral Time-To-Peak algorithm) at a fixed location while the shear wave speed varies both with depth and lateral tracking beam location. Couade *et al.* [68] later demonstrated shear wave speed variation over a cardiac cycle by repeated ARFI pushes with displacement tracking utilizing ultrafast ultrasound imaging at 12000 frames/sec. Authors employed the SuperSonic Shear Imaging (SSI) method [71]

to image the epicardium of 10 sheep hearts in an open chest setup. They reported reduction (~25%) of the systolic shear wave after coronary artery ligation to induce myocardial ischemia. Pernot *et al.* [69] applied a similar SWEI method to an *ex vivo* experiment involving six Langendorff perfused isolated rat hearts and reported higher shear modulus at systole compared to diastole. Hollender *et al.* [70] performed shear wave speed measurements *in vivo* using intracardiac echocardiography (ICE) on six healthy pig models and reported cyclic variation of c_T over a cardiac cycle like the results reported by Couade *et al.* [68]. However, their approach was less invasive than open chest experiments thus moving towards clinical translation. Hollender *et al.* [72] also investigated the potential of intracardiac echocardiography based SWEI for identifying focal infarction in pigs. However, no clear distinction could be made between healthy and infarcted hearts based on the reported data. Later, Pernot *et al.* reported on the differentiation between stunned and infarcted myocardium using passive myocardial stiffness measured at end-diastole (ED) by SWEI. Experimentation was done on 10 sheep in an open chest setup. Authors reported a statistically significant increase in ED SWEI stiffness value in an infarct case when compared to stunned myocardium. The infarcted group also demonstrated further increment in ED SWEI stiffness values after re-perfusion while stunned group remained constant.

All the papers reviewed so far involved animal models either in an open-chest setup or using ICE, however, for clinical application, the preferred imaging mode would be transthoracic closed chest imaging. Song *et al.* [73] measured the myocardial stiffness of LV for the first time *in vivo* by performing transthoracic closed chest imaging of seven healthy human volunteers. Authors utilized pulse inversion harmonic imaging for shear wave tracking. The measurement was limited to end-diastole phase of the cardiac cycle where heart motion was relatively slow [73]. Song *et al.* [74] later investigated the feasibility of the technique for end-diastole SWEI in a cohort

of 20 pediatric volunteers. Recently, Villemain *et al.* [75] reported the differentiation between healthy volunteers and hypertrophic cardiomyopathy patients using passive myocardial stiffness measured at ED by SWEI. Even though these reports are encouraging, there are several technical challenges that remain with SWEI to assess myocardial stiffness non-invasively. First, measurements are localized in both space (excitation site) and time (end-diastole), and would therefore require another imaging modality such as cardiac strain imaging [41] to localize the disease site. A more suitable SWEI approach should cover a larger field-of-view with dynamic measurement over the cardiac cycle [44]. Secondly, myocardial anisotropy might be a complicating factor which has to be addressed before comparing SWEI derived parameters across patient groups [72]. Further details regarding SWEI for cardiac imaging can be found here [44].

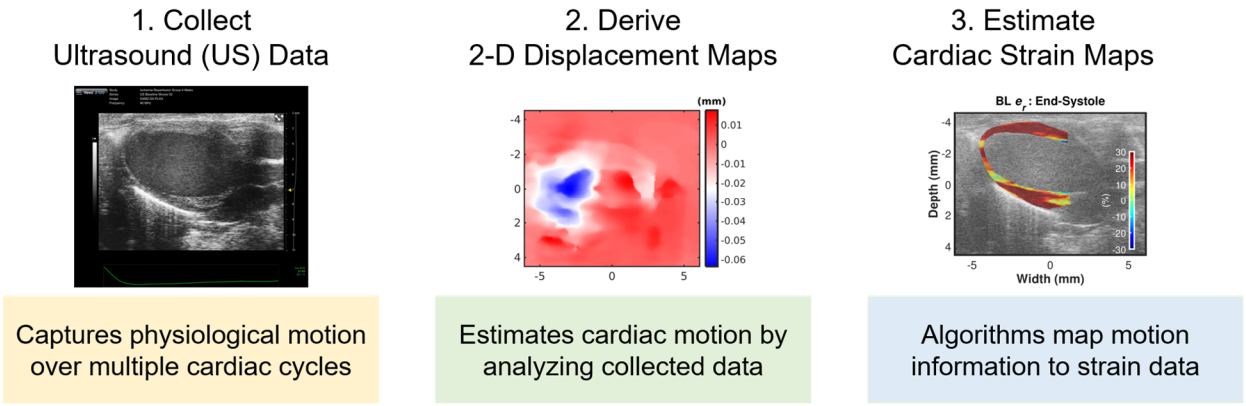

Figure 2.1 High level description of a Cardiac Strain Imaging framework.

2.3 Signal Processing Approaches for Cardiac Strain Imaging (CSI)

In this section, we review the literature reports on the signal processing approaches utilized for CSI. The CSI process can be described as a three-step process on a high level namely – (a) US data collection over several cardiac cycles, (b) motion estimation and (c) cardiac strain derivation as shown in Figure 2.1 and discussed in detail below. CSI can be performed either using a sequence

of ultrasound envelope or B-mode images (envelope detected and log compressed signals) or using radio-frequency (RF) data [76, 77].

2.3.1 Speckle Tracking Echocardiography for Cardiac Strain Estimation

Ultrasound B-mode or envelope-based methods for CSI are commonly termed as speckle tracking echocardiography (STE). Readers interested to learn about the clinical applications of STE are referred to following review papers published between 2010 – 2021 [15, 78-81]. This section focuses more on the technical aspects of STE. A common approach for motion estimation in STE is to search for similar speckle patterns in a sequence of cardiac B-mode images using block matching (BM) [16, 82]. In this approach, similarity between matching blocks is quantified using similarity metrics such as normalized cross-correlation coefficient (NCC), sum of absolute difference (SAD) or sum of squared difference (SSD).

A second popular approach for motion tracking using B-mode ultrasound images are optical flow based motion estimation approaches [83, 84] . These methods assume brightness consistency of a pixel over a short period of time and derive motion by matching pixel intensity across frames. Optical flow-based motion estimation using RF signals was also reported in the literature [85, 86]. Finally, a third approach for motion estimation for STE is the utilization of non-rigid B-mode image registration [87-90]. In these registration methods, cardiac deformation is first modelled as a weighted sets of basis functions and then weights are adjusted appropriately to represent the dense cardiac deformation field [44]. These methods aim to find a spatiotemporal deformation field by iteratively minimizing difference between motion compensated images and a reference [87]. This task is formulated as a global optimization problem where the optimal deformation field minimizes a specific cost function. Smooth basis functions such as B-splines or radial basis functions are typically used to parametrize the myocardial deformation field with

additional regularization terms in the cost function to be minimized [87, 90]. Regularization enforces additional constraints such as smoothness on the derived motion field [87, 88].

Ledesma-Carbayo *et al.* [87] proposed a spatiotemporal elastic registration framework for estimating 2-D displacement fields from a sequence of ultrasound B-mode images of the heart. A parametric model based on B-spline functions was utilized to represent the motion field. They proposed a regularization-free optimization criterion to derive a globally plausible spatiotemporal motion field over the entire image sequence with respect to a reference frame (end-diastole). They then enforced spatial smoothness and temporal coherence on the estimated deformation function by defining B-spline basis functions for both spatial and temporal direction. Finally, the registration problem is solved utilizing a multi-resolution optimization strategy. The approach was validated in a cardiac simulation model revealing the benefit of adding temporal consistency to the framework. They also reported initial clinical validation by performing analysis on *in-vivo* volunteer data from healthy (n=6) and patient (n=6) population. This approach was later extended to 4D data sets (3-D+t) by Metz *et al.* [91] and evaluated on computed tomography (CT) and ultrasound (US) image sequences. Their additional contribution was to enforce a cyclic motion constraint to ensure uniqueness of their optimization solution.

Similar image intensity-based non-rigid image registration framework has been applied in 3-D ultrasound image voxels by Elen *et al.* [88] to derive the cardiac motion field. They also utilized a B-spline transformation model to parametrize the spatial motion field. Their proposed cost function included mutual information as a similarity measure term and two spatial smoothness term as regularizer. The regularization terms enforced spatial smoothness and volume conservation to prevent non-physical estimations. Frame-to-frame image registration was performed to derive the inter-frame displacement field. Finally, inter-frame displacements were accumulated to derive

a Lagrangian representation of the motion field. They showed motion tracking with reasonable performance and accuracy in a simulation study of healthy and infarcted heart. Initial clinical validation was done on *in-vivo* data derived from healthy (n=3) and apical aneurism patient (n=1).

De Craene *et al.* [92, 93] also proposed a 4D image registration approach (3-D+t) to estimate motion and strain sequences from 3-D ultrasound volume sequences. The proposed method referred as Temporal Diffeomorphic Free-Form Deformation (TDFFD) attempted to enforce temporal consistency by the use of continuous spatiotemporal B-spline kernels to represent velocity fields. The proposed approach was evaluated using synthetic 3-D US images, *in-vivo* healthy volunteers (n=9) and Cardiac Resynchronization Therapy (CRT) treated patients (n=13). Zhang *et al.* [94] proposed an elastic image registration framework for 3-D echocardiography images with spatiotemporal regularization (3-D+t approach). The proposed problem formulation closely resembles the approach reported in [87, 88] as authors parameterize the deformation field using tensor product of 1-D cubic B-splines. The approach differs from [87, 88] in terms of regularization where they propose to use two regularization terms (spatial and temporal). The spatial regularization term enforces spatial smoothness while temporal regularization terms enforce smoothness in velocity assuming that any point in myocardium will experience continuous velocity. The temporal penalty term is determined using three consecutive images. They reported improved performance in cardiac motion estimation against no temporal regularization. Nora *et. al.* proposed spatial and sparse regularization with dictionary learning and reported better motion estimation accuracy compared to state-of-the-art methods [95]. Later, they extended their approach to incorporate temporal domain information [96]. Despite regularization being inherently embedded in these NRIR-based methods, they suffer from reduced sensitivity to small inter-frame displacements and lower elastographic signal-to-noise ratio (SNR) due to the use of US B-mode

or envelope data instead of RF data [97]. To address this issue, Bidisha *et al.* proposed a NRIR-based method for RF-based CSI. However, their results did not include analysis on strain estimation accuracy limiting its effectiveness for CSI.

2.3.2 Cardiac Elastography for Myocardial Strain Estimation

RF echo-signal based speckle tracking technique for CSI is commonly termed as Cardiac Elastography (CE) [41] or Myocardial Elastography (ME) [26]. Elastography was originally developed as a technique to estimate local [98] tissue strain via NCC of time-shifted RF signals under an external compression along the ultrasound beam propagation direction [20, 22]. CE on the other hand uses the natural contraction and relaxation of myocardium as a mechanical stimulus for strain estimation [41, 99]. One added advantage of CE is the presence of phase information with RF signals resulting in accurate deformation estimation when compared to B-mode or envelope-based methods (e.g., STE) in detecting small deformations [76, 97, 100]. However, the lack of phase information in the lateral direction (perpendicular to beam direction) makes motion estimation challenging resulting in noisier lateral strain estimates [60, 101]. Further difficulty in accurate 2-D motion estimation results from the "out-of-plane" motion artifacts due to imaging 3-D myocardial deformation using 2-D imaging planes [3, 60, 98, 102]. Therefore, these approaches typically utilize high lateral interpolation factors (e.g., Langeland *et al.* interpolated RF data laterally 30 times with Sinc interpolation [103]) with multi-level tracking and re-correlation strategies to improve the accuracy and precision of the estimates [4, 39, 60, 104]. To further improve the quality of strain estimation, several innovative approaches have been implemented such as displacement regularization [105-107], high frame rate echocardiography [108], spatial angular compounding [109-111] and transverse oscillation approaches [112-114].

2.3.2.1 Improving RF-based Displacement Estimation with Regularization

Regularized displacement estimation algorithms for RF-based ultrasound strain imaging can be broadly categorized into two groups: optimization and BM-based methods. In the first class of algorithms, displacement estimation is modelled as an optimization problem combining measures of speckle similarity and motion continuity [44]. The continuity constraint is usually formulated to penalize large displacement gradients and acts as a regularization term. Pellot-Barakat *et al.* [32] utilized SAD as similarity measure [28] and used an iterative conditional mode algorithm to solve the optimization problem. Brusseau *et al.* [115] modelled motion estimation as a minimization problem with NCC as similarity measure and solved the problem using sequential quadratic programming. Rivaz *et al.* [116] introduced Dynamic Programming Analytic Minimization to efficiently resolve sub-sample displacement by solving the optimization problem. Hashemi *et al.* proposed Global US Elastography algorithm termed as GLUE where a non-linear optimization problem is formulated to estimate displacement in all RF A-lines simultaneously by enforcing a spatial constraint [117]. Majority of these algorithms enforce regularization to produce spatially smooth displacement fields [33, 117-121]. However, in the context of CSI, temporal smoothness may be a reasonable assumption supported by NRIR-based reports as discussed in Section 2.3.1. Rivaz *et al.* [122] applied the concept of temporal consistency in optimization-based displacement estimation using multiple RF frames. The proposed method initially estimates motion between paired images using 2-D analytic minimization (2-D AM) [116]. The initial estimates were then utilized to derive physics based constrains to construct a likelihood function to incorporate data from multiple images. Finally, a posterior probability density was constructed by combining the estimated likelihood function and a spatial smoothening regularization term to derive final displacement estimates. The proposed method was compared against strain image averaging and Lagrangian particle tracking [4] and provided improved performance. Recently,

Ashikuzzaman *et al*. proposed using the GLUE algorithm in spatial and temporal domain termed as GUEST to incorporate temporal continuity in the GLUE framework and validated the algorithm using simulation, phantom and *in vivo* liver data. The results were however limited to axial strain images only making it unclear how generalizable it will be for CSI where lateral and shear components play equally important roles in the derivation of cardiac strain tensors.

Typically, RF-based CSI or CE involves performing BM either with 2-D [4, 123] or 1-D kernels in a 2-D search region [103, 124-128]. Initially, CE was performed using 1-D cross-correlation of time-shifted signals along the ultrasound beam propagation direction [26, 41]. As myocardium undergoes 3-D deformations during a cardiac cycle [1], several approaches of CE have been proposed to estimate cardiac motion and strain in 2-D [2, 4, 16, 39, 57, 60, 100, 103, 124, 128, 129] and even 3-D [3, 98, 102, 130]. For these BM displacement estimation algorithms, n-D kernels (n=1,2 or 3) from pre-deformation RF data are matched with post-deformation kernels in a pre-defined search range using a similarity metric (e.g., NCC, SAD, SSD, mutual information, phase correlation [30, 131, 132]). In this dissertation, we focus on 2-D NCC based BM algorithms where the NCC peak location is used to obtain axial and lateral sub-sample shifts to determine the displacement vector. Regularization can be included in BM algorithms either post estimation or during estimation. Examples of post estimation regularization include median filtering [39, 103, 124], application of geometric shape constraints on the estimated motion fields [133], Gaussian smoothening [134]. Examples of regularization during estimation include application of Viterbi algorithm [34, 118, 135, 136] and Bayesian strain imaging [105-107, 123, 137]. For example, Jiang *et al.* [34] used correlation as similarity measure and used Viterbi algorithm for optimization. Bayesian strain imaging involves the use of prior knowledge to reduce estimation errors using Bayes theorem [137]. McCormick *et al.* [107] applied an iterative Bayesian regularization

algorithm to ultrasound strain imaging with successful application to carotid plaque strain imaging in human subjects [138]. They reported significant improvement in estimation quality compared to conventional peak-hopping error filtering approaches such as median filtering. Byram *et al.* [105, 106] proposed a Bayesian framework with a scaled likelihood function for improved discriminant ability and showed higher displacement accuracy compared to NCC approaches using a generalized-Gaussian-Markov random field prior in their Bayesian framework [137] with 1-D NCC kernels. However, for applications such as cardiac strain imaging, displacement vector estimation using 2-D or 3-D kernel is a key requirement to reduce kernel dimensions for improved spatial resolution and lateral estimation accuracy [139]. However, there are not many reports on the use of temporal consistency concepts for kernel-based displacement estimation. Jiang *et al.* [140] proposed a method of estimating a composite strain image by processing multiple RF frames rather than pairwise processing. The method starts of by selecting three RF frames based on a displacement quality metric (DQM) [140]. Two strain images were estimated from these RF data sets and finally, a composite strain image is obtained by weighted averaging of the pair of strain images. They reported higher SNR with this method compared to simple strain image averaging schemes. Bayer *et al.* [141] explored the idea of temporal continuity based on the assumptions that motion changes gradually over time and accumulation of smaller strain step-size induced displacement would be same as estimated displacement induced from the total large strain step-size. Based on these assumptions and principles, they proposed four algorithms aiming to achieve a temporally smooth displacement field. The first algorithm was accumulation guidance where inter-frame displacements were accumulated to reduce peak-hop errors and used as a guidance for large-step displacement estimation. The second algorithm was named velocity regularization, where a cost function including a temporal smoothness penalty is solved to derive temporally

smooth displacement from three consecutive image frames. The regularization resembles the spatial regularization process described by Jiang and Hall in [136]. The third algorithm named multi-step regularization involved replacing the temporal smoothness constraint with a step-size consistency constraint. Finally, spatial and temporal regularization was combined in a space-time regularization algorithm. Initial investigation in phantom sequences and breast data showed comparable performance with a spatial regularization algorithm [136] and improvement in some specific cases. Initial investigation in phantom sequences and breast data showed comparable performance with the spatial regularization algorithm described by Jiang and Hall [136]. Recently, Mirzaei *et al.* proposed the use of 3-D NCC (2-D+time) and reported robustness against noise corruption for axial strain imaging [142].

2.3.2.2 High Frame Rate Echocardiography (HFRE) for Cardiac Elastography

Several reports on high frame rate echocardiography such as plane/diverging wave imaging [143, 144], multi-line transmission [145] is described in the literature and reviewed in detail by Cikes *et al.* [108]. Grondin *et al.* [126] reported on the use of coherently compounded diverging waves for performing cardiac elastography for the first time. Their initial simulation and *in vivo* feasibility suggested that reasonable strain estimation can be obtained by compounding multiple diverging waves with the added benefit of high frame rate imaging. Later on, Sayseng *et al.* [127] reported on the optimization of transmit parameters related to coherently compounded diverging wave imaging to improve the performance of CE. In 2020, Sayseng *et al.* applied the developed technique to monitor myocardial infarction in canine hearts [146]. Joos *et al.* [147] applied speckle tracking echocardiography on motion-compensated HFRE and reported comparable results obtained using a clinical scanner. Recently, Orlowska *et al.* [148] followed the similar strategies

reported by Grondin *et al.* [126] who performed detailed algorithm optimization with performance bench marking against a clinical system.

2.3.3 Strain Estimation and Quantification Approaches

The final stage of a CSI framework is derivation of cardiac strain along with quantification in a meaningful way to assess myocardial dynamics. Strain estimation can be done by integrating the estimated displacements over a cardiac cycle either using an Eulerian description (observation through fixed spatial location) or Lagrangian description (observation through material coordinates) [4, 15]. For CSI, typically Lagrangian strains are reported as the myocardium deforms over a cardiac cycle with the end-diastolic frame generally being the original reference point [7]. CSI also allows regional analysis of myocardial abnormalities by dividing the entire heart into multiple segments based on image acquisition planes [149, 150]. Furthermore, several quantitative parameters have been derived through analysis of the temporal variation of regional strain curves for example peak strain, end-systolic strain, peak systolic strain, positive peak systolic strains and interventricular dyssynchrony through time-peak-analysis [56, 58, 151, 152]. Additionally, layer-specific (epicardial, mid-myocardial and endocardial) segmental strain analysis has also been reported to study left ventricular function [153]. Interested readers might find the following review papers and consensus reports helpful for designing CSI based experimental studies [76, 77, 149, 154].

List of References

[1] A. J. Teske, B. W. De Boeck, P. G. Melman, G. T. Sieswerda, P. A. Doevendans, and M. J. Cramer, "Echocardiographic quantification of myocardial function using tissue deformation imaging, a guide to image acquisition and analysis using tissue Doppler and speckle tracking," *Cardiovascular ultrasound,* vol. 5, p. 27, 2007.

[2] H. Chen and T. Varghese, "Three-dimensional canine heart model for cardiac elastography," *Medical physics,* vol. 37, pp. 5876-5886, 2010.

[3] C. Papadacci, E. A. Bunting, E. Y. Wan, P. Nauleau, and E. E. Konofagou, "3-D Myocardial ElastographyIn Vivo," *IEEE transactions on medical imaging,* vol. 36, pp. 618-627, 2017.

[4] C. Ma and T. Varghese, "Lagrangian displacement tracking using a polar grid between endocardial and epicardial contours for cardiac strain imaging," *Medical physics,* vol. 39, pp. 1779-1792, 2012.

[5] E. Picano, F. Lattanzi, A. Orlandini, C. Marini, and A. L'Abbate, "Stress echocardiography and the human factor: the importance of being expert," *Journal of the American College of Cardiology,* vol. 17, pp. 666-669, 1991.

[6] M. Cikes and S. D. Solomon, "Beyond ejection fraction: an integrative approach for assessment of cardiac structure and function in heart failure," *Eur Heart J,* vol. 37, pp. 1642-50, Jun 1 2016.

[7] J.-U. Voigt, G. Pedrizzetti, P. Lysyansky, T. H. Marwick, H. Houle, R. Baumann*, et al.*, "Definitions for a common standard for 2-D speckle tracking echocardiography: consensus document of the EACVI/ASE/Industry Task Force to standardize deformation imaging," *European Heart Journal-Cardiovascular Imaging,* vol. 16, pp. 1-11, 2014.

[8] T. Edvardsen, B. L. Gerber, J. Garot, D. A. Bluemke, J. A. Lima, and O. A. Smiseth, "Quantitative assessment of intrinsic regional myocardial deformation by Doppler strain rate echocardiography in humans: validation against three-dimensional tagged magnetic resonance imaging," *Circulation,* vol. 106, pp. 50-6, Jul 2 2002.

[9] A. Heimdal, A. Støylen, H. Torp, and T. Skjærpe, "Real-time strain rate imaging of the left ventricle by ultrasound," *Journal of the American Society of Echocardiography,* vol. 11, pp. 1013-1019, 1998.

[10] S. Urheim, T. Edvardsen, H. Torp, B. Angelsen, and O. A. Smiseth, "Myocardial strain by Doppler echocardiography: validation of a new method to quantify regional myocardial function," *Circulation,* vol. 102, pp. 1158-1164, 2000.

[11] A. Fleming, X. Xia, W. McDicken, G. Sutherland, and L. Fenn, "Myocardial velocity gradients detected by Doppler imaging," ed: The British Institute of Radiology, 1994.

[12] G. R. Sutherland, G. Di Salvo, P. Claus, J. D'hooge, and B. Bijnens, "Strain and strain rate imaging: a new clinical approach to quantifying regional myocardial function," *Journal of the American Society of Echocardiography,* vol. 17, pp. 788-802, 2004.

[13] B. Heyde, O. Mirea, and J. D'hooge, "Cardiac Strain and Strain Rate Imaging," *Ultrasound Elastography for Biomedical Applications and Medicine,* pp. 143-160, 2018.

[14] H. Blessberger and T. Binder, "Two dimensional speckle tracking echocardiography: basic principles," *Heart,* vol. 96, pp. 716-722, 2010.

[15] H. Geyer, G. Caracciolo, H. Abe, S. Wilansky, S. Carerj, F. Gentile*, et al.*, "Assessment of myocardial mechanics using speckle tracking echocardiography: fundamentals and clinical applications," *Journal of the American Society of Echocardiography,* vol. 23, pp. 351-369, 2010.

[16] S. Langeland, P. F. Wouters, P. Claus, H. A. Leather, B. Bijnens, G. R. Sutherland*, et al.*, "Experimental assessment of a new research tool for the estimation of two-dimensional myocardial strain," *Ultrasound in medicine & biology,* vol. 32, pp. 1509-1513, 2006.

[17] S. Langeland, J. D'Hooge, P. F. Wouters, H. A. Leather, P. Claus, B. Bijnens*, et al.*, "Experimental validation of a new ultrasound method for the simultaneous assessment of radial and longitudinal myocardial deformation independent of insonation angle," *Circulation,* vol. 112, pp. 2157-62, Oct 4 2005.

[18] T. Varghese, "Quasi-static ultrasound elastography," *Ultrasound clinics,* vol. 4, p. 323, 2009.

[19] S. K. Alam and B. S. Garra, *Tissue Elasticity Imaging: Volume 1: Theory and Methods*: Elsevier, 2019.

[20] J. Ophir, S. K. Alam, B. Garra, F. Kallel, E. Konofagou, T. Krouskop*, et al.*, "Elastography: ultrasonic estimation and imaging of the elastic properties of tissues," *Proceedings of the Institution of Mechanical Engineers, Part H: Journal of Engineering in Medicine,* vol. 213, pp. 203-233, 1999.

[21] J. Ophir, F. Kallel, T. Varghese, E. Konofagou, S. K. Alam, T. Krouskop*, et al.*, "Elastography," *Comptes Rendus de l'Academie des Sciences-Series IV-Physics,* vol. 2, pp. 1193-1212, 2001.

[22] J. Ophir, I. Cespedes, H. Ponnekanti, Y. Yazdi, and X. Li, "Elastography: a quantitative method for imaging the elasticity of biological tissues," *Ultrasonic imaging,* vol. 13, pp. 111-134, 1991.

[23] B. John and F. Liexiang, "Understanding ARFI and new elastography quantification technologies," *Mountain View, CA: Siemens Medical Solutions,* 2014.

[24] R. G. Barr, "Breast elastography," *Tissue Elasticity Imaging,* pp. 21-46, 2020.

[25] G. Ferraioli, C. Tinelli, B. Dal Bello, M. Zicchetti, G. Filice, C. Filice*, et al.*, "Accuracy of real-time shear wave elastography for assessing liver fibrosis in chronic hepatitis C: a pilot study," *Hepatology,* vol. 56, pp. 2125-2133, 2012.

[26] E. E. Konofagou, J. D'hooge, and J. Ophir, "Myocardial elastography—A feasibility study in vivo," *Ultrasound in medicine & biology,* vol. 28, pp. 475-482, 2002.

[27] P. Chaturvedi, M. F. Insana, and T. J. Hall, "2-D companding for noise reduction in strain imaging," *IEEE transactions on ultrasonics, ferroelectrics, and frequency control,* vol. 45, pp. 179-191, 1998.

[28] L. N. Bohs, B. H. Friemel, B. A. McDermott, and G. E. Trahey, "A real time system for quantifying and displaying two-dimensional velocities using ultrasound," *Ultrasound in medicine & biology,* vol. 19, pp. 751-761, 1993.

[29] L. N. Bohs and G. E. Trahey, "A novel method for angle independent ultrasonic imaging of blood flow and tissue motion," *IEEE Transactions on biomedical engineering,* vol. 38, pp. 280-286, 1991.

[30] G. F. Pinton, J. J. Dahl, and G. E. Trahey, "Rapid tracking of small displacements with ultrasound," *IEEE transactions on ultrasonics, ferroelectrics, and frequency control,* vol. 53, pp. 1103-1117, 2006.

[31] G. F. Pinton and G. E. Trahey, "Continuous delay estimation with polynomial splines," *IEEE transactions on ultrasonics, ferroelectrics, and frequency control,* vol. 53, pp. 2026-2035, 2006.

[32] C. Pellot-Barakat, F. Frouin, M. F. Insana, and A. Herment, "Ultrasound elastography based on multiscale estimations of regularized displacement fields," *IEEE transactions on medical imaging,* vol. 23, pp. 153-163, 2004.

[33] H. Rivaz, E. Boctor, P. Foroughi, R. Zellars, G. Fichtinger, and G. Hager, "Ultrasound elastography: a dynamic programming approach," *IEEE transactions on medical imaging,* vol. 27, pp. 1373-1377, 2008.

[34] J. Jiang and T. J. Hall, "A generalized speckle tracking algorithm for ultrasonic strain imaging using dynamic programming," *Ultrasound in medicine & biology,* vol. 35, pp. 1863-1879, 2009.

[35] F. Kallel and J. Ophir, "A least-squares strain estimator for elastography," *Ultrasonic imaging,* vol. 19, pp. 195-208, 1997.

[36] J. L. Gennisson, T. Deffieux, M. Fink, and M. Tanter, "Ultrasound elastography: principles and techniques," *Diagn Interv Imaging,* vol. 94, pp. 487-95, May 2013.

[37] T. Varghese, "Quasi-Static Ultrasound Elastography," *Ultrasound Clin,* vol. 4, pp. 323-338, Jul 2009.

[38] T. J. Hall, Y. Zhu, and C. S. Spalding, "In vivo real-time freehand palpation imaging," *Ultrasound Med Biol,* vol. 29, pp. 427-35, Mar 2003.

[39] C. Ma, X. Wang, and T. Varghese, "Segmental analysis of cardiac short-axis views using lagrangian radial and circumferential strain," *Ultrasonic imaging,* vol. 38, pp. 363-383, 2016.

[40] N. H. Meshram and T. Varghese, "GPU Accelerated Multilevel Lagrangian Carotid Strain Imaging," *IEEE Transactions on Ultrasonics, Ferroelectrics, and Frequency Control,* 2018.

[41] T. Varghese, J. Zagzebski, P. Rahko, and C. Breburda, "Ultrasonic imaging of myocardial strain using cardiac elastography," *Ultrasonic imaging,* vol. 25, pp. 1-16, 2003.

[42] M. M. Doyley, "Model-based elastography: a survey of approaches to the inverse elasticity problem," *Phys Med Biol,* vol. 57, pp. R35-73, Feb 7 2012.

[43] K. J. Parker, M. M. Doyley, and D. J. Rubens, "Imaging the elastic properties of tissue: the 20 year perspective," *Physics in medicine & biology,* vol. 56, p. R1, 2010.

[44] I. Z. Nenadic, M. W. Urban, J. F. Greenleaf, J.-L. Gennisson, M. Bernal, and M. Tanter, *Ultrasound Elastography for Biomedical Applications and Medicine*: John Wiley & Sons, 2019.

[45] K. Parker, S. Huang, R. Musulin, and R. Lerner, "Tissue response to mechanical vibrations for “sonoelasticity imaging”," *Ultrasound in medicine & biology,* vol. 16, pp. 241-246, 1990.

[46] K. R. Nightingale, M. L. Palmeri, R. W. Nightingale, and G. E. Trahey, "On the feasibility of remote palpation using acoustic radiation force," *The Journal of the Acoustical Society of America,* vol. 110, pp. 625-634, 2001.

[47] M. Fatemi and J. F. Greenleaf, "Vibro-acoustography: An imaging modality based on ultrasound-stimulated acoustic emission," *Proceedings of the National Academy of Sciences,* vol. 96, pp. 6603-6608, 1999.

[48] A. P. Sarvazyan, O. V. Rudenko, S. D. Swanson, J. B. Fowlkes, and S. Y. Emelianov, "Shear wave elasticity imaging: a new ultrasonic technology of medical diagnostics," *Ultrasound Med Biol,* vol. 24, pp. 1419-35, Nov 1998.

[49] J. R. Doherty, G. E. Trahey, K. R. Nightingale, and M. L. Palmeri, "Acoustic radiation force elasticity imaging in diagnostic ultrasound," *IEEE Trans Ultrason Ferroelectr Freq Control,* vol. 60, pp. 685-701, Apr 2013.

[50] K. Nightingale, "Acoustic Radiation Force Impulse (ARFI) Imaging: a Review," *Curr Med Imaging Rev,* vol. 7, pp. 328-339, Nov 1 2011.

[51] M. W. Urban, A. Alizad, W. Aquino, J. F. Greenleaf, and M. Fatemi, "A Review of Vibro-acoustography and its Applications in Medicine," *Curr Med Imaging Rev,* vol. 7, pp. 350-359, Nov 1 2011.

[52] J.-O. Choi, S. W. Cho, Y. B. Song, S. J. Cho, B. G. Song, S.-C. Lee*, et al.*, "Longitudinal 2-D strain at rest predicts the presence of left main and three vessel coronary artery disease in patients without regional wall motion abnormality," *European Journal of Echocardiography,* vol. 10, pp. 695-701, 2009.

[53] R. Jurcut, C. J. Pappas, P. G. Masci, L. Herbots, M. Szulik, J. Bogaert*, et al.*, "Detection of regional myocardial dysfunction in patients with acute myocardial infarction using velocity vector imaging," *Journal of the American Society of Echocardiography,* vol. 21, pp. 879-886, 2008.

[54] J. Grondin, E. Wan, A. Gambhir, H. Garan, and E. E. Konofagou, "Intracardiac myocardial elastography in canines and humans in vivo," *IEEE transactions on ultrasonics, ferroelectrics, and frequency control,* vol. 62, pp. 337-349, 2015.

[55] M. K. Friedberg and C. Slorach, "Relation between left ventricular regional radial function and radial wall motion abnormalities using two-dimensional speckle tracking in children with idiopathic dilated cardiomyopathy," *The American journal of cardiology,* vol. 102, pp. 335-339, 2008.

[56] A. Bhan, A. Sirker, J. Zhang, A. Protti, N. Catibog, W. Driver*, et al.*, "High-frequency speckle tracking echocardiography in the assessment of left ventricular function and remodeling after murine myocardial infarction," *American Journal of Physiology-Heart and Circulatory Physiology,* vol. 306, pp. H1371-H1383, 2014.

[57] J. Luo, K. Fujikura, S. Homma, and E. E. Konofagou, "Myocardial elastography at both high temporal and spatial resolution for the detection of infarcts," *Ultrasound in medicine & biology,* vol. 33, pp. 1206-1223, 2007.

[58] M. Bauer, S. Cheng, M. Jain, S. Ngoy, C. Theodoropoulos, A. Trujillo*, et al.*, "Echocardiographic speckle-tracking based strain imaging for rapid cardiovascular phenotyping in mice," *Circulation research,* vol. 108, pp. 908-916, 2011.

[59] M. De Craene, S. Marchesseau, B. Heyde, H. Gao, M. Alessandrini, O. Bernard*, et al.*, "3-D strain assessment in ultrasound (straus): A synthetic comparison of five tracking methodologies," *IEEE transactions on medical imaging,* vol. 32, pp. 1632-1646, 2013.

[60] R. Lopata, M. M. Nillesen, C. Verrijp, S. Singh, M. Lammens, J. A. van der Laak*, et al.*, "Cardiac biplane strain imaging: initial in vivo experience," *Physics in Medicine & Biology,* vol. 55, p. 963, 2010.

[61] K. Nightingale, M. S. Soo, R. Nightingale, and G. Trahey, "Acoustic radiation force impulse imaging: in vivo demonstration of clinical feasibility," *Ultrasound in medicine & biology,* vol. 28, pp. 227-235, 2002.

[62] K. Nightingale, "Acoustic radiation force impulse (ARFI) imaging: a review," *Current Medical Imaging,* vol. 7, pp. 328-339, 2011.

[63] B. J. Fahey, K. R. Nightingale, S. A. McAleavey, M. L. Palmeri, P. D. Wolf, and G. E. Trahey, "Acoustic radiation force impulse imaging of myocardial radiofrequency ablation:

Initial in vivo results," *IEEE transactions on ultrasonics, ferroelectrics, and frequency control,* vol. 52, pp. 631-641, 2005.

[64] S. J. Hsu, R. R. Bouchard, D. M. Dumont, P. D. Wolf, and G. E. Trahey, "In vivo assessment of myocardial stiffness with acoustic radiation force impulse imaging," *Ultrasound in medicine & biology,* vol. 33, pp. 1706-1719, 2007.

[65] J. J. Dahl, G. F. Pinton, M. L. Palmeri, V. Agrawal, K. R. Nightingale, and G. E. Trahey, "A parallel tracking method for acoustic radiation force impulse imaging," *IEEE transactions on ultrasonics, ferroelectrics, and frequency control,* vol. 54, pp. 301-312, 2007.

[66] V. Kakkad, M. LeFevre, P. Hollender, J. Kisslo, and G. E. Trahey, "Non-invasive measurement of dynamic myocardial stiffness using acoustic radiation force impulse imaging," *Ultrasound in medicine & biology,* vol. 45, pp. 1112-1130, 2019.

[67] R. R. Bouchard, S. J. Hsu, P. D. Wolf, and G. E. Trahey, "In vivo cardiac, acoustic-radiation-force-driven, shear wave velocimetry," *Ultrasonic imaging,* vol. 31, pp. 201-213, 2009.

[68] M. Couade, M. Pernot, E. Messas, A. Bel, M. Ba, A. Hagège*, et al.*, "In vivo quantitative mapping of myocardial stiffening and transmural anisotropy during the cardiac cycle," *IEEE transactions on medical imaging,* vol. 30, pp. 295-305, 2010.

[69] M. Pernot, M. Couade, P. Mateo, B. Crozatier, R. Fischmeister, and M. Tanter, "Real-time assessment of myocardial contractility using shear wave imaging," *Journal of the American College of Cardiology,* vol. 58, pp. 65-72, 2011.

[70] P. J. Hollender, P. D. Wolf, R. Goswami, and G. E. Trahey, "Intracardiac echocardiography measurement of dynamic myocardial stiffness with shear wave velocimetry," *Ultrasound in medicine & biology,* vol. 38, pp. 1271-1283, 2012.

[71] J. Bercoff, M. Tanter, and M. Fink, "Supersonic shear imaging: a new technique for soft tissue elasticity mapping," *IEEE transactions on ultrasonics, ferroelectrics, and frequency control,* vol. 51, pp. 396-409, 2004.

[72] P. Hollender, D. Bradway, P. Wolf, R. Goswami, and G. Trahey, "Intracardiac acoustic radiation force impulse (ARFI) and shear wave imaging in pigs with focal infarctions," *IEEE transactions on ultrasonics, ferroelectrics, and frequency control,* vol. 60, pp. 1669-1682, 2013.

[73] P. Song, H. Zhao, M. W. Urban, A. Manduca, S. V. Pislaru, R. R. Kinnick*, et al.*, "Improved shear wave motion detection using pulse-inversion harmonic imaging with a phased array transducer," *IEEE transactions on medical imaging,* vol. 32, pp. 2299-2310, 2013.

[74] P. Song, X. Bi, D. C. Mellema, A. Manduca, M. W. Urban, P. A. Pellikka*, et al.*, "Pediatric cardiac shear wave elastography for quantitative assessment of myocardial stiffness: a pilot study in healthy controls," *Ultrasound in medicine & biology,* vol. 42, pp. 1719-1729, 2016.

[75] O. Villemain, M. Correia, E. Mousseaux, J. Baranger, S. Zarka, I. Podetti*, et al.*, "Myocardial stiffness evaluation using noninvasive shear wave imaging in healthy and hypertrophic cardiomyopathic adults," *JACC: Cardiovascular Imaging,* vol. 12, pp. 1135-1145, 2019.

[76] J. D'hooge, "Principles and different techniques for speckle tracking," *Myocardial imaging tissue Doppler and speckle tracking,* pp. 17-25, 2007.

[77] J. D'hooge, A. Heimdal, F. Jamal, T. Kukulski, B. Bijnens, F. Rademakers*, et al.*, "Regional strain and strain rate measurements by cardiac ultrasound: principles, implementation and limitations," *European Journal of Echocardiography,* vol. 1, pp. 154-170, 2000.

[78] M. C. Pastore, G. De Carli, G. E. Mandoli, F. D'Ascenzi, M. Focardi, F. Contorni*, et al.*, "The prognostic role of speckle tracking echocardiography in clinical practice: evidence and reference values from the literature," *Heart failure reviews,* pp. 1-11, 2020.

[79] P. Collier, D. Phelan, and A. Klein, "A test in context: myocardial strain measured by speckle-tracking echocardiography," *Journal of the American College of Cardiology,* vol. 69, pp. 1043-1056, 2017.

[80] M. Cameli, G. E. Mandoli, C. Sciaccaluga, and S. Mondillo, "More than 10 years of speckle tracking echocardiography: still a novel technique or a definite tool for clinical practice?," *Echocardiography,* vol. 36, pp. 958-970, 2019.

[81] O. A. Smiseth, H. Torp, A. Opdahl, K. H. Haugaa, and S. Urheim, "Myocardial strain imaging: how useful is it in clinical decision making?," *Eur Heart J,* vol. 37, pp. 1196-207, Apr 14 2016.

[82] B. H. Amundsen, T. Helle-Valle, T. Edvardsen, H. Torp, J. Crosby, E. Lyseggen*, et al.*, "Noninvasive myocardial strain measurement by speckle tracking echocardiography:

validation against sonomicrometry and tagged magnetic resonance imaging," *Journal of the American College of Cardiology,* vol. 47, pp. 789-793, 2006.

[83] M. Sühling, M. Arigovindan, C. Jansen, P. Hunziker, and M. Unser, "Myocardial motion analysis from B-mode echocardiograms," *IEEE Transactions on image processing,* vol. 14, pp. 525–536, 2005.

[84] N. Ouzir, A. Basarab, O. Lairez, and J.-Y. Tourneret, "Robust Optical Flow Estimation in Cardiac Ultrasound Images Using a Sparse Representation," *IEEE transactions on medical imaging,* 2018.

[85] X. Pan, K. Liu, J. Shao, J. Gao, L. Huang, J. Bai*, et al.*, "Performance comparison of rigid and affine models for motion estimation using ultrasound radio-frequency signals," *IEEE transactions on ultrasonics, ferroelectrics, and frequency control,* vol. 62, pp. 1928-1943, 2015.

[86] E. Mercure, G. Cloutier, C. Schmitt, and R. L. Maurice, "Performance evaluation of different implementations of the Lagrangian speckle model estimator for non-invasive vascular ultrasound elastography," *Medical physics,* vol. 35, pp. 3116-3126, 2008.

[87] M. J. Ledesma-Carbayo, J. Kybic, M. Desco, A. Santos, M. Suhling, P. Hunziker*, et al.*, "Spatiotemporal nonrigid registration for ultrasound cardiac motion estimation," *IEEE transactions on medical imaging,* vol. 24, pp. 1113-1126, 2005.

[88] A. Elen, H. Choi, D. Loeckx, H. Gao, P. Claus, P. Suetens*, et al.*, "3-D cardiac strain estimation using spatiotemporal elastic registration of ultrasound images: a feasibility study," *IEEE Trans Med Imaging,* vol. 27, pp. 1580-1591, 2008.

[89] B. Heyde, P. Claus, R. Jasaityte, D. Barbosa, S. Bouchez, M. Vandenheuvel*, et al.*, "Motion and deformation estimation of cardiac ultrasound sequences using an anatomical B-spline transformation model," in *Biomedical Imaging (ISBI), 2012 9th IEEE International Symposium on*, 2012, pp. 266-269.

[90] B. Heyde, S. Cygan, H. F. Choi, B. Lesniak-Plewinska, D. Barbosa, A. Elen*, et al.*, "Regional cardiac motion and strain estimation in three-dimensional echocardiography: A validation study in thick-walled univentricular phantoms," *IEEE transactions on ultrasonics, ferroelectrics, and frequency control,* vol. 59, pp. 668-682, 2012.

[91] C. Metz, S. Klein, M. Schaap, T. van Walsum, and W. J. Niessen, "Nonrigid registration of dynamic medical imaging data using nD+ t B-splines and a groupwise optimization approach," *Medical image analysis,* vol. 15, pp. 238-249, 2011.

[92] M. De Craene, G. Piella, O. Camara, N. Duchateau, E. Silva, A. Doltra*, et al.*, "Temporal diffeomorphic free-form deformation: Application to motion and strain estimation from 3-D echocardiography," *Medical image analysis,* vol. 16, pp. 427-450, 2012.

[93] M. De Craene, G. Piella, N. Duchateau, E. Silva, A. Doltra, H. Gao*, et al.*, "Temporal diffeomorphic free-form deformation for strain quantification in 3-D-US images," in *International Conference on Medical Image Computing and Computer-Assisted Intervention*, 2010, pp. 1-8.

[94] Z. Zhang, X. Song, and D. J. Sahn, "Cardiac motion estimation from 3-D echocardiography with spatiotemporal regularization," in *International Conference on Functional Imaging and Modeling of the Heart*, 2011, pp. 350-358.

[95] N. Ouzir, A. Basarab, H. Liebgott, B. Harbaoui, and J.-Y. Tourneret, "Motion estimation in echocardiography using sparse representation and dictionary learning," *IEEE Transactions on Image Processing,* vol. 27, pp. 64-77, 2017.

[96] N. Ouzir, J. Bioucas-Dias, A. Basarab, and J.-Y. Tourneret, "Robust cardiac motion estimation with dictionary learning and temporal regularization for ultrasound imaging," in *2019 IEEE International Ultrasonics Symposium (IUS)*, 2019, pp. 2326-2329.

[97] C. Ma and T. Varghese, "Comparison of cardiac displacement and strain imaging using ultrasound radiofrequency and envelope signals," *Ultrasonics,* vol. 53, pp. 782-792, 2013.

[98] R. Lopata, M. Nillesen, I. Gerrits, H. Hansen, L. Kapusta, J. Thijssen*, et al.*, "3-D cardiac strain imaging using a novel tracking method," in *4th European Conference of the International Federation for Medical and Biological Engineering*, 2009, pp. 697-700.

[99] E. Konofagou, J. D'hooge, and J. Ophir, "Cardiac elastography-A feasibility study," in *2000 IEEE Ultrasonics Symposium. Proceedings. An International Symposium (Cat. No. 00CH37121)*, 2000, pp. 1273-1276.

[100] B. Chakraborty, Z. Liu, B. Heyde, J. Luo, and J. D'hooge, "2-D Myocardial Deformation Imaging Based on RF-Based Nonrigid Image Registration," *IEEE transactions on ultrasonics, ferroelectrics, and frequency control,* vol. 65, pp. 1037-1047, 2018.

[101] R. G. Lopata, M. M. Nillesen, H. H. Hansen, I. H. Gerrits, J. M. Thijssen, and C. L. De Korte, "Performance evaluation of methods for two-dimensional displacement and strain estimation using ultrasound radio frequency data," *Ultrasound in medicine & biology,* vol. 35, pp. 796-812, 2009.

[102] R. G. Lopata, M. M. Nillesen, J. M. Thijssen, L. Kapusta, and C. L. de Korte, "Three-dimensional cardiac strain imaging in healthy children using RF-data," *Ultrasound in medicine & biology,* vol. 37, pp. 1399-1408, 2011.

[103] S. Langeland, J. D'hooge, T. Claessens, P. Claus, P. Verdonck, P. Suetens*, et al.*, "RF-based two-dimensional cardiac strain estimation: a validation study in a tissue-mimicking phantom," *IEEE transactions on ultrasonics, ferroelectrics, and frequency control,* vol. 51, pp. 1537-1546, 2004.

[104] W. N. Lee, C. M. Ingrassia, S. D. Fung-Kee-Fung, K. D. Costa, J. W. Holmes, and E. E. Konofagou, "Theoretical quality assessment of myocardial elastography with in vivo validation," *IEEE Trans Ultrason Ferroelectr Freq Control,* vol. 54, pp. 2233-45, Nov 2007.

[105] B. Byram, G. E. Trahey, and M. Palmeri, "Bayesian speckle tracking. Part I: An implementable perturbation to the likelihood function for ultrasound displacement estimation," *IEEE transactions on ultrasonics, ferroelectrics, and frequency control,* vol. 60, pp. 132-143, 2012.

[106] B. Byram, G. E. Trahey, and M. Palmeri, "Bayesian speckle tracking. Part II: biased ultrasound displacement estimation," *IEEE transactions on ultrasonics, ferroelectrics, and frequency control,* vol. 60, pp. 144-157, 2012.

[107] M. McCormick, N. Rubert, and T. Varghese, "Bayesian regularization applied to ultrasound strain imaging," *IEEE Transactions on Biomedical Engineering,* vol. 58, pp. 1612-1620, 2011.

[108] M. Cikes, L. Tong, G. R. Sutherland, and J. D'hooge, "Ultrafast cardiac ultrasound imaging: technical principles, applications, and clinical benefits," *JACC: Cardiovascular Imaging,* vol. 7, pp. 812-823, 2014.

[109] H. H. Hansen, R. G. Lopata, and C. L. de Korte, "Noninvasive carotid strain imaging using angular compounding at large beam steered angles: validation in vessel phantoms," *IEEE transactions on medical imaging,* vol. 28, pp. 872-880, 2009.

[110] U. Techavipoo and T. Varghese, "Improvements in elastographic contrast-to-noise ratio using spatial-angular compounding," *Ultrasound in medicine & biology,* vol. 31, pp. 529-536, 2005.

[111] T. Udomchai, Q. Chen, T. Varghese, J. A. Zagzebski, and E. L. Madsen, "Noise reduction using spatial-angular compounding for elastography," *ieee transactions on ultrasonics, ferroelectrics, and frequency control,* vol. 51, pp. 510-520, 2004.

[112] F. Varray and H. Liebgott, "Multi-resolution transverse oscillation in ultrasound imaging for motion estimation," *IEEE transactions on ultrasonics, ferroelectrics, and frequency control,* vol. 60, pp. 1333-1342, 2013.

[113] H. Liebgott, A. Basarab, P. Gueth, D. Friboulet, and P. Delachartre, "Transverse oscillations for tissue motion estimation," *Ultrasonics,* vol. 50, pp. 548-555, 2010.

[114] M. Alessandrini, A. Basarab, L. Boussel, X. Guo, A. Serusclat, D. Friboulet*, et al.*, "A new technique for the estimation of cardiac motion in echocardiography based on transverse oscillations: a preliminary evaluation in silico and a feasibility demonstration in vivo," *IEEE Trans Med Imaging,* vol. 33, pp. 1148-62, May 2014.

[115] E. Brusseau, J. Kybic, J.-F. Déprez, and O. Basset, "2-D locally regularized tissue strain estimation from radio-frequency ultrasound images: Theoretical developments and results on experimental data," *IEEE Transactions on Medical Imaging,* vol. 27, pp. 145-160, 2008.

[116] H. Rivaz, E. M. Boctor, M. A. Choti, and G. D. Hager, "Real-time regularized ultrasound elastography," *IEEE transactions on medical imaging,* vol. 30, pp. 928-945, 2011.

[117] H. S. Hashemi and H. Rivaz, "Global time-delay estimation in ultrasound elastography," *IEEE transactions on ultrasonics, ferroelectrics, and frequency control,* vol. 64, pp. 1625-1636, 2017.

[118] Y. Petrank, L. Huang, and M. O'Donnell, "Reduced peak-hopping artifacts in ultrasonic strain estimation using the Viterbi algorithm," *IEEE transactions on ultrasonics, ferroelectrics, and frequency control,* vol. 56, pp. 1359-1367, 2009.

[119] M. Ashikuzzaman, C. J. Gauthier, and H. Rivaz, "Global Ultrasound Elastography in Spatial and Temporal Domains," *IEEE transactions on ultrasonics, ferroelectrics, and frequency control,* vol. 66, pp. 876-887, 2019.

[120] M. Omidyeganeh, Y. Xiao, M. O. Ahmad, and H. Rivaz, "Estimation of strain elastography from ultrasound radio-frequency data by utilizing analytic gradient of the similarity metric," *IEEE transactions on medical imaging,* vol. 36, pp. 1347-1358, 2017.

[121] L. Guo, Y. Xu, Z. Xu, and J. Jiang, "A PDE-based regularization algorithm toward reducing speckle tracking noise: A feasibility study for ultrasound breast elastography," *Ultrasonic imaging,* vol. 37, pp. 277-293, 2015.

[122] H. Rivaz, E. M. Boctor, M. A. Choti, and G. D. Hager, "Ultrasound elastography using multiple images," *Medical image analysis,* vol. 18, pp. 314-329, 2014.

[123] R. Al Mukaddim, N. H. Meshram, C. C. Mitchell, and T. Varghese, "Hierarchical Motion Estimation With Bayesian Regularization in Cardiac Elastography: Simulation and $ In~ Vivo $ Validation," *IEEE transactions on ultrasonics, ferroelectrics, and frequency control,* vol. 66, pp. 1708-1722, 2019.

[124] W.-N. Lee, C. M. Ingrassia, K. D. Costa, J. W. Holmes, and E. E. Konofagou, "Theoretical quality assessment of myocardial elastography with in vivo validation," *ieee transactions on ultrasonics, ferroelectrics, and frequency control,* vol. 54, pp. 2233-2245, 2007.

[125] I. Zervantonakis, S. Fung-Kee-Fung, W. Lee, and E. Konofagou, "A novel, view-independent method for strain mapping in myocardial elastography: eliminating angle and centroid dependence," *Physics in Medicine & Biology,* vol. 52, p. 4063, 2007.

[126] J. Grondin, V. Sayseng, and E. E. Konofagou, "Cardiac strain imaging with coherent compounding of diverging waves," *IEEE transactions on ultrasonics, ferroelectrics, and frequency control,* vol. 64, pp. 1212-1222, 2017.

[127] V. Sayseng, J. Grondin, and E. E. Konofagou, "Optimization of transmit parameters in cardiac strain imaging with full and partial aperture coherent compounding," *IEEE transactions on ultrasonics, ferroelectrics, and frequency control,* vol. 65, pp. 684-696, 2018.

[128] H. Chen and T. Varghese, "Multilevel hybrid 2-D strain imaging algorithm for ultrasound sector/phased arrays," *Medical physics,* vol. 36, pp. 2098-2106, 2009.

[129] J. Luo and E. E. Konofagou, "High-frame rate, full-view myocardial elastography with automated contour tracking in murine left ventricles in vivo," *IEEE transactions on ultrasonics, ferroelectrics, and frequency control,* vol. 55, pp. 240-248, 2008.

[130] R. G. Lopata, M. M. Nillesen, I. H. Gerrits, J. M. Thijssen, L. Kapusta, and C. L. de Korte, "10B-4 4D cardiac strain imaging: methods and initial results," in *2007 IEEE Ultrasonics Symposium Proceedings*, 2007, pp. 872-875.

[131] S. Langeland, J. D'hooge, H. Torp, B. Bijnens, and P. Suetens, "Comparison of time-domain displacement estimators for two-dimensional RF tracking," *Ultrasound in medicine & biology,* vol. 29, pp. 1177-1186, 2003.

[132] J. Luo and E. E. Konofagou, "A fast normalized cross-correlation calculation method for motion estimation," *IEEE transactions on ultrasonics, ferroelectrics, and frequency control,* vol. 57, pp. 1347-1357, 2010.

[133] D. Rappaport, D. Adam, P. Lysyansky, and S. Riesner, "Assessment of myocardial regional strain and strain rate by tissue tracking in B-mode echocardiograms," *Ultrasound in medicine & biology,* vol. 32, pp. 1181-1192, 2006.

[134] F. Kremer, H. F. Choi, S. Langeland, E. D'Agostino, P. Claus, and J. D'hooge, "Geometric Regularization for 2-D Myocardial Strain Quantification in Mice: An In-Silico Study," *Ultrasound in medicine & biology,* vol. 36, pp. 1157-1168, 2010.

[135] J. Jiang and T. J. Hall, "A coupled subsample displacement estimation method for ultrasound-based strain elastography," *Physics in Medicine & Biology,* vol. 60, p. 8347, 2015.

[136] J. Jiang and T. J. Hall, "A fast hybrid algorithm combining regularized motion tracking and predictive search for reducing the occurrence of large displacement errors," *IEEE transactions on ultrasonics, ferroelectrics, and frequency control,* vol. 58, pp. 730-736, 2011.

[137] D. M. Dumont and B. C. Byram, "Robust tracking of small displacements with a Bayesian estimator," *IEEE transactions on ultrasonics, ferroelectrics, and frequency control,* vol. 63, pp. 20-34, 2015.

[138] M. McCormick, T. Varghese, X. Wang, C. Mitchell, M. Kliewer, and R. Dempsey, "Methods for robust in vivo strain estimation in the carotid artery," *Physics in medicine and biology,* vol. 57, p. 7329, 2012.

[139] H. Shi and T. Varghese, "Two-dimensional multi-level strain estimation for discontinuous tissue," *Physics in Medicine & Biology,* vol. 52, p. 389, 2007.

[140] J. Jiang, T. J. Hall, and A. M. Sommer, "A novel image formation method for ultrasonic strain imaging," *Ultrasound in medicine & biology,* vol. 33, pp. 643-652, 2007.

[141] M. Bayer and T. J. Hall, "Temporal guided search for elastography motion tracking," in *2013 IEEE International Ultrasonics Symposium (IUS)*, 2013, pp. 1268-1271.

[142] M. Mirzaei, A. Asif, M. Fortin, and H. Rivaz, "3-D normalized cross-correlation for estimation of the displacement field in ultrasound elastography," *Ultrasonics,* vol. 102, p. 106053, 2020.

[143] B. Denarie, T. A. Tangen, I. K. Ekroll, N. Rolim, H. Torp, T. Bjåstad*, et al.*, "Coherent plane wave compounding for very high frame rate ultrasonography of rapidly moving targets," *IEEE Trans Med Imaging,* vol. 32, pp. 1265-76, Jul 2013.

[144] M. Tanter and M. Fink, "Ultrafast imaging in biomedical ultrasound," *IEEE Trans Ultrason Ferroelectr Freq Control,* vol. 61, pp. 102-19, Jan 2014.

[145] T. Ling, G. Hang, and J. D'Hooge, "Multi-transmit beam forming for fast cardiac imaging--a simulation study," *IEEE Trans Ultrason Ferroelectr Freq Control,* vol. 60, pp. 1719-31, Aug 2013.

[146] V. Sayseng, R. A. Ober, C. S. Grubb, R. A. Weber, and E. Konofagou, "Monitoring Canine Myocardial Infarction Formation and Recovery via Transthoracic Cardiac Strain Imaging," *Ultrasound Med Biol,* vol. 46, pp. 2785-2800, Oct 2020.

[147] P. Joos, J. Porée, H. Liebgott, D. Vray, M. Baudet, J. Faurie*, et al.*, "High-Frame-Rate Speckle-Tracking Echocardiography," *IEEE transactions on ultrasonics, ferroelectrics, and frequency control,* vol. 65, pp. 720-728, 2018.

[148] M. Orlowska, A. Ramalli, A. Petrescu, M. Cvijic, S. Bezy, P. Santos*, et al.*, "A Novel 2-D Speckle Tracking Method for High-Frame-Rate Echocardiography," *IEEE Trans Ultrason Ferroelectr Freq Control,* vol. 67, pp. 1764-1775, Sep 2020.

[149] J.-U. Voigt, G. Pedrizzetti, P. Lysyansky, T. H. Marwick, H. Houle, R. Baumann*, et al.*, "Definitions for a common standard for 2-D speckle tracking echocardiography: consensus document of the EACVI/ASE/Industry Task Force to standardize deformation imaging," *European Heart Journal-Cardiovascular Imaging,* vol. 16, pp. 1-11, 2015.

[150] A. H. A. W. G. o. M. Segmentation, R. f. C. Imaging:, M. D. Cerqueira, N. J. Weissman, V. Dilsizian, A. K. Jacobs*, et al.*, "Standardized myocardial segmentation and nomenclature for tomographic imaging of the heart: a statement for healthcare professionals from the Cardiac Imaging Committee of the Council on Clinical Cardiology of the American Heart Association," *Circulation,* vol. 105, pp. 539-542, 2002.

[151] C. M. Yu, J. Gorcsan, 3rd, G. B. Bleeker, Q. Zhang, M. J. Schalij, M. S. Suffoletto*, et al.*, "Usefulness of tissue Doppler velocity and strain dyssynchrony for predicting left ventricular reverse remodeling response after cardiac resynchronization therapy," *Am J Cardiol,* vol. 100, pp. 1263-70, Oct 15 2007.

[152] W. N. Lee, J. Provost, K. Fujikura, J. Wang, and E. E. Konofagou, "In vivo study of myocardial elastography under graded ischemia conditions," *Phys Med Biol,* vol. 56, pp. 1155-72, Feb 21 2011.

[153] T. Tsugu, A. Postolache, R. Dulgheru, T. Sugimoto, J. Tridetti, M. L. Nguyen Trung*, et al.*, "Echocardiographic reference ranges for normal left ventricular layer-specific strain: results from the EACVI NORRE study," *Eur Heart J Cardiovasc Imaging,* vol. 21, pp. 896-905, Aug 1 2020.

[154] M. S. Amzulescu, M. De Craene, H. Langet, A. Pasquet, D. Vancraeynest, A. C. Pouleur*, et al.*, "Myocardial strain imaging: review of general principles, validation, and sources of discrepancies," *Eur Heart J Cardiovasc Imaging,* vol. 20, pp. 605-619, Jun 1 2019.

Chapter 3

Photoacoustic Image Beamforming and Oxygen Saturation Estimation: A Literature Review

Photoacoustic imaging (PAI) is a hybrid biomedical imaging modality based on broadband ultrasound (US) signal generation using short pulsed electromagnetic optical irradiation of tissue [1, 2]. US signal generation in PAI is a result of rapid thermal expansion of tissue due to absorption of optical energy by either endogenous chromophores (e.g., oxygenated [HbO_2] and deoxygenated hemoglobin [Hb]), or exogenous contrast agents (e.g., nanoparticles, organic dyes) [1, 3] which can be detected using conventional US transducers [4]. Thus, higher optical contrast at US spatial resolutions can be achieved in PAI making it an attractive imaging modality in biomedicine with both clinical (e.g. cancer detection [5, 6], monitoring microcirculation [7], [8], surgical guidance [9-11], prostate brachytherapy [12]) and preclinical applications (e.g. therapeutic response monitoring [13], cardiovascular [14]). The clinical and pre-clinical applications of PAI have been reviewed by several groups [1, 2, 9, 14-18]. In this chapter, we focus our literature review on two important aspects of PAI – (a) Beamforming methods for PAI reconstruction and (b) Oxygen saturation estimation methods using PAI.

3.1 The Photoacoustic Effect: Basic Principle of PAI

PAI is based on the photoacoustic effect reported back in 1880 by Alexander Graham Bell when he observed sound generation from modulated light [19]. PAI can be considered to be a three-step process – (a) optical irradiation of the tissue region of interest (ROI) and light absorption, (b) thermal expansion causing acoustic wave generation and (c) detection of these generated acoustic waves at tissue surface for image formation [20]. Typically, the tissue ROI is

irradiated with pulsed or time-modulated light [1] from the surface which penetrates the tissue while undergoing multiple scattering and absorption (by optical absorbers referred to as chromophores) [2, 21-24]. This optical absorption causes local temperature rise (<0.1 K) through conversion of optical energy to heat by vibrational and collisional relaxation [1] which in turn induces a rapid thermal expansion of tissue leading to the generation of broadband acoustic waves [2, 21-24]. There are two main pre-requisites for effective PA signal generation as described below [20, 23].

1) Thermal confinement – The pulse width (τ_p) of optical excitation should be less than thermal relaxation time (τ_{th}). τ_{th} denotes the time needed for the heat generated by optical absorption to dissipate due to thermal conduction. This indicates that thermal diffusion during optical illumination should be negligible.
2) Stress confinement – The pulse width (τ_p) of optical excitation should be less than stress relaxation time (τ_s). τ_s denotes the time needed for the stress (induced by the PA effect) to propagate through the heated region. This indicates that there is negligible volume expansion of absorbers during optical illumination.

If thermal and stress confinement are met (which is typically the case as τ_p is on the order of nanoseconds), the initial pressure rise (p_0) due to thermal expansion can be described as follows.

$$p_0(\mathbf{x},\lambda) = \frac{\beta c^2}{C_p}\mu_a(\mathbf{x})\Phi(\mathbf{x},\lambda,\mu_a,\mu_s,g) = \Gamma H(\mathbf{x}) \tag{3.1}$$

where, $\mu_a(\mathbf{x})$ is local absorption coefficient, $\Phi(\mathbf{x},\lambda,\mu_a,\mu_s,g)$ is the local fluence which is a function of absorption coefficient, scattering coefficient (μ_s) and anisotropy factor (g), β denotes volume thermal expansivity, c is speed of sound, C_p is the specific heat capacity at constant pressure, Γ is the Gruneisen coefficient (dimensionless) defined as $\Gamma = \frac{\beta c^2}{C_p}$ and $H(\mathbf{x})$ is the absorbed optical energy defined as $H(\mathbf{x}) = \mu_a(\mathbf{x})\Phi(\mathbf{x},\lambda,\mu_a,\mu_s,g)$. Equation (3.1) indicates that p_0 varies non-linearly with μ_a. This process is described as the optical forward problem in Figure 3.1. The optical inverse problem aims to estimate μ_a using p_0 which will be discussed in Section 0. After generation of p_0, the acoustic wave travels in two opposite directions, being divided into two waves with equal magnitude [20] and will be impacted by tissue acoustic properties such frequency dependent acoustic attenuation before reaching the tissue surface [2]. Finally, the propagating acoustic waves from the initial source are detected at the tissue surface for PA image generation. This process is indicated as the acoustic forward problem Figure 3.1. Note that the initial pressure magnitude in PAI (<10 kPa) is generally significantly lower than diagnostic ultrasound pressure (< 1MPa) [1, 21]. Furthermore, the bandwidth of the PA transient is generally broadband depending on the optical absorber's size (e.g., higher frequency content from smaller optical absorbers). However, the bandwidth of the detected PA signals at tissue surface will be limited by tissue acoustic attenuation and ultrasound transducer bandwidth [1, 21]. For the acoustic inverse problem, we aim to reconstruct p_0 using detected data from the US detector which is discussed in detail in Section 3.2.

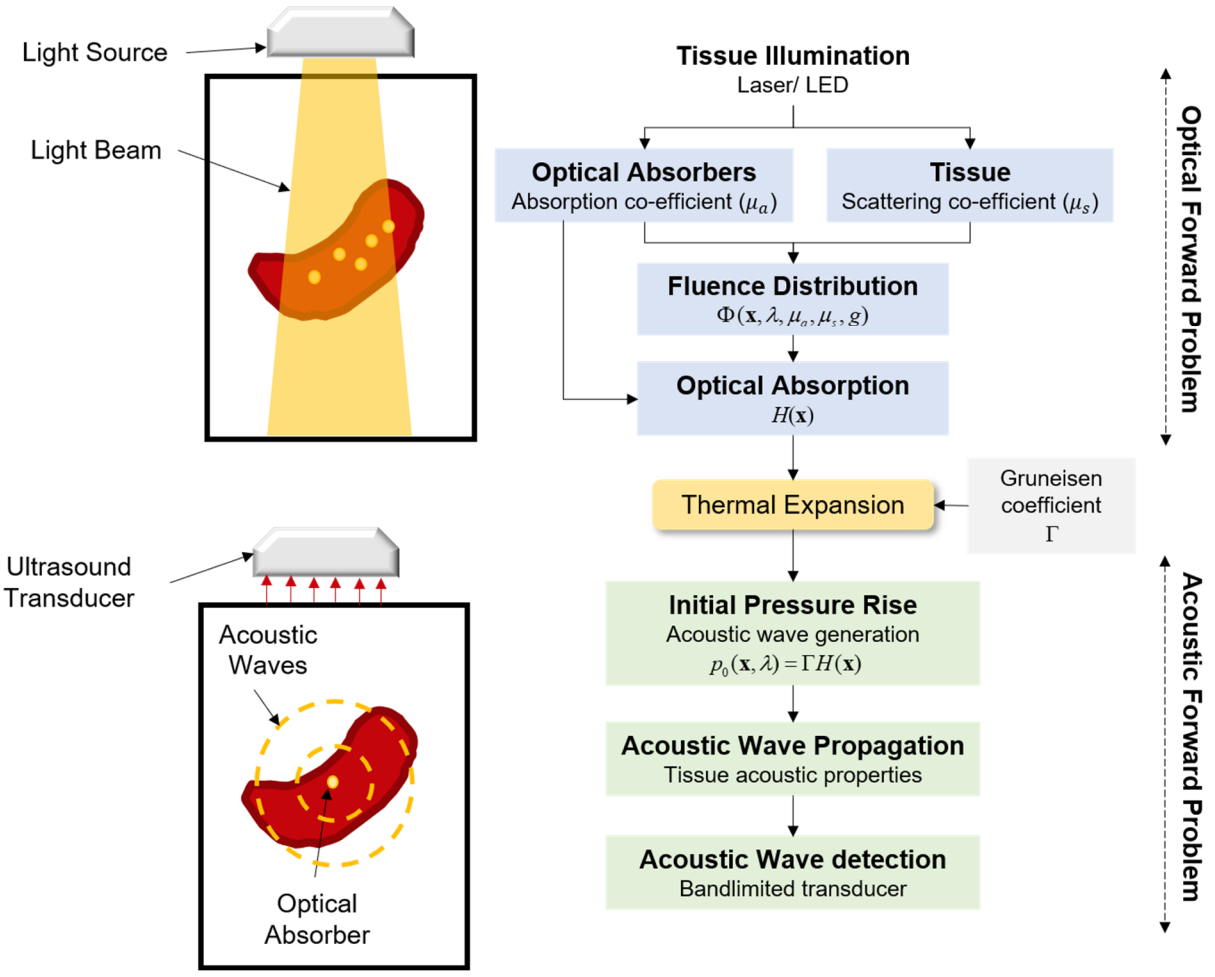

Figure 3.1 Schematic representation of PA signal generation and detection using bandlimited ultrasound transducer

3.2 Photoacoustic Beamforming

PAI can be broadly classified into– (a) Photoacoustic tomography (PAT) and (b) Photoacoustic microscopy (PAM) [1, 25, 26]. This dissertation is focused on PAT specifically on photoacoustic (PA) integrated US imaging systems where acoustic waves generated by pulsed optical irradiation are detected by conventional US array transducers [27]. Image reconstruction or beamforming algorithms use received channel data to form PA images. For its simplicity and speed, delay-and-sum (DAS) is the most common beamforming algorithm utilized. However, DAS has several undesirable characteristics such as wider main lobes, higher sidelobe levels and

incoherent clutter that reduce image quality [4, 27-29]. DAS is particularly unsuitable for PA due to absence of a transmit (Tx) focus which increases both sidelobes and induced off-axis clutter. Therefore, extensive research to translate adaptive beamforming techniques from US to PA image reconstruction is being pursued. Several adaptive beamforming methods have been reported in the peer-reviewed literature for the reduction of these artifacts [30-33]. State-of-the-art adaptive beamforming approaches include data driven adaptive beamforming (e.g., minimum variance (MV) [33], coherence processing [33-35], delay-multiply-and-sum (DMAS) [36-38], iterative reconstruction [39-41]) and the use of machine learning (ML) [42-45]. Other post beamforming approaches to improve PAI quality include signal averaging [46-48], spatial angular compounding [49], singular value decomposition [50] and synthetic aperture focusing [51, 52]. However, in this chapter, we have limited our contextual literature review to beamforming methods using raw channel data and summarized the reviewed papers in Table 3.1.

3.2.1 Minimum variance (MV) beamforming

MV beamforming calculates optimal aperture weighting using data statistics in the aperture domain to reduce contributions from off-axis signals [53, 54]. Park *et al.* adapted MV beamforming for PAI and demonstrated resolution improvement over DAS [33]. Mozaffarzadeh *et al.* combined both MV and eigen-based MV with DMAS to improve the resolution of DMAS beamforming [30, 31, 55]. In eigen-based MV, the covariance matrix utilizes eigen decomposition to determine the signal subspace using a subset of eigen vectors to improve the resolution and sidelobe suppression. Recently, Shamekhi *et al.* combined eigen based-MV with coherence processing and applied the algorithm for linear array PAI [56]. Paridar *et al.* incorporated a sparse regularization constraint to the MV optimization problem thereby improving performance [32]. Even though MV improves resolution and reduces sidelobes when compared to DAS, some level

of sidelobe signals persist. One simple solution is to weight MV images with the coherence factor [33]. However, this may not be an ideal solution in low signal-to-noise ratio environments resulting in undesirable PA signal suppression [57].

3.2.2 Delay-Multiply-and-Sum (DMAS) beamforming

In DMAS, time delayed PA signals in the aperture domain are combinatorically coupled and multiplied before summation. Park *et al.* [38] proposed a DMAS algorithm [58] where time delayed PA signals in the aperture domain are combinatorically coupled and multiplied before summation to enhance signal coherence non-linearly thus gaining higher image contrast. Mozaffarzadeh *et al.* [59] introduced a double stage DMAS algorithm where DAS terms in signal coherence estimation were replaced with DMAS terms. This approach showed improvement in terms of signal-to-noise ratio (SNR) and image contrast when compared to conventional approaches. Kirchner *et al.* demonstrated the applicability of DMAS for multi-spectral PAI by proposing a signed DMAS method where the sign of DAS beamformer is preserved to ensure linearity of the reconstructed results [36]. Ma *et al.* proposed Multiple DAS with Enveloping algorithm where they demonstrated suppression of sidelobe artifacts by calculating the whole N-shaped PA signal for each pixel [60]. Several other variations of DMAS beamformers have also been reported in literature [37, 55, 61, 62].

3.2.3 Coherence based beamforming

Another class of beamforming algorithms utilized to improve PAI quality employ coherence analysis of received channel data, termed as coherence factor (CF). Wang *et al.* applied CF weighting to synthetic aperture focused DAS images and demonstrated improvement in lateral resolution along with better representation of vascular networks in rat dorsal dermis [63]. Zemp *et al.* [29] used CF for PAI of microvasculature with a high-frequency array. Park *et al.* [33]

calculated CF weighting as a ratio of the coherent to incoherent sum of received channel data and weighted MV beamforming to obtain better performance than DAS for point target and inclusion phantoms. Robustness of CF calculations was improved by Wang *et al.* by incorporating local channel SNR [64]. Several variations in CF calculation such as sign coherence factor for high frequency annular-array PAI [65], sign coherence factor for eigen-space MV beamforming [56], CF weighting using DMAS [66] and MV [67] respectively for coherence calculation have also been reported. Another popular coherence-based beamformer is the short-lag spatial coherence (SLSC) beamformer where spatial correlation of channel data at short lag values are utilized to generate PA images [34, 68-70]. SLSC has shown remarkable image quality improvements when applied to PA-based surgical guidance [9-11, 71, 72]. Recently, Graham *et al.* [73] theoretically derived spatial coherence functions for PAI and explored the influence of noise and incident fluence on the spatial coherence functions. The derived spatial coherence functions can be utilized to optimize the SLSC application. However, SLSC image contrast stems from spatial correlation of channel data rather than optical absorption of imaged tissue which is detrimental when multi-wavelength PAI is used for spectral unmixing to estimate blood oxygenation. To address this, Mora *et al.* [74] recently proposed a generalized spatial coherence method combining SLSC and DMAS to preserve PA signal amplitude. However, from the reported results it was not clear how the method will perform for multispectral PAI.

3.2.4 Model based iterative reconstruction

Use of model based iterative reconstruction methods employing signal sparsity and low rankness have also been reported [40, 41, 75-77]. Model based iterative reconstruction methods performs image reconstruction by minimizing the error between experimentally measured and a

forward model (analytical or semi analytical) generated PA data. These methods typically discretize the PA forward problem as follows.

$$\mathbf{p}_r = \mathbf{H}\mathbf{p}_0 \tag{3.2}$$

where, $\mathbf{p}_r \in \mathbb{R}^{LM\times 1}$ denote received PA signals by a L-element array each having M-time samples (raw channel data), $\mathbf{p}_0 \in \mathbb{R}^{N_x N_y \times 1}$ is the beamformed initial pressure distribution image and $\mathbf{H} \in \mathbb{R}^{LM\times N_x N_y}$ is the model or measurement matrix (forward model) which links $\mathbf{p}_r$ and $\mathbf{p}_0$. But, equation (3.2) is an ill-posed problem, thus regularization (e.g., total variation) is added to solve it [39]. Most of these algorithms are in developed PA tomography systems where data collection is done from multiple angles covering the imaged object [40, 41, 75, 76, 78-80]. However, in this dissertation, we are restricting our review to the methods developed only for linear array transducers due to their clinical and pre-clinical relevance. For example, Shang *et al.* [81] proposed a sparsity-based image reconstruction with compressed sensing [82] for linear array PAI. Here authors constructed the forward model by directly measuring the impulse response for each pixel location of the reconstructed image. Then a sparsity-based optimization problem is built incorporating the forward model and solved using an iterative shrinkage/thresholding algorithm [83]. Simulation and phantom validation showed performance improvement over conventional methods. Recently, Vilov *et al.* [84] applied a similar method for performing image reconstruction with data collected from sparse arrays (using only 8 elements out 128 elements available in the transducer). Instead of measuring the impulse response from each location as Shang *et al.* [81], they performed the calculation in a single pixel location and built the model matrix by time shifting. Paridar *et al.* [77] also proposed a sparse beamforming algorithm and solved the optimization problem using a simple iterative algorithm. DAS beamformed data was used to

initialize the iterative solver. The model matrix was data-independent and specific to the linear array geometry and imaging system. Liu *et al.* [85] incorporated dictionary learning using K-SVD to define the sparse transform for regularization and reported better image quality over Wavelet based sparse transforms. All these methods improve image quality by adopting sophisticated data statistics and models with a high computational burden [42]. Recently, Steinberg *et al.* [86] proposed Superiorized Photo-Acoustic Non-NEgative Reconstruction (SPANNER) algorithm for addressing the challenge of real-time implementation. They designed a model matrix considering propagation medium properties and properties of each element (directivity, sensitivity) of a concave array. They have reported results from simulation, point target phantom, *ex vivo* pancreas tissue and *in vivo* contrast enhanced (ICG) prostate imaging with 10 patients. For *in vivo* experiments, the SPANNER method showed statistically significant PA amplitudes before and after injection. Results demonstrated the potential of model-based methods clinically.

Table 3.1 Summary of Reviewed Papers on Adaptive PAI Beamforming

Methods	**Reviewed Papers**	**Application demonstrated**
MV Beamforming	Park *et al.* [33]	Point target and inclusion phantom
	Mozaffarzadeh *et al.* [30]	Simulation and phantom wire targets, single *in vivo* example of human antebrachial vein imaging
	Mozaffarzadeh *et al.* [31, 55]	Simulation and phantom wire targets
	Shamekhi *et al.* [56]	Point target simulation, *ex vivo* (graphite rods in chicken breast) and *in vivo* sentinel lymph node (skin removed and contrast agent used)
	Paridar *et al.* [32]	Simulation and *ex vivo* imaging for point type targets
DMAS Beamforming	Park *et al.* [38]	Acoustic resolution photoacoustic microscopy
	Mozaffarzadeh *et al.* [59]	Simulation and phantom wire targets

DMAS Beamforming	Kirchner *et al.* [36]	Phantom with silicone tubes filled with diluted methylene blue, *in vivo* sO_2 % estimation for human radial artery
	Jeon *et al.* [62]	Phantom with nylon thread and *in vivo* human forearm imaging
	Alshaya *et al.* [61]	Carbon fiber rods in hydrogel phantom
	Ma *et al.* [60]	Simulation and phantom wire targets, single *in vivo* example of human finger joint imaging
Coherence Based Beamforming	Wang *et al.* [63]	Point target phantom and one *in vivo* rat example
	Zemp *et al.* [29]	High frequency imaging with one *in vivo* rat example
	Park *et al.* [33]	Point target and inclusion phantom
	Wang *et al.* [64]	Simulated point target and cyst phantoms, *in vivo* breast imaging
	Chitnis *et al*. [65]	Point target phantom and *in vivo* mouse embryo microvasculature visualization
	Shamekhi *et al.* [56]	Point target simulation, *ex vivo* (graphite rods in chicken breast) and *in vivo* sentinel lymph node (skin removed and contrast agent used)
	Mozaffarzadeh *et al.* [66]	Simulation and phantom point targets, *ex vivo* (graphite rods in chicken breast)
	Mozaffarzadeh *et al.* [67]	Simulation and phantom wire targets
	Mora *et al.* [74]	Simulation, phantom and in vivo human palm imaging
	SLSC [9-11, 34, 68-72, 87]	*ex vivo* and *in vivo* image-guided interventions
Iterative reconstruction	Shang *et al.* [81]	Simulated point target and Shepp–Logan phantom, experimental point target phantom
	Paridar *et al.* [77]	Point target simulation, *ex vivo* (graphite rods in chicken breast) and *in vivo* sentinel lymph node (skin removed and contrast agent used)
	Liu *et al.* [85]	*In vivo* imaging on human hand and two rats

Iterative reconstruction	Vilov *et al.* [84]	Phantom experiments with microfluidic channels
	Steinberg *et al.* [86]	Simulation, point target phantom, *ex vivo* pancreas tissue, *in vivo* contrast enhanced (ICG) prostate imaging with 10 patients
Machine learning	Please refer to **Table 3.2** for details	

3.2.5 Machine learning based methods

In the past few years, ML based algorithms that achieve image quality improvement while maintaining low computational burden have gained momentum [42]. ML models have been used to address PAI issues such as the limited view and use of adaptive beamforming [42, 45, 88-92], reflection artifact removal [43, 93], expanding penetration depth [44] and contrast enhancement in low fluence PAI [94]. The journal papers reviewed for this chapter are summarized in

Table **3.2**. Waibel *et al.* [88] proposed the use of U-Net architecture for direct reconstruction of raw channel data and correction of DAS beamformed data. Their synthetic image generation incorporated fluence contribution and acoustic propagation using open-source simulation software packages (mcxyz [95] and k-Wave [96]). The U-Net performed better for DAS image correction when compared to direct image reconstruction. Authors hypothesized that direct reconstruction requires the U-Net to learn the required time delays from the raw channel data first followed by beamforming which might have a detrimental effect. Anas *et al.* [92] trained a dense convolutional neural network (CNN) to perform beamforming from raw channel data. Compared to the method proposed by Waibel *et al.* [88], they additionally simulated sound of speed heterogeneity, to mimic realistic *in vivo* imaging scenarios. Finally, Kim *et al.* showed that direct reconstruction can be improved if a U-Net is trained using 3-D aperture domain data (after time delay correction) and demonstrated better image quality when compared to training the U-Net on

the raw 2-D channel data [42]. Realistic ground truth images were generated by convolving vascular maps derived from oculi drive with the system of impulse responses of their custom PAUS system. One potential limitation of this method is that their synthetic data generation did not account for acoustic propagation related issues such as attenuation, reverberation, sound of speed heterogeneity. In contrast to the method proposed by Kim *et al.* [42], Lan *et al.* utilized information from both raw channel and DAS beamformed data for DL based beamforming [45]. They proposed Y-Net, which is modification of U-Net to handle two individual encoder networks for channel and DAS beamformed data respectively. Synthetic image generation was done using the k-Wave MATLAB toolbox [96] and the vascular maps derived from oculi drive. The method also provided a comparison against basic U-Net [97] with DAS beamformed data as an input resulting in better image quality.

Vu et al. [89] reported the use of Wasserstein generative adversarial network with gradient penalty (WGAN-GP) to remove limited view artifacts from DAS beamformed images. Other reports on DL based limited view correction and adaptive beamforming can be found here [90, 91, 98-100]. Allman *et al.* [43] trained a CNN to identify point sources and remove reflection artifacts induced by strong acoustic reflections from hyperechoic objects using pre-beamformed raw channel data. Their DL model consisted of two modules, where the first module included a deep CNN of VGG16 architecture [101] and a region proposal network [102] while the second module included Fast-RCNN [103] (Fast Region-based CNN). Their training data synthesis stage considered a wide range of imaging scenarios such noise corruption, source point target location, multiple point targets and impact of bandlimited transducers. Their results showed higher success rate in point source localization and artifact removal when compared to conventional methods in simulation and phantom experiments. Significant optical and acoustic scattering hinders

localization of PA signals from deeper depth. To address this issue, Johnstonbaugh *et al.* [44] proposed the use of a encoder-decoder type neural network to localize PA signals in deep-tissue medium. Their synthetic dataset generation considered both optical and acoustic physics. Superior performance was demonstrated when compared to DAS beamforming. However, the simulation and phantom experiments were limited to point like targets making it unclear how it would perform for the localization of deeper microvasculature *in vivo*. Finally, Hariri *et al.* [94] trained a multi-level wavelet-CNN (MWCNN) [104]to recover high fluence PA images from noisy low fluence PA images. Their proposed method showed better results for *in vivo* Methylene blue (MB) concentration imaging. Even though the results from these ML methods are promising and encouraging, most reported ML models were trained on synthetic data tuned for specific problems thus the generalizability of these methods when applied to *in vivo* imaging requires further investigation. For further details on this topic, interested readers are referred to review papers published during 2020 – 2021 [105-109].

Table 3.2 Summary of Reviewed Papers on Machine learning based PAI Beamforming

Problem Statement	**Paper**	**Deep Learning Architecture**	**Training Sample Size***	**Testing Sample Size**	**Application**
Limited view artifact removal and adaptive beamforming	Waibel *et al.* [88]	U-Net	2880	720	Simulated vessels in transverse view
	Anas *et al.* [92]	Dense CNN	3500	1500	Simulated vessels in transverse view, phantoms with plastic tubes and human hair, *in vivo* skin vasculature
	Vu et al. [89]	WGAN-GP	11200	2800	Simulated disks and micro vessel data
	Kim *et al.* [42]	U-Net with 3-D channel data as input	16000	1000	Simulated microvasculature, wire

Limited view artifact removal and adaptive beamforming					phantom and *in vivo* human finger imaging
	Lan *et al.* [45]	Y-Net	4700	400	Simulated microvasculature, *in vitro* pencil lead in chicken breast and *in vivo* human palm imaging
	Awasthi *et al.* [90]	U-Net with scaled root mean squared loss	1000 (patch wise training with 105000 patches)	100	Simulated phantoms (blood vessels, modified Derenzo, breast and PAT phantom), horse-hair phantom and *in vivo* rat-brain data
Reflection artifact removal	Allman *et al.* [43]	Deep CNN of VGG16 architecture [101], a region proposal network [102] and Fast-RCNN [103]	Sample size varied based on scenario (e.g., baseline training sample size 13872)	Sample size varied based on imaging scenario	Simulation and phantom experiments
Expanding penetration depth	Johnstonbaugh *et al.* [44]	Combination of U-Net and Res-Net [110]	16240	4600	Simulated vessels in transverse view
Low fluence PAI	Hariri *et al.* [94]	MWCNN [104]	3442**	608***	Simulation, phantom and *in vivo* Methylene blue (MB) concentration imaging
	Sample is divided 80:20 for training and validation* * Not explicitly mentioned* **** Test sample size varied based on application*				

3.3 Quantitative Photoacoustic Imaging (qPAI) : Oxygen Saturation Estimation

Several reports on deriving quantitative information from photoacoustic imaging are described in the literature. For example, Hysi *et al.* [111] performed spectral analysis of PA radio-frequency data to study tumor vasculature progression *in vivo*. Landa *et al.* [112] applied PAI for temperature monitoring in photothermal therapy. However, the most prominent and widespread application of qPAI is to determine the spatial distribution and concentrations of optical chromophores [26] present in tissue which in turn can provide valuable physiologically relevant information such as blood oxygen saturation *in vivo*. This section focuses on relevant papers discussing blood oxygen saturation estimation techniques.

3.3.1 Linear spectral unmixing and spectral coloring artifact

To discuss blood oxygen saturation estimation using PAI, we assume that the only chromophores present in the ROI are oxy- and deoxy-hemoglobin ((HbO$_2$ and HbR) respectively and re-represent equation (3.1) in terms of chromophore concentrations and known molar extinction coefficient as follows.

$$p_0(\mathbf{x},\lambda) = \Gamma\Phi(\mathbf{x},\lambda,\mu_a,\mu_s,g)\sum_{k=1}^{K}\varepsilon_k(\lambda)c_k(\lambda) \tag{3.3}$$

where, ε_k and c_k denote the molar extinction coefficient and concentration of the k^{th} chromophore. To estimate the chromophore concentration, PAI data collection is done using multiple wavelengths and can be represented in a matrix form as shown below.

$$\begin{bmatrix} p_0(\lambda_1) \\ . \\ . \\ p_0(\lambda_N) \end{bmatrix} = \Gamma \begin{bmatrix} \Phi(\lambda_1) & . & . & 0 \\ . & . & & . \\ . & & . & . \\ 0 & . & . & \Phi(\lambda_N) \end{bmatrix} \times \begin{bmatrix} \varepsilon_{HbO_2}(\lambda_1) & \varepsilon_{HbR}(\lambda_1) \\ . & . \\ . & . \\ \varepsilon_{HbO_2}(\lambda_N) & \varepsilon_{HbR}(\lambda_N) \end{bmatrix} \times \begin{bmatrix} c_{HbO_2} \\ c_{HbR} \end{bmatrix} \tag{3.4}$$

Then, inversion of equation (3.4) will result in the concentration of oxy- and deoxy-hemoglobin present in the tissue as shown in the following equation.

$$\begin{bmatrix} c_{HbO_2} \\ c_{HbR} \end{bmatrix} = \frac{1}{\Gamma} \times \begin{bmatrix} \varepsilon_{HbO_2}(\lambda_1) & \varepsilon_{HbR}(\lambda_1) \\ . & . \\ . & . \\ \varepsilon_{HbO_2}(\lambda_N) & \varepsilon_{HbR}(\lambda_N) \end{bmatrix}^{\dagger} \times \begin{bmatrix} \frac{1}{\Phi(\lambda_1)} & . & . & 0 \\ . & . & & . \\ . & & . & . \\ 0 & . & . & \frac{1}{\Phi(\lambda_N)} \end{bmatrix} \times \begin{bmatrix} p_0(\lambda_1) \\ . \\ . \\ p_0(\lambda_N) \end{bmatrix} \tag{3.5}$$

where, † denotes the pseudoinverse. Equation (3.5) shows that to estimate the absolute concentration of chromophores, we require information regarding the spatially variant wavelength-dependent fluence distribution Φ which is not readily available and must be estimated from the data which is a challenging problem to solve. Furthermore, it is assumed that the initial pressure distributions are perfectly reconstructed from the measured data which is not valid in practice (e.g., limited view artifacts [113]). However, the most commonly used approach is to assume that Φ is constant over space and wavelength. Then, considering the reconstructed PA image is proportional to the absorption coefficient, the concentrations of HbO_2 and HbR can be calculated using linear least squares method termed as linear spectral unmixing (LSU) [26]. Additionally, non-negativity constraints are also used to make sure physiologically relevant concentration values are extracted [114]. Furthermore, the impact of wavelength on the accuracy of LSU was also investigated and optimal wavelength selection algorithms have been reported [115, 116]. Finally, blood oxygen saturation (sO_2) can be calculated as follows.

$$sO_2(\%) = \frac{c_{HbO_2}}{c_{HbO_2} + c_{HbR}} \tag{3.6}$$

Even though the LSU method provides quick and easy estimates of sO_2, it will result in highly inaccurate results especially deep into tissue as fluence compensation was typically not done [117] . For example, if we consider a blood vessel deep in tissue, then the PA signal from that vessel will not only depend on local μ_a but also on the local fluence which is turn is dependent on the μ_a and μ_s of the surrounding medium (nearby blood vessels, scattering tissues, skin, water) resulting in distortion of the spectrum of the measured PA signals. This distortion of the PA spectrum due to non-uniform fluence distribution is termed as spectral coloring [26, 117] or spectrum corruption [118] in the literature. For further details on spectral coloring effect, readers are referred to the following papers [26, 117]. In the next section, we review approaches reported in the literature to account for fluence distribution.

3.3.2 Fluence corrected oxygen saturation estimation methods

Several approaches have been reported in the literature to solve the optical inverse problem by accounting for the non-uniform fluence distribution. Several published review papers have discussed these methods [26, 119, 120]. In this dissertation, we took the approach of reviewing the related literature by categorizing the proposed algorithms into five broad categories namely – (a) analytical fluence models for direct inversion, (b) iterative error minimization methods, (c) adjunct modality assisted methods, (d) data driven methods and (e) machine learning assisted approaches.

3.3.2.1 Analytical Fluence Models for Direct Inversion

Model-based fluence correction approaches utilize analytical expressions or numerical methods to estimate the local optical fluence distribution using mathematical modelling of light propagation through tissue [26]. One such method was reported by Kim *et al.* [114] where a simple 2-D skin-tissue model and Beer's law was used to estimate local fluence as shown below.

$$\Phi(\lambda, \mathbf{r}) = \Phi_0(\lambda) e^{-\mu_{eff}(\lambda, \mathbf{r})|\mathbf{r}|} \tag{3.7}$$

where, $\Phi(\lambda,\mathbf{r})$ and $\Phi_0(\lambda)$ denote the local fluence at position **r** and incident tissue-surface fluence measured using laser power meter respectively, $|\mathbf{r}|$ denotes distance between skin and pixel location (**r**), μ_{eff} is the effective attenuation coefficient (wavelength and tissue dependent) = $\sqrt{3\mu_a(\mu_a + \mu_s')}$. This model requires prior information regarding chromophore present in the tissue to estimate μ_{eff}. Authors used fluence compensated PA data and a minimum mean square error estimator with non-negativity constraint to obtain the final estimate of chromophore concentrations. Recently, Zhou *et al.* [121] employed the similar model in a comparative study of fluence correction algorithms. Guo *et al.* also utilized Beer's law in a frequency domain method to derive absolute concentration of HbO_2 and HBR under assumption of homogenous non scattering tissue [122]. Under these assumptions, the detected PA signal can be represented using the following equation.

$$p(t) = \left(\frac{\Gamma \Phi_0(\lambda) \mu_a}{2} \right) e^{-\mu_a c t} \tag{3.8}$$

where, c is the speed of sound. The proposed method calculates the spectral ratio between Fourier transform of detected PA signals collected at two wavelengths λ_1 and λ_2 as shown below.

$$\frac{|P(\lambda_1, \omega)|}{|P(\lambda_2, \omega)|} = \frac{\Phi_0(\lambda_1) \sqrt{\left(\omega / \mu_a(\lambda_2) \right)^2 + c^2}}{\Phi_0(\lambda_2) \sqrt{\left(\omega / \mu_a(\lambda_1) \right)^2 + c^2}} \tag{3.9}$$

The system, acoustic attenuation related, and PA efficiency terms get cancelled during the ratio calculation. Then, curve fitting was used to estimate the unknown terms in equation (3.9) – $\mu_a(\lambda_1)$,

$\mu_a(\lambda_2)$ and surface fluence ratio ($\frac{\Phi_0(\lambda_1)}{\Phi_0(\lambda_2)}$). This method was used for optical-resolution photoacoustic microscopy (OR-PAM) therefore may not be a suitable choice for deep tissue sO_2 estimation [119]. In a recent study, Zhou *et al.* [121] employed the diffusion dipole model to represent optical transport through tissue and reported improvement over 1-D Beer's law based modelling [114]. Monte Carlo (MC) modelling of optical transport through tissue has also been reported in the literature for fluence distribution estimation [123]. MC methods solve the radiative transfer equation (RTE) by simulating photon packets undergoing gradual absorption and random scattering during propagation through a medium based on the local optical properties [26, 124]. Bu *et al.* reported MC model based fluence compensation for a model based PA tomography reconstruction method [125]. Recently, Bulsink *et al.* used MC model and tissue structural information derived from ultrasound images to perform fluence correction for LED-based sO_2 estimation system [126]. Other reports on the use of analytical and MC model for fluence correction are described in the following papers [121, 127, 128]. All of these methods reported improvement over conventional linear spectral unmixing without fluence correction however their accuracy would be dependent on accurate modelling of the tissue geometry and unknown optical and acoustic properties thus making *in vivo* applicability challenging [119].

3.3.2.2 Iterative Error Minimization Approaches

Iterative error minimization based methods first formulate a forward image generation model utilizing prior knowledge of underlying physics and assumed optical properties [26, 129]. Then, modelling parameters (e.g., total hemoglobin concentration, local fluence) are iteratively adjusted to minimize the discrepancy between the model generated and experimentally collected PA data. The model parameters minimizing the error are considered as the estimated parameters

for the experimentally collected image [129]. Laufer *et al.* reported on a two-step model-based inversion scheme where time independent diffusion approximation (DA) of the RTE was utilized to estimate the local fluence distribution [130]. For a specific simulation phantom design (a capillary bed), a mathematical forward model is used to estimate the expected PA signal using an acoustic propagation model with the input initial pressure distribution derived using DA-RTE. Then, an inversion step compares the measured PA and model estimated PA data to derive the final chromophore concentration. Naser *et al.* also proposed a similar local fluence correction method based on finite element methods (FEM) and SNR regularization [131]. The method assumes spatially-invariant, wavelength reduced scattering coefficient (μ_s') following power law as below.

$$\mu_s'(a,b) = a\left(\frac{\lambda}{500\ (\text{nm})}\right)^{-b} \tag{3.10}$$

where, regularization was imposed by setting coefficient a and b to be same for all voxels in an imaging frame. First, a forward model estimates local fluence numerically using diffusion approximation of RTE with tissue-surface fluence, μ_s' and initial hemoglobin concentrations as an input [132]. Normalized fluence values for all possible tissue-surface locations were generated by raster scanning a 1-mm diameter ball placed on the surface of gelatin stand-off to empirically determine the tissue-surface fluence. The optical inverse problem was solved using a recursive approach where a l_1-norm objective function was evaluated using the measured PA data and model estimated PA data iteratively for different values of scattering coefficients (a and b). Local fluence estimates were also updated using forward model during the iteration. Final estimated relative hemoglobin concentrations correspond to the value of a and b where the l_1-norm objective function had the global minimum. The optimization region was limited to a SNR mask generated by

comparing measured PA data to an experimentally determined noise distribution thus achieving SNR regularization.

In a recent paper, Buchmann *et al.* proposed a MC model based iterative error minimization method for 3-D PA tomography [133]. Authors employed the MC model to estimate the local fluence in their forward model and designed a least squares error functional to compare the model generated results against experimental data. The proposed method assumed that scattering coefficient remained constant to ensure the validity of their inversion scheme. However, the algorithm validation was limited to a tissue phantom. Additional reports on model-based inversion methods and iterative error minimization for PA fluence correction can be found here [134-137]. These set of algorithms demonstrated encouraging results in simulation experiments however translation of these methods to *in vivo* experimental setups still remain challenging for several reasons. For example, the accuracy of these methods largely depend on the accuracy of the forward model in formulating real image acquisition pathways which will be particularly difficult to achieve in an *in vivo* setup [129]. To address the issue of sensitivity to modelling geometry, a recent publication (January 2021) from Jeng *et al.* [113] proposed an interleaved photoacoustic and ultrasound system with diffusion dipole model based real-time fluence correction. In contrast to conventional broad-beam illumination, authors proposed a fast-swept scanning approach by creating partial PA images through illuminating tissue with 20 narrow laser beams by sequentially firing 20 individual fibers integrated on the US transducer. To perform fluence correction, a diffusion dipole fluence model [23] for i^{th} fiber, defined in terms of unknown effective attenuation co-efficient (μ_{eff}) and reduced scattering coefficient (μ_s') and denoted as $\Phi_i(\vec{r})$ with $\vec{r}$ being the distance from the i^{th} fiber to the pixel of interest was used. Note, $\Phi_i(\vec{r})$ was calculated for all fibers (N_f= 20) at a particular wavelength. Then, a non-linear optimization function is defined to estimate

μ_{eff} and μ_s' by minimizing the error between measured PA signals $\tilde{\Phi}_i(\vec{r})$ for each fiber (sampled from the partial PA images) and model prediction using following equation.

$$\hat{\mu}_{eff}, \hat{\mu}_s' = \arg\min_{\mu_{eff}, \mu_s'} \sum_{i=1}^{N_f} \frac{(\tilde{\Phi}_i(\vec{r}) - \Phi_i(\vec{r}))}{N_f} \tag{3.11}$$

A brute-force search was used to solve equation (3.11). Authors validated the fluence correction method in phantom and *ex vivo* experiments [138] and demonstrated the application of the developed system in the context of PA based needle guidance. In this method, the working assumption is that the PA signal variation at a pixel location among partial PA images is due to the fluence variation only as light has to travel different distances to that location for different fiber locations. The fast sweep scanning method allowed the use of compact light weight lasers, potentially opening up the opportunities for successful clinical translation.

3.3.2.3 Adjunct Modality Assisted Approaches

Adjunct modality assisted approaches combine additional independent tissue optical measurement systems (e.g., diffuse optical tomography (DOT) [139]) with a PAI system to perform fluence correction. For example, Daoudi *et al* [140] and Altaf *et al.* [141] utilized acousto-optics to estimate fluence compensated PA signals for absolute blood oxygen saturation measurement. Acousto-optics (AO) refers to a technique of modulation of optical phase at the focal point of a focused ultrasound beam [142]. The modulation is caused by local density variation induced by the focused US wave inside a medium [142]. Daoudi *et al* [140] and Altaf *et al.* [141] proposed a scheme where a point of interest (point 2) located in a turbid medium is illuminated sequentially from two points (point 1 and 3) on the tissue surface and related the AO measurement to PA measurements using the following equation.

$$\mu_{a,2}(\lambda) = \kappa \sqrt{\frac{p_{1,2}(\lambda) p_{3,2}(\lambda)}{P_{l,123}(\lambda)}} \tag{3.12}$$

where, $\mu_{a,2}$ denotes the local absorption coefficient at point 2, $p_{1,2}$ and $p_{1,3}$ indicate detected PA signals originated from point 2 after sequential illumination from point 1 and 3 respectively. The AO signal is denoted as $P_{l,123}$ where illumination source was point 1, US beam was focused at point 2 and measurement was done at point 3. $P_{l,123}$ was calculated by quantifying speckle contrast changes [143]. By performing dual-wavelength imaging, simple linear spectral unmixing can be used to estimate the absolute sO_2. The proposed method may be well suited for imaging *ex-vivo* samples but may not be applicable *in vivo* due to its specific requirement of dual-illumination and US focusing. This method might also increase acquisition times as the US focal point must be translated sequentially for AO at different depths for achieving deep tissue imaging. DOT enhanced fluence correction has also been proposed by Bauer *et al* [144]. DOT illuminates tissue with an array of light sources and utilizes a set of detectors to measure light leaving the tissue [145]. Then, a model of light propagation is utilized to estimate low resolution 2-D images of optical and scattering coefficients [145]. Authors utilized a hybrid PA-DOT [146] system and extracted the fluence information from the DOT system to correct the non-uniform fluence related errors in raw PA measurements [144]. Other reports on the use of DOT for fluence correction can be found here [139, 147, 148]. Additional examples of adjunct modality based fluence correction methods include utilization of multiple illumination sources [149] and use of reference optical contrast agents [150]. These methods provide better performance compared to raw PA measurements for oxygen saturation measurement at increased system cost due to additional hardware requirements [121].

3.3.2.4 Data driven Approaches

Data driven approaches attempt to reduce or eliminate *apriori* or assumed knowledge requirement of analytical or iterative error-minimization methods by performing fluence correction using derived information from the detected PA signals. For example, Tzoumas *et al.* reported eigenspectral multispectral optoacoustic tomography (eMSOT) with a hypothesis that any unknown fluence distribution can be represented using an affine function of few base spectra irrespective of depth or distribution of tissue optical properties [118]. To estimate the base spectra, principal component analysis (PCA) was applied on 1470 simulated optical fluence distributions considering uniform oxygenation states of hemoglobin. PCA resulted in four significant spectra – a mean fluence spectrum $\Phi_M(\lambda)$ and three eigen spectra: $\Phi_1(\lambda)$, $\Phi_2(\lambda)$ and $\Phi_3(\lambda)$ which were used to define the fluence spectrum of an arbitrary position **r** using following equation.

$$\Phi(\mathbf{r},\lambda) = \Phi_M(\mathbf{r},\lambda) + m_1\Phi_1(\mathbf{r},\lambda) + m_2\Phi_2(\mathbf{r},\lambda) + m_3\Phi_3(\mathbf{r},\lambda) \tag{3.13}$$

where, m_1, m_2 and m_3 were Eigen fluence scaler parameters. A constrained optimization problem was formulated to simultaneously estimate hemoglobin concentration and Eigen fluence parameters requiring data collection for at least 5 wavelengths. eMSOT demonstrated significant error reduction over linear spectral unmixing without fluence correction. However, generalizability of the algorithm *in vivo* would require training data synthesis using more complicated physiological models and diverse chromophore concentrations. Recently, Olefir *et al.* improved the robustness of eMSOT technique to noisy PA data using a Bayesian approach [151].

Dynamic variation of sO_2 levels were utilized to account for non-uniform fluence distributions by *Xia et al.* [152]. The working assumption was that during single wavelength imaging under dynamic variation of sO_2 levels, fluence does not vary if the sO_2 change is small and localized. Authors have validated this method in simulation, phantom and *in vivo* experiments

with controlled variation of oxygenation states. They also reported performance degradation under large change of sO_2. Quantification of sO_2 using with this method under tissue motion may also be challenging.

Fadhel *et al.* recently proposed a fluence correction method where fluence profiles of multiwavelength PA images are matched to the fluence at a reference wavelength [153, 154]. The proposed method first calculates the power spectral ratio between PA data collected at two different wavelengths as shown below.

$$\frac{E(\omega,\lambda_1)}{E(\omega,\lambda_1)} = \frac{p(\omega,\lambda_1)H(\omega)a(\omega)}{p(\omega,\lambda_2)H(\omega)a(\omega)} = \frac{\Phi(\omega,\lambda_1)\mu_a(\omega,\lambda_1)}{\Phi(\omega,\lambda_2)\mu_a(\omega,\lambda_2)} \tag{3.14}$$

where, $E(\omega,\lambda)$ is the power spectrum at wavelength λ, $H(\omega)$ and $a(\omega)$ indicate the impact of system dependent and attenuation related parameters respectively. Authors observed that fluence impacts the frequency content of spectral ratio while absorption coefficient impacts the amplitude. Based on this observation, a frequency filter is designed to perform the fluence matching using the spectral slope estimated within the bandwidth of the transducer.

3.3.2.5 Machine learning assisted oxygen saturation estimation

Machine learning assisted methods reported in literature utilize synthetic data to train a generic model to either quantify absolute sO_2 % or estimate local optical properties [129]. For example, classical random forest regression was applied for quantitative PAI by Kirchner *et al.* [155]. To circumvent the requirement of a large simulation dataset for training, they proposed the use of fluence contribution maps (FIC) to generate context images (CI) as input feature vectors for machine learning model training. For each voxel in an image, CI encodes information about the input PA signals and local fluence due to a particular scanning geometry derived from the FIC.

Therefore, a single simulation results in large number of feature vectors thus reducing the necessity of the simulation of a large number of training images. Their *in silico* results demonstrated better performance than conventional linear spectral unmixing. Recently, several groups have reported on the use of deep learning for performing qPAI. A summary of the methods reviewed in this chapter is presented in **Table 3.3**. Cai *et al.* trained a residual U-net (Res U-net) [97] using 2048 synthetic images generated using a diffusion model of light propagation [156] and tested the model in a simulation setting. Yang *et al.* also proposed a variant of an U-Net namely Deep Residual and Recurrent U-Net (DR2 U-Net) [157] for solving a similar problem [158]. For both methods, training was done using simulated initial pressure distributions which is a major limitation because it assumes that the acoustic inverse problem is solved perfectly which is not the case in pre-clinical and clinical applications. However, the proposed methods provide superior performance when compared to the conventional LSU method. Chen *at al.* demonstrated the use of U-Net for recovering 2-D optical absorption coefficient maps using a single wavelength PA image as input [159]. Training data was sampled using both simulated and phantom experiments. The results showed excellent agreement with ground truth however the simplicity of the training and testing dataset make generalizability of this method unclear. Luke *et al.* proposed O-Net combining two U-Nets in parallel to achieve simultaneous vessel segmentation and sO2 % quantification [160]. In contrast to the studies reported above, Yang *et al.* took the acoustic inverse problem into account and trained an Encoder, Decoder and Aggregator Neural Network (EDA-Net) using PA images generated by optical (MC Model) and acoustic simulation (k-Wave [96]). Realistic training datasets were generated based on 3-D breast phantom. Bench *et al.* further closed the gap between simulation and *in vivo* conditions by generating training 3-D multi-wavelength PA images from CT images of human lung vessels in a multi-layered skin-tissue model [129]. Acoustic inversion

for linear array detectors were also incorporated thus training was done with PA image having limited-view artifacts. An convolutional encoder-decoder network with skip connection (EDS-Net) was trained for simultaneous vessel segmentation and sO2 % quantification like O-Net [129]. The methods discussed above trained the deep learning models based on spatial information of fluence from images [108]. In contrast, Grohl *et al.* proposed an alternative approach for sO2 % quantification by training models using multi-spectral data per pixel [161]. The proposed method was termed Learned Spectral Decoloring where they trained a fully connected feed-forward neural network using simulated initial pressure distributions. Their work reported the use of deep learning assisted sO_2 % quantification *in vivo* for the first time. The key idea behind the method was the generation of training datasets that closely resemble phantom and *in vivo* situations. Authors made their data and code open source which can be found here: https://zenodo.org/record/4304359#.YIePhrVKg54. Other reports on machine learning assisted sO_2 % quantification can be found here [162, 163]. Even though results of machine learning assisted sO_2 % quantification is very encouraging in simulation studies, broader validation studies *in vitro* or *in vivo* are still required to understand the generalizability of these methods [113]. Further details can be found in the review articles published during 2020 – 2021 [105-109].

Table 3.3 Summary of Papers on Deep learning assisted sO_2 (%) quantification

Paper	Deep Learning Architecture	Training Sample Size	Testing Sample Size	Application
Cai *et al.* [156]	Res U-Net	2048	256	*In silico* sO_2% estimation and contrast agent concentration quantification
Yang *et al.* [158]	DR2 U-Net	2560	320	Simulated artery and veins
Chen *et al.* [159]	U-Net	2890	361	Simulation and phantom
Luke et al. [160]	O-Net	3000	1000	*In silico* sO_2% estimation and vessel segmentation
Yang *et al.* [164]	EDA-Net	4880	1440	Simulated breast phantom
Bench *et al.* [129]	EDS-Net	500	40	Simulated vessels
Grohl et al. [161]	Feed-forward neural network	75% of total dataset*	20 % of total dataset	*In silico*, phantom and *in vivo* (porcine brain and human forearm data)
**Total dataset size was not explicitly mentioned in the paper*				

List of References

[1] P. Beard, "Biomedical photoacoustic imaging," *Interface focus,* vol. 1, pp. 602-631, 2011.

[2] M. Xu and L. V. Wang, "Photoacoustic imaging in biomedicine," *Review of scientific instruments,* vol. 77, p. 041101, 2006.

[3] D. Wu, L. Huang, M. S. Jiang, and H. Jiang, "Contrast agents for photoacoustic and thermoacoustic imaging: a review," *International journal of molecular sciences,* vol. 15, pp. 23616-23639, 2014.

[4] T. Harrison and R. J. Zemp, "The applicability of ultrasound dynamic receive beamformers to photoacoustic imaging," *IEEE transactions on ultrasonics, ferroelectrics, and frequency control,* vol. 58, pp. 2259-2263, 2011.

[5] M. Heijblom, W. Steenbergen, and S. Manohar, "Clinical photoacoustic breast imaging: the twente experience," *IEEE pulse,* vol. 6, pp. 42-46, 2015.

[6] J. Jose, D. J. Grootendorst, T. W. Vijn, T. G. van Leeuwen, W. Steenbergen, S. Manohar*, et al.*, "Initial results of imaging melanoma metastasis in resected human lymph nodes using photoacoustic computed tomography," *Journal of biomedical optics,* vol. 16, p. 096021, 2011.

[7] C. P. Favazza, L. V. Wang, and L. A. Cornelius, "In vivo functional photoacoustic microscopy of cutaneous microvasculature in human skin," *Journal of biomedical optics,* vol. 16, p. 026004, 2011.

[8] K. S. Valluru, K. E. Wilson, and J. K. Willmann, "Photoacoustic imaging in oncology: translational preclinical and early clinical experience," *Radiology,* vol. 280, pp. 332-349, 2016.

[9] M. A. Lediju Bell, "Photoacoustic imaging for surgical guidance: Principles, applications, and outlook," *Journal of Applied Physics,* vol. 128, p. 060904, 2020.

[10] A. Wiacek, K. C. Wang, and M. A. L. Bell, "Techniques to distinguish the ureter from the uterine artery in photoacoustic-guided hysterectomies," in *Photons Plus Ultrasound: Imaging and Sensing 2019*, 2019, p. 108785K.

[11] A. Wiacek, K. C. Wang, H. Wu, and M. A. L. Bell, "Dual-wavelength photoacoustic imaging for guidance of hysterectomy procedures," in *Advanced Biomedical and Clinical Diagnostic and Surgical Guidance Systems XVIII*, 2020, p. 112291D.

[12] M. A. L. Bell, N. P. Kuo, D. Y. Song, J. U. Kang, and E. M. Boctor, "In vivo visualization of prostate brachytherapy seeds with photoacoustic imaging," *Journal of biomedical optics,* vol. 19, p. 126011, 2014.

[13] S. Lee, J. H. Kim, J. H. Lee, J. H. Lee, and J. K. Han, "Non-invasive monitoring of the therapeutic response in sorafenib-treated hepatocellular carcinoma based on photoacoustic imaging," *European radiology,* vol. 28, pp. 372-381, 2018.

[14] S. Iskander-Rizk, A. F. van der Steen, and G. van Soest, "Photoacoustic imaging for guidance of interventions in cardiovascular medicine," *Physics in Medicine & Biology,* 2019.

[15] C. Li and L. V. Wang, "Photoacoustic tomography and sensing in biomedicine," *Physics in Medicine & Biology,* vol. 54, p. R59, 2009.

[16] A. Karlas, N.-A. Fasoula, K. Paul-Yuan, J. Reber, M. Kallmayer, D. Bozhko*, et al.*, "Cardiovascular optoacoustics: From mice to men–A review," *Photoacoustics,* vol. 14, pp. 19-30, 2019.

[17] P. K. Upputuri and M. Pramanik, "Recent advances toward preclinical and clinical translation of photoacoustic tomography: a review," *Journal of Biomedical Optics,* vol. 22, p. 041006, 2016.

[18] A. Wiacek and M. A. L. Bell, "Photoacoustic-guided surgery from head to toe," *Biomedical Optics Express,* vol. 12, pp. 2079-2117, 2021.

[19] A. G. Bell, "ART. XXXIV.--On the Production and Reproduction of Sound by Light," *American Journal of Science (1880-1910),* vol. 20, p. 305, 1880.

[20] J. Xia, J. Yao, and L. V. Wang, "Photoacoustic tomography: principles and advances," *Electromagnetic waves (Cambridge, Mass.),* vol. 147, p. 1, 2014.

[21] R. Bouchard, O. Sahin, and S. Emelianov, "Ultrasound-guided photoacoustic imaging: current state and future development," *IEEE transactions on ultrasonics, ferroelectrics, and frequency control,* vol. 61, pp. 450-466, 2014.

[22] L. V. Wang, "Tutorial on photoacoustic microscopy and computed tomography," *IEEE Journal of Selected Topics in Quantum Electronics,* vol. 14, pp. 171-179, 2008.

[23] L. V. Wang and H.-i. Wu, *Biomedical optics: principles and imaging*: John Wiley & Sons, 2012.

[24] L. V. Wang and J. Yao, "A practical guide to photoacoustic tomography in the life sciences," *Nature methods,* vol. 13, p. 627, 2016.

[25] E. Hysi, M. J. Moore, E. M. Strohm, and M. C. Kolios, "A tutorial in photoacoustic microscopy and tomography signal processing methods," *Journal of Applied Physics,* vol. 129, p. 141102, 2021.

[26] B. T. Cox, J. G. Laufer, P. C. Beard, and S. R. Arridge, "Quantitative spectroscopic photoacoustic imaging: a review," *Journal of biomedical optics,* vol. 17, p. 061202, 2012.

[27] A. Needles, A. Heinmiller, J. Sun, C. Theodoropoulos, D. Bates, D. Hirson*, et al.*, "Development and initial application of a fully integrated photoacoustic micro-ultrasound system," *IEEE transactions on ultrasonics, ferroelectrics, and frequency control,* vol. 60, pp. 888-897, 2013.

[28] S. Park, S. R. Aglyamov, and S. Emelianov, "10A-5 beamforming for photoacoustic imaging using linear array transducer," in *2007 IEEE Ultrasonics Symposium Proceedings*, 2007, pp. 856-859.

[29] R. J. Zemp, R. Bitton, K. K. Shung, M.-L. Li, G. Stoica, and L. V. Wang, "Photoacoustic imaging of the microvasculature with a high-frequency ultrasound array transducer," *Journal of biomedical optics,* vol. 12, p. 010501, 2007.

[30] M. Mozaffarzadeh, A. Mahloojifar, M. Orooji, K. Kratkiewicz, S. Adabi, and M. Nasiriavanaki, "Linear-array photoacoustic imaging using minimum variance-based delay multiply and sum adaptive beamforming algorithm," *Journal of biomedical optics,* vol. 23, p. 026002, 2018.

[31] M. Mozaffarzadeh, A. Mahloojifar, V. Periyasamy, M. Pramanik, and M. Orooji, "Eigenspace-based minimum variance combined with delay multiply and sum beamformer: Application to linear-array photoacoustic imaging," *IEEE Journal of Selected Topics in Quantum Electronics,* vol. 25, pp. 1-8, 2018.

[32] R. Paridar, M. Mozaffarzadeh, M. Mehrmohammadi, and M. Orooji, "Photoacoustic image formation based on sparse regularization of minimum variance beamformer," *Biomedical Optics Express,* vol. 9, pp. 2544-2561, 2018.

[33] S. Park, A. B. Karpiouk, S. R. Aglyamov, and S. Y. Emelianov, "Adaptive beamforming for photoacoustic imaging," *Optics letters,* vol. 33, pp. 1291-1293, 2008.

[34] M. A. L. Bell, X. Guo, H. J. Kang, and E. Boctor, "Improved contrast in laser-diode-based photoacoustic images with short-lag spatial coherence beamforming," in *2014 IEEE International Ultrasonics Symposium*, 2014, pp. 37-40.

[35] K. Hollman, K. Rigby, and M. O'donnell, "Coherence factor of speckle from a multi-row probe," in *1999 IEEE Ultrasonics Symposium. Proceedings. International Symposium (Cat. No. 99CH37027)*, 1999, pp. 1257-1260.

[36] T. Kirchner, F. Sattler, J. Gröhl, and L. Maier-Hein, "Signed real-time delay multiply and sum beamforming for multispectral photoacoustic imaging," *Journal of Imaging,* vol. 4, p. 121, 2018.

[37] M. Mozaffarzadeh, A. Hariri, C. Moore, and J. V. Jokerst, "The double-stage delay-multiply-and-sum image reconstruction method improves imaging quality in a led-based photoacoustic array scanner," *Photoacoustics,* vol. 12, pp. 22-29, 2018.

[38] J. Park, S. Jeon, J. Meng, L. Song, J. S. Lee, and C. Kim, "Delay-multiply-and-sum-based synthetic aperture focusing in photoacoustic microscopy," *Journal of biomedical optics,* vol. 21, p. 036010, 2016.

[39] Z. Guo, C. Li, L. Song, and L. V. Wang, "Compressed sensing in photoacoustic tomography in vivo," *Journal of biomedical optics,* vol. 15, p. 021311, 2010.

[40] M. Mozaffarzadeh, A. Mahloojifar, M. Nasiriavanaki, and M. Orooji, "Model-based photoacoustic image reconstruction using compressed sensing and smoothed L0 norm," in *Photons Plus Ultrasound: Imaging and Sensing 2018*, 2018, p. 104943Z.

[41] J. Provost and F. Lesage, "The application of compressed sensing for photo-acoustic tomography," *IEEE transactions on medical imaging,* vol. 28, pp. 585-594, 2008.

[42] M. W. Kim, G.-S. Jeng, I. Pelivanov, and M. O'Donnell, "Deep-learning Image Reconstruction for Real-time Photoacoustic System," *IEEE Transactions on Medical Imaging,* 2020.

[43] D. Allman, A. Reiter, and M. A. L. Bell, "Photoacoustic source detection and reflection artifact removal enabled by deep learning," *IEEE transactions on medical imaging,* vol. 37, pp. 1464-1477, 2018.

[44] K. Johnstonbaugh, S. Agrawal, D. A. Durairaj, C. Fadden, A. Dangi, S. P. K. Karri*, et al.*, "A deep learning approach to photoacoustic wavefront localization in deep-tissue medium," *IEEE Transactions on Ultrasonics, Ferroelectrics, and Frequency Control,* 2020.

[45] H. Lan, D. Jiang, C. Yang, F. Gao, and F. Gao, "Y-Net: Hybrid deep learning image reconstruction for photoacoustic tomography in vivo," *Photoacoustics,* vol. 20, p. 100197, 2020.

[46] C. Kim, T. N. Erpelding, L. Jankovic, M. D. Pashley, and L. V. Wang, "Deeply penetrating in vivo photoacoustic imaging using a clinical ultrasound array system," *Biomedical optics express,* vol. 1, pp. 278-284, 2010.

[47] M. Jaeger, D. C. Harris-Birtill, A. G. Gertsch-Grover, E. O'Flynn, and J. C. Bamber, "Deformation-compensated averaging for clutter reduction in epiphotoacoustic imaging in vivo," *Journal of biomedical Optics,* vol. 17, p. 066007, 2012.

[48] S. A. Telenkov, R. Alwi, and A. Mandelis, "Photoacoustic correlation signal-to-noise ratio enhancement by coherent averaging and optical waveform optimization," *Review of Scientific Instruments,* vol. 84, p. 104907, 2013.

[49] H. J. Kang, M. A. L. Bell, X. Guo, and E. M. Boctor, "Spatial angular compounding of photoacoustic images," *IEEE transactions on medical imaging,* vol. 35, pp. 1845-1855, 2016.

[50] E. R. Hill, W. Xia, M. J. Clarkson, and A. E. Desjardins, "Identification and removal of laser-induced noise in photoacoustic imaging using singular value decomposition," *Biomedical optics express,* vol. 8, pp. 68-77, 2017.

[51] M. K. A. Singh, M. Jaeger, M. Frenz, and W. Steenbergen, "Photoacoustic reflection artifact reduction using photoacoustic-guided focused ultrasound: comparison between plane-wave and element-by-element synthetic backpropagation approach," *Biomedical optics express,* vol. 8, pp. 2245-2260, 2017.

[52] H. K. Zhang, M. A. L. Bell, X. Guo, H. J. Kang, and E. M. Boctor, "Synthetic-aperture based photoacoustic re-beamforming (SPARE) approach using beamformed ultrasound data," *Biomedical optics express,* vol. 7, pp. 3056-3068, 2016.

[53] B. M. Asl and A. Mahloojifar, "Minimum variance beamforming combined with adaptive coherence weighting applied to medical ultrasound imaging," *IEEE transactions on ultrasonics, ferroelectrics, and frequency control,* vol. 56, pp. 1923-1931, 2009.

[54] J.-F. Synnevag, A. Austeng, and S. Holm, "Benefits of minimum-variance beamforming in medical ultrasound imaging," *IEEE transactions on ultrasonics, ferroelectrics, and frequency control,* vol. 56, pp. 1868-1879, 2009.

[55] M. Mozaffarzadeh, A. Mahloojifar, M. Nasiriavanaki, and M. Orooji, "Eigenspace-based minimum variance adaptive beamformer combined with delay multiply and sum:

experimental study," in *Photonics in Dermatology and Plastic Surgery 2018*, 2018, p. 1046717.

[56] S. Shamekhi, V. Periyasamy, M. Pramanik, M. Mehrmohammadi, and B. M. Asl, "Eigenspace-based minimum variance beamformer combined with sign coherence factor: Application to linear-array photoacoustic imaging," *Ultrasonics,* p. 106174, 2020.

[57] R. A. Mukaddim, R. Ahmed, and T. Varghese, "Sub-aperture Processing Based Adaptive Beamforming for Photoacoustic Imaging," *IEEE transactions on ultrasonics, ferroelectrics, and frequency control* 2021.

[58] G. Matrone, A. S. Savoia, G. Caliano, and G. Magenes, "The delay multiply and sum beamforming algorithm in ultrasound B-mode medical imaging," *IEEE transactions on medical imaging,* vol. 34, pp. 940-949, 2014.

[59] M. Mozaffarzadeh, A. Mahloojifar, M. Orooji, S. Adabi, and M. Nasiriavanaki, "Double-stage delay multiply and sum beamforming algorithm: Application to linear-array photoacoustic imaging," *IEEE Transactions on Biomedical Engineering,* vol. 65, pp. 31-42, 2017.

[60] X. Ma, C. Peng, J. Yuan, Q. Cheng, G. Xu, X. Wang*, et al.*, "Multiple delay and sum with enveloping beamforming algorithm for photoacoustic imaging," *IEEE Transactions on Medical Imaging,* vol. 39, pp. 1812-1821, 2019.

[61] A. Alshaya, S. Harput, A. M. Moubark, D. M. Cowell, J. McLaughlan, and S. Freear, "Spatial resolution and contrast enhancement in photoacoustic imaging with filter delay multiply and sum beamforming technique," in *2016 IEEE International Ultrasonics Symposium (IUS)*, 2016, pp. 1-4.

[62] S. Jeon, E.-Y. Park, W. Choi, R. Managuli, K. jong Lee, and C. Kim, "Real-time delay-multiply-and-sum beamforming with coherence factor for in vivo clinical photoacoustic imaging of humans," *Photoacoustics,* vol. 15, p. 100136, 2019.

[63] L. V. Wang, M.-L. Li, H. F. Zhang, K. Maslov, and G. Stoica, "High-resolution photoacoustic tomography in vivo," in *3rd IEEE International Symposium on Biomedical Imaging: Nano to Macro, 2006.*, 2006, pp. 1204-1207.

[64] Y.-H. Wang and P.-C. Li, "SNR-dependent coherence-based adaptive imaging for high-frame-rate ultrasonic and photoacoustic imaging," *IEEE transactions on ultrasonics, ferroelectrics, and frequency control,* vol. 61, pp. 1419-1432, 2014.

[65] P. V. Chitnis, O. Aristizábal, E. Filoux, A. Sampathkumar, J. Mamou, and J. A. Ketterling, "Coherence-weighted synthetic focusing applied to photoacoustic imaging using a high-frequency annular-array transducer," *Ultrasonic imaging,* vol. 38, pp. 32-43, 2016.

[66] M. Mozaffarzadeh, Y. Yan, M. Mehrmohammadi, and B. Makkiabadi, "Enhanced linear-array photoacoustic beamforming using modified coherence factor," *Journal of biomedical optics,* vol. 23, p. 026005, 2018.

[67] M. Mozaffarzadeh, B. Makkiabadi, M. Basij, and M. Mehrmohammadi, "Image improvement in linear-array photoacoustic imaging using high resolution coherence factor weighting technique," *BMC Biomedical Engineering,* vol. 1, p. 10, 2019.

[68] M. A. L. Bell, R. Goswami, J. A. Kisslo, J. J. Dahl, and G. E. Trahey, "Short-lag spatial coherence imaging of cardiac ultrasound data: Initial clinical results," *Ultrasound in medicine & biology,* vol. 39, pp. 1861-1874, 2013.

[69] M. A. Lediju, G. E. Trahey, B. C. Byram, and J. J. Dahl, "Short-lag spatial coherence of backscattered echoes: Imaging characteristics," *IEEE transactions on ultrasonics, ferroelectrics, and frequency control,* vol. 58, pp. 1377-1388, 2011.

[70] B. Pourebrahimi, S. Yoon, D. Dopsa, and M. C. Kolios, "Improving the quality of photoacoustic images using the short-lag spatial coherence imaging technique," in *Photons Plus Ultrasound: Imaging and Sensing 2013*, 2013, p. 85813Y.

[71] E. A. Gonzalez and M. A. L. Bell, "GPU implementation of photoacoustic short-lag spatial coherence imaging for improved image-guided interventions," *Journal of Biomedical Optics,* vol. 25, p. 077002, 2020.

[72] E. A. Gonzalez, A. Jain, and M. A. L. Bell, "Combined ultrasound and photoacoustic image guidance of spinal pedicle cannulation demonstrated with intact ex vivo specimens," *IEEE Transactions on Biomedical Engineering,* 2020.

[73] M. T. Graham and M. A. L. Bell, "Photoacoustic spatial coherence theory and applications to coherence-based image contrast and resolution," *IEEE Transactions on Ultrasonics, Ferroelectrics, and Frequency Control,* vol. 67, pp. 2069-2084, 2020.

[74] J. T. Mora, X. Feng, N. Nyayapathi, J. Xia, and L. Gao, "Generalized spatial coherence reconstruction for photoacoustic computed tomography," *Journal of Biomedical Optics,* vol. 26, p. 046002, 2021.

[75] S. Govinahallisathyanarayana, B. Ning, R. Cao, S. Hu, and J. A. Hossack, "Dictionary learning-based reverberation removal enables depth-resolved photoacoustic microscopy of cortical microvasculature in the mouse brain," *Scientific reports,* vol. 8, pp. 1-12, 2018.

[76] P. Omidi, M. Zafar, M. Mozaffarzadeh, A. Hariri, X. Haung, M. Orooji*, et al.*, "A novel dictionary-based image reconstruction for photoacoustic computed tomography," *Applied Sciences,* vol. 8, p. 1570, 2018.

[77] R. Paridar, M. Mozaffarzadeh, V. Periyasamy, M. Pramanik, M. Mehrmohammadi, and M. Orooji, "Sparsity-based beamforming to enhance two-dimensional linear-array photoacoustic tomography," *Ultrasonics,* vol. 96, pp. 55-63, 2019.

[78] G. Paltauf, J. Viator, S. Prahl, and S. Jacques, "Iterative reconstruction algorithm for optoacoustic imaging," *The Journal of the Acoustical Society of America,* vol. 112, pp. 1536-1544, 2002.

[79] P. Ephrat, L. Keenlislide, A. Seabrook, F. S. Prato, and J. J. Carson, "Three-dimensional photoacoustic imaging by sparse-array detection and iterative image reconstruction," *Journal of Biomedical Optics,* vol. 13, p. 054052, 2008.

[80] Y. Xu and L. V. Wang, "Effects of acoustic heterogeneity in breast thermoacoustic tomography," *IEEE transactions on ultrasonics, ferroelectrics, and frequency control,* vol. 50, pp. 1134-1146, 2003.

[81] R. Shang, R. Archibald, A. Gelb, and G. P. Luke, "Sparsity-based photoacoustic image reconstruction with a linear array transducer and direct measurement of the forward model," *Journal of biomedical optics,* vol. 24, p. 031015, 2018.

[82] D. L. Donoho, "Compressed sensing," *IEEE Transactions on information theory,* vol. 52, pp. 1289-1306, 2006.

[83] J. M. Bioucas-Dias and M. A. Figueiredo, "A new TwIST: Two-step iterative shrinkage/thresholding algorithms for image restoration," *IEEE Transactions on Image processing,* vol. 16, pp. 2992-3004, 2007.

[84] S. Vilov, B. Arnal, E. Hojman, Y. C. Eldar, O. Katz, and E. Bossy, "Super-resolution photoacoustic and ultrasound imaging with sparse arrays," *Scientific reports,* vol. 10, pp. 1-8, 2020.

[85] F. Liu, X. Gong, L. V. Wang, J. Guan, L. Song, and J. Meng, "Dictionary learning sparse-sampling reconstruction method for in-vivo 3-D photoacoustic computed tomography," *Biomedical optics express,* vol. 10, pp. 1660-1677, 2019.

[86] I. Steinberg, J. Kim, M. K. Schneider, D. Hyun, A. Zlitni, S. M. Hooper*, et al.*, "Superiorized Photo-Acoustic Non-NEgative Reconstruction (SPANNER) for Clinical Photoacoustic Imaging," *IEEE Transactions on Medical Imaging,* 2021.

[87] M. Graham, F. Assis, D. Allman, A. Wiacek, E. Gonzalez, M. Gubbi*, et al.*, "In vivo demonstration of photoacoustic image guidance and robotic visual servoing for cardiac catheter-based interventions," *IEEE transactions on medical imaging,* vol. 39, pp. 1015-1029, 2019.

[88] D. Waibel, J. Gröhl, F. Isensee, T. Kirchner, K. Maier-Hein, and L. Maier-Hein, "Reconstruction of initial pressure from limited view photoacoustic images using deep learning," in *Photons Plus Ultrasound: Imaging and Sensing 2018*, 2018, p. 104942S.

[89] T. Vu, M. Li, H. Humayun, Y. Zhou, and J. Yao, "A generative adversarial network for artifact removal in photoacoustic computed tomography with a linear-array transducer," *Experimental Biology and Medicine,* vol. 245, pp. 597-605, 2020.

[90] N. Awasthi, G. Jain, S. K. Kalva, M. Pramanik, and P. K. Yalavarthy, "Deep Neural Network Based Sinogram Super-resolution and Bandwidth Enhancement for Limited-data Photoacoustic Tomography," *IEEE Transactions on Ultrasonics, Ferroelectrics, and Frequency Control,* 2020.

[91] H. K. Zhang, "Democratizing LED-Based Photoacoustic Imaging with Adaptive Beamforming and Deep Convolutional Neural Network," in *LED-Based Photoacoustic Imaging*, ed: Springer, 2020, pp. 183-202.

[92] E. M. A. Anas, H. K. Zhang, C. Audigier, and E. M. Boctor, "Robust photoacoustic beamforming using dense convolutional neural networks," in *Simulation, Image Processing, and Ultrasound Systems for Assisted Diagnosis and Navigation*, ed: Springer, 2018, pp. 3-11.

[93] A. Reiter and M. A. L. Bell, "A machine learning approach to identifying point source locations in photoacoustic data," in *Photons Plus Ultrasound: Imaging and Sensing 2017*, 2017, p. 100643J.

[94] A. Hariri, K. Alipour, Y. Mantri, J. P. Schulze, and J. V. Jokerst, "Deep learning improves contrast in low-fluence photoacoustic imaging," *Biomedical optics express,* vol. 11, pp. 3360-3373, 2020.

[95] S. L. Jacques, "Coupling 3-D Monte Carlo light transport in optically heterogeneous tissues to photoacoustic signal generation," *Photoacoustics,* vol. 2, pp. 137-142, 2014.

[96] B. E. Treeby and B. T. Cox, "k-Wave: MATLAB toolbox for the simulation and reconstruction of photoacoustic wave fields," *Journal of biomedical optics,* vol. 15, p. 021314, 2010.

[97] O. Ronneberger, P. Fischer, and T. Brox, "U-net: Convolutional networks for biomedical image segmentation," in *International Conference on Medical image computing and computer-assisted intervention*, 2015, pp. 234-241.

[98] Z. Sun and X. Yan, "A deep learning method for limited-view intravascular photoacoustic image reconstruction," *Journal of Medical Imaging and Health Informatics,* vol. 10, pp. 2707-2713, 2020.

[99] E. M. A. Anas, H. K. Zhang, J. Kang, and E. Boctor, "Enabling fast and high quality LED photoacoustic imaging: a recurrent neural networks based approach," *Biomedical optics express,* vol. 9, pp. 3852-3866, 2018.

[100] J. Feng, J. Deng, Z. Li, Z. Sun, H. Dou, and K. Jia, "End-to-end Res-Unet based reconstruction algorithm for photoacoustic imaging," *Biomedical optics express,* vol. 11, pp. 5321-5340, 2020.

[101] K. Simonyan and A. Zisserman, "Very deep convolutional networks for large-scale image recognition," *arXiv preprint arXiv:1409.1556,* 2014.

[102] S. Ren, K. He, R. Girshick, and J. Sun, "Faster r-cnn: Towards real-time object detection with region proposal networks," *arXiv preprint arXiv:1506.01497,* 2015.

[103] R. Girshick, "Fast r-cnn," in *Proceedings of the IEEE international conference on computer vision*, 2015, pp. 1440-1448.

[104] P. Liu, H. Zhang, W. Lian, and W. Zuo, "Multi-level wavelet convolutional neural networks," *IEEE Access,* vol. 7, pp. 74973-74985, 2019.

[105] A. DiSpirito III, T. Vu, M. Pramanik, and J. Yao, "Sounding out the hidden data: A concise review of deep learning in photoacoustic imaging," *Experimental Biology and Medicine,* p. 15353702211000310, 2021.

[106] J. Gröhl, M. Schellenberg, K. Dreher, and L. Maier-Hein, "Deep learning for biomedical photoacoustic imaging: A review," *Photoacoustics,* p. 100241, 2021.

[107] C. Yang, H. Lan, F. Gao, and F. Gao, "Review of deep learning for photoacoustic imaging," *Photoacoustics,* vol. 21, p. 100215, 2021.

[108] A. Hauptmann and B. T. Cox, "Deep Learning in Photoacoustic Tomography: Current approaches and future directions," *Journal of Biomedical Optics,* vol. 25, p. 112903, 2020.

[109] H. Deng, H. Qiao, Q. Dai, and C. Ma, "Deep learning in photoacoustic imaging: a review," *Journal of Biomedical Optics,* vol. 26, p. 040901, 2021.

[110] K. He, X. Zhang, S. Ren, and J. Sun, "Deep residual learning for image recognition," in *Proceedings of the IEEE conference on computer vision and pattern recognition*, 2016, pp. 770-778.

[111] E. Hysi, M. N. Fadhel, M. J. Moore, J. Zalev, E. M. Strohm, and M. C. Kolios, "Insights into photoacoustic speckle and applications in tumor characterization," *Photoacoustics,* vol. 14, pp. 37-48, 2019.

[112] F. J. O. Landa, X. L. Deán-Ben, R. Sroka, and D. Razansky, "Volumetric optoacoustic temperature mapping in photothermal therapy," *Scientific reports,* vol. 7, pp. 1-8, 2017.

[113] G.-S. Jeng, M.-L. Li, M. Kim, S. J. Yoon, J. J. Pitre, D. S. Li*, et al.*, "Real-time interleaved spectroscopic photoacoustic and ultrasound (PAUS) scanning with simultaneous fluence compensation and motion correction," *Nature communications,* vol. 12, pp. 1-12, 2021.

[114] S. Kim, Y.-S. Chen, G. P. Luke, and S. Y. Emelianov, "In vivo three-dimensional spectroscopic photoacoustic imaging for monitoring nanoparticle delivery," *Biomedical optics express,* vol. 2, pp. 2540-2550, 2011.

[115] G. P. Luke and S. Y. Emelianov, "Optimization of in vivo spectroscopic photoacoustic imaging by smart optical wavelength selection," *Optics letters,* vol. 39, pp. 2214-2217, 2014.

[116] H. Yoon, G. P. Luke, and S. Y. Emelianov, "Impact of depth-dependent optical attenuation on wavelength selection for spectroscopic photoacoustic imaging," *Photoacoustics,* vol. 12, pp. 46-54, 2018.

[117] R. Hochuli, L. An, P. C. Beard, and B. T. Cox, "Estimating blood oxygenation from photoacoustic images: can a simple linear spectroscopic inversion ever work?," *Journal of biomedical optics,* vol. 24, p. 121914, 2019.

[118] S. Tzoumas, A. Nunes, I. Olefir, S. Stangl, P. Symvoulidis, S. Glasl*, et al.*, "Eigenspectra optoacoustic tomography achieves quantitative blood oxygenation imaging deep in tissues," *Nature communications,* vol. 7, pp. 1-10, 2016.

[119] M. Li, Y. Tang, and J. Yao, "Photoacoustic tomography of blood oxygenation: a mini review," *Photoacoustics,* vol. 10, pp. 65-73, 2018.

[120] F. Cao, Z. Qiu, H. Li, and P. Lai, "Photoacoustic imaging in oxygen detection," *Applied Sciences,* vol. 7, p. 1262, 2017.

[121] X. Zhou, N. Akhlaghi, K. A. Wear, B. S. Garra, T. J. Pfefer, and W. C. Vogt, "Evaluation of fluence correction algorithms in multispectral photoacoustic imaging," *Photoacoustics,* vol. 19, p. 100181, 2020.

[122] Z. Guo, S. Hu, and L. V. Wang, "Calibration-free absolute quantification of optical absorption coefficients using acoustic spectra in 3-D photoacoustic microscopy of biological tissue," *Optics letters,* vol. 35, pp. 2067-2069, 2010.

[123] L. Wang, S. L. Jacques, and L. Zheng, "MCML—Monte Carlo modeling of light transport in multi-layered tissues," *Computer methods and programs in biomedicine,* vol. 47, pp. 131-146, 1995.

[124] D. Marti, R. N. Aasbjerg, P. E. Andersen, and A. K. Hansen, "MCmatlab: an open-source, user-friendly, MATLAB-integrated three-dimensional Monte Carlo light transport solver with heat diffusion and tissue damage," *Journal of biomedical optics,* vol. 23, p. 121622, 2018.

[125] S. Bu, Z. Liu, T. Shiina, K. Kondo, M. Yamakawa, K. Fukutani*, et al.*, "Model-based reconstruction integrated with fluence compensation for photoacoustic tomography," *IEEE transactions on biomedical engineering,* vol. 59, pp. 1354-1363, 2012.

[126] R. Bulsink, M. Kuniyil Ajith Singh, M. Xavierselvan, S. Mallidi, W. Steenbergen, and K. J. Francis, "Oxygen Saturation Imaging Using LED-Based Photoacoustic System," *Sensors,* vol. 21, p. 283, 2021.

[127] Y. Liu, H. Jiang, and Z. Yuan, "Two schemes for quantitative photoacoustic tomography based on Monte Carlo simulation," *Medical physics,* vol. 43, pp. 3987-3997, 2016.

[128] Z. Yuan and H. Jiang, "Quantitative photoacoustic tomography: Recovery of optical absorption coefficient maps of heterogeneous media," *Applied physics letters,* vol. 88, p. 231101, 2006.

[129] C. Bench, A. Hauptmann, and B. T. Cox, "Toward accurate quantitative photoacoustic imaging: learning vascular blood oxygen saturation in three dimensions," *Journal of Biomedical Optics,* vol. 25, p. 085003, 2020.

[130] J. Laufer, D. Delpy, C. Elwell, and P. Beard, "Quantitative spatially resolved measurement of tissue chromophore concentrations using photoacoustic spectroscopy: application to the measurement of blood oxygenation and haemoglobin concentration," *Physics in Medicine & Biology,* vol. 52, p. 141, 2006.

[131] M. A. Naser, D. R. Sampaio, N. M. Muñoz, C. A. Wood, T. M. Mitcham, W. Stefan*, et al.*, "Improved photoacoustic-based oxygen saturation estimation with SNR-regularized local fluence correction," *IEEE transactions on medical imaging,* vol. 38, pp. 561-571, 2018.

[132] M. A. Naser, "Improving the reconstruction image contrast of time-domain diffuse optical tomography using high accuracy Jacobian matrix," *Biomedical Physics & Engineering Express,* vol. 2, p. 015015, 2016.

[133] J. Buchmann, B. Kaplan, S. Powell, S. Prohaska, and J. Laufer, "Quantitative PA tomography of high resolution 3-D images: Experimental validation in a tissue phantom," *Photoacoustics,* vol. 17, p. 100157, 2020.

[134] J. Buchmann, B. A. Kaplan, S. Powell, S. Prohaska, and J. Laufer, "Three-dimensional quantitative photoacoustic tomography using an adjoint radiance Monte Carlo model and gradient descent," *Journal of biomedical optics,* vol. 24, p. 066001, 2019.

[135] B. T. Cox, S. R. Arridge, K. P. Köstli, and P. C. Beard, "Two-dimensional quantitative photoacoustic image reconstruction of absorption distributions in scattering media by use of a simple iterative method," *Applied Optics,* vol. 45, pp. 1866-1875, 2006.

[136] F. M. Brochu, J. Brunker, J. Joseph, M. R. Tomaszewski, S. Morscher, and S. E. Bohndiek, "Towards quantitative evaluation of tissue absorption coefficients using light fluence correction in optoacoustic tomography," *IEEE transactions on medical imaging,* vol. 36, pp. 322-331, 2016.

[137] M. Fonseca, E. Malone, F. Lucka, R. Ellwood, L. An, S. Arridge*, et al.*, "Three-dimensional photoacoustic imaging and inversion for accurate quantification of chromophore distributions," in *Photons Plus Ultrasound: Imaging and Sensing 2017*, 2017, p. 1006415.

[138] M. Kim, G.-S. Jeng, M. O'Donnell, and I. Pelivanov, "Correction of wavelength-dependent laser fluence in swept-beam spectroscopic photoacoustic imaging with a hand-held probe," *Photoacoustics,* vol. 19, p. 100192, 2020.

[139] L. Yin, Q. Wang, Q. Zhang, and H. Jiang, "Tomographic imaging of absolute optical absorption coefficient in turbid media using combined photoacoustic and diffusing light measurements," *Optics letters,* vol. 32, pp. 2556-2558, 2007.

[140] K. Daoudi, A. Hussain, E. Hondebrink, and W. Steenbergen, "Correcting photoacoustic signals for fluence variations using acousto-optic modulation," *Optics express,* vol. 20, pp. 14117-14129, 2012.

[141] A. Hussain, W. Petersen, J. Staley, E. Hondebrink, and W. Steenbergen, "Quantitative blood oxygen saturation imaging using combined photoacoustics and acousto-optics," *Optics letters,* vol. 41, pp. 1720-1723, 2016.

[142] L. Wang, S. L. Jacques, and X. Zhao, "Continuous-wave ultrasonic modulation of scattered laser light to image objects in turbid media," *Optics letters,* vol. 20, pp. 629-631, 1995.

[143] R. Zemp, S. Sakadžić, and L. V. Wang, "Stochastic explanation of speckle contrast detection in ultrasound-modulated optical tomography," *Physical Review E,* vol. 73, p. 061920, 2006.

[144] A. Q. Bauer, R. E. Nothdurft, J. P. Culver, T. N. Erpelding, and L. V. Wang, "Quantitative photoacoustic imaging: correcting for heterogeneous light fluence distributions using diffuse optical tomography," *Journal of Biomedical Optics,* vol. 16, p. 096016, 2011.

[145] D. A. Boas, D. H. Brooks, E. L. Miller, C. A. DiMarzio, M. Kilmer, R. J. Gaudette*, et al.*, "Imaging the body with diffuse optical tomography," *IEEE signal processing magazine,* vol. 18, pp. 57-75, 2001.

[146] S. V. Patwardhan and J. P. Culver, "Quantitative diffuse optical tomography for small animals using an ultrafast gated image intensifier," *Journal of biomedical optics,* vol. 13, p. 011009, 2008.

[147] P. D. Kumavor, C. Xu, A. Aguirre, J. K. Gamelin, Y. Ardeshirpour, B. Tavakoli*, et al.*, "Target detection and quantification using a hybrid hand-held diffuse optical tomography and photoacoustic tomography system," *Journal of biomedical optics,* vol. 16, p. 046010, 2011.

[148] J. C. Ranasinghesagara and R. J. Zemp, "Combined photoacoustic and oblique-incidence diffuse reflectance system for quantitative photoacoustic imaging in turbid media," *Journal of biomedical optics,* vol. 15, p. 046016, 2010.

[149] R. J. Zemp, "Quantitative photoacoustic tomography with multiple optical sources," *Applied optics,* vol. 49, pp. 3566-3572, 2010.

[150] J. R. Rajian, P. L. Carson, and X. Wang, "Quantitative photoacoustic measurement of tissue optical absorption spectrum aided by an optical contrast agent," *Optics express,* vol. 17, pp. 4879-4889, 2009.

[151] I. Olefir, S. Tzoumas, H. Yang, and V. Ntziachristos, "A Bayesian approach to eigenspectra optoacoustic tomography," *IEEE transactions on medical imaging,* vol. 37, pp. 2070-2079, 2018.

[152] J. Xia, A. Danielli, Y. Liu, L. Wang, K. Maslov, and L. V. Wang, "Calibration-free quantification of absolute oxygen saturation based on the dynamics of photoacoustic signals," *Optics letters,* vol. 38, pp. 2800-2803, 2013.

[153] M. N. Fadhel, E. Hysi, H. Assi, and M. C. Kolios, "Fluence-matching technique using photoacoustic radiofrequency spectra for improving estimates of oxygen saturation," *Photoacoustics,* vol. 19, p. 100182, 2020.

[154] M. N. Fadhel and M. C. Kolios, "Method and system for fluence matching in photoacoustic imaging," ed: Google Patents, 2020.

[155] T. Kirchner, J. Gröhl, and L. Maier-Hein, "Context encoding enables machine learning-based quantitative photoacoustics," *Journal of biomedical optics,* vol. 23, p. 056008, 2018.

[156] C. Cai, K. Deng, C. Ma, and J. Luo, "End-to-end deep neural network for optical inversion in quantitative photoacoustic imaging," *Optics letters,* vol. 43, pp. 2752-2755, 2018.

[157] M. Z. Alom, C. Yakopcic, M. Hasan, T. M. Taha, and V. K. Asari, "Recurrent residual U-Net for medical image segmentation," *Journal of Medical Imaging,* vol. 6, p. 014006, 2019.

[158] C. Yang, H. Lan, H. Zhong, and F. Gao, "Quantitative photoacoustic blood oxygenation imaging using deep residual and recurrent neural network," in *2019 IEEE 16th International Symposium on Biomedical Imaging (ISBI 2019)*, 2019, pp. 741-744.

[159] T. Chen, T. Lu, S. Song, S. Miao, F. Gao, and J. Li, "A deep learning method based on U-Net for quantitative photoacoustic imaging," in *Photons Plus Ultrasound: Imaging and Sensing 2020*, 2020, p. 112403V.

[160] G. P. Luke, K. Hoffer-Hawlik, A. C. Van Namen, and R. Shang, "O-Net: a convolutional neural network for quantitative photoacoustic image segmentation and oximetry," *arXiv preprint arXiv:1911.01935,* 2019.

[161] J. Gröhl, T. Kirchner, T. J. Adler, L. Hacker, N. Holzwarth, A. Hernández-Aguilera*, et al.*, "Learned spectral decoloring enables photoacoustic oximetry," *Scientific reports,* vol. 11, pp. 1-12, 2021.

[162] D. A. Durairaj, S. Agrawal, K. Johnstonbaugh, H. Chen, S. P. K. Karri, and S.-R. Kothapalli, "Unsupervised deep learning approach for photoacoustic spectral unmixing," in *Photons Plus Ultrasound: Imaging and Sensing 2020*, 2020, p. 112403H.

[163] I. Olefir, S. Tzoumas, C. Restivo, P. Mohajerani, L. Xing, and V. Ntziachristos, "Deep Learning-Based Spectral Unmixing for Optoacoustic Imaging of Tissue Oxygen Saturation," *IEEE transactions on medical imaging,* vol. 39, pp. 3643-3654, 2020.

[164] C. Yang and F. Gao, "EDA-Net: dense aggregation of deep and shallow information achieves quantitative photoacoustic blood oxygenation imaging deep in human breast," in *International Conference on Medical Image Computing and Computer-Assisted Intervention*, 2019, pp. 246-254.

Chapter 4

Bayesian Regularization for Cardiac Elastography

This chapter[1] focuses on examining the feasibility of applying Bayesian regularization with a hierarchical block matching algorithm for cardiac elastography [1-4]. Cardiac elastography (CE) is an ultrasound radio-frequency (RF) echo-signal based speckle tracking technique for cardiac strain imaging (CSI). Bayesian regularization has been previously implemented by our group [5] for a hierarchical block matching algorithm for carotid elastography [6]. Application of the proposed method provided clinically significant results for *in vivo* plaque imaging [7-9]. Our group previously reported the use of a hierarchical block matching algorithm for CE [10-13]. However, Bayesian regularization was not applied and validated for CE.

This chapter reports on three main contributions. First, a complete strain estimation pipeline for incorporating Bayesian regularization-based hierarchical block matching algorithm, Lagrangian description of motion and myocardial polar strain estimation is presented. Second, we present results with a canine cardiac deformation model [12] and an *in vivo* healthy murine model to evaluate the performance of the hierarchical block matching algorithm with and without Bayesian regularization. Rigorous quantitative analysis demonstrates that Bayesian regularization improves the quality of strain imaging for CE. Third, we present results from an initial comparison study of the proposed strain estimation pipeline against a commercially available CSI software to demonstrate its *in vivo* applicability.

[1] R. Al Mukaddim, N. H. Meshram, C. C. Mitchell, and T. Varghese, "Hierarchical Motion Estimation With Bayesian Regularization in Cardiac Elastography: Simulation and *in vivo* Validation." *IEEE Transactions on Ultrasonics, Ferroelectrics, and Frequency Control*, vol. 66, no. 11, pp. 1708 – 1722 (2019) PMCID: PMC6855404

4.1 Cardiac Strain Estimation Framework with Bayesian Regularized Hierarchical Motion Estimation

4.1.1 Inter-frame Displacement Estimation

In this study, a multi-level block matching algorithm with Bayesian regularization [5] was used for displacement tracking of both simulation and *in vivo* RF data. Inter-frame displacement estimation was performed over a cardiac cycle starting from end-diastolic (ED) phase. We use the term pre-deformation and post-deformation image to describe the current and the next frame used for inter-frame displacement estimation, respectively. Initially, both pre-deformation and post-deformation RF data were up-sampled in the lateral direction (perpendicular to beam propagation direction) by a factor of two using a windowed Sinc interpolator to improve lateral displacement estimates [14-16]. Following upsampling, a coarse to fine pyramid with three levels were constructed for performing an iterative coarse-to-fine motion estimation [5, 11, 13, 17, 18]. Pyramid construction was performed by applying decimation factors presented in Table 4.1 to original RF data with Gaussian smoothening having a variance of $(\frac{d_f}{2})^2$ where d_f denotes the decimation factor.

Following pyramid construction, pre and post-deformation data were divided into a rectangular grid of 2-D kernels. 2-D NCC [18] calculation was performed to compare a kernel between the pre to post-deformation RF frame. NCC calculation was restricted within an empirically chosen search region in the post-deformation frame. This process results in a 2-D similarity metric for each estimation location of the rectangular grid. Parameters employed for 2-D NCC are shown in Table 4.1. Progressively decreasing block sizes were used to improve spatial resolution of the estimated displacement vectors.

Table 4.1 Motion Estimation Algorithm Processing Parameters

Parameter	Value
Hierarchical Block-matching parameters	
Levels in multi-resolution pyramid	3
Lateral interpolation factor	2
Axial decimation factors	[3, 2, 1]
Kernel overlaps [Axial, Lateral*]	[10%, 90%]
Lateral decimation factors	[2, 1, 1]
Axial kernel length (Wavelengths)	[8λ, 3λ, 1λ]
Lateral kernel length (A-lines)	[15, 12, 10]
Axial search range (Wavelengths)	[3λ, 2λ, 1λ]
Lateral search range (A-lines)	[5, 5, 3]
Strain filtering threshold [axial strain, lateral strain]	[2.5%, 2.5%]
Bayesian regularization specific parameters	
Axial strain regularization sigma	0.150
Lateral strain regularization sigma	0.075
Number of iterations**	1/3

**Lateral overlap of 90% corresponds to lateral window shift of 3 A-lines*
***Number of iterations was chosen empirically based on the application. For FEA simulation study, one iteration provided good results while in vivo study required three iterations*

To improve motion estimation accuracy, each similarity metric was regularized using a recursive Bayesian regularization algorithm [5, 6]. In brief, the algorithm tries to remove noisy NCC estimates from a given similarity metric using guidance from left, right, top and bottom neighbors of the similarity matrices. This is achieved by formulating regularization as a maximum *a posteriori* estimation problem in a Bayesian framework. The algorithm requires a parameter referred to as strain regularization sigma (SRS), which is related to the maximum expected strain in both axial and lateral directions. SRS parameter values for axial and lateral directions were chosen empirically and listed in Table 4.1. This process results in regularized similarity metrics, which were used in the next stage to generate displacement vectors.

For subsample displacement estimation, parabolic interpolation was used for level 1 to level 2 while the final level employed Sinc interpolation to achieve unbiased estimation [6, 15]. Subsample estimation using 2-D windowed Sinc interpolation was performed using a multilevel global peak finder scheme [19]. A central-difference gradient was used to estimate strain from corresponding displacement vectors for replacing erroneous displacement estimates due to peak-hopping errors. Inter frame displacement vectors generating strain magnitude > 2.5% were replaced using linear interpolation from neighboring displacement estimates with strain magnitudes less than 2.5%. This is done to inhibit the propagation of peak-hopping errors which present as irrationally high strains [6]. After obtaining displacement vectors and strains at the current level, signal re-correlation using matching block alignment and local temporal stretching is performed for the next level. Signal alignment and stretching improves displacement and strain accuracy by reducing signal decorrelation within the matching block [20-23].

To achieve matching block alignment in our multi-level framework, estimated displacement vectors at each level are used to translate the center of post-deformation matching block in the next higher level. Next, in the align and stretch stage a 9 point least squares fit is used to estimate strain. Using the estimated strain, we stretch the post-deformation block of next level using a 2-D windowed Sinc interpolation for resampling and using a scale factor: $S_i = 1 + e_{ii}$ where e_{ii} denotes the normal strain in that direction. This estimation process is repeated until we reach the final level, i.e., level three in this study. At the final level, we perform a 2-D median filtering of estimated displacement vectors with a [5 pixels × 5 pixels] window to remove any outliers. The displacement estimation procedure is summarized in the flowchart in Figure 4.1.

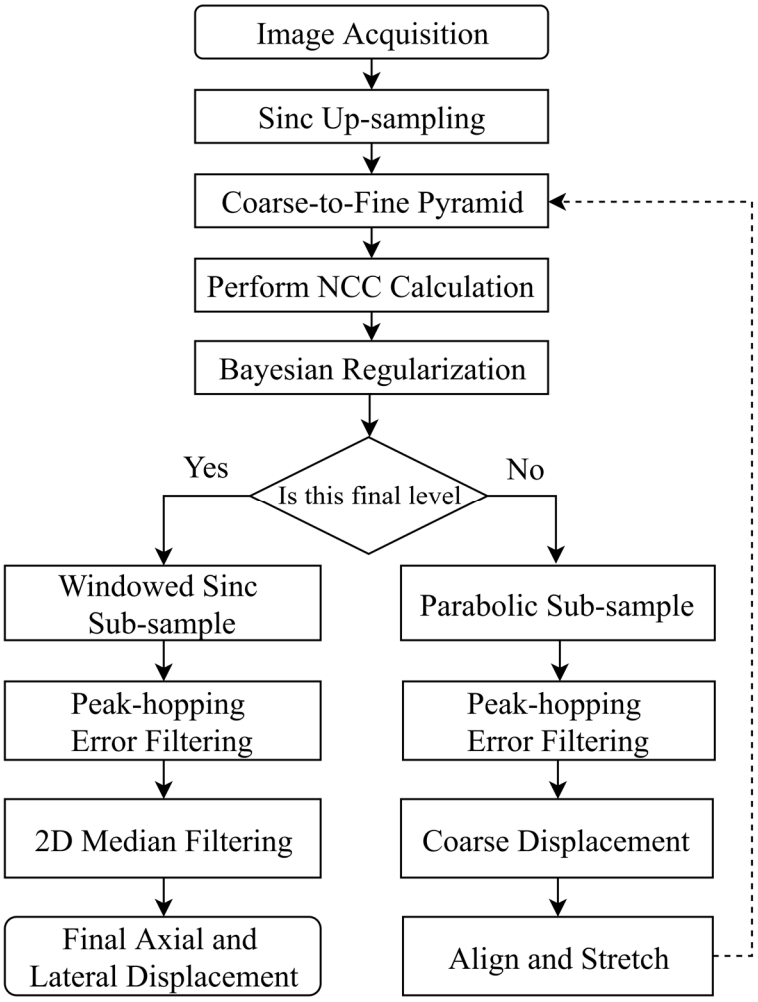

Figure 4.1 Flowchart depicting the various steps involved in the multi-level block matching displacement estimation algorithm with Bayesian regularization. The dotted line indicates that the estimated displacement and strain from the current level guides the search region initialization in the next level.

4.1.2 Lagrangian Description of Motion for Displacement and Polar Strain Estimation

To determine cumulative displacements and strains occurring over a cardiac cycle, inter-frame displacements are integrated over time based on a Lagrangian description of motion. This accumulation process is not trivial as the myocardium changes its location over the cardiac cycle. An ED frame is considered to be the reference frame. Location of each pixel in this frame is defined as the reference state. For every other frame, these locations are updated by translation of axial

and lateral coordinates of pixel locations using the estimated inter-frame axial and lateral displacements respectively. Displacement values derived from updated locations are registered back to reference initial location in the ED frame and accumulated. Pixel registration ensures that the cumulative displacement represents motion along the same tissue geometry [24]. In this way, incremental inter-frame displacements are integrated over a cardiac cycle to obtain cumulative displacement over the cycle. For each individual point, baseline drift is compensated by performing a linear de-trending of temporal displacement and strain curves with the constraint that curves should return to zero after a cardiac cycle [25].

We perform cumulated strain estimation using the resulting cumulated displacement maps. First, the displacement gradient tensor, **G** is calculated, defined as:

$$\mathbf{G} = \begin{pmatrix} \frac{\partial u_x}{\partial x} & \frac{\partial u_x}{\partial y} \\ \frac{\partial u_y}{\partial x} & \frac{\partial u_y}{\partial y} \end{pmatrix} \tag{4.1}$$

where, u_x and u_y denotes estimated displacement in lateral and axial direction respectively. **G** is obtained by differentiating lateral and axial displacement maps using least squares estimator [26] with 0.2 mm and 1 mm kernels respectively. To account for the large myocardial deformation (~30-40%) that occurs from ED to end-systole (ES), an in-plane Lagrangian finite strain tensor, **E** [27-29] is used. **E** is formulated using displacement gradient tensor, **G** as follows [30]:

$$\mathbf{E} = \frac{1}{2}(\mathbf{G} + \mathbf{G}^T + \mathbf{G}^T\mathbf{G}) \tag{4.2}$$

The diagonal components of **E** denoted by e_{xx} and e_{yy} are the cumulative lateral and axial strains respectively.

The strain measure, **E** is coordinate dependent as it involves spatial derivatives in the orthogonal coordinate system used for ultrasound imaging [27, 29]. This poses a challenge in interpretation of these strains in a cardiac coordinate system [31]. In the cardiac coordinate system for apical and parasternal long axis views, we are interested in strains along radial and longitudinal directions, which are defined as follows [28, 31]:

- Radial direction is perpendicular to the endocardial border and provides positive radial strain during contraction. Positive and negative radial strain illustrates thickening and thinning of myocardial walls respectively [32].
- Longitudinal direction is tangential to the endocardial border and provides negative longitudinal strain during contraction. Positive and negative longitudinal strain illustrates lengthening and shortening of the ventricle respectively [32].

To be consistent with the interpretation of strains in the cardiac coordinate system, radial and longitudinal strains are derived from **E** using the coordinate transformation [27]:

$$\mathbf{E}^{rl} = \mathbf{M}\mathbf{E}\mathbf{M}^{T} \tag{4.3}$$

where, **M** is a rotation matrix defined as:

$$\mathbf{M} = \begin{pmatrix} \cos\theta & \sin\theta \\ -\sin\theta & \cos\theta \end{pmatrix} \tag{4.4}$$

where, the superscript rl denotes strain in radial and longitudinal direction respectively in the cardiac coordinate system. The diagonal components of $\mathbf{E}^{rl}$ denoted by e_{rr} and e_{ll} are radial and longitudinal strains respectively. The angle θ used in equation (4.4) is calculated locally along a sampling grid encompassing the entire myocardium. The heart is segmented manually in the ED frame using the B-mode image. This process results in a binary label image. We generate a mesh

of points using this binary label image containing 600 points longitudinally (tangentially) and 40 points radially to the myocardial wall resulting into 24,000 points of interest in the entire myocardium. For a sample point with coordinate value (x_n, y_n), the angle θ was calculated by considering a neighborhood of ten sample points around it along the longitudinal direction and using the following equation for angle of a normal to a line.

$$\theta = \tan^{-1}\left(\frac{x_{n+5} - x_{n-5}}{y_{n-5} - y_{n+5}}\right) \tag{4.5}$$

This angle denotes the radial direction for the point located at (x_n,y_n).

4.2 Experimental Protocol for Validating Proposed CSI Framework

4.2.1 Finite Element Analysis (FEA) Model for Cardiac Elastography

A 3-D FEA model of a healthy canine heart [12] was employed in this study to validate the performance of the proposed strain estimation framework. The original 3-D deformation model of canine heart was developed by the Cardiac Mechanics Research Group at the University of California San Diego (UCSD) [33]. This experimentally validated model allowed simulation of the complex left ventricular mechanics accurately providing a realistic validation setup for cardiac motion estimation algorithms [27, 34]. The original model contained movement of 1296 points located in the canine heart wall acquired at a temporal sampling rate of 250 Hz. Each time point of these movements will correspond to one frame of RF data in the simulation study. These positional deformation information were adapted for ultrasound simulation by a reconstructing a 3-D continuous smooth surface of the canine heart model [12]. Finally, to ensure Rayleigh scattering, over 1×10^6 scatterers were randomly positioned in the myocardium of the cardiac model. From this 3-D model, a 2-D plane was selected to simulate a parasternal long axis (PLAX)

ultrasonic imaging view. To obtain independent strain estimation we utilized the stochastic nature of scatterer generation, generating five independent speckle realizations of the FEA simulation.

A frequency domain ultrasound simulation program [35] was utilized to generate the RF data that incorporated realistic 3-D ultrasound propagation on FEA generated cardiac deformations seeded with a randomly generated scatterer distribution. This simulation approach is used due to its greater flexibility in modelling frequency-dependent ultrasonic imaging properties such as attenuation, dispersion and backscattering over time domain simulation models. The 1-D linear array modeled, consisted of 0.2×10 mm elements with a pitch of 0.2 mm. Conventional Delay and Sum (DAS) beamforming with 128 consecutive elements were utilized to form each A-line. The incident pulse was modeled to be Gaussian shaped with 8 MHz center frequency and 80% bandwidth. The speed of sound and attenuation coefficient were set to 1540 m/s and 0.5 dB/cm-MHz respectively. Each simulated ultrasound image had an 80×100 mm^2 field of view. The ultrasound simulation program related parameters are summarized in Table 4.2. Three regions of interests (ROIs) were placed in anterior, apical and posterior walls of myocardium to quantify the simulated sonographic signal-to-noise ratio (SNR_s). SNR_s calculation was performed using a frequency domain approach described in [36]. The calculated SNR_s for over five scatterer realizations at end-systole frame were 30.38 ± 5.026 dB, 29.34 ± 5.20 dB and 33.76 dB ± 7.64 dB respectively for anterior, apical and posterior wall. Simulation of electronic noise was not performed in this study.

Table 4.2 FEA Simulation Program Parameters

Parameter	Value
Probe specific parameters	
Transducer type	1-D linear array
Number of active elements	128
Single element geometry [width × length]	[0.2 mm × 10 mm]
Pitch	0.2 mm
Aperture size	25.6 mm
Focusing mode	Single
Transmit focus location	40 mm
F-number (Dynamic receive focusing)	1
Number of A-lines	500
Parameters for RF signal reconstruction from scatter frequency response	
Incident pulse	Gaussian-shaped
Center frequency	8 MHz
Pulse bandwidth	80%
Attenuation coefficient	0.5 dB/cm-MHz
Assumed speed of sound	1540.0 m/s
Beamforming method	Delay and sum
RF Sampling frequency	78.84 MHz
Lateral sampling spacing	0.2 mm
Frame rate of acquisition	250 Hz

4.2.2 In vivo Experimental Protocol and Image Acquisition

To validate *in vivo* use of the proposed framework, a 12 weeks old male BALB/CJ mouse obtained from Jackson Labs (ME, USA) was scanned using a Vevo 2100 LAZR imaging system (FUJIFILM VisualSonics, Inc., Toronto, Canada). All *in vivo* procedures were approved by the Institutional Animal Care and Use Committee (IACUC) at the University of Wisconsin-Madison. During the imaging session, the mouse was anesthetized using 1.5% isoflurane with a constant flow of oxygen. Hair was removed from the chest region using depilatory cream. Mouse was placed in the supine position on a heated imaging platform with continuous monitoring of

physiological parameters. High frequency ultrasound imaging was performed using a MS 550D transducer (broadband frequency range of 22– 55 MHz) operating at a center frequency of 40 MHz. 2-D RF data were collected in parasternal long axis (PLAX) view. The field of view was 11×12.08 mm^2 with a sampling frequency of 512 MHz resulting into acquisition of 220 A-lines. Single transmit focusing with the focal depth set at 7 mm from the face of the transducer was used. Imaging frame rate was 235 Hz. 2-D gain (25dB) and time gain compensation (TGC) were adjusted carefully to acquire RF data with optimal signal-to-noise ratio (SNR) for CE. We acquired 1000 frames per imaging plane, which was stored for off-line analysis.

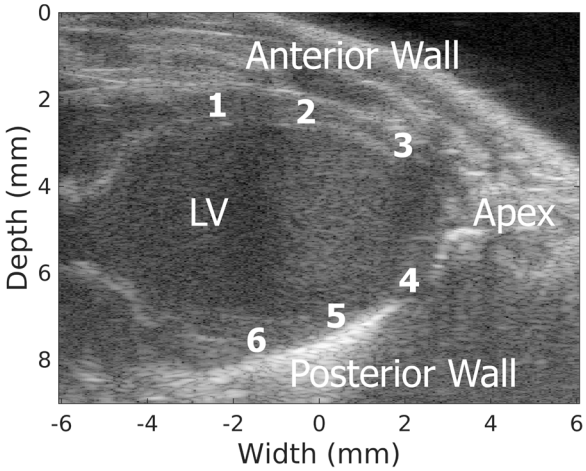

Figure 4.2 Definition of cardiac segments for studying regional variation in displacement and strain. Cardiac segments defined in the PLAX view are: (1) Anterior Base, (2) Anterior Mid, (3) Anterior Apex, (4) Posterior Apex, (5) Posterior Mid and (6) Posterior Base.

4.2.3 Myocardial Region Definition for Segmental Analysis

In this study, we performed segmental analysis of estimated displacement and strains over the entire myocardial wall using American Heart Association (AHA) recommended standard six segment model (employed for global 16-segment model) [37]. Figure 4.2 shows the definition of segments employed for the PLAX view. Segmental analysis was achieved easily as we have already warped the cumulative displacement and strain maps for the ED geometry during

accumulation. Six segments were defined such that all segments have equal length in the ED frame. All the results reported in this work denote displacement and strain measures averaged over the entire cardiac walls on a segment basis.

4.2.4 Comparative Performance Analysis

We evaluated the performance of our hierarchical block matching algorithm using NCC with and without Bayesian regularization. Displacement and strain estimation accuracy using the FEA simulation model was compared over *n=5* randomly generated independent collection of scatterers. True inter-frame displacement estimates were derived from the FEA canine heart model and integrated over time to obtain cumulative true displacement and strain. True and estimated temporal displacement and strain curves for six segments were extracted and compared qualitatively for both approaches. Radial and longitudinal strains were compared in terms of two error metrics, namely - strain error (%) at ES and total temporal relative (TTR) strain error (%). Strain error (%) at ES [38] and total temporal relative strain error (%) were computed using the following equations:

Strain Error (%) at ES =

$$\frac{\sum_{i=1}^{P} |\,\mathrm{ES} - \mathrm{TS}\,|}{\sum_{i=1}^{P} |\,\mathrm{TS}\,|} \times 100 \tag{4.6}$$

Total Temporal Relative Strain Error (%) =

$$\frac{\sum_{t=1}^{T} |\,\mathrm{ES}\,(t) - \mathrm{TS}\,(t)\,|}{\sum_{t=1}^{T} |\,\mathrm{TS}\,(t)\,|} \times 100 \tag{4.7}$$

where ES and TS denote estimated and true strain respectively, ES *(t)* and TS *(t)* denote average of estimated and true strain values respectively at time *t*, *P* is the number of points in the segment of interest and *T* is the number of frames in the cardiac cycle of interest. Strain error (%) at ES quantified the deviation of estimated from ideal FEA strain image at ES while total temporal relative strain error (%) quantified the deviation of estimated from ideal temporal strain curve. Statistical significance was evaluated using paired *t-test* with *p* values less than 0.001.

To demonstrate *in vivo* feasibility, our proposed approach was compared to a commercially available strain estimation software, VevoStrain on the Vevo 2100 LAZR imaging system (FUJIFILM VisualSonics, Inc., Toronto, Canada) for a healthy murine model. Suitable B-mode cine loop containing a cardiac cycle of deformation was loaded into VevoStrain for analysis based on clear visualization of myocardial borders and absence of respiratory artifacts. After endocardial and epicardial borders were delineated in the ED frame, the software automatically tracks myocardial wall deformations using speckle tracking echocardiography. Manual correction of wall tracings was performed to improve quality of tracking and obtain segmental strain curves. VevoStrain reports longitudinal strain curves for epicardial and endocardial wall separately and radial strain curves for the entire myocardial wall. Therefore, endo and epicardial strain curves were averaged along the longitudinal direction. Finally, global radial and longitudinal strain curves were calculated by averaging segmental strain curves for comparison to our approach on the same cine loop. For the *in vivo* study, the elastographic SNR (SNR_e) at ES was computed as:

$$\mathrm{SNR_e\ [in\ decibels]} = 20\log_{10}\left(\frac{\mu}{\sigma}\right) \tag{4.8}$$

where, μ and σ denote the mean and standard deviation of strain (radial/longitudinal) image respectively at ES.

4.3 Findings from FEA Simulation Studies

Axial displacement maps at ES from FEA model, along with those estimated using our multi-level NCC without and with Bayesian regularization are shown in Figure 4.3 (a) – (c) respectively. We refer to the approach without regularization as “NCC” and approach with regularization as “Bayesian" for simplicity in the rest of this chapter. Positive axial displacements shown in red color shades indicate motion away from the transducer and negative axial displacements in blue color shades indicate motion towards the transducer. Figure 4.3 (b) and (c), we observe good agreement between FEA and estimated axial displacements with both methods. Note that in the apical region indicated using arrows in Figure 4.3 (b) and (c), we observe a smoother transition from positive to negative displacement values with regularization when compared to NCC without regularization. Figure 4.3 (d) – (f) represent lateral displacement maps at ES for FEA, NCC and Bayesian respectively. Positive lateral displacements in red color indicate motion to the right and negative lateral displacements in blue color indicate motion to the left. In the displacement transition regions (shown using arrows in Figure 4.3 (e) and (f)), application of Bayesian regularization provided smoother transitions when compared to the NCC approach. Moreover, in the unregularized lateral displacement image (Figure 4.3 (e)), we observe heterogeneity in estimated lateral displacement vectors in the apical region (seen as white bands and indicated using an arrow) and not seen in the FEA result in Figure 4.3 (d). These artifacts were also absent with Bayesian regularization, which provides smooth apical lateral displacement estimation.

Figure 4.4 summarizes the comparison between ES radial and longitudinal strains between the FEA model and estimation results. ES radial strain images from FEA, NCC and Bayesian are shown in Figure 4.4 (a) – (c) respectively. Radial thickening of the myocardial wall was observed

from positive radial strain at ES in the FEA model. NCC provides reliable radial strain estimates in anterior and posterior walls as shown in Figure 4.4 (b). However erroneous negative radial strain values were observed in significant portions of the apical region (indicated using arrows). On the other hand, the radial strain image with Bayesian regularization (Figure 4.4 (d)) provided reliable strain estimation around the myocardium with significantly lower number of negative radial strain values in the apical region when compared to NCC. Figure 4.4 (d) – (f) represent longitudinal strain images for FEA, NCC and Bayesian respectively. Myocardial wall shortening was observed from negative longitudinal strain values in FEA model. Like radial strain, NCC provides reliable longitudinal strain estimation in the anterior and posterior walls. However, the method was prone to errors in the apical region showing positive longitudinal strain values in significant portions of the apex (indicated using arrows). In Figure 4.4 (f), note the significant improvement in strain estimation through incorporation of Bayesian regularization in the longitudinal direction. Regions with highest improvement after regularization are indicated using arrows in Figure 4.4 (d) and (f). Overall, regularized radial and longitudinal strain images showed better qualitative agreement with FEA results.

Figure 4.5 (a) presents the segmental and global radial strain error (%) and Figure 4.5 (b) summarizes the results for longitudinal strain error (%). A logarithmic scale was used for the y-axes in both figures. Application of Bayesian regularization showed statistically significant error reduction of 48.88% ($p<0.001$) globally with highest improvements in anterior and apical regions (see segments 1-4 in Figure 4.5 (a)). Benefit of Bayesian regularization was also evident in longitudinal strain error (%) results (Figure 4.5 (b)) with statistically significant global error reduction of 50.16% ($p<0.001$). For longitudinal strain, highest reductions in error percentages

were observed in anterior mid and apical regions (see segments 2-4 in Figure 4.5 (b)). Table 4.3 summarizes quantitative comparison results between NCC and Bayesian at ES.

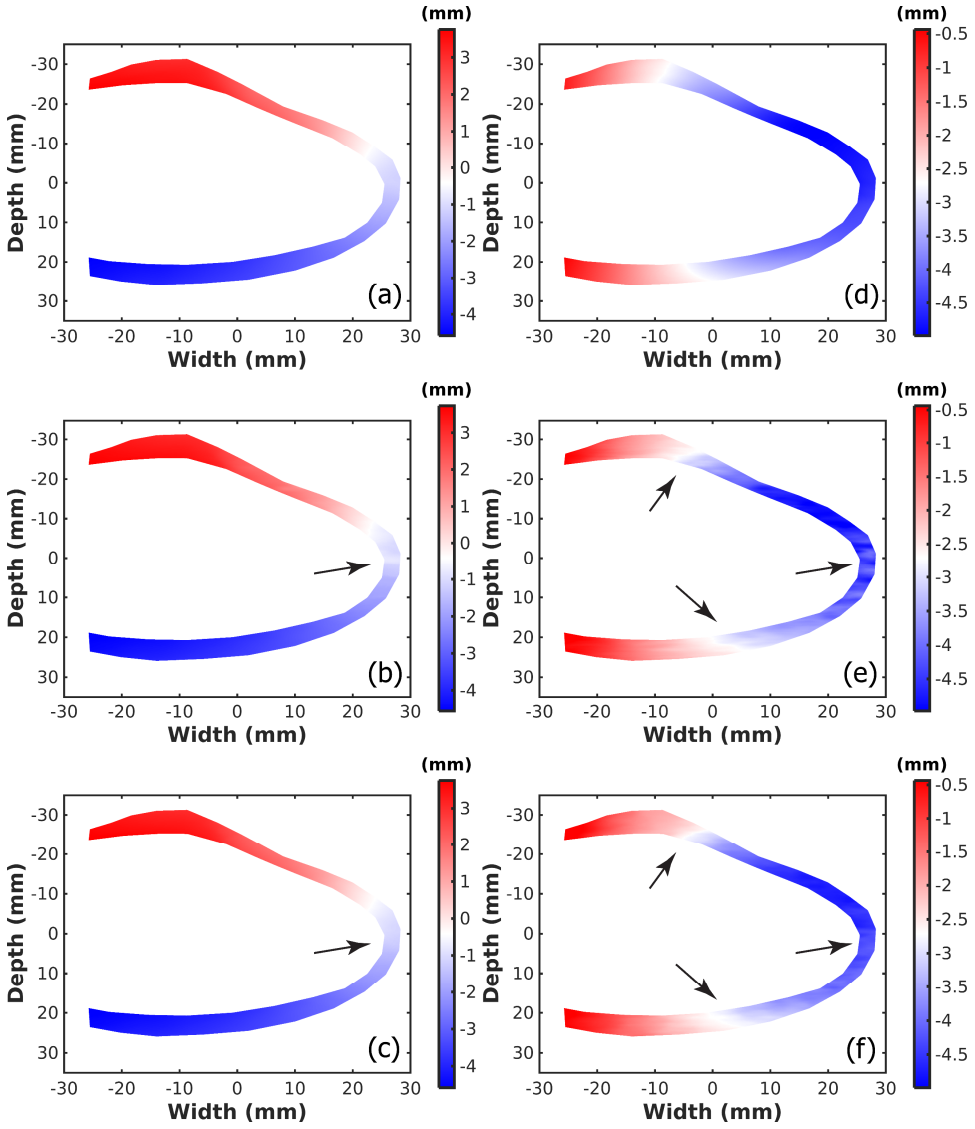

Figure 4.3 End-systole accumulated axial displacement maps from (a) FEA model, (b) NCC and (c) Bayesian. ES accumulated lateral displacement maps from (d) FEA model, (e) NCC and (f) Bayesian. NCC = no regularization. Bayesian = with regularization.

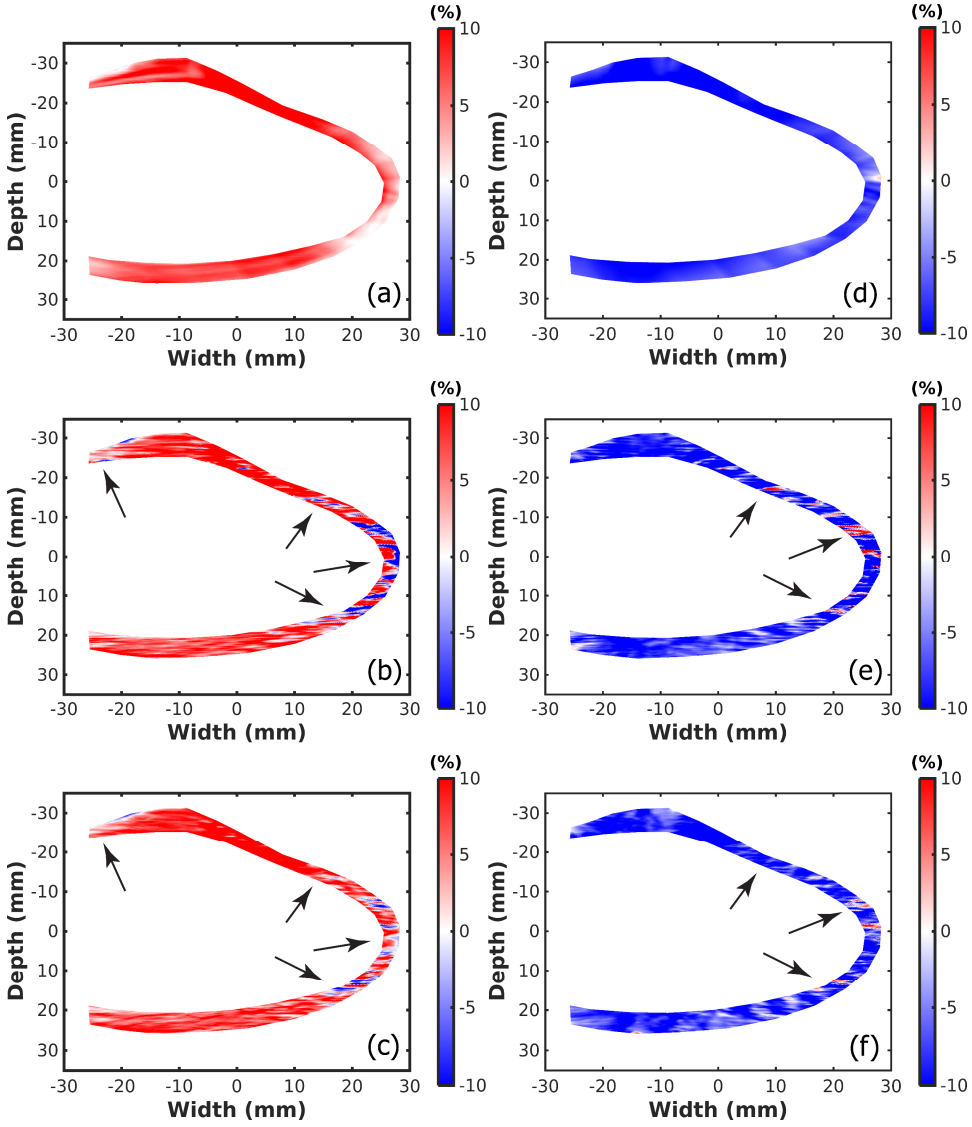

Figure 4.4 End-systole radial strain images from (a) FEA model, (b) NCC and (c) Bayesian. End-systole longitudinal strain images from (d) FEA model, (e) NCC and (f) Bayesian. NCC = no regularization. Bayesian = with regularization.

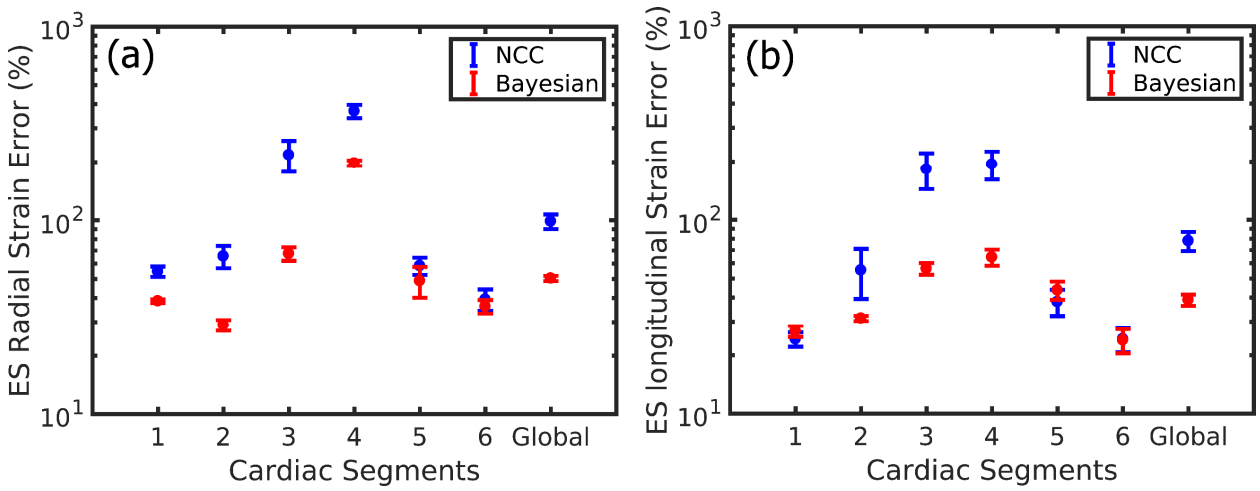

Figure 4.5 Segmental and global strain errors (%) at end-systole. (a) ES radial strain error (%), (b) ES longitudinal strain error (%).

Table 4.3 Comparison of End-Systole Strain Error (%) between NCC and Bayesian

	Radial Strain Error (%) *		Longitudinal Strain Error (%) **	
	NCC	Bayesian	NCC	Bayesian
Segment 1	54.63 ± 3.33	38.51 ± 0.86	24.20 ± 2.09	26.66 ± 1.76
Segment 2	65.36 ± 8.57	28.87 ± 1.88	55.19 ± 15.86	31.22 ± 0.98
Segment 3	217.90 ± 39.97	**67.35 ± 5.39**	182.53 ± 38.48	**56.18 ± 3.39**
Segment 4	367.03 ± 28.97	**197.45 ± 6.63**	193.51 ± 32.16	**64.29 ± 6.10**
Segment 5	58.40 ± 5.93	48.90 ± 8.79	37.96 ± 5.88	43.60 ± 4.67
Segment 6	39.28 ± 4.97	36.16 ± 2.88	24.25 ± 3.53	23.90 ± 3.42
Global	98.57 ± 8.50	**50.39 ± 1.55**	77.92 ± 8.77	**38.83 ± 2.57**

*Segments 5 and 6 did not show statistically significant difference with $p<0.001$.
**Segments 1, 5 and 6 did not show statistically significant difference with $p<0.001$.

Figure 4.6 and Figure 4.7 summarize results from comparative segmental analysis between NCC and Bayesian for radial and longitudinal strain estimations respectively. Figure 4.6 (a)-(f) represent FEA and estimated radial strain curves while Figure 4.7 (a)-(f) represent longitudinal strain curves for the six segments. FEA radial strain curves (shown in black) demonstrated positive peak systolic strains in all six segments indicating cumulative radial thickening over a cardiac cycle. Strain curves estimated using Bayesian regularization (shown in blue) exhibit good

agreement with FEA results in all six segments with positive peak systolic strains and very small standard deviations over realizations. On the contrary, unregularized NCC strain curves (shown in red) showed good agreement with FEA results in the posterior and anterior basal regions (segments 1, 5 and 6) as shown in Figure 4.6 (a), (e) and (f). But NCC strain curves significantly deviated from FEA results for the anterior mid and apical regions (segments 2, 3 and 4) with negative peak systolic strain at segment 4. A similar trend in the estimation performance was observed for the longitudinal strain curves. Good qualitative agreements between FEA and Bayesian strain curves were seen in all segments. NCC produced good strain curves in posterior and anterior basal regions (segments 1, 5 and 6) as shown in Figure 4.7 (a), (e) and (f) but significantly deviated from FEA results for the anterior mid and apical regions (segments 2, 3 and 4). NCC radial and longitudinal strain curves also exhibited higher standard deviations over scatterer realizations when compared to regularized curves. Overall, Bayesian regularization provided better quality strain curves in all six segments and showed very good qualitative agreement with FEA results when compared to the unregularized strain curves utilizing only NCC processing.

Figure 4.8 (a) presents the segmental and global TTR radial strain error (%) results and Figure 4.8 (b) summarizes the TTR longitudinal strain error (%). Statistically significant TTR radial strain error reduction of 78.38 % ($p<0.001$) globally was observed with highest improvements in anterior mid and apical regions (see segments 2-4 in Figure 4.8 (a)) after incorporating Bayesian regularization. Benefits of Bayesian regularization was also clearly evident in TTR longitudinal strain error (%) results (Figure 4.8 (b)) with statistically significant global error reduction of 86.67 % ($p<0.001$). For longitudinal strain, highest reductions in error percentages were observed in the apical region (see segments 3 and 4). Although, we observe a 2.17 × increased error for the anterior basal segment (segment 1) with Bayesian regularization,

this reduction of performance was negligible when compared to improvements in the apical region where NCC has 15.44 and 12.36 × TTR longitudinal strain error (%) in the anterior apical and posterior apical segments respectively. Table 4.4 summarizes the quantitative comparison results between NCC and Bayesian estimated strain curves.

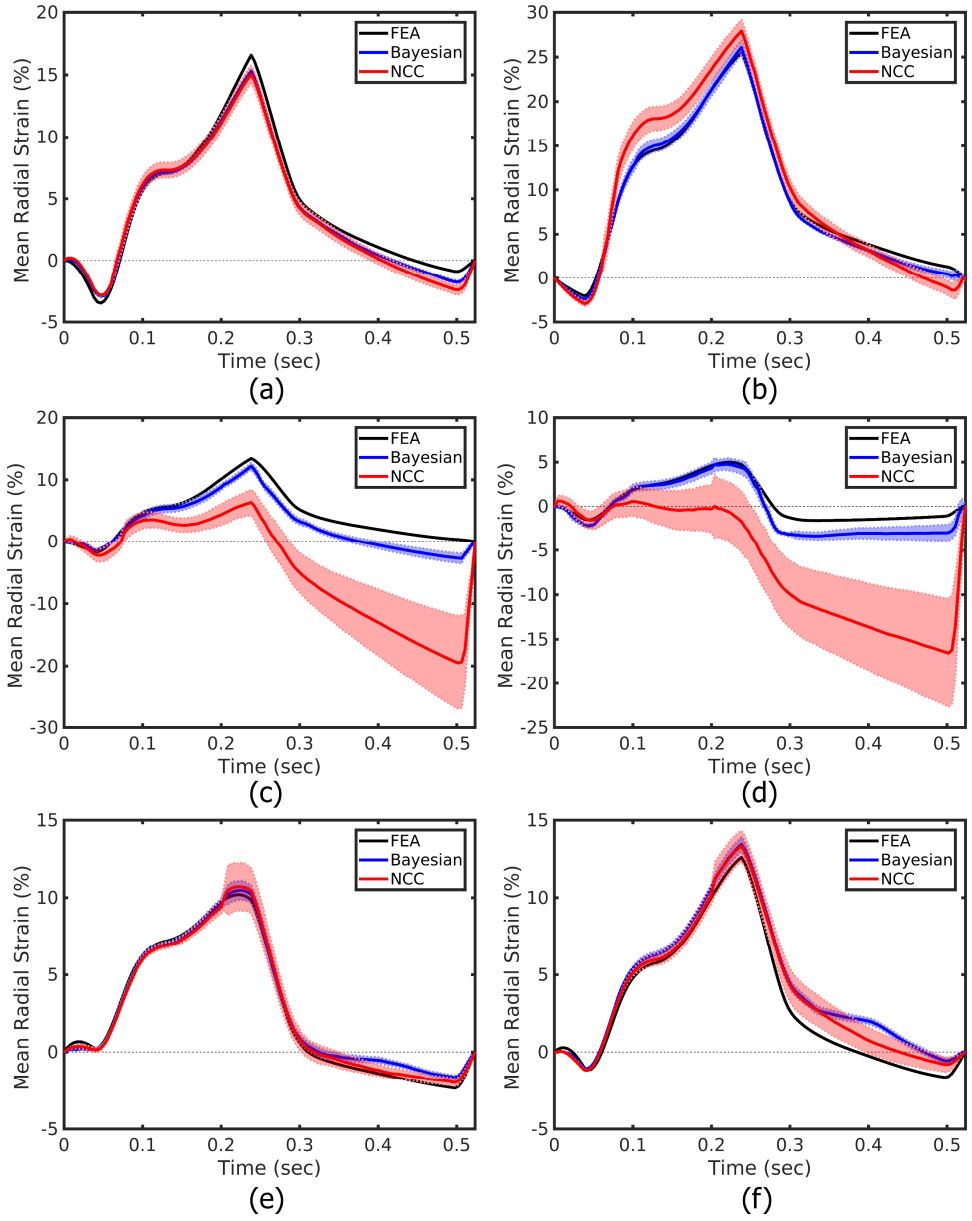

Figure 4.6 Regional radial strain curves from (a) Anterior Base, (b) Anterior Mid, (c) Anterior Apex, (d) Posterior Apex, (e) Posterior Mid and (f) Posterior Base segments respectively. These segments are referred as segments 1-6 respectively in the discussion.

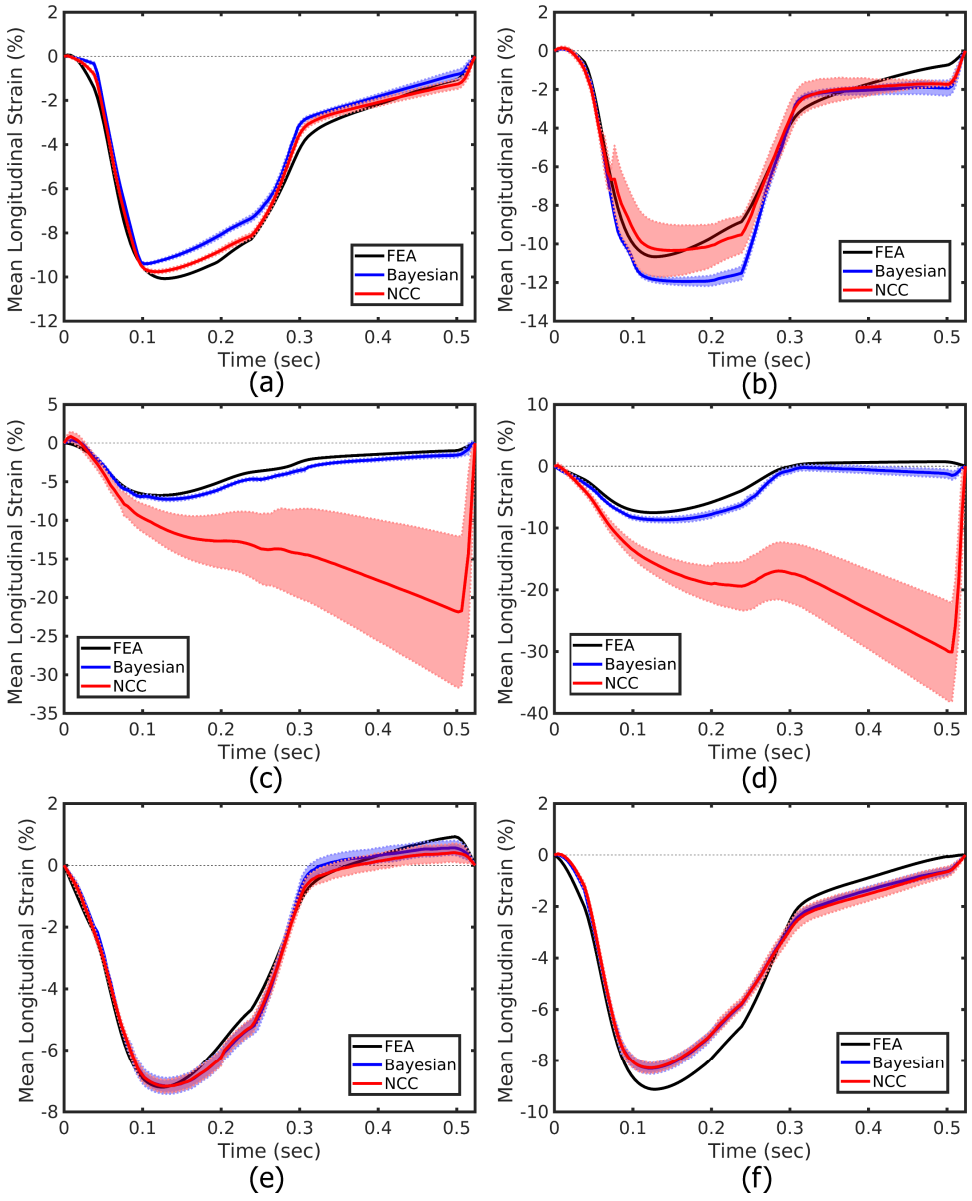

Figure 4.7 Regional longitudinal strain curves from (a) Anterior Base, (b) Anterior Mid, (c) Anterior Apex, (d) Posterior Apex, (e) Posterior Mid and (f) Posterior Base segments respectively.

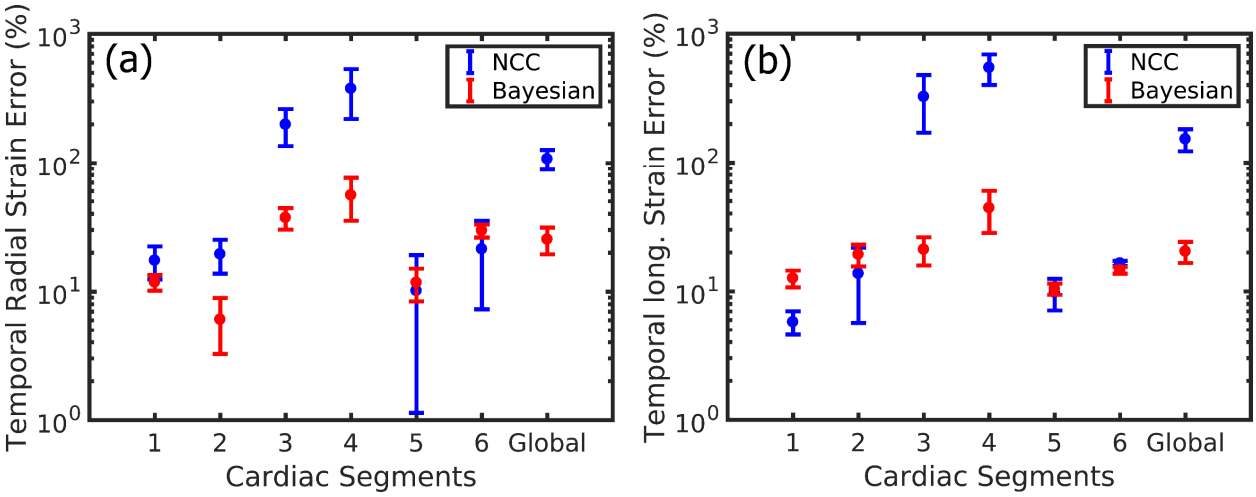

Figure 4.8 Segmental and global TTR strain error (%) results. (a) Temporal radial strain error (%), (b) Temporal longitudinal strain error (%).

Table 4.4 Comparison of Total temporal relative error (TTR %) between NCC and Bayesian

	TTR Radial Strain Error (%) *		TTR Longitudinal Strain Error (%) **	
	NCC	Bayesian	NCC	Bayesian
Segment 1	17.40 ± 4.97	11.81 ± 1.63	5.79 ± 1.22	12.62 ± 1.87
Segment 2	19.48 ± 5.69	6.09 ± 2.85	13.72 ± 8.02	19.28 ± 3.69
Segment 3	199.06 ± 63.33	**37.23 ± 7.07**	325.05 ± 153.76	**21.05 ± 5.17**
Segment 4	376.90 ± 156.96	**55.68 ± 20.35**	545.35 ± 144.52	**44.11 ± 15.80**
Segment 5	10.16 ± 9.02	11.74 ± 3.32	9.81 ± 2.71	10.45 ± 1.05
Segment 6	21.33 ± 14.03	29.62 ± 3.41	16.47 ± 0.72	14.58 ± 0.88
Global	107.39 ± 19.08	**25.36 ± 5.93**	152.70 ± 29.69	**20.35 ± 3.77**

*Segments 5 and 6 did not show statistically significant difference with $p<0.001$.
**Segments 2,5 and 6 did not show statistically significant difference with $p<0.001$.

4.4 Experimental Findings from the *in vivo* Murine Model

Figure 4.9 summarizes the displacement estimation results over a cardiac cycle. Figure 4.9 (a) - (c) show axial displacement maps of the entire myocardium at ES estimated using NCC, and for one iteration and three iterations of Bayesian regularization respectively. A visual analysis of the results shows that the estimated axial displacement vectors were consistent with the expected

inward motion of myocardium during contraction. No qualitative difference in estimated axial displacement maps was observed for NCC and Bayesian regularized images. Figure 4.9 (d) - (f) illustrate lateral displacement maps at ES estimated using NCC, one iteration and three iterations of Bayesian respectively. All approaches provided displacement estimations consistent with the inward myocardial deformation during systole. However, application of Bayesian regularization (both one and three iterations) resulted in higher lateral motion estimation at the posterior wall (Figure 4.9 (e) and (f)) when compared to NCC.

In Figure 4.10, we present strain estimation results for the same mouse over a cardiac cycle. Figure 4.10 (a) - (c) show radial strain images of the entire myocardium at ES estimated using NCC, and one and three iterations of Bayesian regularization respectively. Radial wall thickening was observed in the estimated radial strain results with all the methods. But the NCC strain image exhibited some erroneous negative strain values in the basal segment of the posterior wall. Both one and three iterations of Bayesian regularization were able to correct these erroneous radial strain estimates shown using arrows in Figure 4.10 (b) and (c). In general, better quality radial strain images were obtained using both one and three iterations of regularization (SNR_e = 6.89 and 4.76 dB respectively) compared to the NCC only strain image (SNR_e = 3.83 dB).

Figure 4.10 (d) - (f) show longitudinal strain images of the entire myocardium at ES estimated using NCC without regularization, along with one iteration and three iterations of Bayesian regularization respectively. Longitudinal strain images exhibit ventricular shortening at ES based on negative strain values. NCC provided incorrect positive longitudinal strain values in significant portions of anterior wall and basal segment of posterior wall indicated with yellow arrows in Figure 4.10 (c). With one iteration of Bayesian regularization, improvements in the posterior and apical walls were observed but the anterior wall still suffered from erroneous positive

strain values (shown with yellow arrows) as seen in Figure 4.10 (e). Significant improvement of longitudinal strain estimation was achieved with three iterations of Bayesian regularization (Figure 4.10 (f)). Positive strain estimates in the anterior wall observed with only NCC and one iteration of regularization were corrected using three iterations of regularization. Notable improvement was also seen in the basal segment of the posterior wall with more uniform negative strain values. Highest ES SNR_e was achieved with three iterations (SNR_e = 4.58 dB) compared to one iteration and no regularization (SNR_e = 1.62 dB and 2.29 dB respectively). A small portion of apical wall shown in red arrows in Figure 4.10 (e) and (f) indicated positive strain values in the regularized strain images when compared to the NCC image shown in Figure 4.10 (c). However, this effect was negligible when compared to the improvement achieved by utilizing Bayesian regularization.

Figure 4.11 presents the results for temporal segmental radial and longitudinal strain curves estimated with and without regularization. Radial strain curves are shown in Figure 4.11 (a) and (c). Both approaches were able to resolve radial myocardial wall thickening by exhibiting peak positive radial strains at ES. But regularized radial strain curves in the posterior apical and basal segments (segments 4 and 6 respectively) were smoother compared to unregularized curves indicated using arrows in Figure 4.11 (c). Figure 4.11 (b) and (d) show estimated longitudinal strain curves. The regularized strain curves showed negative peak systolic longitudinal strain indicating ventricular shortening during systole. We observed smooth temporal variation of strain in all six segments over the cardiac cycle as expected from a healthy murine model. But we observed deterioration of performance without regularization as shown in Figure 4.11 (d). All six segments resulted in noisier strain curves when compared to the regularized cases. Erroneous positive longitudinal strain values in segments 2 and 4 as high as 10% was observed towards the end of the cardiac cycle as indicated using arrows Figure 4.11 (d). Higher variations in peak

systolic strain values were also observed in Figure 4.11 (d) compared to Bayesian regularized strain curves in Figure 4.11 (b). Overall, the benefit of Bayesian regularization for estimating regional longitudinal strain curves is clearly visualized from Figure 4.11 (b) and (d).

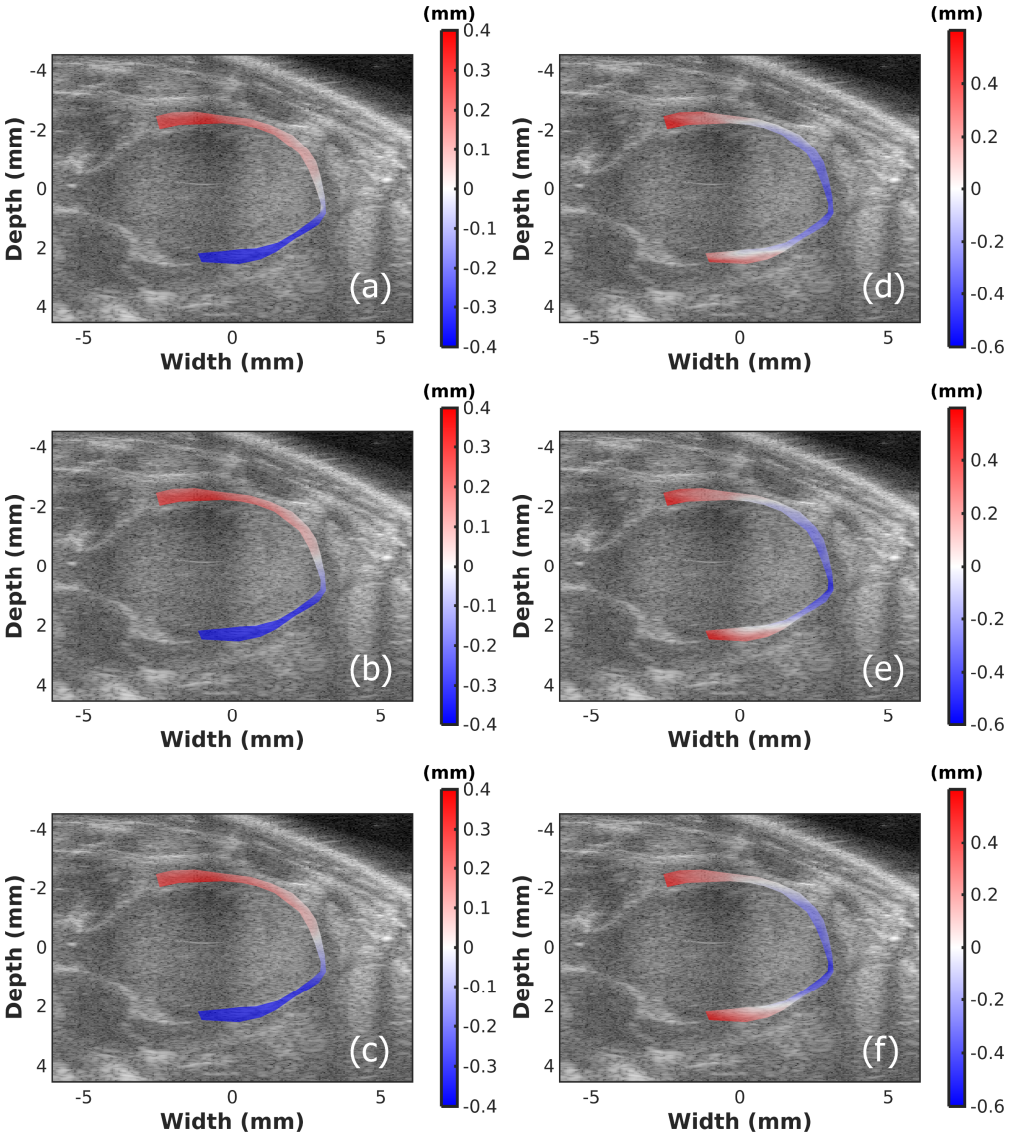

Figure 4.9 ES *in vivo* axial displacement images (a) without regularization, with (b) one iteration and, (c) three iterations of Bayesian regularization respectively. Lateral displacement images (d) without regularization, with (e) one iteration and, (f) three iterations of Bayesian regularization respectively.

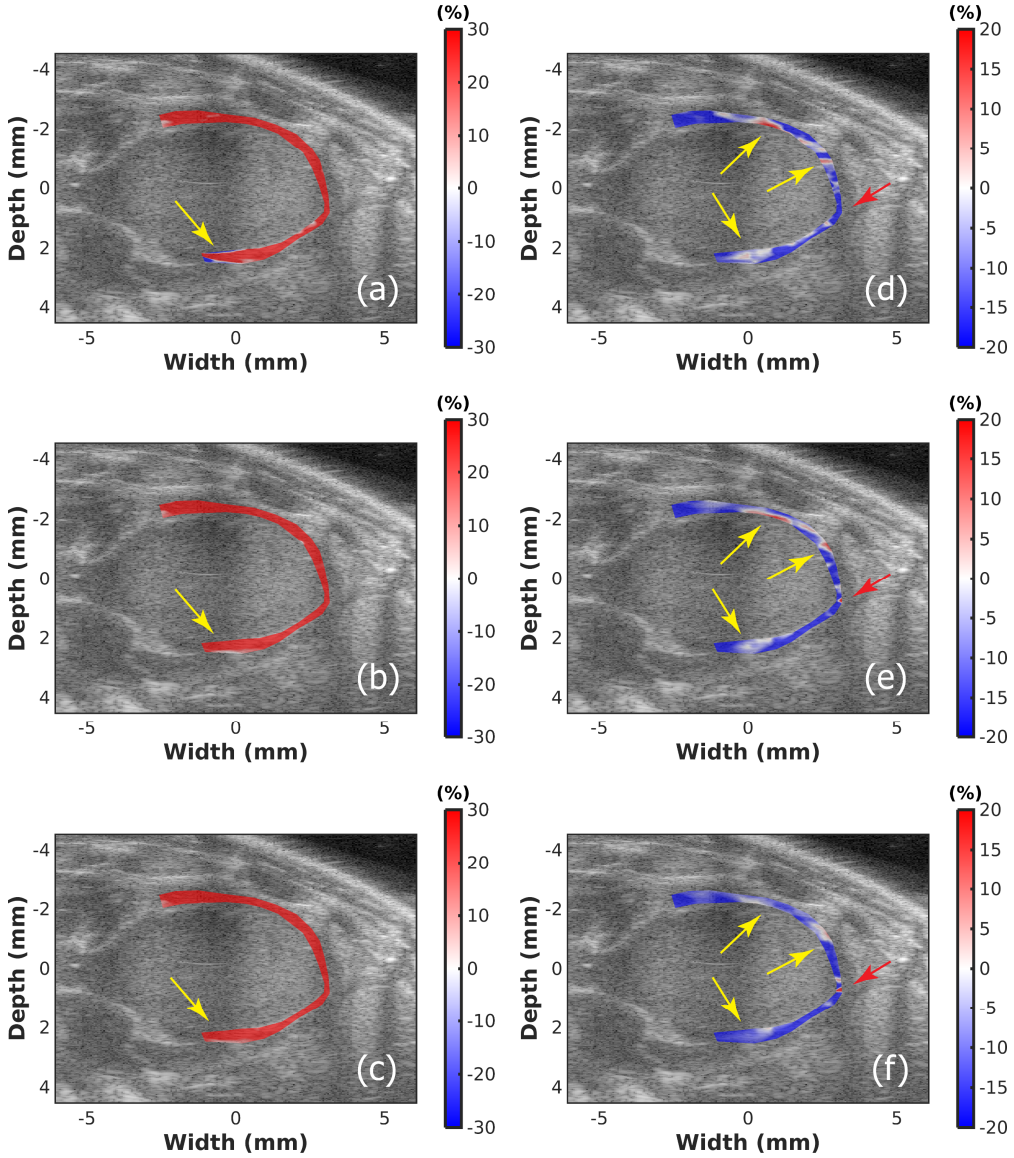

Figure 4.10 ES *in vivo* radial strain images (a) without regularization, with (b) one iteration and, (c) three iterations of Bayesian regularization respectively. Longitudinal strain images (d) without regularization, with (e) one iteration and, (f) three iterations of Bayesian regularization respectively.

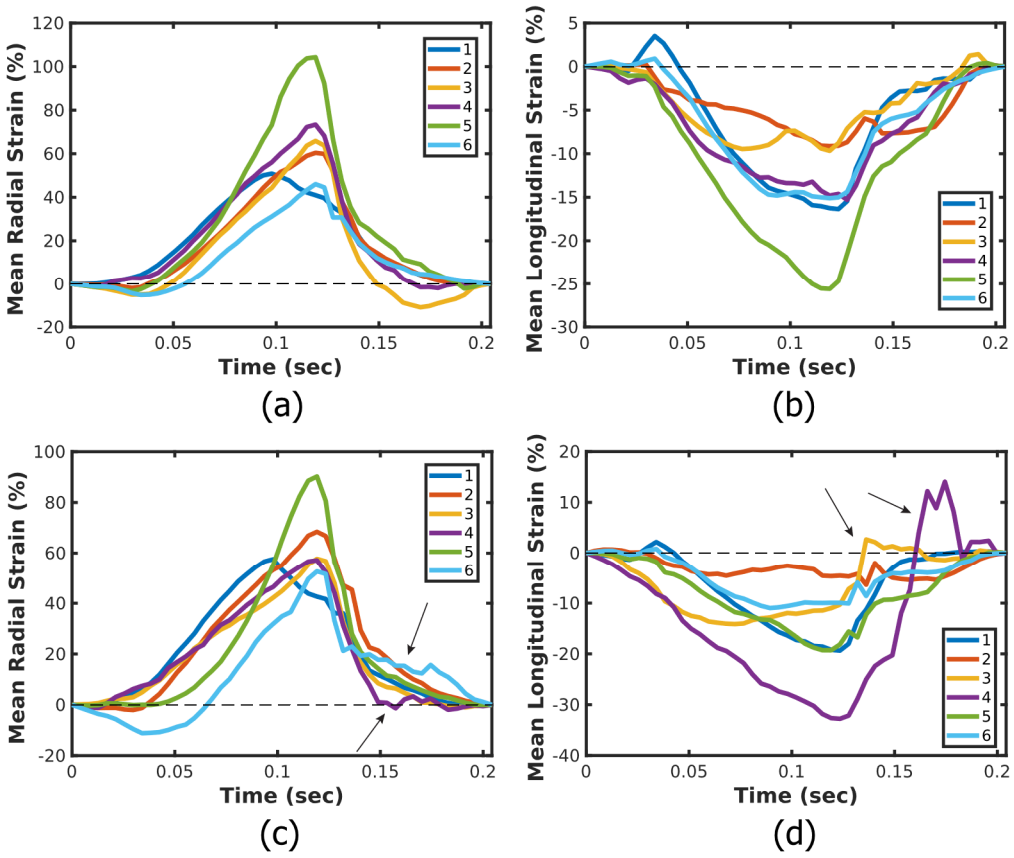

Figure 4.11 *In vivo* segmental radial and longitudinal strain curves. (a) Radial and (b) Longitudinal strain curves with Bayesian regularization, (c) Radial and (d) Longitudinal strain curves with no regularization.

In Figure 4.12, we present comparison results between global strain estimation using regular NCC, Bayesian regularized NCC and speckle tracking echocardiography using VevoStrain. Figure 4.12 (a) shows radial strain results while Figure 4.12 (b) shows longitudinal strain results. In Figure 4.12 (a), all three methods provided positive peak systole strain magnitudes with close resemblance in the overall shape indicating radial wall thickening. For longitudinal strain results in Figure 4.12 (b), negative peaks systolic strain values were observed in estimation from all three methods indicating ventricular shortening at end systole. However, variations of the strain magnitude among CSI and CE approaches were observed.

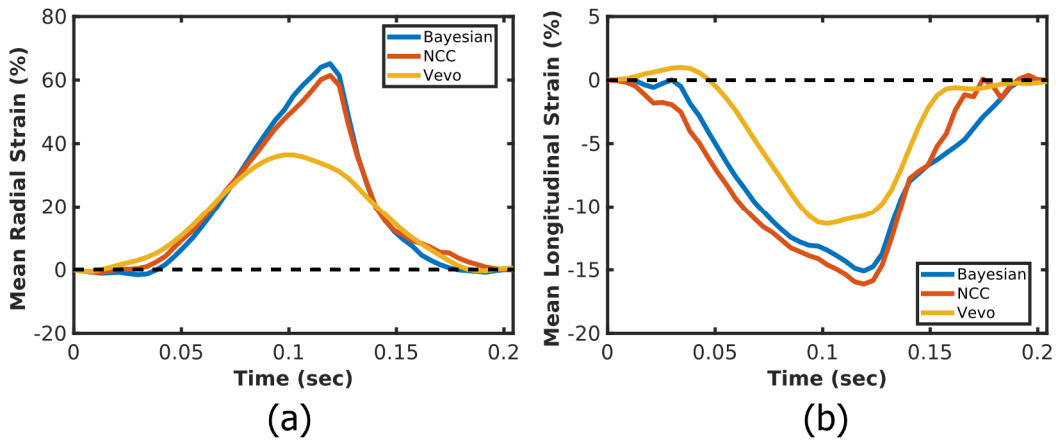

Figure 4.12 Comparison between cardiac strain estimation between cardiac elastography and speckle tracking echocardiography using VevoStrain (FUJIFILM VisualSonics). (a) Radial strain results and (b) Longitudinal strain results.

4.5 Computational Complexity Comparison

The algorithm was implemented in MATLAB (Mathworks Inc., MA) using a standard gateway interface (MEX) in conjunction with C++ and CUDA for cross-platform acceleration. GPU acceleration of computationally intense sections such as Bayesian Regularization and Sinc subsample estimation was achieved by writing a mex wrapper for the original CUDA implementation reported in [19]. All tests were performed on an Intel(R) Xeon(R) CPU E5-2640 v4 at 2.40 GHz, while the CUDA C++ code was run on a Tesla K40c GPU belonging to the Kepler architecture with compute capability 3.5. In the simulation study with RF data dimensions of 8192×500 samples, the proposed algorithm with and without regularization takes 128.63 and 66.67 secs respectively (mean value) to calculate the displacement map between two consecutive frames with parameters presented in Table 4.1. In the *in vivo* study with final RF data dimension of 6016×440 samples, inter-frame displacement estimation execution time with and without regularization was 91.83 and 55.10 secs respectively.

4.6 Discussion on the Results from Simulation and *in vivo* Validation Studies

4.6.1 FEA Simulation Study

In this chapter, we investigated the feasibility of using a multi-level motion estimation framework using NCC coupled with Bayesian regularization for CE. The primary findings of the FEA simulation study can be summarized as follows.

1) Cumulative axial and lateral displacements at ES estimated using both NCC and Bayesian showed good qualitative agreement with FEA results. But Bayesian regularization provided smoother displacement estimates (Figure 4.3).
2) Bayesian regularization improved radial and longitudinal strain images estimated at ES when compared to NCC alone (Figure 4.4). Highest improvements were observed in apical segments (segments 3 and 4). Regularized images had fewer negative radial and positive longitudinal strain values respectively.
3) Quantitative analysis of ES strain images revealed that ES radial strain error (%) decreases from 98.57 ± 8.50% without regularization to 50.39 ± 1.55 % with regularization (Figure 4.5). Similarly, the ES longitudinal error reduces from 77.92 ± 8.77 % without regularization to 38.83 ± 2.57 % with regularization. In both cases, Bayesian regularization resulted in statistically significant error reduction ($p<0.001$) globally (Table 4.3).
4) Bayesian regularization improved the quality of radial and longitudinal temporal strain curves when compared to NCC (Figure 4.6 and Figure 4.7). In anterior and posterior walls, both approaches provided strain curves of comparable quality (segments 1,2,5 and 6). NCC alone fails to estimate strain for apical segments (segments 4 and 5) with higher deviation from FEA results. Use of Bayesian regularization significantly improved NCC results. Bayesian

regularization also provided consistent estimation with lower standard deviation (see error bars in Figure 4.6 and Figure 4.7).

5) Temporal radial strain error (%) decreased from 107.39 ± 19.08 % without regularization to 25.36 ± 5.93 % with regularization (Figure 4.8). Similarly, the temporal longitudinal error reduces from 152.70 ± 29.69 % without regularization to 20.35 ± 3.77 % with regularization. In both cases, Bayesian regularization provided statistically significant error reduction ($p<0.001$) globally (Table 4.4).

Bayesian regularization resulted in smoother displacement vectors when compared to utilizing only NCC (arrows in Figure 4.3). The Bayesian inference process utilizing a regularized similarity metric (from NCC map) incorporates information from neighboring location as a likelihood function significantly reduces errors by not allowing for any abrupt changes resulting in a smooth deformation field. NCC alone can result in some incorrect displacement discontinuities amplified into noisier strain images by the gradient operation. In addition, the lower spatial resolution and lack of phase information in lateral direction pose significant difficulty in lateral motion tracking with NCC [22]. However, within this limitation Bayesian regularization provided reasonable lateral motion estimation.

We observed the highest improvement in strain estimation from Bayesian regularization for the apical segments (segments 3 and 4). In these segments radial and longitudinal strains had significant contributions from shearing components of **E** and we hypothesize that the smoothly varying deformation field with regularization contributed to better estimation of these components. Although we obtained significant improvements some of these errors were not fully corrected using our approach. Several factors might contribute to this. First, the FEA model used in this study contains all deformation information (compression, translation, and torsion) derived

experimentally from a canine heart resulting in a realistic complex 3-D deformation model [12, 33, 34]. Imaging this 3-D deformation using 2-D image planes result in significant "out-of-plane" motion [39, 40]. This issue can be resolved by extending the proposed approach to 3-D image planes using 2-D matrix transducers. Secondly, there exists spatial variations in the elasticity of the myocardial wall (see Figure 4.4 (a) and (d)). Our proposed algorithm attempts to remove noisy NCC estimates from a given similarity metric using guidance from neighboring values. However, in some regions most of the initial similarity metric estimates may be noisy resulting in a noisy final estimate even after regularization. Finally, as mentioned in the discussion on lateral displacement estimation, lower spatial resolution and lack of phase information also introduces errors in lateral displacement estimation. Strain estimation is performed on the cumulated displacement. Any small error in inter-frame displacement estimates is propagated through the accumulation process. Strain estimation through the gradient operation also has a tendency for amplification of displacement estimation noise [26]. Thus, any small error in lateral displacement estimates will cause significantly noisier lateral strain estimates. These issues indicate that motion estimation in lateral direction requires additional improvement.

In the proposed framework, regularization is performed in an iterative manner and the performance of the algorithm is dependent on correctly chosen number of iterations. For the FEA study, we found that a single iteration was sufficient to improve image quality. The number of iterations should be increased with caution as over-regularization might adversely affect the image quality resulting into "banding" artifacts due to over smoothening. Figure 4.13 illustrates the effect of over-regularization on a longitudinal strain image at ES with three iterations of Bayesian regularization.

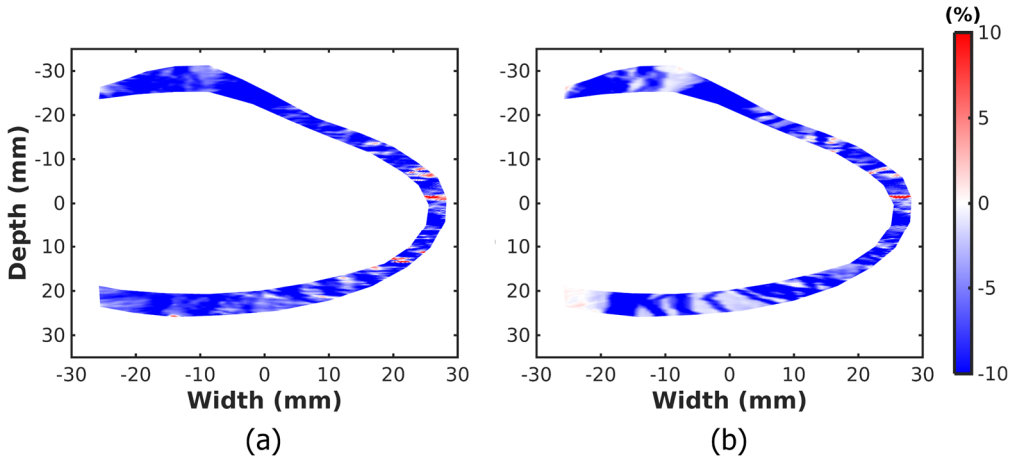

Figure 4.13 Effect of overregularization in strain estimation. End-systole longitudinal images with (a) one iteration and (b) three iterations of Bayesian regularization. Overregularization resulted into "banding" artifacts in the estimated strain image.

4.6.2 In vivo Healthy Murine Model

Myocardial contraction *in vivo* during systole was clearly visible in axial displacement maps (Figure 4.9 (a) – (c)), with anterior wall moving away from the transducer (red shades) and posterior wall moving towards the transducer (blue shades). Estimated lateral displacement maps from all three methods were consistent with the healthy myocardial contraction during systole (Figure 4.9 (d) – (f)). Both one and three iterations of Bayesian regularization provided smoother lateral motion estimations in the apical region. This contributed to improved radial and longitudinal strains. Physiologically inaccurate radial and longitudinal strain values incurred using NCC alone were corrected using Bayesian regularization. Optimal estimation performance required three iterations for the *in vivo* murine model. This emphasizes the importance of correctly choosing the number of iterations for Bayesian regularization. In clinical practice, quantitative estimates of the SNRe could be utilized to determine the optimal number of iterations. In future work, we will look into maximization of the conditional expected value of the SNR_e [10, 41] to determine the optimal number of iterations.

In addition, we were able to resolve to clinically relevant details [28] from longitudinal strain curves such as peak positive strain, ES strain and post-systole strain (see segment 1 and 6 in Figure 4.11 (b)) with Bayesian regularization. These details were suppressed by noise in the NCC only longitudinal strain curves (Figure 4.11 (d)). In Figure 4.11 (d), we observed that strain curves from segments 2 and 3 were noisier. One potential reason for this finding in the apical region of this mouse is that an acoustic shadowing artifact (most likely from a rib or the sternum) is present in the image. As reported in literature [42], acoustic shadowing may result in underestimation of strain and/or the appearance of a regional wall motion abnormality. This made tracking more challenging in those segments and consequently lower quality strain curves.

Comparison of estimated strain curves using CE (NCC and Bayesian) and VevoStrain showed an overall shape agreement but variation in strain magnitudes. Strain estimation in VevoStrain is based on speckle tracking echocardiography, which calculates strain by motion tracking from ultrasound B-mode imaging sequences. In contrast, our proposed method uses ultrasound radio-frequency (RF) signals, which contains additional phase information when compared to B-mode images. A previous study from our group reported that RF signals results into more accurate strain estimates when compared to envelope/B-mode signals [10]. This could explain the magnitude variation between the two methods. Overall, comparable performance of the proposed method against a commercial system shows its potential for *in vivo* CSI.

Some of the previously reported regularization approaches for elastography used assumption of continuous and smooth displacement fields, enforcing an explicit smoothness constraint as a regularizer [43-49]. This assumption limits the application of these approaches to CE where discontinuous deformation is expected (opposing movement of anterior and posterior wall). Incorporation of Bayesian regularization in our multi-level framework provides a balance

between discontinuous motion estimation and error correction. This enables successful application of our framework for CE as shown in FEA simulation and *in vivo* study.

In vivo imaging for murine models was performed with a frame rate of 235 Hz which is comparatively lower than the literature reported values for CE in murine models with 1D tracking or plane wave imaging approaches [50-52]. Our group has previously demonstrated that a frame rate ten times the heart rate provides high SNR_e and reliable strain estimation using RF signals in a phantom study [53]. The murine model in this study had a heart rate of 5 beats per second and was imaged with a frame rate of 235 Hz, leading to 47 frames in a cardiac cycle. Our 2-D hierarchical multi-level NCC approach provides deformation tracking for reliably estimating maximum strains up-to 5% axial and 2.5% lateral strain between consecutive RF frames [5, 6], whereas 1-D NCC kernels with 2-D search approaches fail due to increased signal decorrelation in this applied strain range. Using our multi-level approach with 2-D kernels, we are able to reduce kernel dimensions to accurately track these high strains. Reliable strain estimation in human RF data sets with comparatively lower frame rates was previously reported by our group [10, 11, 13, 54] using this multi-level approach without regularization. Our approach with Bayesian regularization in this chapter provides reliable polar strain estimation for the *in vivo* murine model. However, with higher frame rates, we anticipate additional improvement in strain estimation using the proposed approach.

One limitation of our study is the discrepancy between the transducer center frequency of simulation and *in vivo* experiments. The simulation study was performed based on the 3-D deformation model of a canine heart developed by the Cardiac Mechanics Research Group at the University of California San Diego (UCSD) [33]. The imaging field of view was 80 mm × 100 mm. In the ultrasound imaging simulation, we also modelled an attenuation coefficient of 0.5

dB/cm-MHz. If simulation was performed with 40 MHz center frequency, we will not be able to image the posterior part of heart due to depth-dependent attenuation co-efficient. Thus, the imaging simulation was performed using 8 MHz rather than the 40 MHz center frequency in the *in vivo* study. If we are able to obtain 3-D deformation models for a mouse heart, we would be able to extend the simulation to utilize a 40 MHz center frequency.

List of References

[1] E. Konofagou, J. D'hooge, and J. Ophir, "Cardiac elastography-A feasibility study," in *2000 IEEE Ultrasonics Symposium. Proceedings. An International Symposium (Cat. No. 00CH37121)*, 2000, pp. 1273-1276.

[2] E. Konofagou, T. Harrigan, and S. Solomon, "Assessment of regional myocardial strain using cardiac elastography: Distinguishing infarcted from non-infarcted myocardium," in *2001 IEEE Ultrasonics Symposium. Proceedings. An International Symposium (Cat. No. 01CH37263)*, 2001, pp. 1589-1592.

[3] T. Varghese, C. S. Breburda, J. A. Zagzebski, and P. S. Rahko, "Method and Apparatus for Cardiac Elastography," USA Patent, 2002.

[4] T. Varghese, J. Zagzebski, P. Rahko, and C. Breburda, "Ultrasonic imaging of myocardial strain using cardiac elastography," *Ultrasonic imaging,* vol. 25, pp. 1-16, 2003.

[5] M. McCormick, N. Rubert, and T. Varghese, "Bayesian regularization applied to ultrasound strain imaging," *IEEE Transactions on Biomedical Engineering,* vol. 58, pp. 1612-1620, 2011.

[6] M. McCormick, T. Varghese, X. Wang, C. Mitchell, M. Kliewer, and R. Dempsey, "Methods for robust in vivo strain estimation in the carotid artery," *Physics in medicine and biology,* vol. 57, p. 7329, 2012.

[7] X. Wang, D. C. Jackson, C. C. Mitchell, T. Varghese, S. M. Wilbrand, B. G. Rocque*, et al.*, "Classification of symptomatic and asymptomatic patients with and without cognitive decline using non-invasive carotid plaque strain indices as biomarkers," *Ultrasound in medicine & biology,* vol. 42, pp. 909-918, 2016.

[8] X. Wang, D. C. Jackson, T. Varghese, C. C. Mitchell, B. P. Hermann, M. A. Kliewer*, et al.*, "Correlation of cognitive function with ultrasound strain indices in carotid plaque," *Ultrasound in medicine & biology,* vol. 40, pp. 78-89, 2014.

[9] N. Meshram, T. Varghese, C. Mitchell, D. Jackson, S. Wilbrand, B. Hermann*, et al.*, "Quantification of carotid artery plaque stability with multiple region of interest based ultrasound strain indices and relationship with cognition," *Physics in Medicine & Biology,* vol. 62, p. 6341, 2017.

[10] C. Ma and T. Varghese, "Comparison of cardiac displacement and strain imaging using ultrasound radiofrequency and envelope signals," *Ultrasonics,* vol. 53, pp. 782-792, 2013.

[11] C. Ma and T. Varghese, "Lagrangian displacement tracking using a polar grid between endocardial and epicardial contours for cardiac strain imaging," *Medical physics,* vol. 39, pp. 1779-1792, 2012.

[12] H. Chen and T. Varghese, "Three-dimensional canine heart model for cardiac elastography," *Medical physics,* vol. 37, pp. 5876-5886, 2010.

[13] H. Chen and T. Varghese, "Multilevel hybrid 2-D strain imaging algorithm for ultrasound sector/phased arrays," *Medical physics,* vol. 36, pp. 2098-2106, 2009.

[14] S. Langeland, J. D'hooge, T. Claessens, P. Claus, P. Verdonck, P. Suetens*, et al.*, "RF-based two-dimensional cardiac strain estimation: a validation study in a tissue-mimicking phantom," *IEEE transactions on ultrasonics, ferroelectrics, and frequency control,* vol. 51, pp. 1537-1546, 2004.

[15] M. M. McCormick and T. Varghese, "An approach to unbiased subsample interpolation for motion tracking," *Ultrasonic imaging,* vol. 35, pp. 76-89, 2013.

[16] I. Céspedes, Y. Huang, J. Ophir, and S. Spratt, "Methods for estimation of subsample time delays of digitized echo signals," *Ultrasonic imaging,* vol. 17, pp. 142-171, 1995.

[17] H. Chen, H. Shi, and T. Varghese, "Improvement of elastographic displacement estimation using a two-step cross-correlation method," *Ultrasound in medicine & biology,* vol. 33, pp. 48-56, 2007.

[18] H. Shi and T. Varghese, "Two-dimensional multi-level strain estimation for discontinuous tissue," *Physics in medicine and biology,* vol. 52, p. 389, 2007.

[19] N. H. Meshram and T. Varghese, "GPU Accelerated Multilevel Lagrangian Carotid Strain Imaging," *IEEE Transactions on Ultrasonics, Ferroelectrics, and Frequency Control,* 2018.

[20] S. K. Alam and J. Ophir, "Reduction of signal decorrelation from mechanical compression of tissues by temporal stretching: Applications to elastography," *Ultrasound in Medicine and Biology,* vol. 23, pp. 95-105, 1997.

[21] T. Varghese, J. Ophir, and I. Cespedes, "Noise reduction in elastograms using temporal stretching with multicompression averaging," *Ultrasound in Medicine and Biology,* vol. 22, pp. 1043-1052, 1996.

[22] R. G. Lopata, M. M. Nillesen, H. H. Hansen, I. H. Gerrits, J. M. Thijssen, and C. L. De Korte, "Performance evaluation of methods for two-dimensional displacement and strain estimation using ultrasound radio frequency data," *Ultrasound in medicine & biology,* vol. 35, pp. 796-812, 2009.

[23] H. Li, Y. Guo, and W.-N. Lee, "Systematic performance evaluation of a cross-correlation-based ultrasound strain imaging method," *Ultrasound in medicine & biology,* vol. 42, pp. 2436-2456, 2016.

[24] Z. Qian, W.-N. Lee, E. E. Konofagou, D. N. Metaxas, and L. Axel, "Ultrasound myocardial elastography and registered 3-D tagged MRI: quantitative strain comparison," in *International Conference on Medical Image Computing and Computer-Assisted Intervention*, 2007, pp. 800-808.

[25] A. Elen, H. Choi, D. Loeckx, H. Gao, P. Claus, P. Suetens*, et al.*, "3-D cardiac strain estimation using spatiotemporal elastic registration of ultrasound images: a feasibility study," *IEEE Trans Med Imaging,* vol. 27, pp. 1580-1591, 2008.

[26] F. Kallel and J. Ophir, "A least-squares strain estimator for elastography," *Ultrasonic imaging,* vol. 19, pp. 195-208, 1997.

[27] I. Zervantonakis, S. Fung-Kee-Fung, W. Lee, and E. Konofagou, "A novel, view-independent method for strain mapping in myocardial elastography: eliminating angle and centroid dependence," *Physics in Medicine & Biology,* vol. 52, p. 4063, 2007.

[28] J.-U. Voigt, G. Pedrizzetti, P. Lysyansky, T. H. Marwick, H. Houle, R. Baumann*, et al.*, "Definitions for a common standard for 2-D speckle tracking echocardiography: consensus

document of the EACVI/ASE/Industry Task Force to standardize deformation imaging," *European Heart Journal-Cardiovascular Imaging,* vol. 16, pp. 1-11, 2014.

[29] O. Somphone, M. De Craene, R. Ardon, B. Mory, P. Allain, H. Gao*, et al.*, "Fast myocardial motion and strain estimation in 3-D cardiac ultrasound with sparse demons," in *Biomedical Imaging (ISBI), 2013 IEEE 10th International Symposium on*, 2013, pp. 1182-1185.

[30] W. M. Lai, D. H. Rubin, E. Krempl, and D. Rubin, *Introduction to continuum mechanics*: Butterworth-Heinemann, 2009.

[31] J. D'hooge, A. Heimdal, F. Jamal, T. Kukulski, B. Bijnens, F. Rademakers*, et al.*, "Regional strain and strain rate measurements by cardiac ultrasound: principles, implementation and limitations," *European Journal of Echocardiography,* vol. 1, pp. 154-170, 2000.

[32] A. M. Shah and S. D. Solomon, "Myocardial deformation imaging: current status and future directions," *Circulation,* vol. 125, pp. e244-e248, 2012.

[33] A. D. McCulloch and R. Mazhari, "Regional myocardial mechanics: integrative computational models of flow-function relations," *Journal of Nuclear Cardiology,* vol. 8, pp. 506-519, 2001.

[34] R. Mazhari, J. H. Omens, L. K. Waldman, and A. D. McCulloch, "Regional myocardial perfusion and mechanics: a model-based method of analysis," *Annals of biomedical engineering,* vol. 26, pp. 743-755, 1998.

[35] Y. Li and J. A. Zagzebski, "A frequency domain model for generating B-mode images with array transducers," *IEEE transactions on ultrasonics, ferroelectrics, and frequency control,* vol. 46, pp. 690-699, 1999.

[36] T. Varghese and J. Ophir, "A method for experimental characterization of the noise performance of elastographic systems," *Ultrasonic imaging,* vol. 21, pp. 17-30, 1999.

[37] A. H. A. W. G. o. M. Segmentation, R. f. C. Imaging:, M. D. Cerqueira, N. J. Weissman, V. Dilsizian, A. K. Jacobs*, et al.*, "Standardized myocardial segmentation and nomenclature for tomographic imaging of the heart: a statement for healthcare professionals from the Cardiac Imaging Committee of the Council on Clinical Cardiology of the American Heart Association," *Circulation,* vol. 105, pp. 539-542, 2002.

[38] J. Grondin, V. Sayseng, and E. E. Konofagou, "Cardiac strain imaging with coherent compounding of diverging waves," *IEEE transactions on ultrasonics, ferroelectrics, and frequency control,* vol. 64, pp. 1212-1222, 2017.

[39] R. Lopata, M. M. Nillesen, C. Verrijp, S. Singh, M. Lammens, J. A. van der Laak*, et al.*, "Cardiac biplane strain imaging: initial in vivo experience," *Physics in Medicine & Biology,* vol. 55, p. 963, 2010.

[40] E. E. Konofagou, J. D'hooge, and J. Ophir, "Myocardial elastography—A feasibility study in vivo," *Ultrasound in medicine & biology,* vol. 28, pp. 475-482, 2002.

[41] E. A. Bunting, J. Provost, and E. E. Konofagou, "Stochastic precision analysis of 2-D cardiac strain estimation in vivo," *Physics in Medicine & Biology,* vol. 59, p. 6841, 2014.

[42] C. K. Phoon and D. H. Turnbull, "Cardiovascular imaging in mice," *Current protocols in mouse biology,* vol. 6, pp. 15-38, 2016.

[43] H. Rivaz, E. Boctor, P. Foroughi, R. Zellars, G. Fichtinger, and G. Hager, "Ultrasound elastography: a dynamic programming approach," *IEEE transactions on medical imaging,* vol. 27, pp. 1373-1377, 2008.

[44] H. Rivaz, E. M. Boctor, M. A. Choti, and G. D. Hager, "Real-time regularized ultrasound elastography," *IEEE transactions on medical imaging,* vol. 30, pp. 928-945, 2011.

[45] C. Pellot-Barakat, F. Frouin, A. Herment, J. J. Mai, K. K. Lindfors, J. K. Tsou*, et al.*, "A regularized approach for freehand ultrasound elastography of breast lesions," in *2004 2nd IEEE International Symposium on Biomedical Imaging: Nano to Macro (IEEE Cat No. 04EX821)*, 2004, pp. 952-955.

[46] C. Pellot-Barakat, F. Frouin, M. F. Insana, and A. Herment, "Ultrasound elastography based on multiscale estimations of regularized displacement fields," *IEEE transactions on medical imaging,* vol. 23, pp. 153-163, 2004.

[47] J. Jiang and T. J. Hall, "A fast hybrid algorithm combining regularized motion tracking and predictive search for reducing the occurrence of large displacement errors," *IEEE transactions on ultrasonics, ferroelectrics, and frequency control,* vol. 58, pp. 730-736, 2011.

[48] J. Jiang and T. J. Hall, "A generalized speckle tracking algorithm for ultrasonic strain imaging using dynamic programming," *Ultrasound in medicine & biology,* vol. 35, pp. 1863-1879, 2009.

[49] E. Brusseau, J. Kybic, J.-F. Déprez, and O. Basset, "2-D locally regularized tissue strain estimation from radio-frequency ultrasound images: Theoretical developments and results on experimental data," *IEEE Transactions on Medical Imaging,* vol. 27, pp. 145-160, 2008.

[50] J. Luo, K. Fujikura, S. Homma, and E. E. Konofagou, "Myocardial elastography at both high temporal and spatial resolution for the detection of infarcts," *Ultrasound in medicine & biology,* vol. 33, pp. 1206-1223, 2007.

[51] J. Luo and E. E. Konofagou, "High-frame rate, full-view myocardial elastography with automated contour tracking in murine left ventricles in vivo," *IEEE transactions on ultrasonics, ferroelectrics, and frequency control,* vol. 55, pp. 240-248, 2008.

[52] J. Luo, W.-N. Lee, S. Wang, and E. E. Konofagou, "P4A-2 An In-Vivo Study of Frame Rate Optimization for Myocardial Elastography," in *2007 IEEE Ultrasonics Symposium Proceedings*, 2007, pp. 1933-1936.

[53] H. Chen, T. Varghese, P. S. Rahko, and J. Zagzebski, "Ultrasound frame rate requirements for cardiac elastography: Experimental and in vivo results," *Ultrasonics,* vol. 49, pp. 98-111, 2009.

[54] C. Ma, X. Wang, and T. Varghese, "Segmental analysis of cardiac short-axis views using lagrangian radial and circumferential strain," *Ultrasonic imaging,* vol. 38, pp. 363-383, 2016.

Chapter 5

Adaptive Bayesian Regularization with Local Optimization for Ultrasound Strain Imaging

In this chapter[2], we propose an adaptive iterative Bayesian regularization framework (AIBRF) based on local signal decorrelation levels derived from input radiofrequency (RF) data. The Bayesian regularization algorithm proposed by McCormick *et al.* [1] has been successfully applied for both carotid [2] and cardiac strain imaging (**Chapter 04**) [3]. This regularization scheme was formulated to reduce large displacement or peak-hop errors due to high signal decorrelation of RF signals and was applied in an iterative manner to improve the quality of estimated displacements. However, incorrect choice in the number of iterations can lead to over-regularization and negatively impact the quality of displacement estimates especially in the lateral direction [3]. Previously, the desired number of iterations were determined heuristically based on the clinical application [1, 3, 4]. In addition, the number of required iterations was also shown to be dependent on the strain distribution present in an imaged region [1]. Furthermore, we hypothesize that due to spatial and temporal strain heterogeneities expected with *in vivo* imaging, the number of iterations should be varied locally rather than as a global application of a fixed number of iterations to each displacement estimation location. To address these issues, we utilize local correlation between RF signals to guide the Bayesian regularization based on the underlying strain distribution thus inhibiting the possibility of over-regularization. Furthermore, correlation

[2] Rashid Al Mukaddim, Nirvedh H. Meshram, and Tomy Varghese, "Locally optimized correlation-guided Bayesian adaptive regularization for ultrasound strain imaging." *Physics in Medicine and Biology*, vol. 68, no. 3, 065008 (2020) PMCID: PMC7682728

guidance will automatically determine the optimal number of iterations in local regions eliminating the need for a fixed heuristic determination of the number of iterations.

5.1 Theory Behind Adaptive Bayesian Regularization

5.1.1 Basic Principle of Bayesian Regularization

Assume I_1 and I_2 are two ultrasound RF frames of size $i \times j$ acquired as the pre- and post-deformation frames respectively. In block matching algorithms, I_1 and I_2 are divided into a rectangular grid of 1-D or 2-D matching blocks with Y and X number of grid locations along axial and lateral directions respectively. To compare a matching block between I_1 and I_2, we perform 2-D NCC calculations over a set of possible displacements defined as

$$\Omega = \{u_k : -D_x \le u_k \le D_x\} \times \{u_m : -D_y \le u_m \le D_y\} \tag{5.1}$$

where D_y and D_x are maximum possible axial and lateral displacement estimates respectively in a user defined search grid. This process results in a similarity metric image for each grid location with size of $M \times K$. These similarity metric images can be treated as probability density (PDF) images, through application of a basic transformation [1] and regularized using Bayes' theorem to improve motion estimation accuracy.

The regularization estimator calculates the posterior probability density (PPD), $\Pr(\mathbf{u}_{\mathbf{x}} \mid \mathbf{u}_{\mathcal{N}_x})$ for a possible displacement estimate, $\mathbf{u}_{\mathbf{x}} = [u_{axial}, u_{lateral}]$ of the matching block located at grid location, $\mathbf{x} = [x_{axial}, x_{lateral}]$ given observed displacements at neighboring matching blocks, $\mathbf{u}_{\mathcal{N}_x}$ in a Bayesian framework

$$\Pr(\mathbf{u}_{\mathbf{x}} \mid \mathbf{u}_{\mathcal{N}_x}) = \frac{\Pr(\mathbf{u}_{\mathcal{N}_x} \mid \mathbf{u}_{\mathbf{x}}) \Pr(\mathbf{u}_{\mathbf{x}})}{\Pr(\mathbf{u}_{\mathcal{N}_x})} \tag{5.2}$$

where, $\mathbf{u}_{\mathcal{N}_x}$ is the set of displacements at neighboring matching blocks, $\Pr(\mathbf{u}_{\mathbf{x}})$ is the prior probability density obtained by mapping the similarity metric image to a probability density image and $\Pr(\mathbf{u}_{\mathcal{N}_x} | \mathbf{u}_{\mathbf{x}})$ is the likelihood function. In the original implementation, four immediate neighbors (left, right, top and bottom) were considered for $\mathbf{u}_{\mathcal{N}_x}$. In conventional ultrasound motion tracking, the estimated displacement vector maximizes $\Pr(\mathbf{u}_{\mathbf{x}})$ [5]. This estimate will be considered as the NCC estimate in this chapter. However, in the Bayesian framework, information from neighboring matching blocks modifies the prior PDF, $\Pr(\mathbf{u}_{\mathbf{x}})$ resulting in a regularized motion tracking framework.

Assuming the neighbors are independent, the likelihood function $\Pr(\mathbf{u}_{\mathcal{N}_x} | \mathbf{u}_{\mathbf{x}})$ is defined as follows.

$$\Pr(\mathbf{u}_{\mathcal{N}_x} | \mathbf{u}_{\mathbf{x}}) = \prod_{\mathbf{x}' \in \mathcal{N}_x} \Pr(\mathbf{u}_{\mathbf{x}'} | \mathbf{u}_{\mathbf{x}}) \tag{5.3}$$

where, $\Pr(\mathbf{u}_{\mathbf{x}'} | \mathbf{u}_{\mathbf{x}})$ is the probability that a neighboring block at $\mathbf{x}'$ has a displacement $\mathbf{u}_{\mathbf{x}'}$ given displacement $\mathbf{u}_{\mathbf{x}}$ at $\mathbf{x}$. The independence assumption can be invalid due to expected correlation among neighboring matching blocks but is necessary to simplify mathematical modelling for Bayesian regularization. Application of Bayesian regularization for medical image registration [4, 6] have also made a similar independence assumption for modelling the likelihood function. In the case of ultrasound strain estimation, some degree of independence can be achieved by utilizing no kernel overlaps in both axial and lateral directions along with a iterative application of the algorithm [1]. $\Pr(\mathbf{u}_{\mathbf{x}'} | \mathbf{u}_{\mathbf{x}})$ term is modelled as follows.

$$\Pr\left(\mathbf{u}_{\mathbf{x}'} \mid \mathbf{u}_{\mathbf{x}}\right) \propto \max_{\mathbf{v}_{\mathbf{x}'} \in \mathcal{N}_{\mathbf{u}_{\mathbf{x}'}}} \left[\Pr\left(\mathbf{v}_{\mathbf{x}'}\right) \times \exp^{\left(\frac{-\|\mathbf{v}_{\mathbf{x}'} - \mathbf{u}_{\mathbf{x}}\|^2}{2\sigma_u^2}\right)} \right] \tag{5.4}$$

where $\mathbf{v}_{\mathbf{x}'}$ is the displacement at $\mathbf{x}'$, $\mathcal{N}_{\mathbf{u}_{\mathbf{x}'}}$ is a set of possible displacements evaluated in a neighborhood where $\mathbf{u}_{\mathbf{x}'}$ is evaluated and σ_u is the variance of a Gaussian weighting term. To evaluate equation (5.4), we need to consider all the possible displacements defined by the domain, Ω in equation (5.1) at the neighboring matching block location $\mathbf{x}' \in \mathcal{N}_x$. For each possible displacement, we consider a subset of local displacements around it, $\mathbf{v}_{\mathbf{x}'} \in \mathcal{N}_{\mathbf{u}_{\mathbf{x}'}}$ and weight them with a Gaussian term. The Gaussian term is modelled such that $\left\|\mathbf{v}_{\mathbf{x}'} - \mathbf{u}_{\mathbf{x}}\right\| < \epsilon$ with ϵ being a constant. In an approximate sense, a Gaussian model of spatial displacement variation is imposed by equation (5.4). The maximum among these Gaussian weighted displacements is utilized in equation (5.4). The variance σ_u controls the type of displacements allowed by the model. McCormick *et al.* coupled σ_u with the maximum expected strain in an image by introducing a parameter called strain regularization sigma (SRS), σ_ε [1]. PPD is then estimated by multiplying likelihood function with the prior PDF. Finally, regularized displacement estimate is determined using a *maximum a posteriori* (MAP) principle shown in eq. (5.5).

$$\mathbf{u}_{map} = \arg\max_{\mathbf{u}_{\mathbf{x}}} \Pr(\mathbf{u}_{\mathbf{x}} \mid \mathbf{u}_{\mathcal{N}_x}) \tag{5.5}$$

Integer displacements are derived by determining the axial and lateral shift corresponding to the maximum value of PPD. Subsample precision of the displacement is obtained using interpolation of PPD.

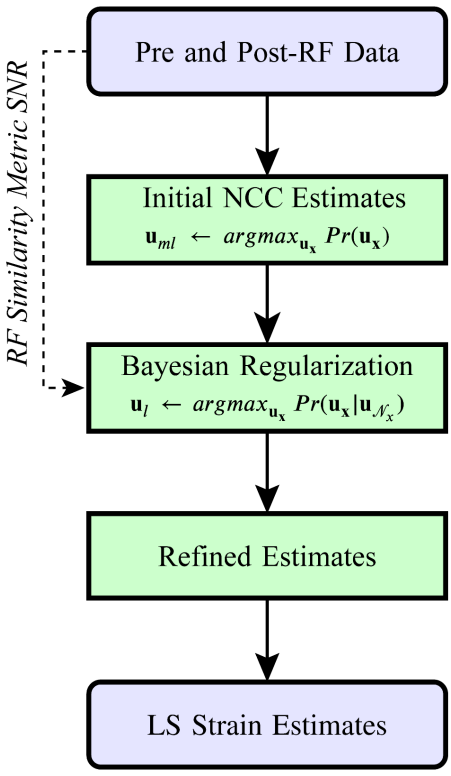

(a)

Algorithm 1: Adaptive refinement using Bayesian Regularization

Input : $\mathbf{u}_{NCC}$: NCC displacement vector
$SNR_\rho^{(NCC)}$: NCC signal-to-noise ratio
τ : Decorrelation threshold
l_{max}: Maximum number of iterations
ζ : Improvement tolerance
TOL: Iteration tolerance
$r^{(up)}$: Upper regularization ratio
$r^{(low)}$: Lower regularization ratio

Output: $\mathbf{u}_{reg}$: Regularized displacement vector

$\mathbf{u}_0 \leftarrow \mathbf{u}_{NCC}$
$SNR_\rho^{(0)} \leftarrow SNR_\rho^{(NCC)}$
$MAP_l \leftarrow 0$
for $l \leftarrow 1$ **to** l_{max} **do**
  $\mathbf{u}_l \leftarrow argmax_{\mathbf{u}_x} Pr(\mathbf{u}_x|\mathbf{u}_{\mathcal{N}_x})$
  $\rho_{mc}^{(l)} \leftarrow$ Estimate $\rho_{mc}^{(l)}$ for $\mathbf{u}_l$
  if $l = 1$ **then**
    if $(SNR_\rho^{(0)} < \tau)$ **then**
      MAP_l++
      $\mathbf{u}_{reg} \leftarrow \mathbf{u}_l$
    else
      $\mathbf{u}_{reg} \leftarrow \mathbf{u}_0$
  else
    if $(\rho_{mc}^{(l)} - \rho_{mc}^{(l-1)}) > \zeta$ **then**
      MAP_l++
      $\mathbf{u}_{reg} \leftarrow \mathbf{u}_l$
  if $(|MAP_l - MAP_{l-1}| < TOL$ **and** $MAP_l^{ratio} < r^{(up)})$ **or** $(MAP_l^{ratio} < r^{(low)})$ **then**
    break

(b)

Figure 5.1 (a) Flowchart describing AIBRF. (b) Proposed algorithm for adaptive refinement of NCC displacement estimates using Bayesian regularization.

5.1.2 Adaptive Application of Bayesian Regularization

Equation (5.4) can be applied iteratively to regularize the initial NCC similarity metric image. At each iteration, influence from neighboring matching blocks beyond the adjacent blocks get incorporated into the regularization process. Thus, we expect that based on the degree of signal decorrelation between pre- and post-deformation RF echo signal data, the number of required iterations will vary locally within the displacement estimated. Based on this observation, we propose the AIBRF framework for a locally optimized correlation-guided adaptive iterative

Bayesian regularization framework for ultrasound strain imaging. The key steps of the proposed framework are summarized in Figure 5.1 (a). Axial and lateral displacement estimates obtained using 2-D NCC are used as an input to the AIBRF. In the original implementation, these estimates were refined using a fixed number of iterations. In the proposed framework, we provide RF data as an additional input to the BRF to locally control the number of iterations. Finally, refined axial and lateral displacement estimates are passed through a least squares spatial gradient operator to derive underlying tissue strain [7].

5.1.2.1 Quality metrics for optimizing Bayesian regularization

We consider two quality metrics for determining local signal de-correlation during the regularization process. Firstly, we derive a quality metric for the un-regularized similarity metric by converting peak cross-correlation estimate of the NCC function into a signal-to-noise ratio [8, 9] measure defined as follows.

$$SNR_{\rho} = \frac{\rho_{\max}}{1-\rho_{\max}} \tag{5.6}$$

where ρ_{max} is the peak cross-correlation coefficient.

Secondly, we evaluate the quality of estimated displacements after each iteration by performing 2-D NCC calculation between RF data I_1 and I_2 after motion compensation. We term this metric as motion compensated *SNR* and denote using $\rho_{mc}^{(l)}$ for iteration *l*. To derive $\rho_{mc}^{(l)}$ between I_1 and I_2, we consider a kernel, W_1 of size $r \times c$ from I_1 around the point (x_1, y_1). A post-deformation kernel, W_2 of same size is extracted from the corresponding point (x_2, y_2) in the image I_2 by re-sampling post-RF data with linear interpolation using the following equation [10, 11].

$$x_2 = (1+\varepsilon_x)\, x_1 + u_x$$
$$y_2 = (1-\varepsilon_y)\, y_1 + u_y \tag{5.7}$$

where, ε_y and ε_x are the estimated axial and lateral strains derived by applying a central-difference gradient operator on the estimated axial (u_y) and lateral (u_x) displacements respectively. Linear interpolation was chosen due to its simplicity and lower computational load compared to other approaches (e.g., bicubic/Sinc).

5.1.2.2 Algorithm for Adaptive Bayesian Regularization

The algorithm for adaptive refinement of NCC estimates using Bayesian regularization is presented in Figure 5.1 (b). The key steps of the proposed algorithm are follows.

(i). Initialize the algorithm by estimating NCC displacement, $\mathbf{u}_{NCC}$ and $SNR_{\rho}^{(NCC)}$. $SNR_{\rho}^{(NCC)}$ is estimated using equation (5.6) and considered as a de-correlation measure of the unregularized similarity metric.

(ii). Set iteration, *l=1* and regularization location counter $MAP_l = 0$. The parameter MAP_l keeps track of the number of grid locations requesting regularization in the next iteration, *l+1*.

(iii). Estimate Bayesian regularized displacement, $\mathbf{u}_l$ using equation (5.5).

(iv). Using $\mathbf{u}_l$, estimate motion compensated *SNR*, $\rho_{mc}^{(l)}$.

(v). For iteration equal to one, if $SNR_{\rho}^{(NCC)}$ is less than decorrelation threshold, τ then refined displacement estimate, $\mathbf{u}_{reg}$ is updated using current regularized estimate, $\mathbf{u}_l$ and MAP_l is incremented otherwise $\mathbf{u}_{NCC}$ is assigned to $\mathbf{u}_{reg}$.

(vi). If iteration is greater than 1 then

   a. If there is an improvement in motion compensated *SNR* with current estimate compared to estimate from previous iteration i.e. $\left(\rho_{mc}^{(l)} - \rho_{mc}^{(l-1)}\right) > \zeta$ where, ζ is an improvement tolerance then $\mathbf{u}_{reg}$ is updated using current regularized estimate, $\mathbf{u}_l$ and MAP_l is incremented.

b. If there is no improvement, then retain previous iteration's estimate.

(vii). Repeat step (iii) – (vi) for all grid locations (grid dimension of $X \times Y$).

(viii). Estimate percentage of locations requiring regularization using following equation.

$$MAP_l^{ratio} = \frac{MAP_l}{(X \times Y)} \tag{5.8}$$

(ix). To adaptively stop regularization after an optimal number of iterations, we have defined two stopping criteria based on MAP_l^{ratio}. We stop regularization if either of the following conditions get satisfied

a. The number of locations requiring regularization between consecutive iterations is within a tolerance, TOL and MAP_l^{ratio} is less than the upper regularization ratio, $r^{(up)}$

b. MAP_l^{ratio} is less than the lower regularization ratio, $r^{(low)}$

(x). If none of the conditions stated in step (ix) are met and $l+1$ is less than the maximum number of iterations, l_{max} then continue to step (iii).

Note that the grid locations where MAP_l is incremented are marked for regularization in the next iteration while the remaining locations will not be regularized. Thus, the number of required iterations will vary for different local locations in contrast to the same number of iterations for all locations in the original implementation. The parameters decorrelation threshold, τ and improvement tolerance, ζ are used to inhibit under-regularization and over-regularization respectively. Parameter TOL is designed to stop regularization when the number of locations requesting regularization between consecutive iterations does not vary significantly indicating that additional regularization is unlikely to provide any additional benefit. At very high applied deformations, it might be the case that MAP_l between initial iterations are within TOL thus stopping regularization even though it requires further refinement. Upper regularization ratio, $r^{(up)}$ is used to impede this. Additionally, to prevent the algorithm from stalling by trying to improve

the grid locations near edges (especially in the simulation study), we break the regularization loop if MAP_l^{ratio} falls below the lower regularization ratio $r^{(low)}$. This rule is used to improve computational efficiency and our initial experiments demonstrate that the performance of the proposed approach was not compromised.

5.1.3 Algorithm Implementation

We incorporate the adaptive Bayesian regularization framework into our multi-level 2-D BM algorithm for strain estimation. We denote displacement estimation methods without regularization, with fixed number of iterations and adaptive regularization as NCC, MAP-Iter and MAP-Adapt respectively. A coarse-to-fine pyramid with three levels was constructed by applying the decimation factors reported in Table 5.1 to the up sampled RF data with Gaussian smoothening. Smoothening was performed using a discrete Gaussian function with variance of $\left(f/2\right)^2$ where f denotes the decimation factor. This approach combines the robustness of envelope tracking at higher strains with precision of RF data at lower strains [12-14]. B-mode data used for coarse motion tracking at the first level ensures global estimation of displacement reducing errors incurred with larger deformations, while the rest of the levels use RF data for precise displacement and strain estimation. To improve spatial resolution of the estimated displacements, the coarse-to-fine search strategy with progressively decreasing kernel size was utilized (Table 5.1). The processing kernel overlap was 10% and 90% in the axial and lateral directions respectively. The final processing kernel size was 1 wavelength by 10 A-lines. Parabolic interpolation was used for levels 1 and 2 while the final level used 2-D windowed Sinc interpolation [15-17] for unbiased subsample displacement estimation. Signal alignment and stretching was used at each level to improve displacement estimation accuracy [2, 11, 18]. To compute the $SNR_\rho^{(NCC)}$ term for MAP-Adapt, 2-

D windowed Sinc interpolation with a window radius of 8 points was used to precisely locate the peak of the NCC function. This was necessary due to the non-linear relationship between SNR_ρ and peak NCC coefficient $\rho_{\max}$. 2-D displacement estimation and regularization related parameters are summarized in Table 5.1.

Table 5.1 Displacement Estimation Algorithm Processing Parameters

Parameter	**Value**
Multi-level Block-matching parameters	
Levels in multi-resolution pyramid	3
Lateral interpolation factor	2
Axial decimation factors	[3, 2, 1]
Kernel overlaps [Axial, Lateral]	[10%, 90%]
Lateral decimation factors	[2, 1, 1]
Axial kernel length (Wavelengths)	[8 λ, 3 λ, 1 λ]
Lateral kernel length (A-lines)	[15, 12, 10]
Axial search range (Wavelengths) *	[3 λ, 2 λ, 1 λ]
Lateral search range (A-lines) *	[5, 5, 3]
Bayesian regularization specific parameters	
Axial strain regularization sigma	0.150
Lateral strain regularization sigma	0.075
Number of iterations	[1,5]
Adaptive Bayesian regularization specific parameters	
Maximum number of iterations, l_{max}	10
Decorrelation threshold, τ	90
Improvement tolerance, ζ	0.01
Iteration tolerance, TOL (pixels)	100
Lower regularization ratio, $r^{(low)}$	0.15
Upper regularization ratio, $r^{(up)}$	0.80

**Search range reported for cardiac strain imaging applications (simulation and in vivo)*
Updated appropriately for quasi-static elastography applications (simulation)

5.2 Validation Experiments for Adaptive Bayesian Regularization

5.2.1 Numerical Quasi-static Elastography Simulation Study

Two experiments using numerical phantom simulations were used to evaluate the performance of the MAP-Adapt algorithm. First, a uniform tissue mimicking phantom with background modulus of 2 kPa was simulated to test algorithm performance for tracking displacements in a homogeneous medium. Second, an inclusion phantom with a stiffer inclusion in soft background was simulated to characterize algorithm performance for lesion visualization. Finite-element analysis (FEA) model generated displacement fields were applied on the top surface of each phantom axially to produce nominal strain of 0.5 %, 1.0 %, 3.0 %, 5.0 %, 7.0 %, 9.0 % and 11.0 %. For each applied deformation, ten independent scatterer distributions were generated to obtain statistically significant results. Details about the FEA can be found in [1]. RF data were generated using a frequency domain ultrasound simulation program developed in our laboratory [19]. A 1-D linear array with 128 elements and a kerf of 0.2 mm was modeled. Each individual element had a height of 10 mm and width of 0.15 mm. The linear array was operating at a center of frequency of 8.0 MHz and RF data was sampled at a frequency of 78.84 MHz. A single transmit focus was set at a depth of 20 mm. Conventional Delay and Sum (DAS) beamforming with 128 consecutive elements were used to form each A-line. The speed of sound and attenuation coefficient were set to 1540 m/s and 0.5 dB/cm-MHz respectively.

To reduce the effects of boundaries, a 20×25 mm^2 region of interest (ROI) around the transducer's focus was considered for quantitative evaluation. Estimation accuracy was evaluated using displacement mean absolute error (*MAE)*, jitter error [20] and normalized strain error (%), $\Delta\varepsilon$:

$$MAE = \frac{\sum_{i=1}^{n} |u_e - u_t|}{n} \tag{5.9}$$

$$jitter = \mathrm{var}(u_e - u_t) \tag{5.10}$$

$$\Delta\varepsilon = \frac{\sum |\varepsilon_{ES} - \varepsilon_{TS}|}{\sum |\varepsilon_{TS}|} \times 100 \tag{5.11}$$

In equations (5.9) and (5.10), u_e and u_t denote estimated and FEA displacements respectively. In equation (5.11), ε_{ES} and ε_{TS} denote estimated and FEA strains respectively. Experimental strain filters [21] were generated for each method by calculating elastographic signal-to-noise ratio (SNR_e) [22] :

$$SNR_e \text{ [dB]} = 20 \times \log\left(\frac{m_e}{s_e}\right) \tag{5.12}$$

where, m_e and s_e denote the mean and standard deviation of estimated strain respectively.

Detectability in inclusion phantom strain images were quantified by calculating Contrast to Noise ratio (CNR_e) [23, 24] :

$$CNR_e\text{[dB]} = 20 \times \log\left(\sqrt{\frac{2(m_b - m_t)^2}{\sigma_b^2 + \sigma_t^2}}\right) \tag{5.13}$$

where, m_b and m_t are spatial strain average of background (w_b) and target (w_t) window respectively, σ_b^2 and σ_t^2 denote spatial variance of w_b and w_t respectively. A rectangular ROI of size 3.35×3.35 mm^2 was placed inside the lesion as w_t. Two rectangular ROIs were placed at same depth as the target ROI (w_t) but offset 9.25 and 9.73 mm laterally to the left and right respectively

from the center of the inclusion were used as background ROIs. Area of each background ROI was half the area of w_t.

5.2.2 Finite Element Analysis (FEA) Model for Canine Cardiac Simulation

A 3-D FEA model of a healthy canine heart [25, 26] was employed to compare the performance of NCC, MAP-Adapt and MAP-Iter approaches in the presence of complex cardiac deformation. Over 1×10^6 scatterers were randomly positioned in the myocardium of the 3-D model to ensure Rayleigh scattering statistics. A 2-D parasternal long axis (PLAX) ultrasonic imaging view from this 3-D model was used. The description of the RF data simulation is the same as that presented for quasi-static elastography simulation above. RF data were collected at a 78.84 MHz sampling frequency. Each simulated ultrasound image had an 80×100 mm^2 field of view.

5.2.3 In vivo Cardiac Imaging of Murine Model

To demonstrate *in vivo* feasibility, cardiac strain estimation was done in a healthy murine model (10-12 weeks old male athymic nude mouse acquired from Jackson Labs, ME, USA). All *in-vivo* procedures were approved by the Institutional Animal Care and Use Committee (IACUC) at the University of Wisconsin-Madison. The mouse was anesthetized using 1.5% isoflurane and placed in the supine position on a heated imaging platform with a constant flow of oxygen. A representative image of *in vivo* cardiac image acquisition experimental setup is shown in Figure 5.2. A Vevo 2100 LAZR imaging system (FUJIFILM VisualSonics, Inc., Toronto, Canada) was employed for collecting ultrasound RF data. High frequency ultrasound imaging was performed using a MS 550D transducer operating at a center frequency of 40 MHz. 2-D conventional focused ultrasound RF data at a 512 MHz sampling frequency along the PLAX and parasternal short axis (PSAX) views were acquired. We acquired 1000 frames per imaging plane, which was stored for off-line analysis. During image acquisition, electrocardiogram (ECG) and respiratory signals were

continuously monitored and acquired. A single cardiac cycle was chosen for strain estimation gated to ECG and respiratory signal. Image acquisition related parameters are summarized in Table 5.2.

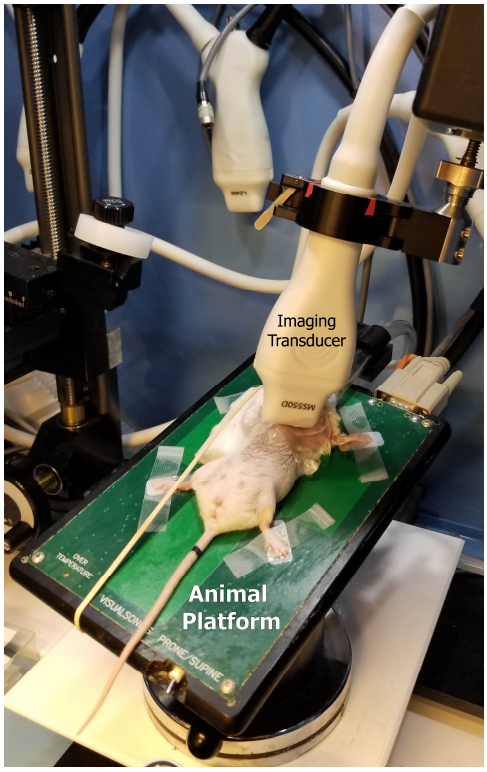

Figure 5.2 Representative image of *in vivo* cardiac image acquisition experimental setup.

Table 5.2 *In vivo* Image Acquisition Parameters

Parameter	**PLAX**	**PSAX**
Transducer	MS550D	
Center frequency (MHz)	40	
Field of view ($mm^{2)}$	11 × 12.08	10 × 8.08
Number of A-lines	220	148
Imaging Framerate (Hz)	235	347
Sensitivity	Standard	
2-D Gain (dB)	25	

5.2.4 Adaptive Bayesian Regularization for Cardiac Strain Imaging

A cardiac strain estimation pipeline [27] described in detail in **Chapter 4** was employed to estimate myocardial strain from FEA canine cardiac simulation and *in vivo* murine model data. Incremental axial and lateral displacements were estimated using approaches reported in Section 0. These incremental displacements were integrated over time based on a Lagrangian description of motion from end-diastole (ED) to end-systole (ES). In plane Lagrangian finite strain tensors were then derived from the accumulated displacements using a least squares (LS) strain estimator [7] with 0.2 mm and 1 mm kernels in axial and lateral directions respectively. Cartesian to cardiac coordinate transformation was utilized to calculate myocardial strain for ease of interpretation. Radial and longitudinal strain curves were derived from PLAX view while the PSAX view was used to derive radial and circumferential strain curves. ES strain images and segmental strain curves from both FEA and *in vivo* models were compared for NCC, MAP-Adapt and MAP-Iter approaches. FEA model results were quantitatively compared using eqn. (5.11).

5.3 Findings from Numerical Quasi-static Elastography Simulation Study

5.3.1 Uniform Phantom Simulation Results

Displacement and strain estimation accuracy for MAP-Adapt as a function of applied deformation is compared against NCC and MAP-Iter with 1 and 5 iterations. Our previous studies showed that in some cases a single iteration of Bayesian regularization was sufficient while others required three or larger number of iterations [27]. Therefore, we investigated cases with both low and high number of iterations for MAP-Iter in this study. MAP-Iter with 1 and 5 iterations will be termed as MAP-Iter=1 and MAP-Iter=5 respectively. Strain errors are strongly influenced by the choice of LS kernel length and amount of smoothening [14]. Thus, we decided to use a small kernel length (3.2 *mm* for both axial and lateral direction) for LS and perform no spatial filtering

(e.g., median filtering) so that any noise in the estimated displacement fields gets amplified in the strain images. Ground truth strain images were derived by applying the same LS strain estimator on the FEA displacement fields. Error bars denote twice the standard error computed over ten independent simulations at each applied deformation. Statistical analysis was performed using the paired t-test with the aforementioned ten independent simulation instances.

Representative results from a uniform phantom simulation study at low (3 %) and high (7 %) applied deformations are presented in Figure 5.3 and Figure 5.4 respectively for qualitative comparison between NCC, MAP-Iter=1, MAP-Iter=5 and MAP-Adapt methods. Qualitatively all methods provide fairly similar axial displacement and strain results. In the case of axial strain, MAP-Iter=5 strain image (Figure 5.3 (i) [g]) was smoother when compared to MAP-Iter=1 (Figure 5.3 (i) [f]) and MAP-Adapt images (Figure 5.3 (i) [h]). Note that for lateral displacement and strain images, Map-Iter=1 and MAP-Adapt displacement results were smoother (Figure 5.3 (ii) [b] and [d] respectively) when compared to NCC (Figure 5.3 (ii) [a]). Subsequently, lateral strain images estimated by MAP-Iter=1 (Figure 5.3 (ii) [f]) and MAP-Adapt (Figure 5.3 (ii) [h]) had higher uniformity when compared to NCC (Figure 5.3 (ii) [e]). On the other hand, observe the severe deterioration in the displacement and strain image quality with MAP-Iter=5 (Figure 5.3 (ii) [c] and [g]). Impact of over-regularization appears as “vertical banding” artifacts in these lateral strain images.

Figure 5.4 summarizes the estimation results at 7 % applied deformation. Visual inspection shows that Bayesian methods provide higher quality axial displacement (Figure 5.4 (i) [b – d]) and strain images (Figure 5.4 (i) [f – h]) when compared to NCC (presence of peak-hop errors in Figure 5.4 (i) [a] and [e]). Lateral displacement and strain images at 7 % applied deformation indicate that higher quality results were obtained using MAP-Iter=1 (Figure 5.4 (ii) [b] and [f]) and MAP-Adapt

(Figure 5.4 (ii) [d] and [h]) when compared to NCC (observe presence of peak-hop errors in Figure 5.4 (ii) [a] and [e]) or MAP-Iter=5 (vertical bands in Figure 5.4 (ii) [c] and [g]).

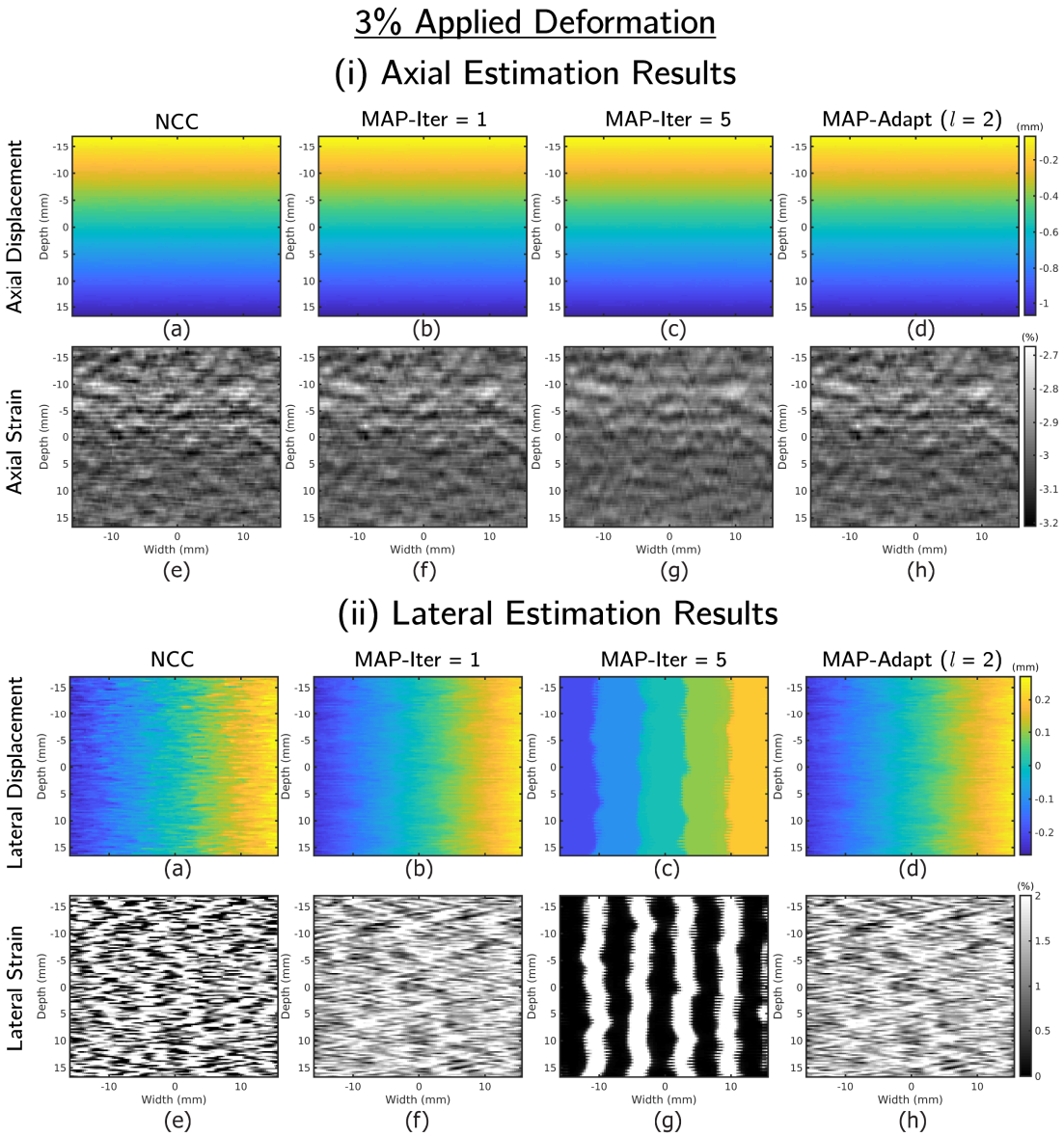

Figure 5.3 Representative axial (i) and lateral (ii) estimation results from uniform phantom simulation at 3 % applied deformation. Displacement images estimated by (a) NCC, (b) MAP-Iter=1, (c) MAP-Iter=5 and (d) MAP-Adapt along with corresponding strain images estimated by (e) NCC, (f) MAP-Iter=1, (g) MAP-Iter=5 and (h) MAP-Adapt respectively. *l* = maximum required iterations by MAP-Adapt.

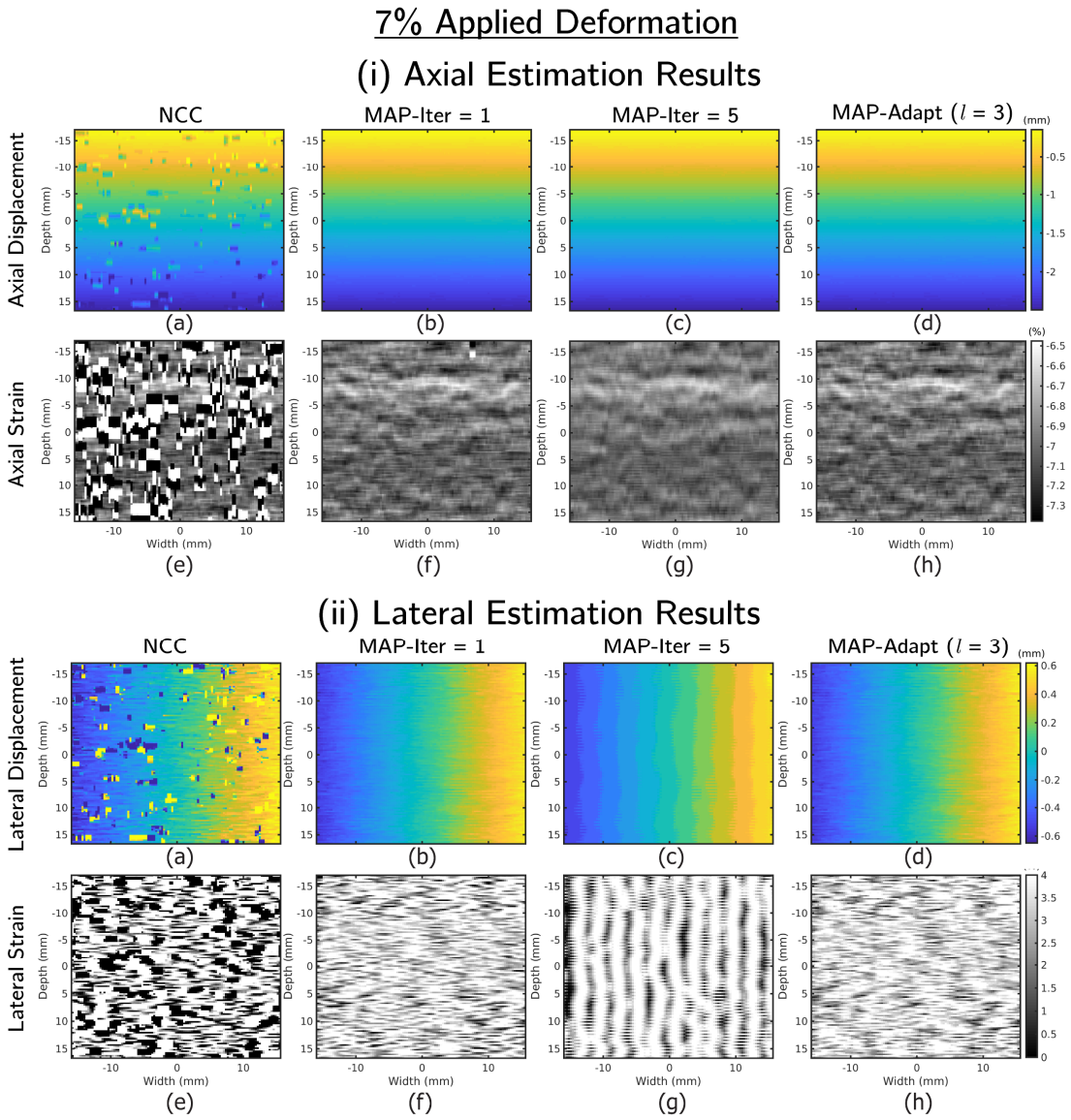

Figure 5.4 Representative axial (i) and lateral (ii) estimation results from uniform phantom simulation at 7 % applied deformation. Displacement images estimated by (a) NCC, (b) MAP-Iter=1, (c) MAP-Iter=5 and (d) MAP-Adapt and corresponding strain images estimated by (e) NCC, (f) MAP-Iter=1, (g) MAP-Iter=5 and (h) MAP-Adapt respectively. *l* = maximum required iterations by MAP-Adapt.

Figure 5.5 (a) – (c) demonstrate the results for axial displacement MAE (d_y^{MAE}), jitter error (d_y^{Var}) and normalized axial strain error ($\Delta\varepsilon_{axial}$) respectively. Figure 5.5 (a) shows that all methods had similar axial displacement MAEs at low and moderate strains (up to 5 % strain). At higher

strains, MAP-Adapt and MAP-Iter=5 provided lower d_y^{MAE} values compared to NCC and MAP-Iter=1. At 11 % strain, due to significant decorrelation, all methods fail to provide any reliable estimate. Figure 5.5 (b) shows that MAP-Iter=5 had the least amount of jitter errors compared to other methods. MAP-Adapt had slightly higher jitter errors compared to MAP-Iter=5 but retained improved performance compared to NCC and MAP-Iter=1. Similar trend was observed in axial strain error results presented in Figure 5.5 (c). Best performance in terms of $\Delta\varepsilon_{axial}$ was achieved with MAP-Iter = 5. However, improvements were on par with MAP-Adapt as it had slightly higher axial strain error ($\Delta\varepsilon_{axial|5\%}$ =1.51 %) compared to MAP-Iter=5 ($\Delta\varepsilon_{axial|5\%}$ =1.29 %). These results indicate that strain estimation performance in the axial direction was dominated by jitter errors. Figure 5.5 (d) – (f) present the results for lateral displacement MAE (d_x^{MAE}), jitter error (d_x^{Var}) and normalized lateral strain error ($\Delta\varepsilon_{lateral}$) respectively. Figure 5.5 (d) shows that MAP-Iter=5 had higher lateral displacement MAEs when compared to MAP-Adapt and MAP-Iter=1. This result demonstrates the impact of over regularization on lateral displacement estimates. At 4.5 % strain, MAP-Adapt demonstrated superior performance ($p < 0.001$) with lower lateral displacement MAE (d_x^{MAE} = 23.73 μm) when compared to MAP-Iter=1 (d_x^{MAE} = 114.16 μm). NCC has higher MAEs when compared to MAP-Adapt showing the benefit of regularization. Similar trends were observed in lateral jitter error results presented in Figure 5.5 (e). MAP-Adapt had the least amount of jitter errors up to 3.5 % strain. However, there was performance degradation of MAP-Adapt (d_x^{Var} = 1.74 μm^2) compared to MAP-Iter=5 (d_x^{Var} = 0.79 μm^2) at 4.5 % strain. Figure 5.5 (f) shows that most accurate lateral strain estimation was achieved with MAP-Adapt except for the 4.5 % strain. For instance, at 1.5 % lateral strain, MAP-Iter=5's lateral strain error ($\Delta\varepsilon_{lateral|1.5\%}$ = 104.49 %) was significantly reduced using MAP-Adapt approach ($\Delta\varepsilon_{lateral|1.5\%}$ = 27.51 %) with p-value

less than 0.001. At 4.5 % strain, MAP-Iter with 5 iterations showed improved performance. Note that maximum required number of iterations vary as a function of applied deformation as shown in Figure 5.5 (g).

Figure 5.6 (a) and (b) represent experimental axial and lateral strain filter results respectively. NCC axial strain filter showed comparable performance with Bayesian regularization methods for low strains (0.5 % to 3 %). Note that SNR_e values drastically reduce at higher applied deformations (5.0% to 9.0%). MAP-Iter=5 had the highest axial SNR_e values at all applied deformations and MAP-Iter=1 had the worst axial estimation performance among Bayesian regularization approaches. MAP-Adapt had comparable performance with MAP-Iter=5 up to 7 % strain. For instance, at 7 % strain, MAP Adapt and MAP-Iter=5 had SNR_e of 35.10 dB and 36.40 dB respectively. However, MAP-Iter=5 performed significantly better ($p < 0.01$) than MAP-Adapt at 9 % strain (SNR_e = 34.22 dB and 28.11 dB respectively). Our findings from error analysis in Figure 5.5 (a) – (c) corroborate these results. For lateral strain, NCC had the lowest SNR_e values for all applied deformations. MAP-Adapt and MAP-Iter=1 performed significantly better than NCC and MAP-Iter=5 up to 3.5 % strain. For instance, at 1.5 % strain, MAP Adapt and MAP-Iter=5 had SNR_e of 9.18 dB and -0.39 dB respectively ($p < 0.001$). Although MAP-Iter=5 had slightly higher SNR_e value at 0.25 % strain, it severally underestimated the underlying strain (median estimated $\varepsilon_{lateral} = 0.0012\%$). A distinct peak was observed in the strain filter of MAP-Iter=5 at 4.5 % strain showing improved performance with higher iterations at high strain. Overall, MAP-Adapt approach achieved a balance between axial and lateral displacement and strain estimation accuracy without the over-regularization seen with MAP-Iter=5.

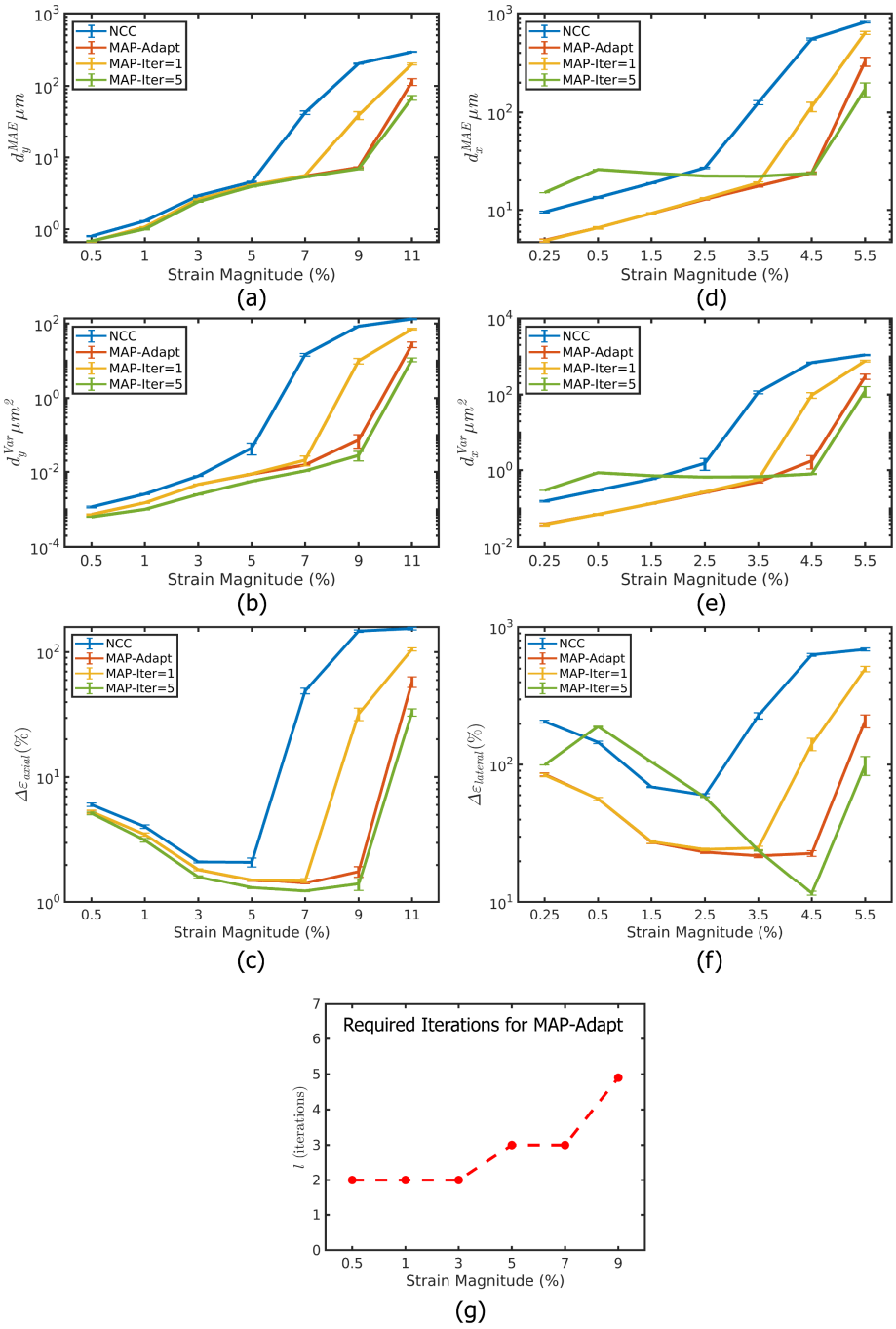

Figure 5.5 Uniform phantom simulation error analysis as a function of the applied deformation. (a) Axial displacement MAE (μm), (b) axial displacement jitter error (μm^2), (c) axial normalized strain error (%), (d) lateral displacement MAE (μm), (e) lateral displacement jitter error (μm^2), (f) lateral normalized strain error (%) and (g) Maximum required number of iterations as a function of applied deformation for MAP-Adapt.

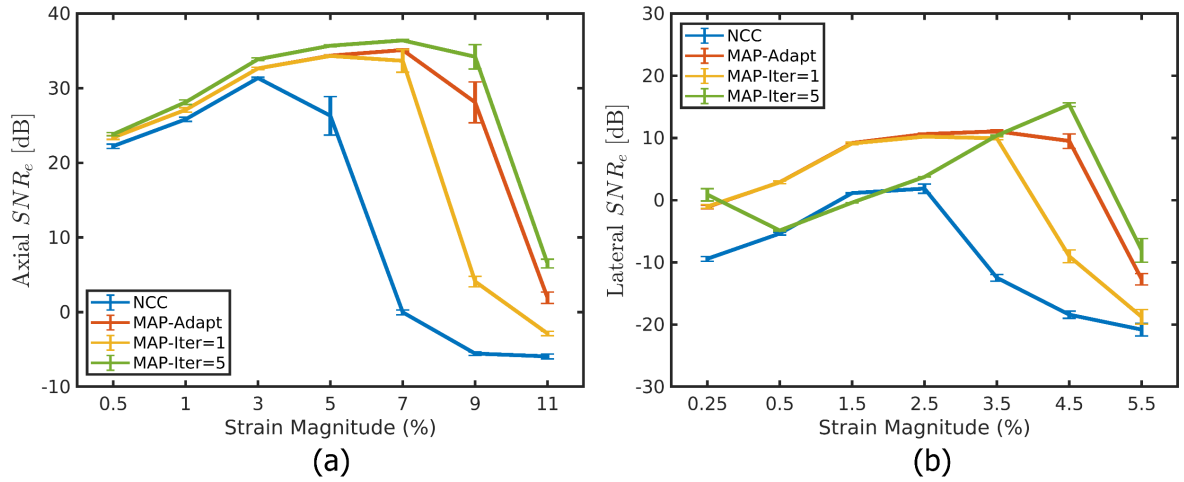

Figure 5.6 Comparison of experimental strain filters estimated using NCC, adaptive Bayesian and Bayesian with fixed iterations. (a) Axial strain filter and (b) lateral strain filter.

5.3.2 Inclusion Phantom Simulation Results

In this section, we present representative results from the inclusion phantom study at low (3 %) and high (7 %) applied deformation for a qualitative comparison. Figure 5.7 summarizes the estimation results at 3 % applied deformation. Axial displacement and strain images are shown in Figure 5.7 (i). Qualitatively all methods provide similar axial displacement results (Figure 5.7 (i) [a – d]). In case of axial strain, NCC had some erroneous strain values near the bottom right of the lesion (Figure 5.7 (i) [e]) which were corrected by all Bayesian regularization methods (Figure 5.7 (i) [f – h]). Lateral displacement and strain images at 3 % applied deformation are shown in Figure 5.7 (ii). Note that Map-Iter=1 and MAP-Adapt methods provide smoother displacement images (Figure 5.7 (ii) [b] and [d] respectively) compared to NCC (Figure 5.7 (ii) [a]). Subsequently, lateral strain images estimated by MAP-Iter=1 (Figure 5.7 (ii) [f]) and MAP-Adapt (Figure 5.7 (ii) [h]) had higher quality with clearer lesion boundary and smoother background compared to NCC (Figure 5.7 (ii) [e]). Severe deterioration of displacement and strain image quality was observed

with MAP-Iter=5 (Figure 5.7 (ii) [c] and [g]). Impact of over-regularization appears as "vertical banding" artifacts in these results.

Figure 5.8 summarizes the estimation results at 7 % applied deformation. Figure 5.8 (i) shows the axial displacement and axial strain images estimated using the methods previously described. Visual inspection shows that MAP-Adapt and MAP-Iter=5 provide higher quality displacement (Figure 5.8 (i) [c – d]) and strain images (Figure 5.8 (i) [g – h]). Axial displacement images estimated by NCC and MAP-Iter=1 (Figure 5.8 (i) [a – b]) suffer from peak-hop errors causing significant reduction of corresponding strain image quality (Figure 5.8 (i) [e – f]). Lateral displacement and strain images at 7 % applied deformation are shown in Figure 5.8 (ii). MAP-Adapt provided the best displacement (Figure 5.8 (ii) [d]) and strain (Figure 5.8 (ii) [h]) images showing the improvement obtained with adaptive Bayesian regularization. NCC (Figure 5.8 (ii) [a] and [e]) and MAP-Iter=1 (Figure 5.8 (ii) [b] and [f]) suffer from peak-hop errors while the vertical banding artifact due to over-regularization was seen in MAP-Iter=5 results (Figure 5.8 (ii) [c] and [g]).

Figure 5.9 (a) – (c) demonstrate the results for axial displacement MAE (d_y^{MAE}), jitter error (d_y^{Var}) and normalized axial strain error ($\Delta\varepsilon_{axial}$) respectively from the inclusion phantom simulation study. In case of axial displacement and strain estimation, both MAP-Adapt and MAP-Iter=5 provided improved performance compared to NCC and MAP-Iter=1 over the entire range of applied deformations. NCC and MAP-Iter=1 suffered from performance degradation at moderate and higher strains (5% or higher) due to under-regularization. Figure 5.9 (d) – (f) present the results for lateral displacement MAE (d_x^{MAE}), jitter error (d_x^{Var}) and normalized lateral strain error ($\Delta\varepsilon_{lateral}$) respectively. These results demonstrate the superiority of MAP-Adapt over MAP-

Iter=5 with significantly lower d_x^{MAE}, d_x^{Var} and $\Delta\varepsilon_{lateral}$ up to 3.5 % strain ($p < 0.001$). At 4.5 % strain, MAP-Iter=5 showed the best performance. Overall, a balance between under-regularization and over-regularization was achieved using MAP-Adapt approach.

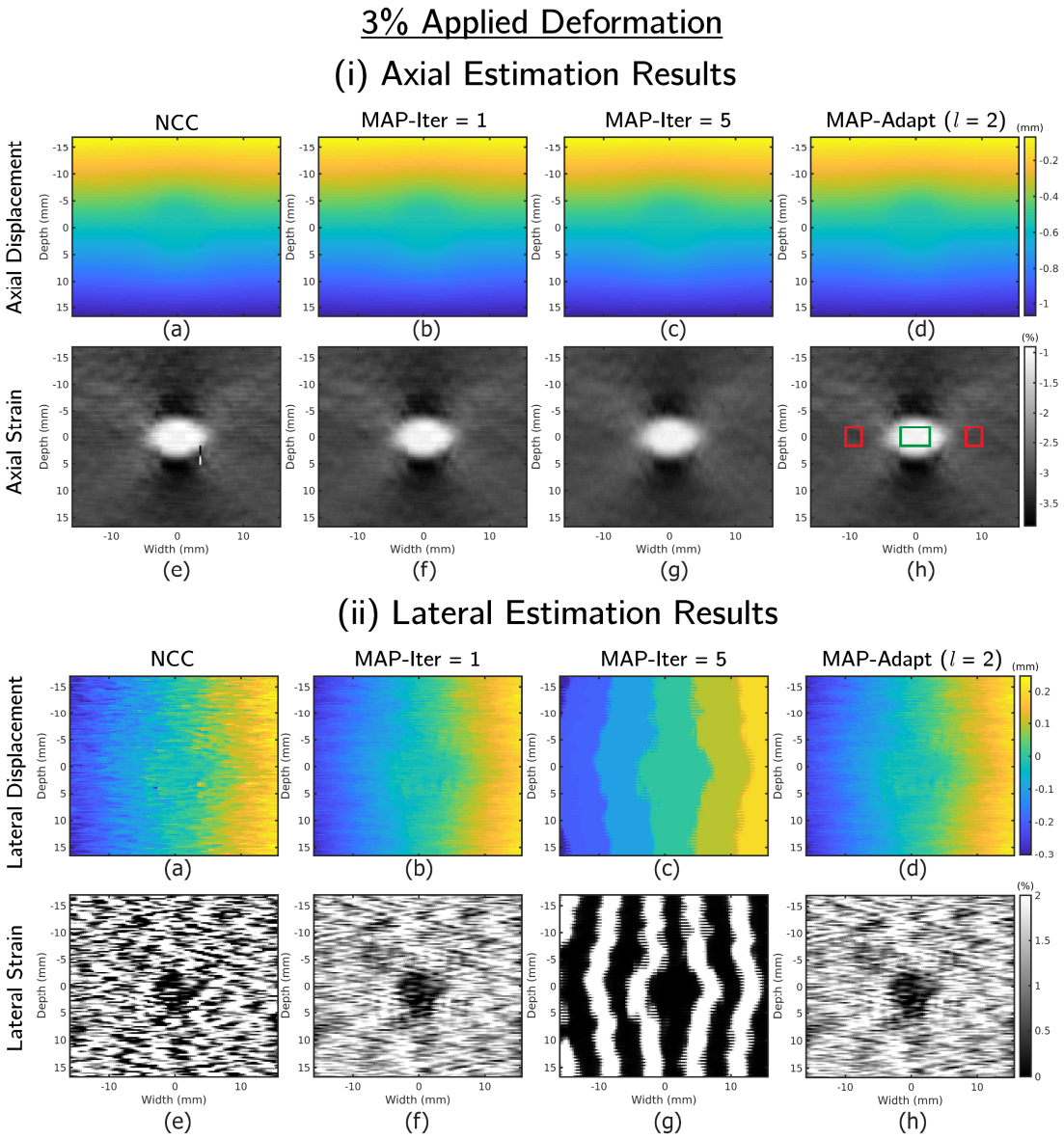

Figure 5.7 Representative axial (i) and lateral (ii) estimation results from inclusion phantom simulation at 3 % applied deformation. Displacement images estimated by (a) NCC, (b) MAP-Iter=1, (c) MAP-Iter=5 and (d) MAP-Adapt and corresponding strain images estimated by (e) NCC, (f) MAP-Iter=1, (g) MAP-Iter=5 and (h) MAP-Adapt respectively. *l* = maximum required iterations by MAP-Adapt.

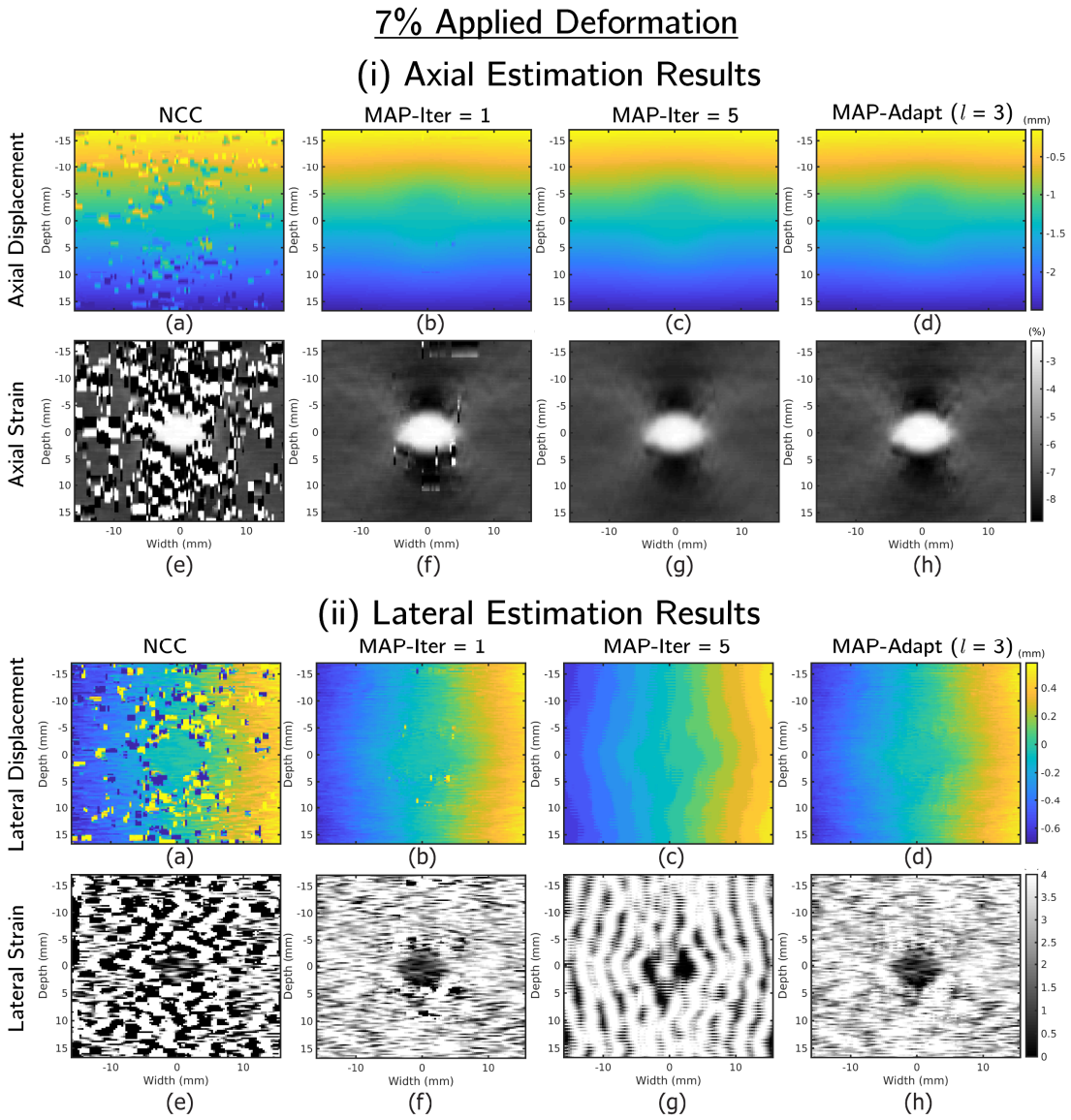

Figure 5.8 Representative axial (i) and lateral (ii) estimation results from inclusion phantom simulation at 7 % applied deformation. Displacement images estimated by (a) NCC, (b) MAP-Iter=1, (c) MAP-Iter=5 and (d) MAP-Adapt along with corresponding strain images estimated by (e) NCC, (f) MAP-Iter=1, (g) MAP-Iter=5 and (h) MAP-Adapt respectively. *l* represents the maximum required iterations for the MAP-Adapt algorithm.

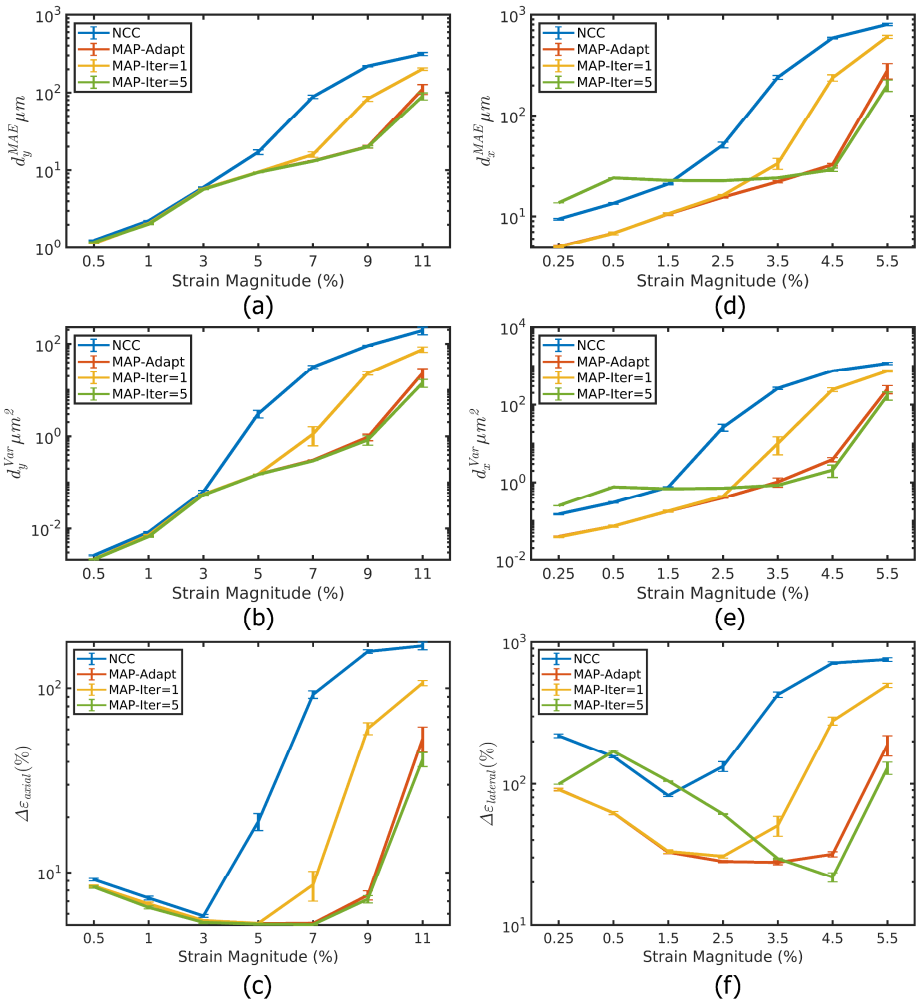

Figure 5.9 Inclusion phantom simulation error analysis as a function of the applied deformation. (a) Axial displacement MAE (μm), (b) axial displacement jitter error (μm^2), (c) axial normalized strain error (%), (d) lateral displacement MAE (μm), (e) lateral displacement jitter error (μm^2), and (f) lateral normalized strain error (%).

To compare the methods quantitatively, CNR_e as a function of applied deformation is compared in Figure 5.10. Figure 5.10 (a) – (b) show the axial and lateral CNR_e results respectively. The MAP-Adapt approach had higher axial CNR_e values compared to other methods. For lateral strain, MAP-Adapt retained its improved performance at all deformations expect 0.25 % lateral strain. However, strain error analysis shows that MAP-Adapt had lower lateral strain error (

$\Delta\varepsilon_{lateral\,|\,0.25\%}$ = 91.15 %) compared to MAP-Iter=5 ($\Delta\varepsilon_{lateral\,|\,0.25\%}$ = 99.39 %). Overall, qualitative and quantitative analysis demonstrate that MAP-Adapt method provides improved image quality at both low and high applied deformations.

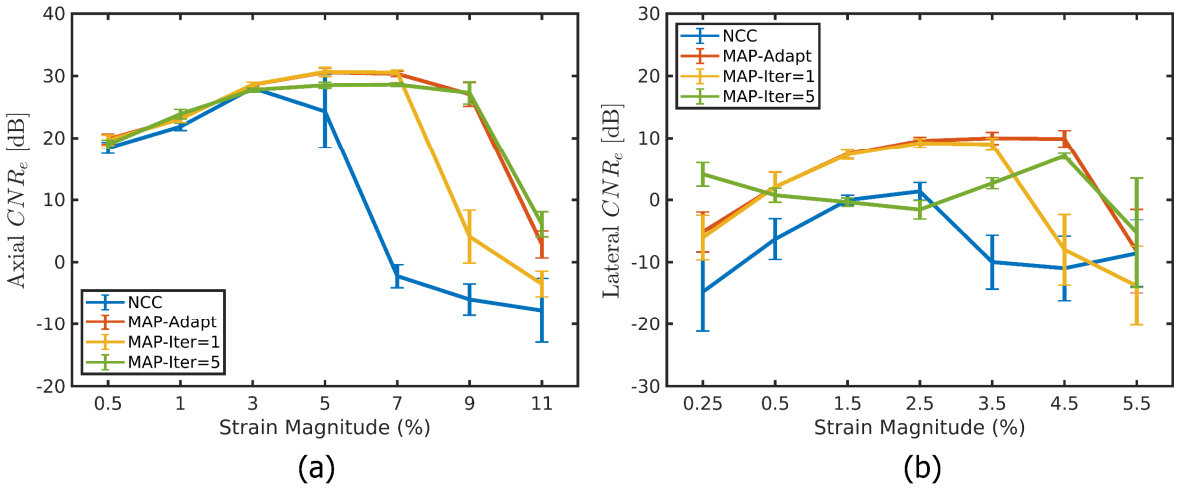

Figure 5.10 *CNR*$_e$ analysis of strain images estimated using NCC, adaptive Bayesian and Bayesian with fixed iterations. (a) Axial *CNR*$_e$ results and (b) Lateral *CNR*$_e$ results.

Adaptive variation in the required iterations against applied deformation for the MAP-Adapt method is presented in Figure 5.11. Figure 5.11 (a) shows that at low and moderate strains, two iterations were sufficient for regularization while increased number of iterations were required at higher strains. We also quantified the number of displacement image pixels (MAP_l) refined after each iteration (Figure 5.11 (b)). Figure 5.11 (b) shows that MAP_l exponentially decreases with the number of iterations. This result demonstrates that after the initial iteration, MAP_l does not change significantly, and algorithm stops the regularization process when the conditions stated in step (ix) of algorithm description is reached. Hence, the number of iterations is varied locally (per grid locations) rather than globally setting the number of iterations, in the proposed MAP-Adapt approach illustrating the adaptive and optimal nature of the regularization scheme. Here we do not over-regularize displacement estimates that do not require correction.

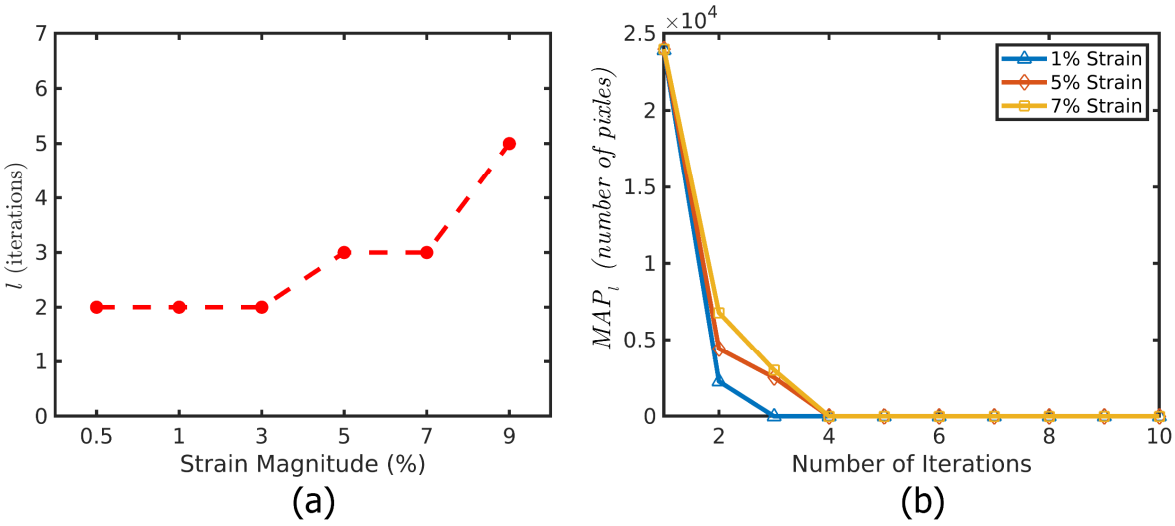

Figure 5.11 Adaptive variation of number of iterations against applied deformation. (a) Number of required iterations. (b) Number of pixels refined at each iteration.

5.3.3 Performance evaluation as a function of MAP-Adapt parameters

Strain estimation accuracy of MAP-Adapt as a function of different choices of decorrelation threshold (τ), improvement tolerance (ζ) and iteration tolerance (TOL) are presented in Figure 5.12. Uniform phantom simulations at applied deformations of 3% and 7% were utilized. Figure 5.12 (a) – (c) show the impact of ζ on axial strain error, lateral strain error and number of required iterations respectively. At higher strain, smaller value of ζ will perform better. However, choosing too small a value for ζ has a detrimental impact on lateral strain estimation accuracy at 3 % strain [Figure 5.12 (b)]. Optimal performance was achieved at $\zeta = 0.005$ resulting in a balance between strain estimation accuracy and the number of required iterations. Figure 5.12 (d) – (f) show the variation of axial strain error, lateral strain error and number of required iterations respectively as a function of decorrelation threshold (τ). Axial and lateral error for both low and high strain reaches a plateau at $\tau = 65$ with no significant impact on the number of iterations. Impact of TOL on estimation performance is summarized in Figure 5.12 (g) – (i). No variation among estimation accuracy was observed [Figure 5.12 (g) – (h)]. However, lower TOL required

larger number of iterations prior to stopping regularization. Note that, for this particular instance, $r^{(low)}$ threshold was not utilized. Thus, these results also demonstrate that improvement of computational efficiency was achieved with the use of $r^{(low)}$ threshold without comprising estimation performance.

5.3.4 FEA Canine Cardiac Simulation Results

ES myocardial stain images are presented in Figure 5.13 for comparison among NCC, MAP-Iter=3 and MAP-Adapt methods. Figure 5.13 (a) – (d) show ES radial strain images for FEA, NCC, MAP-Iter=3 and MAP-Adapt respectively. Apical and some portion of anterior region of myocardial wall had erroneous negative radial strain values in NCC result (indicated with arrows in Figure 5.13 (b)). These errors were resolved using Bayesian regularization approaches (Figure 5.13 (c) – (d)) resulting in close similarity with FEA result (Figure 5.13 (a)). However, MAP-Iter=3 result presents with the "banding artifact" as shown with an arrow in Figure 5.13 (c). Figure 5.13 (e) – (d) show ES longitudinal strain images for FEA, NCC, MAP-Iter=3 and MAP-Adapt respectively. MAP-Adapt provided the best longitudinal strain image (Figure 5.13 (f)) having excellent agreement with FEA result (Figure 5.13 (e)). NCC image had some erroneous positive strain values near apex as indicated with an arrow in Figure 5.13 (f). MAP-Iter=3 result severely underestimated the underlying strain as several regions with almost zero strains (arrows in Figure 5.13 (g)) were observed around the myocardium. Axial strain error ($\Delta\varepsilon_{axial}$ %), lateral strain error ($\Delta\varepsilon_{lateral}$ %), radial strain error ($\Delta\varepsilon_{radial}$ %) and longitudinal strain error ($\Delta\varepsilon_{long}$ %) were quantified for ES myocardial strain images are presented in Table 5.3. Quantitative results confirm our qualitative observations with best performance obtained with the MAP-Adapt method.

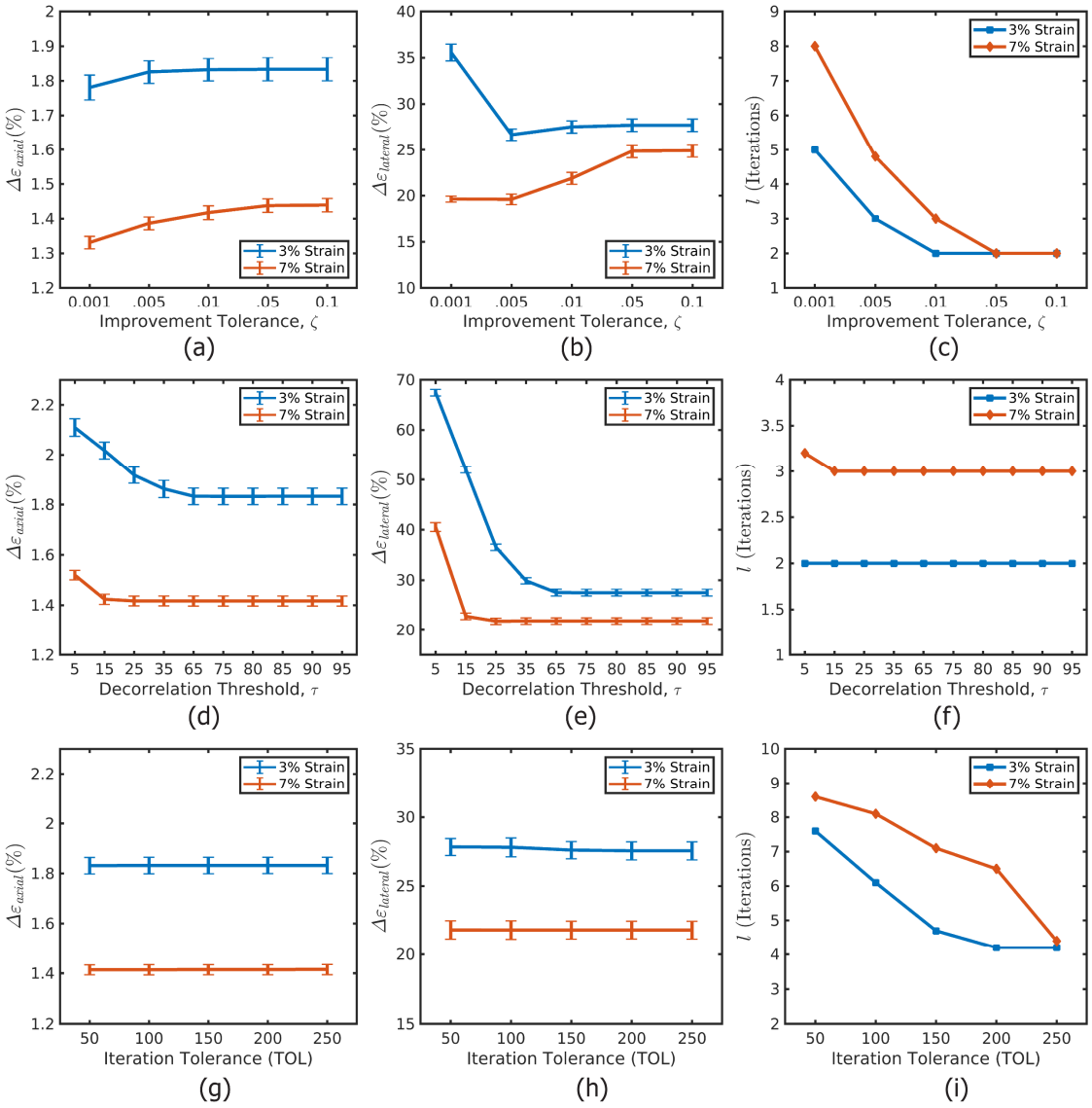

Figure 5.12 Variation of (a) axial strain error (%), (b) lateral strain error (%) and (c) number of iterations as a function of improvement tolerance (ζ). Variation of (d) axial strain error (%), (e) lateral strain error (%) and (f) number of iterations as a function of decorrelation threshold (τ). Variation of (g) axial strain error (%), (h) lateral strain error (%) and (i) number of iterations as a function of iteration tolerance (TOL).

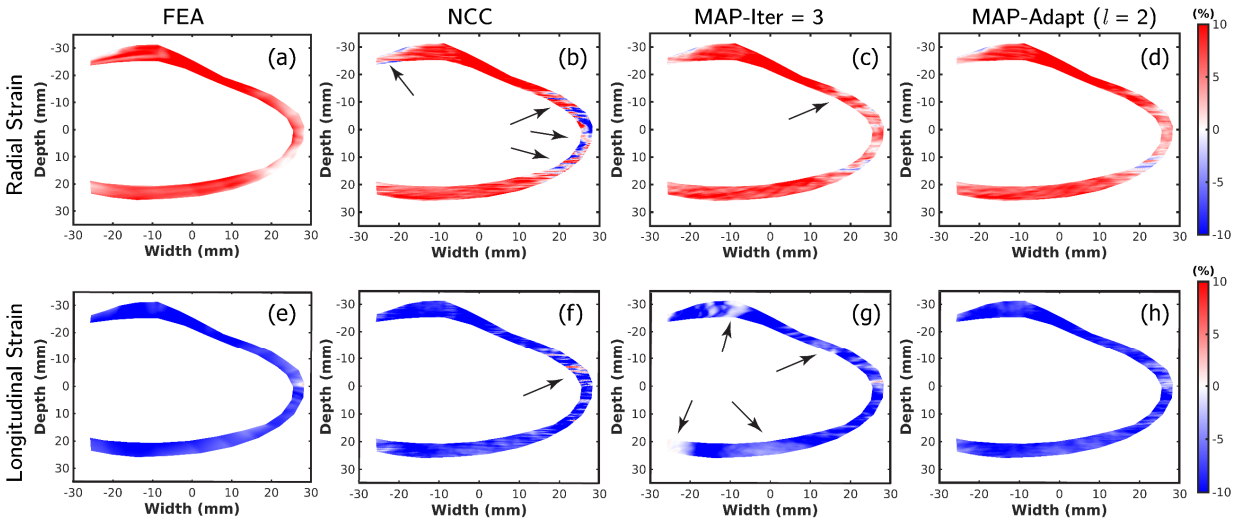

Figure 5.13 ES radial strain images for (a) FEA, (b) NCC, (c) MAP-Iter=3 and (d) MAP-Adapt respectively. ES longitudinal strain images for (e) FEA, (f) NCC, (g) MAP-Iter=3 and (h) MAP-Adapt respectively. *l* = required iterations by MAP-Adapt.

Table 5.3 Comparison of ES estimation errors

Methods	$\Delta\varepsilon_{axial}$ (%)	$\Delta\varepsilon_{lateral}$ (%)	$\Delta\varepsilon_{radial}$ (%)	$\Delta\varepsilon_{long}$ (%)
NCC	47.22	49.81	54.44	33.22
MAP-Adapt	**28.23**	**26.46**	**28.10**	**18.05**
MAP-Iter=1	28.62	26.55	29.00	18.24
MAP-Iter=2	29.34	37.93	29.44	25.24
MAP-Iter=3	32.41	58.10	32.86	41.08

Figure 5.14 shows the results for performance evaluation of NCC, MAP-Adapt and MAP-Iter as a function of the number of iterations. Median error computed over 125 frames from one cardiac cycle of FEA simulation is used comparison. Figure 5.14 (a) – (d) show results for $\Delta\varepsilon_{axial}$, $\Delta\varepsilon_{lateral}$, $\Delta\varepsilon_{radial}$ and $\Delta\varepsilon_{long}$ respectively. In all cases, NCC presented with the largest errors. Best performance was achieved with the MAP-Adapt method. For MAP-Iter approaches, as the number of iterations increased $\Delta\varepsilon_{lateral}$, $\Delta\varepsilon_{radial}$ and $\Delta\varepsilon_{long}$ also increased drastically when compared to MAP-Adapt.

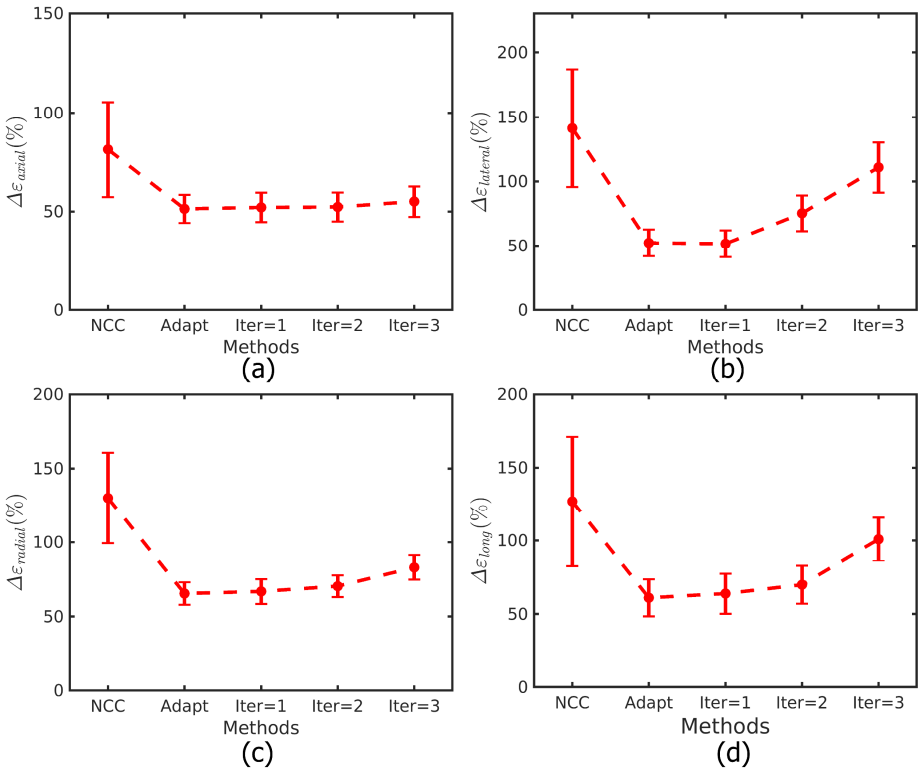

Figure 5.14 Performance evaluation of NCC, MAP-Adapt and MAP-Iter as a function of the number iterations. Figs. 14 (a) – (d) show axial strain error (%), lateral strain error (%), radial strain error (%) and longitudinal strain error (%) respectively.

5.3.5 Computational Cost

The algorithm was run in MATLAB (Mathworks Inc., MA) with a standard gateway interface (C++ MEX) and CUDA for cross-platform acceleration. All experiments were done on an Intel(R) Xeon(R) CPU E5-2640 v4 at 2.40 GHz, while the CUDA C++ code was run on a Tesla K40c GPU belonging to the Kepler architecture with compute capability 3.5. Computational cost is expected to vary depending on the input RF data dimension and algorithm processing parameters as presented in Table 5.1. Therefore, we present the execution timing analysis from the uniform phantom study in Table 5.4. The final RF data dimension was 8192×400 and mean execution time

for ten independent simulations is reported. With higher number of iterations for Bayesian regularization, the computational load is increased resulting in longer execution times (Table 5.4).

Table 5.4 Execution Timing Analysis (n=10)

Methods	Time (secs)
NCC	64.40
MAP-Adapt [Minimum, Maximum] *	[134.80, 261.34]
MAP-Iter=1	80.88
MAP-Iter=5	230.21

* MAP-Adapt execution times varied based on signal decorrelation. Lowest and highest execution times were recorded at 0.5 % and 9 % applied deformation.

5.4 *In vivo* Example of Adaptive Bayesian Regularization for Cardiac Strain Imaging

Figure 5.15 summarizes *in vivo* estimation results from the murine model in parasternal long axis view. PLAX B-mode image at end-diastole with segmentation scheme is presented in Figure 5.15 (i). Figure 5.15 (ii) and (iii) present radial and longitudinal strain estimation results respectively. For healthy myocardial function, radial and longitudinal strain images should exhibit uniformly positive and negative strain values respectively throughout the myocardium. Figure 5.15 (ii) [a] and [c] show ES *in vivo* radial strain images estimated with NCC and MAP-Adapt respectively. Radial wall thickening (positive strain magnitudes) at ES was observed in all estimated results. However, the NCC strain image showed some erroneous negative strain values in the anterior region (segments 1 and 2) indicating presence of ischemia in a healthy mouse. These errors were corrected with MAP-Adapt. Figure 5.15 (iii) [a] and [c] show ES *in vivo* longitudinal strain images estimated with NCC and MAP-Adapt respectively. Ventricular shortening (negative strain magnitudes) at ES was observed in all estimated results. The NCC longitudinal strain image exhibited some erroneous positive strain values in significant portions of myocardial wall. Higher quality longitudinal strain image was realized with the MAP-Adapt approach.

Figure 5.15 (ii) [b] and [d] show segmental radial strain curves estimated using NCC and MAP-Adapt approach respectively. All approaches resolve radial myocardial wall thickening by exhibiting peak positive radial strains at ES. Bayesian regularized radial strain curves in the anterior basal and mid segments (segments 1 and 2 respectively) were smoother compared to unregularized curves. Furthermore, regularized strain curves achieved improved homogeneity in temporal variation across six segments compared to NCC results. Figure 5.15 (iii) [b] and [d] show estimated segmental longitudinal strain curves. All approaches were able to resolve ventricular shortening during systole by exhibiting peak negative longitudinal strains at ES. Smooth temporal variation of strain in all six segments near end of the cardiac cycle was observed in regularized strain curves (Figure 5.15 (iii) [d]) compared to NCC (Figure 5.15 (iii) [b]). Overall, higher quality ES strain images and segmental strain curves were achieved with MAP-Adapt approach. Note that the median value of the required iterations by MAP-Adapt for estimating the results presented in Figure 5.15 were four.

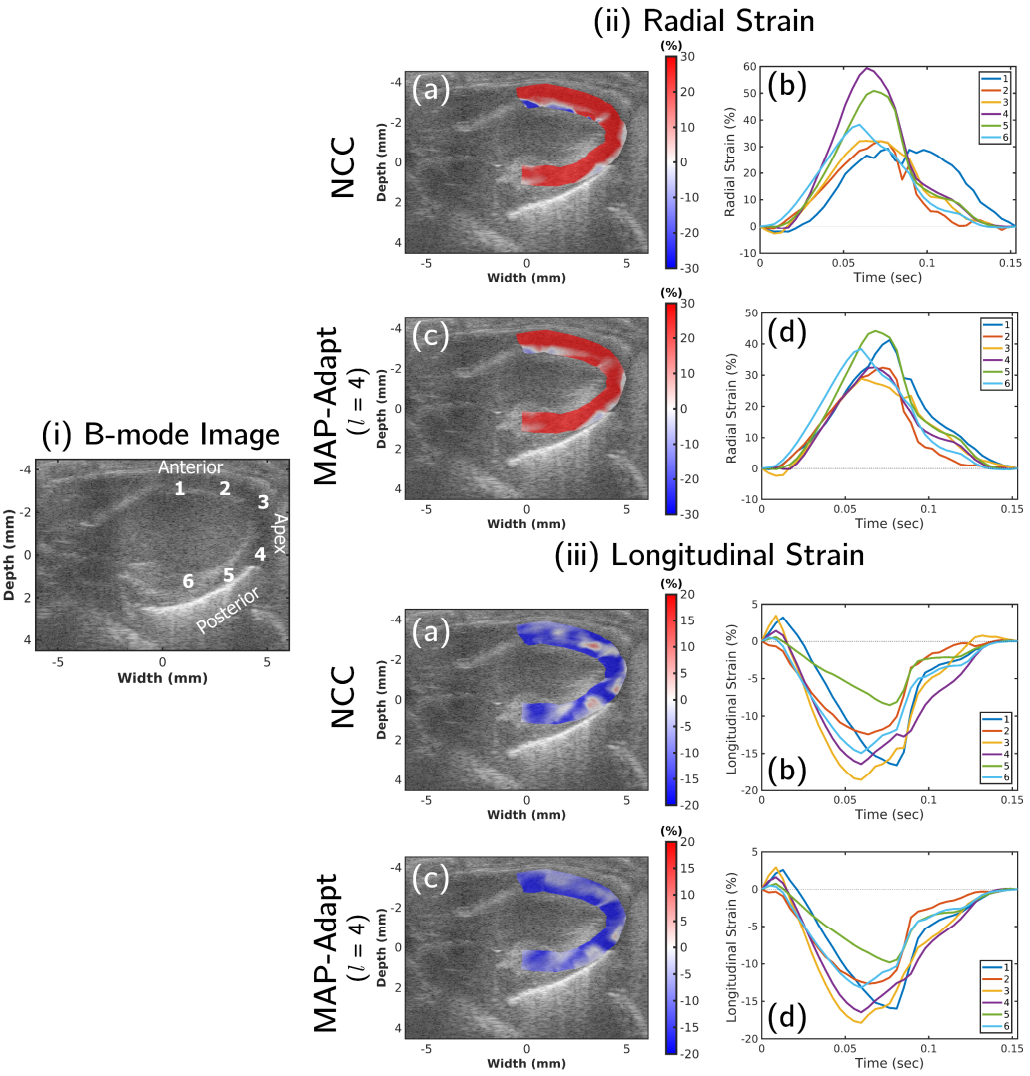

Figure 5.15 (i) PLAX B-mode image at end-diastole with segmentation scheme. (ii) Radial strain estimation results. ES *in vivo* myocardial strain images with (a) NCC and (c) MAP-Adapt respectively. *In vivo* segmental strain curves with (b) NCC and (d) MAP-Adapt respectively. (iii) Longitudinal strain estimation results. ES *in vivo* myocardial strain images with (a) NCC and (c) MAP-Adapt respectively. *In vivo* segmental strain curves with (b) NCC and (d) MAP-Adapt respectively. *l* = median maximum required iterations by MAP-Adapt.

Figure 5.16 summarizes *in vivo* estimation results from the murine model in parasternal short axis view. Figure 5.16 (ii) and (iii) present radial and circumferential strain estimation results respectively. For normal cardiac function, the radial and circumferential strain images should

exhibit uniformly positive and negative strain values respectively throughout the myocardium. Figure 5.16 (ii) [a] and [c] show ES *in vivo* radial strain images estimated with NCC and MAP-Adapt respectively. Radial wall thickening (positive strain magnitudes) at ES was observed in all estimated results. No significant difference was observed between NCC and MAP-Adapt estimates. Figure 5.16 (iii) [a] and [c] show ES *in vivo* circumferential strain images estimated with NCC and MAP-Adapt respectively. Circumferential strain estimated by NCC is less homogeneously negative (segments 1, 2, 3 and 6) compared to MAP-Adapt result. Although improvement was achieved with MAP-Adapt method (Figure 5.16 (iii) [c]), presence of erroneous positive circumferential strain values was still observed in the posterior segments (segments 2, 3 and 4).

Figure 5.16 (iii) [b] and [d] show segmental radial strain curves with NCC and MAP-Adapt respectively. Circumferential strain curves with NCC and MAP-Adapt methods are presented in Figure 5.16 (iii) [b] and [d] respectively. Radial estimation results indicate smooth temporal variation as expected from a healthy murine model without any significant difference between NCC and MAP-Adapt approach. Improved performance with MAP-Adapt was noted in circumferential strain curves. Regularized strain curves (Figure 5.16 (iii) [d]) achieved better homogeneity and smoothness (segments 2 and 4) in temporal variation across six segments compared to NCC results (Figure 5.16 (iii) [c]). Note that the median value of the required iterations by MAP-Adapt for estimating these results were three.

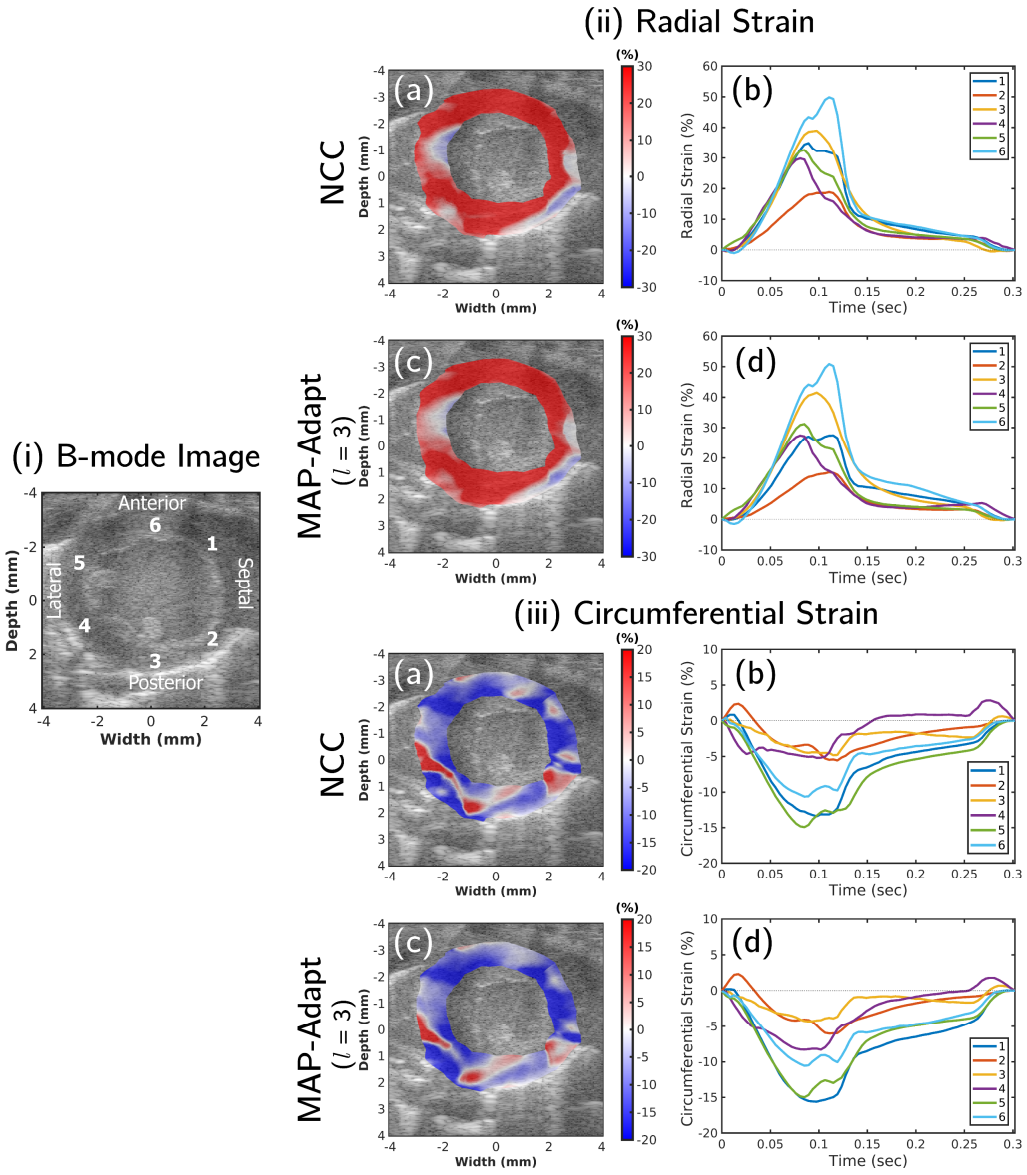

Figure 5.16 (i) PSAX B-mode image at end-diastole with segmentation scheme. (ii) Radial strain estimation results. ES *in vivo* myocardial strain images with (a) NCC and (c) MAP-Adapt respectively. *In vivo* segmental strain curves with (b) NCC and (d) MAP-Adapt respectively. (iii) Circumferential strain estimation results. ES *in vivo* myocardial strain images with (a) NCC and (c) MAP-Adapt respectively. *In vivo* segmental strain curves with (b) NCC and (d) MAP-Adapt respectively. *l* = median maximum required iterations by MAP-Adapt.

5.5 Adaptive Bayesian Regularization Achieves Optimal Performance in Simulation and *in vivo* Experiments

5.5.1 Numerical Phantom Simulation Studies

The results from uniform phantom simulation study show that Bayesian based methods outperform conventional NCC approach both in terms of motion estimation accuracy and elastographic signal-to-noise ratio. These findings corroborate those previously reported in literature [1, 28]. The key finding from the uniform phantom error analysis study demonstrates that the MAP-Adapt approach achieved concurrent estimation quality improvements in both axial and lateral directions. With higher fixed number of iterations (e.g. MAP-Iter=5), we achieve similar improvements in only the axial displacement and strain estimation accuracy when compared to MAP-Adapt [observe that performance of MAP-Adapt is close to that of MAP-Iter=5 in Figure 5.5 (a) – (c) and Figure 5.6 (a)]. However, this improvement was achieved at the expense of severe performance degradation in the lateral direction [Figure 5.5 (d) – (f) and Figure 5.6 (b)]. Bayesian regularization [1] and other optimization based motion estimation approaches [10, 29-34] were designed to limit the occurrence of large displacement errors or peak-hopping errors by imposing a motion continuity constraint as a regularization term. Estimation bias introduced through the regularization term have been shown to reduce estimation variance significantly. However, for Bayesian regularization, over-regularization tends to have a negative impact on lateral estimation resulting in higher bias and variance as shown in this paper. To gain further insight into the mechanism of over-regularization, posterior pdfs after each iteration of Bayesian regularization was carefully studied. After each iteration, as information from neighboring blocks further away from adjacent blocks gets incorporated into the posterior pdf through the likelihood function presented in equation (5.4). This process leads to peak-hop error filtering by attenuating false correlation peaks while enhancing the peak closest to the dominant peak of the neighboring

matching blocks. With additional iterations, the probabilities get concentrated more around the dominant correlation peak. Therefore, after an optimal number of iterations, the posterior pdf from Bayesian regularization is expected to resolve into a 2-D unimodal Gaussian distribution.

However, if the number of iterations is set beyond the optimal operating point, the lateral projection of the posterior pdf becomes a delta function due to the lower lateral sampling frequency of RF data. Thus, when sub-sample displacement estimation is performed through interpolation (parabolic/Sinc), estimation error incurred, as displacements are not resolved with the necessary sub-sample precision. These errors appear as vertical bands in lateral displacement maps (Figure 5.3 and Figure 5.4 (ii) [c]) and as regions with very high and low strains in lateral strain maps (Figure 5.3 and Figure 5.4 (ii) [g]). The impact of over-regularization on lateral displacement and strain is more pronounced at lower strains than higher strains (compare Figure 5.3 (ii) [c] to Figure 5.4 (ii) [c]). Probable reasons are due to the diffuse nature of initial pdf at higher strains that require larger number of iterations to converge to an optimal unimodal pdf and the requirement of higher subsample precision at lower strains. Keeping this principle in mind, in our proposed approach we limit the number of unnecessary regularizations by locally determining the optimal iteration requirement based on RF signal decorrelation. RF signal decorrelation was evaluated by assessing the correlation information between pre-RF and motion-compensated post-RF data after each iteration. This correlation information had been previously used as a framework for performance evaluation of strain imaging algorithms [35]. In this work, we use it to optimize Bayesian regularization. Regions with higher signal decorrelation utilize larger number of iterations when compared to regions with lower signal decorrelation. Thus, possibilities of over-regularization were reduced, and improved motion estimation accuracy was achieved in the lateral direction as shown in Figure 5.5 (d) – (f) and Figure 5.6 (b) while maintaining comparable estimation accuracy

in the axial direction. Axial and lateral strain filters estimated with MAP-Adapt corroborates trends previously reported in literature [21, 36, 37]. However, note that the bandpass nature of the lateral strain filter was not observed for MAP-Iter=5 as a result of over-regularization. Based on these results, we claim that a trade-off exists between axial and lateral strain estimation accuracy, which was achieved with our proposed MAP-Adapt method.

The results from our inclusion phantom study further substantiates our claim. Higher number of iterations might an attractive approach for MAP-Iter method to estimate axial strain images (Figure 5.7 (i) and Figure 5.8 (i)). However, this results in negative impact on lateral strain images with "vertical banding" artifacts seen in Figure 5.7 (ii) and Figure 5.8 (ii). Further understanding of the proposed method can be attained by closely analyzing Figure 5.8 and Figure 5.11. Figure 5.8 (i) [f] and Figure 5.8 (ii) [f] show that MAP-Iter=1 was able to refine most of the peak-hopping errors present in the NCC results. MAP-Adapt approach identifies locations, which were not corrected with initial iterations by using $\rho_{mc}^{(l)}$ and increases iterations for those specific locations (Figure 5.11 (b)). As a result, peak-hopping errors were corrected and at same time sub-sample precision was maintained in the lateral direction, achieving a balance between under-regularization and over-regularization. Quantitative results presented in Figure 5.9 corroborate the aforementioned qualitative observations. The results from CNR_e study also show the superior performance of MAP-Adapt methods over other approaches (Figure 5.10). Although MAP-Iter=5, produces higher lateral CNR_e value at very small deformations (0.25 % strain), visual inspection reveals that the inclusion was not discerned in the estimated strain image. At such low deformation, strain estimation performance is limited by electronic and quantization noise [21]. In our study, we utilized a lateral interpolation factor of two. The resultant lateral sampling frequency together with absence of phase information and resolution limitations of ultrasound imaging systems further

impede reliable tracking of small lateral deformations [14, 38, 39]. Therefore, all methods incurred very high lateral strain estimation errors up to 0.5 % lateral strain. The quality of MAP-Adapt lateral strain images can be improved further with the application of median filtering. However, for the comparative study, we followed an approach similar to [40], which did not use any median filtering for numerical simulation study.

Impact of parameter selection on the performance of MAP-Adapt approach was investigated using uniform phantom simulation. Proper choice of improvement tolerance and decorrelation threshold provide a balance between under-regularization and over-regularization. Smaller value of ζ will drive the algorithm towards higher regularization as evident from the improvement in axial strain estimation accuracy [Figure 5.12 (a)]. However, this improvement will be at a cost of performance degradation in the lateral direction at low strain and corresponding increased number of iterations [Figure 5.12 (b) – (c)] resulting in over-regularization. Optimal choice of ζ will impede over-regularization with concurrent axial and lateral strain estimation quality at a reasonable computational load. Figure 5.12 (d) – (f) show that smaller value of decorrelation threshold results in higher strain estimation error with performance approaching that obtained with NCC. These results suggest that τ should be chosen high enough to inhibit any instances of under-regularization. With τ and ζ fixed, no variation in strain estimation quality was observed with the range of iteration tolerance evaluated in this work. However, Figure 5.12 (i) suggests that proper choice of TOL will result in computationally efficient implementation with improved estimation quality.

5.5.2 FEA Canine Simulation Study

Accurate lateral displacement estimation is crucial for cardiac elastography or strain imaging applications [41]. Myocardial polar strains (radial, longitudinal and circumferential) are

derived using axial, lateral and shear strain components. Thus, estimation error in any of these strain tensors directly impacts the quality of myocardial strain images [42]. The results from this study show that MAP-Adapt achieves optimal regularization thus producing the best radial and longitudinal strain images at ES (Figure 5.13 and Table 5.3). The data presented in Figure 5.14 show that over-regularization severely deteriorates the lateral estimation quality. This result corroborates with our findings from numerical phantom simulation study. The degradation of lateral estimation quality severely impacted the longitudinal strain estimation with a 65% increase in median error compared to MAP-Adapt method. The quality degradation for radial strain estimation is not as severe as the longitudinal case because the axial component has more contributions to radial strain than lateral strain [27].

5.5.3 In vivo Cardiac Strain Imaging Study

In this study, *in vivo* feasibility of MAP-Adapt method has been shown. End-systolic strain is a recommended parameter to investigate cardiac dynamics [43]. Physiologically inaccurate radial and longitudinal strain values from NCC were corrected by MAP-Adapt method (Figure 5.15). For PSAX view, higher improvement was observed in circumferential strain image quality when compared to radial strain result with MAP-Adapt (Figure 5.16). However, some erroneous positive strain values were still retained in the posterior segments (segments 2, 3 and 4). These errors can be attributed to lateral strain estimation quality as it contributes more to circumferential strain estimation [44]. Segmental analysis was done for *in vivo* estimated strains and segmental temporal strain curves were presented for PLAX and PSAX views respectively. Overall, both NCC and MAP-Adapt resolved clinically relevant details [43] such as peak positive strain, ES strain, and post systole strain reliably. However, smoother temporal variation was achieved using the Bayesian approach when compared to NCC which corroborates our previous findings [27].

Adaptive behavior of the proposed method was also observed in these *in vivo* examples. Imaging frame rates for PLAX and PSAX data acquisition were 235 Hz and 347 Hz respectively. As the median heart rate of the mouse under anesthesia was 340 bpm, it was expected that higher signal decorrelation will be observed while performing inter-frame motion estimation with PLAX data compared to PSAX data. Accordingly, MAP-Adapt required higher number of iterations (four) for PLAX data motion estimation compared to PSAX case (three). We anticipate that this adaptive nature will be crucial when the proposed Bayesian regularization will be used in clinical cardiac imaging as optimal performance will be automatically achieved based on input RF data.

One other important finding is that better lateral estimation with MAP-Adapt was observed in PLAX view compared to PSAX view (errors in the circumferential strain image). Moreover, we did not observe significant difference in estimation quality in PSAX view between NCC and MAP-Adapt for radial strain tensors. These findings might be attributed to lower incurred inter-frame lateral motion due to higher imaging frame rate [42, 45, 46]. One possible solution might be the use of dynamic frame skip [2], by using a short frame skip when strain rate is high and a long frame skip when strain rate is low.

List of References

[1] M. McCormick, N. Rubert, and T. Varghese, "Bayesian regularization applied to ultrasound strain imaging," *IEEE Transactions on Biomedical Engineering,* vol. 58, pp. 1612-1620, 2011.

[2] M. McCormick, T. Varghese, X. Wang, C. Mitchell, M. Kliewer, and R. Dempsey, "Methods for robust in vivo strain estimation in the carotid artery," *Physics in medicine and biology,* vol. 57, p. 7329, 2012.

[3] R. Al Mukaddim, N. H. Meshram, C. C. Mitchell, and T. Varghese, "Hierarchical Motion Estimation With Bayesian Regularization in Cardiac Elastography: Simulation and *In Vivo*

Validation," *IEEE transactions on ultrasonics, ferroelectrics, and frequency control,* vol. 66, pp. 1708-1722, 2019.

[4] G. Xiao, J. M. Brady, J. A. Noble, M. Burcher, and R. English, "Nonrigid registration of 3-D free-hand ultrasound images of the breast," *IEEE Transactions on medical imaging,* vol. 21, pp. 405-412, 2002.

[5] B. Byram, G. E. Trahey, and M. Palmeri, "Bayesian speckle tracking. Part I: An implementable perturbation to the likelihood function for ultrasound displacement estimation," *IEEE transactions on ultrasonics, ferroelectrics, and frequency control,* vol. 60, pp. 132-143, 2012.

[6] P. M. Hayton, M. Brady, S. M. Smith, and N. Moore, "A non-rigid registration algorithm for dynamic breast MR images," *Artificial Intelligence,* vol. 114, pp. 125-156, 1999.

[7] F. Kallel and J. Ophir, "A least-squares strain estimator for elastography," *Ultrasonic imaging,* vol. 19, pp. 195-208, 1997.

[8] I. Cespedes, J. Ophir, and S. K. Alam, "The combined effect of signal decorrelation and random noise on the variance of time delay estimation," *IEEE transactions on ultrasonics, ferroelectrics, and frequency control,* vol. 44, pp. 220-225, 1997.

[9] B. H. Friemel, L. N. Bohs, K. R. Nightingale, and G. E. Trahey, "Speckle decorrelation due to two-dimensional flow gradients," *IEEE transactions on ultrasonics, ferroelectrics, and frequency control,* vol. 45, pp. 317-327, 1998.

[10] M. Omidyeganeh, Y. Xiao, M. O. Ahmad, and H. Rivaz, "Estimation of strain elastography from ultrasound radio-frequency data by utilizing analytic gradient of the similarity metric," *IEEE transactions on medical imaging,* vol. 36, pp. 1347-1358, 2017.

[11] S. K. Alam and J. Ophir, "Reduction of signal decorrelation from mechanical compression of tissues by temporal stretching: Applications to elastography," *Ultrasound in Medicine and Biology,* vol. 23, pp. 95-105, 1997.

[12] H. Shi and T. Varghese, "Two-dimensional multi-level strain estimation for discontinuous tissue," *Physics in Medicine & Biology,* vol. 52, p. 389, 2007.

[13] H. Li, Y. Guo, and W.-N. Lee, "Systematic performance evaluation of a cross-correlation-based ultrasound strain imaging method," *Ultrasound in medicine & biology,* vol. 42, pp. 2436-2456, 2016.

[14] R. G. Lopata, M. M. Nillesen, H. H. Hansen, I. H. Gerrits, J. M. Thijssen, and C. L. De Korte, "Performance evaluation of methods for two-dimensional displacement and strain estimation using ultrasound radio frequency data," *Ultrasound in medicine & biology,* vol. 35, pp. 796-812, 2009.

[15] I. Céspedes, Y. Huang, J. Ophir, and S. Spratt, "Methods for estimation of subsample time delays of digitized echo signals," *Ultrasonic imaging,* vol. 17, pp. 142-171, 1995.

[16] M. M. McCormick and T. Varghese, "An approach to unbiased subsample interpolation for motion tracking," *Ultrasonic imaging,* vol. 35, pp. 76-89, 2013.

[17] N. H. Meshram and T. Varghese, "GPU accelerated multilevel Lagrangian carotid strain imaging," *IEEE transactions on ultrasonics, ferroelectrics, and frequency control,* vol. 65, pp. 1370-1379, 2018.

[18] T. Varghese, J. Ophir, and I. Cespedes, "Noise reduction in elastograms using temporal stretching with multicompression averaging," *Ultrasound in Medicine and Biology,* vol. 22, pp. 1043-1052, 1996.

[19] Y. Li and J. A. Zagzebski, "A frequency domain model for generating B-mode images with array transducers," *IEEE transactions on ultrasonics, ferroelectrics, and frequency control,* vol. 46, pp. 690-699, 1999.

[20] G. F. Pinton and G. E. Trahey, "Continuous delay estimation with polynomial splines," *IEEE transactions on ultrasonics, ferroelectrics, and frequency control,* vol. 53, pp. 2026-2035, 2006.

[21] T. Varghese and J. Ophir, "A theoretical framework for performance characterization of elastography: The strain filter," *IEEE transactions on ultrasonics, ferroelectrics, and frequency control,* vol. 44, pp. 164-172, 1997.

[22] J. Ophir, F. Kallel, T. Varghese, E. Konofagou, S. K. Alam, T. Krouskop*, et al.*, "Elastography," *Comptes Rendus de l'Academie des Sciences-Series IV-Physics,* vol. 2, pp. 1193-1212, 2001.

[23] M. Bilgen and M. Insana, "Predicting target detectability in acoustic elastography," in *1997 IEEE Ultrasonics Symposium Proceedings. An International Symposium (Cat. No. 97CH36118)*, 1997, pp. 1427-1430.

[24] T. Varghese and J. Ophir, "An analysis of elastographic contrast-to-noise ratio," *Ultrasound in medicine & biology,* vol. 24, pp. 915-924, 1998.

[25] H. Chen and T. Varghese, "Three-dimensional canine heart model for cardiac elastography," *Medical physics,* vol. 37, pp. 5876-5886, 2010.

[26] A. D. McCulloch and R. Mazhari, "Regional myocardial mechanics: integrative computational models of flow-function relations," *Journal of Nuclear Cardiology,* vol. 8, pp. 506-519, 2001.

[27] R. Al Mukaddim, N. H. Meshram, C. C. Mitchell, and T. Varghese, "Hierarchical Motion Estimation with Bayesian Regularization in Cardiac Elastography: Simulation and in-vivo Validation," *IEEE transactions on ultrasonics, ferroelectrics, and frequency control,* 2019.

[28] D. M. Dumont and B. C. Byram, "Robust tracking of small displacements with a Bayesian estimator," *IEEE transactions on ultrasonics, ferroelectrics, and frequency control,* vol. 63, pp. 20-34, 2015.

[29] J. Jiang and T. J. Hall, "A coupled subsample displacement estimation method for ultrasound-based strain elastography," *Physics in Medicine & Biology,* vol. 60, p. 8347, 2015.

[30] J. Jiang and T. J. Hall, "A fast hybrid algorithm combining regularized motion tracking and predictive search for reducing the occurrence of large displacement errors," *IEEE transactions on ultrasonics, ferroelectrics, and frequency control,* vol. 58, pp. 730-736, 2011.

[31] J. Jiang and T. J. Hall, "A generalized speckle tracking algorithm for ultrasonic strain imaging using dynamic programming," *Ultrasound in medicine & biology,* vol. 35, pp. 1863-1879, 2009.

[32] H. S. Hashemi and H. Rivaz, "Global time-delay estimation in ultrasound elastography," *IEEE transactions on ultrasonics, ferroelectrics, and frequency control,* vol. 64, pp. 1625-1636, 2017.

[33] H. Rivaz, E. Boctor, P. Foroughi, R. Zellars, G. Fichtinger, and G. Hager, "Ultrasound elastography: a dynamic programming approach," *IEEE transactions on medical imaging,* vol. 27, pp. 1373-1377, 2008.

[34] H. Rivaz, E. M. Boctor, M. A. Choti, and G. D. Hager, "Real-time regularized ultrasound elastography," *IEEE transactions on medical imaging,* vol. 30, pp. 928-945, 2011.

[35] J. Jiang, T. J. Hall, and A. M. Sommer, "A novel performance descriptor for ultrasonic strain imaging: A preliminary study," *IEEE transactions on ultrasonics, ferroelectrics, and frequency control,* vol. 53, pp. 1088-1102, 2006.

[36] P. Verma and M. M. Doyley, "Revisiting the cramér rao lower bound for elastography: Predicting the performance of axial, lateral and polar strain elastograms," *Ultrasound in medicine & biology,* vol. 43, pp. 1780-1796, 2017.

[37] E. E. Konofagou, T. Varghese, and J. Ophir, "Theoretical bounds on the estimation of transverse displacement, transverse strain and Poisson's ratio in elastography," *Ultrasonic Imaging,* vol. 22, pp. 153-177, 2000.

[38] Z. Liu, C. Huang, and J. Luo, "A systematic investigation of lateral estimation using various interpolation approaches in conventional ultrasound imaging," *IEEE transactions on ultrasonics, ferroelectrics, and frequency control,* vol. 64, pp. 1149-1160, 2017.

[39] J. Luo and E. E. Konofagou, "Effects of various parameters on lateral displacement estimation in ultrasound elastography," *Ultrasound in medicine & biology,* vol. 35, pp. 1352-1366, 2009.

[40] X. Pan, J. Gao, S. Tao, K. Liu, J. Bai, and J. Luo, "A two-step optical flow method for strain estimation in elastography: Simulation and phantom study," *Ultrasonics,* vol. 54, pp. 990-996, 2014.

[41] W.-N. Lee, C. M. Ingrassia, K. D. Costa, J. W. Holmes, and E. E. Konofagou, "Theoretical quality assessment of myocardial elastography with in vivo validation," *ieee transactions on ultrasonics, ferroelectrics, and frequency control,* vol. 54, pp. 2233-2245, 2007.

[42] E. A. Bunting, J. Provost, and E. E. Konofagou, "Stochastic precision analysis of 2-D cardiac strain estimation in vivo," *Physics in Medicine & Biology,* vol. 59, p. 6841, 2014.

[43] J.-U. Voigt, G. Pedrizzetti, P. Lysyansky, T. H. Marwick, H. Houle, R. Baumann*, et al.*, "Definitions for a common standard for 2D speckle tracking echocardiography: consensus document of the EACVI/ASE/Industry Task Force to standardize deformation imaging," *European Heart Journal-Cardiovascular Imaging,* vol. 16, pp. 1-11, 2014.

[44] W.-N. Lee, Z. Qian, C. L. Tosti, T. R. Brown, D. N. Metaxas, and E. E. Konofagou, "Preliminary validation of angle-independent myocardial elastography using MR tagging in a clinical setting," *Ultrasound in medicine & biology,* vol. 34, pp. 1980-1997, 2008.

[45] V. Sayseng, J. Grondin, and E. E. Konofagou, "Optimization of transmit parameters in cardiac strain imaging with full and partial aperture coherent compounding," *IEEE transactions on ultrasonics, ferroelectrics, and frequency control,* vol. 65, pp. 684-696, 2018.

[46] H. Chen, T. Varghese, P. S. Rahko, and J. Zagzebski, "Ultrasound frame rate requirements for cardiac elastography: Experimental and in vivo results," *Ultrasonics,* vol. 49, pp. 98-111, 2009.

Chapter 6

Spatiotemporal Bayesian Regularization for Cardiac Strain Imaging

In **Chapter 04** of this dissertation, we demonstrated the use of Bayesian regularization in the context of a multi-level block matching-based (BM) cardiac strain imaging (CSI) and reported significant performance improvement over conventional 2-D normalized cross-correlation coefficient (NCC) based method without regularization. The proposed algorithm incorporated information from a local spatial neighborhood to regularize 2-D NCC matrices. In this chapter[3], we extend the Bayesian regularization algorithm into the temporal domain with an underlying assumption of smooth variation in velocity over a short span of time during tissue deformation [1] and validate it using simulation and *in vivo* cardiac dataset. Note that all previous reports on Bayesian strain imaging utilized information only from its spatial neighbors [1-9].

This chapter reports on two main contributions. First, two schemes for incorporating temporal domain information into our Bayesian regularization algorithm is proposed and implemented into a Lagrangian cardiac strain estimation framework [10]. Second, we report results from a comparative study involving conventional NCC, spatial and spatiotemporal Bayesian regularization using data from finite-element-analysis (FEA) canine cardiac simulations and ten healthy murine hearts collected *in vivo*.

[3]Rashid Al Mukaddim, Nirvedh H. Meshram, Ashley M. Weichmann, Carol C. Mitchell and Tomy Varghese, "Spatiotemporal Bayesian Regularization For Cardiac Strain Imaging: Simulation and *in vivo* Results." *IEEE Open Journal of Ultrasonics, Ferroelectrics, and Frequency Control*, under review (2021)

6.1 Basic Principle of Spatiotemporal Bayesian Regularization (STBR)

For mathematical details on conventional spatial Bayesian regularization (SBR), please refer to **Chapter 05** of this dissertation. In this section, we present the basic principles utilized to extend SBR into the temporal domain. For STBR, we consider a set of four consecutive RF frames for displacement estimation. First, inter-frame 2-D NCC estimation is performed, resulting in three similarity metric images (SMI) for each BM location. Specifically, for a BM location $\mathbf{x}$, we have past, present and future temporal unregularized SMIs denoted by SMI(t-1,$\mathbf{x}$), SMI(t,$\mathbf{x}$) and SMI(t+1,$\mathbf{x}$) respectively with SMI(t,$\mathbf{x}$) being regularized by the proposed STBR method as shown in Figure 6.1. To enforce temporal continuity assuming smooth variation of velocity over time, we propose two schemes for incorporating temporal information into Bayesian regularization as described below.

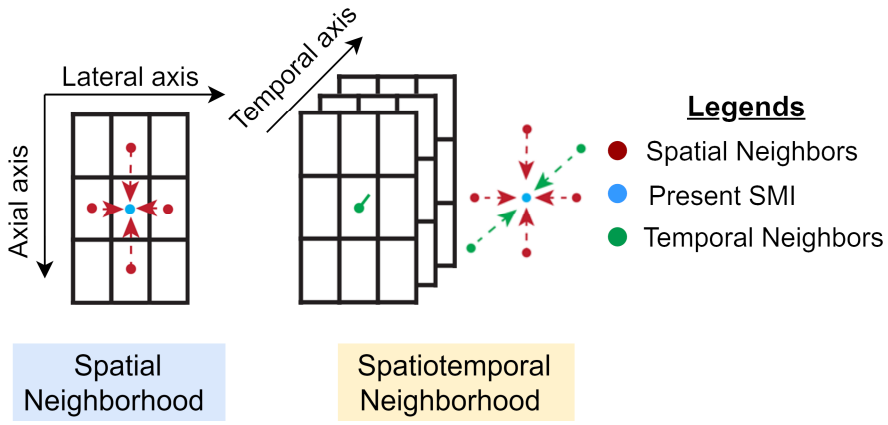

Figure 6.1 Neighborhood definition for spatial and spatiotemporal Bayesian regularization. The SMI being regularized is denoted by the blue circle while its spatial and temporal neighbors are indicated by red and green circles, respectively. Each rectangle represents a SMI.

6.1.1 Spatial then Temporal Bayesian (STBR-1)

In this scheme, first one iteration of SBR is applied on all SMIs independently resulting in spatially regularized SMI for each BM location. Then, temporal regularization is done by

considering these regularized SMI as the prior with a likelihood function incorporating information from its past and future temporal neighbors using following equation.

$$\Pr(\mathbf{u}_{\mathbf{x}} \mid \mathbf{u}_{\mathcal{N}_t}) \propto \Pr(\mathbf{u}_{\mathcal{N}_t} \mid \mathbf{u}_{\mathbf{x}}) \times \Pr(\mathbf{u}_{\mathbf{x}} \mid \mathbf{u}_{\mathcal{N}_x}) \tag{6.1}$$

where, $\Pr(\mathbf{u}_{\mathbf{x}} \mid \mathbf{u}_{\mathcal{N}_t})$ is the posterior PDF after temporal regularization, $\mathbf{u}_{\mathcal{N}_t}$ is the set of displacement vectors from a temporal neighborhood, $\mathcal{N}_t$ defined with two adjacent neighbors (past and future) and $\Pr(\mathbf{u}_{\mathbf{x}} \mid \mathbf{u}_{\mathcal{N}_x})$ is PPD after one iteration of SBR. To define the temporal likelihood function [$\Pr(\mathbf{u}_{\mathcal{N}_t} \mid \mathbf{u}_{\mathbf{x}})$], models like those reported in **Chapter 05** are utilized and a 2-D temporal Gaussian term with a width vector $\boldsymbol{\sigma}_{\mathbf{t}}$ is defined. Finally, the regularized displacement estimator determines the integer displacement vector as the point where $\Pr(\mathbf{u}_{\mathbf{x}} \mid \mathbf{u}_{\mathcal{N}_t})$ maximizes is obtained using sub-sample precision through interpolation. We term this method as the **STBR-1** displacement estimator.

6.1.2 Simultaneous Spatiotemporal Bayesian Regularization (STBR-2)

In the second scheme, STBR is done simultaneously on the present unregularized SMI using following equation.

$$\Pr(\mathbf{u}_{\mathbf{x}} \mid \mathbf{u}_{\mathcal{N}_{xt}}) \propto \Pr(\mathbf{u}_{\mathcal{N}_{xt}} \mid \mathbf{u}_{\mathbf{x}}) \times \Pr(\mathbf{u}_{\mathbf{x}}) \tag{6.2}$$

where, $\Pr(\mathbf{u}_{\mathbf{x}} \mid \mathbf{u}_{\mathcal{N}_{xt}})$ is the posterior PDF after spatiotemporal regularization, $\mathbf{u}_{\mathcal{N}_{xt}}$ is the set of displacement vectors from a spatiotemporal neighborhood, $\mathcal{N}_{xt}$ defined with two adjacent temporal neighbors (past and future) and four adjacent spatial neighbors for the present SMI (left, right, top and bottom). To define the spatiotemporal likelihood function [$\Pr(\mathbf{u}_{\mathcal{N}_{xt}} \mid \mathbf{u}_{\mathbf{x}})$], models like those reported in **Chapter 05** are utilized with appropriate use of Gaussian terms for

modulation depending on either spatial or temporal neighbors. Finally, *maximum a posteriori* (MAP) principle was applied on $\Pr(\mathbf{u}_{\mathbf{x}} \mid \mathbf{u}_{\mathcal{N}_{xt}})$ to determine integer displacement with sub-sample precision obtained through interpolation. This approach is termed as the **STBR-2** displacement estimator in this chapter.

6.2 Experimental Protocols to Validate STBR for Cardiac Strain Imaging

6.2.1 Cardiac Finite-Element Analysis Simulation Study

To evaluate the performance of STBR for CSI, a simulation study was performed using a 3-D FEA model of a healthy canine heart [11, 12] containing complex cardiac deformation over a cardiac cycle. A detailed description of FEA analysis, scatterer generation and simulation was previously described in **Chapter 04** and **05**. Cardiac cycle RF data (125 frames) in 2-D parasternal long axis (PLAX) US imaging view extracted from the 3-D model was generated using a frequency domain US simulation program [13]. Five independent scatterer realizations were simulated for statistical analysis. For each scatterer realization, two sets of RF datasets were generated by superimposing additive, white Gaussian noise (AWGN) on the simulated noise-less RF signals to achieve sonographic signal-to-noise (SNR_s) of 30 dB and 0 dB respectively [5]. AWGN profiles were generated relative to the noiseless RF signal derived from a 2-D region of interest (ROI) placed on the anterior wall.

6.2.2 In vivo Murine Cardiac Imaging

In vivo feasibility study was done by collecting cardiac RF data from 10 BALB/CJ mice (7 male, 3 female, median age = 10 weeks, acquired from Jackson Labs, Bar Harbor, ME, USA) using a Vevo 2100 LAZR imaging system (FUJIFILM VisualSonics, Inc., Toronto, Canada). All *in-vivo* procedures were approved by the Institutional Animal Care and Use Committee (IACUC) at the

University of Wisconsin-Madison. High frequency US imaging was performed using a MS 550D transducer (center frequency = 40 MHz). We acquired 1000 frames in PLAX view, which were stored in inphase/quadrature (IQ) format for off-line CSI. Electrocardiogram (ECG) and respiratory signals were continuously monitored and simultaneously acquired during RF data collection. Finally, one cardiac cycle of RF data (sampling frequency = 512 MHz) was extracted from the collected 1000 frames by applying ECG and respiratory gating and used for CSI. Further details regarding data collection can be found here [10].

6.2.3 STBR Algorithm Implementation

The STBR algorithm is incorporated into a multi-level BM algorithm [14] and implemented using MATLAB and CUDA to run on a GPU (NVIDIA Tesla K80) for cross-platform acceleration. Figure 6.2 presents pseudocode for the STBR algorithm where RFData and SearchParameters are structures containing four consecutive RF frames and displacement estimation parameters, respectively. The algorithm is as follows.

1) For all input frames, RF data are up-sampled using a 2-D windowed Sinc interpolator [15, 16] and a multi-level pyramid are formed by data decimation.
2) At each level, inter-frame 2-D-NCC are estimated for all frames and stored in a 3-D SMI store array.
3) A First-in-First-out (FIFO) buffer and a 3-D Bayesian store array are initialized on GPU and CPU memory respectively for Bayesian regularization.
4) STBR is applied iteratively for all SMI using either equation 4 or 5. Perform Scaling in Figure 2 denotes the normalization applied on SMIs to generate the PDFs. In this chapter, we have limited STBR to a single iteration thus requiring only past and future neighbors for PPD calculation. However, to integrate information beyond adjacent temporal neighbors, we need

more than four RF frames as an input to the algorithm resulting in higher memory requirement on the GPU. To avoid illegal memory access on GPU, the FIFO buffer holds required SMI data on GPU device memory for a specific time, t while results after performing regularization on GPU are copied back to the CPU Bayesian store array.

5) Finally, subsample motion estimation [15] with 2-D Sinc interpolation is done and RF data prepared (by aligning and stretching [17]) for the next level.

6) Repeat steps (1) – (5) for the given number of levels.

Algorithm 1 Spatiotemporal Bayesian Regularization

```
1:  procedure SPATIOTEMPORALBAYES(RFData, SearchParamters)
2:      Perform up-sampling using Sinc Interpolation
3:      Multi-level pyramid formation by data decimation
4:      for level = 0 to TotalLevels do
5:          Initialize 3D SMI Store Array
6:          Time Loop for inter-frame 2D-NCC
7:          Initialize First-in-First-out (FIFO) Buffer
8:          Initialize Bayesian Store Array
9:          for iteration = 0 to max do
10:             Perform Scaling
11:             for time,t = 0 to totaltime do
12:                 Update FIFO Buffer
13:                 Perform Spatiotemporal Regularization
14:                 Bayesian Store Array ← PPD
15:             end for
16:         end for
17:         Time Loop for SubSample Motion Estimation
18:         Aligning and stretching for next level
19:     end for
20: end procedure
```

Figure 6.2 Algorithm for STBR incorporated into a multi-level block matching displacement estimator. SMI = Similarity metric image, PPD = Posterior Probability Density.

6.2.4 Lagrangian Cardiac Strain Imaging

Lagrangian radial and longitudinal strain tensors were derived using a cardiac strain estimation framework proposed in **Chapter 04**. Inter-frame displacement estimation was performed with the multi-level BM algorithm [14] with and without regularization (SBR, STBR-1 and STBR-2). The displacement estimation parameters used for FEA simulation and *in vivo*

studies are summarized in Table 6.1. For STBR, width vector $\boldsymbol{\sigma_t}$ was set empirically. Default axial and lateral direction $\boldsymbol{\sigma_t}$ values for FEA simulation and *in vivo* study were [0.01,0.01] and [0.1,0.1] respectively. A mesh of 24000 points covering the entire myocardium was generated by utilizing user-defined segmentation of epicardial and endocardial walls of the heart at end-diastole (ED) of a cardiac cycle (R-Wave of ECG) [10, 18]. The cardiac mesh was then used to integrate the inter-frame incremental displacements over time based on a Lagrangian description of motion starting from ED [2, 9, 10]. Before accumulation, 2-D median filtering was performed to remove any outliers from the estimated displacement vectors. The Lagrangian strain tensor (**E**) was derived by applying a least squares (LS) strain estimator on the accumulated displacement vectors to estimate axial, lateral and shear strain components [10, 19]. Axial and lateral LS strain estimator kernel dimensions were 0.5 mm and 1 mm respectively. Finally, radial (e_r) and longitudinal (e_l) strains were derived by applying a coordinate transformation on **E**. Further details regarding strain estimation and coordinate transformation can be found here [10]. End-systole (ES) strain images and segmental strain curves from both FEA simulation and *in vivo* mice data were investigated to qualitatively compare NCC, SBR, STBR-1 and STBR-2.

Table 6.1 Displacement Estimation Parameters for FEA Simulation and *in vivo* Studies

	Value	Unit
Number of levels	3	-
RF data sampling factor [Axial: Lateral]	1:2	-
Axial decimation factors	[3,2,1]	-
Lateral decimation factors	[2,1,1]	-
Axial kernel length	[8λ, 5λ, 1λ]	Wavelengths
Lateral kernel length	[15, 12 ,10]	A-lines
Kernel overlaps [Axial, Lateral]	[10*,90]	%
Median filter kernel [Axial, Lateral]	[5** × 5]	pixels
Subsample estimation	2-D Sinc	-

* *In vivo* axial kernel overlap was 50 %

** *In vivo* median filter axial kernel dimension was 7 pixels

6.2.5 Quantitative Performance Analysis

Theoretical strain tensors were derived from the 3-D cardiac FEA simulation and used to compare the strain estimation accuracy among NCC, SBR, STBR-1 and STBR-2 respectively. Quantitative performance analysis was done by evaluating the strain bias (%), normalized strain error (%) or Δ_ε (%) and total temporal relative error (TTR) as follows.

$$\text{Strain bias (\%)} = \mathrm{E}\left[\varepsilon_{true} - \varepsilon_{estimated}\right] \tag{6.3}$$

$$\Delta_\varepsilon\ (\%) = \frac{\sum_{i=1}^{P}\left|\varepsilon_{true} - \varepsilon_{estimated}\right|}{\sum_{i=1}^{P}\left|\varepsilon_{true}\right|} \times 100 \tag{6.4}$$

$$\text{TTR (\%)} = \frac{\sum_{t=1}^{T}\left|\varepsilon_{true}(t) - \varepsilon_{estimated}(t)\right|}{\sum_{t=1}^{T}\left|\varepsilon_{true}(t)\right|} \times 100 \tag{6.5}$$

where, ε_{true} and $\varepsilon_{estimated}$ denote estimated and theoretical strain while $\varepsilon_{true}(t)$ and $\varepsilon_{estimated}(t)$ denote the estimated and true strain value, respectively, P is the number of points in the cardiac mesh (24000 points) and T is the total number of frames in a cardiac cycle (125 frames). We computed strain bias and Δ_ε for each method at all time points and for all scatterer realizations and concatenated the results in 1-D arrays for statistical analysis resulting in a sample size of 620 [20]. TTR quantified the resemblance between the true and estimated strain curves per scatterer realizations resulting in a sample of size of 5 [10]. One-way analysis of variance (ANOVA) with the Bonferroni multiple comparison test was done to determine statistical significance among NCC, SBR, STBR-1 and STBR-2. Statistical analysis was performed using MATLAB Statistics and Machine Learning Toolbox Version 11.4 (R2018b).

To compare the algorithm performance *in vivo*, strain filters [21] were derived for the accumulated radial and longitudinal strains at all time points for each method by performing stochastic precision analysis [21-23]. First, the local elastographic signal-to-noise (SNR_e) was computed as follows.

$$\mathrm{SNR_e} = \frac{\mu}{\sigma} \tag{6.6}$$

where, μ and σ the mean and standard deviation of strain values within a 5 pixel × 9 pixel ROI centered at each cardiac mesh point. The window was translated over the entire cardiac mesh and calculation was repeated for all time points within a cardiac cycle resulting into strain-SNR_e pairs which were used to generate a 2-D histogram representing the SNR_e PDF, $f(\mathrm{SNR_e}, \varepsilon)$ and a 1-D histogram representing the strain PDF, $f(\varepsilon)$. Then, $f(\mathrm{SNR_e}, \varepsilon)$ was normalized by $f(\varepsilon)$ resulting into the conditional PDF, $f(\mathrm{SNR_e}, \varepsilon)$. Finally, the strain filter or the conditional expected value of the SNR_e was derived using the follow equation.

$$E(\mathrm{SNR_e} \,|\, \varepsilon) = \int_0^{+\infty} \mathrm{SNR_e} \times f(\mathrm{SNR_e} \,|\, \varepsilon)\, d\mathrm{SNR_e} \tag{6.7}$$

To perform comparative analysis among NCC, SBR, STBR-1 and STBR-2, we qualitatively compared the corresponding strain filters. Additionally, $E(\mathrm{SNR_e} \,|\, \varepsilon)$ values for radial and longitudinal strains at 46 % and -17.69 % strains were compared using ANOVA with the Bonferroni multiple comparison test following an approach reported in [24].

6.3 STBR Performance Assessment using Cardiac FEA Simulation Study

Figure 6.3 (a) – (e) show end-systole (ES) radial strain images obtained using FEA model, NCC, SBR, STBR-1 and STBR-2, respectively. Input RF data for this example had SNR_s value of

0 dB. Radial thickening of myocardium at ES was observed in the FEA result with positive strain values. The myocardium was divided into six equal segments denoted as segments 1 – 6 respectively in Figure 6.3 (a). Segments 1 – 6 denote anterior base, anterior mid, anterior apex, posterior apex, posterior mid and posterior base segments respectively. NCC had noisy estimates in apical and posterior segments (3 – 6) with spuriously elevated positive and negative strain values. Regularization (SBR, STBR-1 and STBR-2) reduced strain noise when compared to NCC in segments 3 – 6. STBR-1 suffered from under-estimation in anterior base (segment 1).

Segmental radial strain curves corresponding to Figure 6.3 are summarized in Figure 6.4. Figure 6.4 (a) – (f) compare the segmental radial strain curves estimated using NCC, SBR, STBR-1 and STBR-2 for anterior base, anterior mid, anterior apex, posterior apex, posterior mid and posterior base segments respectively against FEA results. NCC results had higher deviation from the FEA in apical and posterior segments (Figure 6.4 (c) – (f)). Significant improvement in strain estimation quality was achieved with SBR, STBR-1 and STBR-2 methods. Note that STBR improved the quality further in posterior mid and posterior base segments compared to SBR (observe the STBR-2 results in Figure 6.4 (e)). However, STBR-2 underestimated radial strain in anterior base segment corroborating the finding from Figure 6.3.

Figure 6.5 (a) – (e) show ES longitudinal strain images obtained using FEA, NCC, SBR, STBR-1 and STBR-2, respectively. Longitudinal shortening of myocardium at ES was observed in the FEA result with uniform negative strain values. NCC provides noisy estimates in apical and posterior segments (3 – 6) indicated spurious high positive negative strain values. All regularization methods (SBR, STBR-1 and STBR-2) reduced strain noise compared to NCC in segments 3 – 6 with better qualitative agreement with FEA result. No significant qualitative difference was observed among SBR, STBR-1 and STBR-2 results.

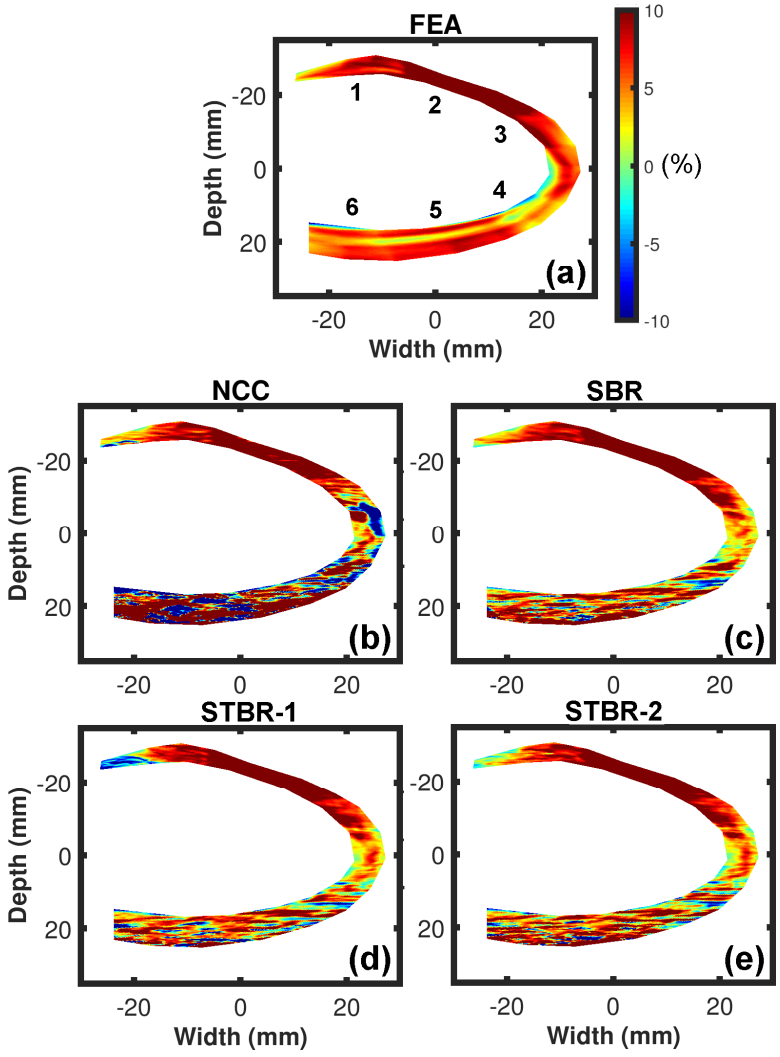

Figure 6.3 Qualitative comparison of ES radial strain estimation for FEA simulation. (a) – (e) denote FEA, NCC, SBR, STBR-1 and STBR-2 results, respectively. SBR = Spatial Bayesian regularization, STBR-1 = Spatial then temporal Bayesian regularization and STBR-2 = Simultaneous STBR.

Comparison of segmental longitudinal strain curves shown in Figure 6.5 are summarized in Figure 6.6. Figure 6.6 (a) – (f) compare the segmental longitudinal strain curves estimated using NCC, SBR, STBR-1 and STBR-2 for the 6 segments versus FEA results. NCC results had higher deviation from the FEA in apical and posterior segments (Figure 6.6 (c) – (f)). Significant improvement in strain estimation quality was achieved with SBR, STBR-1 and STBR-2 methods when compared to NCC with significant difference among each other.

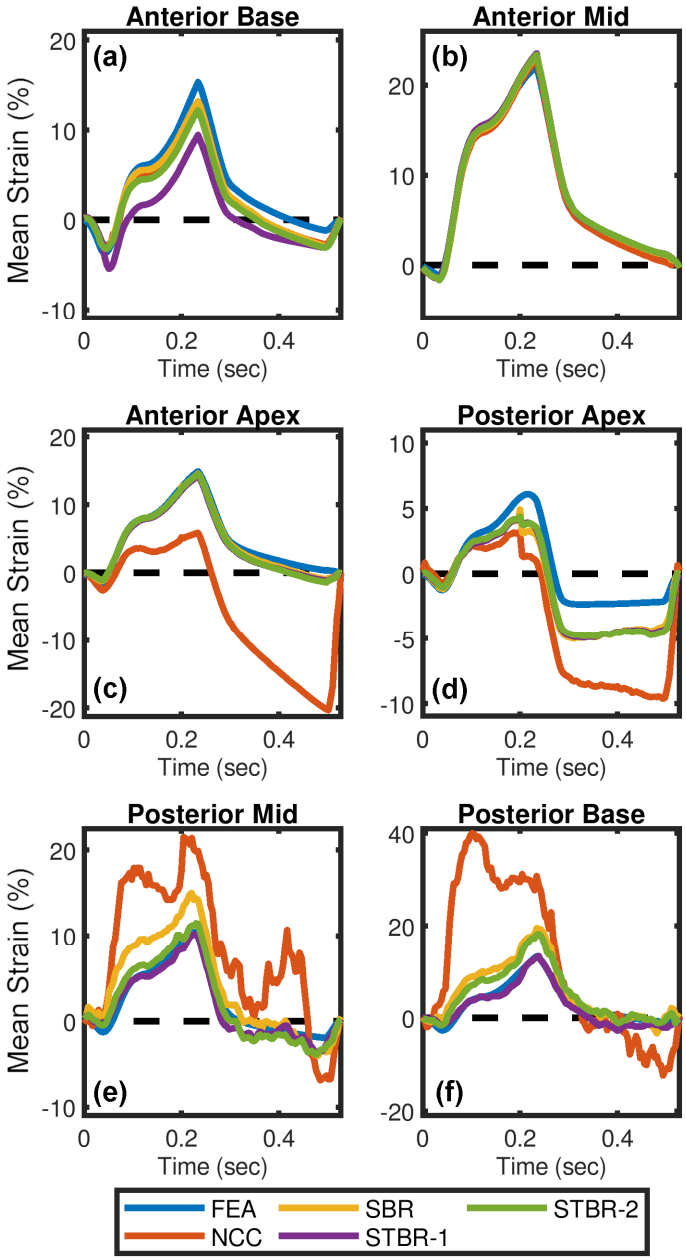

Figure 6.4 Qualitative comparison of radial strain curves for FEA simulation. Radial strain curves comparison among NCC, SBR, STBR-1 and STBR-2 for (a) anterior base, (b) anterior mid, (c) anterior apex, (d) posterior apex, (e) posterior mid and (f) posterior base segments respectively.

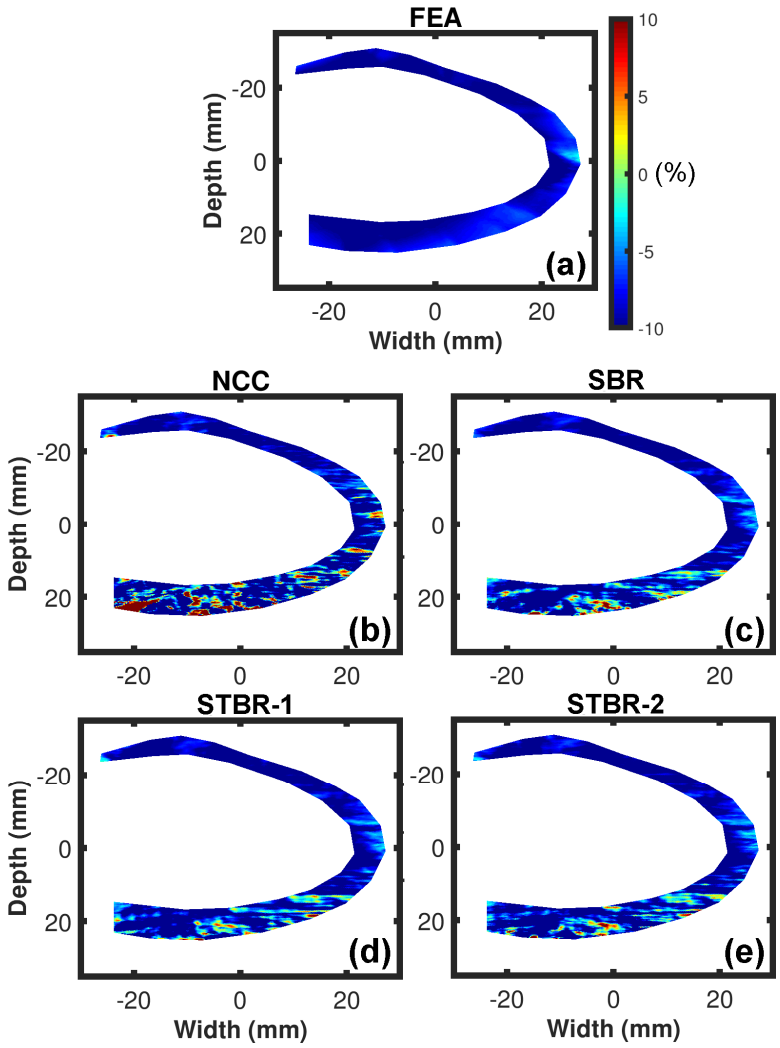

Figure 6.5 Qualitative comparison of ES longitudinal strain estimation for FEA simulation. (a) – (e) denote FEA, NCC, SBR, STBR-1 and STBR-2 results, respectively. SBR = Spatial Bayesian regularization, STBR-1 = Spatial then temporal Bayesian regularization and STBR-2 = Simultaneous STBR.

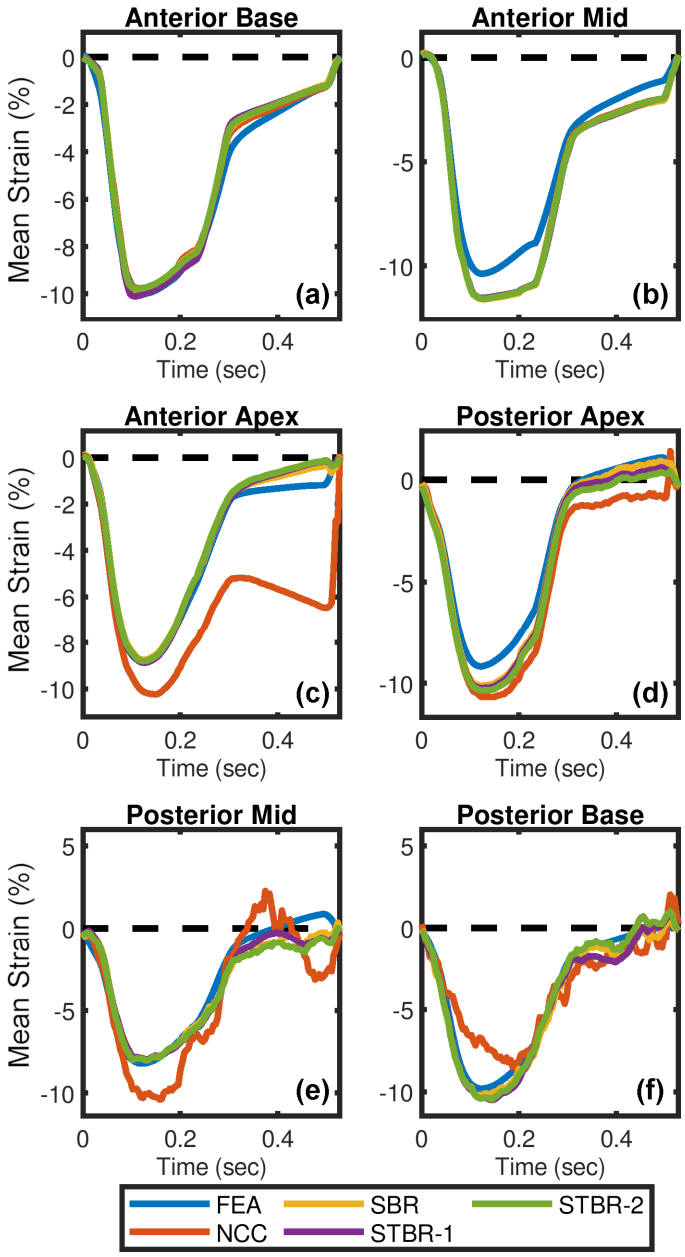

Figure 6.6 Qualitative comparison of longitudinal strain curves for FEA simulation. Longitudinal strain curves comparison among NCC, SBR, STBR-1 and STBR-2 for (a) anterior base, (b) anterior mid, (c) anterior apex, (d) posterior apex, (e) posterior mid and (f) posterior base segments respectively.

Figure 6.7 summarizes the comparison results for strain estimation bias. Figure 6.7 (a) – (b) show radial strain estimation bias for input RF data with $SNR_s = 30$ dB and 0 dB respectively. Both spatial and STBR methods had lower radial strain estimation bias with statistical significance

($p<0.001$). For 30 dB data, STBR-2 had the lowest mean estimation bias (0.16%) but was not significantly different than SBR (0.17%). For 0 dB data, SBR had the lowest mean estimation bias with statistical significance with all other methods ($p<0.01$). Figure 6.7 (c) – (d) show longitudinal strain estimation bias for input RF data with SNR_s = 30 dB and 0 dB respectively. All regularization methods had lower longitudinal strain estimation bias with statistical significance ($p<0.001$) compared to NCC with no statistically significant difference among each other. For example, for 30 dB data, mean e_l estimation bias for NCC, SBR, STBR-1 and STBR-2 were 1.01 %, 0.18%, 0.15% and 0.18% respectively.

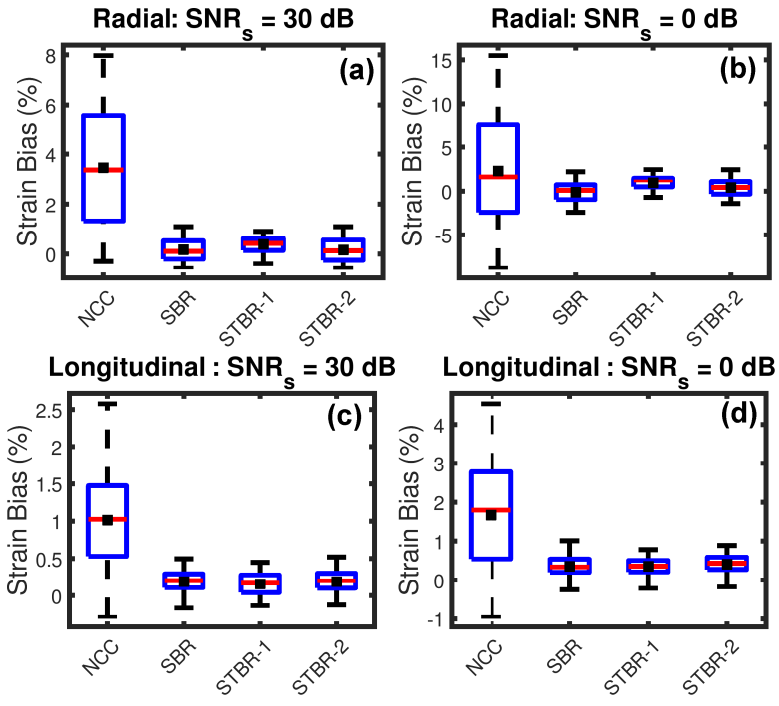

Figure 6.7 Strain estimation bias comparison (n = 620). (a) – (b) Radial strain estimation bias for input RF data with SNR_s = 30 dB and 0 dB respectively. (c) – (d) Longitudinal strain estimation bias for input RF data with SNR_s = 30 dB and 0 dB respectively. Red line and black square in the box-whisker plot denote median and mean statistics, respectively.

Figure 6.8 summarizes the comparison results for normalized strain error or Δ_ε (%). Figure 6.8 (a) – (b) show radial strain Δ_ε (%) for input RF data with SNR_s = 30 dB and 0 dB respectively while Figure 6.8 (c) – (d) show longitudinal strain Δ_ε (%) for input RF data with SNR_s = 30 dB and 0 dB respectively. All regularization methods performed significantly better than NCC ($p<0.001$) with no statistically significant differences among each other.

Figure 6.9 (a) – (b) show radial TTR for input RF data with SNR_s = 30 dB and 0 dB respectively while Figure 6.9 (c) – (d) show longitudinal TTR for input RF data with SNR_s = 30 dB and 0 dB respectively. All regularization methods performed significantly better than NCC. For 30 dB data, SBR had the lowest TTR for radial and longitudinal strains. For 0 dB data, STBR-2 and SBR had the lowest TTR for radial and longitudinal strains, respectively. However, the values did not differ significantly (For SNRs = 0 dB, mean e_r TTR for NCC, SBR, STBR-1 and STBR-2 were 169.44%, 32.07%, 30.04% and 27.70% respectively).

Figure 6.10 shows the variation of strain estimation bias as a function of the width vector σ_t for both STBR-1 and STBR-2 algorithms. Figure 6.10 (a) – (b) show the variation of radial strain estimation bias as a function of $\boldsymbol{\sigma_t}$ for STBR-1 and STBR-2 respectively while Figure 6.10 (c) – (d) show the variation of longitudinal strain estimation bias. Width vector = [0.01, 0.01] had the lowest bias for all cases therefore used as a default parameter in FEA study.

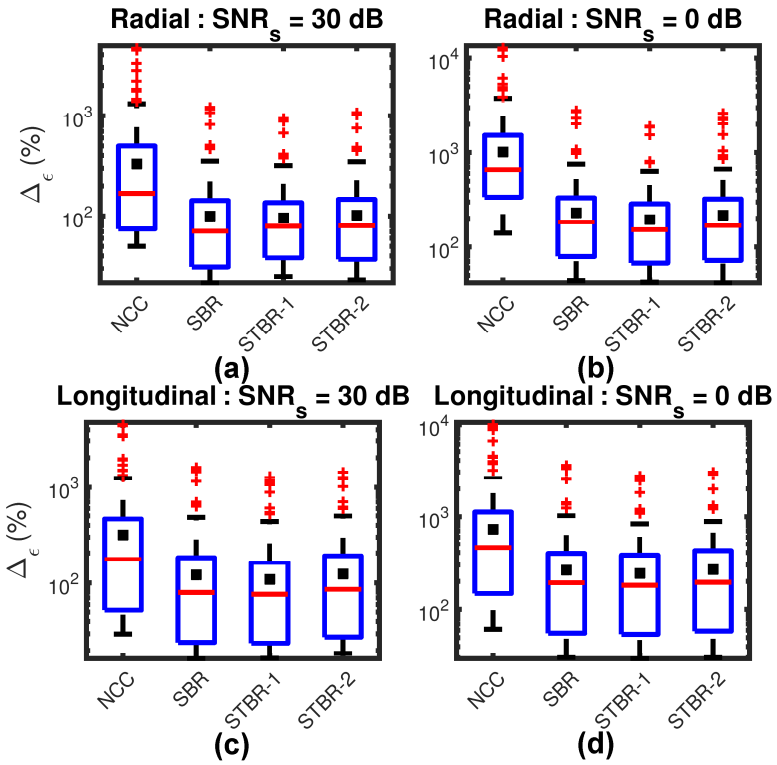

Figure 6.8 Normalized strain error or $\Delta_\varepsilon(\%)$ comparison (n = 620). (a) – (b) Radial $\Delta_\varepsilon(\%)$ for input RF data with SNR_s = 30 dB and 0 dB respectively. (c) – (d) Longitudinal $\Delta_\varepsilon(\%)$ for input RF data with SNR_s = 30 dB and 0 dB respectively.

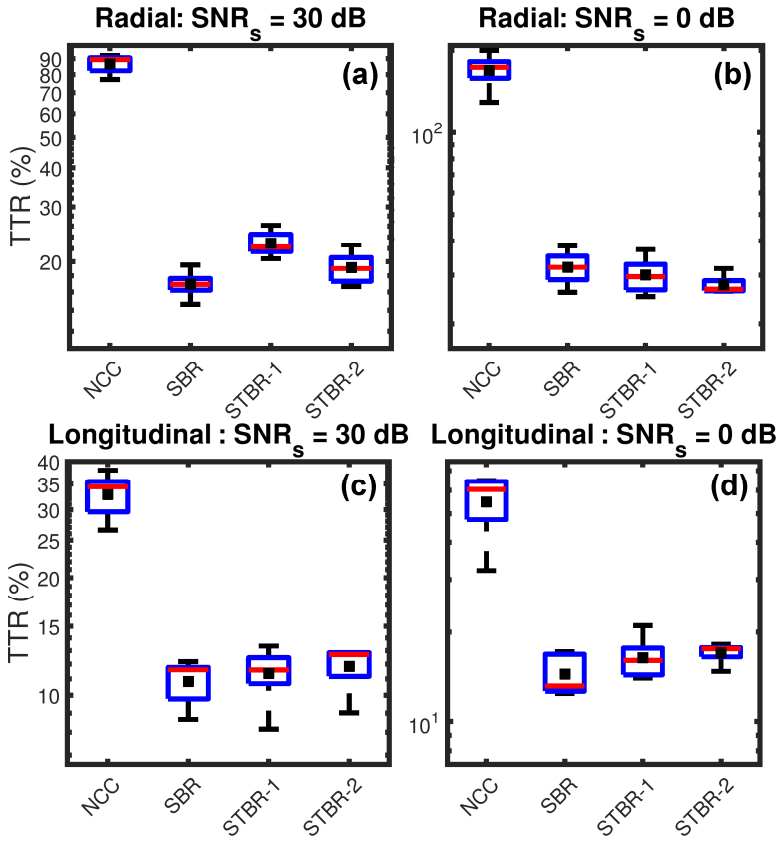

Figure 6.9 Total temporal relative (TTR) error comparison (n = 5). (a) – (b) Radial TTR for input RF data with SNR_s = 30 dB and 0 dB respectively. (c) – (d) Longitudinal TTR for input RF data with SNR_s = 30 dB and 0 dB respectively.

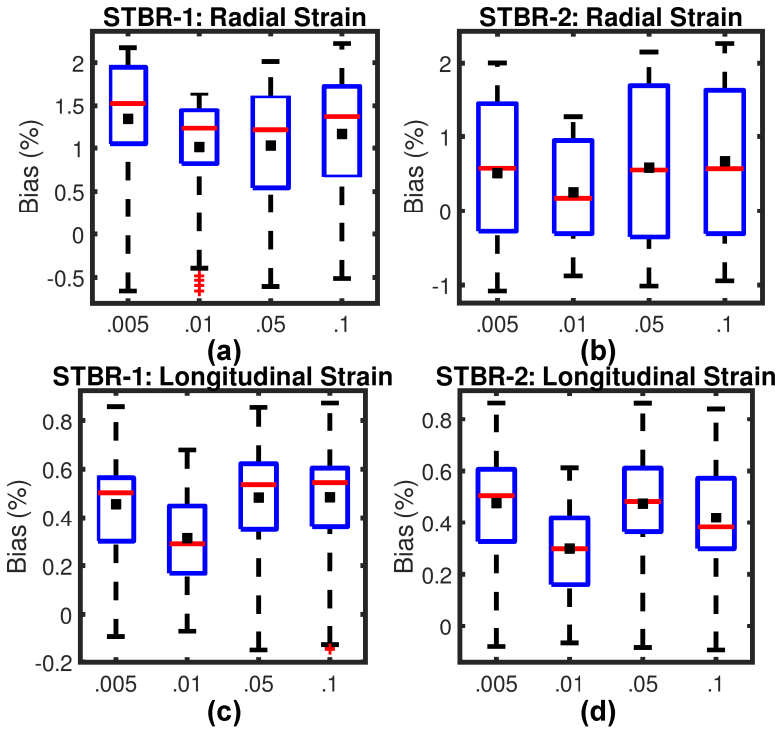

Figure 6.10 Variation of strain estimation bias as a function of σ_t (n = 125). (a) – (b) Variation of radial strain estimation bias as a function of σ_t for STBR-1 and STBR-2 respectively. (b) Variation of longitudinal strain estimation bias as a function of σ_t for STBR-1 and STBR-2 respectively.

6.4 *In vivo* Murine Cardiac Strain Imaging for STBR Validation

Figure 6.11 (a) – (d) show ES radial strain images obtained using NCC, SBR, STBR-1 and STBR-2, respectively for a healthy mouse heart. Radial thickening of myocardium at ES was observed in all results. However, NCC depicts patches of spuriously high non-physiological negative strain values throughout the entire myocardium. All regularization methods significantly reduced these erroneous strain values providing performance improvement. The best strain distribution was achieved with STBR-2 *in vivo* (observed regions indicated with arrows) correlating with the physiological expectation from a healthy mouse heart.

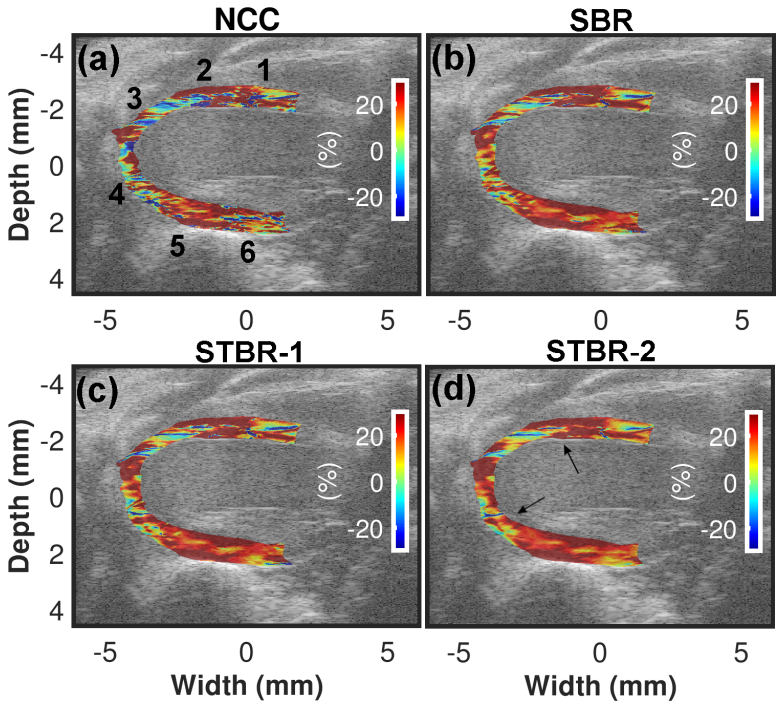

Figure 6.11 *In vivo* end-systole radial strain image comparison. (a) – (d) Radial strain images estimated with NCC, SBR, STBR-1 and STBR-2 respectively. Segments 1-6 shown in Fig. 11 (a) denote anterior base, anterior mid, anterior apex, posterior apex, posterior mid and posterior base segments respectively.

Figure 6.12 (a) – (f) compare segmental radial strain curves estimated using NCC, SBR, STBR-1 and STBR-2 for the 6 segments respectively. NCC without regularization resulted in noisy radial strain curves. For example, observe the peak shift and temporal jitter noise in anterior mid and posterior apex segments respectively. Significantly better radial strain curves were obtained using Bayesian regularization (both spatial and spatiotemporal). STBR-2 had the best quality curves quantified in terms of physiological relevant strain variation and temporal smoothness thus corroborating the ES strain image quality observation from Figure 6.11.

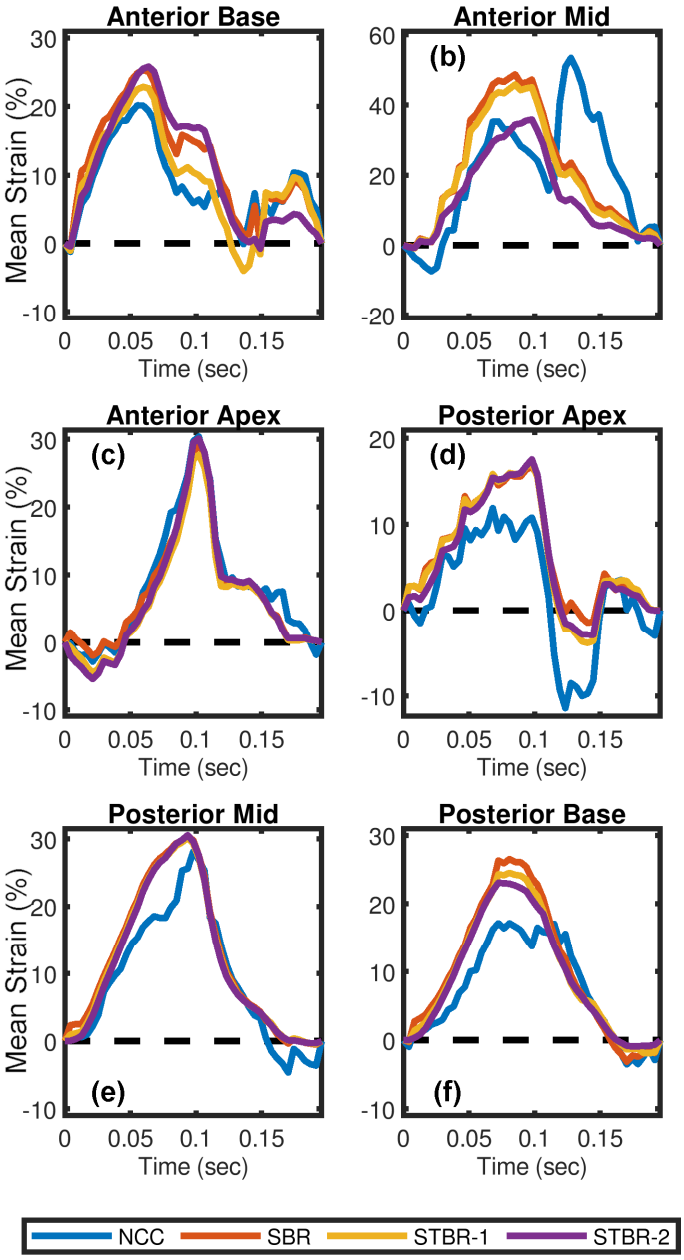

Figure 6.12 *In vivo* qualitative strain comparison of radial curves. Radial strain curves comparison among NCC, SBR, STBR-1 and STBR-2 for (a) anterior base, (b) anterior mid, (c) anterior apex, (d) posterior apex, (e) posterior mid and (f) posterior base segments respectively.

Figure 6.13 (a) – (d) show ES longitudinal strain images obtained using NCC, SBR, STBR-1 and STBR-2, respectively for a healthy mouse heart. Longitudinal shortening of myocardium at ES was observed in all results. However, NCC result had patches of spuriously high

unphysiological positive strain values throughout the entire myocardium with higher concentration in the apical and posterior base segments. All regularization methods significantly reduced those erroneous strain values providing performance improvement. The most homogeneous strain distribution was achieved with STBR-2 *in vivo* with significant improvement in the apical regions (observed regions indicated with arrows).

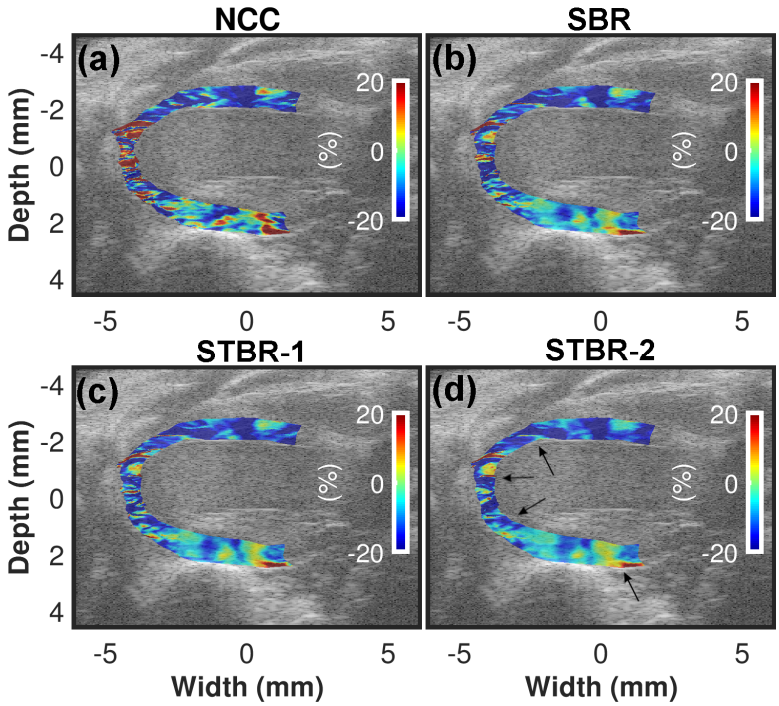

Figure 6.13 *In vivo* end-systole longitudinal strain image comparison. (a) – (d) Longitudinal strain images estimated with NCC, SBR, STBR-1 and STBR-2 respectively.

Figure 6.14 (a) – (f) qualitatively compare segmental radial strain estimated using NCC, SBR, STBR-1 and STBR-2 for anterior base, anterior mid, anterior apex, posterior apex, posterior mid and posterior base segments respectively. NCC resulted in noisy longitudinal strain curves in the apical [Figure 6.14 (c)] and posterior base [Figure 6.14 (f)] segments. SBR provided significant performance improvement in all segments except anterior apex [Figure 6.14 (c)] with reduced ES longitudinal strain value. STBR-2 had the best quality curves quantified in terms of physiological

relevant strain variation and temporal smoothness thus corroborating the ES strain image quality observation from Figure 6.13.

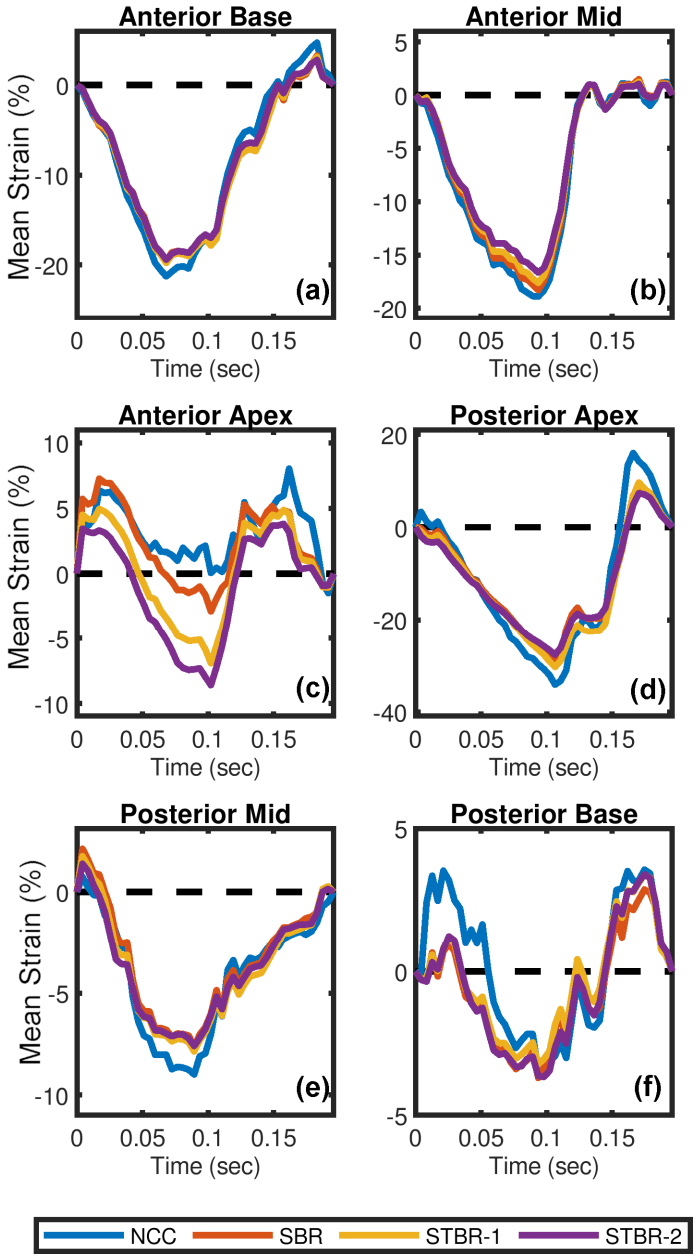

Figure 6.14 *In vivo* qualitative comparison of longitudinal strain curves. Longitudinal strain curves comparison among NCC, SBR, STBR-1 and STBR-2 for (a) anterior base, (b) anterior mid, (c) anterior apex, (d) posterior apex, (e) posterior mid and (f) posterior base segments respectively.

Figure 6.15 summarizes the results for *in vivo* stochastic precision analysis performed using ten healthy mice for radial (Figure 6.15 (a)) and longitudinal (Figure 6.15 (b)) strain filter comparisons, respectively. The strain filter presented in Figure 6.15 denote the mean of strain filters estimated individually for ten mice. Strain filter comparsion illustrate performance improvement with Bayesian regularization for both radial and longitudinal strain when compared to NCC. SBR and STBR-1, where the strain filters were coincident with each other indicating no performance improvement with STBR-1. However, STBR-2 produced the strain filters with higher $E(\mathrm{SNR}_e|\varepsilon)$ values for both e_r and e_l strains. Figure 6.15 (c) – (d) illustrate the comparison of $E(\mathrm{SNR}_e|\varepsilon)$ values for each method at 46 % accumulated radial strain and -17.69 % accumulated longitudinal strain, respectively. All regularization methods performed significantly better than NCC ($p<.0.05$). Note that STBR-2 had the higher $E(\mathrm{SNR}_e|\varepsilon)$ values both for radial and longitudinal strains even though it was not statistically significant when compared to SBR and STBR-1. The mean $E(\mathrm{SNR}_e|\varepsilon)$ values at 46% accumulated radial strain for NCC, SBR, STBR-1 and STBR-2 were 5.03, 9.43, 9.42 and 10.58, respectively. The mean $E(\mathrm{SNR}_e|\varepsilon)$ values at -17.69% accumulated longitudinal strain for NCC, SBR, STBR-1 and STBR-2 were 7.24, 11.68, 12.06 and 13.62, respectively.

Figure 6.16 (a) – (b) show the variation of *in vivo* radial strain and longitudinal estimation performance as a function of $\boldsymbol{\sigma_t}$. For both STBR-1 and STBR-2, we have generated strain filters with $\boldsymbol{\sigma_t}$ = [0.01,0.01] and [0.1,0.1] respectively. Figure 6.16 show that $\boldsymbol{\sigma_t}$ = [0.1,0.1] provided higher $E(\mathrm{SNR}_e|\varepsilon)$ values for both methods with best performance achieved with STBR-2 when assessed for radial and longitudinal strain results.

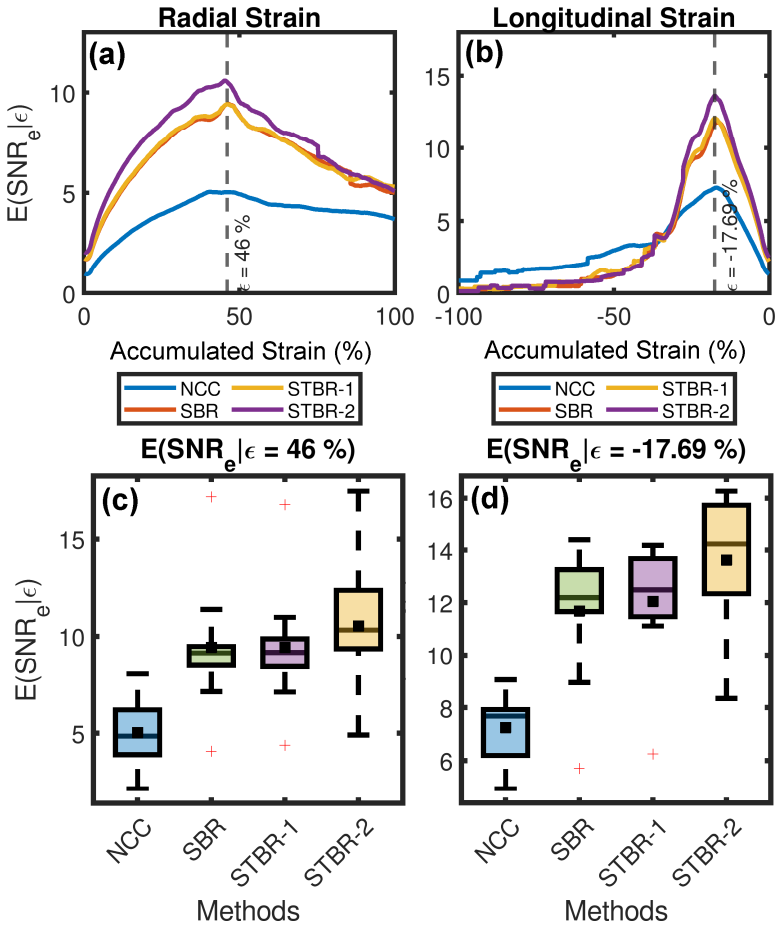

Figure 6.15 *In vivo* stochastic precision analysis (n = 10). (a) – (b) Radial and longitudinal strain filter comparison, respectively. (c) – (d) Comparison of $E(\mathrm{SNR}_e|\varepsilon)$ for each method at 46 % accumulated radial strain and -17.69 % accumulated longitudinal strain, respectively.

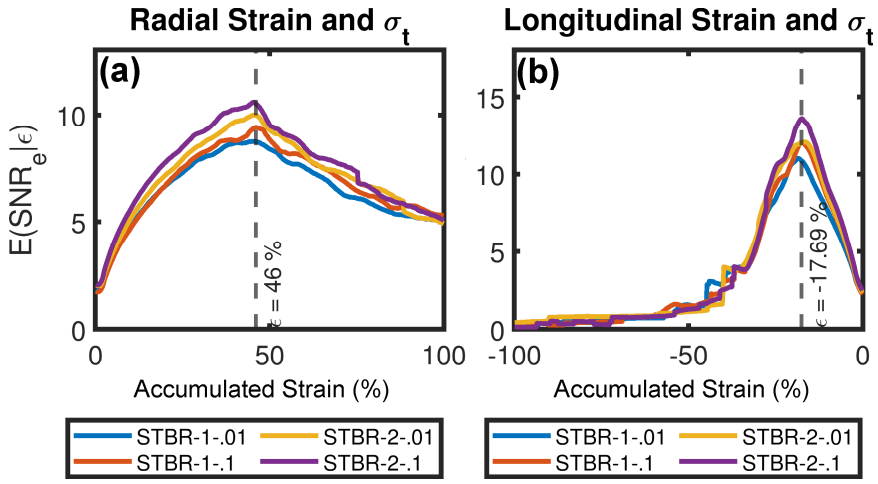

Figure 6.16 Variation of *in vivo* strain estimation performance as a function of σ_t. (a) – (b) Radial and longitudinal strain estimation performance as a function of σ_t.

Table 6.2 presents computational times for NCC, SBR, STBR-1 and STBR-2 for inter-frame displacement estimation. The results are measured in seconds and evaluated for a mouse RF dataset. The final RF data dimension was 6016×440 and mean execution time for 49 frames covering a complete cardiac cycle is reported. Bayesian methods required more computational time than NCC with highest time required by STBR-1.

Table 6.2 Summary of Computational Time (Seconds)

NCC	SB	STB-1	STB-2
73.20	114.30	316.15	156.86

6.5 Discussion on the Findings from STBR Validation Studies

In this chapter, we evaluated two STBR approaches (STBR-1 and STBR-2) and compared them against conventional NCC and spatial Bayesian regularization (SBR) using FEA and *in vivo* small animal studies both qualitatively and quantitatively. The key findings from these studies are summarized as follows.

a) Both spatial and spatiotemporal regularization methods performed significantly better than NCC for both FEA simulation and *in vivo* studies.
b) For the FEA simulation study, STBR-1 and STBR-2 performed as good as SBR in most of the cases. Few cases resulted in lower estimation errors with STBR however without any statistical significance.
c) Incorporation of temporal domain information resulted in better ES strain images and smoother strain curves *in vivo*.
d) STBR-2 is the preferred spatiotemporal regularization scheme because of lower errors in FEA simulation and higher SNR_e *in vivo*.

Qualitative comparison of ES radial strain images and temporal strain curves derived from RF data with SNRs = 0 dB showed the robustness of Bayesian regularization to handle significant noise corruption when compared to NCC. Posterior segments had higher noise compared to anterior segments in the FEA simulation because of the modelled frequency dependent acoustic attenuation and noise profile calculation with data derived from anterior segments. However, better qualitative agreement with FEA results in posterior segments (apex, mid and base) with STBR-1 and STBR-2 were seen compared to NCC and SBR indicating benefit of using temporal regularization for low SNR regions [Figure 6.3 (c) – (d) and Figure 6.4 (d) – (f)]. No statistically significant difference between SBR and STBR methods for SNRs = 30 dB data was observed. These results suggest that for high SNR input data, additional regularization with temporal information may not be necessary. Additionally, spatial then temporal regularization (STBR-1) resulted in under-estimation of radial strain in apical anterior base segment (Figure 6.3 (d) and 1.4 (a)) suggesting iterative application of Bayesian regularization with only temporal information might result in undesirable bias due to “over-regularization [2]”. SBR, STBR-1 and STBR-2

longitudinal results demonstrated good agreement with FEA results compared to NCC with no clear distinction between them [Figure 6.5 and Figure 6.6]. These results might be attributed to the simulated higher lateral sampling frequency (500 A-lines) and lateral Sinc interpolation used before displacement estimation [16]. These qualitative findings correlate well with the quantitative evaluation of strain bias, normalized strain error and total temporal relative error. Note that, higher TTRs with STBR-1 compared to SBR and STBR-2 resulted from underestimation with only temporal regularization. Overall, these results suggest that STBR-2 regularization is preferred over STBR-1 when performing STBR for CSI. Additionally, adaptive application of either SBR or STBR-2 might be a preferred approach for Bayesian regularization depending on local signal decorrelation and input RF data for future studies.

In vivo qualitative results suggest benefits from using temporal information for CSI observed with uniform strain distribution and strain curves with smooth temporal variation and physiological relevance (Figure 6.11 – Figure 6.14). Quantitative stochastic analysis results (Figure 6.15) corroborate the qualitative findings with STBR-2 demonstrating the best performance in terms of $E(\mathrm{SNR}_e|\varepsilon)$. Even though STBR-2 had higher radial and longitudinal $E(\mathrm{SNR}_e|\varepsilon)$ values compared to all other methods, the results were not statistically significant possibly due to small sample size (n = 10) and the choice of a conservative post-hoc test (Bonferroni) for multiple comparisons after ANOVA for four algorithms. Additionally, the best performance with STBR-2 correlates with our conclusion from FEA simulation study where STBR-2 is preferred over STBR-1 due to lower errors.

We also demonstrated performance variation with the choice of $\boldsymbol{\sigma_t}$ (temporal Gaussian width vector) in FEA simulation and *in vivo* experiments [Figure 6.10 and Figure **6.16**] with

optimal $\boldsymbol{\sigma_t}$ being 0.01 and 0.1, respectively. One interesting observation from these results is the dependence of $\boldsymbol{\sigma_t}$ to image acquisition frame rate (simulation = 250 Hz for canine heart and *in vivo* = 213 Hz mouse heart) suggesting lower $\boldsymbol{\sigma_t}$ for data collected at higher frame rate. Our previous *in vivo* STBR for carotid strain imaging also corroborates the finding (optimal $\boldsymbol{\sigma_t}$ = 0.005 for carotid artery with imaging frame rate = 538 Hz). $\boldsymbol{\sigma_t}$ can be considered as a tuning parameter controlling the type of displacements allowed by the model [note that likelihood function construction]. Lower $\boldsymbol{\sigma_t}$ enforce higher temporal continuity and vice versa. Thus, it is reasonable to expect the optimal choice to be tissue and imaging frame rate specific. In this dissertation, we set $\boldsymbol{\sigma_t}$ empirically, a potential drawback which must be addressed before employing STBR for future *in vivo* studies. Possible solutions include dynamic variation of $\boldsymbol{\sigma_t}$ based on local signal decorrelation [2, 25, 26] or designing tissue-specific presets for displacement estimation parameters as suggested by Ashikuzzaman *et al*. [27].

Computational timing analysis showed that STBR methods require more time to execute when compared to NCC or SBR (Table 6.2). Additional timing requirement stems from the referred time loops shown in Figure 6.2 [Algorithm 1]. There are several methods to improve computation efficiency. For example, currently NCC calculation is done within a temporal for loop which calls a NCC computation CUDA kernel having 2-D blocks of threads. The temporal loop can be replaced with 3-D blocks of threads achieving better parallelization. However, higher memory requirement will be a potential challenge while adopting this approach.

Several state-of-art US imaging techniques with plane or diverging wave imaging have also been implemented for cardiac and vascular strain imaging applications [28-30]. These techniques achieve significantly higher frame rates compared to focused line-by-line image

acquisition approaches. We anticipate more robust Bayesian regularization for these applications using both spatial and temporal domain information simultaneously.

One limitation of the current study is the use of data only from healthy models for both FEA and *in vivo* studies. To better understand the robustness and efficacy of the STBR, diseased heart models [20] (e.g., ischemia, dyssynchrony) should also be considered in future studies. Another limitation is the algorithm implementation for linear arrays as opposed to phased array transducers. This must be addressed before possible application of STBR to *in vivo* human studies. Finally, our analysis was limited to a single iteration of temporal regularization thus sampling information only from its immediate past and future neighbors. Iterative application will be investigated in future studies to better understand the effect of neighborhood size for STBR.

List of References

[1] R. Al Mukaddim, A. M. Weichmann, C. C. Mitchell, and T. Varghese, "Ultrasound strain imaging using spatiotemporal Bayesian regularized multi-level block matching method," in *Medical Imaging 2021: Ultrasonic Imaging and Tomography*, 2021, p. 116020R.

[2] R. Al Mukaddim, N. H. Meshram, and T. Varghese, "Locally optimized correlation-guided Bayesian adaptive regularization for ultrasound strain imaging," *Physics in Medicine & Biology,* vol. 65, p. 065008, 2020.

[3] B. Byram, G. E. Trahey, and M. Palmeri, "Bayesian speckle tracking. Part I: An implementable perturbation to the likelihood function for ultrasound displacement estimation," *IEEE transactions on ultrasonics, ferroelectrics, and frequency control,* vol. 60, pp. 132-143, 2012.

[4] B. Byram, G. E. Trahey, and M. Palmeri, "Bayesian speckle tracking. Part II: biased ultrasound displacement estimation," *IEEE transactions on ultrasonics, ferroelectrics, and frequency control,* vol. 60, pp. 144-157, 2012.

[5] D. M. Dumont and B. C. Byram, "Robust tracking of small displacements with a Bayesian estimator," *IEEE transactions on ultrasonics, ferroelectrics, and frequency control,* vol. 63, pp. 20-34, 2015.

[6] M. McCormick, N. Rubert, and T. Varghese, "Bayesian regularization applied to ultrasound strain imaging," *IEEE Transactions on Biomedical Engineering,* vol. 58, pp. 1612-1620, 2011.

[7] C. C. Mitchell, R. Al Mukaddim, A. M. Weichmann, K. W. Eliceiri, M. E. Graham, and T. Varghese, "Carotid Strain Imaging with a Locally Optimized Adaptive Bayesian Regularized Motion Tracking Algorithm," in *2020 IEEE International Ultrasonics Symposium (IUS)*, 2020, pp. 1-4.

[8] R. Al Mukaddim and T. Varghese, "Improving Ultrasound Lateral Strain Estimation Accuracy using Log Compression of Regularized Correlation Function," *2020 42nd Annual International Conference of the IEEE Engineering in Medicine and Biology Society (EMBC). IEEE,* 2020.

[9] R. Al Mukaddim and T. Varghese, "Cardiac Strain Imaging with Dynamically Skipped Frames: A Simulation Study," in *2020 IEEE International Ultrasonics Symposium (IUS)*, 2020, pp. 1-4.

[10] R. Al Mukaddim, N. H. Meshram, C. C. Mitchell, and T. Varghese, "Hierarchical Motion Estimation With Bayesian Regularization in Cardiac Elastography: Simulation and *In Vivo* Validation," *IEEE transactions on ultrasonics, ferroelectrics, and frequency control,* vol. 66, pp. 1708-1722, 2019.

[11] H. Chen and T. Varghese, "Three-dimensional canine heart model for cardiac elastography," *Medical physics,* vol. 37, pp. 5876-5886, 2010.

[12] A. D. McCulloch and R. Mazhari, "Regional myocardial mechanics: integrative computational models of flow-function relations," *Journal of Nuclear Cardiology,* vol. 8, pp. 506-519, 2001.

[13] Y. Li and J. A. Zagzebski, "A frequency domain model for generating B-mode images with array transducers," *IEEE transactions on ultrasonics, ferroelectrics, and frequency control,* vol. 46, pp. 690-699, 1999.

[14] H. Shi and T. Varghese, "Two-dimensional multi-level strain estimation for discontinuous tissue," *Physics in Medicine & Biology,* vol. 52, p. 389, 2007.

[15] N. H. Meshram and T. Varghese, "GPU accelerated multilevel Lagrangian carotid strain imaging," *IEEE transactions on ultrasonics, ferroelectrics, and frequency control,* vol. 65, pp. 1370-1379, 2018.

[16] M. M. McCormick and T. Varghese, "An approach to unbiased subsample interpolation for motion tracking," *Ultrasonic imaging,* vol. 35, pp. 76-89, 2013.

[17] R. G. Lopata, M. M. Nillesen, H. H. Hansen, I. H. Gerrits, J. M. Thijssen, and C. L. De Korte, "Performance evaluation of methods for two-dimensional displacement and strain estimation using ultrasound radio frequency data," *Ultrasound in medicine & biology,* vol. 35, pp. 796-812, 2009.

[18] C. Ma and T. Varghese, "Lagrangian displacement tracking using a polar grid between endocardial and epicardial contours for cardiac strain imaging," *Medical physics,* vol. 39, pp. 1779-1792, 2012.

[19] I. Zervantonakis, S. Fung-Kee-Fung, W. Lee, and E. Konofagou, "A novel, view-independent method for strain mapping in myocardial elastography: eliminating angle and centroid dependence," *Physics in Medicine & Biology,* vol. 52, p. 4063, 2007.

[20] M. De Craene, S. Marchesseau, B. Heyde, H. Gao, M. Alessandrini, O. Bernard*, et al.*, "3D strain assessment in ultrasound (straus): A synthetic comparison of five tracking methodologies," *IEEE transactions on medical imaging,* vol. 32, pp. 1632-1646, 2013.

[21] T. Varghese and J. Ophir, "A theoretical framework for performance characterization of elastography: The strain filter," *IEEE transactions on ultrasonics, ferroelectrics, and frequency control,* vol. 44, pp. 164-172, 1997.

[22] E. A. Bunting, J. Provost, and E. E. Konofagou, "Stochastic precision analysis of 2D cardiac strain estimation in vivo," *Physics in Medicine & Biology,* vol. 59, p. 6841, 2014.

[23] C. Ma and T. Varghese, "Analysis of 2-d ultrasound cardiac strain imaging using joint probability density functions," *Ultrasound in medicine & biology,* vol. 40, pp. 1118-1132, 2014.

[24] V. Sayseng, J. Grondin, and E. E. Konofagou, "Optimization of transmit parameters in cardiac strain imaging with full and partial aperture coherent compounding," *IEEE transactions on ultrasonics, ferroelectrics, and frequency control,* vol. 65, pp. 684-696, 2018.

[25] B. H. Friemel, L. N. Bohs, K. R. Nightingale, and G. E. Trahey, "Speckle decorrelation due to two-dimensional flow gradients," *IEEE transactions on ultrasonics, ferroelectrics, and frequency control,* vol. 45, pp. 317-327, 1998.

[26] M. Omidyeganeh, Y. Xiao, M. O. Ahmad, and H. Rivaz, "Estimation of strain elastography from ultrasound radio-frequency data by utilizing analytic gradient of the similarity metric," *IEEE transactions on medical imaging,* vol. 36, pp. 1347-1358, 2017.

[27] M. Ashikuzzaman, C. J. Gauthier, and H. Rivaz, "Global Ultrasound Elastography in Spatial and Temporal Domains," *IEEE transactions on ultrasonics, ferroelectrics, and frequency control,* vol. 66, pp. 876-887, 2019.

[28] M. Cikes, L. Tong, G. R. Sutherland, and J. D'hooge, "Ultrafast cardiac ultrasound imaging: technical principles, applications, and clinical benefits," *JACC: Cardiovascular Imaging,* vol. 7, pp. 812-823, 2014.

[29] S. Korukonda, R. Nayak, N. Carson, G. Schifitto, V. Dogra, and M. M. Doyley, "Noninvasive vascular elastography using plane-wave and sparse-array imaging," *IEEE transactions on ultrasonics, ferroelectrics, and frequency control,* vol. 60, pp. 332-342, 2013.

[30] J. Grondin, V. Sayseng, and E. E. Konofagou, "Cardiac strain imaging with coherent compounding of diverging waves," *IEEE transactions on ultrasonics, ferroelectrics, and frequency control,* vol. 64, pp. 1212-1222, 2017.

Chapter 7

Dynamic Frame Skip and Log Compressed Correlation Function for Ultrasound Strain Imaging

This chapter focuses on two signal processing approaches: (a) dynamic frame skip (DFS) and (b) log compression of the correlation function in the context of improving Bayesian regularization for ultrasound strain imaging. In Section 7.1[4], we investigate if the DFS algorithm can provide improved estimation of cardiac strain tensor components (radial and longitudinal strain) when compared to a conventional inter frame tracking approach. In Section 7.2[5], we investigative the utility of log compression of the regularized correlation function to tackle over-regularization artifacts seen with Bayesian regularization (refer to **Chapters 04** and **05** for more details).

7.1 Dynamic Frame Skip (DFS) for Cardiac Strain Imaging

In **Chapter 04**, we proposed and validated a cardiac strain imaging framework with Bayesian regularization using simulation and *in vivo* data. In this sub-section, we are primarily focused on investigating the feasibility of using dynamic frame skip (DFS) to further improve cardiac strain imaging accuracy. Optimal frame selection to improve strain estimation quality has been investigated by several groups. Jiang *et al.* [1] proposed to select optimal frames by assessing a displacement quality metric [2]. Xia *et al.* [3] used a one-predication-one-correction method for

[4] Rashid Al Mukaddim, and Tomy Varghese, "Cardiac Strain Imaging with Dynamically Skipped Frames: A Simulation Study." *IEEE International Ultrasonics Symposium Proceedings, 2020.*

[5] Rashid Al Mukaddim, and Tomy Varghese, "Improving Ultrasound Lateral Strain Estimation Accuracy using Log Compression of Regularized Correlation Function." *2020 42nd Annual International Conference of the IEEE Engineering in Medicine & Biology Society (EMBC), IEEE, 2020.*

dynamic frame pairing in quasi-static elastography. Zayed *et al.* [4] utilized principal component analysis and a multi-layer perceptron classifier to choose suitable frame pairs. In this chapter, we extend the DFS approach reported by Daniels and Varghese [5], and previously used by McCormick *et al.* [6] for carotid strain imaging to cardiac strain imaging. Dynamic frame skip relies on automatically selecting pre- and post-deformation frames with sufficient deformation to ensure reliable 2-D tracking of both axial and lateral displacement vectors. McCormick *et al.* [7] applied DFS for carotid strain imaging by determining frame skip (FS) criterion based on absolute axial strain in a rectangular region of interest (ROI) of the image. The ROI was chosen by discarding top and bottom portions of the image such that it only contained the arterial wall [7]. For cardiac applications, we are interested in optimizing the strain estimation accuracy within the myocardial wall. Thus, three ROIs were placed at anterior, apical, and posterior segments of myocardium at end-diastole (ED) to automatically determine DFS criterion. FS was determined from the two axial strain criteria defined as follows. The first criterion was to increase skip until mean absolute ROI strain (ROI_{MAA}) exceeds a threshold, τ_{max}. Second, a limit was imposed on the percentage of ROI pixels, ROI_{per} greater than τ_{max}. The maximum allowed FS was 5 frames. After tracking was done with an optimal FS, estimated axial and lateral displacements were used to update the positions of anterior, apical and posterior DFS ROIs to evaluate skip criteria for following frame pairs. The algorithm initially utilizes the previous FS which was increased if it satisfied all the above-mentioned criteria. Otherwise, FS was decreased until all criteria were satisfied. The DFS algorithm is summarized in Figure 7.1. In this chapter, τ_{max} and ROI_{per} values were empirically chosen to be 1.5 % and 10 % respectively.

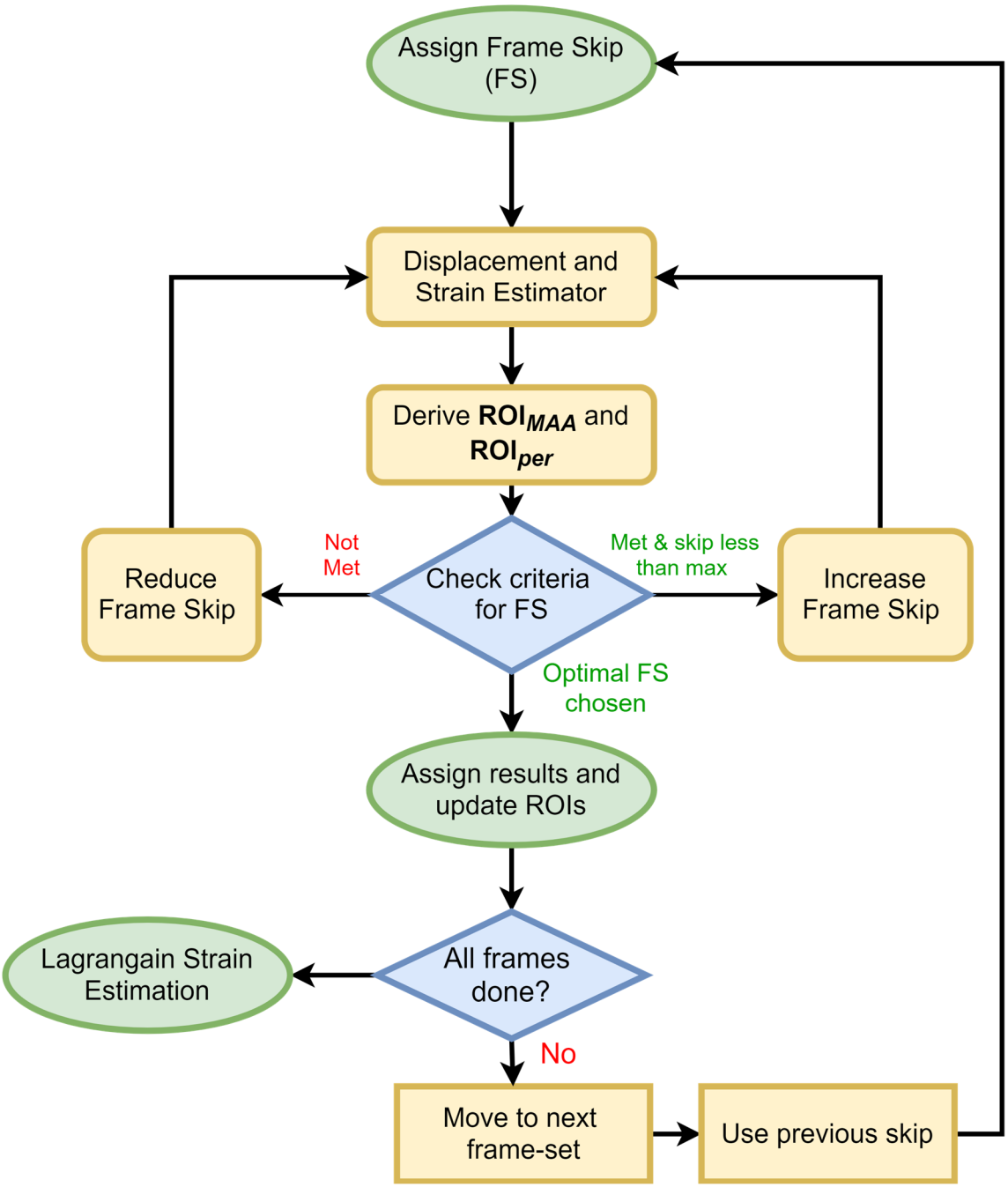

Figure 7.1 Flowchart representation of Dynamic Frame Skip Algorithm.

7.1.1 Simulation Study to Investigate Feasibility of DFS

7.1.1.1 Cardiac Strain Imaging with Bayesian Regularization

DFS was integrated into our cardiac strain imaging pipeline with Bayesian regularization-based hierarchical block-matching algorithm for displacement estimation reported in **Chapter 04**. Default setup for displacement estimation was three levels of tracking, one iteration of Bayesian regularization with no lateral interpolation. Axial kernel dimensions for three levels were 8λ, 6λ, and 5λ respectively while lateral kernel dimensions were 15, 13 and 11 A-lines respectively. Kernels had an overlap of 10 % and 50 % in axial and lateral directions respectively. 2-D windowed Sinc interpolation [8] was used to determine sub-sample displacement estimates. Lagrangian strain estimation was performed after delineating the myocardium and integrating incremental displacement estimates over a cardiac cycle [9]. A modified Akima piecewise cubic Hermite interpolation was used to interpolate estimates for skipped frames. Strain estimation was also done with skip = 0, termed as continuous frame skip (CFS) to compare with DFS. For ease of interpretation of results in the cardiac coordinate system, the cardiac strain tensor was derived using Lagrangian strain tensor through coordinate transformation. Further details regarding the CSI framework can be found in **Chapter 04**. Additionally, the impact of the maximum iteration number for Bayesian regularization on DFS performance was also investigated.

7.1.1.2 Canine Cardiac Deformation Simulation Study

A 3-D finite element analysis (FEA) canine cardiac deformation model [10] was used for the simulation study. Here 125 frames of radiofrequency (RF) data in parasternal long axis view covering one cardiac cycle of deformation were simulated. A 128-element linear array was simulated using a frequency domain ultrasound imaging program [11] and used to collect 500 A-lines at a sampling frequency of 78.8 MHz for each frame. A Gaussian-shaped transmit pulse with

8 MHz center frequency and 80% fractional bandwidth was used. To quantitatively compare performance between CFS and DFS, total temporal relative (TTR) error (%) was computed using:

$$\text{TTR}\ (\%) = \frac{\sum_{t=1}^{T} \left| \text{ES}(t) - \text{TS}(t) \right|}{\sum_{t=1}^{T} \left| \text{TS}(t) \right|} \times 100 \tag{7.1}$$

where estimated and ground-truth strain were denoted by ES and TS respectively, t is the time index. Further details regarding the simulation framework can be found in **Chapter 04**.

7.1.2 Experimental Findings from the DFS Feasibility Study

Regional analysis was performed by dividing the myocardial wall into six segments based on American Heart Association (AHA) classification to evaluate the performance of DFS. Segments 1 – 6 represent anterior base, anterior mid, anterior apex, posterior apex, posterior mid and posterior base segments, respectively. Figure 7.2 shows the comparison between DFS and CFS for estimation of regional axial displacement temporal curves. No apparent performance difference was observed between DFS and CFS. The comparison results between DFS and CFS for estimation of regional lateral displacement temporal curves are shown in Figure 7.3. Note that DFS showed improved qualitative agreement with ground truth when compared to CFS. Quantitative analysis shows that DFS reduced axial and lateral displacement TTR of CFS by 24.89 % and 46.07 % respectively. Figure 7.4 shows the comparison between DFS and CFS for estimation of regional temporal radial strain. No apparent performance difference was observed, expect for segment 4 where DFS results were comparatively better than CFS. Figure 7.5 presents comparison between DFS and CFS for estimation of regional temporal longitudinal strain. In segment 1 and 4, DFS had comparatively better agreement with true strain results when compared to CFS. TTRs comparison between DFS and CFS as a function of the maximum regularization

iteration value is presented Table 7.1. DFS with a single iteration provided the best performance in terms of strain TTRs (shown in bold font in Table 7.1). With increased number of iterations, both DFS and CFS resulted in higher TTRs attributed to the over-regularization artifact previously discussed in **Chapter 05**. However, DFS still maintained lower errors than CFS. One solution to tackle over regularization would be employing adaptive Bayesian regularization as reported in **Chapter 05**. One additional solution is also presented in Section 7.2 of this chapter.

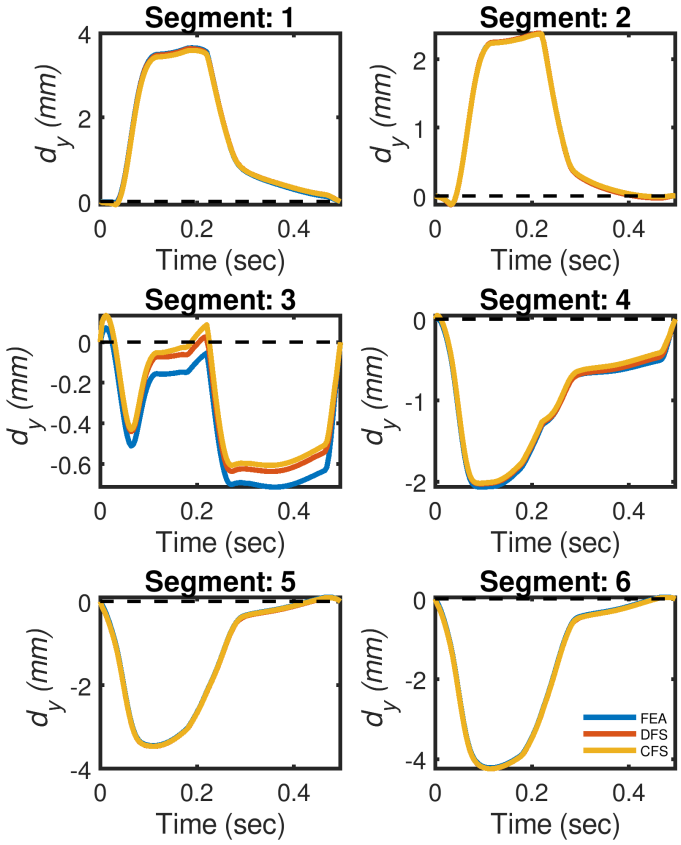

Figure 7.2 Regional axial displacement estimation performance comparison between DFS and CFS.

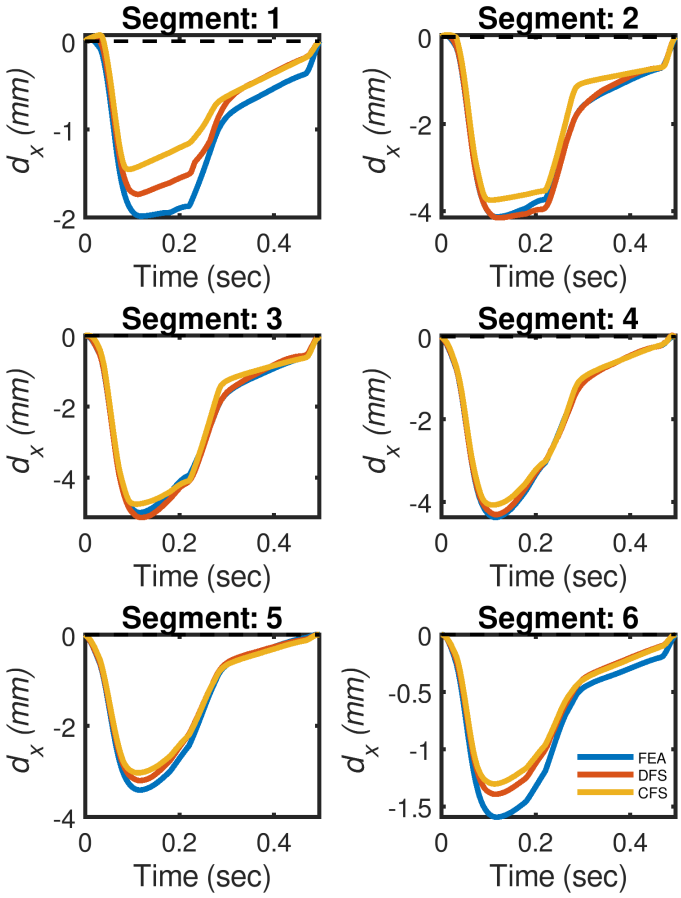

Figure 7.3 Regional lateral displacement estimation performance comparison between DFS and CFS.

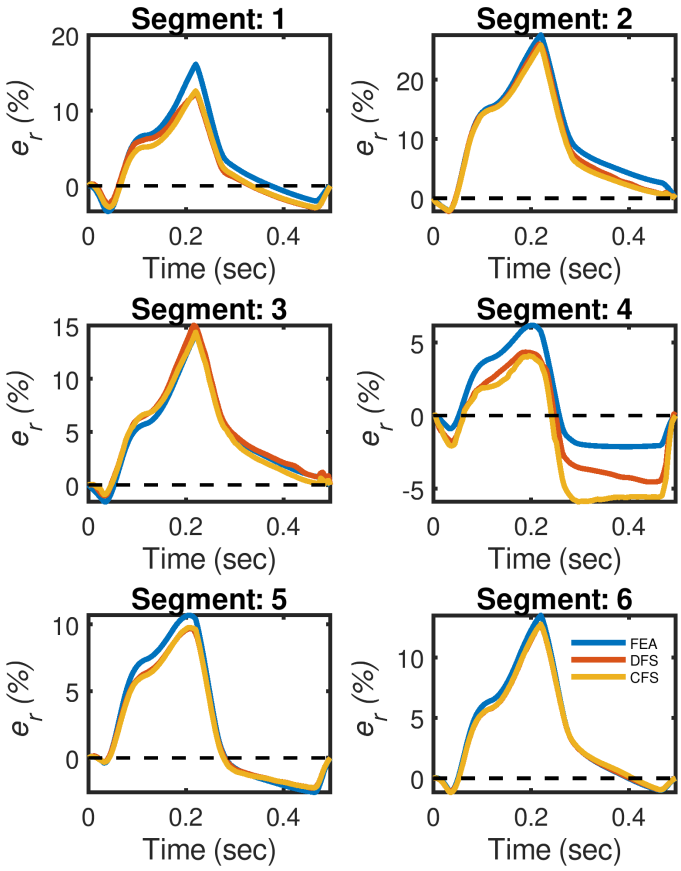

Figure 7.4 Regional radial strain estimation performance comparison between DFS and CFS.

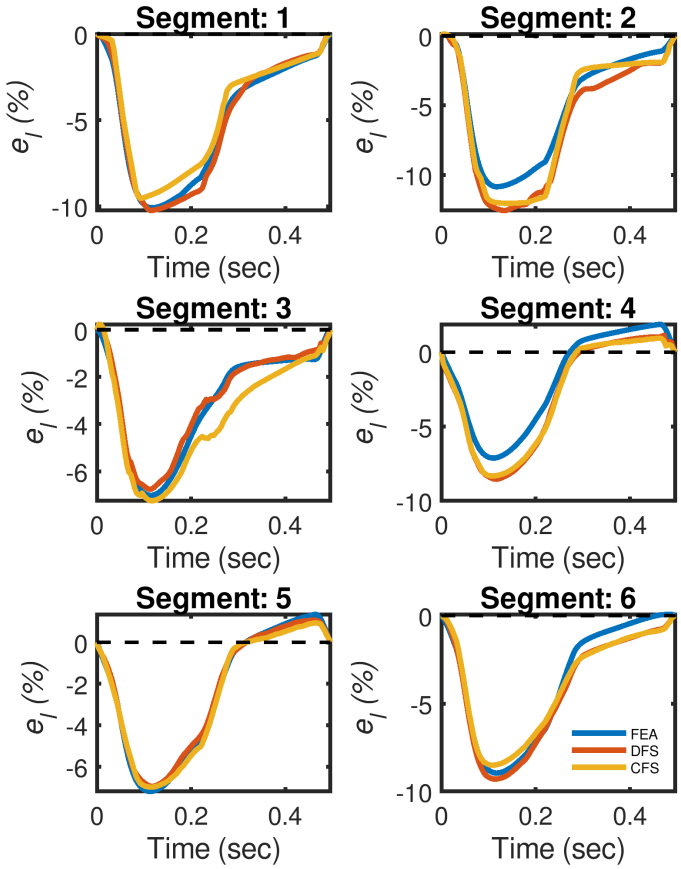

Figure 7.5 Regional longitudinal strain estimation performance comparison between DFS and CFS.

Table 7.1 TTR Comparison Between DFS and CFS: No Lateral Interpolation

	Iteration 1		Iteration 2		Iteration 3	
	DFS	CFS	DFS	CFS	DFS	CFS
Axial	**18.37**	22.39	26.42	21.89	22.19	25.00
Lateral	29.92	30.89	**26.87**	50.19	33.09	61.71
Radial	**17.32**	22.35	23.56	26.25	22.17	30.6
Longitudinal	**14.52**	15.87	22.26	22.83	26.61	31.77

7.1.3 Discussion on the use of the DFS Algorithm for CSI

In section 7.1, we have investigated the impact of using DFS for cardiac strain imaging using a realistic 3-D deformation model of the canine heart. DFS and CFS performed similarly in estimating axial displacement due to phase information and higher sampling frequency of RF data along the axial or beam direction. Performance improvement was more evident in lateral displacement estimation results which could be for following three reasons. First, magnitude dependence of strain estimation quality as shown by Varghese *et al.* [12] using strain filter. Second, tracking small deformations using envelope signals results in strain quality degradation [13]. Third, Bayesian regularization performs better under higher deformation (between 1% to 5%) [14]. Improved displacement quality resulted in accurate axial and lateral strain estimates [Table 7.1]. Consequently, components of cardiac strain tensor (radial and longitudinal strain) had fewer estimation errors when compared to CFS [Table 7.1]. Note that the performance improvements in apical segments (segments 3 – 4) shown in Figure 7.4 and Figure 7.5, is attributed to improved lateral-shear strain estimation with the DFS method. These results suggest that DFS can be potentially utilized to enhance cardiac strain imaging quality. However, these are preliminary results and several other factors such as kernel dimension optimization, performance in the case of noise corrupted RF data, lateral interpolation factor and simulation models of diseased hearts (e.g., ischemic) should be investigated to decide conclusively if there are clear benefits of using DFS over CFS for cardiac strain imaging. For example, higher lateral interpolation might be sufficient to reduce some of the errors seen with CFS. In future studies, DFS will be applied for *in vivo* murine cardiac strain imaging.

7.2 Log Compression of the Regularized Correlation Function

Bayesian regularization for ultrasound strain imaging proposed by McCormick *et al.* [15] can be iteratively applied to improve the quality of displacement estimation. At each iteration, new data from kernels located further from the current grid location are incorporated into the likelihood function resulting in attenuation of the magnitude of any secondary random peak. After the desired number of iterations, the probability values get concentrated around the peak that is similar to the dominant peaks of neighboring kernels. Thus, the PPD converges to a 2-D unimodal Gaussian distribution as shown in Figure 7.6 (a). Though significant improvement can be achieved in the axial direction, we observed that the PPD shown in Figure 7.6 (a) incurs lateral estimation errors in the estimation of subsample lateral displacements through interpolation (e.g., parabolic/cosine/Sinc) due to the delta like profile along the lateral direction [blue curve in Figure 7.6 (c)]. This behavior is due to over-regularization, where the lateral displacement subsample resolution gets bounded by the sub-line resolution of up-sampled RF data. One computationally intensive solution would be to interpolate RF data with a high interpolation factor [16] in the lateral direction. For instance, Byram *et al.* [17] used RF data with sampling frequency of 10 GHz to avoid using any subsample estimators. Another robust approach is to adaptively vary desired iteration as discussed in **Chapter 05**. Here, we propose a logarithmic transformation of PPD [Figure 7.6 (b)] as a low-cost alternative to recover the lateral displacements with improved subsample resolution. As shown in Figure 7.6 (c), Log(PPD) does not shift the mode of PPD but enables a more manageable data presentation using interpolation.

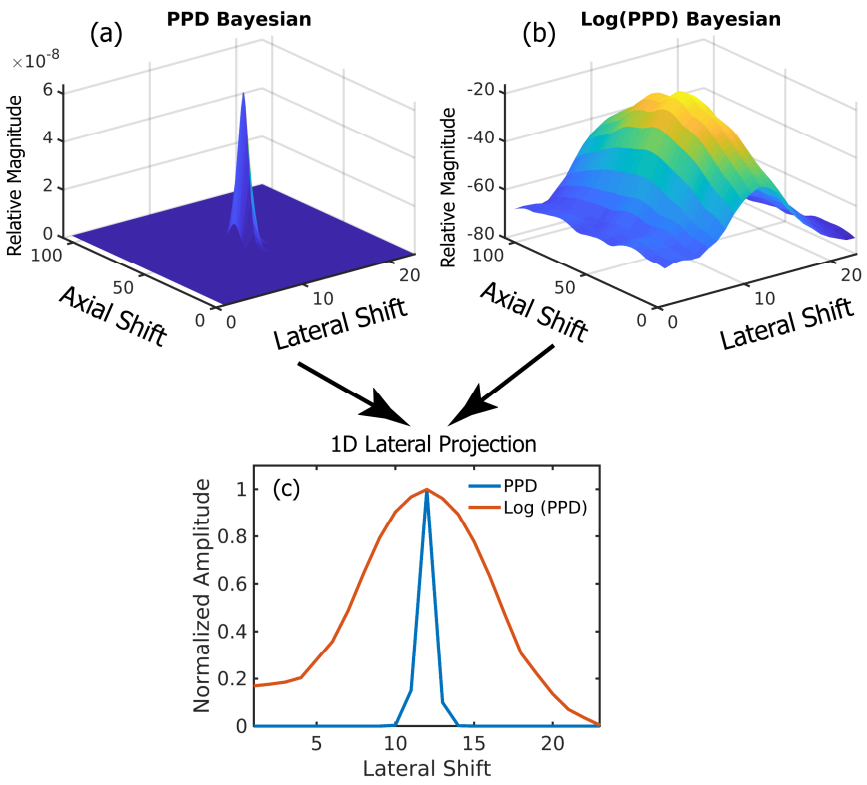

Figure 7.6 (a) PPD after Bayesian regularization. (b) Log of the PPD. (c) Lateral profiles of PPD along the integer axial shift location corresponding the peak.

7.2.1 Experimental Protocol to Investigate the Feasibility of Log Compressed Regularized Correlation Function

7.2.1.1 Displacement and Strain Estimation

Three levels of tracking using a hierarchical 2-D BM algorithm with Bayesian regularization is used in this study [9, 18, 19]. RF data were up sampled by a factor of 2 in both axial and lateral directions. Final level used a spatial kernel dimension of 1 wavelength by 10 A-lines. Axial and lateral kernel overlaps were 10% and 90% respectively. At each level, three iterations of Bayesian regularization were performed. Subsample estimation was performed with parabolic interpolation using both PPD and Log(PPD) for comparison. These approaches will be termed as “parabolic” and “log+parabolic” in this chapter. No additional filtering was performed

on the estimated displacements. A linear least squares with kernel dimension of 3.2×3.2 mm was then used for strain estimation [20].

7.2.1.2 Numerical Simulation Study

Numerical finite-element analysis (FEA) models of uniform and inclusion phantoms under 3% and 7% uniaxial deformation were used for our comparative study. Ultrasound imaging was performed using a 128 element 1-D linear array (element dimension = 10×0.15 mm^2) operating at a center frequency of 8.0 MHz. The array was modelled using a frequency-domain ultrasound simulation program [11]. Delay-and-sum beamforming was used to generate each A-line of RF data. Ten independent scatterer distributions were utilized for statistical analysis with a paired *t-test* used to compute significance. Displacement bias, variance and normalized strain error, $\Delta\varepsilon$ were calculated in a ROI around the focus of the transducer (20 mm) using the following equations.

$$\text{bias}(\mu m) = E\left[\left|\tau_e - \tau_t\right|\right] \tag{7.2}$$

$$\text{variance}(\mu m^2) = \text{var}(\tau_e - \tau_t) \tag{7.3}$$

$$\Delta\varepsilon = \left(\sum(\varepsilon_{ES} - \varepsilon_{TS})^2 \Big/ \sum \varepsilon_{TS}^2\right)\times 100 \tag{7.4}$$

where, τ_e and τ_t denote estimated and FEA displacement respectively. In equation (7.4), ε_{ES} and ε_{TS} denote estimated and FEA strain respectively. Additionally, signal-to-noise ratio (SNR) and contrast-to-noise ratio (CNR) were calculated in the uniform and inclusion phantom respectively

7.2.2 Results from the Simulation Comparative Study

Due to the low lateral sampling frequency, the impact of over-regularization is more readily observed in lateral estimation results. We present qualitative results in Figure 7.7 and Figure 7.8 showing lateral estimation results for 3% and 7% deformation respectively. “Vertical banding”

artifacts are clearly visible in displacement and strain images obtained with parabolic interpolation [Figure 7.7 (a) and (c)]. Improvement in image quality with reduction in banding artifacts were achieved with log+parabolic processing [Figure 7.7 (b) and (d)]. Log+parabolic displacement image [Figure 7.8 (a)] showed smoother transitions from low to high values compared to parabolic alone [Figure 7.8 (b)]. Thus, the log+parabolic strain image Figure 7.8 (d)] achieved improved homogeneity than the parabolic strain image [Figure 7.8 (c)]. Table 7.2 summarizes the quantitative analysis results. No significant difference was observed in the axial estimation accuracy. However, log+parabolic had significantly lower lateral displacement bias, variance and strain errors when compared to parabolic ($p < 0.001$) for both the low and high deformation. SNR results are summarized in Table 7.3. Significant improvement in lateral SNR were achieved with the log+parabolic approach ($p < 0.001$).

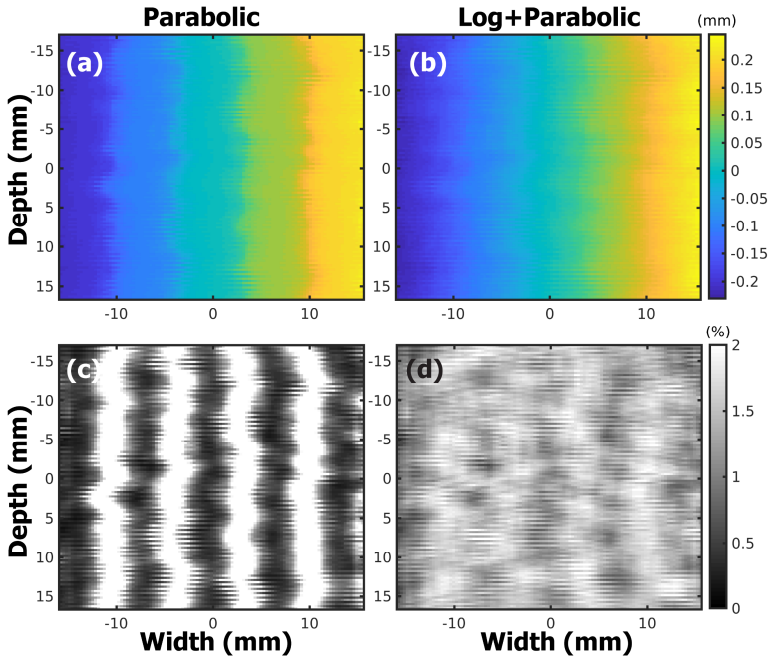

Figure 7.7 Uniform phantom at 3% deformation. Panels (a) and (b) show lateral displacement images with parabolic interpolation before and after log compression. Panels (c) and (d) show corresponding strain images.

Table 7.2 Comparison of Estimation Accuracy Before and After Log Compression of PPD Uniform Phantom Results (n = 10)

		3% Applied Deformation		**7% Applied Deformation**	
		Parabolic	**Log+Parabolic**	**Parabolic**	**Log+Parabolic**
Axial Estimates*	Bias (μm)	2.43 ± 0.04	2.40 ± 0.04	5.33 ± 0.08	5.28 ± 0.08
	Jitter (μm^2)	0.002±9.11×10^{-5}	0.003±9.11×10^{-5}	0.01±3.09×10^{-4}	0.01±3.15×10^{-4}
	$Strain_{Error}$ (%)	1.62 ± 0.03	1.58 ± 0.03	1.28 ± 0.02	1.27 ± 0.02
Lateral Estimates	Bias (μm)	12.91 ± 0.11	**5.86 ± 0.18**	12.86 ± 0.31	**10.78 ± 0.36**
	Jitter (μm^2)	0.22 ± 0.005	**0.05 ± 0.003**	0.25 ± 0.01	**0.17 ± 0.01**
	$Strain_{Error}$ (%)	56.33 ± 0.49	**15.17 ± 0.48**	13.94 ± 0.26	**10.37 ± 0.42**

**No difference along axial directions*

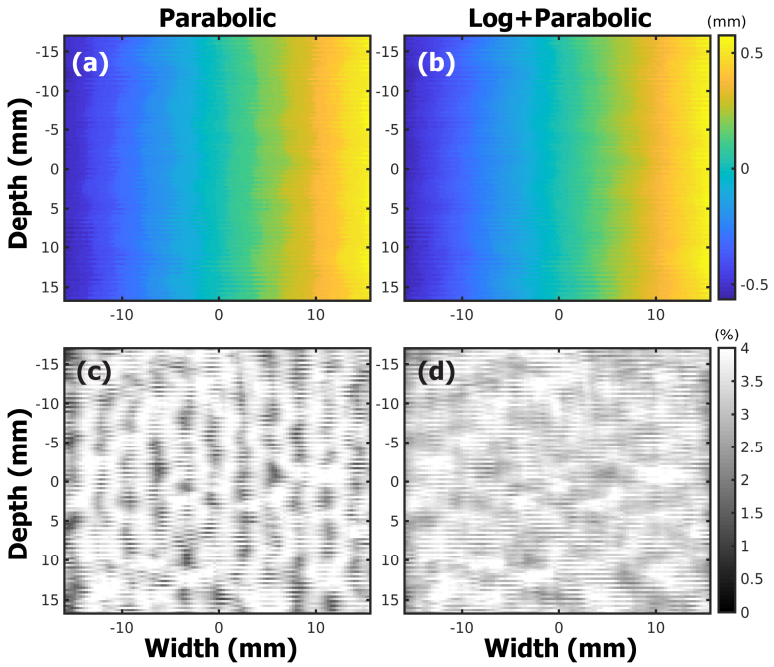

Figure 7.8 Uniform phantom at 7% deformation. Panels (a) and (b) show lateral displacement images with parabolic interpolation before and after log compression, while (c) and (d) show corresponding strain images.

Table 7.3 SNRs* Before and After Log Compression of PPD

	3% Deformation		7% Deformation	
Methods	**Axial**	**Lateral**	**Axial**	**Lateral**
Parabolic	33.76±0.18	4.51±0.08	35.98±0.15	14.83±0.17
Log+Parabolic	33.92±0.18	14.61±0.27	36.04±0.15	17.61±0.36

*SNR results are in decibels (dB)

Figure 7.9 (a) – (b) show 3% axial strain images using parabolic and log+parabolic estimation respectively, while Figure 7.9 (c) – (d) show the corresponding images for 7% axial strain. No difference was observed among these results due to presence of phase information and high sampling frequency in the axial direction. CNR values in Table 7.4 corroborate this observation. Figure 7.10 and Figure 7.11 show lateral estimation results for the 3% and 7%

deformation, respectively. Note that the inclusion appearance is distorted due to the banding artifacts in the parabolic results [Figure 7.10 (a) and (c)]. Improved lateral strain images with clearer inclusion boundary delineation was achieved with log and parabolic processing [Figure 7.10 (b) and (d)]. Observe that the 7% lateral strain image with parabolic interpolation had banding artifacts both in background and inside the inclusion [Figure 7.11 (a) and (c)]. These issues were resolved with log+parabolic processing [Figure 7.11 (b) and (d)]. Significant improvement in lateral CNR was achieved with log and parabolic ($p < 0.001$).

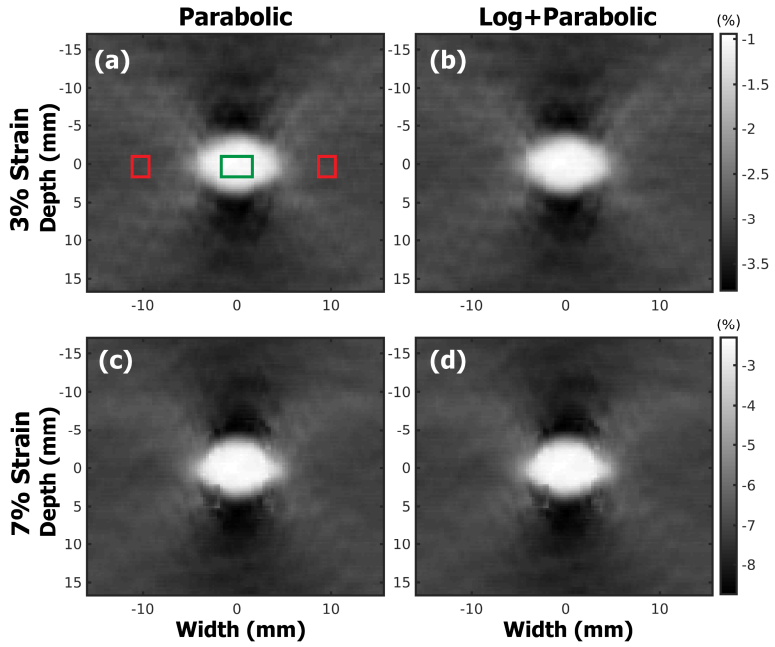

Figure 7.9 Axial strain images from an inclusion phantom. Panels (a) and (b) show 3% axial strain, while (c) and (d) show 7% axial strain with parabolic interpolation before and after log compression. Green ROI = target, Red ROI = background.

Table 7.4 CNRs* Before and After Log Compression of PPD

Methods	3% Deformation		7% Deformation	
	Axial	**Lateral**	**Axial**	**Lateral**
Parabolic	15.21±0.83	1.31±0.13	17.41±1.63	3.13±0.22
Log+Parabolic	15.28±0.83	3.12±0.28	17.49±1.63	4.79±0.41

*CNR results are in decibels (dB)

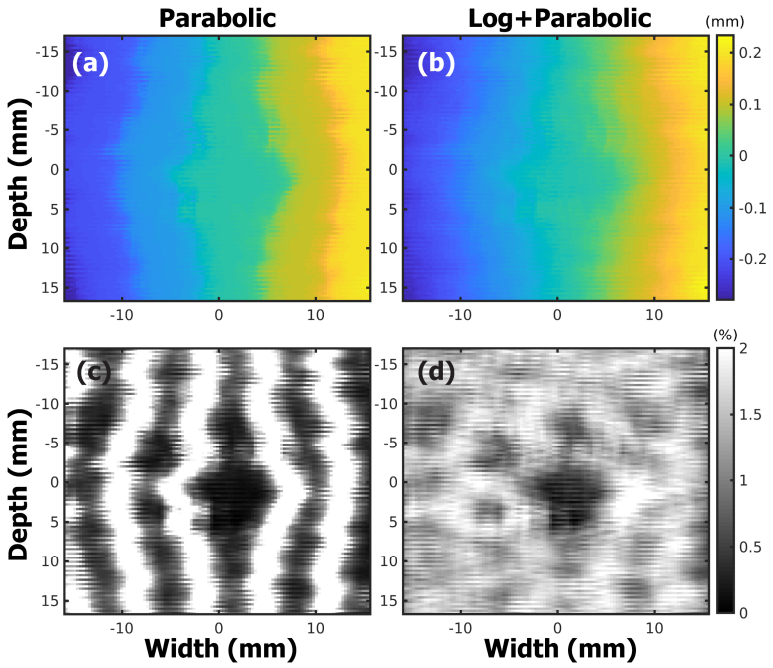

Figure 7.10 Inclusion phantom at 3% deformation. Panels (a) and (b) show lateral displacement images with parabolic interpolation before and after log compression. Panels (c) and (d) show corresponding strain images.

In this section, the use of log compressed regularized NCC to reduce banding artifacts due to over-regularization was investigated. Peaks similar to a Delta function in the lateral projection of PPD cannot be represented with conventional interpolation schemes. Our results demonstrate that log compression enables improved subsample estimation with significant reduction of lateral banding errors without additional computational burden or bias. As sub-sample displacement

estimation is more critical at lower when compared to higher deformations, the benefit of our proposed approach is therefore more evident at lower strains. Future work will focus on using cosine and *Sinc* interpolation [8] and *in vivo* validation. Furthermore, this approach will be compared against adaptive Bayesian regularization to benchmark its performance against more sophisticated algorithms developed to tackle over-regularization.

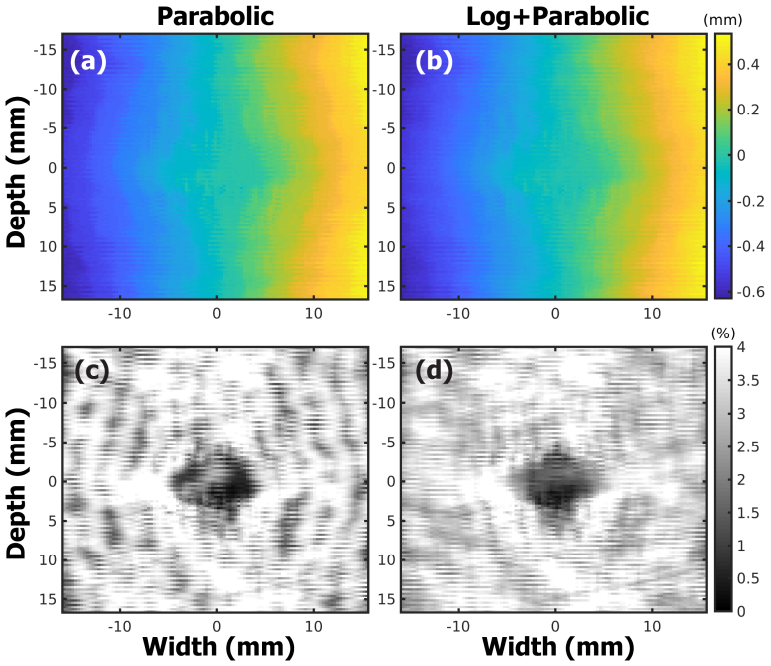

Figure 7.11 Inclusion phantom at 7% deformation. Panels (a) and (b) show lateral displacement images with parabolic interpolation before and after log compression, while (c) and (d) show corresponding strain images.

List of References

[1] J. Jiang, T. J. Hall, and A. M. Sommer, "A novel image formation method for ultrasonic strain imaging," *Ultrasound in medicine & biology,* vol. 33, pp. 643-652, 2007.

[2] J. Jiang, T. J. Hall, and A. M. Sommer, "A novel performance descriptor for ultrasonic strain imaging: A preliminary study," *IEEE transactions on ultrasonics, ferroelectrics, and frequency control,* vol. 53, pp. 1088-1102, 2006.

[3] R. Xia, G. Tao, and A. K. Thittai, "Dynamic frame pairing in real-time freehand elastography," *IEEE transactions on ultrasonics, ferroelectrics, and frequency control,* vol. 61, pp. 979-985, 2014.

[4] A. Zayed and H. Rivaz, "Fast Strain Estimation and Frame Selection in Ultrasound Elastography using Machine Learning," *IEEE Transactions on Ultrasonics, Ferroelectrics, and Frequency Control,* 2020.

[5] M. J. Daniels and T. Varghese, "Dynamic frame selection for in vivo ultrasound temperature estimation during radiofrequency ablation," *Physics in Medicine & Biology,* vol. 55, p. 4735, 2010.

[6] M. McCormick, T. Varghese, X. Wang, C. Mitchell, M. Kliewer, and R. Dempsey, "Methods for robust in vivo strain estimation in the carotid artery," *Physics in medicine and biology,* vol. 57, p. 7329, 2012.

[7] M. McCormick, T. Varghese, X. Wang, C. Mitchell, M. Kliewer, and R. Dempsey, "Methods for robust in vivo strain estimation in the carotid artery," *Physics in Medicine & Biology,* vol. 57, p. 7329, 2012.

[8] M. M. McCormick and T. Varghese, "An approach to unbiased subsample interpolation for motion tracking," *Ultrasonic imaging,* vol. 35, pp. 76-89, 2013.

[9] R. Al Mukaddim, N. H. Meshram, C. C. Mitchell, and T. Varghese, "Hierarchical Motion Estimation With Bayesian Regularization in Cardiac Elastography: Simulation and *In Vivo* Validation," *IEEE transactions on ultrasonics, ferroelectrics, and frequency control,* vol. 66, pp. 1708-1722, 2019.

[10] H. Chen and T. Varghese, "Three-dimensional canine heart model for cardiac elastography," *Medical physics,* vol. 37, pp. 5876-5886, 2010.

[11] Y. Li and J. A. Zagzebski, "A frequency domain model for generating B-mode images with array transducers," *IEEE transactions on ultrasonics, ferroelectrics, and frequency control,* vol. 46, pp. 690-699, 1999.

[12] T. Varghese and J. Ophir, "A theoretical framework for performance characterization of elastography: The strain filter," *IEEE transactions on ultrasonics, ferroelectrics, and frequency control,* vol. 44, pp. 164-172, 1997.

[13] R. G. Lopata, M. M. Nillesen, H. H. Hansen, I. H. Gerrits, J. M. Thijssen, and C. L. De Korte, "Performance evaluation of methods for two-dimensional displacement and strain estimation using ultrasound radio frequency data," *Ultrasound in medicine & biology,* vol. 35, pp. 796-812, 2009.

[14] R. Al Mukaddim, N. H. Meshram, and T. Varghese, "Locally optimized correlation-guided Bayesian adaptive regularization for ultrasound strain imaging," *Physics in Medicine & Biology,* vol. 65, p. 065008, 2020.

[15] M. McCormick, N. Rubert, and T. Varghese, "Bayesian regularization applied to ultrasound strain imaging," *IEEE Transactions on Biomedical Engineering,* vol. 58, pp. 1612-1620, 2011.

[16] Z. Liu, C. Huang, and J. Luo, "A systematic investigation of lateral estimation using various interpolation approaches in conventional ultrasound imaging," *IEEE transactions on ultrasonics, ferroelectrics, and frequency control,* vol. 64, pp. 1149-1160, 2017.

[17] B. Byram, G. E. Trahey, and M. Palmeri, "Bayesian speckle tracking. Part II: biased ultrasound displacement estimation," *IEEE transactions on ultrasonics, ferroelectrics, and frequency control,* vol. 60, pp. 144-157, 2012.

[18] N. H. Meshram and T. Varghese, "GPU accelerated multilevel Lagrangian carotid strain imaging," *IEEE transactions on ultrasonics, ferroelectrics, and frequency control,* vol. 65, pp. 1370-1379, 2018.

[19] H. Shi and T. Varghese, "Two-dimensional multi-level strain estimation for discontinuous tissue," *Physics in medicine and biology,* vol. 52, p. 389, 2007.

[20] F. Kallel and J. Ophir, "A least-squares strain estimator for elastography," *Ultrasonic imaging,* vol. 19, pp. 195-208, 1997.

Chapter 8

Real-Time *in vivo* Photoacoustic Imaging of Myocardial Ischemia

In recent years, efforts have concentrated on *in-vivo* quantitative imaging by capitalizing on the absorption spectra of endogenous contrast agents such as hemoglobin [1, 2], leading to the use of dual-wavelength photoacoustic imaging (PAI) to estimate blood oxygen saturation (% sO_2). Differing absorption spectra of oxyhemoglobin (HbO_2) and deoxyhemoglobin (HHb) enables quantification of blood oxygenation with this approach [3]. Real-time PAI and its sensitivity to blood oxygenation levels coupled with the recent development of PA integrated micro-ultrasound systems [4] make it suitable for diagnosis and monitoring of myocardial ischemia *in-vivo*. This chapter[6] focuses on the use of such a commercially available PA imaging system (Vevo 2100 LAZR, FUJIFILM VisualSonics, Inc., Toronto, Canada) for the diagnosis and monitoring of myocardial ischemia in murine models.

Initial reports of PAI for murine cardiovascular dynamics was reported in [5]. They utilized a 30-MHz linear array to image the beating heart of athymic nude mice at ~50 frames per second. Li *et al*. (2011) tried to establish a correlation between the extent of myocardial ischemia and variation of PA signal intensity in rats submerged in water under tracheal intubation, on a section of the left ventricular wall. They used a wavelength of 532 nm and a single element transducer with center frequency of 3.5 MHz for reception [6]. They reported an exponential decay in the PA signal intensity with time after left anterior descending (LAD) artery occlusion. In this chapter, we report on the utilization of a commercially available dual-wavelength PAI solution to generate parametric maps of blood oxygen saturation, % sO_2 that were overlaid on high resolution high-

[6] Rashid Al Mukaddim, Allison Rodgers, Timothy A. Hacker, Andrew Heinmiller and Tomy Varghese, "Real-time *in vivo* photoacoustic imaging in the assessment of myocardial dynamics in murine model of myocardial ischemia." *Ultrasound in Medicine and Biology*, vol. 44, no. 10, pp. 2155-2164 (2018) PMCID: PMC6135705

frequency ultrasound images of the myocardium and show that PAI is sensitive to changes in myocardial oxygenation associated with acute myocardial ischemia.

8.1 Murine Models and Photoacoustic Data Analysis

8.1.1 Murine model of Myocardial Ischemia

Ten 10-12 weeks old male BALB/CJ mice obtained from Jackson Labs (ME, USA) were studied using PAI and high frequency ultrasound (HFUS) imaging. Myocardial ischemia was established in each murine model using the procedure described below. All *in vivo* procedures were performed under an approved protocol by the Institutional Animal Care and Use Committee (IACUC) at the University of Wisconsin-Madison.

Following induction of isoflurane anesthesia (3%), the mouse was intubated with an 18-gauge catheter and placed on a ventilator at 120-130 breaths per minute with a stroke volume of 150 μL and maintained on 2% isoflurane. A left lateral incision through the fourth intercostal space was made to expose the heart. After visualizing the left coronary artery, a 7-0 clear prolene suture was placed through the myocardium in the anterolateral wall and secured [7, 8]. Coronary artery entrapment was confirmed by observing blanching of the distal circulation (ventricular apex) and ECG changes indicative of myocardial ischemia. The lungs were over inflated, and the ribs and muscle layers were closed by absorbable sutures. The skin was closed by additional suturing using 6-0 clear nylon or silk sutures. The mouse was then recovered from anesthesia and extubated.

8.1.2 Photoacoustic (PA) and High-frequency Ultrasound Imaging

Longitudinal variations of perfusion and cardiac function of the heart after ischemia, was evaluated using PA and HFUS. Imaging sessions were performed before LAD ligation (baseline) and at 30 minutes, 80 minutes, 120 minutes and 24 hours after LAD ligation. The objective of

imaging after LAD ligation (from 30 minutes to 24 hours) was to study the ability of PAI in the early detection of ischemia in the ventricular wall. All imaging was performed using a Vevo LAZR imaging system (FUJIFILM VisualSonics, Inc., Toronto, Canada). During imaging sessions, mice were anesthetized using 1.5 % isoflurane and a constant flow of oxygen was maintained. Hair was removed from the chest region using depilatory cream to ensure better transmission of optical energy. Mice were placed supine on a heated imaging platform for imaging with continuous monitoring of physiological parameters.

2-D PAI was performed in "Oxy-Hemo" mode to obtain parametric maps of oxygen saturation (% sO_2) and hemoglobin (Hbt) concentration in the anterior myocardium. In this mode, an automated imaging sequence is used to perform dual-wavelength PAI at 750 and 850 nm. Parametric maps of % sO_2 and Hbt are then generated using the algorithm reported in [4, 9, 10], implemented on the system. Mice hearts were imaged in a parasternal long axis (PLAX) view using a LZ 400 transducer (FUJIFILM VisualSonics, Inc., Toronto, Canada) with broadband frequency range from 18 – 38 MHz and operating at a center frequency of 30 MHz. The imaging parameters used for PAI are presented in **Table 8.1**.

Table 8.1 PAI Presets

Imaging Parameter	Set Value
PA Gain	52 dB
2-D Gain	27 dB
Image Width	10.36 mm
Image Depth	15.00 mm
Image Depth Offset	2.00 mm
Focus Depth	10.00 mm
Persistence	10
Correct Energy	On
Threshold Hbt	20 %

A large amount of centrifuged acoustic gel was applied on the chest and in the transducer cavity to ensure that no air bubbles were present in the imaging plane. This precaution was taken to avoid reverberation artifacts which can interfere with PA images. Special attention was also paid to keeping the heart in the imaging plane such that the anterior myocardium or interventricular septum or anterior wall LV lies within a depth of 9-11 mm where laser energy is focused. The transducer was also placed horizontally keeping the skin surface at a depth of 7.5 mm or higher to avoid any reverberation artifacts from the skin whenever possible. Manual time gain compensation (TGC) was applied to improve the signal to noise ratio at this depth setting and to compensate for the attenuation of light as its energy drops with depth in the tissue. The imaging parameters were optimized by experimenting on two mice models in the group and then saved as a preset in the scanner for the remainder of the animal models. Figure 8.1 presents a representative Oxy-Hemo PA image of the mouse heart using the above-mentioned preset. Note that our study focused only on the anterior myocardium, since most of the light energy is absorbed here leaving very little energy for posterior myocardium to generate any reasonable PA estimates which is also evident from Figure 8.1. 3-D PAI was then performed using the acquisition motor with a scanning range of 6 mm and step size of 0.16 mm resulting in 37 2-D slices/volume. Persistence (frame averaging) of 10 was also maintained during 3-D PA acquisition. Figure 8.2 illustrates a representative case of 3-D Oxy-Hemo PA image.

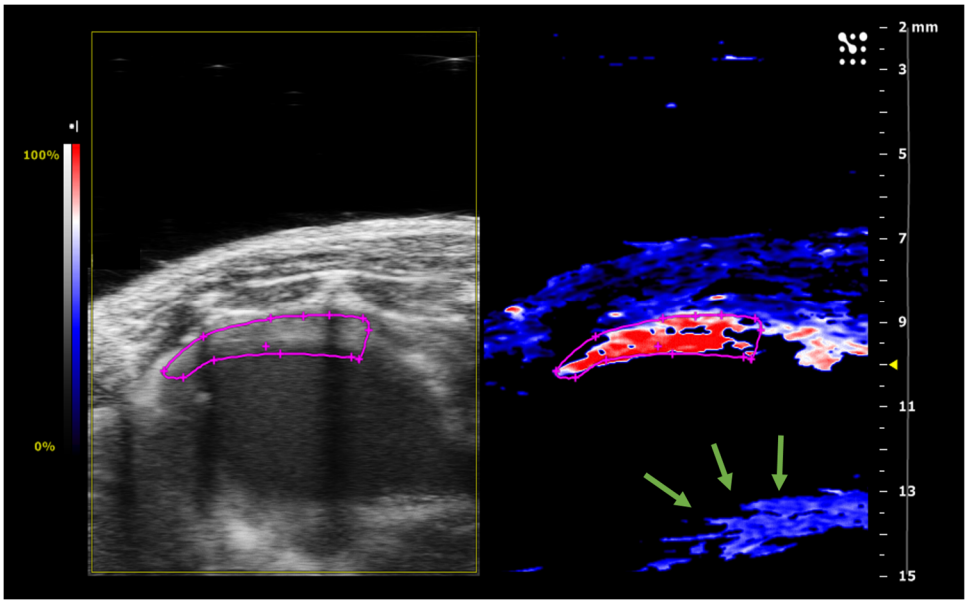

Figure 8.1 Representative Oxy-Hemo PA Image of Mice Heart at baseline (before LAD ligation). Left panel shows the ultrasound image while right panel shows the corresponding Oxy-Hemo PA image. The region outlined in pink represents the region of interest (ROI). The anterior myocardium is placed within a depth range of 9-11 mm with the skin surface at 7 mm maintained parallel to the transducer face. The reverberation artifact (indicated by green arrows) is seen at a depth of 13-14 mm caused due to the PA signal being reflected between the skin layer and transducer face. High oxygen saturation (% sO_2) (in red) is visible in the anterior myocardium within the ROI. No estimates are obtained in posterior myocardium (black region in the Oxy-Hemo Image).

HFUS was performed using two transducers - MS 550D (broadband frequency range of 22 – 55 MHz) operating at center frequency of 40 MHz and LZ 400 transducer (broadband frequency range of 18 – 38 MHz) operating at center frequency of 30 MHz. 2-D B-mode images were collected in both PLAX and short axis (PSAX) views using MS 550D while LZ 400 was used to collect only PSAX views. Image width, depth, gain and TGC were adjusted carefully to optimize image quality by maximizing the signal-to-noise ratio and adjusting for the attenuation of light with depth. A 235 Hz frame rate was maintained over all ultrasound only imaging sessions. This frame rate ensured optimal temporal resolution and captured the motion of the rapidly beating

mouse heart without distortion which is critical in performing 2-D echocardiographic measurements. Cine loops containing 1000 frames per imaging plane were stored digitally for further analysis.

3-D imaging was performed along the parasternal long axis view using the acquisition motor by translating the transducer perpendicular to the long axis imaging orientation. For all mice, scanning range of 5 mm with step size of 0.14 mm was maintained resulting in 36 2-D slices/volume.

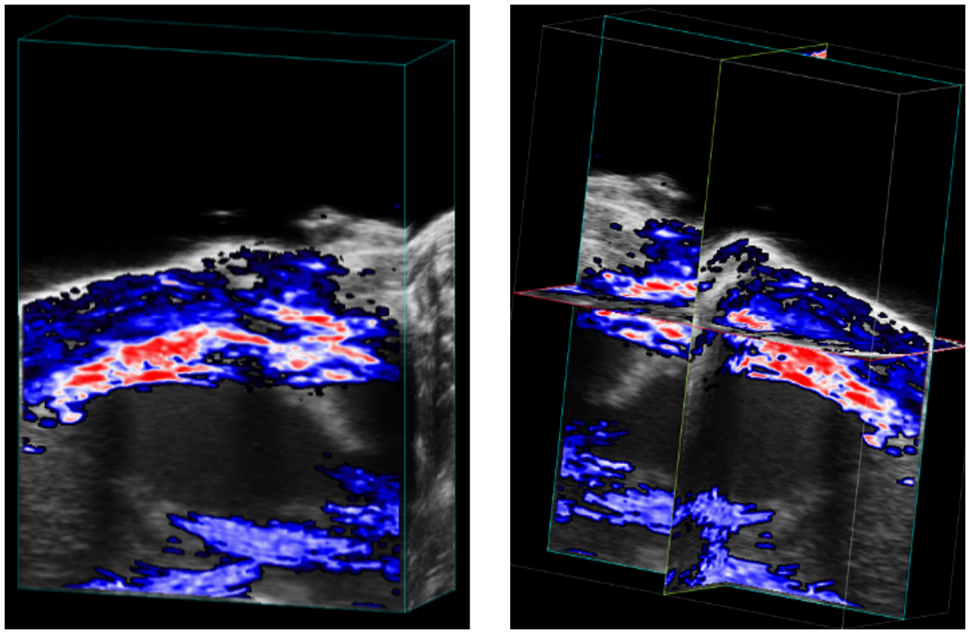

Figure 8.2 Representative 3-D Oxy-Hemo PA Image of Mice Heart at baseline (before LAD ligation). Left panel shows the cube-view representation of $sO_{2\ average}$ estimates overlaid on ultrasound images while the right panel presents an orthogonal representation of the same heart.

8.1.3 Photoacoustic (PA) Image Analysis

Quantitative analysis of Oxy-Hemo PA images were performed offline using VevoLab Software commercially available with Vevo LAZR imaging system. For each imaging session, an average of 20 frames per cine loop of Oxy-Hemo data were collected and digitally stored. Given

that frame averaging was used while acquiring OxyHemo images (average of 10 frames per wavelength), each frame represents an average of % sO_2 values throughout multiple cardiac cycles. The system is therefore not sensitive enough to detect variation of % sO_2 over one cardiac cycle. However, in this work, our main focus was to detect the general trend in the variation of % sO_2 after induction of LAD ligation which is still measurable using the frame averaging scheme. Even with persistence of 10, we experienced signal dropouts in some of the collected frames. Therefore, a single frame with reasonable amount of % sO_2 estimate was chosen for analysis. A ROI was delineated manually in the anterior myocardium based on the anatomical ultrasound images. Delineated ROI encompassed the entire myocardium and sometimes a thin portion of ventricular chamber adjacent to endocardium. Both the OxyZated™ and HemoMeaZure™ tool were utilized to quantify oxygen saturation (% sO_2) and total hemoglobin (Hbt) respectively within the ROI. The software reports two measures of oxygen saturation, namely % $sO_{2\ Average}$ and % $sO_{2\ Total}$. Values of % $sO_{2\ Total}$ calculates the average oxygen saturation in all pixels including those with a zero/void estimate within the ROI while % $sO_{2\ Average}$ calculates the average oxygen saturation within the ROI after excluding the zero/void estimates [11]. After LAD ligation we sometimes observe loss of PA signal in the ROI due to presence of a suture in the path of light transmission. This also resulted in higher numbers of zero/void estimates within ROI than for the baseline case which could introduce a small bias in the longitudinal study. To avoid this issue, % $sO_{2\ Average}$ was chosen as the measure of oxygen saturation in our study. The percent change of oxygen saturation (% $sO_{2\ Average}$) between baseline and post- LAD ligation cases were calculated using the following formula:

$$\nabla sO_2\ (\%) = \frac{sO_{2\ Post} - sO_{2\ Baseline}}{sO_{2\ Baseline}} \times 100 \tag{8.1}$$

Quantitative results from VevoLab software were exported to excel files for statistical analysis using MATLAB (The MathWorks, Inc., Natick, MA, USA).

8.1.4 Two-Dimensional Echocardiographic Measurements

Conventional echocardiographic measurements were derived from both grayscale B-mode and M-mode images acquired along the PLAX views. PLAX cardiac measurement protocol for VevoLab software was utilized for performing the measurement of left ventricular (LV) ejection fraction (% EF), fractional shortening (% FS) and stroke volume (SV μL).

EF and SV were derived from PLAX B-mode images obtained using LZ550D transducer. For performing the measurements, endocardial wall was delineated at end diastole (ED) and end systole (ES) of a cardiac cycle. Software then automatically traces out the intermediate frames and calculates the left ventricle volume at ED ($LV_{vol;d}$) and left ventricle volume at ES ($LV_{vol;s}$). Finally, EF (%) was calculated as $EF\ (\%) = \frac{LV_{vol;d} - LV_{vol;s}}{LV_{vol;d}} \times 100$ while SV (μL) was calculated as $SV\ (\mu L) = LV_{vol;d} - LV_{vol;s}$.

M-mode PLAX images were used to derive the measure of FS using LZ400 transducer. A section of the cine loop without breathing motion artifacts was chosen for analysis. LV trace tool was used to delineate the left ventricular anterior wall (LVAW) and posterior wall (LVPW). Based on the delineation, the software automatically calculates the ED diameter (LV_{EDD}) and ES diameter (LV_{ESD}). Finally, FS (%) was calculated as $FS\ (\%) = \frac{LV_{EDD} - LV_{ESD}}{LV_{EDD}} \times 100$.

These measurements provide anatomical information about the heart after induction of myocardial ischemia. Quantitative results from VevoLab software were exported to excel files for statistical analysis using MATLAB.

8.1.5 Statistical Analysis

All data are represented as mean ± standard deviation. One-way analysis of variance (ANOVA) with Tukey-Kramer post hoc test was performed for the five observation time points (Baseline, 30 minutes, 80 minutes, 120 minutes and 24 hours) to determine the statistical difference between observations. A $p < 0.05$ was considered statistically significant. Correlation obtained using linear regression and Pearson correlation coefficient (*r-value*) was reported. All statistical analysis was performed using MATLAB (Statistics and Machine Learning Toolbox Release 2017b, The MathWorks, Inc., Natick, Massachusetts, United States).

8.2 Quantification of oxygen saturation levels post LAD ligation

The main results of the reported study are visualization and quantification of alterations in oxygen saturation levels post LAD ligation using dual-wavelength PA imaging. The variation in the % $sO_{2\ Average}$ also exhibits a positive linear relationship with conventional echocardiographic measurements.

8.2.1 Detection of alterations in oxygenation level in anterior myocardium after LAD ligation

Representative PA images of myocardial ischemia are presented in Figure 8.3. Figure 8.3 (a) shows baseline PA image with very high oxygen saturation (dark red) in the anterior myocardium indicating high perfusion. Figure 8.3 (b) – (e) illustrates the oxygen saturation levels at 30 minutes, 80 minutes, 120 minutes and 24 hours after LAD ligation. Qualitative observations indicate a reduction of % sO_2 level shown in blue in the PA-US co-registered images. We also

observed a decrease in the total colored area in post-surgery cases when compared to the baseline indicating lower % sO_2 level in the anterior myocardium.

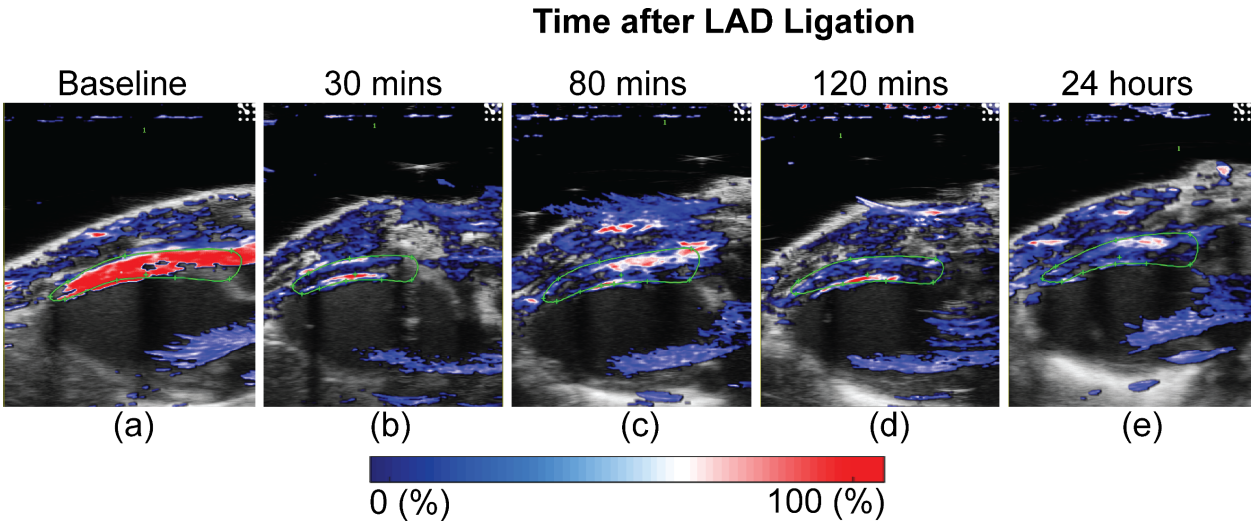

Figure 8.3 Dual-wavelength *in-vivo* PA monitoring of acute myocardial ischemia. Representative Oxy-Hemo PA images at (a) baseline, (b) 30 minutes, (c) 80 minutes, (d) 120 minutes and (e) 24 hours after LAD ligation. The heat map represents % sO_2 levels ranging from 0% (dark blue) to 100% (dark red). ROI in the anterior myocardium is shown in green. Figure (b) and (d) represents images where a thin sliver of the ventricular chamber could have been included in chosen ROI for analysis (red line right against the inside of the anterior myocardium).

To obtain statistically significant results, the experiment was repeated over seven additional mice. All mice experienced similar rapid decreases in blood oxygen saturation (% sO_2) starting at 30 minutes after LAD ligation with $p < 0.001$. One-way ANOVA with Tukey-Kramer post hoc test indicate statistical difference of blood oxygen saturation (% sO_2) at baseline compared to post ligation time points ($p < 0.001$). There was no statistically significant difference of % sO_2 level among post ligation observations compared to each other. Figure 8.4 shows the box-and-whisker plots of blood oxygen saturation (% sO_2) at five time points of observation. The plot illustrates that % sO_2 level at 30, 80, 120 minutes and 24 hours are close to each other and

lower than baseline % sO_2 level. One outlier is observed at 120 minute's which can be attributed to the physiological variability among the mice. Highest variability is observed at 24 hours which might be caused by the variation in response to ischemia among mice. Even then, the oxygenation level after 24 hours remained significantly lower than the baseline ($p < 0.001$) showing the effect of permanent ligation on anterior myocardium of LV. In general, LAD ligation was associated with significant decrease ($p < 0.001$) in blood oxygen saturation (% sO_2) post-LAD ligation (30 min: 33.05% ± 6.80; 80 min: 36.59% ± 5.22; 120 min: 36.70% ± 9.46; 24 h: 40.55% ± 13.04) when compared to baseline (87.83% ± 5.73). This reduction of oxygenation level is a clear suggestion of ischemia revealing the sensitivity of PAI for real time monitoring.

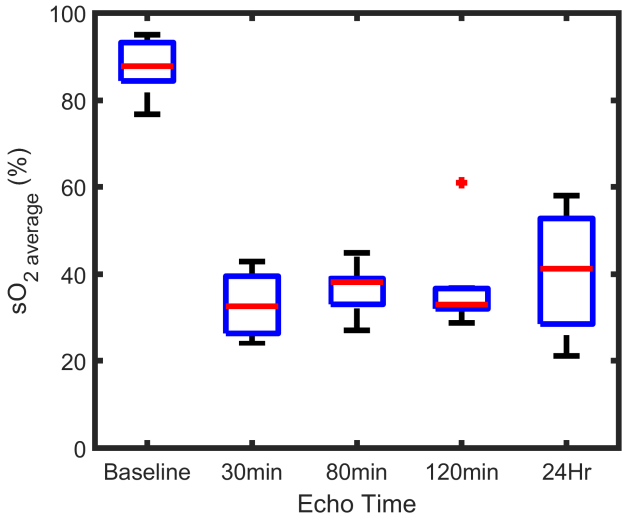

Figure 8.4 Variation in blood oxygen saturation levels (% sO_2) over time. Box-and-whisker plots of blood oxygen saturation (% sO_2) at five time points of observation (at baseline, 30 minutes, 80 minutes, 120 minutes and 24 hours). Box-and-whisker plot present min and max values (whiskers), and the 25th and 75th percentile (box), finite outlier (red plus) and median % sO_2 level. The trend indicates rapid fall from baseline to 30 minutes with a 62.97% reduction.

8.2.2 Relationship between variation of % $sO_{2\ Average}$ and echocardiographic measurements

To obtain a relationship between cardiac perfusion and cardiac structural changes, *PA in vivo* oxygen saturation measurements were correlated with % EF, % FS and SV μL derived from 2-D echocardiographic measurements. It has been reported previously that myocardial infarction in mice models were associated with declines in EF, FS and SV with time after ligation [12-16]. Our results corroborate these previous reports revealing declines in % EF, % FS and SV μL over time. **Table 8.2** summarizes results obtained from echocardiographic measurements. Statistically significant difference was observed in post-ligation cases compared to baseline ($p<0.001$).

Table 8.2 Conventional echocardiographic measurements over monitoring period

Measurement	Baseline	30 min	80 min	120 min	24 Hours	$p <$
% EF	48.05±6.47	26.04±11.16	28.76±9.45	23.95±8.88	28.15±14.92	0.001
% FS	29.05±4.98	15.65±7.39	14.53±6.55	13.24±6.91	16.95±10.55	0.001
SV (μL)	33.73±6.81	15.99±5.92	19.79±5.05	17.52±7.18	19.12±8.04	0.001

Correlation analysis of % sO_2 was performed with EF, FS and SV to understand the relationship between functional and perfusion changes associated with myocardial ischemia. Our analysis reveals a positive linear ($p <0.001$) relationship of blood oxygen saturation with each of the conventional echocardiographic measurements as shown in Figure 8.5. In Table 8.3, we present the Pearson correlation coefficient (r) along with the corresponding p-values for blood oxygen saturation with EF, FS and SV respectively for all mice.

Table 8.3 Correlation of blood oxygen saturation with EF, FS and SV.

Parameters	**Baseline – Day 1**	
	r value	***p value*** <
Ejection Fraction (%)	0.66	0.001
Fractional Shortening (%)	0.67	0.001
Stroke Volume (µL)	0.77	0.001

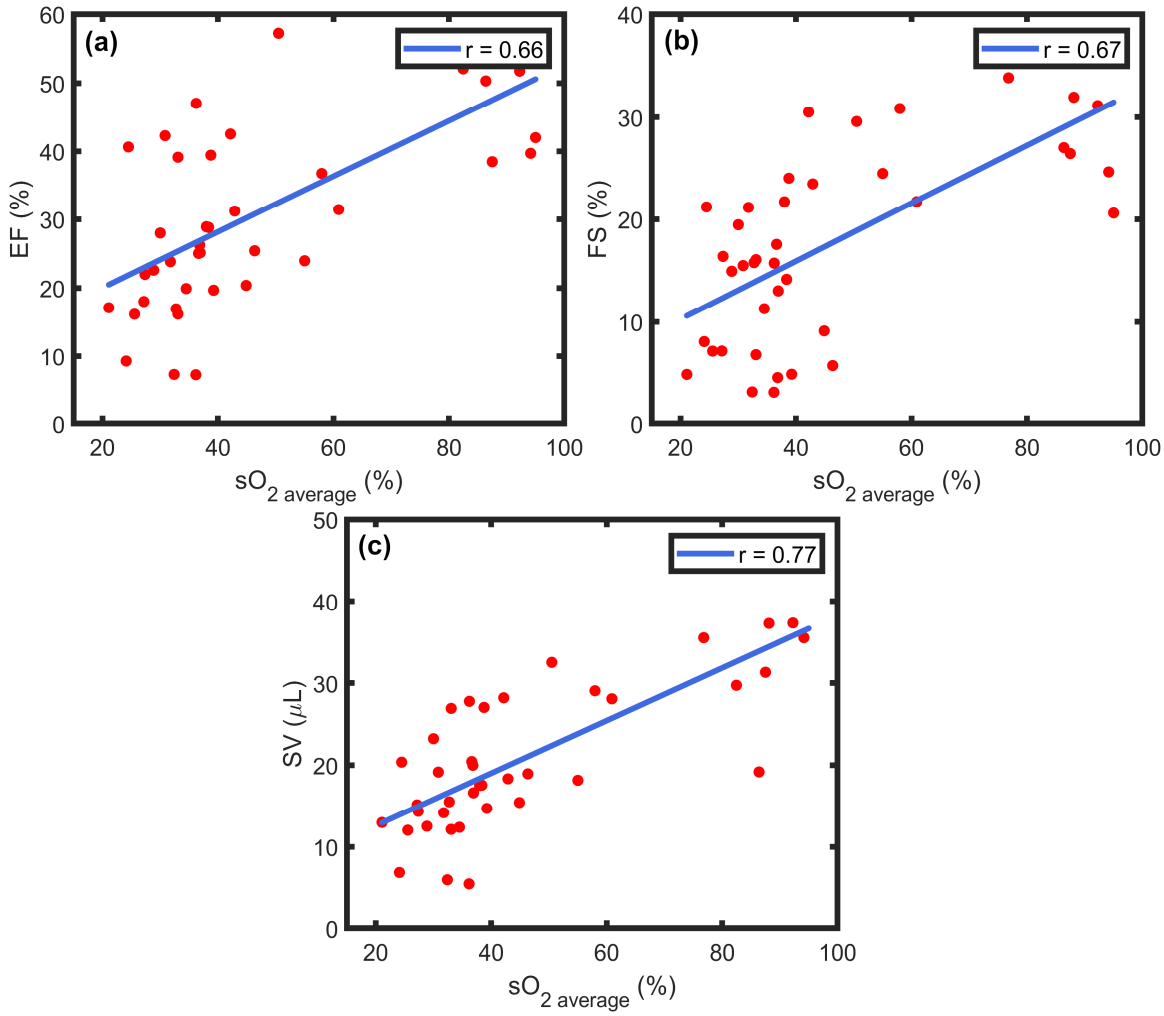

Figure 8.5 Linear regression of blood oxygenation, % sO_2 against parameters from 2-D echocardiography measurements. Positive correlation of blood oxygenation (% sO_2) with (a) Ejection Fraction (*r=0.66*), (b) Fractional Shortening (*r=0.67*) and (c) Stroke Volume *(r=0.77*) was found. All relationships have a *p value* less than 0.001.

8.3 Discussion of utility of a Commercial dual-wavelength system for % sO_2 mapping

Our results indicate that cardiac dysfunction associated with myocardial ischemia in a murine model can be detected using PAI. In Figure 4, we show that blood oxygen saturation decreases over time when compared to baseline measurements ($p < 0.001$). We consider this alteration of % sO_2 being indicative of myocardial ischemia. PAI contrast is "absorption-based" because the PA signal can be considered to be proportional to optical absorption properties of tissue [3]. In dual-wavelength PAI, the absorption spectral difference between oxyhemoglobin (HbO_2) and deoxyhemoglobin (HHb) is utilized to generate estimates of relative blood oxygen saturation, % sO_2. In particular, equation (2) is utilized in the Vevo 2100 LAZR imaging system to estimate blood oxygen saturation of blood [4].

$$sO_2 = \frac{[HbO_2]}{[HbO_2 + HHb]} = \frac{A_{\lambda 2}\varepsilon_{HHb}^{\lambda 1} - A_{\lambda 1}\varepsilon_{HHb}^{\lambda 2}}{A_{\lambda 1}\Delta\varepsilon_{HHb}^{\lambda 2} - A_{\lambda 2}\Delta\varepsilon_{HHb}^{\lambda 1}} \tag{8.2}$$

Where [HbO_2] and [HHb] are the molar concentrations of oxyhemoglobin and deoxyhemoglobin respectively, A_λ is the PA signal intensity at wavelength λ, ε_{HHb} and ε_{HbO_2} are molar extinction coefficient of deoxyhemoglobin and oxyhemoglobin respectively, $\Delta\varepsilon_{HHB} = \varepsilon_{HBO_2} - \varepsilon_{HHB}$. In cardiac muscle, PAI contrast can be attributed to oxygenated hemoglobin present in blood perfused into the anterior myocardium. At baseline, the continuous flow of arterial blood contributed to the PAI contrast with high oxygen saturation values in the PA image. In our experimental setup, a permanent LAD ligation was performed to restrict the flow of arterial blood into the myocardium. We then observed a significant decline in % sO_2 from baseline measurements after ligation at the 30 minutes time step. The decline in % sO_2 can be caused either by a decrease in arterial blood with rich oxygenation affecting the [HbO_2] term or by possible pooling of venous blood affecting

the [*HHb*] term in equation (2). In the current setup, it is difficult to state with specificity the exact contributing factor to the % sO_2 decline. We hypothesize that the major contributor is reduced arterial blood flow as LAD ligation was performed in these mice.

In this study, we present observations from baseline to 24 hours post-LAD ligation to image changes in perfusion of the heart at possible initial stages of myocardial infarction. Acute ischemic insult of heart shortly following the beginning of MI is well reported in literature [17-19]. Our results indicate that PAI can track a rapid fall in the oxygenation due to LAD ligation which could lead to an MI. The accuracy of measuring real tissue oxygen saturation has been previously reported in phantom studies [20, 21]. These studies support the use of PAI for detection of oxygen saturation changes associated with acute myocardial ischemia with LAD ligation. At 30 minutes post ligation, a 62.37% decrease in % sO_2 was observed when compared to baseline measurements. This preliminary study provides us with possible future directions to assess chronic changes associated with MI using PAI.

A persistence of 10 (frame averaging) was utilized to generate reasonable % sO_2 estimates as the estimation of % sO_2 using multi-wavelength imaging is very prone to system noise. This persistence setting generates the % sO_2 estimate in one frame by taking average of 10 frames per wavelength (in this case 750 nm and 850 nm). Thus, each acquired frame represents an average of % sO_2 values throughout multiple cardiac cycles. This results in reduced sensitivity in detecting subtle variation of % sO_2 over a single cardiac cycle and limits us to detect less severe ischemic events. However, in this work, our main focus was to detect the general trend in the variation of % sO_2 after induction of permanent LAD ligation which is still measurable using the frame averaging scheme. One possible solution is to have an ECG gated method for acquiring PA images.

This would greatly improve accuracy and precision of the measurements and potentially make this much more sensitive to assessing less severe ischemic events.

Change of % EF, % FS and SV (μL) are indicative of left ventricular dysfunction after MI. We have shown statistically significant positive linear correlation ($p < 0.001$) of tissue oxygenation with EF, FS and SV in this study. This linear relationship substantiates our claim that dual-wavelength PAI has potential to be a real-time monitoring tool for myocardial ischemia. While performing PAI, we were cautious to ensure that no bubbles are present in the images to avoid bubble related artifacts. Presence of bubbles causes unreliable tissue oxygenation estimates and in some case may corrupt information inside the ROI where analysis is performed. We recommend application of large amount of centrifuged gel to overcome these artifacts. Another key challenge in PAI imaging are reverberation artifacts appearing at a depth twice that of the skin surface. General recommendation is to use higher standoff to push the artifact out of the field of view. In our work, the skin surface was placed at depth of around 7.5 mm to avoid reverberation artifacts. Even after using clear sutures in our study, we sometimes observe a significant loss of PA signal. Although light propagated though the suture without interference, we suspect that the suture was blocking the light induced ultrasound signal. Therefore, care should be taken to avoid possible suture locations while imaging the myocardium which can be quite challenging.

Limitations with use of PAI for studying myocardial dynamics include the following; First, the VisualSonics system performs Oxy-Hemo imaging with a frame rate of 5 Hz resulting in lower temporal resolution when compared to conventional echocardiography. Thus, it may not be possible to accurately time-register PA signals with ECG events in the heart. Secondly, in our study we focused on the anterior myocardium as most of light energy is absorbed in this region.

This imposed a fundamental limit on the penetration depth achievable using PAI. Resolving these issues will further enhance the potential of PAI for routine cardiovascular assessment.

List of References

[1] M. Xu and L. V. Wang, "Photoacoustic imaging in biomedicine," *Review of scientific instruments,* vol. 77, p. 041101, 2006.

[2] L. V. Wang and S. Hu, "Photoacoustic tomography: in vivo imaging from organelles to organs," *Science,* vol. 335, pp. 1458-1462, 2012.

[3] P. Beard, "Biomedical photoacoustic imaging," *Interface focus,* p. rsfs20110028, 2011.

[4] A. Needles, A. Heinmiller, J. Sun, C. Theodoropoulos, D. Bates, D. Hirson*, et al.*, "Development and initial application of a fully integrated photoacoustic micro-ultrasound system," *IEEE transactions on ultrasonics, ferroelectrics, and frequency control,* vol. 60, pp. 888-897, 2013.

[5] R. Zemp, L. Song, R. Bitton, K. Shung, and L. Wang, "Realtime photoacoustic microscopy of murine cardiovascular dynamics," *Optics express,* vol. 16, pp. 18551-18556, 2008.

[6] Z. Li, H. Li, H. Chen, and W. Xie, "In vivo determination of acute myocardial ischemia based on photoacoustic imaging with a focused transducer," *Journal of biomedical optics,* vol. 16, pp. 076011-076011-6, 2011.

[7] D. Kumar, T. A. Hacker, J. Buck, L. F. Whitesell, E. H. Kaji, P. S. Douglas*, et al.*, "Distinct mouse coronary anatomy and myocardial infarction consequent to ligation," *Coronary artery disease,* vol. 16, pp. 41-44, 2005.

[8] D. K. Singla, T. A. Hacker, L. Ma, P. S. Douglas, R. Sullivan, G. E. Lyons*, et al.*, "Transplantation of embryonic stem cells into the infarcted mouse heart: formation of multiple cell types," *Journal of molecular and cellular cardiology,* vol. 40, pp. 195-200, 2006.

[9] J. Laufer, C. Elwell, D. Delpy, and P. Beard, "In vitro measurements of absolute blood oxygen saturation using pulsed near-infrared photoacoustic spectroscopy: accuracy and resolution," *Physics in Medicine & Biology,* vol. 50, p. 4409, 2005.

[10] X. Wang, X. Xie, G. Ku, L. V. Wang, and G. Stoica, "Noninvasive imaging of hemoglobin concentration and oxygenation in the rat brain using high-resolution photoacoustic tomography," *Journal of biomedical optics,* vol. 11, p. 024015, 2006.

[11] L. J. Rich and M. Seshadri, "Photoacoustic monitoring of tumor and normal tissue response to radiation," *Scientific reports,* vol. 6, p. 21237, 2016.

[12] S. Kanno, D. L. Lerner, R. B. Schuessler, T. Betsuyaku, K. A. Yamada, J. E. Saffitz*, et al.*, "Echocardiographic evaluation of ventricular remodeling in a mouse model of myocardial infarction," *Journal of the american society of echocardiography,* vol. 15, pp. 601-609, 2002.

[13] M. Bauer, S. Cheng, M. Jain, S. Ngoy, C. Theodoropoulos, A. Trujillo*, et al.*, "Echocardiographic Speckle-Tracking Based Strain Imaging for Rapid Cardiovascular Phenotyping in MiceNovelty and Significance," *Circulation research,* vol. 108, pp. 908-916, 2011.

[14] X.-M. Gao, A. M. Dart, E. Dewar, G. Jennings, and X.-J. Du, "Serial echocardiographic assessment of left ventricular dimensions and function after myocardial infarction in mice," *Cardiovascular research,* vol. 45, pp. 330-338, 2000.

[15] F. Yang, Y.-H. Liu, X.-P. Yang, J. Xu, A. Kapke, and O. A. Carretero, "Myocardial infarction and cardiac remodelling in mice," *Experimental Physiology,* vol. 87, pp. 547-555, 2002.

[16] R. D. Patten, M. J. Aronovitz, L. Deras-Mejia, N. G. Pandian, G. G. Hanak, J. J. Smith*, et al.*, "Ventricular remodeling in a mouse model of myocardial infarction," *American Journal of Physiology-Heart and Circulatory Physiology,* vol. 274, pp. H1812-H1820, 1998.

[17] M. A. Pfeffer, J. M. Pfeffer, M. C. Fishbein, P. J. Fletcher, J. Spadaro, R. A. Kloner*, et al.*, "Myocardial infarct size and ventricular function in rats," *Circulation research,* vol. 44, pp. 503-512, 1979.

[18] H. Swan, J. S. Forrester, G. Diamond, K. Chatterjee, and W. W. Parmley, "Hemodynamic spectrum of myocardial infarction and cardiogenic shock," *Circulation,* vol. 45, pp. 1097-1110, 1972.

[19] K. T. Weber, J. S. Janicki, R. O. Russell, C. E. Rackley, H. Swan, L. Resnekov*, et al.*, "Identification of high risk subsets of acute myocardial infarction: derived from the

myocardial infarction research units cooperative study data bank," *The American journal of cardiology,* vol. 41, pp. 197-203, 1978.

[20] L. J. Rich and M. Seshadri, "Photoacoustic imaging of vascular hemodynamics: validation with blood oxygenation level–dependent MR imaging," *Radiology,* vol. 275, pp. 110-118, 2014.

[21] L. M. Yamaleyeva, Y. Sun, T. Bledsoe, A. Hoke, S. B. Gurley, and K. B. Brosnihan, "Photoacoustic imaging for in vivo quantification of placental oxygenation in mice," *The FASEB Journal,* vol. 31, pp. 5520-5529, 2017.

Chapter 9

Spatiotemporal Coherence Weighting for Photoacoustic Image Beamforming

This chapter focuses on the use of a high frequency linear array photoacoustic (PA) imaging system to assess myocardial health in a murine model. We are interested in deriving blood-dominated cardiac pathological information in myocardial wall to complement functional information derived from ultrasound (US) imaging. However, when a rapidly moving murine heart is imaged with photoacoustic imaging (PAI), reliable localization of PA signal from the myocardial wall becomes challenging due to signals picked up by the wide-band high frequency transducer from surrounding muscle and blood circulating inside left ventricular (LV) chamber. Consequently, reconstructed PA images with conventional delay-and-sum (DAS) beamforming have temporally varying noise which causes reduced myocardial PA signal specificity thus making image interpretation difficult. In this chapter[7], we address noise suppression utilizing signal processing of received raw channel photoacoustic radiofrequency (PA-RF) data. We demonstrate that dominant PA signals from the myocardial wall can be differentiated from background noise signals utilizing spatiotemporal coherence in the aperture domain. We propose to use both spatial and temporal information in the aperture domain during beamforming to calculate a coherence factor (CF) termed spatiotemporal coherence factor (STCF) to weight DAS and MV beamformed PA images. Under low SNR, the benefit of using temporal information across a transmit pulse

[7] Rashid Al Mukaddim, and Tomy Varghese, "Spatiotemporal Coherence Weighting for *in vivo* Cardiac Photoacoustic Image Beamformation." *IEEE Transactions on Ultrasonics, Ferroelectrics, and Frequency Control*, vol. 68, no. 3, pp. 586 – 598 (2021) PMCID: PMC8011040

length for CF-type methods has been previously demonstrated for US imaging [1]. Here, assuming dominant PA signals are sustained over adjacent time frames after laser irradiation, temporal information is added to STCF for improved suppression of linear array PAI noise artifacts.

Three main contributions are reported in this chapter. First, STCF is proposed and extensive simulation studies by varying inherent contrast between dominant absorbers and backgrounds, acoustic absorption levels, non-uniform optical fluence distribution and channel SNR is presented. Second, *in vivo* feasibility is demonstrated by using the proposed method to reconstruct PA M-mode image for ECG and respiratory signal gated murine cardiac imaging without temporal averaging. Third, the use of coherence based beamformers (CF and STCF) for single wavelength cardiac PAI is compared against conventional [DAS and minimum variance (MV)] methods in an objective manner.

9.1 Conventional and Proposed Beamforming Approaches for PAI Reconstruction

9.1.1 Delay-and-sum and Coherence Factor Beamforming

Consider a linear array with *M* equally spaced transducer elements that receive PA signals at time *t*. DAS beamforming can be used to reconstruct the PA image from the detected signals using the following equation:

$$y_{DAS}(t) = \sum_{m=1}^{M} w_m(t) \times x_m(t - \tau_m) = W(t)^H X(t) \tag{9.1}$$

In equation (9.1), $y_{DAS}(t)$ is the beamformed image, $w_m(t)$ is the aperture weight for an element m, $x_m(t)$ is the received signal by m^{th} element, τ_m is the time delay applied to element m to focus at a specific point in the image, $W(t)$ and $X(t)$ are *M-element* vectors containing the aperture weights and the time delayed versions of the detected signals respectively, and $(\bullet)^H$ denotes a

conjugate transpose operation. For DAS, *W(t)* is a vector of ones. DAS with uniform aperture weighting, however, suffers from reduced off axis interference signal rejection thus degrading image quality [2].

Improved off-axis signal rejection can be achieved with MV beamforming [2-4], that adaptively calculates aperture weights to maximize the signal-to-interference-plus-noise ratio [3]. Optimal MV aperture weights, $W_{MV}(t)$ are given by:

$$W_{MV}(t) = \frac{R(t)^{-1}a}{a^H R(t)^{-1}a} \tag{9.2}$$

where *R(t)* is the covariance matrix expressed as $R(t) = E\left[X(t)X(t)^H\right]$ and *a* is the steering vector. Before calculating minimum variance optimal weights, received PA signals are pre-steered with appropriate delays to implement dynamic receive focusing. Thus, the steering vector become an array of ones [5]. To achieve good estimation of the covariance matrix, sub-array averaging has been proposed [3]. Sub-array averaged estimated covariance matrix is given by:

$$R_{SA}(t) = \frac{1}{M-S+1}\sum_{s=1}^{M-S+1} X_s(t)X_s(t)^H \tag{9.3}$$

where *S* is the number of subarray elements and $X_s(t)$ is the subarray signal vector. Finally, output of MV beamformer is:

$$y_{MV}(t) = \frac{1}{M-S+1}\sum_{s=1}^{M-S+1} W_{MV-SA}(t)^H X_s(t) \tag{9.4}$$

To achieve additional contrast enhancement and sidelobe reduction for both DAS and MV beamformed images, CF weighting has been proposed [2, 3, 6, 7]. CF adaptively considers aperture

signal coherence by calculating the ratio of coherent and incoherent sums of detected PA signals [3]. CF is defined as:

$$CF(t) = \frac{\left|\sum_{m=1}^{M} x_m(t-\tau_m)\right|^2}{M\sum_{m=1}^{M}\left|x_m(t-\tau_m)\right|^2} \tag{9.5}$$

DAS and MV beamformers with CF weighting (DAS-CF and MV-CF) are given by:

$$y_{DAS-CF}(t) = CF(t) \times y_{DAS}(t) \tag{9.6}$$

$$y_{MV-CF}(t) = CF(t) \times y_{MV}(t) \tag{9.7}$$

9.1.2 Spatiotemporal Coherence Factor (STCF) Weighting

Conventional CF weighting considers the spatial spectrum of aperture data for a single frame. In this chapter, we extend CF to the temporal domain by considering multiple adjacent image acquisitions for beamforming. To perform beamforming with STCF, we consider of set of K (odd) adjacent PAI frames with $\left(K - 1/2 + 1\right)^{th}$ frame being the frame of interest, K_c. DAS and MV beamformed images are produced using equation (1) and (4) for frame, K_c. To calculate STCF, we consider a 2-D spatiotemporal matrix, $X_{MK}(t,k)$ with dimensions $M \times K$. Each column of $X_{MK}(t,k)$ contains an *M-element* array of time-delayed received PA signal for the k^{th} frame. Thus, $X_{MK}(t,k)$ has the following form:

$$X_{MK}(t,k)=\begin{bmatrix} x_1\left(t-\tau_1,-\frac{K-1}{2}\right) & . & . & x_1\left(t-\tau_1,\frac{K-1}{2}\right) \\ . & & . & . \\ . & & . & . \\ x_M\left(t-\tau_M,-\frac{K-1}{2}\right) & . & . & x_M\left(t-\tau_M,\frac{K-1}{2}\right) \end{bmatrix}$$

Using $X_{MK}(t,k)$, STCF is calculated by following equation:

$$STCF(t,K_c)=\frac{\left|\sum_{k=-\frac{K-1}{2}}^{\frac{K-1}{2}}\sum_{m=1}^{M}x_m(t-\tau_m,k)\right|^2}{K\times M\times\sum_{k=-\frac{K-1}{2}}^{\frac{K-1}{2}}\sum_{m=1}^{M}\left|x_m(t-\tau_m,k)\right|^2} \tag{9.8}$$

Finally, STCF weighting is incorporated into DAS and MV beamformers (DAS-STCF and MV-STCF) using:

$$y_{DAS-STCF}(t,K_c)=STCF(t,K_c)\times y_{DAS}(t) \tag{9.9}$$

$$y_{MV-STCF}(t,K_c)=STCF(t,K_c)\times y_{MV}(t) \tag{9.10}$$

9.2 Simulation and *in vivo* Validation Studies and Quantitative Analysis

9.2.1 Numerical Simulation Studies

k-Wave Matlab toolbox was used to perform all numerical simulation experiments reported in the paper [8]. Numerical phantoms were designed by placing four 0.1 mm radius spherical absorbers as point targets in a scattering background simulated by randomly distributing 10,000 independent 0.1 mm scatterers. Scattering background was simulated assuming that *in vivo* tissue comprises of both optical absorbers (hemoglobin, lipid or water) and scatterers (fibrous tissue,

collagen) [9]. Point targets were positioned along the vertical axis separated by 4 mm with the first point target located 8 mm from the transducer surface. A linear array with 128 elements, 72 μm element width, 18 μm kerf and 84 MHz sampling frequency operating at 21 MHz central frequency and 55% fractional bandwidth was utilized as the sensor in k-Wave to detect PA signals. These parameters modeled a commercial PA LZ 250 transducer (FUJIFILM VisualSonics, Inc., Toronto, Canada) [10, 11]. The speed of sound was assumed to be 1540 m/s. Imaging field of view (FOV) was 25 × 11.5 mm^2. k-Wave computational grid with a node spacing of 15 μm covered the entire FOV. For statistical analysis, all simulations were repeated using 30 independent realizations.

9.2.1.1 Simulating Inherent Tissue Contrast

Optical absorbers are expected to have higher PAI contrast compared to scattering from background tissue. Furthermore, absorption induced contrast is dependent on the concentration of chromophores present in tissue [12]. To simulate this contrast, we varied initial pressure distribution, $p_0(r)$ of point targets relative to the maximum initial pressure amplitude of the background. Background initial pressure amplitudes were sampled from a zero mean normal distribution. Lower and higher inherent contrasts were simulated by setting point targets, $p_0(r)$ to be 6 and 10 times the maximum initial pressure amplitude of the background respectively. These initial pressure distributions were input to the k-Wave toolbox [8] to solve for acoustic wave propagation within a 2-D loss-less homogenous propagation medium governed by:

$$\frac{\partial \mathbf{u}}{\partial t} = -\frac{1}{\rho_0}\nabla p, \frac{\partial \rho}{\partial t} = -\rho_0 \nabla \cdot \mathbf{u}, p = c^2 \rho \tag{9.11}$$

where, $\mathbf{u}$ is the acoustic particle velocity, ρ_0 and ρ denote ambient and acoustic density, c is the speed of sound and p is the acoustic pressure. Temporally varying noise backgrounds were produced by generating 30 independent background scattering distributions ($n = 30$).

9.2.1.2 Simulating Acoustic Absorption

The effect of acoustic absorption on beamforming performance was investigated by simulating different power law absorption exponent values [8]. The attenuation coefficient was set to $\alpha_0 = 0.3$ dB MHz^{-y} cm^{-1} [13] where y is the power law exponent. $p_0(r)$ of point targets were set to 10 times maximum initial pressure amplitude of the background and k-Wave was used to generate acoustic RF data.

9.2.1.3 Optical Fluence Distribution

Initial pressure, p_0 of an absorber located at r after absorbing optical energy can be modeled using [14]: $p_0(r) = \Gamma \times A(\lambda, r)$, where, Γ is the dimensionless Grueneisen parameter and $A(\lambda,r)$ is the absorbed energy density which is dependent on spatially variant optical fluence distribution and optical absorption co-efficient, $\mu_a(\lambda, r)$. To evaluate performance under varying optical fluence distributions, a hybrid simulation approach is adopted using MCmatlab [15] and k-Wave toolbox [8] for optical and acoustic simulations respectively. MCmatlab calculated $A(\lambda,r)$ through Monte Carlo simulation of light propagation in a 3-D voxel space using the optical simulation parameters listed in Table 9.1. Setting Γ to be 0.129 [16], point targets, $p_0(r)$ were calculated for k-Wave to generate acoustic RF signals. Finally, Gaussian random noise was added to have a channel signal-to-noise ($SNR_{channel}$) ratio of -3 dB. A schematic diagram summarizing key steps of our hybrid photoacoustic imaging simulation is presented in Figure 9.1.

9.2.1.4 Noise Corrupted Photoacoustic Channel Data

To model noise floors present in real imaging systems, zero-mean Gaussian random noise with standard deviation, σ_{noise} was added to channel data to achieve desired channel SNR, $SNR_{channel}$ in dB. Noise standard deviation is given by:

$$\sigma_{noise}(m) = \frac{S_{rms}(m)}{10^{\left(\frac{SNR_{channel}}{20}\right)}} \tag{9.12}$$

where, $S_{rms}(m)$ is the root-mean squared amplitude for the m^{th} channel.

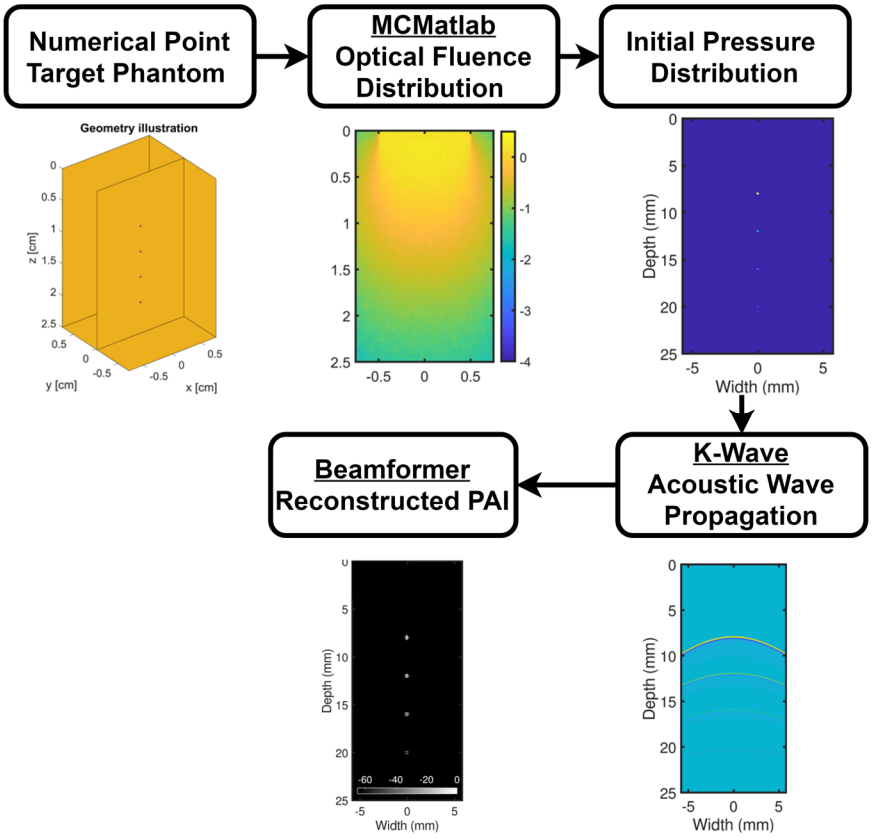

Figure 9.1 Schematic diagram with key steps of the hybrid photoacoustic imaging simulation. Optical fluence distribution estimated using MCMatlab is used to generate the initial pressure distribution

for k-Wave acoustic simulation. Finally, a beamforming algorithm is utilized to reconstruct PA images from the received channel data.

Table 9.1 Optical Simulation Parameters

Parameter	Value	Unit
Simulation cuboid	2×1.5×1.5	cm^3
Vessel absorption (μ_a)	5.21	cm^{-1}
Vessel scattering (μ_s)	58.82	cm^{-1}
Vessel oxygen saturation	75.0	%
Background absorption (μ_a)	0.01	cm^{-1}
Background scattering (μ_s)	[10,15,112]	cm^{-1}
Optical Wavelength	850	nm
Collimated top-hat beam radius	0.5	cm

9.2.2 In vivo Murine Cardiac Photoacoustic Imaging

To demonstrate *in vivo* feasibility, cardiac PAI in parasternal long axis (PLAX) view was performed with four healthy murine models (10-12 months old BALB/CJ mouse acquired from Jackson Labs, ME, USA). All *in-vivo* procedures were approved by the Institutional Animal Care and Use Committee (IACUC) at the University of Wisconsin-Madison. Imaging was done by placing the mouse in supine position on a heated platform under 1.5% isoflurane and constant flow of oxygen. A Vevo 2100 LAZR imaging system (FUJIFILM VisualSonics, Inc., Toronto, Canada) was used for collecting PAI data. 1000 frames of pre-beamformed PA RF channel data at 850 nm wavelength were acquired using a LZ 250 transducer (256-element array) operating at a nominal frequency of 21 MHz. Four sequential laser pulses are required to cover maximum FOV for LZ 250 with 64-element parallel acquisition per pulse. This reduces the imaging frame rate to one fourth the laser repetition rate [17]. Therefore, FOV was adjusted [green rectangles in Fig. 14 (a) and 15 (a)] to limit acquisition with only 64-elements to achieve maximum possible PAI frame rate (20 Hz) on Vevo LAZR. Simultaneous ECG and respiratory signals were collected using the dedicated physiological monitoring system. A custom MATLAB script (MathWorks, Inc., Natick,

MA, USA) acquired from VisualSonics was utilized to reconstruct a single cardiac cycle of PA data by temporally rearranging collected frames using image time stamp information, along with ECG and respiratory signals. Finally, beamforming was performed on the rearranged frames to reconstruct cardiac PAI cine loops. End-diastolic (ED) and end-systolic (ES) PAI frames were selected using reconstructed PAI M-mode image.

9.2.3 Quantitative Parameters for Performance Evaluation

For simulation studies, quantitative evaluations were done by calculating the *SNR* as [4]:

$$SNR = 20 \times \log_{10} \left(\frac{Signal}{Noise} \right) \tag{9.13}$$

where, *Signal* denotes the difference between maximum and minimum signal amplitude of a 2×1 mm^2 rectangular region-of-interest (ROI) including the point target [green rectangle in Figure 9.2 (a)] and *Noise* represents the standard deviation of two noise regions [red dotted rectangles in Figure 9.2 (a)] within the original ROI. 1-D lateral curves through the center of each point target were used to calculate Full-width-at-half-maximum (FWHM) at -6 dB quantifying the lateral point spread function (PSF). FWHM was determined as the lateral distance in mm between the curve points at the peak half maximum level.

In *in vivo* cardiac PAI, optical absorbers present in muscle tissue between skin and myocardium, the myocardial wall and circulating blood in LV chamber act as initial pressure sources. In the context of myocardial ischemia detection, we are interested in differentiating PA signals that arise only from the myocardial wall [18]. Thus, a beamformer with improved contrast between myocardial wall and surrounding background structures (either muscle or LV chamber blood) is ideal. Quantitative analysis to assess *in vivo* cardiac PAI quality at ED and ES phase was

done using SNR, contrast ratio (CR) and generalized contrast ratio (gCNR) as defined below [19, 20].

$$SNR = 20 \times \log_{10}\left(\frac{m_{myo}}{\sigma_b}\right) \tag{9.14}$$

$$CR = 20 \times \log_{10}\left(\frac{m_{myo}}{m_b}\right) \tag{9.15}$$

$$gCNR = 1 - \sum_{k=0}^{N-1} \min\left\{h_{myo}(x_k), h_b(x_k)\right\} \tag{9.16}$$

In equations (9.14) and (9.15), m_{myo} and m_b denote the mean signal amplitudes within myocardial wall and background ROIs (either surrounding muscle or LV chamber blood), respectively and σ_b denote the standard deviation of signal amplitudes within the rectangular ROI placed in the gel region. Equation (9.16) is a histogram-based discrete expression [19] equivalent to the original probability density-based definition of gCNR [20] where, h_{myo} and h_b represent myocardial wall and background histograms derived with 100 bins over the signal dynamic range with bin centers denominated by k. The white, blue, black and green dotted ROIs shown in DAS images in Figure 9.14 and Figure 9.15 represent ROIs for gel noise, muscle, myocardium and LV chamber blood, respectively. All metrics were evaluated using envelope detected PA data.

9.3 Findings from Simulation and *in vivo* Validation Studies

We compare the performance of our proposed DAS-STCF and MV-STCF against DAS, DAS-CF, MV and MV-CF beamformers. A 64-element ($M = 64$) aperture was utilized to perform DAS beamforming. For the MV beamformer, we set the sub-array length, $S = 16$ and use diagonal loading with $\Delta = 1/(100 \times S)$ to estimate the covariance matrix. Diagonal loading ensures stability

of the covariance matrix [3]. For STCF, the default ensemble length was 5. Envelope detected normalized log compressed images with dynamic range of 65 dB are presented for qualitative comparison. Plots are presented as mean ± standard error computed over thirty independent simulation instances.

9.3.1 Results from Numerical Simulation Studies

9.3.1.1 Inherent Tissue Contrast

Figure 9.2 shows beamforming results for point targets positioned in a high contrast background. Figure 9.2 (a) – (f) show the output of DAS, DAS-CF, DAS-STCF, MV, MV-CF and MV-STCF, respectively. Visually point targets can be detected in DAS and MV results but higher levels of background signals were seen. CF shows improvement in background signal rejection compared to only DAS and MV beamformers. Figure 9.2 (c) and (f) show that STCF provides significant noise reduction with the best quality reconstructed images. Figure 9.3 (a) – (b) present lateral PSF results from low contrast background at depths of 8 and 20 mm, respectively. Figure 9.3 (c) – (d) show PSF results from high contrast background at depths of 8 and 20 mm, respectively. Table 9.2 summarizes the -6 dB FWHM values for both low and high contrast background simulation. With STCF weighting, -6 dB FWHM values were same as CF but sidelobe levels were comparatively lower.

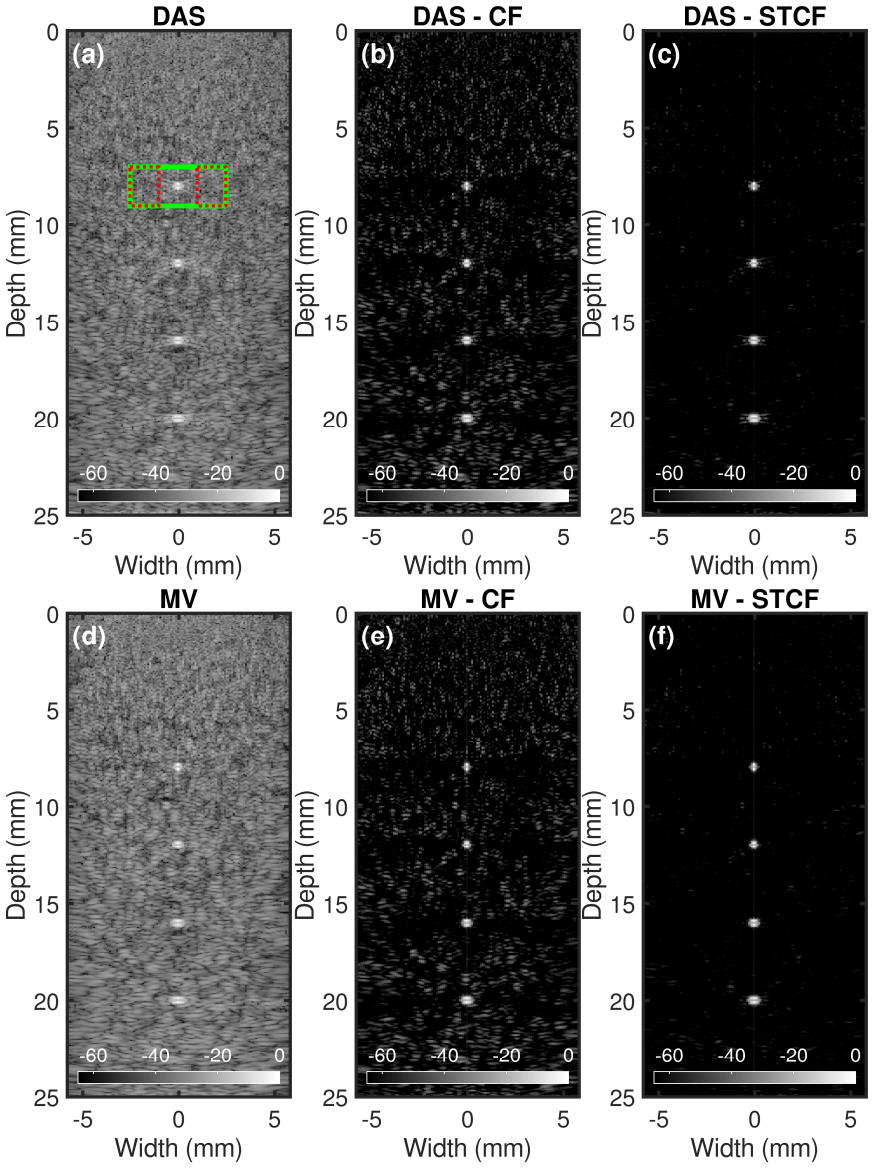

Figure 9.2 Beamformed images of simulated point targets in a high contrast background. (a) DAS, (b) DAS-CF, (c) DAS-STCF, (d) MV, (e) MV-CF and (f) MV-STCF. Display dynamic range is 65 dB. Green and red (dotted) rectangles denote signal and noise ROIs, respectively. STCF weighted images had the lowest level of background signal or noise.

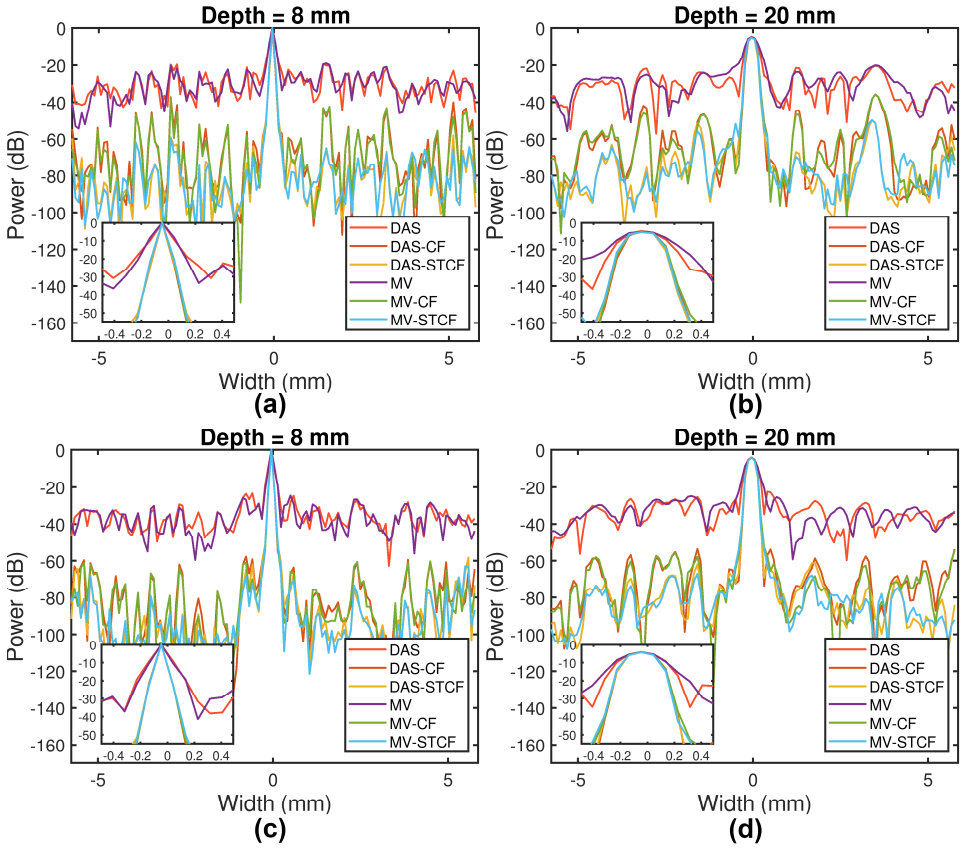

Figure 9.3 Lateral profiles of PSF of at depth of (a) 8 mm and (b) 20 mm for low contrast, (c) 8 mm and (d) 20 mm for high contrast background. Profiles around center of the point targets are zoomed in and displayed in the insets. Both CF and STCF weighting had similar FWHM values with improvement over DAS and MV beamformer alone.

Table 9.2 -6 dB FWHM (mm) Values with Inherent Contrast Variation

	Depth = 8 mm		Depth = 20 mm	
Methods	**Low**	**High**	**Low**	**High**
DAS	0.14	0.14	0.37	0.37
DAS-CF	0.10	0.10	0.28	0.29
DAS-STCF	0.10	0.10	0.28	0.29
MV	0.15	0.14	0.43	0.39
MV-CF	0.10	0.10	0.30	0.29
MV-STCF	0.10	0.10	0.29	0.29

Figure 9.4 (a) – (b) show results of SNR variation as a function of low and high inherent contrast of point targets at a depth of 8 and 20 mm, respectively. Significant SNR improvement with STCF is seen. For instance, consider the depth of 20 mm for low contrast case where mean SNR (dB) of DAS, DAS-CF, DAS-STCF, MV, MV-CF and MV-STCF were 29.62, 44.57, 62.39, 29.25, 44.58 and 63.06, respectively. Overall, both qualitative and quantitative results from these experiments show superior performance of beamforming with STCF.

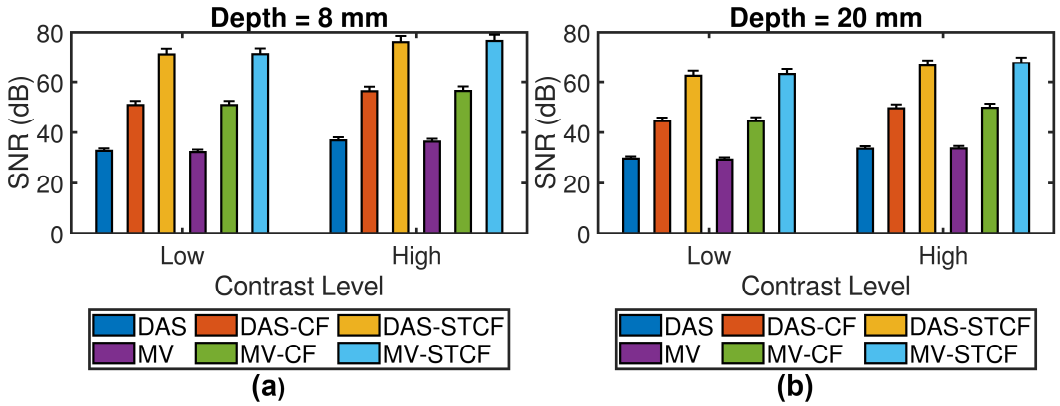

Figure 9.4 Variation of SNR for the simulated point targets with contrast variation at a depth of (a) 8 mm and (b) 20 mm, respectively. STCF weighting had higher SNR values attributed to better background signal suppression.

9.3.1.2 Acoustic Absorption

Figure 9.5 shows beamformed images of simulated point targets with power law exponent, $y = 1.5$. Figure 9.5 (a) – (f) show the output of DAS, DAS-CF, DAS-STCF, MV, MV-CF and MV-STCF, respectively. CF shows improvement in background signal rejection compared to DAS and MV beamformers. With STCF, point targets were resolved with lowest amount of background noise signal. Figure 9.6 (a) – (b) present PSF results at depths of 8 and 20 mm, respectively. STCF weighted results had comparatively lower sidelobe levels. Table 9.3 summarizes the -6 dB FWHM

values for y = 1.5. Both CF and STCF weighting had similar FWHM values with improvement over DAS and MV beamformers.

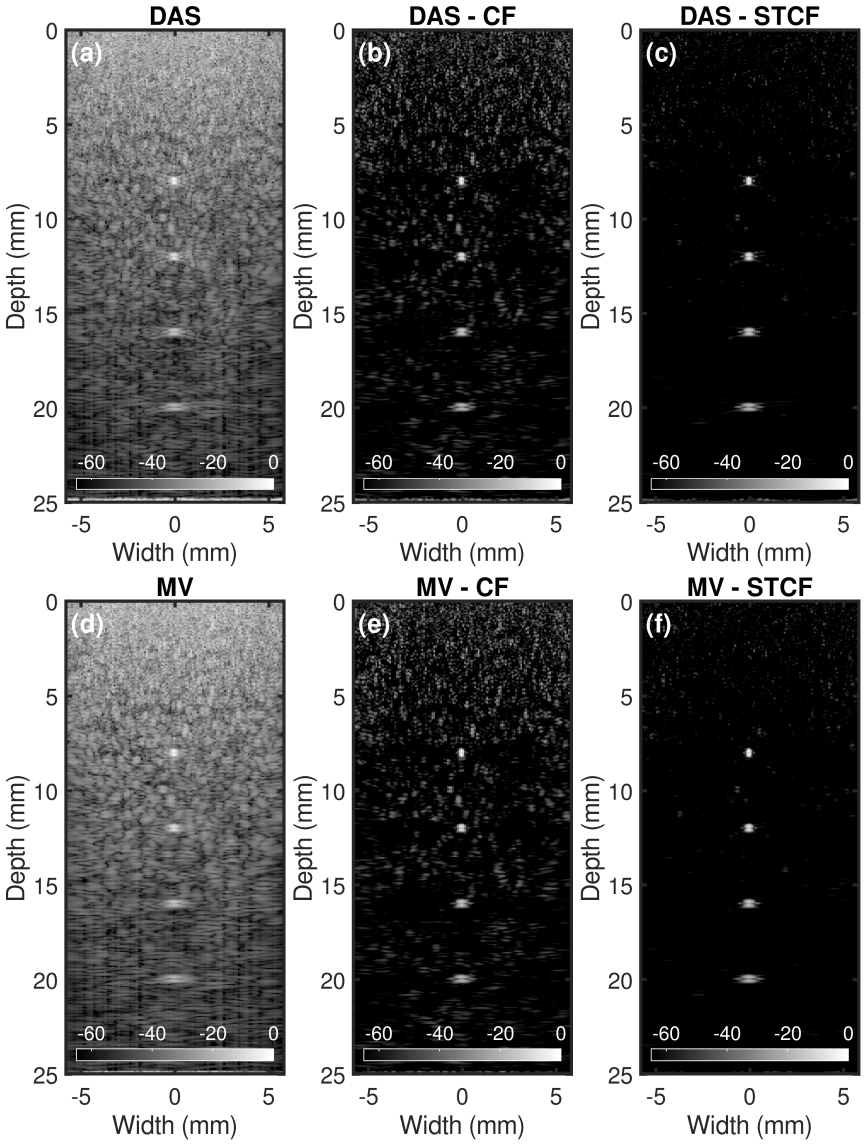

Figure 9.5 Beamformed images of simulated point targets under acoustic absorption with power law exponent, y = 1.5. (a) DAS, (b) DAS-CF, (c) DAS-STCF, (d) MV, (e) MV-CF and (f) MV-STCF. Display dynamic range is 65 dB.

Table 9.3 -6 DB FWHM (mm) values with acoustic absorption (y = 1.5)

Methods	Depth = 8 mm	Depth = 20 mm
DAS	0.23	0.65
DAS-CF	0.16	0.51
DAS-STCF	0.16	0.51
MV	0.24	0.72
MV-CF	0.16	0.52
MC-STCF	0.16	0.52

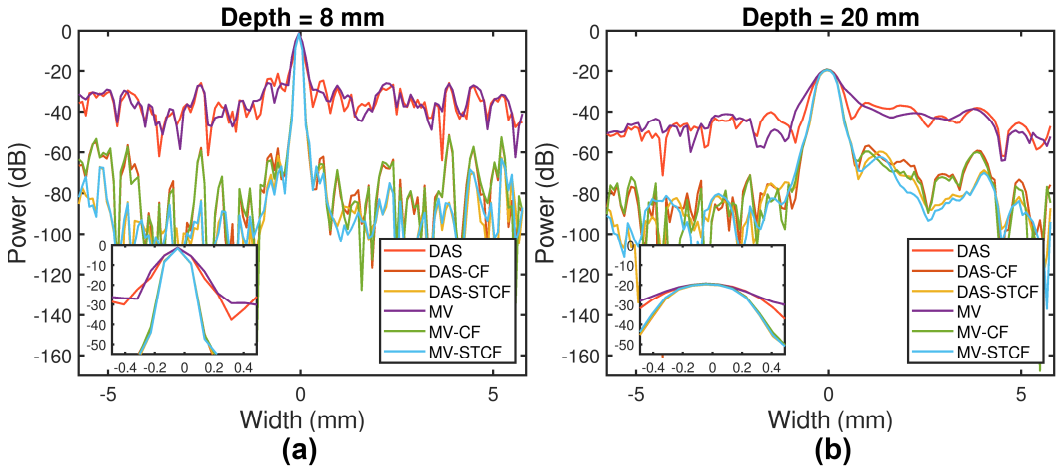

Figure 9.6 Lateral profiles of the PSF at depth of (a) 8 mm and (b) 20 mm for acoustic absorption simulation with y = 1.5. Impact of acoustic attenuation and resultant depth dependent blurring effect is apparent in 20 mm results.

Figure 9.7 (a) – (b) show the variation of SNR as a function of y at a depth of 8 mm and 20 mm, respectively. Beamforming with STCF resulted in higher SNR values compared to other methods. At a depth of 20 mm and y = 1.5, mean SNR (dB) of DAS, DAS-CF, DAS-STCF, MV, MV-CF and MV-STCF were 29.89, 42.09, 55.08, 29.92, 42.41 and 57.70, respectively. At very high attenuation (y=2), STCF and CF had similar performance in terms of SNR.

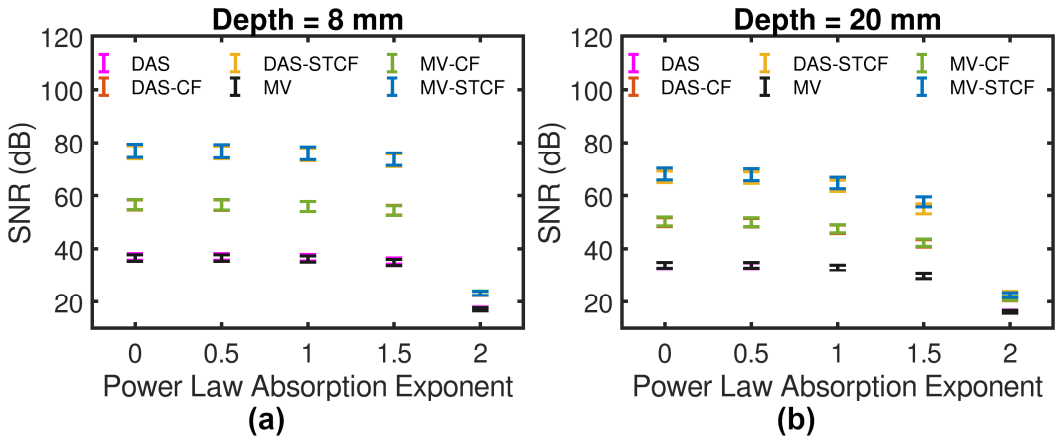

Figure 9.7 Variation of SNR with power law absorption exponent at a depth of (a) 8 mm and (b) 20 mm, respectively.

9.3.1.3 Optical Fluence Distribution

Figure 9.8 shows beamforming results for point targets positioned in a background with optical scattering, μ_s value of 15 cm^{-1}. Figure 9.8 (a) – (f) show the output of DAS, DAS-CF, DAS-STCF, MV, MV-CF and MV-STCF. respectively. Point targets beyond 15 mm were not discernable with DAS and MV. Use of CF reduced background noise but significant improvement in noise rejection with better target detectability was achieved with STCF. Peak amplitudes of the point targets were attenuated over depth.

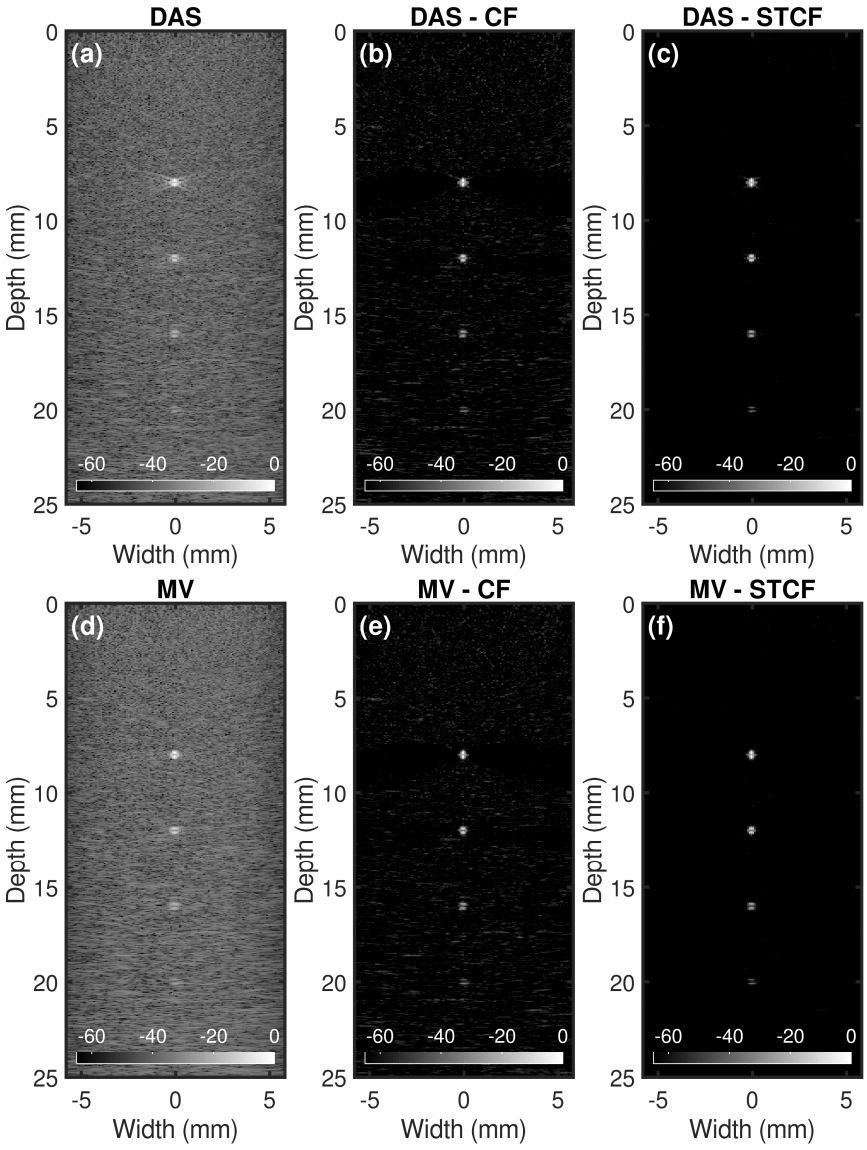

Figure 9.8 Beamformed images of simulated point targets under optical absorption and scattering (μ_s = 15 cm^{-1}). (a) DAS, (b) DAS-CF, (c) DAS-STCF, (d) MV, (e) MV-CF and (f) MV-STCF. Display dynamic range is 65 dB.

Figure 9.9 (a) – (b) show variation of SNR as a function of μ_s at depths of 8 mm and 20 mm, respectively. Beamforming with STCF resulted in higher SNR values compared to other methods. At a depth of 20 mm and μ_s = 15 cm^{-1}, mean SNR (dB) of DAS, DAS-CF, DAS-STCF, MV, MV-CF and MV-STCF were 19.19, 29.02, 44.68, 18.38, 28.65 and 44.30 respectively. Figure 9.10 shows DAS-STCF beamformer point target detectability with increased background optical

scattering. With higher μ_s, deeper point targets became difficult to detect resulting in reduced *SNR* [Figure 9.10 (b)].

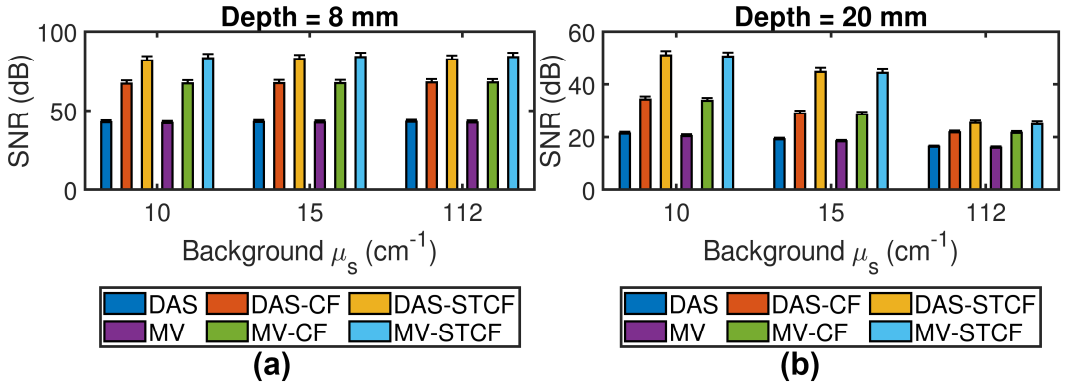

Figure 9.9 Variation of SNR with background scattering (μ_s) at a depth of (a) 8 mm and (b) 20 mm, respectively.

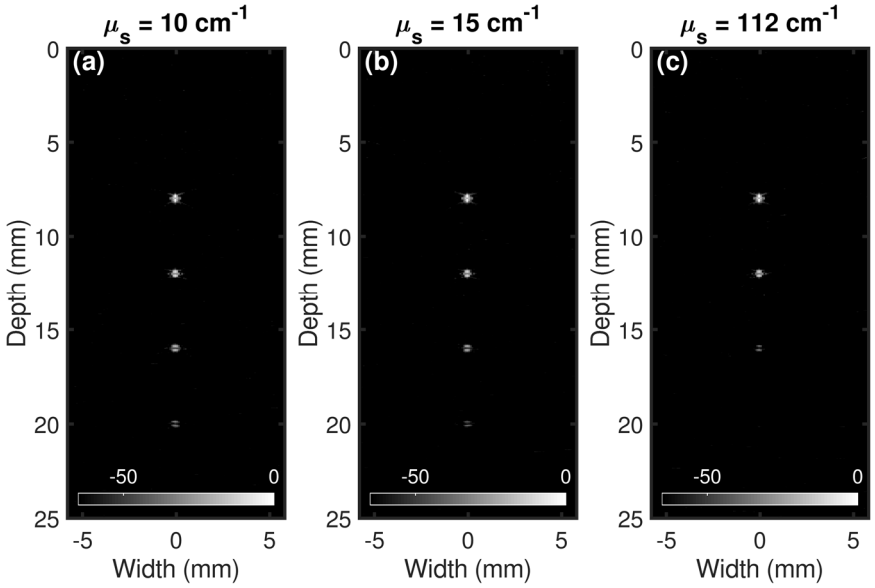

Figure 9.10 Variation of DAS-STCF beamformer point target discernibility with background scattering of (a) μ_s = 10 cm^{-1}, (b) μ_s = 15 cm^{-1}and (c) μ_s = 112 cm^{-1}respectively. Display dynamic range is 65 dB.

9.3.1.4 Noise Corrupted Channel Data

Figure **9.11** (a) – (b) show the variation of SNR with $SNR_{channel}$ at depths of 8 mm and 20 mm, respectively. Note that beamforming with STCF had the highest SNRs for all channel noise

levels and methods. For instance, for a depth of 20 mm and $SNR_{channel}$ = -9 dB, mean SNR (dB) of DAS, DAS-CF, DAS-STCF, MV, MV-CF and MV-STCF were 25.25, 43.21, 59.15, 24.65, 43.09 and 58.82, respectively. These results show robustness of STCF under noise corruption of channel data.

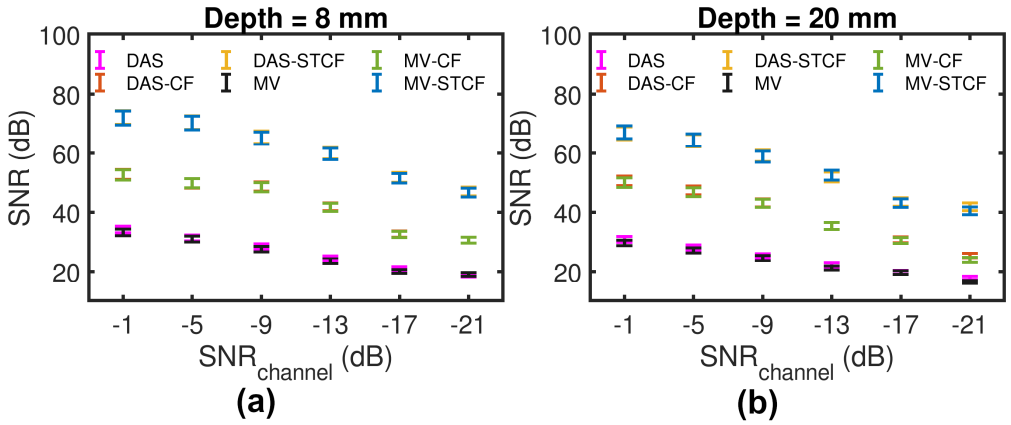

Figure 9.11 Variation of SNR with channel data SNR at a depth of (a) 8 mm and (b) 20 mm, respectively.

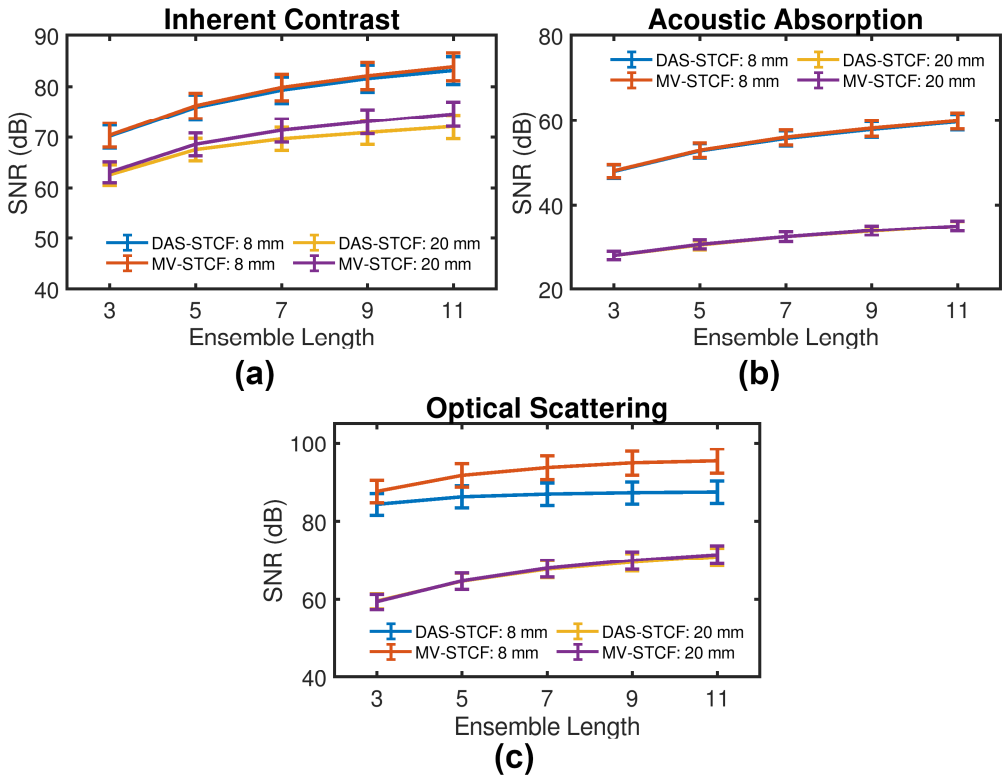

Figure 9.12 Variation of STCF beamformer SNR with ensemble length under (a) no acoustic and optical absorption, (b) acoustic absorption and (c) optical scattering, respectively.

9.3.1.5 Sensitivity to Ensemble Length

Figure 9.12 shows STCF beamformer performance sensitivity with ensemble length using channel data with (a) no acoustic or optical absorption (inherent contrast experiment data), (b) acoustic absorption with power law exponent of 2 and (c) background optical scattering coefficient of 10 cm^{-1}, respectively. Note that all channel data were corrupted with Gaussian random noise for a resultant channel SNR of 5 dB. For each experiment, we evaluated performance for shallow (8 mm) and deep (20 mm) targets. With increased ensemble length, steady improvement in SNR was observed in all cases expect for shallow target under optical scattering [Brown and blue curves in Figure 9.12 (c)].

9.3.2 Results from in vivo Murine Cardiac PAI

PAI M-mode results are summarized in Figure 9.13, where Figure 9.13 (a) – (f) show the output of DAS, DAS-CF, DAS-STCF, MV, MV-CF and MV-STCF, respectively. Movement of anterior myocardium is clearly visible in all results. However, STCF methods result in significant reduction of temporally varying noise signals from LV chamber and gel region. Figure 9.14 shows corresponding *in vivo* cardiac PA images at ED. US B-mode image with PA imaging FOV [green rectangle] is shown in Figure 9.14 (a). Beamformed image from Vevo LAZR system is shown in Figure 9.14 (b). Figure 9.14 (c) – (h) show the results of DAS, DAS-CF, DAS-STCF, MV, MV-CF and MV-STCF, respectively. Improved myocardial signal specificity and higher signal rejection in LV chamber and acoustic gel region is observed with STCF. Similarly, Figure 9.15 shows *in vivo* cardiac PA images at ES, where the beamformed image from Vevo LAZR system is presented in Figure 9.15 (b). Figure 9.15 (c) – (h) show images with DAS, DAS-CF, DAS-STCF, MV, MV-CF and MV-STCF beamforming, respectively. Finally, quantitative results for ED and ES PAI are summarized in Figure 9.16. Plots are presented as mean ± standard error computed over four independent mice datasets. Figure 9.16 (a) shows that STCF weighting resulted in higher SNR values both at ED and ES. CR and gCNR results between myocardium and surrounding muscle tissue are presented in Figure 9.16 (b) and (d). Note that CF and STCF weighting performed equally well with clear improvement over using DAS and MV beamformers alone. CR and gCNR results between myocardium and LV chamber blood are presented in Figure 9.16 (c) and (e). STCF weighted images had higher CR and gCNR values compared to CF weighted and conventional (DAS and MV) beamformed images. Figure 9.17 shows the sensitivity of *in vivo* STCF beamforming performance with ensemble length. Figure 9.17 (a) shows that SNR improvement with ensemble length up to 7 following which the curves plateau. Figure 9.17 (b) and (d) indicate no variation in CR and gCNR between myocardium and muscle with ensemble

length. Figure 9.17 (c) and (e) show that CR and gCNR values between myocardium and LV chamber blood increased with ensemble length increments until K = 7, after which the curves plateau.

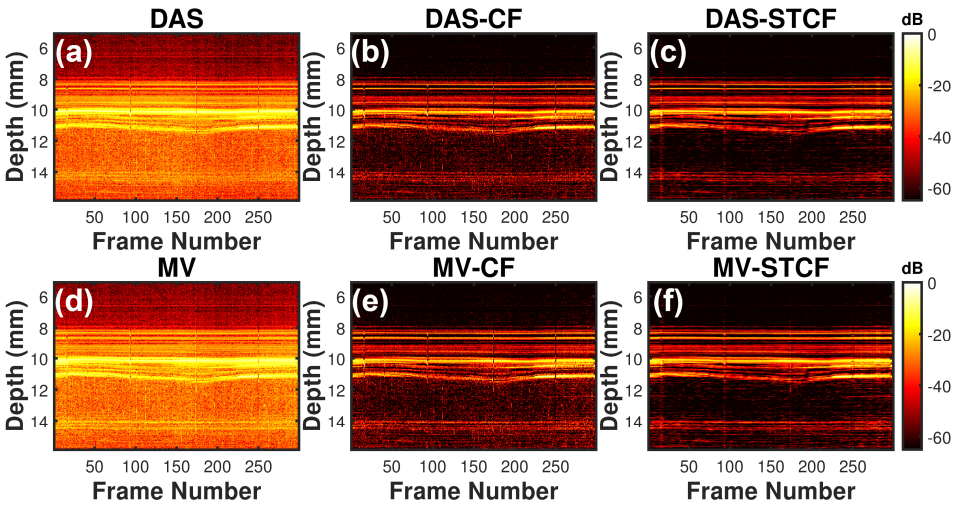

Figure 9.13 Cardiac PAI M-mode image reconstructed using (a) DAS, (b) DAS-CF, (c) DAS-STCF, (d) MV, (e) MV-CF and (f) MV-STCF. Display dynamic range is 65 dB.

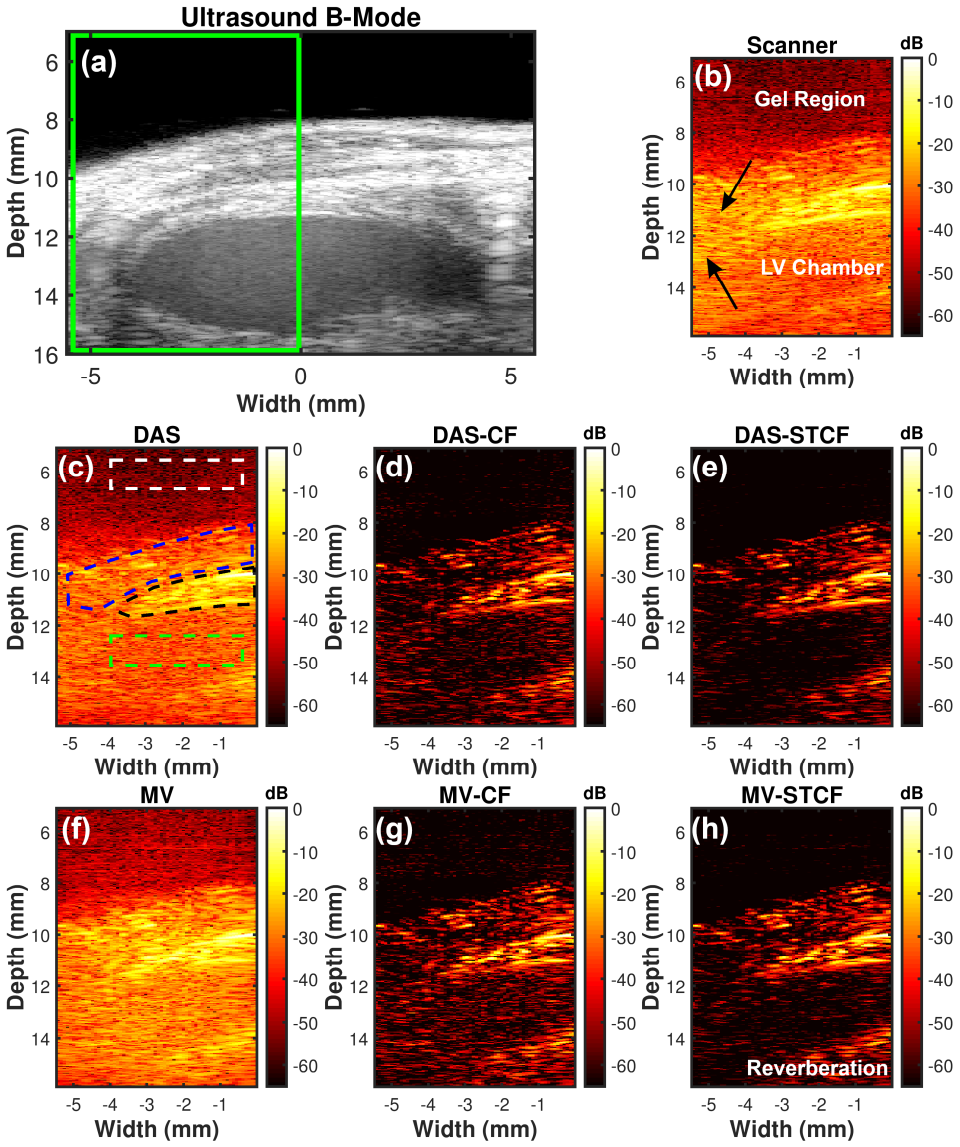

Figure 9.14 *In vivo* cardiac photoacoustic images at ED. (a) US B-mode, (b) System PA image, (c) DAS, (d) DAS-CF, (e) DAS -STCF, (f) MV, (g) MV-CF and (h) MV-STCF. Arrows in Fig. 14 (b) indicate signals impeding contrast between myocardium and surrounding muscle. ROI definitions in Fig. 14 (c): Green = LV chamber blood, black = myocardial wall, blue = muscle and white = noise. STCF weighting better suppressed signals from gel region and LV chamber.

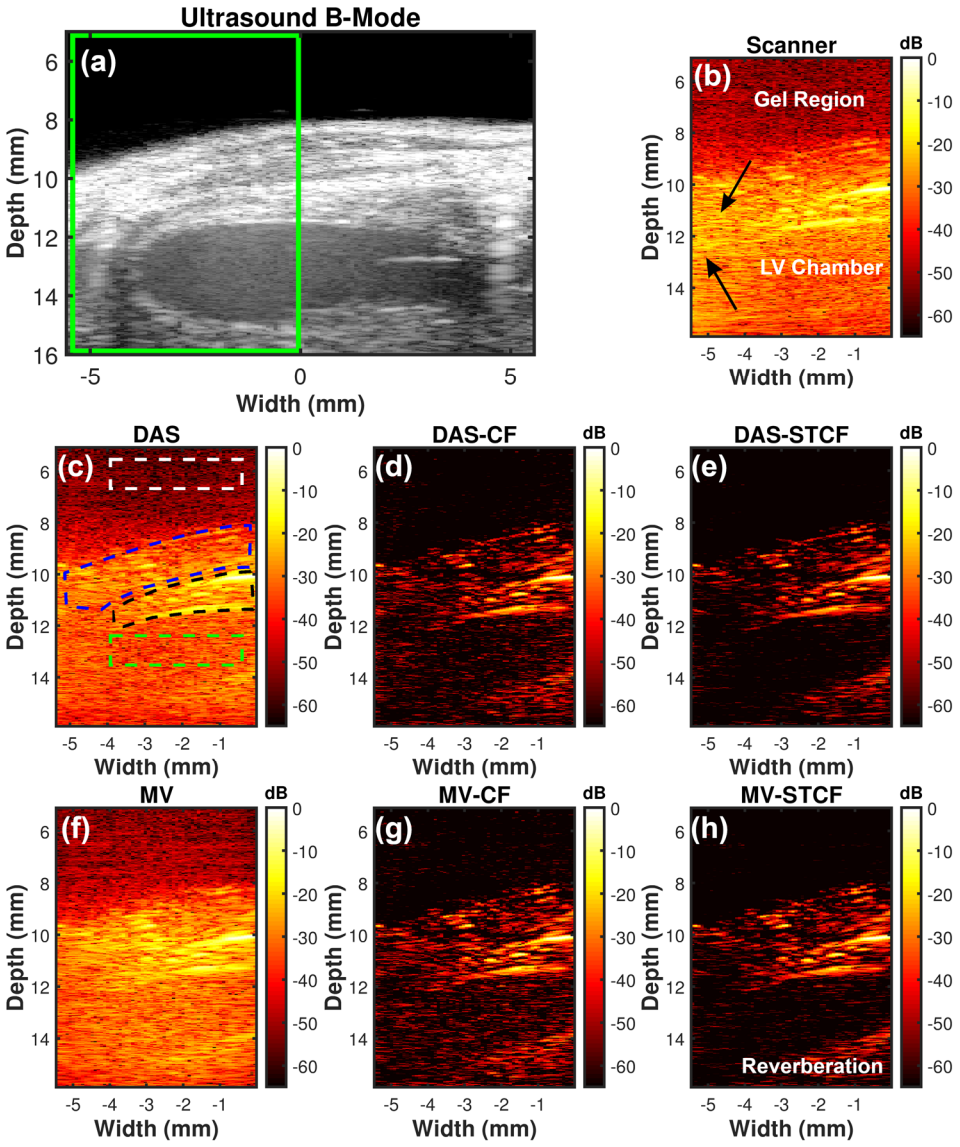

Figure 9.15 *In vivo* cardiac photoacoustic images at ES. (a) US B-mode, (b) System PA image, (c) DAS, (d) DAS-CF, (e) DAS -STCF, (f) MV, (g) MV-CF and (h) MV-STCF. Arrows in Fig. 15 (b) indicate signals impeding contrast between myocardium and surrounding muscle. ROI definitions in Fig. 15 (c): Green = LV chamber blood, black = myocardial wall, blue = muscle and white = noise. STCF weighting better suppressed signals from gel region and LV chamber.

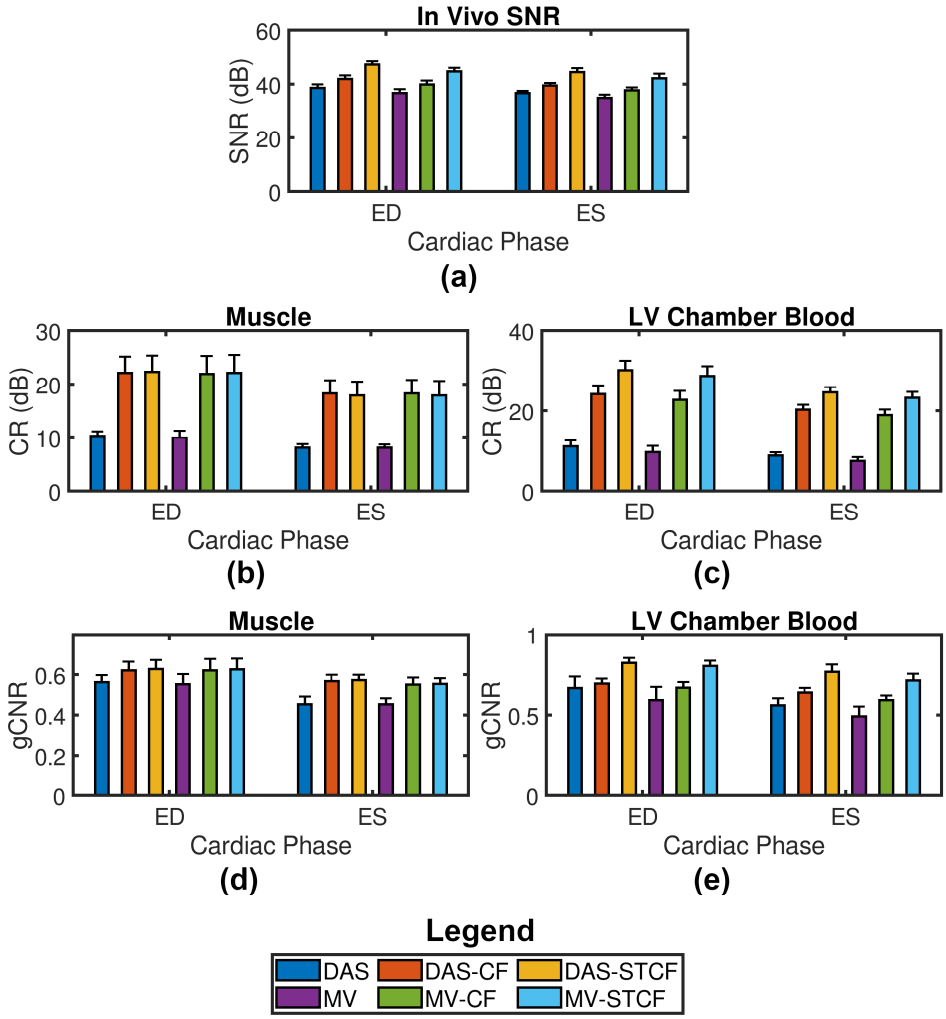

Figure 9.16 (a) *In vivo* SNR comparison. (b) and (d) show CR and gCNR comparison between myocardial wall and muscle, respectively. (c) and (e) show CR and gCNR comparison between myocardial wall and LV chamber blood, respectively.

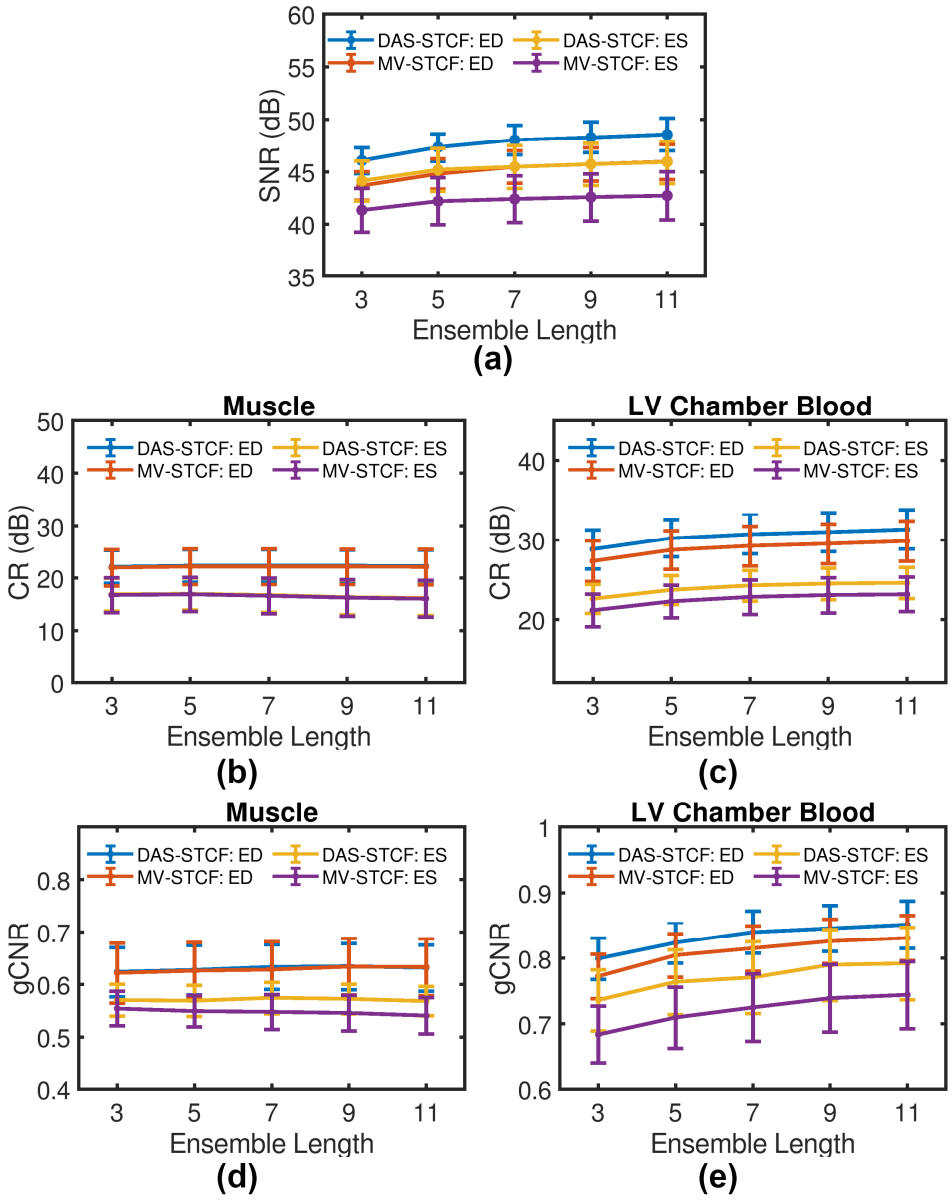

Figure 9.17 (a) SNR variation with ensemble length (K). (b) and (d) show CR and gCNR variation between myocardial wall and muscle, respectively. (c) and (e) show CR and gCNR variation between myocardial wall and LV chamber blood, respectively.

9.4 Discussion on Findings from Simulation and *in vivo* Experiments

9.4.1 Numerical STCF Simulation Studies

In the numerical simulation studies, we have investigated the impact of inherent contrast, acoustic absorption, optical attenuation and channel SNR on the performance of conventional and coherence-based beamformers. The primary findings of our simulation studies can be summarized as follows.

Experiments with inherent contrast variation were performed to model SNR variation in PA channel data with optical energy used for acoustic excitation. Lower optical fluence results in low SNR data reducing contrast between optical absorber and tissue scattering [21]. Under low contrast conditions, PA pressure waves are difficult to distinguish from background scattering. Using STCF, temporal coherence in PA pressure waves was exploited resulting in improved separation of point target PA signals from background scattering signals, lower sidelobe levels and higher SNR values [Figure 9.2 – Figure 9.4].

Acoustic signal loss due to absorption in soft biological tissues is a well-known phenomenon [22, 23]. Resultant attenuation shows a power law frequency dependence. Due to its broadband nature, PA signals are affected by frequency dependent attenuation [24] resulting in depth dependent blurring of features and magnitude errors [25]. Furthermore, *in vivo* pre-clinical cardiac PAI data was obtained using a high frequency linear array (f_c = 21 MHz) necessitating studying acoustic attenuation in simulations at various levels of acoustic absorption. Results show DAS-STCF and MV-STCF provide higher SNR values when compared to other methods at all depths for attenuation power law exponent values less than 2, showing the robustness of STCF [Fig. 7]. However, at very high attenuation (y = 2), SNR values for STCF weighted beamformers converge to the performance of CF-based beamformer because acoustic attenuation becomes the

primary performance limiting factor rather than background noise, indicating that additional signal processing is necessary to improve image quality. Attenuation correction approaches can be applied post beamforming to address this issue [26, 27].

To account for the impact of the non-uniform optical fluence distribution due to photon scattering in biological tissues on PA beamforming, a hybrid simulation approach was adopted in this work [Figure 9.1]. In our tissue model, all point targets were treated as 0.1 mm radius blood vessels imaged transversely with 75 % oxygen saturation. Since they are placed along the same lateral coordinate with axial location variation, $A(\lambda,r)$ of the point targets appear to have an exponential decay over depth. Therefore, at increased depths, low intensity PA signal wavefronts get buried under noise ($SNR_{channel}$ = -3 dB) which are not resolved with conventional and CF-based beamformers. However, utilizing temporal coherence, low intensity wavefronts are separated from the noise background resulting in better target detectability at 20 mm with subsequent improvement in SNR [Figure 9.8 and Figure 9.9]. We further evaluated beamforming performance background scattering coefficient values of soft and fibrous breast tissues reported in the literature [28-30]. We found that with a drastic drop in $A(\lambda,r)_{|r=20mm}$ due to high level of optical scattering (μ_s= 112 cm^{-1}), both signal and noise wavefronts had similar spatiotemporal coherence resulting in target signal suppression with STCF. Thus, with low energy optical fluence, STCF may fail to resolve deeper PAI targets [Figure 9.10]. A proposed deep learning method [29] can be coupled with STCF to address this issue.

Ensemble length, K is a key algometric parameter for STCF weighting and was carefully investigated in our simulations with the results summarized in Figure 9.12. In the presence of inherent contrast with no acoustic and optical attenuation, both shallow and deep targets demonstrate steady SNR improvement (> 8 dB) with increment of K from 3 to 9 [Figure 9.12 (a)].

This is an expected outcome since only temporally varying background signals contribute to the noise floor, which are suppressed during temporal coherence calculations. Similar trend was observed for experiments incorporating acoustic absorption [Figure 9.12 (b)]. However, shallow targets had higher SNR than deeper targets due to the depth-dependent nature of acoustic attenuation. For experiments with background optical scattering coefficient = 10 cm^{-1}, no significant performance improvement was seen by increasing K for the target at 8 mm depth [Figure 9.12 (c)]. However, SNR of MV-STCF was 18 dB higher than MV-CF SNR with K = 7 indicating that even for shallow targets with high optical absorption, STCF provides significant improvement. For 20 mm target, more than 10 dB performance gain was obtained with increasing K from 3 to 9. At deeper depths, the low intensity PA wavefront becomes increasingly difficult to separate from the noise background, where increasing K had an evident impact [Figure 9.12 (c)]. Taking all these factors together, for ensemble lengths greater than 5, STCF always perform better or same as CF methods.

Typically experimental and *in vivo* channel data get corrupted by background noise, comprised of electronic and thermal noise [31, 32]. Optical scattering of tissues further contribute to the noise floor [32] resulting in low SNR channel data. Thus, performance evaluation was done by varying the *SNR* of channel data. Qualitative observation of channel data revealed that beyond $SNR_{channel}$ = -9 dB, PA pressure wavefronts were difficult to discern. Consequently, added noise contributed to significant destructive interference [33] during DAS and MV beamforming resulting in images with non-resolvable optical absorbers. Superiority of the proposed STCF was demonstrated as significantly higher SNR values were seen even with low SNR channel data [Figure 9.11].

One limitation of our simulation studies was that no relative motion was modelled for the dominant optical absorber's location over time. This was done under the assumption that little, or no motion will be encountered within short ensemble periods. However, if large relative motion occurs, realignment of dominant PA wave fronts by performing motion estimation in the aperture domain can be performed before STCF calculation. Overall, the performance of STCF weighting was robust for different contrast, acoustic absorption, optical scattering and channel SNR levels. STCF weighted DAS and MV beamformers produced higher quality PA images compared to other methods (DAS and MV with and without CF). This quality enhancement is attributed to improved suppression of background noise and spatiotemporally incoherent signals. Subsequently, STCF images exhibit a greater dynamic range than conventional and CF PA images enabling better visualization of low intensity PA signals.

9.4.2 In vivo Cardiac STCF PAI Beamforming

In vivo feasibility of STCF beamformers was demonstrated by performing PA imaging of the healthy murine heart. Our group has previously demonstrated the use of oxygen saturation (sO_2) as a measure to differentiate between healthy and infarcted hearts [18]. To obtain a reliable estimate of sO_2 in a rapidly beating organ such as the mouse heart (typical heart rate of 400-500 bpm), high persistence (frame averaging) is essential. This resulted in significantly reduced temporal resolution [34], and thereby sensitivity for detecting subtle variations in sO_2 over a single cardiac cycle and in the detection of less severe ischemic events. To address these concerns, imaging was done using the maximum possible PAI frame rate (20 Hz) on the Vevo LAZR without any frame averaging. Offline processing was employed to reconstruct a single cardiac cycle of PA data. This process led to ECG and respiratory signal gated "pseudo-high frame rate" cardiac PA imaging. However, contrast between myocardial wall and surrounding background structure was

impeded in the scanner reconstructed and conventional beamformed PA images due to spuriously high amplitude PA signals from muscle [indicated by arrows in Figure 9.14 (b) and Figure 9.15 (b)] and LV chamber.

Benefits of coherence-based beamforming over DAS has been reported previously for cardiac US [35, 36]. In this paper, we explore CF beamforming for *in vivo* cardiac PAI to enhance PA signals only from the myocardium by suppressing other noise artifacts. With the use of CF weighting, random noise signals from the gel region were suppressed to lie below the display dynamic range. This resulted in improved contrast between skin and gel region and better correspondence between US and PA images [Figure 9.14 and Figure 9.15]. In addition, due to the temporal variation of these random noise signals, STCF weighting produced higher SNR values when compared to other methods [Figure 9.16 (a)], thus corroborating our findings from numerical simulation studies [Figure 9.4]. PA signals from muscle and myocardium have lower temporal variation compared to signals from LV chamber blood [Figure 9.13 (a) and (d)]. Thus, comparable contrast (CR) and lesion detectability (gCNR) were observed using CF and STCF in contrast to conventional beamforming results between myocardial wall and muscle [Figure 9.16 (b) and (d)]. This is an expected outcome based on our results from simulation studies where similar FWHM values for non-temporally varying point targets were obtained with CF and STCF.

Our results demonstrate that contrast degradation between myocardium and LV chamber blood, was not suppressed using only CF. Due to pseudo-high frame rate of the reconstructed cine loop, we observed that PA wave fronts from myocardium had both spatial and temporal coherence over a short span of time with higher amplitude. On the other hand, PA wave fronts from LV chamber blood had low STCF with amplitudes at the same level as noise signals from gel region. This variation could be primarily due to the following two reasons. First, highly absorbing blood

inside the coronary artery (murine arterial oxygen saturation ≈ 90 – 95% [18, 37]) and scattering tissues (with reduced scattering coefficients (μ_s') of heart wall, whole blood, skin and soft tissue are 6.84 cm^{-1} , 5.88 cm^{-1}, 17.06 cm^{-1} and 9.55 cm^{-1} respectively [28] at 850 nm) causes significant light attenuation before it reaches LV chamber, thus creating a strong bias towards the myocardium surface [38]. Second, PA transients from the large volume of high velocity circulating blood (in early filling, E wave and late or atrial filling phase, A wave during diastole) inside the LV generates mainly destructive interference, while low velocity blood flow (diastolic coronary flow velocity ≈ 20 cm/sec [39]) in the coronary artery on the myocardial surface generates constructive interference resulting in PA amplitude differences between myocardium and LV chamber [33]. The E and A wave velocity [40] of mitral valve flow during diastole were roughly 54.2 cm/sec and 43.8 cm/sec respectively [41]. Therefore, no viable signal can be retrieved from the LV chamber except temporally varying noise which reduces contrast between myocardium and LV chamber [Figure 9.14 (b) and Figure 9.15 (b)]. This also corroborates our numerical simulation findings where low fluence and noisy channel data was correlated with point target depth. Observe that the PA signal level and background noise were similar at a 20 mm depth [Figure 9.10]. Furthermore, previous studies on murine myocardial ischemia and PAI were focused on the anterior myocardium due to penetration depth limitations [18, 37, 42]. Under these circumstances the benefit of using STCF becomes more evident as it results in higher CR and gCNR between myocardium and LV chamber when compared to other methods [Figure 9.16 (c) and Figure 9.16 (e)] by suppressing non-viable LV chamber PA signals.

Ensemble length analysis also indicates that gains in SNR, CR and gCNR are obtained with higher ensemble length with high temporally varying noise [Figure 9.17 (a), (c) and (e)] with no evident impact in the presence of slow or no temporal variation in PA signals [Figure 9.17 (b) and

(d)]. Note also that reverberation artifacts (at depth > 14 mm) persist for CF beamformers [Figure 9.14 – Figure 9.15 (h)].

Results from simulation studies show that increasing ultrasound absorption and optical attenuation reduces channel SNR, negatively impacting the SNR of STCF beamformed images. For *in vivo* data sets, the quality of received channel data depends on a complex interplay of inter-frame laser energy, depth-dependent fluence distribution, cardiac motion, positioning of the animal in imaging FOV and ultrasound attenuation of generated PA signals (e.g. normalized signal loss of freshly excised heart at 40 MHz = 36 dB/cm [43]) . Thus, SNR and CR obtained with STCF *in vivo* was lower than simulation results. One interesting finding is that DAS-STCF had slightly higher SNR, CR and gCNR when compared to MV-STCF *in vivo*. One implication of this finding is that with STCF improved performance is obtained with a less computationally intensive beamformer.

PAI has been used to monitor radiofrequency ablation lesion formation in the passively beating *ex-vivo* left atrium [44] where Savitzky–Golay smoothing was employed to reduce SNR degradation from cardiac motion. Results from this chapter suggests that CF and STCF beamformers can be used to reduce SNR degradation. Recently, use of PAI to guide cardiac catheter interventions have been demonstrated *in vivo* where DAS beamformed images were used to localize the catheter tip inside the right atrium [45]. We anticipate that STCF weighting can be potentially applied to visualize the tip at higher dynamic ranges. In future work, we will apply this technique to perform cardiac PAI for infarcted murine hearts by estimating *in vivo* oxygen saturation (sO_2). Poor SNR in single wavelength PA data for estimating sO_2 was shown to have a significant noise bias [46]. We anticipate that with STCF weighting, noise signals can be separated out, enabling improved sO_2 estimation with SNR-regularization [46].

Finally, results in this work show that better adaptive beamforming can be obtained using temporal information in context of cardiac PAI. We anticipate similar idea can be extended to other variants of adaptive beamformers such as DMAS [4, 47-51], high resolution CF [52], modified-CF [7], SNR-dependent CF [21] and SLSC [34, 53, 54] to further improve resultant image quality.

List of References

[1] M. Xu, X. Yang, M. Ding, and M. Yuchi, "Spatio-temporally smoothed coherence factor for ultrasound imaging [Correspondence]," *IEEE transactions on ultrasonics, ferroelectrics, and frequency control,* vol. 61, pp. 182-190, 2014.

[2] S. Park, A. B. Karpiouk, S. R. Aglyamov, and S. Y. Emelianov, "Adaptive beamforming for photoacoustic imaging," *Optics letters,* vol. 33, pp. 1291-1293, 2008.

[3] B. M. Asl and A. Mahloojifar, "Minimum variance beamforming combined with adaptive coherence weighting applied to medical ultrasound imaging," *IEEE transactions on ultrasonics, ferroelectrics, and frequency control,* vol. 56, pp. 1923-1931, 2009.

[4] M. Mozaffarzadeh, A. Mahloojifar, M. Orooji, K. Kratkiewicz, S. Adabi, and M. Nasiriavanaki, "Linear-array photoacoustic imaging using minimum variance-based delay multiply and sum adaptive beamforming algorithm," *Journal of biomedical optics,* vol. 23, p. 026002, 2018.

[5] J.-F. Synnevag, A. Austeng, and S. Holm, "Benefits of minimum-variance beamforming in medical ultrasound imaging," *IEEE transactions on ultrasonics, ferroelectrics, and frequency control,* vol. 56, pp. 1868-1879, 2009.

[6] P. V. Chitnis, O. Aristizábal, E. Filoux, A. Sampathkumar, J. Mamou, and J. A. Ketterling, "Coherence-weighted synthetic focusing applied to photoacoustic imaging using a high-frequency annular-array transducer," *Ultrasonic imaging,* vol. 38, pp. 32-43, 2016.

[7] M. Mozaffarzadeh, Y. Yan, M. Mehrmohammadi, and B. Makkiabadi, "Enhanced linear-array photoacoustic beamforming using modified coherence factor," *Journal of biomedical optics,* vol. 23, p. 026005, 2018.

[8] B. E. Treeby and B. T. Cox, "k-Wave: MATLAB toolbox for the simulation and reconstruction of photoacoustic wave fields," *Journal of biomedical optics,* vol. 15, p. 021314, 2010.

[9] J. Laufer, D. Delpy, C. Elwell, and P. Beard, "Quantitative spatially resolved measurement of tissue chromophore concentrations using photoacoustic spectroscopy: application to the measurement of blood oxygenation and haemoglobin concentration," *Physics in Medicine & Biology,* vol. 52, p. 141, 2006.

[10] D. M. Egolf, R. K. Chee, and R. J. Zemp, "Sparsity-based reconstruction for super-resolved limited-view photoacoustic computed tomography deep in a scattering medium," *Optics letters,* vol. 43, pp. 2221-2224, 2018.

[11] P. Zhang, L. Li, L. Lin, P. Hu, J. Shi, Y. He*, et al.*, "High-resolution deep functional imaging of the whole mouse brain by photoacoustic computed tomography in vivo," *Journal of biophotonics,* vol. 11, p. e201700024, 2018.

[12] P. Beard, "Biomedical photoacoustic imaging," *Interface focus,* vol. 1, pp. 602-631, 2011.

[13] C. Li and L. V. Wang, "Photoacoustic tomography and sensing in biomedicine," *Physics in Medicine & Biology,* vol. 54, p. R59, 2009.

[14] L. V. Wang, "Tutorial on photoacoustic microscopy and computed tomography," *IEEE Journal of Selected Topics in Quantum Electronics,* vol. 14, pp. 171-179, 2008.

[15] D. Marti, R. N. Aasbjerg, P. E. Andersen, and A. K. Hansen, "MCmatlab: an open-source, user-friendly, MATLAB-integrated three-dimensional Monte Carlo light transport solver with heat diffusion and tissue damage," *Journal of biomedical optics,* vol. 23, p. 121622, 2018.

[16] D.-K. Yao, C. Zhang, K. I. Maslov, and L. V. Wang, "Photoacoustic measurement of the Grüneisen parameter of tissue," *Journal of biomedical optics,* vol. 19, p. 017007, 2014.

[17] A. Needles, A. Heinmiller, J. Sun, C. Theodoropoulos, D. Bates, D. Hirson*, et al.*, "Development and initial application of a fully integrated photoacoustic micro-ultrasound system," *IEEE transactions on ultrasonics, ferroelectrics, and frequency control,* vol. 60, pp. 888-897, 2013.

[18] R. A. Mukaddim, A. Rodgers, T. A. Hacker, A. Heinmiller, and T. Varghese, "Real-Time in Vivo Photoacoustic Imaging in the Assessment of Myocardial Dynamics in Murine Model of Myocardial Ischemia," *Ultrasound in Medicine & Biology,* vol. 44, pp. 2155-2164, 2018.

[19] K. M. Kempski, M. T. Graham, M. R. Gubbi, T. Palmer, and M. A. L. Bell, "Application of the generalized contrast-to-noise ratio to assess photoacoustic image quality," *Biomedical Optics Express,* vol. 11, pp. 3684-3698, 2020.

[20] A. Rodriguez-Molares, O. M. H. Rindal, J. D'hooge, S.-E. Måsøy, A. Austeng, M. A. L. Bell*, et al.*, "The generalized contrast-to-noise ratio: a formal definition for lesion detectability," *IEEE Transactions on Ultrasonics, Ferroelectrics, and Frequency Control,* vol. 67, pp. 745-759, 2019.

[21] Y.-H. Wang and P.-C. Li, "SNR-dependent coherence-based adaptive imaging for high-frame-rate ultrasonic and photoacoustic imaging," *IEEE transactions on ultrasonics, ferroelectrics, and frequency control,* vol. 61, pp. 1419-1432, 2014.

[22] W. J. Fry, "Mechanism of acoustic absorption in tissue," *The Journal of the Acoustical Society of America,* vol. 24, pp. 412-415, 1952.

[23] P. Wells, "Absorption and dispersion of ultrasound in biological tissue," *Ultrasound in medicine & biology,* vol. 1, pp. 369-376, 1975.

[24] J. Yao and L. V. Wang, "Sensitivity of photoacoustic microscopy," *Photoacoustics,* vol. 2, pp. 87-101, 2014.

[25] B. E. Treeby, J. Jaros, and B. T. Cox, "Advanced photoacoustic image reconstruction using the k-Wave toolbox," in *Photons Plus Ultrasound: Imaging and Sensing 2016*, 2016, p. 97082P.

[26] P. Burgholzer, H. Grün, M. Haltmeier, R. Nuster, and G. Paltauf, "Compensation of acoustic attenuation for high-resolution photoacoustic imaging with line detectors," in *Photons Plus Ultrasound: Imaging and Sensing 2007: The Eighth Conference on Biomedical Thermoacoustics, Optoacoustics, and Acousto-optics*, 2007, p. 643724.

[27] B. E. Treeby, E. Z. Zhang, and B. T. Cox, "Photoacoustic tomography in absorbing acoustic media using time reversal," *Inverse Problems,* vol. 26, p. 115003, 2010.

[28] S. L. Jacques, "Optical properties of biological tissues: a review," *Physics in Medicine & Biology,* vol. 58, p. R37, 2013.

[29] K. Johnstonbaugh, S. Agrawal, D. A. Durairaj, C. Fadden, A. Dangi, S. P. K. Karri*, et al.*, "A deep learning approach to photoacoustic wavefront localization in deep-tissue medium," *IEEE Transactions on Ultrasonics, Ferroelectrics, and Frequency Control,* 2020.

[30] D. Waibel, J. Gröhl, F. Isensee, T. Kirchner, K. Maier-Hein, and L. Maier-Hein, "Reconstruction of initial pressure from limited view photoacoustic images using deep learning," in *Photons Plus Ultrasound: Imaging and Sensing 2018*, 2018, p. 104942S.

[31] D. Allman, A. Reiter, and M. A. L. Bell, "Photoacoustic source detection and reflection artifact removal enabled by deep learning," *IEEE transactions on medical imaging,* vol. 37, pp. 1464-1477, 2018.

[32] C. Kim, T. N. Erpelding, L. Jankovic, M. D. Pashley, and L. V. Wang, "Deeply penetrating in vivo photoacoustic imaging using a clinical ultrasound array system," *Biomedical optics express,* vol. 1, pp. 278-284, 2010.

[33] E. Hysi, M. N. Fadhel, M. J. Moore, J. Zalev, E. M. Strohm, and M. C. Kolios, "Insights into photoacoustic speckle and applications in tumor characterization," *Photoacoustics,* vol. 14, pp. 37-48, 2019.

[34] M. A. L. Bell, X. Guo, H. J. Kang, and E. Boctor, "Improved contrast in laser-diode-based photoacoustic images with short-lag spatial coherence beamforming," in *2014 IEEE International Ultrasonics Symposium*, 2014, pp. 37-40.

[35] G. Matrone, A. Ramalli, J. d'Hooge, P. Tortoli, and G. Magenes, "A Comparison of Coherence-Based Beamforming Techniques in High Frame-Rate Ultrasound Imaging with Multi-Line Transmission," *IEEE Transactions on Ultrasonics, Ferroelectrics, and Frequency Control,* 2019.

[36] M. A. L. Bell, R. Goswami, J. A. Kisslo, J. J. Dahl, and G. E. Trahey, "Short-lag spatial coherence imaging of cardiac ultrasound data: Initial clinical results," *Ultrasound in medicine & biology,* vol. 39, pp. 1861-1874, 2013.

[37] J. Lv, Y. Peng, S. Li, Z. Guo, Q. Zhao, X. Zhang*, et al.*, "Hemispherical photoacoustic imaging of myocardial infarction: in vivo detection and monitoring," *European radiology,* vol. 28, pp. 2176-2183, 2018.

[38] X. L. Deán-Ben, S. J. Ford, and D. Razansky, "High-frame rate four dimensional optoacoustic tomography enables visualization of cardiovascular dynamics and mouse heart perfusion," *Scientific reports,* vol. 5, p. 10133, 2015.

[39] W.-T. Chang, S. Fisch, M. Chen, Y. Qiu, S. Cheng, and R. Liao, "Ultrasound based assessment of coronary artery flow and coronary flow reserve using the pressure overload model in mice," *JoVE (Journal of Visualized Experiments),* p. e52598, 2015.

[40] M. L. Lindsey, Z. Kassiri, J. A. Virag, L. E. de Castro Brás, and M. Scherrer-Crosbie, "Guidelines for measuring cardiac physiology in mice," *American Journal of Physiology-Heart and Circulatory Physiology,* vol. 314, pp. H733-H752, 2018.

[41] S. Gao, D. Ho, D. E. Vatner, and S. F. Vatner, "Echocardiography in mice," *Current protocols in mouse biology,* vol. 1, pp. 71-83, 2011.

[42] Z. Li, H. Li, W. Xie, and H. Chen, "In vivo determination of acute myocardial ischemia based on photoacoustic imaging with a focused transducer," *Journal of Biomedical Optics,* vol. 16, p. 076011, 2011.

[43] C. L. Dent, M. J. Scott, S. A. Wickline, and C. S. Hall, "High-frequency ultrasound for quantitative characterization of myocardial edema," *Ultrasound in medicine & biology,* vol. 26, pp. 375-384, 2000.

[44] S. Iskander-Rizk, P. Kruizinga, R. Beurskens, G. Springeling, F. Mastik, N. M. de Groot*, et al.*, "Real-time photoacoustic assessment of radiofrequency ablation lesion formation in the left atrium," *Photoacoustics,* vol. 16, p. 100150, 2019.

[45] M. Graham, F. Assis, D. Allman, A. Wiacek, E. Gonzalez, M. Gubbi*, et al.*, "In vivo demonstration of photoacoustic image guidance and robotic visual servoing for cardiac catheter-based interventions," *IEEE transactions on medical imaging,* vol. 39, pp. 1015-1029, 2019.

[46] M. A. Naser, D. R. Sampaio, N. M. Muñoz, C. A. Wood, T. M. Mitcham, W. Stefan*, et al.*, "Improved photoacoustic-based oxygen saturation estimation with SNR-regularized local fluence correction," *IEEE transactions on medical imaging,* vol. 38, pp. 561-571, 2018.

[47] G. Matrone, A. S. Savoia, G. Caliano, and G. Magenes, "The delay multiply and sum beamforming algorithm in ultrasound B-mode medical imaging," *IEEE transactions on medical imaging,* vol. 34, pp. 940-949, 2014.

[48] M. Mozaffarzadeh, A. Mahloojifar, M. Nasiriavanaki, and M. Orooji, "Eigenspace-based minimum variance adaptive beamformer combined with delay multiply and sum: experimental study," in *Photonics in Dermatology and Plastic Surgery 2018*, 2018, p. 1046717.

[49] M. Mozaffarzadeh, A. Mahloojifar, M. Orooji, S. Adabi, and M. Nasiriavanaki, "Double-stage delay multiply and sum beamforming algorithm: Application to linear-array photoacoustic imaging," *IEEE Transactions on Biomedical Engineering,* vol. 65, pp. 31-42, 2017.

[50] M. Mozaffarzadeh, A. Mahloojifar, V. Periyasamy, M. Pramanik, and M. Orooji, "Eigenspace-based minimum variance combined with delay multiply and sum beamformer: Application to linear-array photoacoustic imaging," *IEEE Journal of Selected Topics in Quantum Electronics,* vol. 25, pp. 1-8, 2018.

[51] J. Park, S. Jeon, J. Meng, L. Song, J. S. Lee, and C. Kim, "Delay-multiply-and-sum-based synthetic aperture focusing in photoacoustic microscopy," *Journal of biomedical optics,* vol. 21, p. 036010, 2016.

[52] M. Mozaffarzadeh, B. Makkiabadi, M. Basij, and M. Mehrmohammadi, "Image improvement in linear-array photoacoustic imaging using high resolution coherence factor weighting technique," *BMC Biomedical Engineering,* vol. 1, p. 10, 2019.

[53] M. A. L. Bell, N. Kuo, D. Y. Song, and E. M. Boctor, "Short-lag spatial coherence beamforming of photoacoustic images for enhanced visualization of prostate brachytherapy seeds," *Biomedical optics express,* vol. 4, pp. 1964-1977, 2013.

[54] B. Pourebrahimi, S. Yoon, D. Dopsa, and M. C. Kolios, "Improving the quality of photoacoustic images using the short-lag spatial coherence imaging technique," in *Photons Plus Ultrasound: Imaging and Sensing 2013*, 2013, p. 85813Y.

Chapter 10

Adaptive Photoacoustic Beamforming with Sub-Aperture Processing

We previously extended coherence factor (CF) calculations into the spatiotemporal domain (STCF) and showed improved image quality over delay-and-sum (DAS) and minimum variance (MV) beamforming for *in vivo* cardiac photoacoustic imaging in **Chapter 09** [1, 2]. However, further *in vivo* investigation revealed that CF and STCF weighting may also lead to undesirable signal suppression from the myocardial wall along with sidelobe suppression. Furthermore, most of the reported adaptive methods (e.g., coherence-based methods) [1-7] have shown performance improvement for coherent targets when compared to DAS. However, for diffuse scattering arising from constructive or destructive interference of spatially randomly distributed optical absorbers [8], they tend to suppress the signal of interest.

Optimal image reconstruction should recover both coherent and diffuse photoacoustic (PA) signals while suppressing clutter and sidelobes. To this end, in this chapter[8], we propose image formation based on sub-aperture processing to preserve DAS amplitude levels for myocardial wall PA signals while achieving sidelobe and clutter suppression like CF based beamformers. Here, the received channel data are first split into two non-overlapping sub-apertures as in dual apodization with normalized cross-correlation (DAX) [9] and acoustic sub-aperture processing (ASAP) [10] developed for B-mode and contrast enhanced ultrasound (CEUS) imaging respectively. A pair of sub-aperture PA images were then reconstructed using the DAS algorithm. Amplitude and phase correlation of the sub-aperture PA images were utilized to generate a weighting matrix to suppress

[8] Rashid Al Mukaddim, Rifat Ahmed, and Tomy Varghese, "Sub-aperture Processing Based Adaptive Beamforming for Photoacoustic Imaging." *IEEE Transactions on Ultrasonics, Ferroelectrics, and Frequency Control*, Early Access (2021) PMCID: Pending

sidelobe and clutter signals. Finally, the full-aperture DAS image was weighted using the weighting matrix to generate a PA sub-aperture (PSAP) image. In [11], ASAP was coupled with spatiotemporal filtering and temporal correlation estimation to improve contrast-enhanced PAI. A limited *ex vivo* study was performed using DAX on contrast-based PAI [12]. In PSAP, we utilize the spatial correlation function derived from sub-aperture beamformed images to enhance non-contrast PAI where optical contrast is attributed to endogenous chromophores *in vivo*.

10.1 Basic Principles of Photoacoustic Sub-aperture Processing (PSAP)

10.1.1 Beamforming using Sub-apertures

Let $\mathbf{X}(t) = [x_1(t-\tau_m);\ \ldots.;\ x_M(t-\tau_M)]$ represent the received time-delayed PA channel data from an M-element linear array with the time delay of element m denoted by τ_m. For PSAP, using the received time-delayed PA channel data $\boldsymbol{X}(t)$, two set of images, $\mathbf{S_1}(t)$ and $\mathbf{S_2}(t)$ are reconstructed using two non-overlapping sub-apertures with no common elements, denoted by the vectors $\mathbf{W_1}(t)$ and $\mathbf{W_2}(t)$ [9, 10, 13-19]. Sub-aperture reconstructed images are represented using the following equations.

$$\begin{aligned}\mathbf{S_1}(t) &= \mathbf{W_1}(t)^H \mathbf{X}(t)\\ \mathbf{S_2}(t) &= \mathbf{W_2}(t)^H \mathbf{X}(t)\end{aligned} \tag{10.1}$$

To construct $\mathbf{W_1}(t)$ and $\mathbf{W_2}(t)$ we follow an approach reported in [9]. $\mathbf{W_1}(t)$ is made of ones and zeros with an alternating pattern of N elements on and N elements off. $\mathbf{W_2}(t)$ is complementary to $\mathbf{W_1}(t)$ and uses the opposite alternating pattern of N elements on and N elements off. An example of sub-apertures $\mathbf{W_1}(t)$ and $\mathbf{W_2}(t)$ formed with 4-4 alternating element pattern is shown in Figure 10.1. Here, we assume that any signal from on-axis main lobe will be highly correlated between $\mathbf{S_1}(t)$ and $\mathbf{S_2}(t)$ while off-axis interfering signals such as sidelobe and incoherent clutter will be

decorrelated [9, 13]. Therefore, quantifying the similarity between $\mathbf{S}_1(t)$ and $\mathbf{S}_2(t)$ will enable determination of a weighting matrix for DAS PA to suppress sidelobe and incoherent clutter. A schematic diagram for PSAP is presented in Figure 10.2. Seo *et al.* [9] used a similar approach for ultrasound B-mode images and Stanziola *et al.* [10] later extended the approach for CEUS. Here, we demonstrate that this approach results in significant clutter reduction in PA.

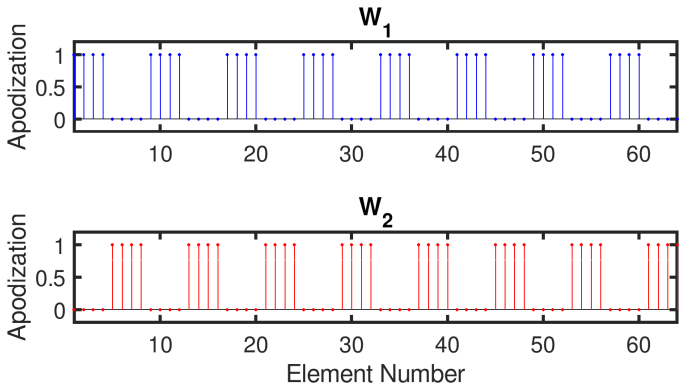

Figure 10.1 Sub-aperture $\mathbf{W}_1(t)$ and $\mathbf{W}_2(t)$ formed with 4-4 alternating element pattern.

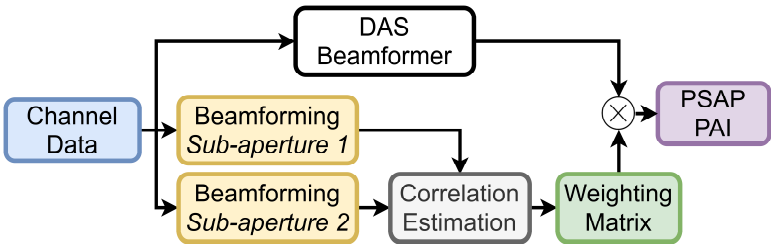

Figure 10.2 Schematic diagram presenting the PSAP method.

10.1.2 Weighting Matrix Generation for PSAP

Two approaches are reported in this chapter to generate the weighting matrix. The first approach is based on using 2-D normalized cross-correlation (NCC) termed as PSAP_{NCC} and second approach utilizes phase differences between sub-aperture beamformed images termed as $\text{PSAP}_{\text{Phase}}$.

10.1.2.1 PSAP$_{NCC}$ Weighting Matrix

Our first approach follows DAX weighting reported by Shin *et al.* [15] where the pixel-wise 2-D NCC coefficient, $\rho(i,j)$ at zero lag was computed between $\mathbf{S_1}$ and $\mathbf{S_2}$ to quantify the degree of similarity:

$$\rho(i,j)=\frac{\sum_{k=i-K}^{i+K}\sum_{h=j-H}^{j+H}\left(\mathbf{S_1}(k,h)-\overline{s}_1\right)\left(\mathbf{S}_2(k,h)-\overline{s}_2\right)}{\sqrt{\sum_{k=i-K}^{i+K}\sum_{j-H}^{j+H}\left(\mathbf{S_1}(k,h)-\overline{s}_1\right)^2\times\sum_{k=i-K}^{i+K}\sum_{j-H}^{j+H}\left(\mathbf{S}_2(k,h)-\overline{s}_2\right)^2}} \tag{10.2}$$

where, i and j denote i^{th} sample of j^{th} A-line with a kernel dimension of 2K+1 samples by 2H+1 A-lines, $\overline{s}_1$ and $\overline{s}_2$ are the mean values over the 2-D kernel. Using $\rho(i,j)$, the weighting matrix *NCCw(i,j)* was computed as follows [9]:

$$NCC_W(i,j)=\max\left(\rho(i,j),\varepsilon\right) \tag{10.3}$$

where, ε is a minimum NCC threshold value chosen to be 0.001 in this work. Here, signals with correlation values less than ε were considered as sidelobe and incoherent clutter and subsequently suppressed using the weighting matrix. In both sidelobe and incoherent clutter regions, typical NCC values are low ranging from -1 to -0.8. Thus, weighting DAS-beamformed RF data directly with the NCC matrix introduces a sign reversal rather than artifact suppression. Therefore, a max operator was used in equation (3) to ensure that the resultant weighting matrix has positive weights ranging from ε (0.001) to 1 resulting in 20log10(0.001) = 60 dB amplitude reduction applied to clutter signals [15]. Furthermore, NCC$_W$ calculation was robust to noise due the use of 2-D kernel and data up-sampling using linear interpolation, therefore no additional filtering (e.g., 2-D median filter) was necessary [15]. Finally, the DAS beamformed data was multiplied by the weighting matrix to generate a PSAP$_{NCC}$ image as shown:

$$PSAP_{NCC}(i,j) = NCC_W(i,j) \times DAS(i,j) \tag{10.4}$$

10.1.2.2 $PSAP_{Phase}$ Weighting Matrix

Since main lobe signals are highly correlated between sub-aperture beamformed images, they result in zero or small phase differences, whereas interfering signals will be out-of-phase resulting in an increased phase difference. Therefore, in our second approach, we utilized phase information derived from the complex cross-correlation between the sub-aperture beamformed images to determine the weighting matrix [10, 13]. For $\mathbf{S_1}$ and $\mathbf{S_2}$, corresponding complex valued IQ signals $\mathbf{s_1}$ and $\mathbf{s_2}$ were derived using Hilbert transformation. The complex cross-correlation function, *R* was calculated as follows:

$$R(i,j) = \mathbf{s_1}(i,j) \times \mathbf{s_2^*}(i,j) \tag{10.5}$$

The weighting matrix was determined using the phase angle of *R* to suppress any off-axis signals following an approach reported by Stanziola *et al.* [10] as shown below:

$$Phase_W(i,j) = \exp\left(-\frac{k^2}{k_0^2}\right) \tag{10.6}$$

where *k* denotes the phase angle of *R(i,j)* and k_0 is an empirically determined phase factor to attenuate out-of-phase signals. Phase$_W$ estimation is a point wise calculation (no kernel), thus the resultant weighting matrix was more sensitive to noise when compared to NCC$_W$. Therefore, 2-D median filtering was applied to the weighting matrix for reducing noise. Finally, the DAS beamformed data is multiplied by the weighting matrix to generate PSAP$_{Phase}$ images as shown:

$$PSAP_{Phase}(i,j) = Phase_W(i,j) \times DAS(i,j) \tag{10.7}$$

10.2 Description of Simulation and *in vivo* Validation Experiments

10.2.1 Numerical Simulations

All simulations were performed using the k-Wave MATLAB toolbox [20]. To detect PA channel data, a 128-element linear array transducer with 72-μm element width, 18-μm kerf and 84-MHz sampling frequency operating at a center frequency of 21-MHz, and 100% fractional bandwidth was modelled in k-Wave. For all simulations, the imaging field-of-view (FOV) was divided into a 2-D k-Wave grid having a node spacing of 15-μm in both axial and lateral directions. The speed of sound and medium density was assumed to be 1540 m/s and 1000 kg/m^3, respectively. For all quantitative evaluations, envelope detected PA beamformed data were used.

10.2.1.1 Point Target Simulation

Four 100-μm diameter spherical absorbers were placed in a homogenous background with zero optical absorption to model a point target numerical phantom. They were positioned along the vertical axis with an inter-point target separation of 4 mm starting from a depth of 8 mm from the transducer surface. Imaging FOV was 22 × 11.5 mm^2. Each point target had an initial pressure value of 3 Pa. Optical and acoustic attenuation was not simulated. For quantitative evaluation, the main-lobe-to-sidelobe (MLSL) ratio was computed [21]:

$$MLSL = 20 \times \log_{10}\left(\frac{\mu_{\max} - \mu_{\min}}{\sigma_n}\right) \tag{10.8}$$

where, $\mu_{\max}$ and $\mu_{\min}$ denote the maximum and minimum signal amplitude within a 2×5 mm^2 rectangular region-of-interest (ROI) centered on each point target and σ_n represents the standard deviation of signal amplitudes from two 2×2 mm^2 ROIs within the signal ROI. The full-width-at-

half-maximum (FWHM) at -6 dB was also calculated using 1-D lateral plots through the point targets, quantifying the distance in millimeters between points at the peak half maximum level.

10.2.1.2 Diffuse Inclusion Simulation

To understand how well PSAP preserves signals from diffuse targets, we performed simulations with inclusions having randomly distributed optical absorbers. A hybrid simulation approach using MCMatlab [22] and k-Wave [20] software packages was used [1]. Two 3 mm-diameter circular targets were placed along the vertical axis of a 16×11.5 mm^2 phantom at a depth of 7 mm and 13 mm, respectively. Each circular target contained randomly distributed optical absorbers with a spatial density of 299 absorbers/mm^2 [23, 24]. Ten independent optical absorber realizations were generated for statistical analysis. First, spatially variant (r = optical absorber spatial location) and wavelength (λ) dependent absorbed optical energy density [$A(\lambda,r)$] was calculated using MCMatlab with the simulation parameters listed in Table 10.1. Then, $A(\lambda,r)$ was utilized to determine the initial pressure distribution (p_0) for the acoustic simulation as follows [25]:

$$p_0(\lambda, r) = \Gamma \times A(\lambda, r) \tag{10.9}$$

where, Γ is the dimensionless Grueneisen parameter set to be 0.129 in this work [26]. To evaluate the performance of PSAP under varying level of channel noise, white noise was also added to the simulated channel data resulting in SNRs (SNR_c) ranging from -25 to 25 dB.

Quantitative analysis was done using contrast ratio (CR) and generalized contrast-to-ratio (gCNR) [23, 27] as described in **Chapter 09**.

Table 10.1 Diffuse Inclusion Optical Simulation Parameters

Parameter	Value	Unit
Simulation cuboid	1.6×1.2×0.5	cm^3
Water coupling layer	1	mm
Vessel absorption (μ_a at 7mm, 13 mm)	(4.43,5.60)	cm^{-1}
Vessel scattering (μ_s at 7mm, 13 mm)	(58.82,58.82)	cm^{-1}
Vessel oxygen saturation (7 mm, 13 mm)	(35.0,95.0)	%
Background absorption (μ_a)	0.01	cm^{-1}
Background scattering (μ_s)	10	cm^{-1}
Optical Wavelength	850	nm
Collimated top-hat beam radius	0.5	cm
Incident laser energy	30	mJ

10.2.1.3 Microvasculature Simulation

To understand how well PSAP preserves signals of interest in anatomically relevant heterogeneous media, we performed simulations mimicking typical *in vivo* microvasculature networks using 40 reference vascular images collected from the fundus oculi drive [28, 29]. Database contained binary images of blood vessels manually extracted from digital color images of the retina with white pixels denoting vessel segmentation. We use these binary images in our hybrid simulation framework to simulate raw channel data. First, optical absorbers were randomly distributed inside the blood vessels with a spatial density of 299 absorbers/mm^2. Then, MCMatlab [22] was used to derive the absorbed optical energy density [$A(\lambda,r)$] with parameters listed in Table 10.2. Finally, equation 12 was used to generate the initial pressure distribution and acoustic simulation was done using k-Wave [20]. CR and gCNR were computed for quantitative comparison. Rectangular ROIs containing vessel signals were defined randomly using ground truth images as target ROIs. The same ROIs were shifted to adjacent background locations and denoted as background ROIs.

Table 10.2 Microvasculature Optical Simulation Parameters

Parameter	Value	Unit
Simulation cuboid	1.6×1.2×0.5	cm^3
Water coupling layer	3	mm
Vessel absorption (μ_a)	5.6	cm^{-1}
Vessel scattering (μ_s)	58.82	cm^{-1}
Vessel oxygen saturation	75	%
Background absorption (μ_a)	0.01	cm^{-1}
Background scattering (μ_s)	10	cm^{-1}
Optical Wavelength	850	nm
Collimated top-hat beam radius	0.5	cm
Incident laser energy	30	mJ

10.2.2 In vivo Cardiac PAI Experiments

In vivo cardiac PAI data from five healthy murine models were collected using an experimental protocol approved by the Institutional Animal Care and Use Committee (IACUC) at the University of Wisconsin-Madison and described in detail in **Chapter 09** [1]. Data collection was done in PA RF mode to access raw channel data. Typical total acquisition time for *in vivo* data collection was 50 seconds. End-diastolic (ED) and end-systolic (ES) PAI frames were selected using reconstructed PAI M-mode images to perform quantitative analysis using CR and gCNR. Target ROIs were manually drawn on the epicardium and endocardium to locate myocardial wall PA signals. Then, the target ROIs were shifted to the left ventricular (LV) chamber and denoted as background ROIs. For delay-and-sum (DAS) PAI images, we have consistently observed dominant PA signals concentrated in the endocardial and epicardial walls corroborating findings from literature [30]. To ensure, that our quantitative analysis is not biased by PA signals that may appear as temporally varying noise between the endocardial and epicardial wall during cardiac motion, ROIs were limited only to the epicardial and endocardial walls. Therefore, the target ROI

was the summation of these two ROIs. Furthermore, shifting the target ROIs in the LV chamber ensured that both target and background ROIs had equal area during CR and gCNR evaluation.

10.2.3 Algorithm Implementation and Data Processing

All beamforming algorithms were implemented to run on a GPU in MATLAB (Mathworks Inc., MA) for cross-platform acceleration. DAS and DAS_{CF} (DAS with coherence factor weighting) beamforming were included in a comparative study and described in detail in **Chapter 09**. DAS and DAS_{CF} beamforming were performed using a 64-element, dynamic apodization having a constant f-number of 1 and uniform aperture weighting. With the 64-element aperture, apodization was constant after 5.76 mm. For both $PSAP_{NCC}$ and $PSAP_{Phase}$, sub-aperture data were upsampled by a factor of 2 both axially and laterally using linear interpolation before calculating the weighting matrix [31, 32]. Upsampling was done to improve robustness of NCC and phase estimation. Default parameter settings for $PSAP_{NCC}$ and $PSAP_{Phase}$ are summarized in Table 10.3 and Table 10.4, respectively. Choice of these parameters are justified in Sections 1.3 and 1.4 where simulation and experimental results are discussed. One-way analysis of variance (ANOVA) with the Bonferroni multiple comparison test was used to determine statistical significance among DAS, DAS_{CF}, $PSAP_{NCC}$ and $PSAP_{Phase}$. Statistical analysis was performed using SPSS Version 23 (IBM SPSS Statistics for Windows, Version 23.0, IBM Corp., Armonk, NY, USA).

Table 10.3 $PSAP_{NCC}$ Parameters

Experiment	Parameter	Value
Point Target	Sub-aperture alternating elements (N) 2-D NCC Kernel (Wavelength, A-lines)	8-8 (4.5λ,3)
Diffuse Inclusion Microvasculature *In vivo*	Sub-aperture alternating elements (N) 2-D NCC Kernel (Wavelength, A-lines)	2-2 (1.5λ,3)

Table 10.4 $PSAP_{Phase}$ Parameters

Experiment	Parameter	Value
Point Target	Sub-aperture alternating elements (N)	8-8
	Phase factor (k_0)	$\pi/9$
	Median filter kernel (pixels, pixels)	(11,11)
Diffuse Inclusion Microvasculature *In vivo*	Sub-aperture alternating elements (N)	2-2
	Phase factor (k_0)	$\pi/3.5$
	Median filter kernel (pixels, pixels)	(5,5)

10.3 Findings from Numerical Simulation Studies

10.3.1 Point Target Simulation

Figure 10.3 (a) – (d) show beamformed images obtained using DAS, DAS_{CF}, $PSAP_{NCC}$ and $PSAP_{Phase}$, respectively. Significant sidelobes are apparent in the DAS image, that are suppressed by both CF weighting and PSAP. Qualitatively, DAS_{CF} provided the best reconstructed image.

Figure 10.4 (a) – (b) show the lateral profiles of the point spread function (PSF) at depths of 8 and 20 mm respectively. Both CF and PSAP significantly reduced sidelobe levels when compared to DAS but DAS_{CF} had better lateral resolution. Table 10.5 summarizes MLSL and FWHM at -6 dB. The best and worst values of MLSL and FWHM were denoted with blue and red colors respectively in Table 10.5. Results show that both CF and PSAP provide better image quality than DAS. They also have the lowest MLSL and highest FWHM values at all depths coorborating our qualitiave observations from Figure 10.3 – Figure 10.4.

The variation in MLSL and FWHM as a function of alternating element numbers is shown in Figure 10.5. Note the trade-off between MLSL [Figure 10.5 (a) – (b)] and resolution [Figure 10.5 (c) – (d)] when selecting the alternating element numbers. We observed reduction in MLSL for all point targets (red, blue and green curves) except at 20 mm depth with the 16-16 alternating

pattern when compared to 8-8 for $PSAP_{NCC}$. For $PSAP_{Phase}$, a MLSL peak was achieved for all targets using the 8-8 alternating pattern except the one at 8 mm which shows a slight reduction from its peak. These observations suggest that selecting alternating element numbers with an 8-8 pattern achieves a balance for both $PSAP_{NCC}$ and $PSAP_{Phase}$. The results also suggest that lower N is preferred for shallower depth [red curves in Figure 10.5 (a) – (b)] and vice versa [black curves in Figure 10.5 (a) – (b)].

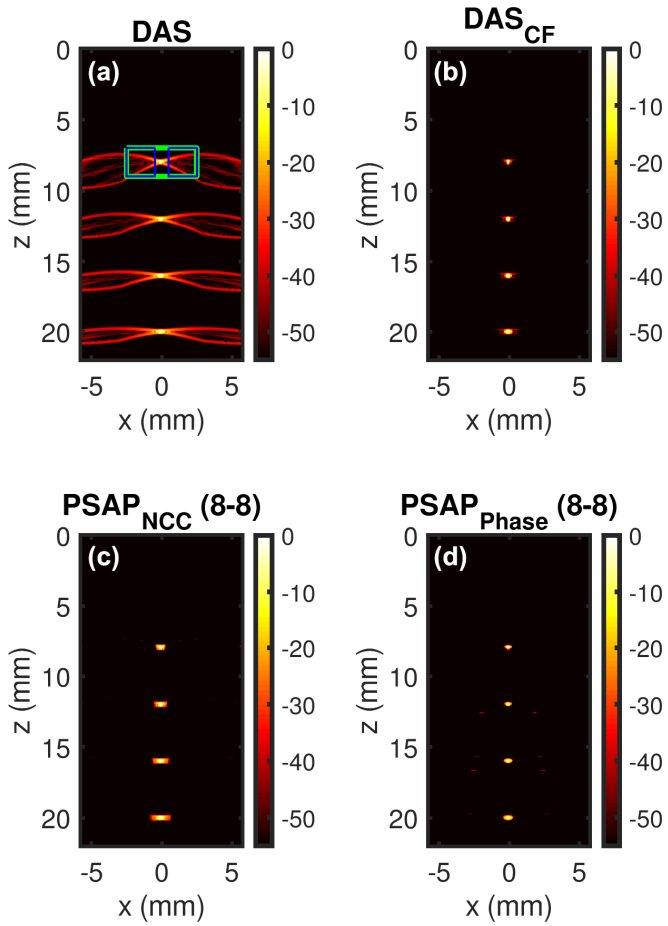

Figure 10.3 Beamformed images of simulated point targets (a) DAS, (b) DAS_{CF}, (c) $PSAP_{NCC}$ (8-8) and (d) $PSAP_{Phase}$ (8-8). Display dynamic range is 55 dB. Green and blue rectangles denote signal and noise ROIs, respectively. For $PSAP_{NCC}$ and $PSAP_{Phase}$, axial kernel length and phase factor (k_0) were 4.5λ and $\pi/9$ respectively.

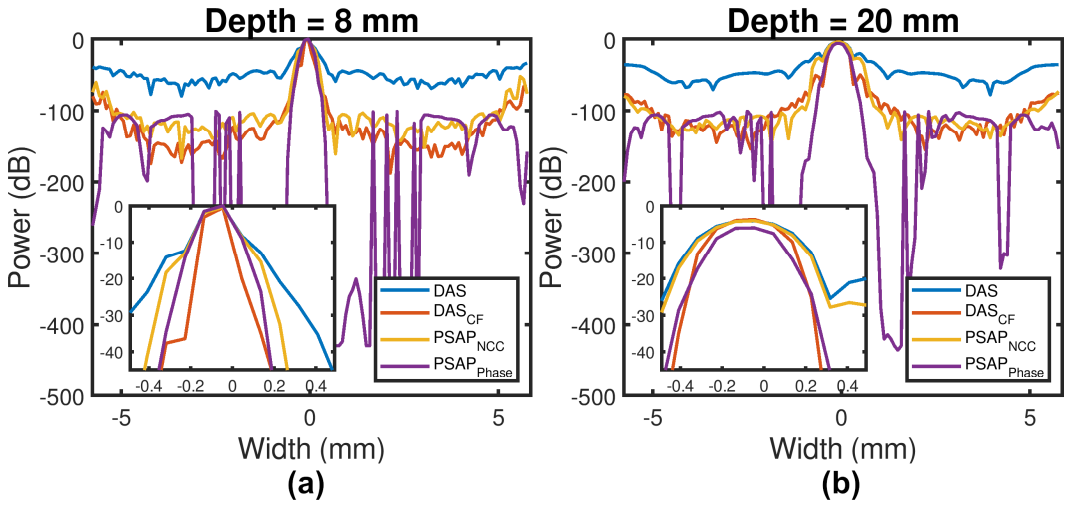

Figure 10.4 Lateral profiles of PSF of at depth of (a) 8 mm and (b) 20 mm for all methods. Both CF and PSAP significantly reduced sidelobe level of DAS.

Table 10.5 Comparison of MLSL (dB) and FWHM at -6 dB Values*

	MLSL (dB)				FWHM at -6 dB (mm)			
Depth (mm)	DAS	DAS_{CF}	$PSAP_{NCC}$	$PSAP_{Phase}$	DAS	DAS_{CF}	$PSAP_{NCC}$	$PSAP_{Phase}$
8	41.15	75.7	70.5	80.3	0.21	0.17	0.21	0.20
12	38.16	70.4	71.2	57.8	0.32	0.24	0.30	0.29
16	35.91	66.0	60.4	59.1	0.41	0.33	0.40	0.36
20	33.81	61.8	46.5	80.7	0.53	0.41	0.50	0.38

*The best and worst values are in blue and red colors, respectively.

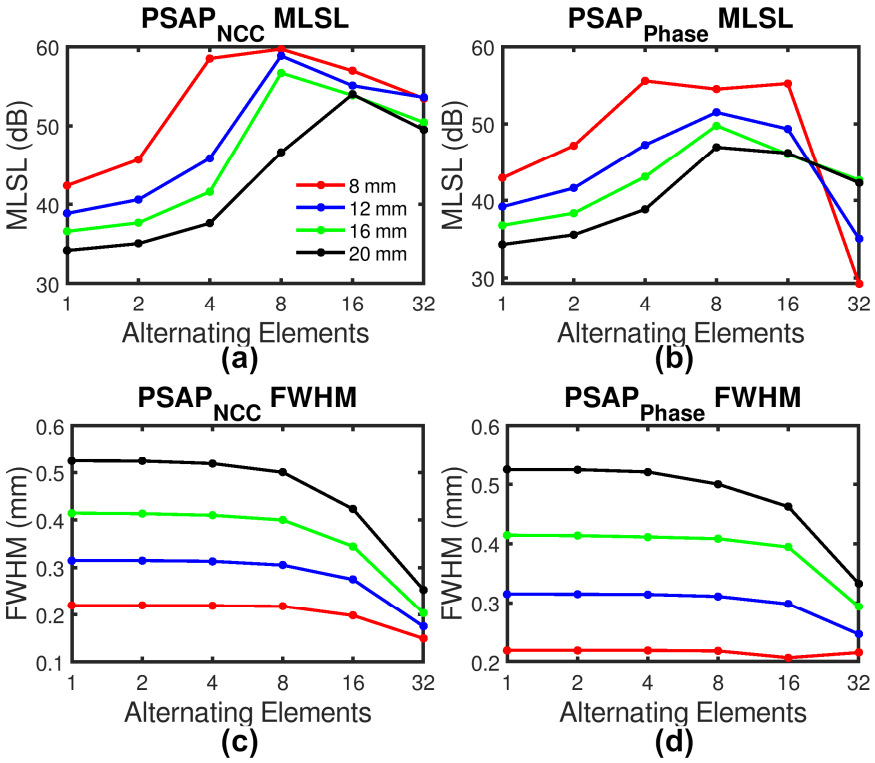

Figure 10.5 Variation of MLSL with alternating element number for (a) $PSAP_{NCC}$ and (b) $PSAP_{Phase}$ respectively. Variation of FWHM at -6 dB with alternating element number for (a) $PSAP_{NCC}$ and (b) $PSAP_{Phase}$ respectively. For $PSAP_{NCC}$ and $PSAP_{Phase}$, axial kernel length and phase factor (k_0) were 2.5λ and $\pi/3$ respectively.

The performance of $PSAP_{NCC}$ as a function of axial kernel length are shown in Figure 10.6. With higher axial kernel lengths, a steady improvement in MLSL was seen for shallower targets when compared to deeper targets with no signifcant variation at 20 mm as shown in Figure 10.6 (a) – (e). Higher axial kernel lengths did not impact FWHM except for the 20 mm target [Figure 10.6 (f)]. A 8-8 alternating pattern was used.

Figure 10.7 shows $PSAP_{Phase}$ performance as a function of phase factor (k_0). Better sidelobe suppression was achieved with lower phase factors resulting in higher MLSL values as seen in Figure 10.7 (a) – (e). Furthermore, reduction of FWHM values at depth was observed with

lower k_0 [Figure 10.7 (f)]. A 8-8 alternating pattern was used. These results indicate that the phase factor can be adjusted to adatively control the level of sidelobe suppression of coherent targets.

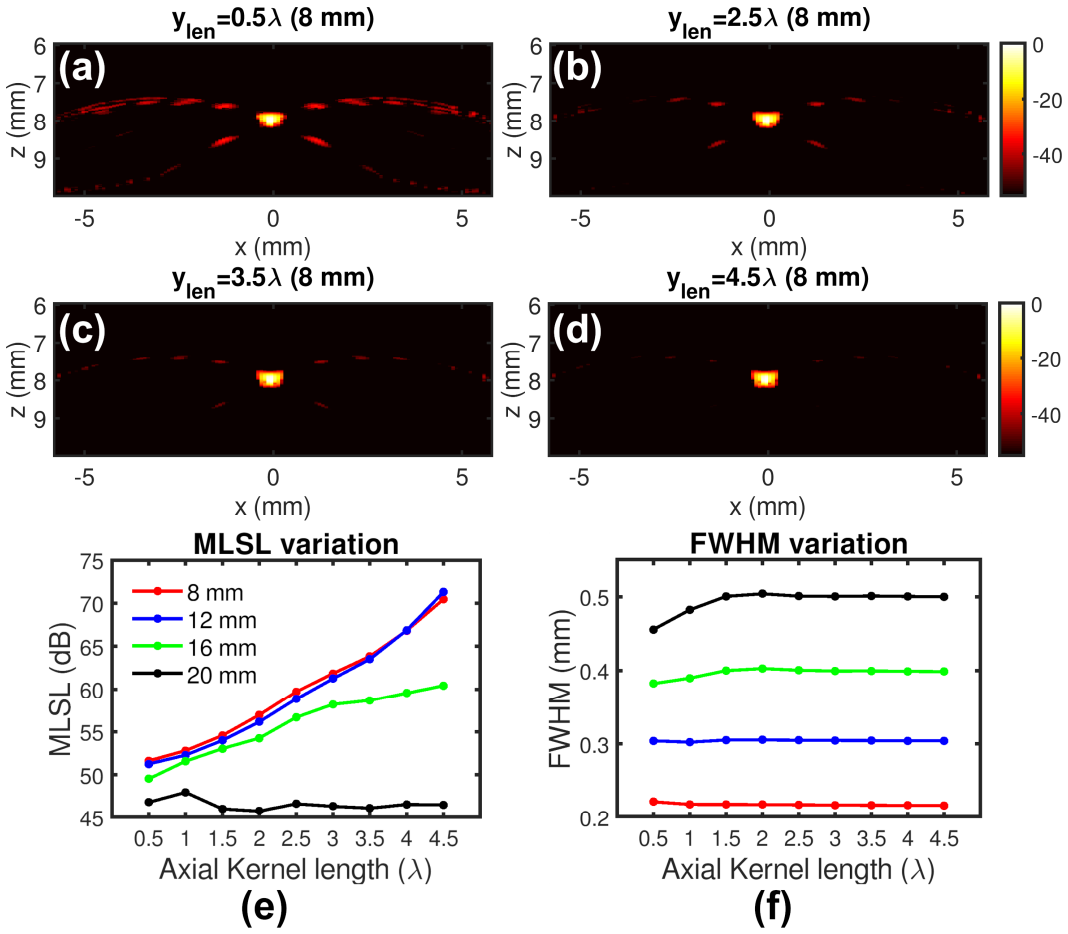

Figure 10.6 Variation of $PSAP_{NCC}$ performance with axial kernel length. Point target at 8 mm depth beamformed using an axial kernel length of (a) 0.5λ, (b) 2.5λ, (c) 3.5λ and (d) 4.5λ respectively. Variation of MLSL and FWHM at -6 dB are shown in (e) and (f) respectively.

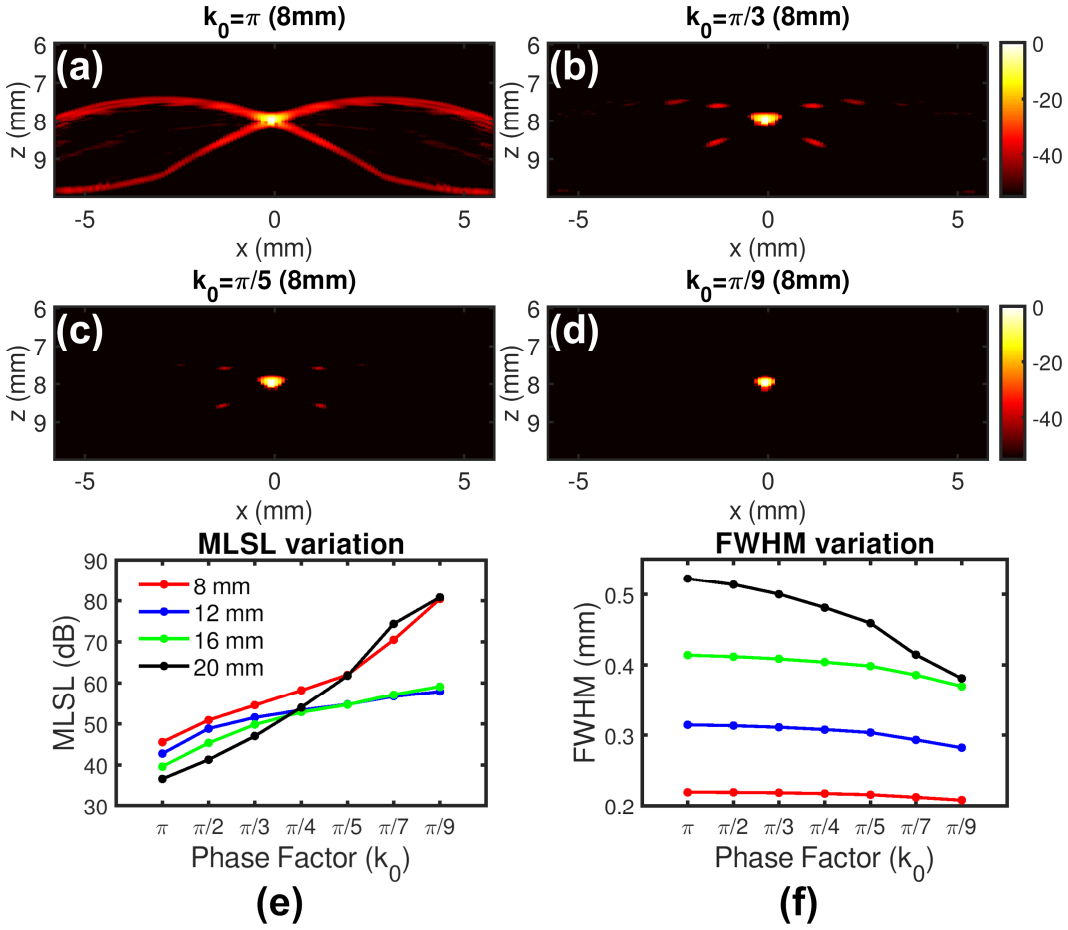

Figure 10.7 Variation in $PSAP_{Phase}$ performance with phase factor. Point target at 8 mm depth beamformed using a phase factor of (a) π, (b) $\pi/3$, (c) $\pi/5$ and (d) $\pi/9$ respectively. Variation of MLSL and FWHM at -6 dB are shown in (e) and (f) respectively.

10.3.2 Diffuse Inclusion Simulation

Representative qualitative results with diffuse inclusions are shown in Figure 10.8. Figure 10.8 (a) – (e) show the ground truth initial pressure disribution, along with the reconstrcuted images using DAS, DAS_{CF}, $PSAP_{NCC}$ and $PSAP_{Phase}$, respectively. Strong sidelobes are seen in the DAS image [Figure 10.8 (b)]. CF reduced sidelobes seen with DAS along with the undesirable supression of PA signals inside the inclusion [Figure 10.8 (c)]. On the other hand, $PSAP_{NCC}$ and $PASP_{Phase}$ produced higher quality images with reduced sidelobe and better PA signal preservation

inside the inclusion that more closely resembled ground truth image [Figure 10.8 (d) – (e)]. However, strong sidelobes near the border of the shallow target in Figure 10.8 (b) causes positive correlation between sub-aperture images with the chosen parameters. This resulted in additional noise in the border regions of the PSAP images [Figure 10.8 (d) – (e)].

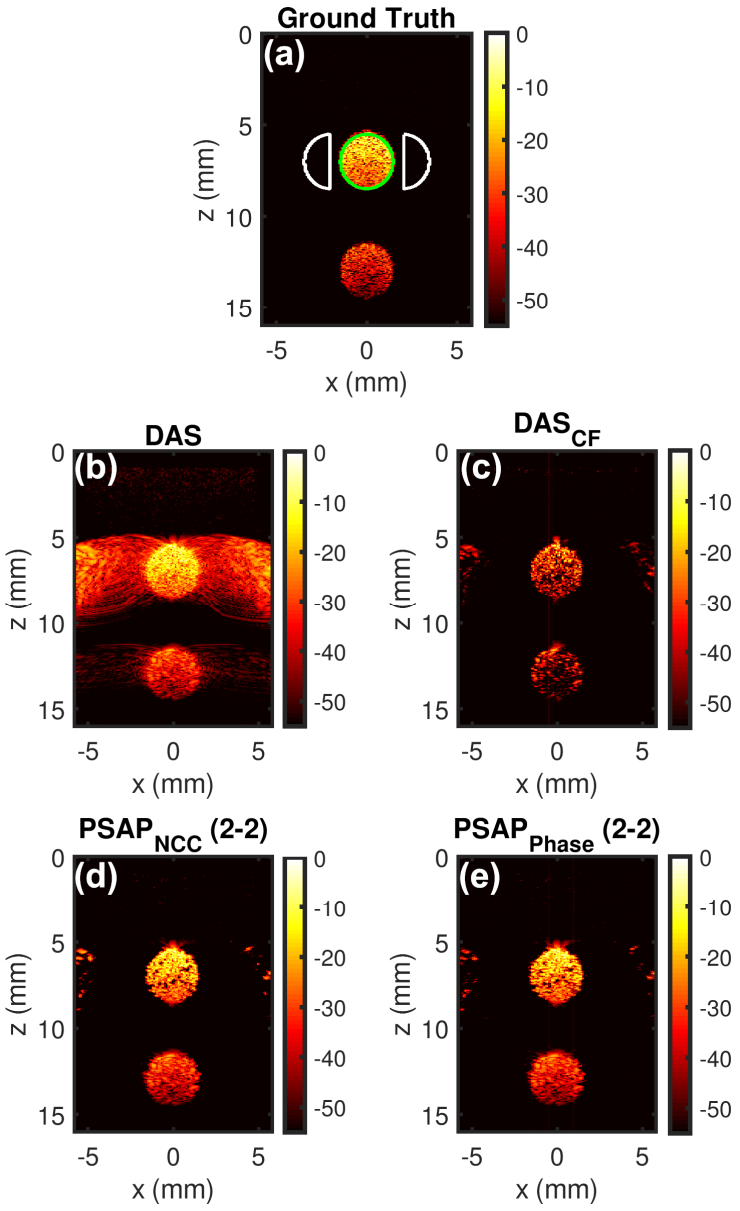

Figure 10.8 Beamformed images of simulated 3-mm diameter diffuse targets. (a) ground truth initial pressure distribution, (b) DAS, (c) DAS_{CF}, (d) $PSAP_{NCC}$ (2-2) and (e) $PSAP_{Phase}$. (2-2). Display dynamic range is 55 dB. Green and white ROIs denote signal and noise ROIs, respectively.

Figure 10.9 (a) – (c) present the CF, NCC_W and $Phase_W$ weighting matrices used to obtain the corresponding DAS_{CF}, $PSAP_{NCC}$ and $PSAP_{Phase}$ images shown in Figure 10.8. A linear scale ranging from 0 to 1 was used to display the results. Observe that the CF weighting matrix had unusable lower weight values inside both lesions. However, NCC_W and $Phase_W$ both robustly estimated higher weighting values insde the lesions and lower weighting values inside sidelobe and clutter regions, thus hindering the undesirable signal suppression observed in the DAS_{CF} result (Figure 10.9 (c)).

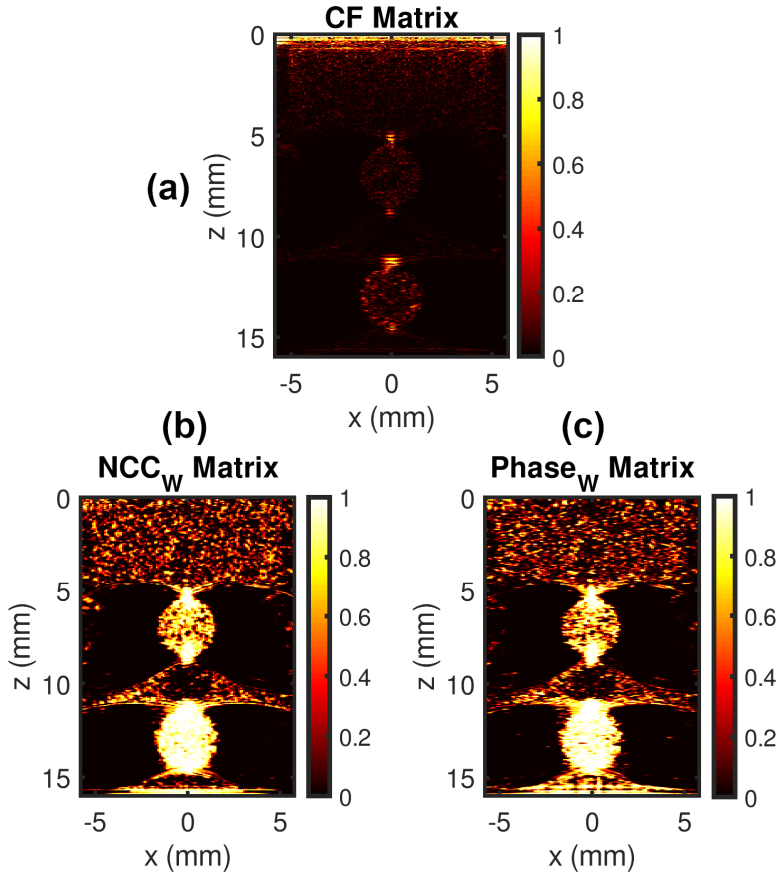

Figure 10.9 Weighting matrix comparison between CF and PSAP processing in diffuse inclusion simulation. (a) – (c) show CF, NCC_W and $Phase_W$ weighting matrix respectively in a linear scale from 0 to 1.

Figure 10.10 summarizes statistical analysis, where both CF and PSAP show statistically significant differences in CR when compared to DAS with PSAP methods achieving the highest

values [Figure 10.10 (a) – (b)]. PSAP significantly improved inclusion detectability when compared to both DAS and DAS_{CF} as shown in Figure 10.10 (c) – (d) where $PSAP_{NCC}$ and $PSAP_{Phase}$ had higher gCNR values ($p<0.001$) with no significant differences between each other.

The choice of sub-aperture patterns was also investigated for diffuse inclusions. Figure 10.11 (a) and (b) show that peak CRs for inclusions located at shallower and deeper depth were achieved with 2-2 and 4-4 alternating patterns respectively for both $PSAP_{NCC}$ and $PSAP_{Phase}$. But gCNR results [Figure 10.11 (c) – (d)] show peaks with 2-2 alternating pattern indicating an ideal choice for diffuse inclusion detection. Thus, the 2-2 alternating pattern was chosen for subsequent analysis of microvasculature simulations and *in vivo* data.

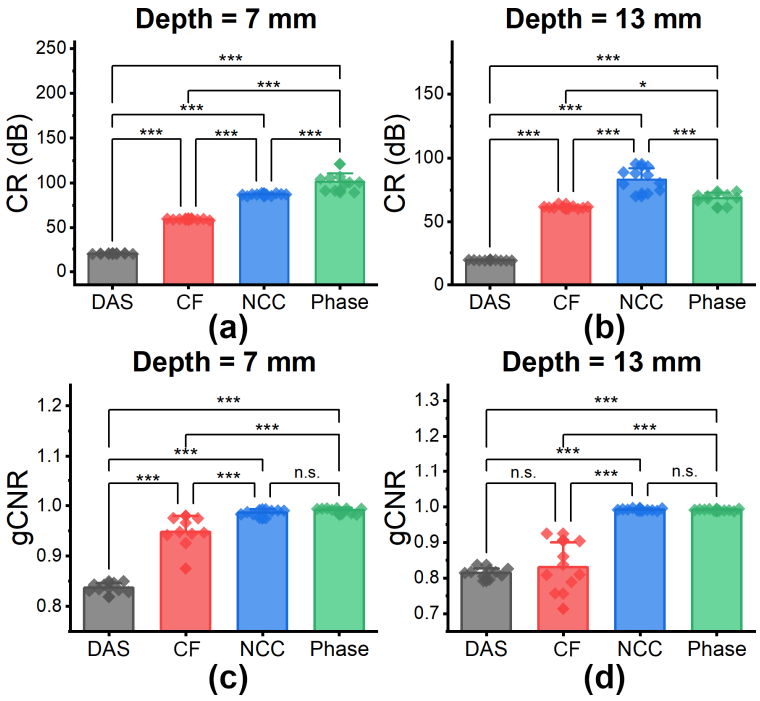

Figure 10.10 Statistical analysis for performance comparison among DAS, DAS-CF and PSAP (*n = 10*). Comparison of CR for lesions located at a depth of (a) 7 mm and (b) 13 mm respectively. Comparison of gCNR for lesions located at a depth of (a) 7 mm and (b) 13 mm respectively. Here, **** is p<0.001*.

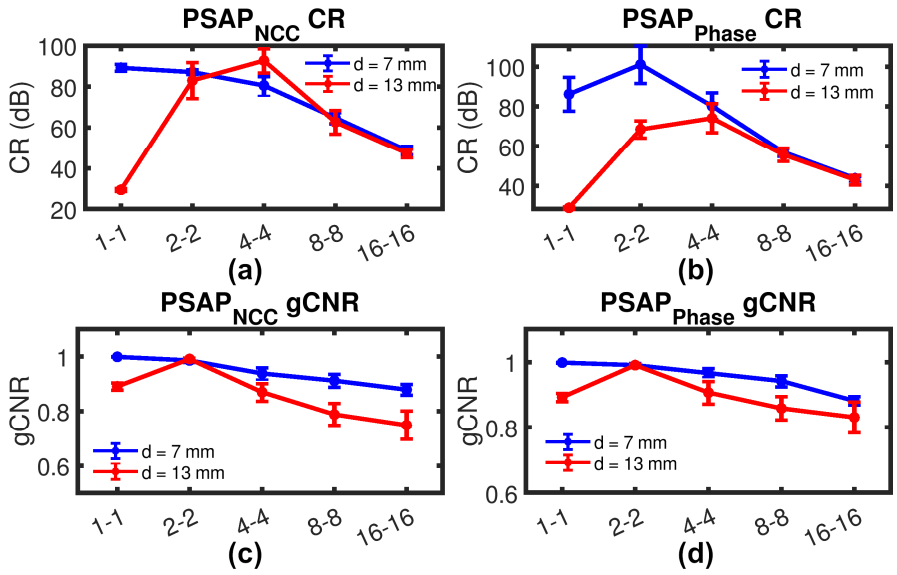

Figure 10.11 Impact of sub-aperture size on lesion contrast and detectability. CR variation with the choice of sub-aperture for (a) $PSAP_{NCC}$ and (b) $PSAP_{Phase}$ respectively. gCNR variation with the choice of sub-aperture for (c) $PSAP_{NCC}$ and (d) $PSAP_{Phase}$ respectively.

Variations in CR and gCNR as a function of channel SNR (SNR_c) is presented in Figure 10.12. Figure 10.12 (a) – (b) show CR variations at depths of 7 and 13 mm, respectively. For the 7 mm deep inclusion, DAS_{CF}, $PSAP_{NCC}$ and $PSAP_{Phase}$ present with higher CR than DAS for all SNR_c levels. $PSAP_{NCC}$ and $PSAP_{Phase}$ showed higher CR values than DAS_{CF} for SNR_c < -15 dB (Figure 10.12 (a)). At the deeper depth (13 mm), DAS_{CF}, $PSAP_{NCC}$ and $PSAP_{Phase}$ had higher CR than DAS for SNR_c < -15 dB after which the inclusion is not visualized due to high noise levels. Figure 10.12 (c) – (d) show gCNR variation at depths of 7 and 13 mm, respectively. Figure 10.12 (c) shows that PSAP results had higher gCNR than DAS and DAS_{CF} for the shallow target at all SNR_c levels. For the deeper target, PSAP results had higher gCNR for low levels of noise (SNR_c > 5 dB) after which the results converge to the results obtained with DAS_{CF}. DAS_{CF}, $PSAP_{NCC}$ and $PSAP_{Phase}$ had higher gCNR than DAS for SNR_c < -15 dB after which the inclusion was not distinguished from the background.

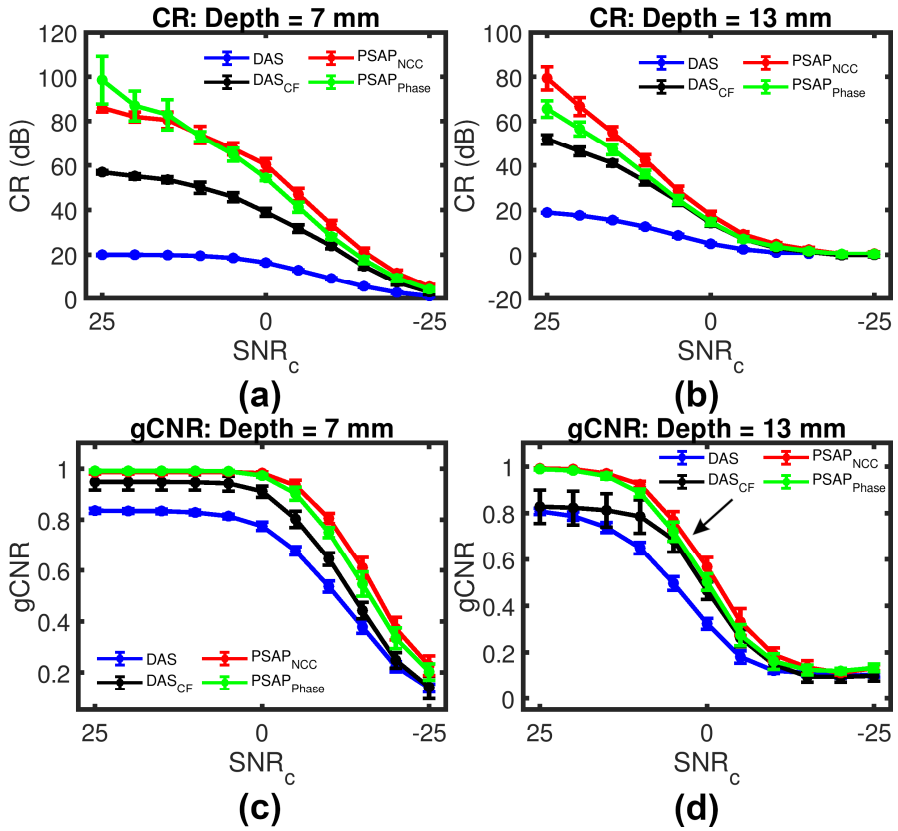

Figure 10.12 Diffuse inclusion simulation CR and gCNR analysis as function of channel SNR. (a) – (b) CR variation at a depth of 7 and 13 mm, respectively. (c) – (d) gCNR variation at a depth of 7 and 13 mm, respectively.

Table 10.6 provides computational times computed over ten simulation instances of the diffuse inclusion simulation. Note that, PSAP requires more computational time due to additional sub-aperture beamforming and weighting matrix calculation.

Table 10.6 Summary of Computational Times (Secs)

Experiment	DAS & DAS_{CF}	$PSAP_{NCC}$	$PSAP_{Phase}$
Diffuse Inclusion*	0.14	0.33	1.85

* Average time over 10 simulation realizations

10.3.3 Microvasculature Simulation Results

A representative result from the microvasculature simulation is shown in Figure 10.13 (a) – (e) with ground truth initial pressure disribution, reconstructed images with DAS_{CF}, $PSAP_{NCC}$ and $PSAP_{Phase}$, respectively. Representative target and background ROI definitions for quantitative analysis are shown in Figure 10.13. DAS image show severe clutter artifacts due to high sidelobe levels. With CF, clutter was reduced but the PA signal amplitude inside blood vessels were also undesirably suppressed thus negatively impacting deeper vessel detectability. $PSAP_{NCC}$ and $PSAP_{Phase}$ produced significantly better images when compared to DAS and DAS_{CF} achieving both clutter supression and blood vessel PA signal preservation. Figure 10.13 (f) shows the axial profiles across the blue line ROI shown in Figure 10.13 (a). Note that PSAP preserves DAS amplitude levels in the blood vessels and at the same time reduces clutter compared to DAS_{CF}.

Figure 10.14 demonstrates that statistically significant improvements in CR and gCNR were achieved with PSAP when compared to DAS and DAS_{CF}. Figure 10.14 also demonstrate that CF weighting stretches the dynamic range resulting in higher CR without improving the target detectability (no significant difference between DAS and DAS_{CF} gCNR values). With PSAP, improvements both in contrast and target detectability was achieved. The choice of sub-aperture was also investigated for microvasculature simulations as shown in Figure 10.15. Peak CR and gCNR values were obtained with the 2-2 alternating pattern for both $PSAP_{NCC}$ and $PSAP_{Phase}$. Figure 10.15 also shows that performance can be severely impacted if larger number of alternating elements are chosen.

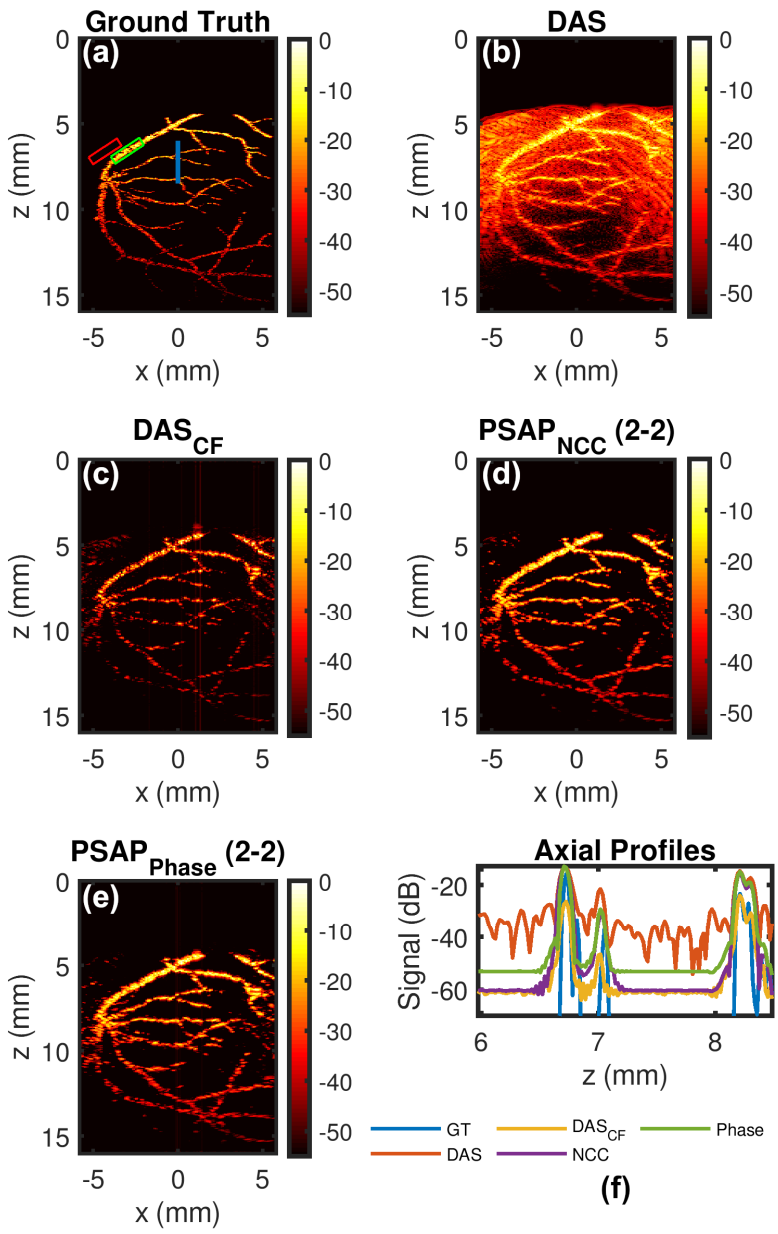

Figure 10.13 Beamformed images of simulated microvasculature. (a) ground truth initial pressure distribution, (b) DAS, (c) DAS_{CF}, (d) $PSAP_{NCC}$ (2-2) and (e) $PSAP_{Phase}$. (2-2). Signal variation across an axial line ROI shown in (f). Display dynamic range is 55 dB. Green and red rectangles in (a) denote signal and clutter ROIs, respectively. Blue line in (a) denotes axial profile ROI.

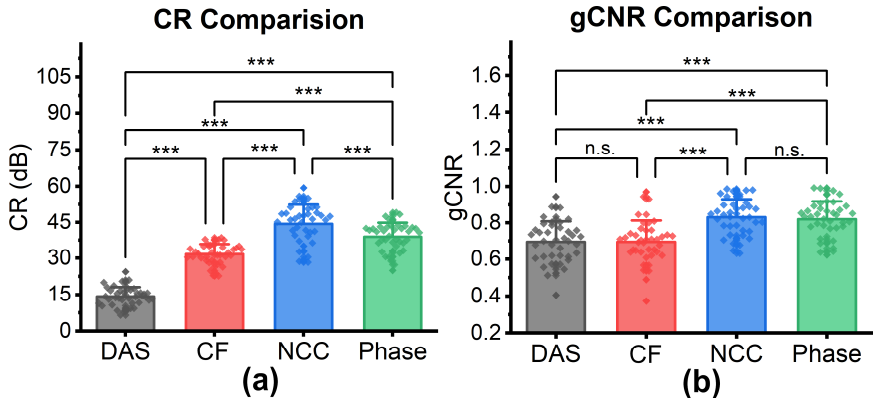

Figure 10.14 Statistical analysis for performance comparison among DAS, DAS_{CF} and PSAP (*n = 40*). Comparison of (a) CR and (b) gCNR for microvasculature simulation data. Here, *** is p<0.001.

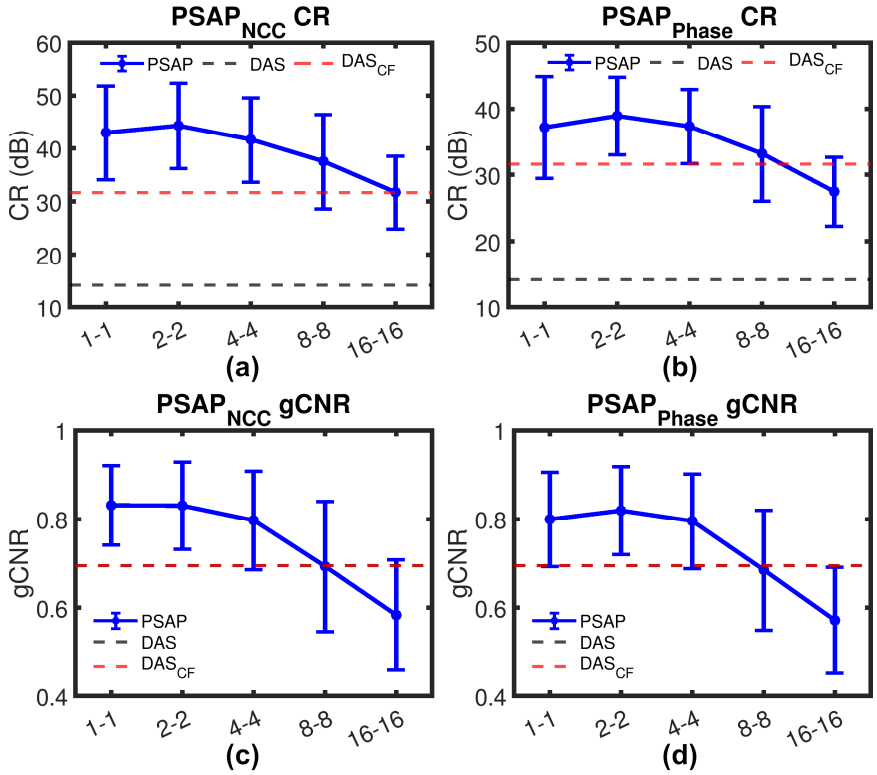

Figure 10.15 Impact of sub-aperture size on microvasculature contrast and detectability. CR variation with the choice of subaperture for (a) $PSAP_{NCC}$ and (b) $PSAP_{Phase}$ respectively. gCNR variation with the choice of subaperture for (c) $PSAP_{NCC}$ and (d) $PSAP_{Phase}$ respectively.

10.4 Experimental Findings from *in vivo* Cardiac PAI Study

Figure 10.16 (b) – (e) shows *in vivo* cardiac PA images at ED reconstructed using DAS, DAS_{CF}, $PSAP_{NCC}$ and $PSAP_{Phase}$, respectively. Corresponding US B-mode image with PAI aquisition ROI and relevant anatomical locations is shown in Figure 10.16 (a). Myocardial wall PA signals and background clutter signals are shown in blue and white ROIs in the DAS image. Note that DAS_{CF} reduced clutter signals with simualtanous supression of myocardial wall PA signals. On the other hand, $PSAP_{NCC}$ and $PSAP_{Phase}$ showed improved myocardial wall signal specificity and reduced clutter in the LV chamber and thus provided higher quality image when compared to DAS and DAS_{CF}. *In vivo* cardiac PA images at ES are shown in Figure 10.17, we observe similar findings as in ED images. Figure 10.18 shows that $PSAP_{NCC}$ and $PSAP_{Phase}$ had higher CR and gCNR values compared to DAS and DAS_{CF}.

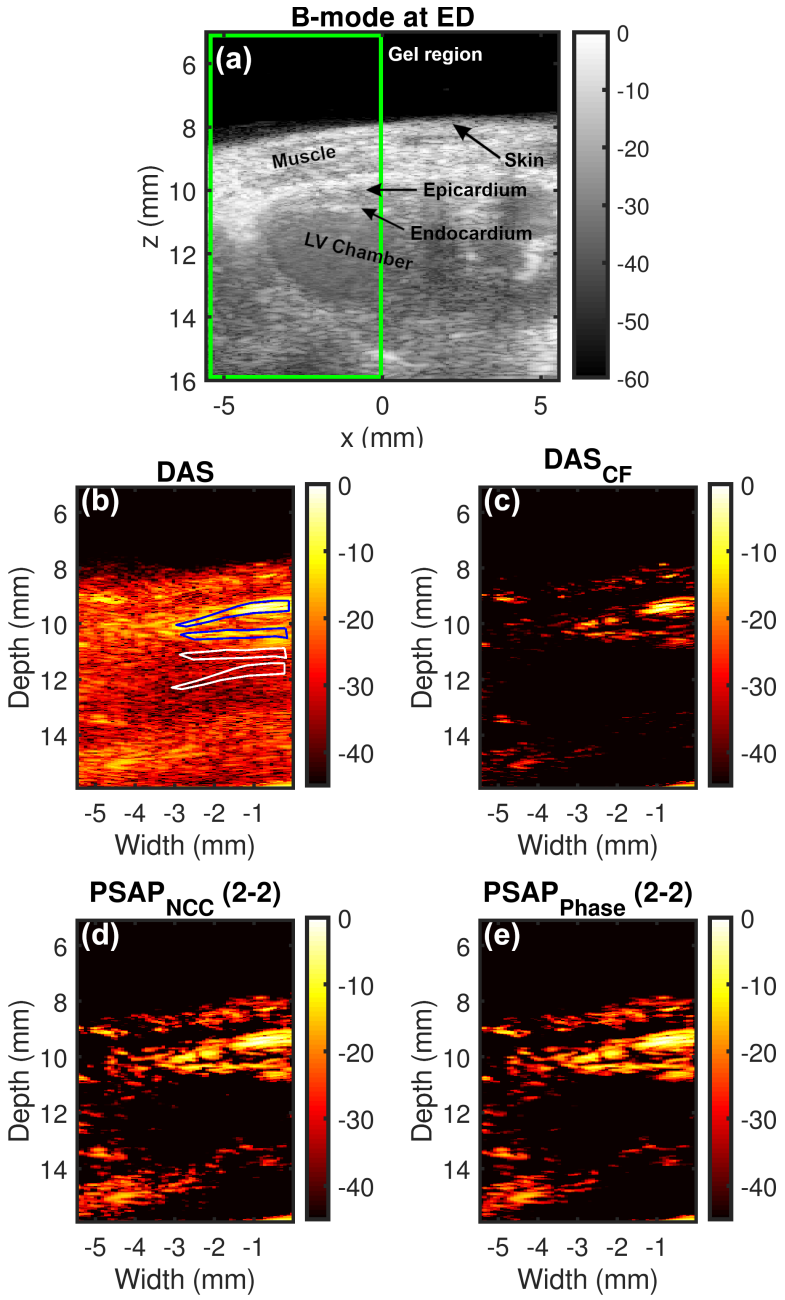

Figure 10.16 *In vivo* cardiac photoacoustic images at ED. (a) US B-mode, (b) (b) DAS, (c) DAS_{CF}, (d) $PSAP_{NCC}$ (2-2) and (e) $PSAP_{Phase}$. (2-2). Green rectangle denotes PAI ROI. Blue and white ROIs indicate myocardial wall and clutter signals respectively.

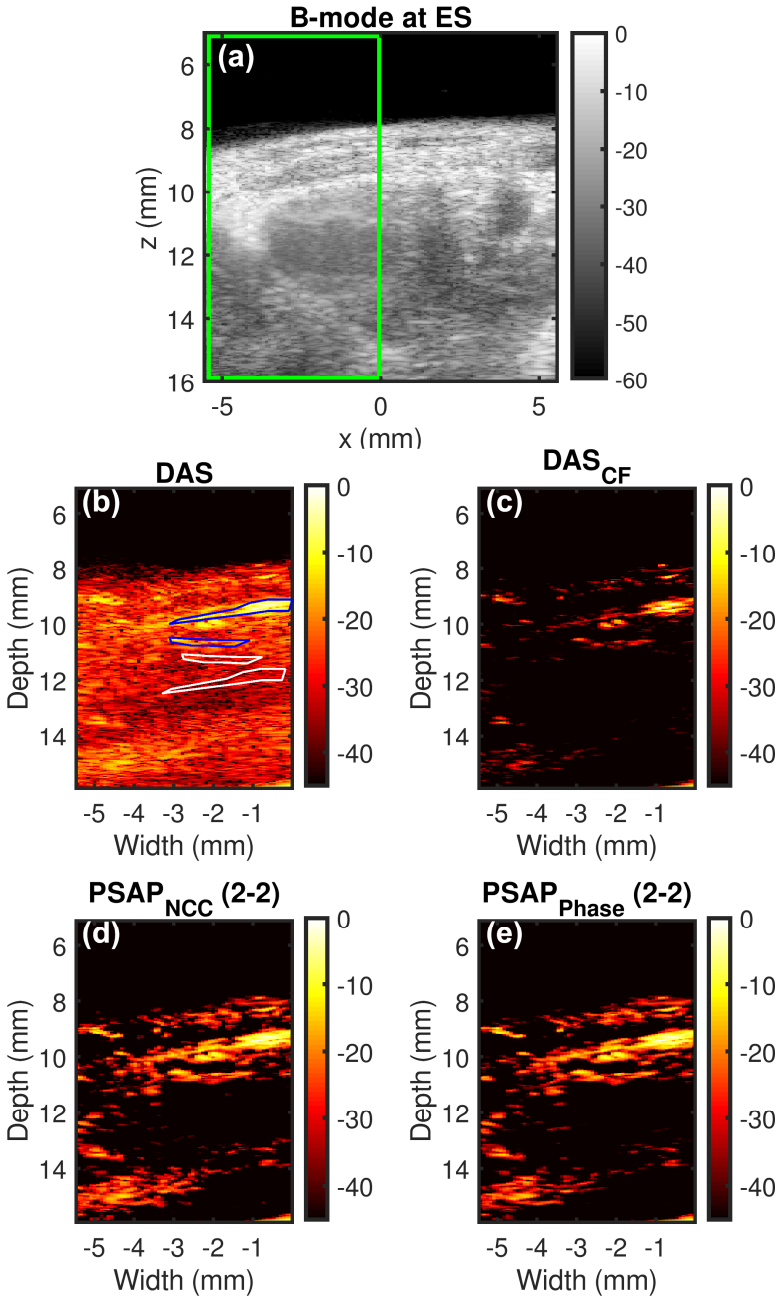

Figure 10.17 *In vivo* cardiac photoacoustic images at ES. (a) US B-mode, (b) (b) DAS, (c) DAS_{CF}, (d) $PSAP_{NCC}$ (2-2) and (e) $PSAP_{Phase}$. Green rectangle denotes PAI ROI. Blue and white ROIs indicate myocardial wall and clutter signals respectively.

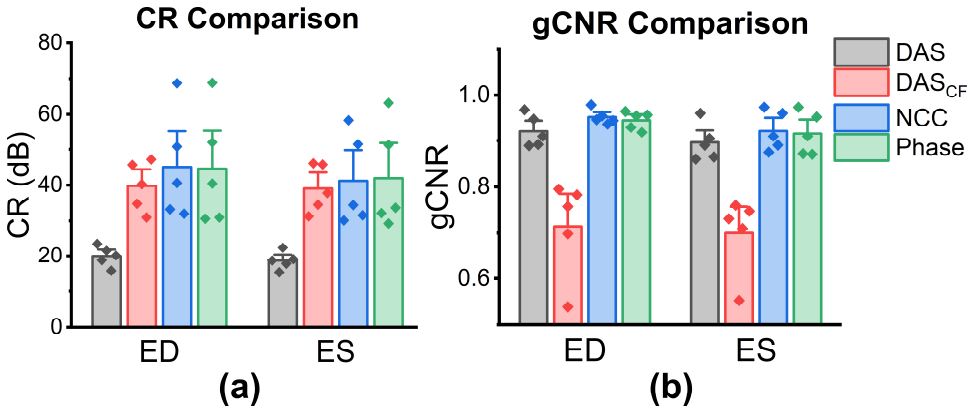

Figure 10.18 *In vivo* statistical analysis for performance comparison among DAS, DAS$_{CF}$ and PSAP (*n* = *5*). (a) and (b) show CR and gCNR. *n = 5* corresponds to the number of animal models.

10.5 Discussion on the implication of using PSAP algorithms for PAI beamforming

In this chapter, we presented our PSAP algorithms, validated using numerical simulations and *in vivo* animal studies both qualitatively and quantitatively. The key findings from these studies can be summarized as follows.

a) PSAP reduces PA clutter seen in DAS PA images utilizing similarity information between sub-aperture beamformed images.
b) PSAP improves PA target detectability at all depths by preserving DAS signal amplitude inside the target while achieving CF like clutter suppression in the background.
c) Optimal PSAP performance is parameter dependent and varies with application.

The variation in DAS image quality with f-number was evaluated using both point target and diffuse inclusion simulations. A f-number of 1 was chosen as it provided higher MLSL for point targets and higher CR and gCNR for inclusions **(Appendix A: DAS and DAS$_{CF}$ Performance Optimization for PSAP Comparison Study)**. For coherent targets, PSAP reduces DAS sidelobe levels when compared to DAS$_{CF}$ while maintaining DAS resolution [Figure 10.3 and Figure 10.4]. But DAS$_{CF}$ provided the best quality images in terms of MLSL and FWHM with comparable performance with PSAP [Table 10.5]. For PSAP$_{NCC}$ and PSAP$_{Phase}$, choice of the

alternating sub-aperture element number (N) showed a depth-dependent variation in MLSL [Figure 10.5]. Varying the alternating pattern affects the PSF shape generated by each sub-aperture which in turn changes the correlation of sidelobe signals [10]. Furthermore, from the DAS image [Figure 10.3 (a)], we observe depth-dependent variation of full aperture PSF due to variation in scattering intensity over depth [10]. Thus, larger number of alternating elements provide better MLSL deeper in tissue with 8-8 achieving a balance.

Two key algorithmic parameters – axial kernel length for PSAP-NCC and phase factor for PSAP-Phase were also investigated. Figure 10.6 (a) – (d) and Figure 10.7 (a) – (d) show that lower axial kernel length and higher phase factor introduces positive correlation between sub-aperture beamformed images in sidelobe regions resulting in point-like artifacts in the images. These artifacts were seen in point target simulations due to the strong sidelobes in the original DAS image. Increasing axial kernel length steadily improved MLSL for shallower targets [8 and 12 mm shown by red and blue curves in Figure 10.6 (e)] as they had wider sidelobes when compared to deeper targets [16 and 20 mm shown by green and black curves in Figure 10.6 (e)]. On the other hand, we observed steady improvement in performance (MLSL and FWHM) when lower phase factor values were chosen for $PSAP_{Phase}$ [Figure 10.7]. Therefore, these results suggest that both axial kernel length and phase factor values should be adjusted based on the application to achieve desired sidelobe suppression. Overall, the results from point target simulations suggest that larger alternating element number (8-8), higher axial kernel length and lower phase factor is preferred when using PSAP for coherent target PAI [10].

Several groups including ours have reported on CF weighting for sidelobe lobe suppression [1, 3, 5, 33, 34]. However, analysis in this chapter shows that although CF weighting suppresses clutter signals, it also leads to undesirable target PA signal suppression specifically at depths where

the target signal is weaker due to optical attenuation [Figure 10.8 and Figure 10.13]. CF was originally developed for US imaging to tackle phase aberration [35] and utilizes very strict measures of coherence. This causes weak PA signals at depth to have lower coherence values thus suppressing them at the level of clutter signals. On the other hand, our PSAP approaches separate target PA signals from clutter using correlation (amplitude and phase) between sub-aperture beamformed images. Here, target PA signals were highly correlated both at shallower and deeper depths when compared to clutter signals due to the use of non-overlapping sub-apertures [9, 10, 13, 15]. Therefore, weaker PA signals at depth were better preserved with PSAP when compared to CF. Quantitative results show that DAS_{CF}, $PSAP_{NCC}$ and $PSAP_{Phase}$ provide higher CR values than DAS. However, we are also interested in improving signal detectability which is better quantified using gCNR [27]. Adaptive methods often nonlinearly alter the image dynamic range and histogram to which gCNR is invariant [23, 27]. gCNR analysis reveals that significant improvement is achieved using PSAP when compared to DAS_{CF} [Figure 10.10 and Figure 10.14]. Figure 10.11 and Figure 10.15 also indicate that lower N is preferred for maintaining a balance between main lobe signal preservation and clutter signal suppression. With higher N, target PA signals start to get negatively correlated and suppressed through the PSAP weighting matrix. This results in lower CR and PA signal detectability (gCNR). Furthermore, lower axial kernel length and higher phase factor values were chosen to inhibit any undesirable suppression of target PA signal [Table 10.3 and Table 10.4]. Overall, the results for diffuse and microvasculature simulations suggest that lower alternating element number (2-2), lower axial kernel length and higher phase factor is preferred when using PSAP for diffuse target PAI.

PSAP and CF also showed similar CR trends as a function of SNR_c with better performance than DAS [Figure 10.12 (a) – (b)]. However, PSAP processing provides improved target

detectability (gCNR values) when compared to DAS and DAS_{CF} under low noise levels for both target depths. Additionally, PSAP processing had larger SNR_c operating regions for shallower versus deeper targets, observed by the left shift of the gCNR curve indicated by an arrow in Figure Figure 10.12 (d). For lower SNR_c channel data with simulated optical attenuation, main lobe strength in the sub-aperture beamformed images degrades severely for deeper targets resulting in decorrelation during NCC and phase estimation. These results indicate that for PA imaging targets severely corrupted by incoherent clutter noise, PSAP processing is unable to distinguish between signal and noise providing similar performance as DAS_{CF}.

We also observed few erroneous vertical lines in DAS_{CF} images in Figure 10.8 (c) and Figure 10.13 (d) respectively, probably due to the Hilbert transformation of CF weighted beamformed PA RF data for envelope detection. CF weighting may have extended the signal bandwidth resulting in violation of the bandlimited signal assumption required with the Hilbert transform. This may happen in any weighting-based beamforming algorithm, however in DAS_{CF} results, we observed it within our imaging dynamic range. However, it did not impact the quantitative analysis, because the vertical line artifacts were outside our chosen ROI locations. Approaches to reduce the vertical line artifact include determining the envelope of beamformed PAI RF data first then weighting using the CF matrix or beamforming in the IQ domain by taking Hilbert transform of channel data or bandpass filtering of the RF data prior to Hilbert envelope detection. Additionally, we have investigated a filtered version of CF weighting by applying a spatial averaging filter with a kernel of size [1.5λ × 3 A-lines] on the CF map and observed that the filtered version of DAS_{CF} provides vertical line artifact reduction and minor improvements in the CR and gCNR when compared to the classical CF algorithm. Please refer to **Appendix A: DAS and DAS_{CF} Performance Optimization for PSAP Comparison Study** for further details.

PSAP however does require additional computational time and memory for sub-aperture processing and weighting matrix generation. For real-time processing, parallel processing with GPUs can be harnessed by beamforming DAS and sub-aperture images in parallel from collected raw channel data.

A limitation of our simulations was that frequency dependent acoustic attenuation was not modelled. Typically, broadband PA signals are impacted by acoustic attenuation [36] especially when high frequency transducers are used for imaging resulting in depth dependent blurring of features and signal loss [37]. Future work will incorporate acoustic attenuation into the simulation model. Another limitation was the use of a planar phantom and performing simulations in 2-D. In the future, simulations with 3-D phantoms will be performed as the dimensions of the US beam is not negligible in the elevational direction. Finally, another limitation of the proposed technique is the use of the fixed alternating pattern number for sub-aperture generation. As the PSF with PAI varies over depth, we anticipate further performance improvement using depth-dependent dynamic sub-aperture generation by varying the alternating pattern number [14].

Benefits of PSAP are clear in the presented ED and ES images in Figure 10.16 and Figure 10.17. Note that PA signals in the LV chamber appear as temporally varying random noise in the DAS cine loop. This makes interpretation of myocardial PA signals difficult especially during the systolic phase. This random variation can be attributed to higher blood flow velocities inside the LV chamber and strong optical absorption in the coronary artery [1, 38, 39]. This leads to a strong bias of PA signals towards the myocardial (endocardium and epicardium) walls and results in non-viable PA signals from the LV chamber [1, 30]. These random noise signals can be suppressed using CF as shown in Figure 10.16 – Figure 10.17 (c). However, CF also undesirably suppresses myocardial wall PA signals further corroborating our findings from simulation studies. One

implication of undesirable myocardial wall PA signal suppression is that it can lead to inaccurate diagnosis of ischemia [1, 40, 41] as only healthy murine hearts were imaged in this study. In contrast to CF, PSAP enables suppression of non-viable LV chamber PA signals while preserving DAS amplitude levels in the myocardial wall. This is a critical advantage over CF because DAS amplitude preservation is desired when multi-wavelength PAI is employed for oxygen saturation quantification [42]. Quantitative analysis shows that DAS_{CF}, provides higher CR values but reduced wall PA signal detectability as also indicated by the gCNR reduction when compared to DAS in Figure 10.18. In contrast, $PSAP_{NCC}$ and $PSAP_{Phase}$ provided improvements in both CR and gCNR when compared to DAS demonstrating the *in vivo* feasibility of PSAP. Future *in vivo* validation studies will focus on application of PSAP for murine ischemia-reperfusion detection using single- and multi-wavelength cardiac PAI.

In this chapter, we have focused on imaging the murine heart wall using linear array PAI. Researchers have also illustrated use of PAI to guide *in vivo* cardiac catheter interventions [43]. Furthermore, PAI has been used for imaging prostate brachytherapy seeds [44, 45], percutaneous radiofrequency ablation needle detection [46] and surgical guidance [47]. One recurring challenge in these applications is the PA image quality [47], and novel beamforming approaches have been proposed to tackle this challenge [7, 44, 48, 49]. Simulation and *in vivo* results presented in this chapter suggest that PSAP can potentially improve image quality for the above-mentioned applications by clutter reduction while maintaining target detectability thus contributing towards solving the image quality challenge. PSAP also be combined with adaptive beamforming methods such as minimum variance, DMAS beamforming [6, 7, 21, 50] for further image improvements.

List of References

[1] R. A. Mukaddim and T. Varghese, "Spatiotemporal Coherence Weighting for *In Vivo* Cardiac Photoacoustic Image Beamformation," *IEEE transactions on ultrasonics, ferroelectrics, and frequency control* 2020.

[2] R. A. Mukaddim, A. M. Weichmann, and T. Varghese, "Photoacoustic Delay-and-Sum Beamforming with Spatiotemporal Coherence Factor," *2020 IEEE International Ultrasonics Symposium (IUS), IEEE, 2020.,* 2020.

[3] P. V. Chitnis, O. Aristizábal, E. Filoux, A. Sampathkumar, J. Mamou, and J. A. Ketterling, "Coherence-weighted synthetic focusing applied to photoacoustic imaging using a high-frequency annular-array transducer," *Ultrasonic imaging,* vol. 38, pp. 32-43, 2016.

[4] S. Jeon, E.-Y. Park, W. Choi, R. Managuli, K. jong Lee, and C. Kim, "Real-time delay-multiply-and-sum beamforming with coherence factor for in vivo clinical photoacoustic imaging of humans," *Photoacoustics,* vol. 15, p. 100136, 2019.

[5] M. Mozaffarzadeh, Y. Yan, M. Mehrmohammadi, and B. Makkiabadi, "Enhanced linear-array photoacoustic beamforming using modified coherence factor," *Journal of biomedical optics,* vol. 23, p. 026005, 2018.

[6] S. Shamekhi, V. Periyasamy, M. Pramanik, M. Mehrmohammadi, and B. M. Asl, "Eigenspace-based minimum variance beamformer combined with sign coherence factor: Application to linear-array photoacoustic imaging," *Ultrasonics,* p. 106174, 2020.

[7] S. Park, A. B. Karpiouk, S. R. Aglyamov, and S. Y. Emelianov, "Adaptive beamforming for photoacoustic imaging," *Optics letters,* vol. 33, pp. 1291-1293, 2008.

[8] E. Hysi, M. N. Fadhel, M. J. Moore, J. Zalev, E. M. Strohm, and M. C. Kolios, "Insights into photoacoustic speckle and applications in tumor characterization," *Photoacoustics,* vol. 14, pp. 37-48, 2019.

[9] C. H. Seo and J. T. Yen, "Sidelobe suppression in ultrasound imaging using dual apodization with cross-correlation," *IEEE transactions on ultrasonics, ferroelectrics, and frequency control,* vol. 55, pp. 2198-2210, 2008.

[10] A. Stanziola, C. H. Leow, E. Bazigou, P. D. Weinberg, and M.-X. Tang, "ASAP: Super-contrast vasculature imaging using coherence analysis and high frame-rate contrast

enhanced ultrasound," *IEEE transactions on medical imaging,* vol. 37, pp. 1847-1856, 2018.

[11] G. Zhang, B. Wang, A. Stanziola, A. Shah, J. Bamber, and M.-X. Tang, "High Signal-to-Noise Ratio Contrast-Enhanced Photoacoustic Imaging using Acoustic Sub-Aperture Processing and Spatiotemporal Filtering," in *2019 IEEE International Ultrasonics Symposium (IUS)*, 2019, pp. 494-497.

[12] C. H. Seo and M. O'Donnell, "High contrast photoacoustic imaging with dual apodization with cross-correlation: ex-vivo study," in *Photons Plus Ultrasound: Imaging and Sensing 2011*, 2011, p. 78991X.

[13] C. H. Leow, N. L. Bush, A. Stanziola, M. Braga, A. Shah, J. Hernández-Gil*, et al.*, "3-d microvascular imaging using high frame rate ultrasound and asap without contrast agents: Development and initial in vivo evaluation on nontumor and tumor models," *IEEE transactions on ultrasonics, ferroelectrics, and frequency control,* vol. 66, pp. 939-948, 2019.

[14] C. H. Seo and J. T. Yen, "Evaluating the robustness of dual apodization with cross-correlation," *IEEE transactions on ultrasonics, ferroelectrics, and frequency control,* vol. 56, pp. 291-303, 2009.

[15] J. Shin, Y. Chen, H. Malhi, and J. T. Yen, "Ultrasonic reverberation clutter suppression using multiphase apodization with cross correlation," *IEEE transactions on ultrasonics, ferroelectrics, and frequency control,* vol. 63, pp. 1947-1956, 2016.

[16] J. Shin and J. T. Yen, "Synergistic enhancements of ultrasound image contrast with a combination of phase aberration correction and dual apodization with cross-correlation," *IEEE transactions on ultrasonics, ferroelectrics, and frequency control,* vol. 59, pp. 2089-2101, 2012.

[17] J. Shin and J. T. Yen, "Effects of dual apodization with cross-correlation on tissue harmonic and pulse inversion harmonic imaging in the presence of phase aberration," *IEEE transactions on ultrasonics, ferroelectrics, and frequency control,* vol. 60, pp. 643-649, 2013.

[18] J. Shin and J. T. Yen, "Improved image quality using phase aberration correction and dual apodization with cross-correlation," in *2011 IEEE International Ultrasonics Symposium*, 2011, pp. 393-396.

[19] J. T. Yen and C. H. Seo, "Sidelobe suppression in ultrasound imaging using dual apodization with cross-correlation," ed: Google Patents, 2012.

[20] B. E. Treeby and B. T. Cox, "k-Wave: MATLAB toolbox for the simulation and reconstruction of photoacoustic wave fields," *Journal of biomedical optics,* vol. 15, p. 021314, 2010.

[21] M. Mozaffarzadeh, A. Mahloojifar, M. Orooji, S. Adabi, and M. Nasiriavanaki, "Double-stage delay multiply and sum beamforming algorithm: Application to linear-array photoacoustic imaging," *IEEE Transactions on Biomedical Engineering,* vol. 65, pp. 31-42, 2017.

[22] D. Marti, R. N. Aasbjerg, P. E. Andersen, and A. K. Hansen, "MCmatlab: an open-source, user-friendly, MATLAB-integrated three-dimensional Monte Carlo light transport solver with heat diffusion and tissue damage," *Journal of biomedical optics,* vol. 23, p. 121622, 2018.

[23] K. M. Kempski, M. T. Graham, M. R. Gubbi, T. Palmer, and M. A. L. Bell, "Application of the generalized contrast-to-noise ratio to assess photoacoustic image quality," *Biomedical Optics Express,* vol. 11, pp. 3684-3698, 2020.

[24] L. R. Dixon, "The complete blood count: physiologic basis and clinical usage," *The Journal of perinatal & neonatal nursing,* vol. 11, pp. 1-18, 1997.

[25] L. V. Wang, "Tutorial on photoacoustic microscopy and computed tomography," *IEEE Journal of Selected Topics in Quantum Electronics,* vol. 14, pp. 171-179, 2008.

[26] D.-K. Yao, C. Zhang, K. I. Maslov, and L. V. Wang, "Photoacoustic measurement of the Grüneisen parameter of tissue," *Journal of biomedical optics,* vol. 19, p. 017007, 2014.

[27] A. Rodriguez-Molares, O. M. H. Rindal, J. D'hooge, S.-E. Måsøy, A. Austeng, M. A. L. Bell*, et al.*, "The generalized contrast-to-noise ratio: a formal definition for lesion detectability," *IEEE Transactions on Ultrasonics, Ferroelectrics, and Frequency Control,* vol. 67, pp. 745-759, 2019.

[28] J. Staal, M. D. Abràmoff, M. Niemeijer, M. A. Viergever, and B. Van Ginneken, "Ridge-based vessel segmentation in color images of the retina," *IEEE transactions on medical imaging,* vol. 23, pp. 501-509, 2004.

[29] M. W. Kim, G.-S. Jeng, I. Pelivanov, and M. O'Donnell, "Deep-learning Image Reconstruction for Real-time Photoacoustic System," *IEEE Transactions on Medical Imaging,* 2020.

[30] X. L. Deán-Ben, S. J. Ford, and D. Razansky, "High-frame rate four dimensional optoacoustic tomography enables visualization of cardiovascular dynamics and mouse heart perfusion," *Scientific reports,* vol. 5, p. 10133, 2015.

[31] R. Al Mukaddim, N. H. Meshram, C. C. Mitchell, and T. Varghese, "Hierarchical Motion Estimation With Bayesian Regularization in Cardiac Elastography: Simulation and $ In~ Vivo $ Validation," *IEEE transactions on ultrasonics, ferroelectrics, and frequency control,* vol. 66, pp. 1708-1722, 2019.

[32] M. M. McCormick and T. Varghese, "An approach to unbiased subsample interpolation for motion tracking," *Ultrasonic imaging,* vol. 35, pp. 76-89, 2013.

[33] B. M. Asl and A. Mahloojifar, "Minimum variance beamforming combined with adaptive coherence weighting applied to medical ultrasound imaging," *IEEE transactions on ultrasonics, ferroelectrics, and frequency control,* vol. 56, pp. 1923-1931, 2009.

[34] M. Mozaffarzadeh, B. Makkiabadi, M. Basij, and M. Mehrmohammadi, "Image improvement in linear-array photoacoustic imaging using high resolution coherence factor weighting technique," *BMC Biomedical Engineering,* vol. 1, p. 10, 2019.

[35] K. Hollman, K. Rigby, and M. O'donnell, "Coherence factor of speckle from a multi-row probe," in *1999 IEEE Ultrasonics Symposium. Proceedings. International Symposium (Cat. No. 99CH37027)*, 1999, pp. 1257-1260.

[36] J. Yao and L. V. Wang, "Sensitivity of photoacoustic microscopy," *Photoacoustics,* vol. 2, pp. 87-101, 2014.

[37] B. E. Treeby, J. Jaros, and B. T. Cox, "Advanced photoacoustic image reconstruction using the k-Wave toolbox," in *Photons Plus Ultrasound: Imaging and Sensing 2016*, 2016, p. 97082P.

[38] J. Lv, Y. Peng, S. Li, Z. Guo, Q. Zhao, X. Zhang*, et al.*, "Hemispherical photoacoustic imaging of myocardial infarction: in vivo detection and monitoring," *European radiology,* vol. 28, pp. 2176-2183, 2018.

[39] W.-T. Chang, S. Fisch, M. Chen, Y. Qiu, S. Cheng, and R. Liao, "Ultrasound based assessment of coronary artery flow and coronary flow reserve using the pressure overload model in mice," *JoVE (Journal of Visualized Experiments),* p. e52598, 2015.

[40] R. A. Mukaddim, A. Rodgers, T. A. Hacker, A. Heinmiller, and T. Varghese, "Real-Time in Vivo Photoacoustic Imaging in the Assessment of Myocardial Dynamics in Murine Model of Myocardial Ischemia," *Ultrasound in Medicine & Biology,* vol. 44, pp. 2155-2164, 2018.

[41] Z. Li, H. Li, W. Xie, and H. Chen, "In vivo determination of acute myocardial ischemia based on photoacoustic imaging with a focused transducer," *Journal of Biomedical Optics,* vol. 16, p. 076011, 2011.

[42] M. Li, Y. Tang, and J. Yao, "Photoacoustic tomography of blood oxygenation: a mini review," *Photoacoustics,* vol. 10, pp. 65-73, 2018.

[43] M. Graham, F. Assis, D. Allman, A. Wiacek, E. Gonzalez, M. Gubbi*, et al.*, "In vivo demonstration of photoacoustic image guidance and robotic visual servoing for cardiac catheter-based interventions," *IEEE transactions on medical imaging,* vol. 39, pp. 1015-1029, 2019.

[44] M. A. L. Bell, N. Kuo, D. Y. Song, and E. M. Boctor, "Short-lag spatial coherence beamforming of photoacoustic images for enhanced visualization of prostate brachytherapy seeds," *Biomedical optics express,* vol. 4, pp. 1964-1977, 2013.

[45] D. Allman, A. Reiter, and M. A. L. Bell, "Photoacoustic source detection and reflection artifact removal enabled by deep learning," *IEEE transactions on medical imaging,* vol. 37, pp. 1464-1477, 2018.

[46] K. J. Francis and S. Manohar, "Photoacoustic imaging in percutaneous radiofrequency ablation: device guidance and ablation visualization," *Physics in Medicine & Biology,* vol. 64, p. 184001, 2019.

[47] M. A. Lediju Bell, "Photoacoustic imaging for surgical guidance: Principles, applications, and outlook," *Journal of Applied Physics,* vol. 128, p. 060904, 2020.

[48] B. Pourebrahimi, S. Yoon, D. Dopsa, and M. C. Kolios, "Improving the quality of photoacoustic images using the short-lag spatial coherence imaging technique," in *Photons Plus Ultrasound: Imaging and Sensing 2013*, 2013, p. 85813Y.

[49] J. Park, S. Jeon, J. Meng, L. Song, J. S. Lee, and C. Kim, "Delay-multiply-and-sum-based synthetic aperture focusing in photoacoustic microscopy," *Journal of biomedical optics,* vol. 21, p. 036010, 2016.

[50] M. Mozaffarzadeh, A. Mahloojifar, V. Periyasamy, M. Pramanik, and M. Orooji, "Eigenspace-based minimum variance combined with delay multiply and sum beamformer: Application to linear-array photoacoustic imaging," *IEEE Journal of Selected Topics in Quantum Electronics,* vol. 25, pp. 1-8, 2018.

Chapter 11

Improving Minimum Variance Beamforming with Sub-Aperture Processing for Photoacoustic Imaging

Minimum variance (MV) beamforming improves resolution and reduces sidelobes when compared to delay-and-sum (DAS) beamforming for photoacoustic imaging (PAI). However, some level of sidelobe signal and incoherent clutter persist degrading MV PAI quality. One simple solution is to weight MV images with coherence factor [1-4]. However, this may not be an ideal solution in low signal-to-noise ratio environments resulting in undesirable PA signal suppression as demonstrated in **Chapters 09** and **10** [5]. In this chapter, we propose to utilize our developed photoacoustic sub-aperture processing (PSAP) method [5] with MV to address the sidelobe corruption problem while preserving resolution improvement obtained with MV.

11.1 Principles of Photoacoustic Sub-aperture Processing (PSAP) for Minimum Variance (MV) Beamforming

We first generate two MV beamformed images, $MV_1(t)$ and $MV_2(t)$ using two non-overlapping sub-apertures having no common elements [5-7]. Details regarding MV beamforming and sub-aperture generation is described in **Chapters 09** and **10** respectively. Then, 2-D normalized cross-correlation (NCC) between $MV_1(t)$ and $MV_2(t)$ is performed to separate on-axis main-lobe signals and interfering side-lobe signals. $NCC(t)$ is used to estimate a dynamic weighting matrix, $PSAP_W(t)$ using following equation:

$$\mathbf{PSAP_W}(t) = \max(\mathbf{NCC}(t), \varepsilon) \tag{11.1}$$

where, ε is a minimum NCC threshold value to estimate a weighting matrix having a range of [ε , 1]. Finally, $PSAP_W(t)$ is multiplied with $MV(t)$ [MV beamformed image with the full-aperture]

resulting in a PSAP MV beamformed image denoted as $MV_{PSAP}(t)$. Here, we design the first sub-aperture with ones and zeros with an alternating pattern of N elements on and N elements off, with the second sub-aperture is complementary to the first one. Further details on PSAP is presented in [5].

11.2 Simulation Validation Studies and Quantitative Analysis

The proposed method was validated using numerical simulations with point targets, diffuse inclusion and microvasculature networks. A similar simulation methodology as reported in **Chapter 10** has been adopted for this chapter and described in detail in **Chapter 10**. For point target simulations, we computed the main-lobe-to-sidelobe (MLSL) ratio (dB) and full-width-at-half-maximum (FWHM) at -6 dB values. Diffuse inclusion and microvasculature simulations were quantified using contrast ratio (CR) and generalized contrast-to-ratio (gCNR) [8, 9].

A comparative study was designed with DAS, MV and MV_{PSAP} beamforming. DAS was performed with a 64-element aperture, uniform apodization and f-number of 1. MV beamforming used sub-arrays with length $S = 24$ and diagonal loading $\Delta = 1/(100 \times S)$ to estimate $\mathbf{R_{SA}}(t)$. MV_{PSAP} parameters used are listed in Table 11.1 MVPSAP Parameters. Parameter choices were chosen based on parametric studies reported in [5]. Algorithms were run on a GPU and MATLAB Parallel Computing toolbox for accelerated computation.

Table 11.1 MV_{PSAP} Parameters

Experiment	**Parameter**	**Value**
Point Target	Alternating elements (N) NCC Kernel (Wavelength, A-lines)	16-16 (4.5λ,3)
Diffuse Inclusion Micro-vasculature	Alternating elements (N) NCC Kernel (Wavelength, A-lines)	1-1 (1λ,3)

11.3 MV_{PSAP} Improves Conventional MV Performance

Figure 11.1 (a) – (c) show point target beamformed images with DAS, MV and MV_{PSAP}, respectively. Note the presence of strong sidelobe signals with DAS. MV reduces sidelobes seen with DAS but does not suppress it completely. Incorporation of PSAP with MV provided the best beamformed image with significant performance improvement over DAS and MV. Figure 11.2 (a) – (b) show the point spread function (PSF) at a depth of 8 mm and 20 mm, respectively. MV_{PSAP} had the narrowest PSF with lowest sidelobe level. Table 11.2 and Table 11.3 summarize the results for MLSL and FWHM comparison. Improvement in lateral resolution (lowest FWHM) and sidelobe reduction (highest MLSL) was achieved using MV_{PSAP}.

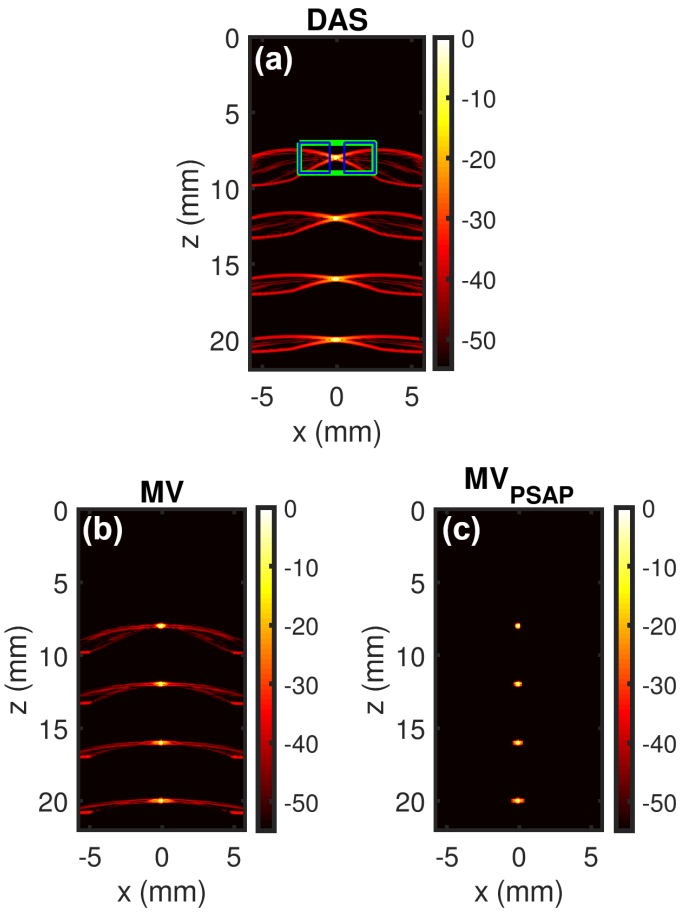

Figure 11.1 Beamformed images from point target simulations. (a) DAS, (b) MV and (c) MV_{PSAP}. Display dynamic range 55 dB.

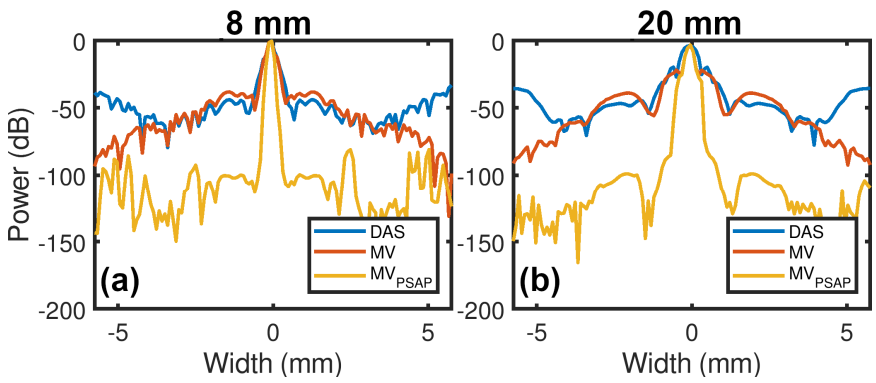

Figure 11.2 Lateral PSF at depths of (a) 8 and (b) 20 mm, respectively. MV_{PSAP} has the narrowest PSF with lowest sidelobe level.

Table 11.2 MLSL (dB) Results

Depth	**DAS**	**MV**	**MV_{PSAP}**
8 mm	41.15	50.84	**84.63**
12 mm	38.16	47.40	**107.85**
16 mm	35.91	46.89	**100.12**
20 mm	33.82	42.26	**95.05**

Table 11.3 –6dB FWHM (mm) Values

	DAS	**MV**	**MV_{PSAP}**
8 mm	0.22	0.21	**0.19**
12 mm	0.32	0.17	**0.16**
16 mm	0.41	0.22	**0.21**
20 mm	0.53	0.26	**0.25**

Beamformed images for the diffuse inclusion simulation using DAS, MV and MV_{PSAP} are shown in Figure 11.3 (b) – (d). The ground truth initial pressure distribution with target (green circle) and background (white half-circles) ROIs is presented in Figure 11.3 (a). For DAS, we observe high sidelobe signal levels specially near the borders for shallow targets as indicated by

arrows (Figure 11.3 (b)). MV results show significant image quality improvements with suppression of the strong border region clutter signals. Further, performance enhancement with increased sidelobe suppression was achieved with MV_{PSAP}.

CR and gCNR comparison results for diffuse inclusion simulation are shown in Figure 11.4 (a) – (b) respectively. MV_{PSAP} had the highest CR and gCNR among the three methods. For example, mean gCNR values (n = 10) for the inclusion at 8 mm, for DAS = 0.84, MV = 0.89 and MV_{PSAP} = **0.99**, demonstrate that improvement in both contrast and target detectability is achieved using PSAP for MV.

Figure 11.5 (b) – (d) show microvasculature beamformed images with DAS, MV and $MV_{PSAP,}$ respectively. The ground truth initial pressure distribution is presented in Figure 11.5 (a). Note that DAS image suffer from high level of sidelobe signals specially near the borders for shallower vessels (white arrows in Figure 11.5 (b)). Results using MV show suppression of the strong sidelobe signals, but unexpected background clutter persist. Best quality image was achieved with MV_{PSAP} (Figure 11.5 (d)) showing a close resemblance with the ground truth image. CR and gCNR were computed by placing small rectangular ROIs covering the shallowest vessels as target ROIs and then translating them into the sidelobe regions as background ROIs. MV_{PSAP} had the highest CR and gCNR values (Mean CR [dB] for DAS = 15.38, MV = 22.42, MV_{PSAP} = **46.32** and mean gCNR for DAS = 0.71, MV = 0.81, MV_{PSAP} = **0.82**).

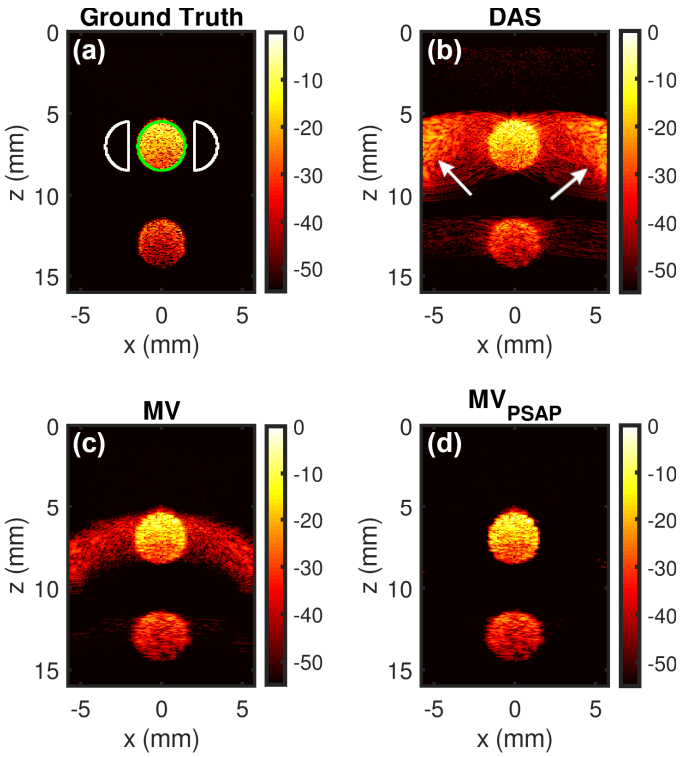

Figure 11.3 Diffuse inclusion beamforming results. (a) Ground truth initial pressure distribution, (a) DAS, (b) MV and (c) MV_{PSAP}. Display dynamic range 55 dB.

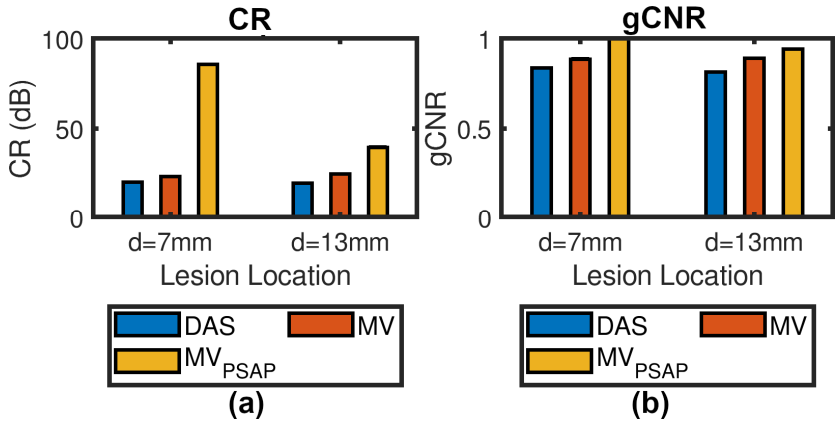

Figure 11.4 (a) CR and (b) gCNR comparison for diffuse inclusion.

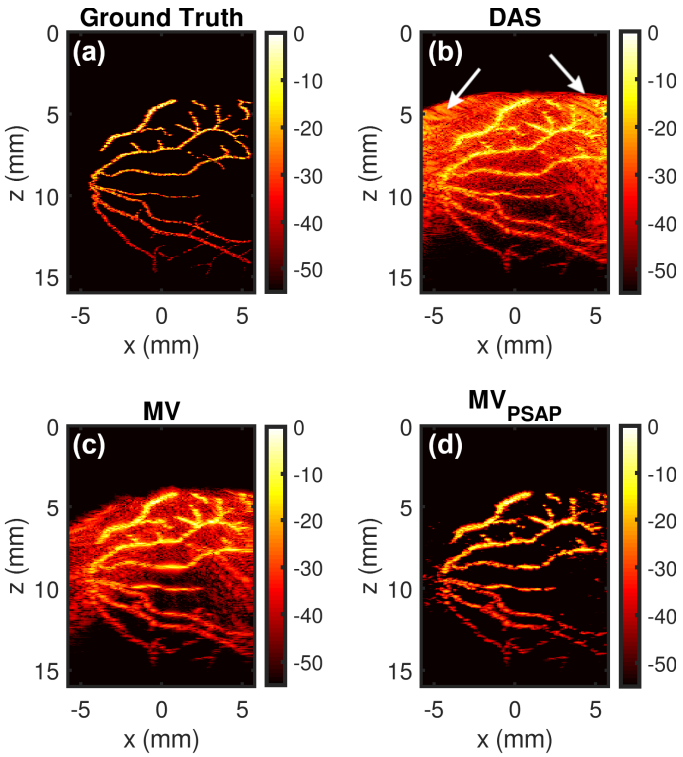

Figure 11.5 Simulated microvasculature beamformed images. (a) Ground truth initial pressure distribution, (a) DAS, (b) MV and (c) MV_{PSAP}. Display dynamic range 55 dB.

The results presented in this chapter show that the proposed hybrid beamforming algorithm coupled with better resolution from MV along with sidelobe signal suppression from PSAP. The resulting MV_{PSAP} images demonstrated higher contrast and improved target detectability. Future work will involve validation in more complicated simulation environments (e.g., addition of channel noise, acoustic attenuation), phantom experiments and *in vivo* applications.

List of References

[1] R. A. Mukaddim and T. Varghese, "Spatiotemporal Coherence Weighting for *In Vivo* Cardiac Photoacoustic Image Beamformation," *IEEE transactions on ultrasonics, ferroelectrics, and frequency control* 2020.

[2] S. Shamekhi, V. Periyasamy, M. Pramanik, M. Mehrmohammadi, and B. M. Asl, "Eigenspace-based minimum variance beamformer combined with sign coherence factor: Application to linear-array photoacoustic imaging," *Ultrasonics,* p. 106174, 2020.

[3] S. Park, A. B. Karpiouk, S. R. Aglyamov, and S. Y. Emelianov, "Adaptive beamforming for photoacoustic imaging," *Optics letters,* vol. 33, pp. 1291-1293, 2008.

[4] R. A. Mukaddim, A. M. Weichmann, and T. Varghese, "Photoacoustic Delay-and-Sum Beamforming with Spatiotemporal Coherence Factor," *2020 IEEE International Ultrasonics Symposium (IUS), IEEE, 2020.,* 2020.

[5] R. A. Mukaddim, R. Ahmed, and T. Varghese, "Sub-aperture Processing Based Adaptive Beamforming for Photoacoustic Imaging," *IEEE transactions on ultrasonics, ferroelectrics, and frequency control* 2021.

[6] C. H. Seo and J. T. Yen, "Sidelobe suppression in ultrasound imaging using dual apodization with cross-correlation," *IEEE transactions on ultrasonics, ferroelectrics, and frequency control,* vol. 55, pp. 2198-2210, 2008.

[7] J. T. Yen and C. H. Seo, "Sidelobe suppression in ultrasound imaging using dual apodization with cross-correlation," ed: Google Patents, 2012.

[8] K. M. Kempski, M. T. Graham, M. R. Gubbi, T. Palmer, and M. A. L. Bell, "Application of the generalized contrast-to-noise ratio to assess photoacoustic image quality," *Biomedical Optics Express,* vol. 11, pp. 3684-3698, 2020.

[9] A. Rodriguez-Molares, O. M. H. Rindal, J. D'hooge, S.-E. Måsøy, A. Austeng, M. A. L. Bell*, et al.*, "The generalized contrast-to-noise ratio: a formal definition for lesion detectability," *IEEE Transactions on Ultrasonics, Ferroelectrics, and Frequency Control,* vol. 67, pp. 745-759, 2019.

Chapter 12

Spatiotemporal Singular Value Decomposition for *in vivo* Cardiac Photoacoustic Imaging

In this chapter[9], we present a spatiotemporal singular value decomposition (SVD) processing method using ECG and respiratory signal (ECG-R) gating with *in vivo* cardiac murine photoacoustic imaging (PAI) data beamformed with delay-and-sum (DAS) [1]. SVD has been previously used for artifact and clutter reduction in ultrasound (US) imaging [2], power Doppler [3, 4] and ultrafast functional US imaging [4-6] demonstrating remarkable improvement in sensitivity. Spatiotemporal SVD allows for signal separation between tissue, blood, and random noise components by decomposing raw data into spatiotemporal singular vectors, enabling selection of singular vectors with relevant spatiotemporal fluctuations [4]. SVD to improve image reconstruction performance for photoacoustic computed tomography systems (PACT) has also been reported [7, 8]. For example, Wang *et al.* proposed a fast spatiotemporal image reconstruction algorithm with SVD for dynamic PACT and reported accuracy improvement over conventional approaches [8]. In this chapter, however, we focus on improving the quality of photoacoustic images collected using linear array US transducers. For linear array PAI, SVD has been used for identification and reduction of laser-induced noise using the spatial singular value spectrum [9]. Spatiotemporal clutter filtering with SVD has also been applied for contrast enhanced PAI in a phantom study [10]. The novelty of our approach is to utilize the natural deformation of myocardial tissue to achieve PA image enhancement using spatiotemporal SVD processing. The purpose of

[9] Rashid Al Mukaddim, Ashley M. Weichmann, Carol C. Mitchell and Tomy Varghese, "Enhancement of *in vivo* Cardiac Photoacoustic Signal Specificity using Spatiotemporal Singular Value Decomposition." *Journal of Biomedical Optics*, vol. 26, no. 4, 046001 (2021) PMCID: Pending

this study is to demonstrate PA signal enhancement in myocardial tissue when compared to surrounding muscle tissue and blood within the LV chamber.

Briefly, a custom ECG-R gating algorithm along with a DAS and minimum variance (MV) beamformer are used to reconstruct a cardiac cycle of PAI data. We hypothesize that blood signals from the LV chamber will have low spatiotemporal coherence when compared to signals from the myocardial wall and surrounding tissue region appearing as random temporally incoherent clutter signals. Moreover, as the myocardium contracts and relaxes during a cardiac cycle, myocardial echo signals will have lower spatiotemporal coherence when compared to quasi-static surrounding tissue and any diffuse quasi-static clutter. Based on the aforementioned hypotheses, spatiotemporal SVD processing was applied to enhance the contribution from myocardial tissue.

12.1 Principles behind Spatiotemporal SVD for *in vivo* cardiac PAI

Figure 12.1 presents a schematic diagram describing the spatiotemporal SVD algorithm for ECG-R gated *in vivo* cardiac PAI which is described in detail below.

12.1.1 In vivo murine cardiac PAI data acquisition

Eight healthy BALB/CJ mice (median age of 10 weeks, five males, three females) acquired from The Jackson Laboratory (Bar Harbor, ME USA) were used to perform an *in vivo* validation study for the proposed SVD processing framework. All *in vivo* experiments were approved by the Institutional Animal Care and Use Committee (IACUC) at the University of Wisconsin-Madison. A Vevo 2100-LAZR photoacoustic-ultrasonic imaging system (FUJIFILM VisualSonics, Inc., Toronto, Canada) was utilized for collecting PAI data. After removing chest hair with depilatory cream, Nair (Church & Dwight Co., Ewing, NJ), mice were placed in the supine position on a heated platform under anesthesia (1.5-3.5% isoflurane) and continuous flow of oxygen (1-2 L/min)

via a nose cone. ECG and respiratory signals were collected using dedicated physiological monitoring system with the Vevo 2100-LAZR. Spectra 360 electrode gel (Parker Labs, Fairfield, NJ) was applied on the physiological signal monitoring system electrodes to ensure optimal contact with each paw ensuring high-quality ECG and respiratory signal acquisition. The supply of isoflurane and oxygen flow rate was titrated to maintain a consistent heart rate between 310-340 beats per minute (bpm) as best as possible during imaging.

A LZ 250 transducer (256-element linear array) having a pitch of 90 μm, center frequency of 21 MHz and bandwidth from 13 MHz to 24 MHz was used for data collection [11]. LithoClear, (Next Medical Products, Branchburg, NJ) a high viscosity acoustic gel was applied within the cup of the transducer along with a liberal amount to the animals' chest to ensure optimal acoustic coupling between the transducer and mice, while also allowing for a gel offset to reduce reverberation artifacts. Acoustic gel was centrifuged prior to imaging to remove air bubbles that would cause artifacts in PAI. Parasternal long axis (PLAX) imaging view was used with US B-mode imaging. B-mode images had a depth of 16 mm and width of 11.04 mm with a depth offset of 5 mm and focus at 11 mm. The skin surface of the mice was placed at an approximate depth of 8 mm whenever possible to avoid reverberation artifacts from the skin [12, 13]. A cine loop of US B-mode was collected to confirm normal cardiac function for each mouse. Then, 1000 frames of co-registered beamformed US and pre-beamformed PA channel data were acquired using an optical wavelength of 850 nm where oxygenated hemoglobin has dominant absorption [14] with simultaneous acquisition of ECG and respiratory signals. With the LZ 250, two sequential laser pulses are required to cover the chosen US imaging width [11.04 mm] with 64-element parallel acquisition per pulse resulting in a PAI frame rate of one half the laser repetition rate [15]. To perform PAI at the maximum laser repetition rate of the system dedicated Nd:YAG laser [20 Hz],

PA imaging width was adjusted to be approximately half of the US imaging width resulting in an acquisition with only 64-elements [green rectangle in Figure 12.1] [16, 17]. No frame or A-line averaging was performed during PA data collection. PA gain (40 dB) and time gain compensation (TGC) were kept constant throughout the experiment to allow inter-animal comparison. Finally, in-phase and quadrature (IQ) sampled PA channel data were exported for offline beamforming and SVD processing.

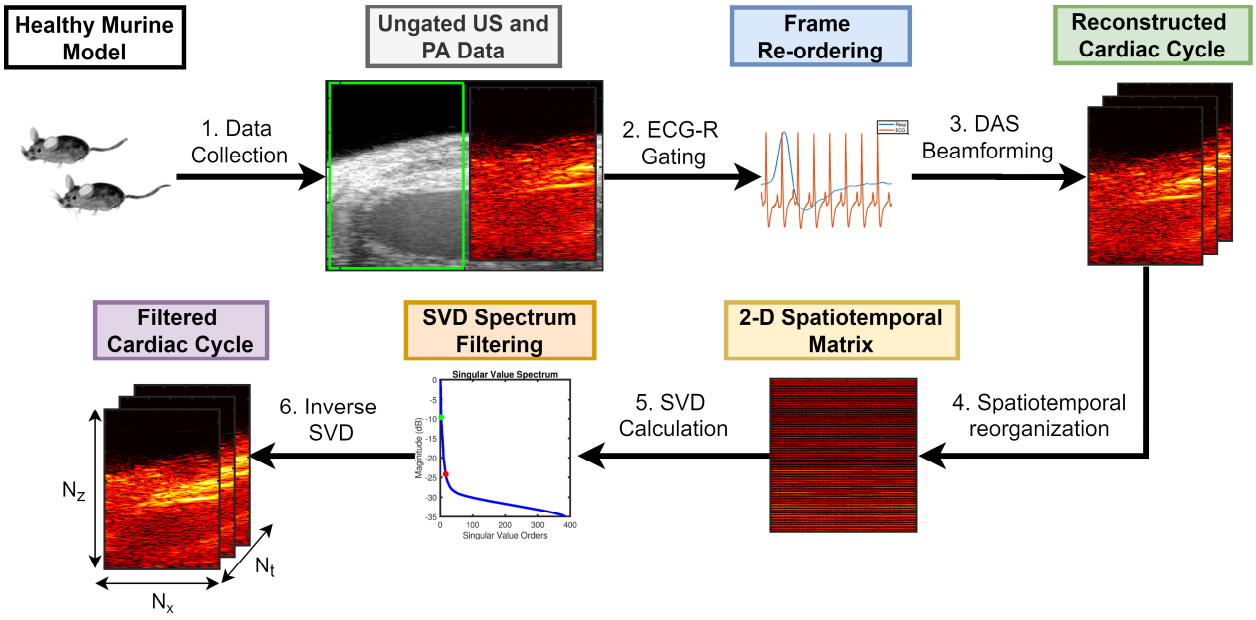

Figure 12.1 Schematic diagram illustrating the spatiotemporal Singular Value Decomposition (SVD) processing algorithm for ECG and Respiratory (ECG-R) gated *in vivo* cardiac photoacoustic imaging.

12.1.2 Cardiac Cycle Reconstruction using ECG-R Gating and Beamforming

A cardiac cycle of PA channel data was reconstructed by performing respiratory signal gating to discard frames and avoid motion artifacts, followed by re-ordering of gated frames using ECG signals and individual frame time stamps. To ensure accurate respiratory signal gating, a publicly available open source respiratory signal processing toolbox named BreathMetrics

(https://github.com/zelanolab/breathmetrics) was used [18]. Respiratory signal was analyzed to determine all inhalation peak time points with corresponding inhalation onsets and exhalation pause onsets. Then, gating was done per inhalation peak with gate start and end time corresponding to the inhalation onset and exhalation pause onset times, respectively as shown in Figure 12.2. Any PA and US frames within the gated region were discarded from subsequent analysis. Finally, the remaining usable frames were re-ordered by calculating the delay between the image time stamps and nearest ECG R-waves reconstructing a cardiac cycle of US and PA channel data. Additionally, an ECG curve for the gated cardiac cycle PA data was reconstructed using the image time stamps of the re-ordered frames after ECG-R gating and the original ECG timing information. To reconstruct the gated ECG curve, we sampled the original ECG signal by finding time indices closest to the image time stamps of the re-ordered usable frames after performing ECG-R gating.

PA complex radio-frequency IQ data were reconstructed from PA channel data using DAS beamforming with 64-element aperture, uniform aperture weighting and dynamic apodization with f-number of 1. For details regarding DAS beamforming please refer to **Chapter 09**. Dynamic receive focusing was performed by calculating one-way US signal propagation delay assuming the speed of sound to be 1540 ms^{-1}. Beamforming process was accelerated by implementation using CUDA to run on a GPU in MATLAB (Mathworks Inc., MA). All beamforming was done on an Intel(R) Xeon(R) CPU E5-2640 v4 at 2.40 GHz and a Tesla K40c GPU (compute capability 3.5). This resulted into a three-dimensional (3-D) complex valued matrix **P** used for SVD processing with dimensions N_x = 64 A-lines, N_z =296 samples along depth and Nt $\approx$ 300 – 400 frames.

Additionally, time delayed PA channel data were also beamformed using a minimum variance (MV) beamforming algorithm [19]. For MV, the optimal aperture apodization function was determined by minimizing the variance of beamformed data using the following equation:

$$\mathbf{W}_{\mathbf{MV}}(t) = \frac{\mathbf{R}_{\mathbf{SA}}(t)^{-1} a}{a^{H} \mathbf{R}_{\mathbf{SA}}(t)^{-1} a} \tag{12.1}$$

where, $\mathbf{W}_{\mathbf{MV}}(t)$ is the minimum variance aperture weighting vector, a (the steering vector) is a unit vector in our case due to dynamic receive focusing, $\mathbf{R}_{\mathbf{SA}}(t)$ is the co-variance matrix estimated by dividing the full array into overlapping sub-arrays having a length of $N_s = 16$ and t is the time-of-arrival of PA acoustic waves. MV beamforming was accelerated using the Parallel Computing Toolbox in MATLAB.

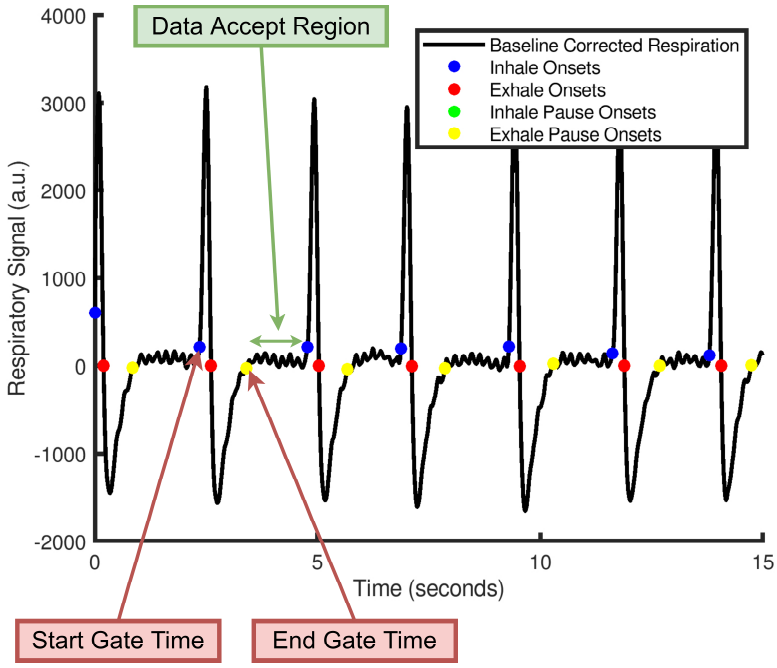

Figure 12.2 Respiration gating using BreathMetrics for performing ECG-R gated *in vivo* cardiac PAI

12.1.3 Spatiotemporal Singular Value Decomposition (SVD) Processing

Theoretical background on spatiotemporal SVD processing is presented in this section. For SVD processing, a 3-D complex valued matrix **P** is constructed using stacks of ECG-R gated DAS beamformed PAI cardiac cycle data. The matrix **P** has two dimensions in space denoted by N_x and N_z corresponding to the number of transducer elements and number of samples along the depth axis respectively and one dimension in time (N_t) corresponding to the number of frames in the

ECG-R gated cardiac cycle data. A spatiotemporal reorganization was applied on the matrix **P** to construct a two-dimensional (2-D) Casorati matrix, **S** with dimensions of ($N_x \times N_z$) by N_t [4]. Each column vector of **S** represents a PA image. Then, SVD is performed on **S** which can be represented as follows.

$$\mathbf{S} = \mathbf{U}\mathbf{\Delta}\mathbf{V}^{*} \tag{12.2}$$

where $\mathbf{\Delta}$ is a diagonal matrix with dimensions [$\min(N_x \times N_z, N_t)$ by $\min(N_x \times N_z, N_t)$] containing the singular values in the diagonal and two unitary matrices **U** with dimensions [($N_x \times N_z$) by $\min(N_x \times N_z, N_t)$] and **V** dimensions [$N_t$ by $\min(N_x \times N_z, N_t)$] containing the spatial and temporal singular vectors corresponding to each singular value, respectively.

For cardiac PAI, we are interested in enhancing signals from myocardial tissue depicting natural contraction and relaxation over a cardiac cycle. The key assumption here is that myocardial tissue should have lower spatiotemporal coherence compared to PA signals from diffuse quasi-static clutter and surrounding muscle regions and higher spatiotemporal coherence compared to fast moving blood volumes inside the LV chamber. The assumed spatiotemporal PA signal fluctuation will be characterized by matrix **V** containing the temporal singular vectors. Therefore, to enhance myocardial PA signals, singular values and vectors associated with myocardial tissue displacements were preserved by filtering both lower and higher order singular values of the singular value spectrum (SVS). The low-order cutoff used to separate myocardial PA signal from quasi-static clutter and surrounding muscle was manually selected and denoted as r_{st} here and in the rest of the chapter. After application of ECG-R gating, we observed that high amplitude PA signals from the surrounding muscle regions was depicted as quasi-static clutter while myocardial PA signals had deformation characteristics associated with natural contraction and relaxation of the heart over a cardiac cycle. Spatiotemporal SVD thereby decomposed the raw PA data into

spatiotemporal singular vectors. The singular vectors from quasi-static clutter and surrounding muscle had the lowest spatiotemporal fluctuations thereby contributing to lower order singular values. On the other hand, myocardial tissue had higher spatiotemporal fluctuations, therefore utilizing a lower-order cut-off enhanced the myocardial PA signals over quasi-static clutter and surrounding muscle. The high-order cut-off used to suppress random PA noise was calculated using the gradient of SVS and selected at the singular value order where gradient becomes less than 20 and denoted by r_{rt}. The filtered SVS can be presented using a truncated diagonal matrix $\mathbf{\Delta}^{ST}$ as shown below.

$$\mathbf{\Delta}^{ST} = \mathbf{\Delta} \times \mathbf{I}^{ST} \tag{12.3}$$

where $\mathbf{I}^{ST}$ is a diagonal matrix to filter $\mathbf{\Delta}$. For $\mathbf{I}^{ST}$, diagonal elements between r_{st} and r_{rt} were set to one and rest were set to zeros. A typical SVS derived from our cardiac PAI data with chosen low- and high-order cutoff is shown in Figure 12.3. A filtered Casorati matrix, $\mathbf{S}^{ST}$ through inverse SVD calculation was derived using the following equation.

$$\mathbf{S}^{ST} = \mathbf{U}\mathbf{\Delta}^{ST}\mathbf{V}^{*} \tag{12.4}$$

Finally, a 3-D matrix of SVD processed cardiac PAI data, $\mathbf{P}^{ST}$ was reconstructed by applying a spatiotemporal reorganization on $\mathbf{S}^{ST}$.

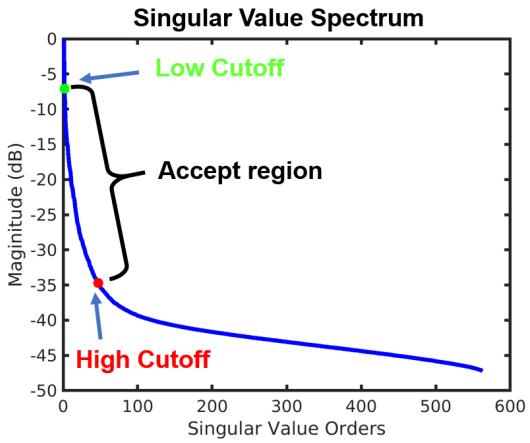

Figure 12.3 Singular value spectrum derived from SVD of in vivo cardiac PAI murine data. Green and red dots show the low and high-order cutoff respectively for SVD filtering.

12.1.4 Quantitative Analysis

To perform quantitative analysis, three cardiac time points (during systole, at end-systole and during diastole) were identified using US M-Mode image derived from the reconstructed ECG-R gated cardiac cycle of the co-registered US B-mode cine-loop (Figure 12.4 (a)). We define systole as the cardiac phase when the LV chamber begins to contract until just before it reaches its smallest dimension, end-systole as the cardiac time point at which LV chamber is at the smallest dimension and diastole as the cardiac phase when the LV chamber begins to expand until it reaches its largest dimension. Note that imaging field of view (FOV) was set to focus on the interventricular septum while maintaining enough offset between the skin and transducer face to avoid reverberation artifacts during photoacoustic imaging. Then, corresponding B-mode images were used to manually draw target and background regions of interest (ROI) as shown with blue and red polygons respectively in Figure 12.4 (b). Both target and background ROI were constructed to have equal areas. Finally, the corresponding DAS, MV and SVD processed PA images were evaluated by calculating the contrast ratio (CR) [16, 17], generalized contrast-to-noise ratio (gCNR) [20, 21] and signal-to-noise ratio (SNR) [22] as defined in **Chapter 09**.

For statistical analysis, a one-way analysis of variance (ANOVA) with the Bonferroni multiple comparison test was used to compare among DAS, MV and SVD-4. Note that SVD-4 denotes spatiotemporal SVD processed image with $r_{st} = 4$. Statistical analysis and graphing were done with Origin, Version 2020 (OriginLab Corporation, Northampton, MA, USA).

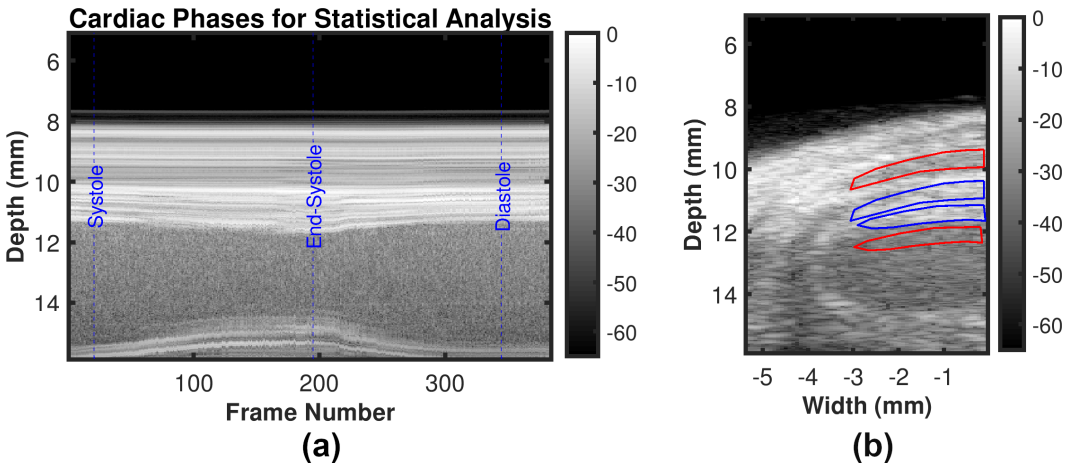

Figure 12.4 Ultrasound guided statistical analysis of *in vivo* PAI. (a) US M-mode image derived from the reconstructed cardiac cycle after ECG-R gating. Chosen cardiac phases are shown with blue dashed line on the M-mode image. (b) Representative target (blue polygon) and background (red polygon) ROIs overlayed on PAI co-registered US image.

12.2 Spatiotemporal SVD enhances myocardial specificity and reduces clutter noise

Figure 12.5 (a) – (c) show representative examples of DAS, MV and SVD processed images during systole, at end systole (ES) and during diastole of a cardiac cycle, respectively. US B-mode and PA images reconstructed with DAS, MV, SVD-0, and SVD-4 are presented from left to right chronologically for each sub-figure. PA signal strength from the myocardium in DAS and MV images were low making myocardial signal localization difficult. With SVD-0, no significant qualitative difference was observed in the myocardial wall region. However, significant

myocardial PA signal enhancement was achieved with SVD-4. Specifically, we observe ES radial wall thickening in the SVD-4 image, which was not clearly visualized in the DAS, MV and SVD-0 results [Figure 12.5 (b)]. Radial wall thickening was also confirmed with the corresponding US B-mode image [Figure 12.5 (b) left most image].

Figure 12.6 (a) – (c) show another set of representative examples of DAS, MV and SVD processed images during systole, at end systole (ES) and during diastole of a cardiac cycle, respectively. US B-mode and PA images reconstructed with DAS, MV, SVD-0, and SVD-4 are presented from left to right chronologically for each sub-figure. In DAS and MV results, spurious high amplitude PA clutter (diffuse quasi-static) signals are observed in the surrounding muscle and background regions (indicated using black arrows in Figure 12.6 DAS images). Although some level of clutter reduction was observed with SVD-0, high amplitude PA signals persist in the regions indicated with arrows in DAS results. Finally, with SVD-4 significant PAI diffuse quasi-static clutter reduction was achieved when compared to DAS, MV and SVD-0 thus enhancing signal specificity and detectability of myocardial PA signals.

Findings from a parametric study to investigate the performance of the proposed algorithm as a function of lower order singular value cut-off (r_{st}) are summarized in Figure 12.7 and Figure 12.8. Representative end-systole spatiotemporal SVD processed images for different r_{st} values are presented in Figure 12.7. Results with r_{st} = 0, 1, 2, 4 and 6 are presented from left to right chronologically. The impact of the r_{st} cutoff is evident in these results in terms of myocardial signal enhancement and background signal suppression, with the best quality image obtained at $r_{st} = 4$. However, choosing too high a value for r_{st} may suppress signals from myocardial tissue as seen in Figure 12.7 for $r_{st} = 6$. Figure 12.8 (a) – (c) show the variation of CR, gCNR and SNR as a function of r_{st} for systolic, end-systolic and diastolic phase SVD processed PA images, respectively. We

observe peak CR, gCNR and SNR were achieved with r_{st} = 4 after which the curves plateau. Therefore, SVD processed image with r_{st} = 4 was used in the quantitative comparative study against DAS and MV beamforming.

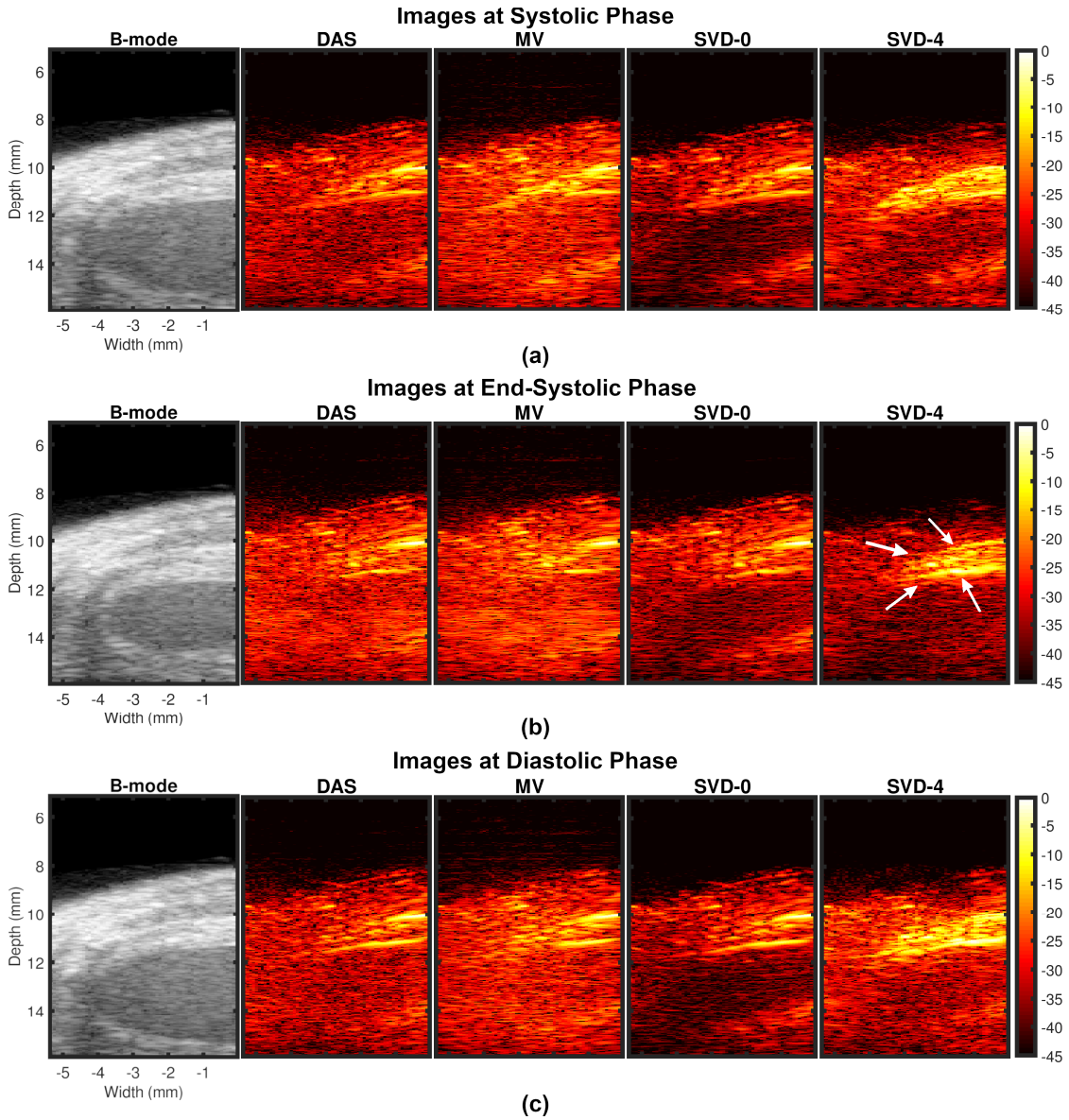

Figure 12.5 Representative SVD processed images at three different cardiac time points demonstrating improved PAI signal specificity after processing. (a) – (c) show results at systolic, end-systolic, and diastolic phase of a cardiac cycle, respectively. US B-mode and PA images for DAS, MV, SVD-0, and SVD-4 are presented from left to right chronologically for each sub-figure. SVD-0 and SVD-4 denote spatiotemporal SVD processed images with r_{st} = 0 and 4, respectively.

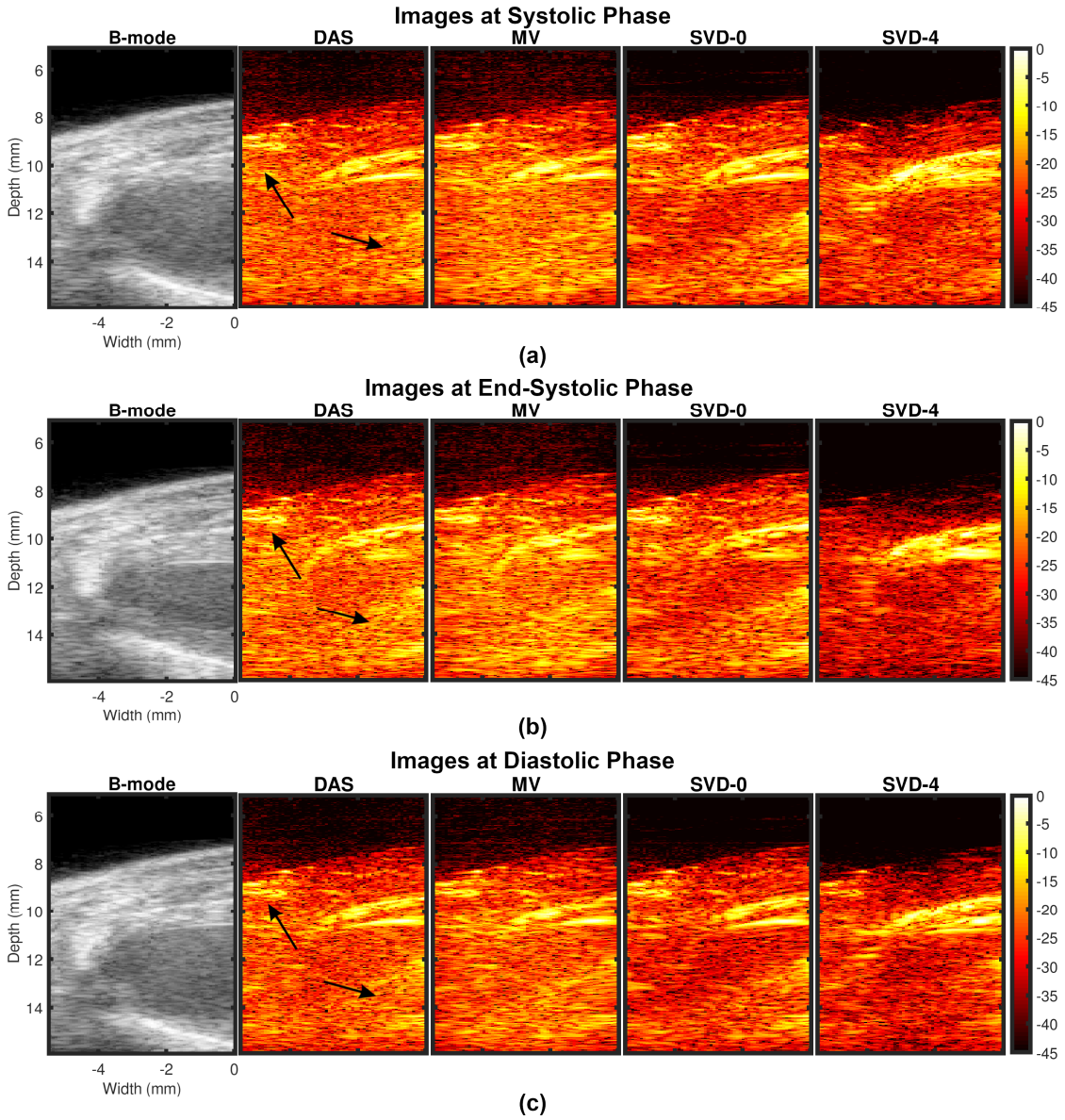

Figure 12.6 Representative SVD processed images at three different cardiac time points demonstrating PAI diffuse and quasi-static clutter reduction after processing. (a) – (c) show results at systolic, end-systolic, and diastolic phase of a cardiac cycle, respectively. US B-mode and PA images for DAS, MV, SVD-0, and SVD-4 are presented from left to right chronologically for each sub-figure. SVD-0 and SVD-4 denote spatiotemporal SVD processed images with r_{st} = 0 and 4, respectively.

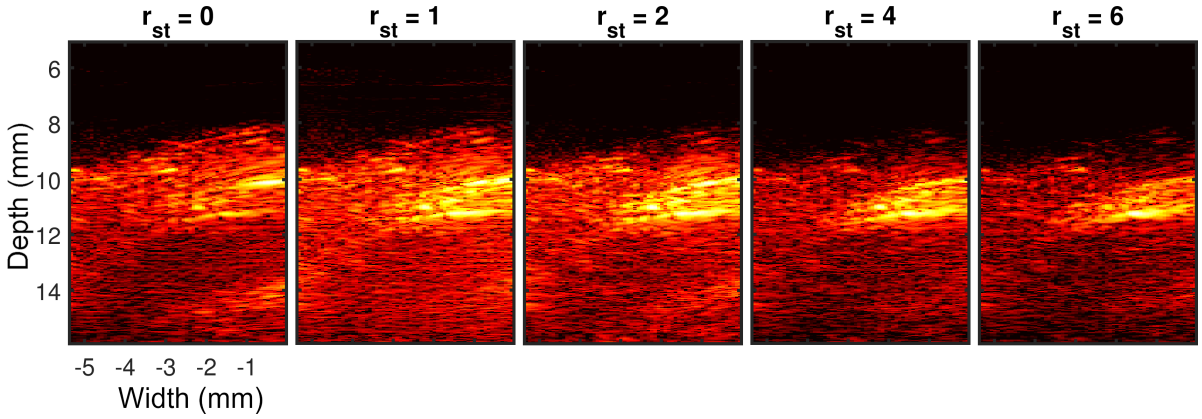

Figure 12.7 End-systole spatiotemporal SVD processed images as a function of lower singular valuer order cut-off threshold (r_{st}). Results with r_{st} = 0, 1, 2, 4 and 6 are presented from left to right chronologically.

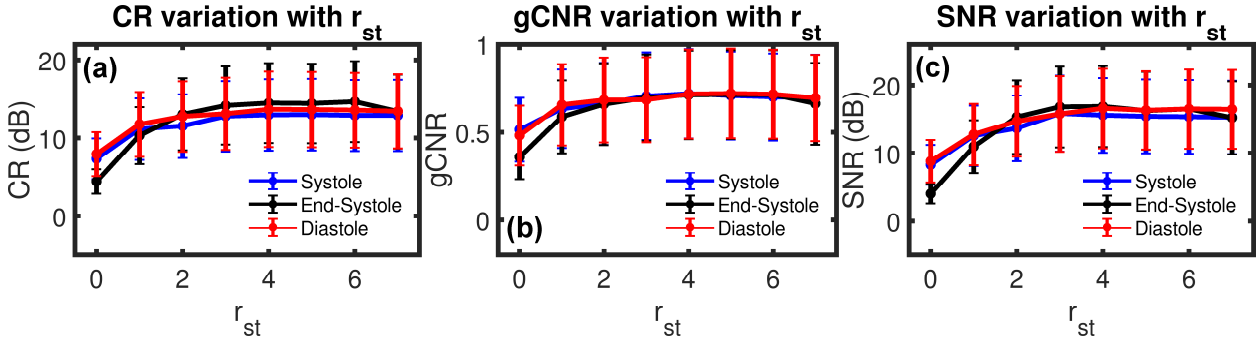

Figure 12.8 Variation of (a) CR, (b) gCNR and (c) SNR as a function of r_{st} for spatiotemporal SVD processed images evaluated at systolic (blue), end-systolic (black) and diastolic (red) phase of a cardiac cycle.

Quantitative comparison results using CR, gCNR and SNR are summarized in Figure 12.9 – Figure 12.11, respectively. Results are presented using box-whisker plots with raw data plotted on the right side. Mean of each distribution is denoted by the black diamond symbol.

Figure 12.9 (a) – (c) show the CR results during systolic, at end-systolic, and during the diastolic phase of a cardiac cycle, respectively. SVD-4 had higher CR values compared to DAS and MV with statistical significance for all cases. No statistically significant differences were observed between DAS and MV. For example, at ES, mean CR values for DAS, MV and SVD-4 were 4.20, 5.28 and 14.49 dB, respectively.

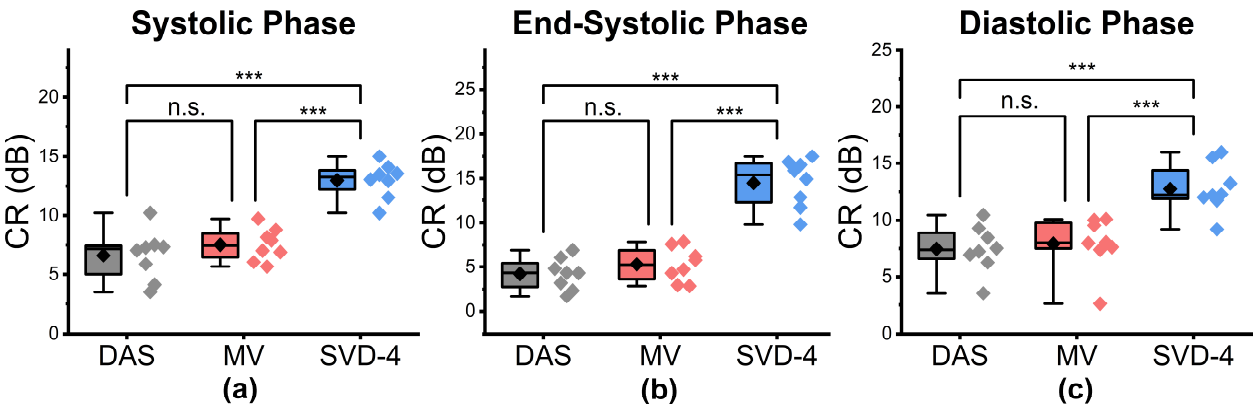

Figure 12.9 Statistical analysis for contrast ratio (CR) comparison among DAS, MV and SVD-4 (*n* = *8*). (a) – (c) show results at systolic, end-systolic, and diastolic phase of a cardiac cycle, respectively. SVD-4 presents with statistically higher CR values when compared to DAS and MV.

Figure 12.10 (a) – (c) show the gCNR results during systolic, end-systolic, and during the diastolic phase of a cardiac cycle, respectively. SVD-4 had higher gCNR values when compared to DAS and MV with statistical significance for all cases. No statistically significant difference was observed between DAS and MV. Larger differences were observed in the ES phase when compared to systolic and diastolic phases. For example, at ES, mean gCNR values for SVD-4 was 115.15 % higher than DAS while at systolic phase, it was 56.52 % higher.

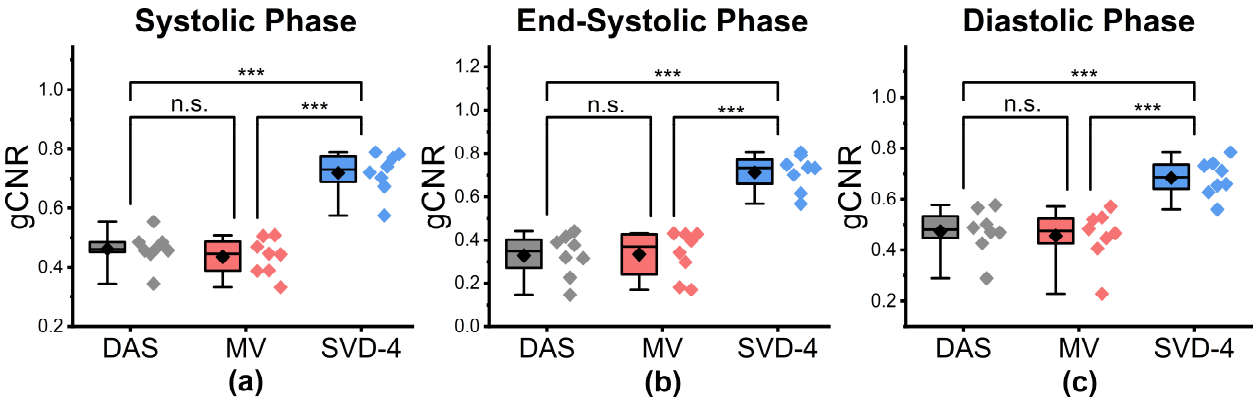

Figure 12.10 Statistical analysis for gCNR comparison among DAS, MV and SVD-4 (*n* = *8*). (a) – (c) show results at systolic, end-systolic, and diastolic phase of a cardiac cycle, respectively. SVD-4 shows statistically higher gCNR values when compared to DAS and MV.

Figure 12.11 (a) – (c) show the SNR results during systolic, at end-systolic, and during the diastolic phase of a cardiac cycle, respectively. For all three phases, SVD-4 had statistically higher SNR than DAS. When compared to MV, SVD-4 had statistically higher SNR at ES and systole with no statistically significant difference during the diastolic phase. However, highest mean SNR values were achieved in all three phases using SVD-4. For example, mean SNR of DAS, MV and SVD-4 were 8.84, 10.41 and 14.69 dB for the diastolic phase results.

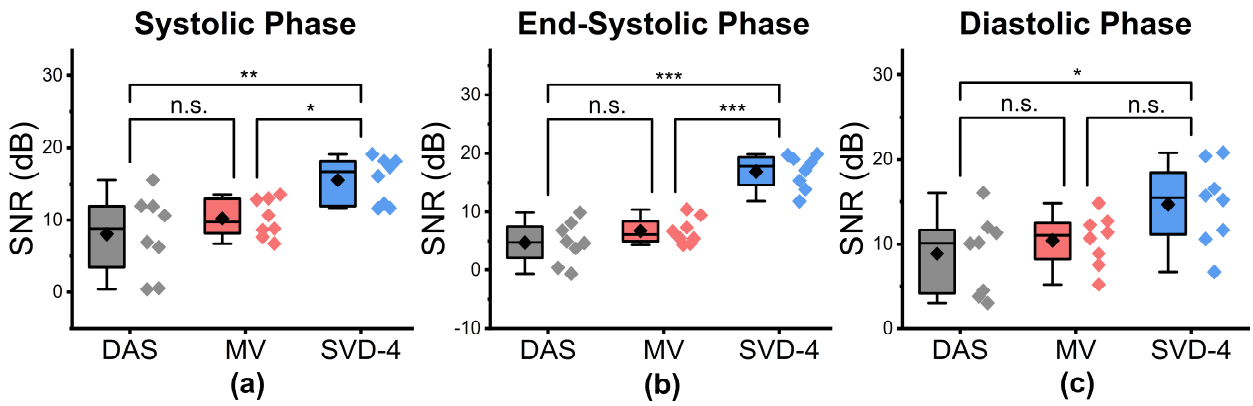

Figure 12.11 Statistical analysis for SNR comparison among DAS, MV and SVD-4 (*n* = *8*). (a) – (c) show results at systolic, end-systolic, and diastolic phase of a cardiac cycle, respectively. SVD-4 had statistically higher SNR values than DAS.

Table 12.1 summarizes the computation times required to reconstruct a PA cardiac cycle using DAS, MV and spatiotemporal SVD processing for two mice. For example, DAS requires 45.81 secs to reconstruct a complete 3-D cardiac cycle having a dimension of 296×64×300 samples while MV requires significantly more time (446.58 secs). Note that enhanced PAI with spatiotemporal SVD can be achieved with a very low additional computation burden (1.71 secs). Similar performance trends were observed for mouse 2 with computational time scaled by N_t (461 frames).

Table 12.1 Summary of Computational Times (Seconds)

	DAS Total (per frame)	MV Total (per frame)	SVD*
Mouse 1	45.81 (0.12)	446.58 (1.16)	1.71
Mouse 2	54.40 (0.12)	506.61 (1.10)	2.45

Mouse 1, N_t = 300 frames, Mouse 2, N_t = 461 frames
**Additional time needed to process entire cardiac cycle using spatiotemporal SVD after DAS.*
DAS = Delay-and-sum, MV= Minimum Variance, SVD = Singular Value Decomposition

12.3 Discussion on the experimental findings to validate Spatiotemporal SVD processing

In this chapter, a spatiotemporal SVD algorithm with ECG and Respiratory (ECG-R) gating for *in vivo* cardiac PAI has been proposed and validated. *In vivo* feasibility with eight healthy mice demonstrated significantly improved performance with SVD-4 processing over conventional DAS and MV beamformed images. The proposed SVD processing is a data driven approach where spatiotemporal characteristics of cardiac PAI are utilized to enhance signal contribution from myocardial tissue under the following assumptions based on literature findings and experimental observations. First, highly absorbing blood inside the coronary artery (murine arterial oxygen saturation $\approx$ 90 – 95% [12, 23]) having low blood flow velocity (diastolic coronary flow velocity $\approx$20 cm/sec [24]) should contribute to the PA signals from myocardial tissue at 850 nm. Second, highly scattering mice skin and muscle due to the presence of connective tissues and anisotropic layers of collagen [25] having lower optical absorption coefficients at 850 nm (for example, male BALB/CJ mice skin optical absorption coefficient at 850nm $\approx$ 1 cm^{-1} [25]) compared to oxygenated blood should result in low amplitude PA signals compared to myocardial tissue. During data collection, we observed the presence of spurious high amplitude PA clutter signals from surrounding muscle which were quasi-static in nature. Third, PA transients from the large volume of high velocity circulating blood (in early filling, E wave and late or atrial filling

phase, A wave during diastole) inside the LV generates mainly destructive interference during DAS beamforming, resulting in non-viable PA signals with random spatiotemporal fluctuations. Note that, the **E** and **A** wave velocity [26] of mitral valve flow during diastole have previously been reported to be approximately 54.2 cm/sec and 43.8 cm/sec respectively [27]. Furthermore, short duration pulses provided to the flash lamp within the laser source may also contribute to random PA noise [9]. Therefore, in the proposed method, singular values and vectors corresponding to cardiac tissue displacements associated with the natural contraction and relaxation of the heart over a cardiac cycle were preserved by discarding the first few singular values for the low-order SVD cutoff to suppress spurious high amplitude quasi-static clutter and by suppressing random PA signal fluctuations using high-order SVD cut-off (Figure 12.3). To ensure that a suitable dataset is generated for SVD processing, a custom ECG-R gating algorithm was developed using an open-source Matlab toolbox (Figure 12.2).

Qualitative results presented in Figure 12.5 – Figure **12.6** show that significant improvement in myocardial signal specificity is achieved with $r_{st} = 4$ which was also validated by quantitative analysis. Note that, no additional temporal smoothing was applied to preserve the original spatial and temporal resolution demonstrating a significant improvement over prior approaches using higher persistence [12, 13]. With SVD processing, significant enhancement of myocardial signal was demonstrated with improved contrast between the myocardium and background as demonstrated by CR comparison results (Figure 12.9). Additionally, gCNR comparison was done to confirm that this contrast enhancement was not due to mere dynamic range alternations, but due to improvement in target detectability. gCNR results presented in Figure 12.10 show that myocardial signal detectability is significantly improved using spatiotemporal SVD processing when compared to conventional DAS or MV results. Higher

gCNR improvement observed at ES compared to either systolic or diastolic phases can be attributed to the high strain rate at ES with the thickest wall dimension [28]. SNR results demonstrate statistically significant improvement with SVD-4 over DAS for all cardiac phases (Figure 12.11). We observed an exception in the diastolic phase where MV and SVD-4 had non-significant differences. In contrast to CR and gCNR (both measure target detectability), SNR additionally considers the smoothness of the background regions. To understand the SNR trend, we also evaluated the mean PA amplitude of the target region and standard deviation of background region individually and found that SVD-4 had higher mean PA amplitudes demonstrating improved myocardial signal enhancement in all phases corroborating the improvement in CR and gCNR. However, reduction in background standard deviation in the diastolic phase was not as significant as in the end-systole and systolic phase resulting in non-significant SNR improvement statistically between MV and SVD images even though SVD-4 had higher mean SNR value. Overall, qualitative and quantitative results demonstrate that spatiotemporal SVD processing can potentially improve *in vivo* cardiac PAI quality.

Note that myocardial tissue identified in SVD processed PA images showed similar anatomical variation as a function of time as observed in B-mode images. For example, in Figure 12.5 (b), thickening and shortening of anterior wall is evident from the B-mode image at ES. Observe thickening and shortening of the anterior wall from SVD-4 images [myocardial boundaries indicated with arrows in Figure 12.5 (b)] with clear visualized contrast when compared to the background. Binary maps were generated by applying a threshold on the SVD-4 images (from Figure 12.5) at the systolic, end-systolic and diastolic phases which are shown in Figure 12.12. Anatomical variation at the different cardiac phases is clearly observed in Figure 12.12, demonstrating that both spatial and temporal localization of myocardial PA signals is achieved

using spatiotemporal SVD processing. One common approach in PA-based oxygen saturation (% sO_2) estimation is to use a quality control ROI [14, 29]. In the future, we will utilize SVD processed images to define our quality control ROI utilizing improved target detectability and perform multispectral imaging to evaluate the myocardial % sO_2 as a function of time over a cardiac cycle.

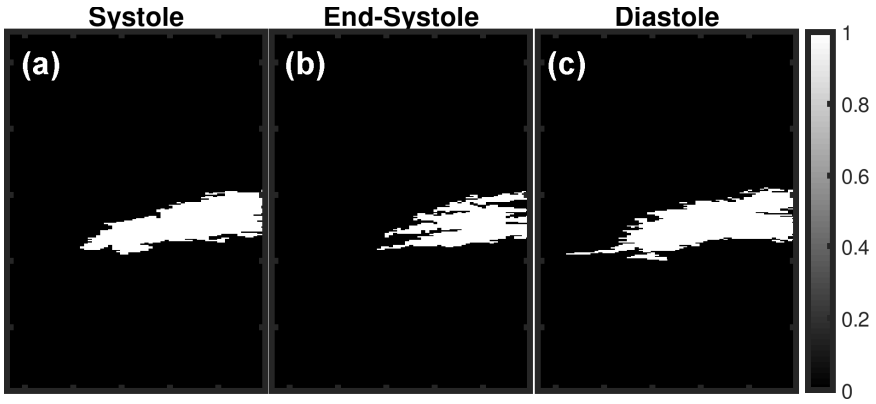

Figure 12.12 (a) – (c) Binary maps of the myocardial wall generated by applying a threshold on SVD-4 images at systolic, end-systolic and diastolic phases of cardiac cycle, respectively.

The performance of SVD processing depends on the choice of the lower singular value order cut-off threshold (r_{st}) which was chosen empirically by evaluating a range of r_{st} values [Figure 12.7 and Figure 12.8]. However, this is not an optimal solution when the proposed algorithm must be applied to larger datasets. In future work, we will investigate the feasibility for automated determination of the low order cut-off threshold by estimating the mean frequency of each temporal singular vectors contained in the matrix **V** [5].

In this chapter, the focus was on *in vivo* murine cardiac PAI where the myocardial signals are diffuse in nature. PAI has also been used for imaging prostate brachytherapy seeds [30, 31], percutaneous radiofrequency ablation needle detection [32] and surgical guidance [33] where the signals of interest are more coherent. We anticipate that our proposed spatiotemporal SVD

processing can be applied for those applications with appropriate adjustment of singular value thresholds. Adaptive beamforming methods such as MV, DMAS beamforming [34] can be also be coupled with SVD processing to improve murine cardiac PAI quality if channel data is accessible. However, researchers must be mindful of any non-linearity introduced by these adaptive beamforming algorithms.

Despite the presented encouraging results, this study still has some limitations. First, SVD processing was considered as decomposing the matrix **S** into weighted, ordered sum of separable matrices as hypothesized for ultrafast functional US imaging [4, 5]. However, from our study we observed some overlap between the myocardial and background signal subspace even after applying SVS thresholding. Therefore, to account for the background signal, additional signal processing approaches may be necessary. One potential approach might be the use of photoacoustic sub-aperture processing (PSAP) developed in our lab to suppress incoherent clutter for DAS PA images [35]. An example using PSAP processing to suppress background signals in the SVD processed images is presented in **Appendix B: Background suppression using PSAP**. Second, the low and higher order singular value cut-offs were chosen empirically and were fixed for all mice that were imaged. However, it is anticipated that adaptive methods [5, 6] for selecting the singular value cutoff may further improve performance by accounting for physiological variation (for example, heart rate under anesthesia) that occur with different mice. Third, any singular value below the low order and above the high order singular value cutoff was set to zero in our implementation. However, adaptive weighting functions based on the singular values [2] can be designed to weight the SVS to further enhance myocardial PA signals. Fourth, only healthy murine models were considered in this study. However, efficacy should be evaluated for murine

cardiovascular disease models such ischemia-reperfusion [36] for further validation which will be performed in future studies.

List of References

[1] R. A. Mukaddim and T. Varghese, "Singular value decomposition processing for in vivo cardiac photoacoustic imaging," in *Medical Imaging 2021: Ultrasonic Imaging and Tomography*, 2021.

[2] F. W. Mauldin, D. Lin, and J. A. Hossack, "The singular value filter: A general filter design strategy for PCA-based signal separation in medical ultrasound imaging," *IEEE transactions on medical imaging,* vol. 30, pp. 1951-1964, 2011.

[3] R. Nayak, V. Kumar, J. Webb, M. Fatemi, and A. Alizad, "Non-invasive small vessel imaging of human thyroid using motion-corrected spatiotemporal clutter filtering," *Ultrasound in medicine & biology,* vol. 45, pp. 1010-1018, 2019.

[4] C. Demené, T. Deffieux, M. Pernot, B.-F. Osmanski, V. Biran, J.-L. Gennisson*, et al.*, "Spatiotemporal clutter filtering of ultrafast ultrasound data highly increases Doppler and fUltrasound sensitivity," *IEEE transactions on medical imaging,* vol. 34, pp. 2271-2285, 2015.

[5] J. Baranger, B. Arnal, F. Perren, O. Baud, M. Tanter, and C. Demené, "Adaptive spatiotemporal SVD clutter filtering for ultrafast Doppler imaging using similarity of spatial singular vectors," *IEEE transactions on medical imaging,* vol. 37, pp. 1574-1586, 2018.

[6] P. Song, A. Manduca, J. D. Trzasko, and S. Chen, "Ultrasound small vessel imaging with block-wise adaptive local clutter filtering," *IEEE transactions on medical imaging,* vol. 36, pp. 251-262, 2016.

[7] M. B. Roumeliotis, R. Z. Stodilka, M. A. Anastasio, E. Ng, and J. J. Carson, "Singular value decomposition analysis of a photoacoustic imaging system and 3-D imaging at 0.7 FPS," *Optics express,* vol. 19, pp. 13405-13417, 2011.

[8] K. Wang, J. Xia, C. Li, L. V. Wang, and M. A. Anastasio, "Fast spatiotemporal image reconstruction based on low-rank matrix estimation for dynamic photoacoustic computed tomography," *Journal of biomedical optics,* vol. 19, p. 056007, 2014.

[9] E. R. Hill, W. Xia, M. J. Clarkson, and A. E. Desjardins, "Identification and removal of laser-induced noise in photoacoustic imaging using singular value decomposition," *Biomedical optics express,* vol. 8, pp. 68-77, 2017.

[10] G. Zhang, B. Wang, A. Stanziola, A. Shah, J. Bamber, and M.-X. Tang, "High Signal-to-Noise Ratio Contrast-Enhanced Photoacoustic Imaging using Acoustic Sub-Aperture Processing and Spatiotemporal Filtering," in *2019 IEEE International Ultrasonics Symposium (IUS)*, 2019, pp. 494-497.

[11] L. J. Rich, S. R. Chamberlain, D. R. Falcone, R. Bruce, A. Heinmiller, J. Xia*, et al.*, "Performance Characteristics of Photoacoustic Imaging Probes with Varying Frequencies and Light-delivery Schemes," *Ultrasonic Imaging,* vol. 41, pp. 319-335, 2019.

[12] R. A. Mukaddim, A. Rodgers, T. A. Hacker, A. Heinmiller, and T. Varghese, "Real-Time in Vivo Photoacoustic Imaging in the Assessment of Myocardial Dynamics in Murine Model of Myocardial Ischemia," *Ultrasound in Medicine & Biology,* vol. 44, pp. 2155-2164, 2018.

[13] R. A. Mukaddim, A. Rodgers, T. A. Hacker, and T. Varghese, "Real-Time Monitoring of Myocardial Ischemia in a Murine Model using in-vivo Photo-acoustic Imaging," *Proceedings of the 63rd Annual Convention, American Institute of Ultrasound in Medicine, New York.,* 2018.

[14] K. E. Wilson, S. V. Bachawal, L. Tian, and J. K. Willmann, "Multiparametric spectroscopic photoacoustic imaging of breast cancer development in a transgenic mouse model," *Theranostics,* vol. 4, p. 1062, 2014.

[15] A. Needles, A. Heinmiller, J. Sun, C. Theodoropoulos, D. Bates, D. Hirson*, et al.*, "Development and initial application of a fully integrated photoacoustic micro-ultrasound system," *IEEE transactions on ultrasonics, ferroelectrics, and frequency control,* vol. 60, pp. 888-897, 2013.

[16] R. A. Mukaddim, A. M. Weichmann, and T. Varghese, "Photoacoustic Delay-and-Sum Beamforming with Spatiotemporal Coherence Factor," *2020 IEEE International Ultrasonics Symposium (IUS), IEEE, 2020.,* 2020.

[17] R. A. Mukaddim and T. Varghese, "Spatiotemporal Coherence Weighting for *In Vivo* Cardiac Photoacoustic Image Beamformation," *IEEE transactions on ultrasonics, ferroelectrics, and frequency control* 2020.

[18] T. Noto, G. Zhou, S. Schuele, J. Templer, and C. Zelano, "Automated analysis of breathing waveforms using BreathMetrics: a respiratory signal processing toolbox," *Chemical senses,* vol. 43, pp. 583-597, 2018.

[19] J.-F. Synnevag, A. Austeng, and S. Holm, "Benefits of minimum-variance beamforming in medical ultrasound imaging," *IEEE transactions on ultrasonics, ferroelectrics, and frequency control,* vol. 56, pp. 1868-1879, 2009.

[20] K. M. Kempski, M. T. Graham, M. R. Gubbi, T. Palmer, and M. A. L. Bell, "Application of the generalized contrast-to-noise ratio to assess photoacoustic image quality," *Biomedical Optics Express,* vol. 11, pp. 3684-3698, 2020.

[21] A. Rodriguez-Molares, O. M. H. Rindal, J. D'hooge, S.-E. Måsøy, A. Austeng, M. A. L. Bell*, et al.*, "The generalized contrast-to-noise ratio: a formal definition for lesion detectability," *IEEE Transactions on Ultrasonics, Ferroelectrics, and Frequency Control,* vol. 67, pp. 745-759, 2019.

[22] M. Mozaffarzadeh, A. Mahloojifar, M. Orooji, S. Adabi, and M. Nasiriavanaki, "Double-stage delay multiply and sum beamforming algorithm: Application to linear-array photoacoustic imaging," *IEEE Transactions on Biomedical Engineering,* vol. 65, pp. 31-42, 2017.

[23] J. Lv, Y. Peng, S. Li, Z. Guo, Q. Zhao, X. Zhang*, et al.*, "Hemispherical photoacoustic imaging of myocardial infarction: in vivo detection and monitoring," *European radiology,* vol. 28, pp. 2176-2183, 2018.

[24] W.-T. Chang, S. Fisch, M. Chen, Y. Qiu, S. Cheng, and R. Liao, "Ultrasound based assessment of coronary artery flow and coronary flow reserve using the pressure overload model in mice," *JoVE (Journal of Visualized Experiments),* p. e52598, 2015.

[25] C. P. Sabino, A. M. Deana, T. M. Yoshimura, D. F. da Silva, C. M. França, M. R. Hamblin*, et al.*, "The optical properties of mouse skin in the visible and near infrared spectral regions," *Journal of Photochemistry and Photobiology B: Biology,* vol. 160, pp. 72-78, 2016.

[26] M. L. Lindsey, Z. Kassiri, J. A. Virag, L. E. de Castro Brás, and M. Scherrer-Crosbie, "Guidelines for measuring cardiac physiology in mice," *American Journal of Physiology-Heart and Circulatory Physiology,* vol. 314, pp. H733-H752, 2018.

[27] S. Gao, D. Ho, D. E. Vatner, and S. F. Vatner, "Echocardiography in mice," *Current protocols in mouse biology,* vol. 1, pp. 71-83, 2011.

[28] M. McCormick, T. Varghese, X. Wang, C. Mitchell, M. Kliewer, and R. Dempsey, "Methods for robust in vivo strain estimation in the carotid artery," *Physics in Medicine & Biology,* vol. 57, p. 7329, 2012.

[29] M. A. Naser, D. R. Sampaio, N. M. Muñoz, C. A. Wood, T. M. Mitcham, W. Stefan*, et al.*, "Improved photoacoustic-based oxygen saturation estimation with SNR-regularized local fluence correction," *IEEE transactions on medical imaging,* vol. 38, pp. 561-571, 2018.

[30] M. A. L. Bell, N. Kuo, D. Y. Song, and E. M. Boctor, "Short-lag spatial coherence beamforming of photoacoustic images for enhanced visualization of prostate brachytherapy seeds," *Biomedical optics express,* vol. 4, pp. 1964-1977, 2013.

[31] D. Allman, A. Reiter, and M. A. L. Bell, "Photoacoustic source detection and reflection artifact removal enabled by deep learning," *IEEE transactions on medical imaging,* vol. 37, pp. 1464-1477, 2018.

[32] K. J. Francis and S. Manohar, "Photoacoustic imaging in percutaneous radiofrequency ablation: device guidance and ablation visualization," *Physics in Medicine & Biology,* vol. 64, p. 184001, 2019.

[33] M. A. Lediju Bell, "Photoacoustic imaging for surgical guidance: Principles, applications, and outlook," *Journal of Applied Physics,* vol. 128, p. 060904, 2020.

[34] T. Kirchner, F. Sattler, J. Gröhl, and L. Maier-Hein, "Signed real-time delay multiply and sum beamforming for multispectral photoacoustic imaging," *Journal of Imaging,* vol. 4, p. 121, 2018.

[35] R. Al Mukaddim, R. Ahmed, and T. Varghese, "Sub-aperture Processing Based Adaptive Beamforming for Photoacoustic Imaging," *IEEE Transactions on Ultrasonics, Ferroelectrics, and Frequency Control,* 2021.

[36] D. Kumar, T. A. Hacker, J. Buck, L. F. Whitesell, E. H. Kaji, P. S. Douglas*, et al.*, "Distinct mouse coronary anatomy and myocardial infarction consequent to ligation," *Coronary artery disease,* vol. 16, pp. 41-44, 2005.

Chapter 13

In vivo Estimation of Myocardial Oxygenation with Physiological Signal Gating and Motion Compensation

Photoacoustic Imaging (PAI) with high persistence (multiple frame averaging) has been reported in **Chapter 08** of this dissertation to quantify murine myocardial relative oxygen saturation (sO_2) *in vivo*. But the proposed method may not be suitable to identify subtle sO_2 variation associated with ischemia and suffer from lower spatiotemporal resolution due to averaging. In this chapter, we propose a physiological signal gated PAI technique with motion compensation that addresses these issues and term this method as OPMC (**O**xygenation estimation with **P**hysiological signal gating and **M**otion **C**ompensation). Image and signal processing methods developed and reported in **Chapters 04, 09 – 12** in this dissertation are employed in this chapter to implement an improved *in vivo* myocardial relative oxygen saturation (sO_2) estimation framework. OPMC

13.1 Proposed Workflow to Estimate Myocardial Oxygenation

Figure 13.1 shows a schematic diagram summarizing key steps of the proposed framework to estimate murine myocardial relative oxygen saturation *in vivo*.

13.1.1 In vivo murine cardiac single wavelength PAI data acquisition

Raw photoacoustic (PA) channel data at 710, 734, 760, 800 and 850 nm were collected from three BALB/CJ mice (male, 10 weeks old, Jackson Lab) using a Vevo 2100 LAZR imaging system in PA RF mode. Data collection was done with an LZ 250 transducer (f_c = 21 MHz) with a field-of-view covering the anterior myocardium resulting in 64-element parallel receive and

simultaneous acquisition of physiological signals (ECG and respiratory). For further details, interested readers are referred to **Chapter 12** as the same data acquisition protocol is employed in this chapter.

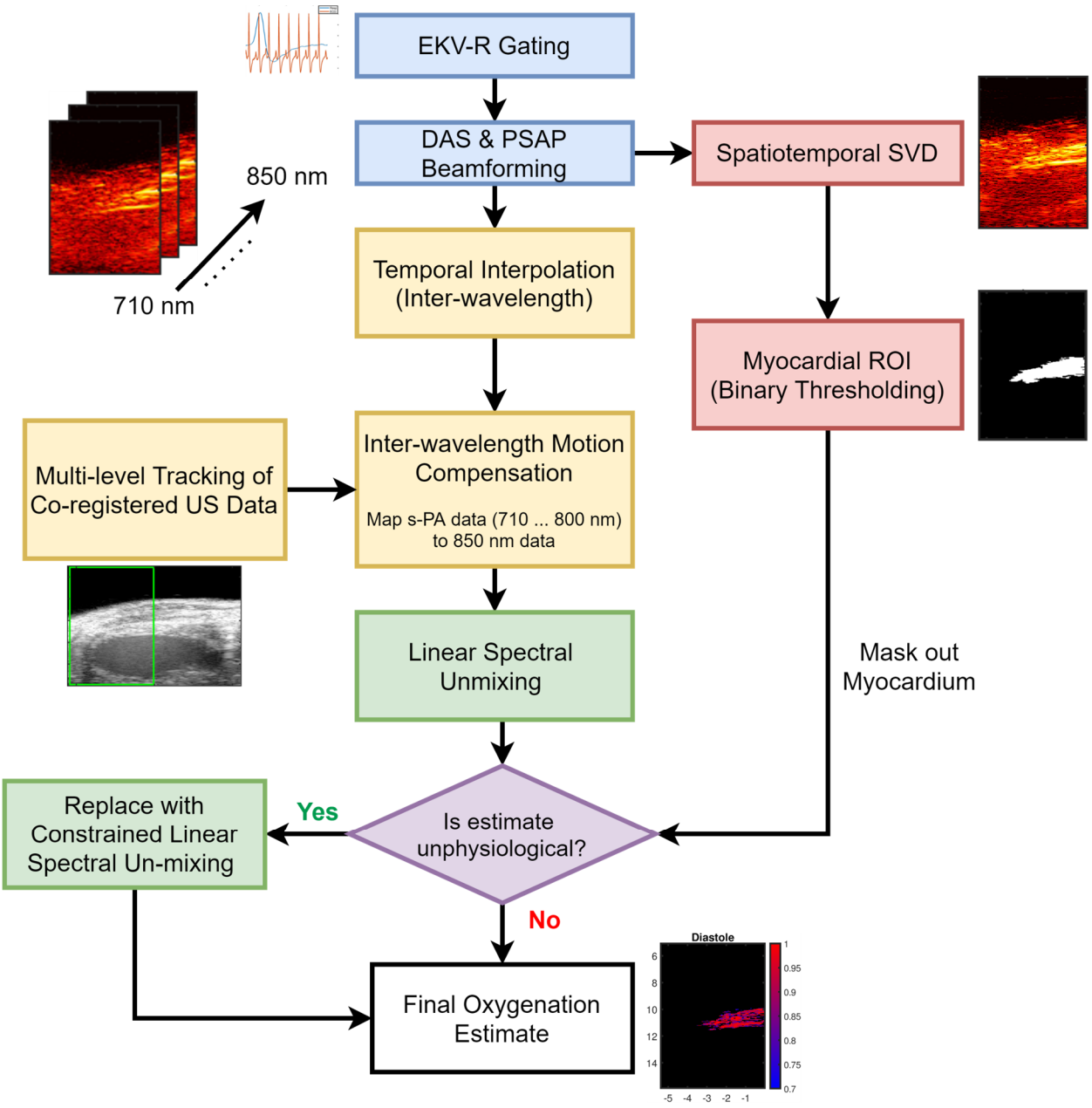

Figure 13.1 Proposed Framework to estimate murine myocardial relative oxygen saturation *in vivo*. s-PA = single wavelength PA data.

13.1.2 Physiological Signal Gating and DAS Beamforming

For each PA wavelength, physiological signal gating was applied to reconstruct a cardiac cycle of channel data following an approach reported in **Chapter 12** and beamforming using delay-and-sum (DAS) and photoacoustic sub-aperture processing (PSAP) [**Chapter 10 and 11**] was done. Parameters used for beamforming are the same as that reported in **Chapters 10** and **12**. At the same time, co-registered ultrasound B-mode images were also beamformed using DAS for each wavelength. Temporal linear interpolation was applied on beamformed data (DAS PA, PSAP and DAS B-mode) to ensure at least 100 frames per cardiac cycle per wavelength.

13.1.3 Inter-wavelength Motion Compensation

For multi-wavelength PAI to estimate sO_2, same tissue must be probed using optical pulses at multiple wavelengths to produce a PAI spectrum as a function of the optical wavelength. However, presence of physiological motion will corrupt the derived PAI spectrum thus resulting in inaccurate sO_2 estimation [1]. To ensure stable spectral decomposition, imaging was done with 5 optical wavelengths in this work [1, 2]. This process introduced unique challenges associated with periodic myocardial motion. First, due to system limitations, imaging was done sequentially requiring 50 seconds per wavelength of data collection with additional time required to switch from one wavelength to another. Second, during this relatively long data acquisition period, there was variability in heart rate (e.g., around 20-30 beats per minutes) among single wavelength PA (s-PA) data. In order to address these challenges, we first applied physiological signal gating and temporal interpolation to temporally align s-PA data. However, due to the heart rate variability mentioned above, the data were still not aligned perfectly. To address this issue, we utilized co-registered ultrasound B-mode data to register s-PA data collected at 710, 734, 760, 800 nm to the 850 nm dataset [1]. Inter-wavelength axial and lateral displacements were estimated by applying

a three-level displacement tracking algorithm on the co-registered ultrasound B-mode images to perform motion compensation [3]. During motion estimation, 710, 734, 760, 800 nm data were considered as motion corrupted while 850 nm data was considered as the reference frame. Table 13.1 summarizes the motion estimation parameters used in this study. Motion compensation is repeated for all the frames over the reconstructed cardiac cycle (100 frames) as discussed in Section 13.1.2).

Table 13.1 Inter-wavelength Displacement Estimation Parameters

Parameters	**Values**	**Units**
Axial Kernel	8, 5, 1	Wavelengths (λ)
Lateral Kernel	31, 21, 21	Interpolated A-lines
Interpolation Factor (axial: lateral)	2: 2	-
Kernel Overlap (axial, lateral)	(10, 75)	%
Median Filtering Kernel	5 × 5	pixel

13.1.4 Myocardial Oxygenation Estimation Linear Spectral Unmixing

Using motion compensated multi-wavelength PAI data, linear spectral unmixing (LSU) was applied to extract chromophore concentration of oxy- and deoxy-hemoglobin (HbO_2 and HbR). Linear spectral unmixing was described in detail in **"Chapter 03 Section 3.3.1: Linear spectral unmixing and spectral coloring artifact"** of this dissertation. Note that, fluence compensation was not implemented for this study thus resulting in a relative estimate of myocardial sO_2.

13.1.5 Dynamic Myocardial Region of Interest Generation and Correction of Inaccurate LSU Estimates

To quantitatively analyze myocardial sO_2 estimates over a cardiac cycle, dynamic regions of interest (ROIs) were generated by applying a binary thresholding filter on the spatiotemporal singular value decomposition (ST-SVD) processed PSAP images at 850 nm. For methodological details and related parameters regarding ST-SVD processing and PSAP processing, please refer to **Chapters 10 – 12**. The LSU estimated sO_2 parametric maps were first masked out using the dynamic ROIs. We term these results as LSU+M in the rest of this chapter. Then, the non-physiological sO_2 estimates ($sO_2 < 0$ % or $sO_2 > 100$ %) detected within the ROIs were replaced using a constrained sO_2 estimation approach with a non-negativity constraint proposed by Kim *et al.* [4]. Briefly, the method describes the expected local absorption spectrum ($\mu_a'(\lambda, \mathbf{r})$) using following equation.

$$\mu_a'(\lambda, \mathbf{r}) = C\left[HbO_2\right](\mathbf{r})\varepsilon_{HbO_2}(\lambda) + C\left[HbR\right](\mathbf{r})\varepsilon_{HbR}(\lambda) \tag{13.1}$$

where, $C\left[HbO_2\right]$ and $C\left[HbR\right]$ are the concentrations of oxy- and deoxy-hemoglobin (HbO_2 and HbR) respectively at a pixel location, **r** and ε denotes the known molar extinction coefficient. Imposing two constraints (non-negativity of chromophore concentrations) such that $C\left[HbO_2\right] + C\left[HbR\right] = 1$ and $0 < C\left[HbO_2\right], C\left[HbR\right] < 1$, all possible local absorption spectra were reconstructed. Then, $C\left[HbO_2\right]$ and $C\left[HbR\right]$ values were determined by minimizing the least squared error between normalized local PA spectrum (extracted from motion compensated multi-spectral PAI data) and expected local absorption spectra as follows.

$$C\left[HbO_2\right]^*, C\left[HbR\right]^* = \underset{C[HbO_2], C[HbR]}{\arg\min}\ E\left[\left(p^*(\lambda, \mathbf{r}) - \mu_a'(\lambda, \mathbf{r})\right)^2\right] \tag{13.2}$$

where, $p^*(\lambda, \mathbf{r})$ is the normalized local PA spectrum estimated from experimental data. Equation (13.2) was solved numerically to estimate $C\left[HbO_2\right]$ and $C\left[HbR\right]$. Finally, the relative oxygen saturation was estimated as follows.

$$sO_2(\%) = \frac{C\left[HbO_2\right]^*}{C\left[HbO_2\right]^* + C\left[HbR\right]^*} \tag{13.3}$$

This approach is termed as CLSU+M in this chapter. Temporal progression of myocardial sO_2 over a cardiac cycle was extracted by averaging all the estimates within the dynamic ROIs. Additionally, to derive the temporal trend and noise suppression, a 7-point temporal moving average filter was applied on the raw temporal progression curves.

13.1.6 Comparative Analysis

Myocardial sO_2 (%) estimated using the proposed method was compared against the sO_2 (%) values estimated using a high persistence dual-wavelength PAI method reported in **Chapter 08**. Additionally, healthy cardiac function was also confirmed by estimating cardiac strain tensors using the cardiac strain imaging approaches reported in **Chapters 04 – 05**.

13.2 Proposed Method Improves Temporal Sensitivity of Myocardial Oxygenation Estimation

This section presents preliminary results on myocardial oxygen saturation estimation from three healthy mice using the proposed method.

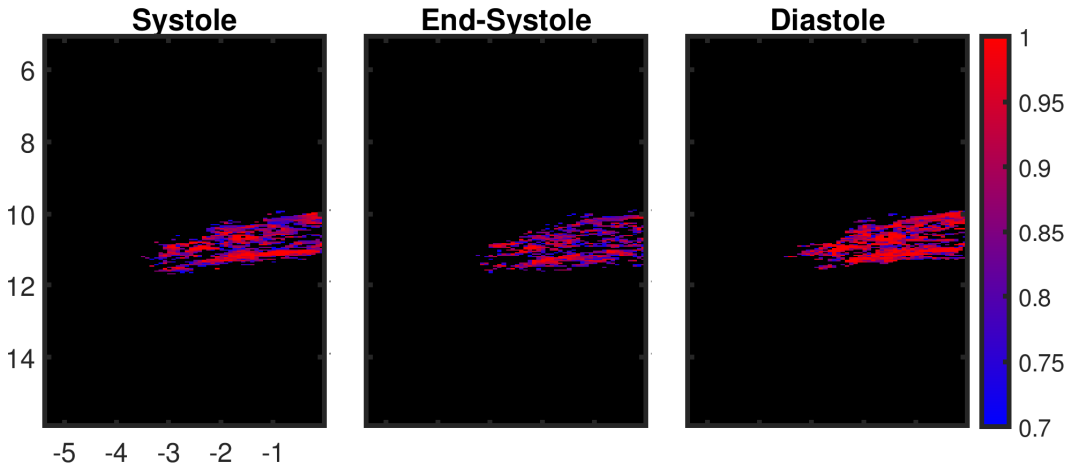

Figure 13.2 (a) – (c) Myocardial sO_2 images estimated during systole, end-systole and diastole phase of a cardiac cycle respectively. ROIs were generated automatically using PSAP and spatiotemporal SVD processing.

Figure 13.2 (a) – (c) show myocardial sO_2 maps estimated during systole, end-systole and diastole phase of a cardiac cycle respectively for Mouse 1. We observed higher oxygenation at the beginning of systole (more red pixels) which reduced at ES (more blue pixels) and finally recovering to higher oxygenation at diastole (uniformly red). Note that ROIs were generated automatically using PSAP and spatiotemporal SVD processing as described in Section 13.1.5.

A representative example of the temporal progression of myocardial sO_2 over a cardiac cycle for the same mouse is presented in Figure 13.3. Figure 13.3 (a) shows raw sO_2 using LSU (blue), LSU+M (brown) and CLSU+M (yellow) without moving average filtering. Motion compensation provided higher estimates compared to LSU without any motion correction. CLSU+M followed the similar trend as LSU+M but resulted in higher sO_2 attributed to the replacement operation. Figure 13.3 (b) presents the result of myocardial sO_2 estimated with dual-wavelength OxyHemo mode commercially available in Vevo 2100 imaging system and high persistence. Note that the results are presented for 20 frames, each of them produced by incoherent averaging over 10 consecutive frames. Therefore, image acquisition frame rate was only 5 Hz and

estimates cannot be temporally synchronized to different phases of a cardiac cycle such as end-systole. Figure 13.3 (d) shows final sO_2 estimates using LSU (blue), LSU+M (brown) and CLSU+M (yellow) after moving average filtering while Figure 13.3 (c) show the corresponding PAI M-mode image. We observed higher sO_2 values at end-diastole (≈80%) which gradually reduced during systole (≈72%) and finally recovering to higher oxygenation at diastole (≈80%). This observation correlates with the myocardial motion seen in PAI M-mode image. The turning point for CLSU+M (marked with an arrow on the yellow curve in Figure 13.3 (d)) matches with the turning point of left ventricular (LV) chamber towards increased volume after end-systole (observe the endocardial border marked with an arrow in Figure 13.3 (d)). Additionally, these results show that the proposed method will allow us to temporally synchronize myocardial sO_2 estimates to different phases of a cardiac cycle thus providing higher temporal sensitivity when compared to the reported commercial method in **Chapter 08**.

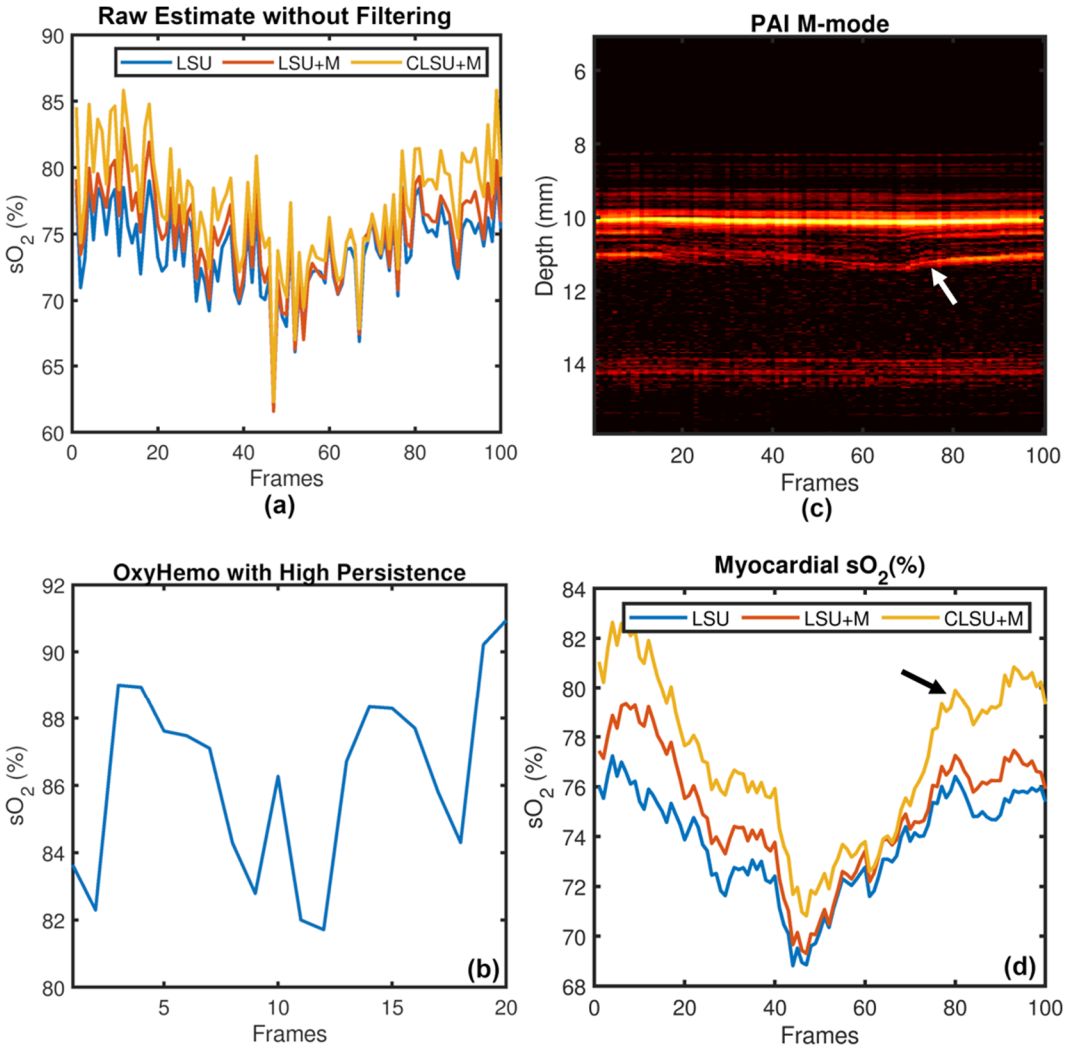

Figure 13.3 A representative example of temporal progression of myocardial sO_2 over a cardiac cycle. (a) Raw sO_2 obtained using the proposed method without a moving average filter, (b) sO_2 estimation using OxyHemo mode in Vevo 2100 imaging system and high persistence, (c) PAI M-mode image and (d) Final sO_2 estimate using the proposed method after application of a moving average filter. LSU = Linear spectral unmixing, LSU+M = Linear spectral unmixing with inter-wavelength motion compensation and CLSU+M = Replacement with constrained linear spectral unmixing with inter-wavelength motion compensation.

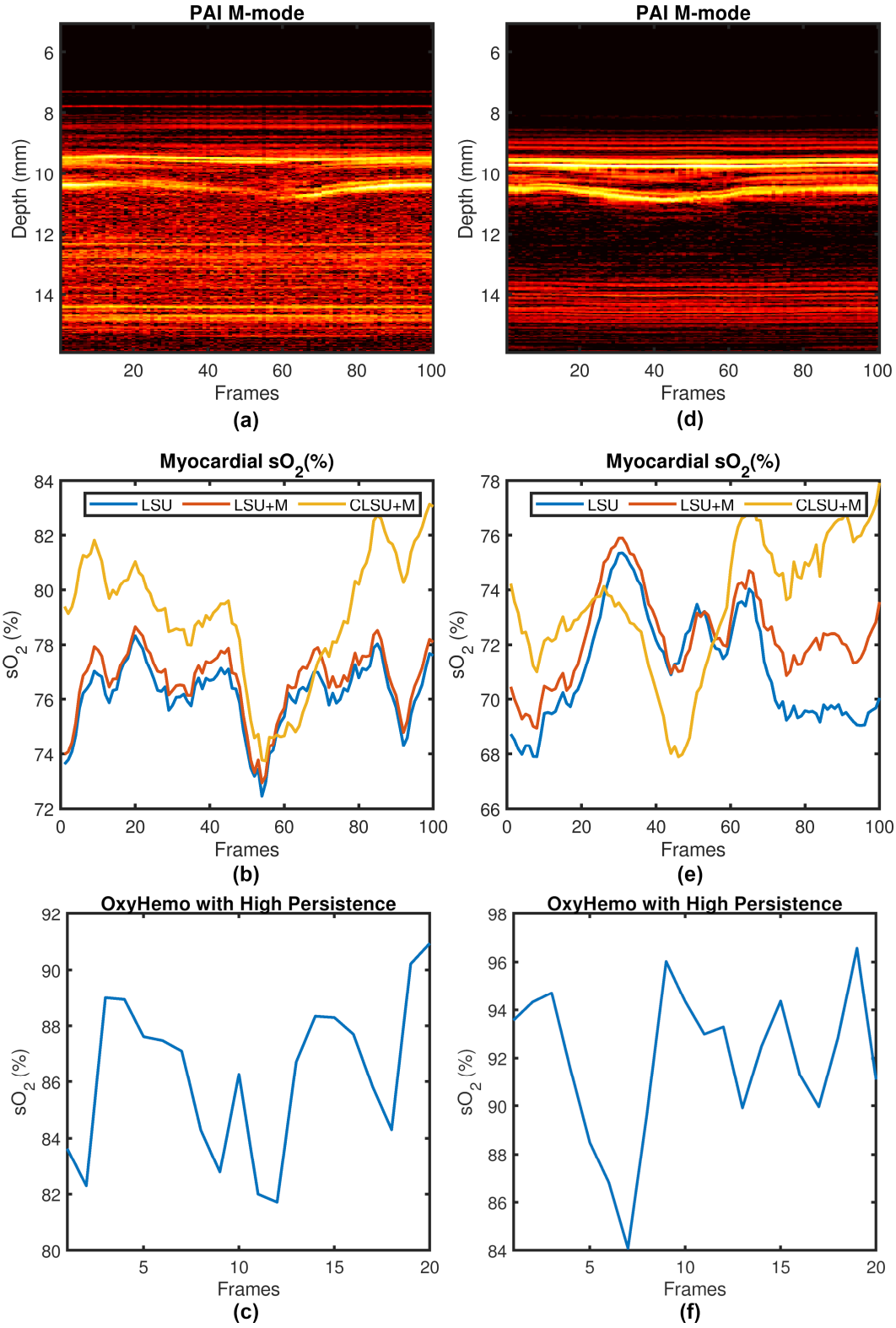

Figure 13.4 Panels (a) – (c) show PAI M-mode, sO_2 estimation with proposed method and commercial solution with high persistence for Mouse 02. (d) – (f) show the same results for Mouse 03.

Results from a comparative study using two more mice are represented in Figure 13.4. Figure 13.4 (a) – (c) show PAI M-mode, sO_2 estimation with proposed method and commercial solution with high persistence respectively for Mouse 02 while (d) – (f) show the same results for Mouse 03. We observe similar trends in temporal progression of myocardial sO_2 in Mouse 02 – 03 like Mouse 01 with higher sO_2 values at end-diastole, gradual reduction during systole and final recovery to higher oxygenation during diastole [Figure 13.4 (b) and (e)]. The PAI M-mode images corroborate our findings [Figure 13.4 (a) and (b)]. Even though, estimates using commercial software with high persistence provided high sO_2 values [Figure 13.4 (c) and (f)] as expected from healthy mice hearts, they lacked the temporal sensitivity demonstrated by our proposed framework.

13.3 Discussion on Experimental Findings and Future Directions

In this chapter, we proposed a multi-wavelength PAI approach to estimate murine myocardial relative oxygen saturation *in vivo* with physiological signal gating and inter-wavelength motion compensation. Methods developed in **Chapters 10 – 12** (Photoacoustic Sub-aperture Processing and Spatiotemporal Singular Value Decompaction) enabled dynamic ROI generation to quantify myocardial sO_2 signals with coherent averaging (moving average filter) to extract temporal progression of sO_2 values over a cardiac cycle. Proposed method resulted in temporal synchronization of estimated sO_2 values to different phases of a cardiac cycle such as systole, end-systole, diastole and end-diastole. We observed higher myocardial sO_2 values at diastolic phase compared to systolic phase of a cardiac cycle. We hypothesize that this finding correlates with the left coronary artery flow variation between diastole and systole observed in both human [5, 6] and mice [7, 8] studies with increased blood flow in diastole. For example, for normal human heart, the coronary arteries accessed through transthoracic Doppler ultrasound

demonstrated higher velocity blood flow in diastole when the heart muscle is relaxed [5]. Similar results were reported by Hartley *et al.* [8] by performing Doppler ultrasound examination of coronary arteries of wild-type and ApoE$^{-/-}$ mice. Even though results presented in this chapter are quite encouraging and interesting, several important factors require further investigation to understand the robustness of the proposed workflow which are listed below. First, fluence compensation was not incorporated in this work therefore these estimates might suffer from spectral coloring as distance between skin and epicardial layer exceeds 1 mm [9, 10]. To address this issue, we will utilize the fluence correction approach proposed by Fadhel *et al.* where fluence profiles of multi-wavelength PA images are matched to the fluence at a reference wavelength [11, 12]. Second, our results in this chapter were limited to only three mice. However, further experiments with a larger cohort are necessary to understand the strengths and weakness of the proposed method. Third, robustness should be evaluated using more complicated murine models such myocardial infarction and ischemia-reperfusion injury *in vivo*. Finally, further simulation studies are required to adapt the fluence matching algorithm from Fadhel *et al.* [11, 12] with motion compensation and the constrained linear spectral unmixing method used in this chapter [4]. Even under the stated limitations, our initial results are very promising and demonstrate that our proposed method is sensitive to subtle variations in myocardial oxygenation *in vivo*.

List of References

[1] G.-S. Jeng, M.-L. Li, M. Kim, S. J. Yoon, J. J. Pitre, D. S. Li*, et al.*, "Real-time interleaved spectroscopic photoacoustic and ultrasound (PAUS) scanning with simultaneous fluence compensation and motion correction," *Nature communications,* vol. 12, pp. 1-12, 2021.

[2] M. A. Naser, D. R. Sampaio, N. M. Muñoz, C. A. Wood, T. M. Mitcham, W. Stefan*, et al.*, "Improved photoacoustic-based oxygen saturation estimation with SNR-regularized local fluence correction," *IEEE transactions on medical imaging,* vol. 38, pp. 561-571, 2018.

[3] H. Shi and T. Varghese, "Two-dimensional multi-level strain estimation for discontinuous tissue," *Physics in Medicine & Biology,* vol. 52, p. 389, 2007.

[4] S. Kim, Y.-S. Chen, G. P. Luke, and S. Y. Emelianov, "In vivo three-dimensional spectroscopic photoacoustic imaging for monitoring nanoparticle delivery," *Biomedical optics express,* vol. 2, pp. 2540-2550, 2011.

[5] L. Cortigiani, F. Rigo, S. Gherardi, F. Bovenzi, S. Molinaro, E. Picano*, et al.*, "Prognostic implication of Doppler echocardiographic derived coronary flow reserve in patients with left bundle branch block," *Eur Heart J,* vol. 34, pp. 364-73, Feb 2013.

[6] A. G. Goodwill, G. M. Dick, A. M. Kiel, and J. D. Tune, "Regulation of Coronary Blood Flow," *Compr Physiol,* vol. 7, pp. 321-382, Mar 16 2017.

[7] J. Wikström, J. Grönros, G. Bergström, and L. M. Gan, "Functional and morphologic imaging of coronary atherosclerosis in living mice using high-resolution color Doppler echocardiography and ultrasound biomicroscopy," *J Am Coll Cardiol,* vol. 46, pp. 720-7, Aug 16 2005.

[8] C. J. Hartley, A. K. Reddy, L. H. Michael, M. L. Entman, V. Chintalagattu, A. Y. Khakoo*, et al.*, "Coronary flow reserve in mice: effects of age, coronary disease, and vascular loading," *Annu Int Conf IEEE Eng Med Biol Soc,* vol. 2010, pp. 3780-3, 2010.

[9] R. Hochuli, L. An, P. C. Beard, and B. T. Cox, "Estimating blood oxygenation from photoacoustic images: can a simple linear spectroscopic inversion ever work?," *Journal of biomedical optics,* vol. 24, p. 121914, 2019.

[10] B. T. Cox, J. G. Laufer, P. C. Beard, and S. R. Arridge, "Quantitative spectroscopic photoacoustic imaging: a review," *Journal of biomedical optics,* vol. 17, p. 061202, 2012.

[11] M. N. Fadhel, E. Hysi, H. Assi, and M. C. Kolios, "Fluence-matching technique using photoacoustic radiofrequency spectra for improving estimates of oxygen saturation," *Photoacoustics,* vol. 19, p. 100182, 2020.

[12] M. N. Fadhel and M. C. Kolios, "Method and system for fluence matching in photoacoustic imaging," ed: Google Patents, 2020.

Chapter 14

In vivo Murine Cardiac Strain Imaging with Adaptive Bayesian Regularization

Murine models of cardiovascular disease (e.g., myocardial infarction and ischemia-reperfusion injury) focus on providing mechanistic insights into disease progression and translation of pre-clinical therapies into the clinic [1]. For accurate investigation of these models, non-invasive cardiovascular imaging plays a critical role [2]. In particular, ultrasound-based cardiac strain imaging (CSI) has demonstrated higher sensitivity when compared to conventional echocardiography for assessing these models [3]. CSI is an ultrasound radio-frequency (RF) signal-based approach for estimation of myocardial tissue elasticity by utilizing the natural contraction and relaxation of the myocardium [4-11]. However, accurate strain estimation in murine models poses unique challenges due their small size and rapid heart rate [12]. Higher heart rates result in increased RF signal decorrelation and additional out-of-plane motion thus degrading the quality of CSI. To address these issues, we have previously developed a multi-level block matching (BM) algorithm with Bayesian regularization for CSI (**Chapter 04**) [13-16]. Later, we developed an adaptive scheme which utilizes local RF data statistics to further optimize Bayesian regularization (**Chapter 05**). In this chapter, we report on a Lagrangian CSI framework incorporating Adaptive Bayesian Regularization (ABR-CSI) [17] into a multi-level BM algorithm and investigate the feasibility of this method for longitudinal monitoring of cardiac remodeling in murine models of myocardial infarction and ischemia-reperfusion injury *in vivo*.

14.1 *In vivo* Validation Study Design for ABR-CSI

Figure 14.1 summarizes the key steps involved in the *in vivo* longitudinal study designed to validate the ABR-CSI.

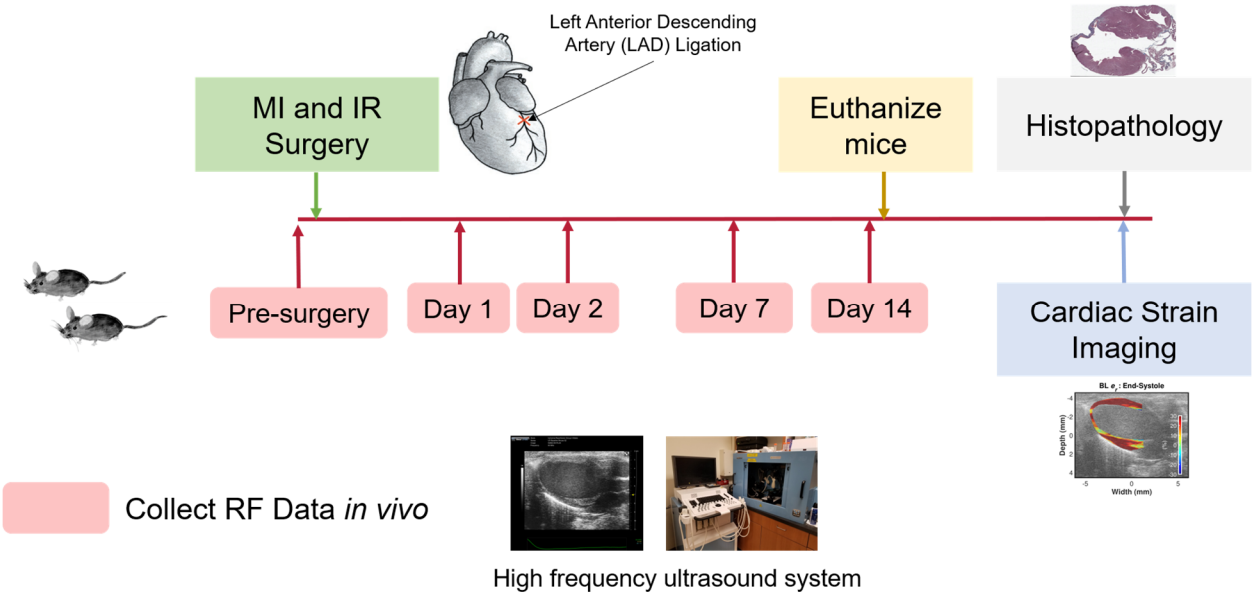

Figure 14.1 Schematic diagram illustrating the in vivo validation study for ABR-CSI

14.1.1 Murine Model and in vivo RF Data Collection

Three male BALB/CJ 10 weeks old mice acquired from The Jackson Laboratory, Bar Harbor, ME USA were imaged pre-surgery (BL) and 1,2,7 and 14 days post-surgery. RF data collection was done using a MS 550D transducer (center frequency, $f_c = 40$ MHz) at 235 fps in the parasternal long axis view (Vevo 2100, Fujifilm Visualsonics). For details regarding RF data collection, please refer to **Chapters 04** and **12** of this dissertation. Mice were randomly assigned to 1 of 3 surgery groups: sham, myocardial infarction (MI) and ischemia reperfusion (IR). The sham mouse underwent thoracotomy with no manipulation of the heart. For the MI mouse, myocardial infarction was induced by permanent ligation of the left anterior descending coronary artery (LAD) via thoracotomy. For the IR mouse, myocardial ischemia was first induced by

ligating the LAD and then blood flow was restored by releasing the tie after 45 minutes for reperfusion. All *in vivo* experimental protocols were approved by the University of Wisconsin School of Medicine and Public Health Institutional Animal Care and Use Committee.

14.1.2 Lagrangian CSI framework incorporating Adaptive Bayesian Regularization

ECG and respiratory gating were applied offline to extract one cardiac cycle of RF data for CSI. To estimate interframe axial and lateral displacements, a three-level normalized cross-correlation (NCC) based BM algorithm [13, 18, 19] with locally optimized correlation based adaptive Bayesian regularization was utilized [17]. Bayesian regularization improves displacement estimation by enforcing spatial continuity in a local BM neighborhood through iterative application of Bayes theorem [20]. ABR was developed to dynamically determine the optimal iteration for Bayesian regularization per BM location by taking spatial and temporal strain heterogeneities that are expected *in vivo* into consideration. ABR evaluates a local optimality criterion based on NCC signal-to-noise ratio and motion compensation between pre- and post-deformation RF frames to achieve dynamic regularization [17, 21]. For further details on ABR, please refer to **Chapter 05** of this dissertation. For motion estimation, RF data were first interpolated laterally by a factor of 2 and then tracked with 2-D kernels with final dimensions of [1λ, 11 A-lines] and [50%, 95%] overlap in the axial and lateral direction, respectively. Maximum allowed Bayesian iterations for ABR was 10. For accurate sub-sample estimation, 2-D windowed Sinc interpolation was utilized [22, 23]. Finally, 2-D median filtering in a 5 pixel × 5 pixel neighborhood was applied to remove any outliers.

For cardiac strain estimation, myocardial walls were manually segmented at end-diastole (R-Wave of ECG) to generate a mesh of 24000 points covering the entire myocardium, and used for accumulating interframe displacements over a cardiac cycle [24, 25]. The Lagrangian strain

tensor, **E** was derived by estimating axial, lateral and shear strain components using a least squares strain estimator. Finally, radial (e_r) and longitudinal (e_l) strains were derived by applying coordinate transformation using a rotation matrix, **M** shown below.

$$\mathbf{M} = \begin{pmatrix} \cos\theta & \sin\theta \\ -\sin\theta & \cos\theta \end{pmatrix} \tag{14.1}$$

where, angle θ denotes the radial direction calculated for each cardiac mesh point. For further details on Lagrangian strain estimation, please refer to **Chapter 04** of this dissertation. End-systole (ES) radial and longitudinal strain images were derived to qualitatively evaluate mouse cardiac function. Segmental radial and longitudinal strain curves over a cardiac cycle were also derived by dividing the myocardium into six segments (anterior base, anterior mid, anterior apex, posterior apex, posterior mid and posterior base denoted as segments 1 – 6) [26] and temporal progression of segmental ES and peak strain values were compared among sham, MI and IR mice. Additionally, intraventricular dyssynchrony was quantified by calculating the standard deviation of segmental time-to-peak strains normalized to cardiac cycle length (R-R interval in ECG) [12, 27].

14.1.3 Histopathological Analysis

After the 14th day post-surgery imaging session, the mice were euthanized, hearts were harvested and fixed in 10% formalin for histopathological analysis. Harvested myocardial tissues were embedded in paraffin highlighting the aortic outflow tract to achieve an orientation roughly approximating the ultrasonographic PLAX plane. To confirm the heart orientation, small stripes of histology tissue inks were placed on the anterior surface of the heart following the convention shown in Figure 14.2. Anterior stripe (shown in green in Figure 14.2) through apex and aortic outflow tract approximated the plane through the aortic outflow tract to match a whole slide image

(WSI) section with the *in vivo* PLAX ultrasound data. Short plane stripe (shown in blue in Figure 14.2) was used to aid in alignment of multiple sections for 3-D reconstruction. After inking, 5 μm-thick sections were taken at 100 μm intervals through the entire heart in the long axis orientation and stained with Masson's trichome (MT) for quantification of fibrosis. The stained slides were digitized using a 20× uScopeHXII digital microscope (Microscopes International, Dallas, TX 75208-1953). To automatically classify regions of fibrosis in the digital WSI, a 3-class Random Tree pixel classifier was designed using QuPath [28] (an open-source software for digital pathology image analysis accessed through: https://qupath.github.io/) by manually delineating collagen, non-collagen and background regions in a representative WSI. Note that, collagen and non-collagen regions were stained as blue and dark purple in the MT stained WSIs. Finally, classified images from QuPath [28] were loaded into MATLAB to quantify percentage of fibrosis in the infarct and viable regions. First, infarct and viable regions were manually delineated using the MT-stained WSI. Then, collagen content was expressed as a percentage with respect to total area of the affected region using the classification from QuPath [28]

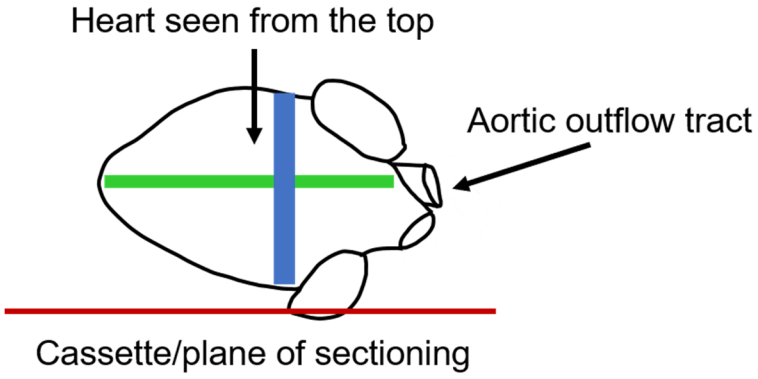

Figure 14.2 Inking convention for matching histopathology WSIs to *in vivo* ultrasound PLAX view. Image courtesy: Dr. Melissa Graham, Director, Comparative Pathology Laboratory, Research Animal Resources and Compliance (RARC), UW-Madison

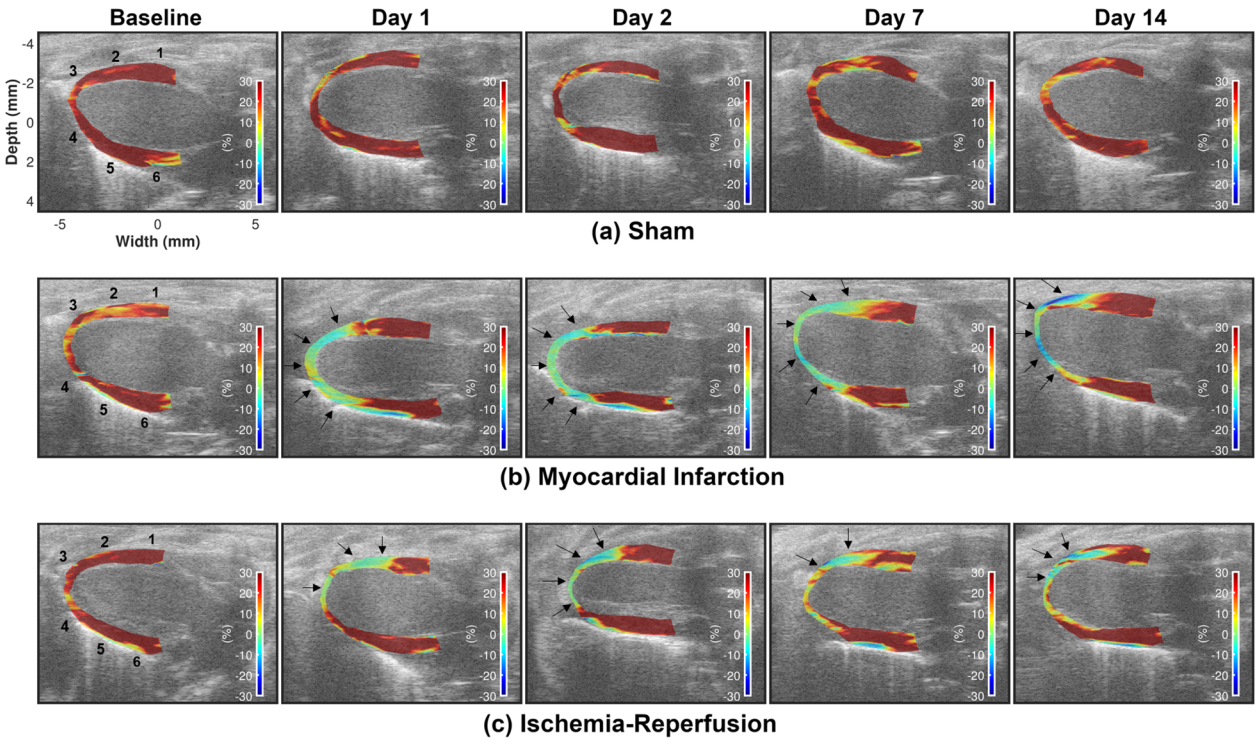

Figure 14.3 ES accumulated radial strain images over time for (a) sham, (b) MI and (c) IR mice, respectively. Strain display dynamic range is from -30% to +30%. Positive strain value (red) = myocardial wall thickening, negative strain value (blue) = myocardial wall thinning and zero strain value (light green) = no wall motion.

14.2 Temporal Progression of Cardiac Strain differentiates among Sham, MI and IR mice

Figure 14.3 (a) – (c) show the progression of ES radial strain images over time for sham, MI and IR mice, respectively. For normal LV function, thickening of myocardial wall is expected during systole with reverse changes during diastole [3, 29]. This would be reflected as positive radial strain values mapped as red in the chosen colormap in Figure 14.3. At baseline (pre-surgery), all three mice demonstrated normal LV function with uniformly red strain maps at ES indicating myocardial thickening. The sham mouse preserved normal cardiac function in the radial strain images resulting in uniformly red strain maps at ES for all post-surgery imaging sessions [Figure 14.3 (a)]. The post-surgery ES strain images for the MI mouse showed a marked reduction or sign

reversal of strain magnitudes (light green or blue) in the apical segments when compared to baseline as indicated with the black arrows in Figure 14.3 (b). Furthermore, infarct, border and viable regions can be clearly identified in the MI radial strain images having predominantly blue, mixture of yellow + light blue + red, and red colors, respectively. The IR mouse also demonstrated motion abnormalities post-surgery with marked reduction or sign reversal of strain magnitudes (light green or blue) in anterior mid (segment 2) and anterior apical (segment 3) segments (infarcted region marked with arrows).

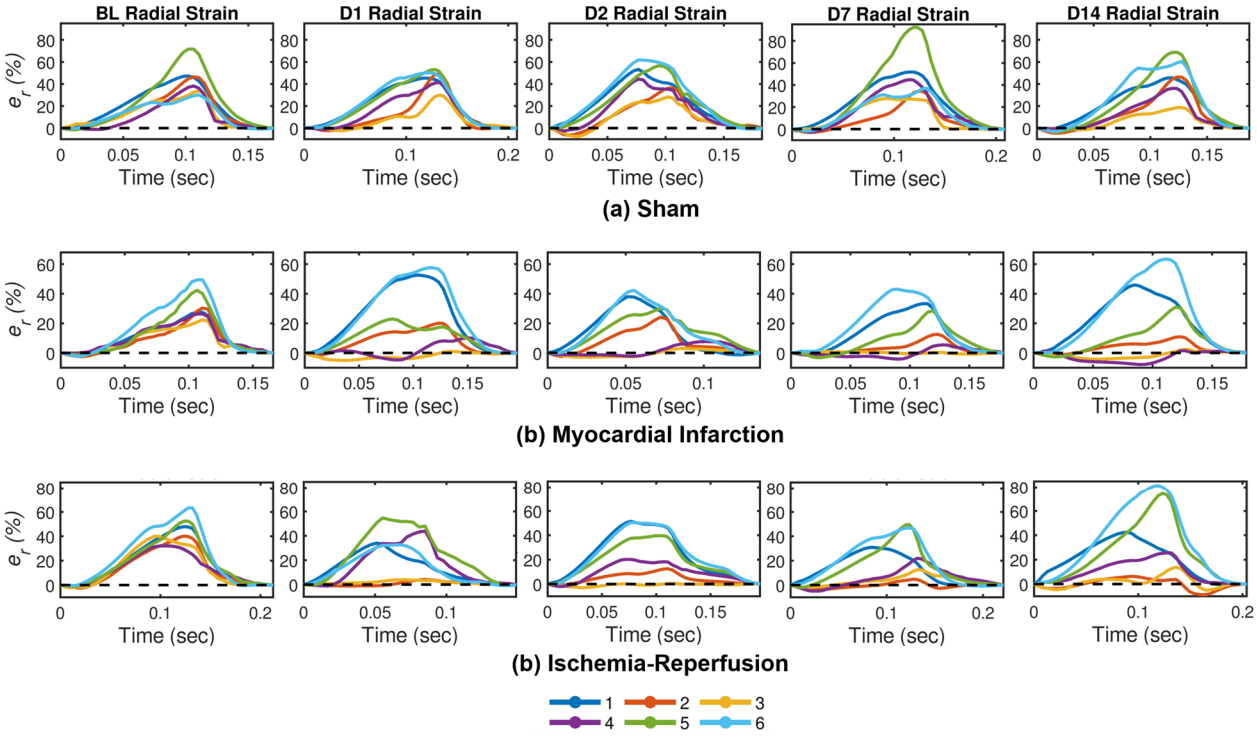

Figure 14.4 Temporal progression of segmental radial strain curves over a cardiac cycle for (a) sham, (b) MI and (c) IR mice, respectively. Anterior base, anterior mid, anterior apex, posterior apex, posterior mid and posterior base regions are denoted as segments 1 – 6 in these curves.

Figure 14.4 (a) – (c) compare the temporal progression of segmental radial strain curves over a cardiac cycle for sham, MI and IR mice, respectively. At baseline, all three mice had peak positive radial strain values in all segments with synchronicity among the segments (observe the

low intraventricular dyssynchrony at baseline in Table 14.1). Sham mouse maintained the similar trends in the segmental radial strain curves post-surgery cases indicating normal cardiac function (e.g., intraventricular dyssynchrony at Day 14 was 0.02 [Table 14.1]). Note that an apical infarct can be clearly identified in the MI mouse with subsequent reduction of peak radial and strain values in apical segments (segments 3 – 4 shown in yellow and violet colors in Figure 14.4) with late time-to-peak strain values compared to viable regions (segments 1, 5 – 6) resulting in higher intraventricular dyssynchrony values (e.g., intraventricular dyssynchrony at Day 14 was 0.13 [Table 14.1]). Anterior mid segment (segment 2 plotted using brown color in Figure 14.4) showed progressive deterioration over time indicating the ability for cardiac remodeling monitoring with ABR-CSI. Infarcted and viable regions can also be separated in the IR mouse with a clear decline in peak positive strain values observed in anterior mid and anterior apical segments (segments 2 – 3 in Figure 14.4). We also observed slight reduction in peak radial strain value in posterior apical segment thus demarcating it as border region between infarct and viable regions. Furthermore, the late time-to-peak strain values in segments 2 – 3 contributed to higher intraventricular dyssynchrony values post-surgery (e.g., intraventricular dyssynchrony at Day 14 was 0.11 [Table 14.1]).

Figure 14.5 compares the ES (Figure 14.5 (a)) and peak (Figure 14.5 (b)) segmental radial strain values over time among sham, MI and IR mice respectively. Sham mouse had both positive ES and peak strain values over time corroborating qualitative observations seen in Figure 14.3 and Figure 14.4. For example, ES e_r values for anterior base at baseline = 46.88%, D1 = 45.05%, D2 = 44.22%, D7 = 47.40% and D14 = 39.94%. Based on Figure 14.5, MI mouse had an apical infarct with anterior mid being a border region. For example, ES e_r values for anterior apex at baseline = 17.30%, D1 = -2.88%, D2 = -2.06%, D7 = -0.31% and D14 = -1.31% while for posterior mid at

baseline = 33.01%, D1 = 15.87%, D2 = 25.55%, D7 = 13.20% and D14 = 22.44%. For the IR case, a clear separation in strain values between infarct and viable regions were observed with infarct being localized to the anterior mid and anterior apical segments (segments 2 – 3) and posterior apex being a border region. The infarcted regions showed steady decline in e_r strain values post-surgery while viable regions showed similar or higher peak strain values when compared to baseline. For example, peak e_r values for anterior apex at baseline = 40.12%, D1 = 3.81%, D2 = 3.98%, D7 = 12.64% and D14 = 13.80% while for posterior mid at baseline = 52.43%, D1 = 54.63%, D2 = 39.68%, D7 = 49.61% and D14 = 74.46%.

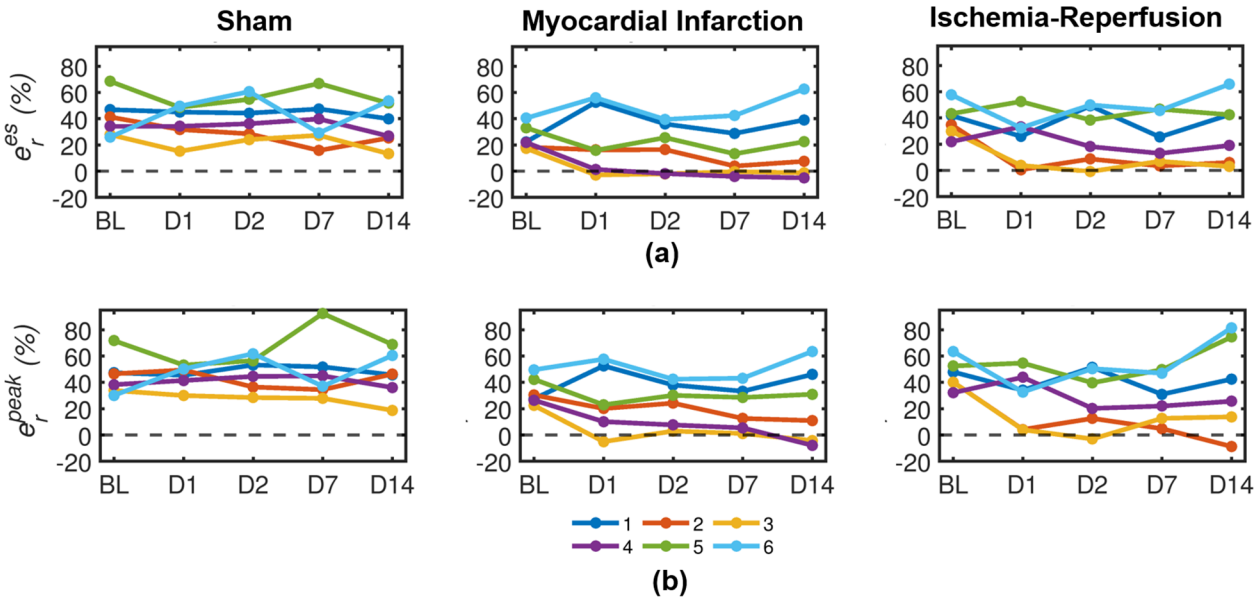

Figure 14.5 Comparison of segmental strains at (a) ES and (b) peak radial strain values over time among sham, MI and IR mice respectively. For each sub-figure, sham, MI and IR results are presented from left to right.

Table 14.1 Intraventricular Dyssynchrony Quantified using Radial Time-to-peak Strain

	Baseline	Day 1	Day 2	Day 7	Day 14
Sham	0.02	0.02	0.07	0.06	0.02
MI	0.01	0.20	0.13	0.21	0.13
IR	0.05	0.08	0.13	0.08	0.11

Temporal progression of strain at ES in the longitudinal strain images for sham, MI and IR mice are summarized in Figure 14.6 (a) – (c) respectively. For normal LV function, shortening of myocardial wall is expected during systole with reverse changes during diastole [3, 29]. This would be reflected as negative longitudinal strain values mapped as blue in the chosen colormap in Figure 14.6. All three mice demonstrated normal LV function along longitudinal direction at the pre-surgery time point with predominantly blue strain maps at ES indicating myocardial wall shortening. Sham mouse preserved this normal cardiac function longitudinally resulting in predominantly blue strain maps at ES for all post-surgery imaging sessions [Figure 14.6. (a)]. There were few small patches of zero or positive longitudinal strain values in sham strain images indicated by the red arrows. In the post-surgery ES strain images for the MI mouse, there was a marked reduction or sign reversal of strain magnitudes (light green or red) in the apical segments when compared to baseline as indicated by the black arrows in Figure 14.6 (b). At Day 14, infarct and viable regions can be clearly identified in the MI longitudinal strain image depicting predominantly a mixture of yellow + light blue + red, and uniformly blue colors, respectively. The IR mice also demonstrated motion abnormalities post-surgery with a marked reduction or sign reversal of strain magnitudes (light green or red) in anterior mid (segment 2) and anterior apical (segment 3) segments (infarcted region marked with black arrows in Figure 14.6 (c)). In the IR ES longitudinal strain images, a small patch within the posterior mid segment (segment 5) showed positive strain values starting from baseline up to Day 14 indicated with red arrows. Additionally, few erroneous positive strain values were also observed in anterior base segment (segment 1) indicated with red arrows in Figure 14.6 (c). These errors were attributed to the quasi-static clutter signals due to reverberation signals from the chest wall, ribs or sternum thus blocking the

myocardial motion in those segments. Several approaches have been reported in peer-reviewed literature to address this issue [30] (e.g., singular value filtering by Mauldin *et al.* [31]).

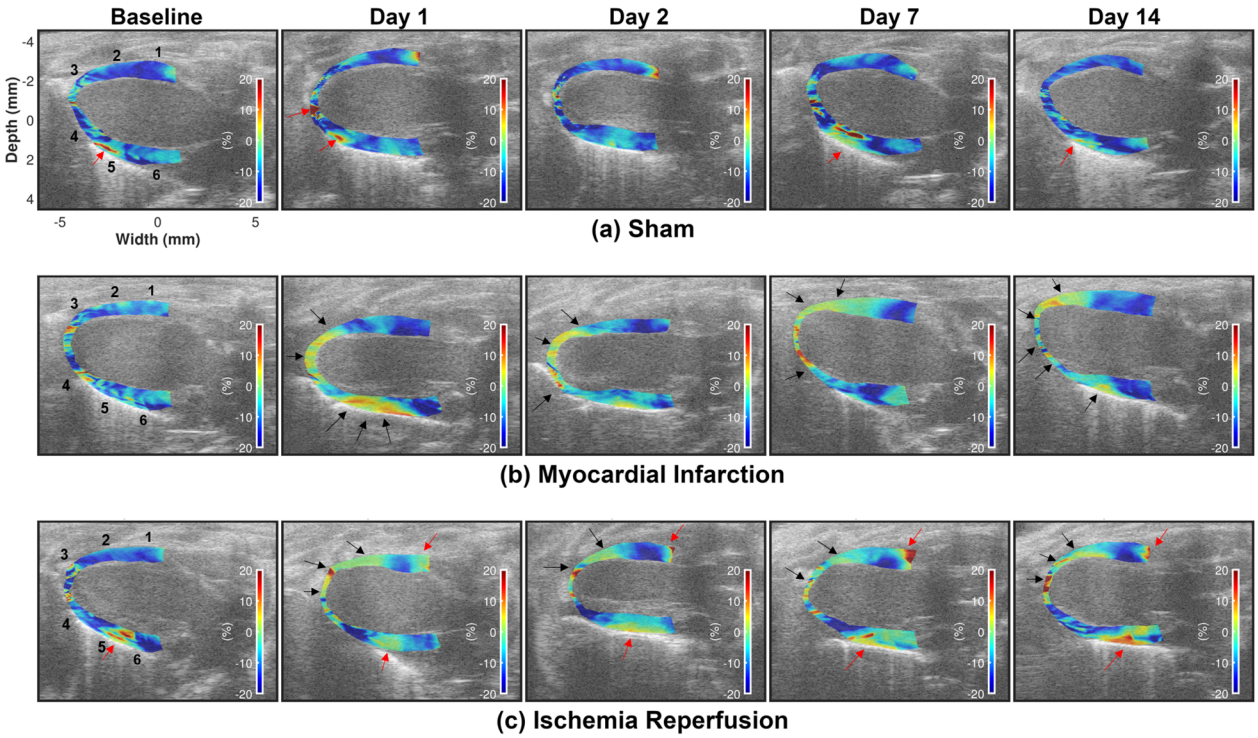

Figure 14.6 ES accumulated longitudinal strain images over time for (a) sham, (b) MI and (c) IR mice, respectively. Strain display dynamic range is from -20% to +20%. Negative strain value (blue) = myocardial wall shortening, positive strain value (red) = myocardial wall elongation and zero strain value (light green) = no wall motion.

The temporal progression of segmental longitudinal strain curves over a cardiac cycle for sham, MI and IR mice were compared in Figure 14.7. At baseline, all three mice had peak negative longitudinal strain values in all segments with synchronicity among the segments (observe low intraventricular dyssynchrony at baseline in Table 14.2) thus denoting normal cardiac function [Figure 14.7 (a) – (c)]. Sham mouse maintained a similar trend in segmental longitudinal strain curves [Figure 14.7 (a)] in post-surgery imaging time points with consistently low standard deviation of time-to-peak strain values (e.g., intraventricular dyssynchrony values at Baseline and

Day 14 were 0.07 and 0.04 [Table 14.2]. For the MI mouse, impact of permanent ligation can be observed mostly in the apical segments (segments 3 and 4) based on the reduction and sign reversal of longitudinal strain curves post-surgery [Figure 14.7 (b)]. At day 1, segments 3 and 5 were dyskinetic [32, 33] characterized by early systolic lengthening, followed by late and post-systolic shortening with reduced strain in posterior apical segment (segment 4). At day 14, segments 4 and 5 recovered longitudinal motion while segments 3 became more dyskinetic. However, no significant variation in intraventricular dyssynchrony was observed from baseline for the MI mouse except Day 1 [Table 14.2]. Similar trends were observed for the IR mouse with infarct being localized in anterior mid and anterior apex segments (brown and yellow curves in Figure 14.7 (c)). We also observed ventricular dyskinesis in segment 3 as early as day 1 with significant impairment at day 14. Furthermore, segments 2 and 6 were hypokinetic (less systolic shortening together with marked post-systolic shortening [32]) starting from day 2 with a significant increase in severity at day 14 indicating the impact of IR surgery on the LV function. But we did not observe any significant increase in intraventricular dyssynchrony when compared to the baseline imaging time point for the IR mouse [Table 14.2].

Table 14.2 Intraventricular Dyssynchrony Quantified using Longitudinal Time-to-Peak Strain

	Baseline	Day 1	Day 2	Day 7	Day 14
Sham	0.07	0.09	0.06	0.07	0.04
MI	0.05	0.17	0.05	0.08	0.06
IR	0.03	0.07	0.09	0.08	0.04

Figure 14.8 compares the ES (Figure 14.8 (a)) and peak (Figure 14.8 (b)) segmental longitudinal strain values over time among sham, MI and IR mice respectively. Sham mouse demonstrated consistent negative ES and peak strain values over time. For example, ES e_l values for anterior base at baseline = -12.89%, D1 = -11.05%, D2 = -8.49%, D7 = -11.46% and D14 = -

13.00%. ES and peak longitudinal strain values for the anterior apical segment was significantly impaired for the MI mouse whereas basal segments (both anterior and posterior) maintained the values observed at baseline indicating viable tissue regions. For example, ES e_l values for anterior apex at baseline = -4.18%, D1 = 1.87%, D2 = 2.33%, D7 = 2.18% and D14 = 0.58%. Other segments demonstrated reduction or sign reversal at Day 1 with steady recovery till Day 14 [Figure 14.8 (b)]. For the IR case, segments 2 – 3 and 6 showed impaired longitudinal strain values when compared to baseline with reduction or sign reversal of ES and peak e_l values [Figure 14.8 (c)] corroborating our observation of dyskinesia and hypokinesia based on Figure 14.7. For example, ES e_l values for anterior apex at baseline = -14.68%, D1 = 1.87%, D2 = 1.00%, D7 = -0.94% and D14 = 4.21%.

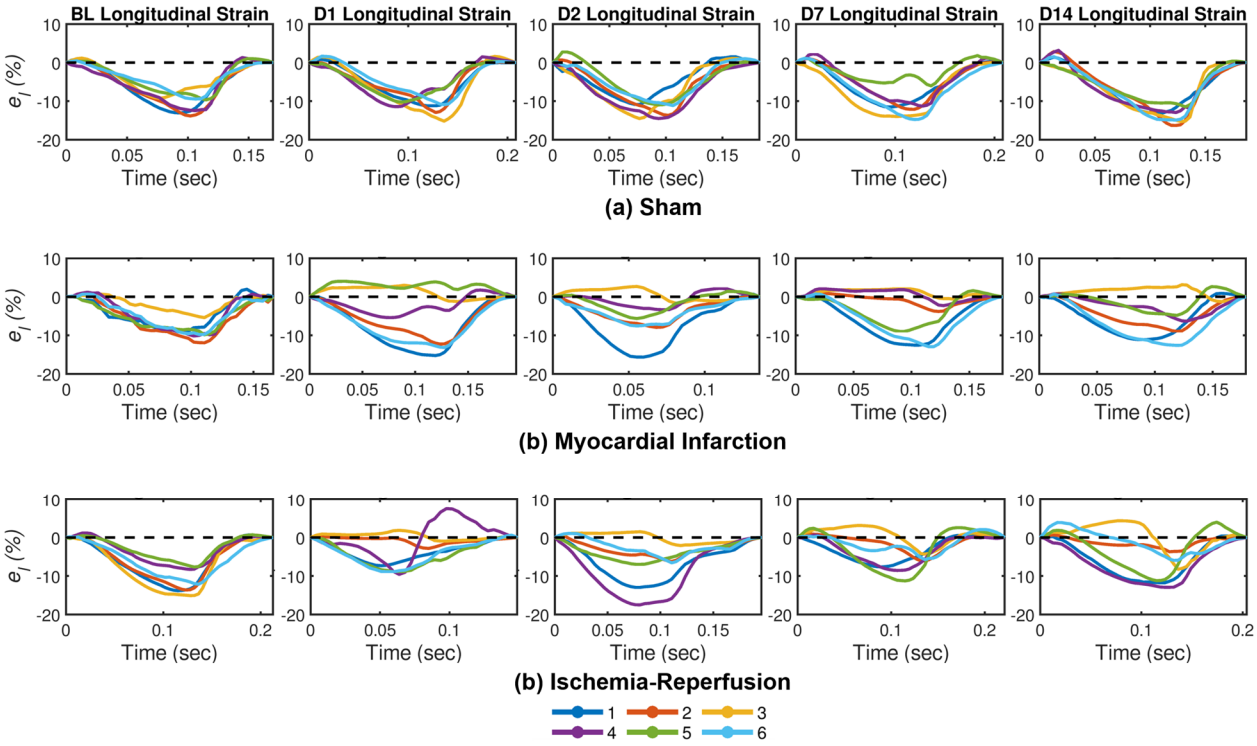

Figure 14.7 Temporal progression of segmental longitudinal strain curves over a cardiac cycle for (a) sham, (b) MI and (c) IR mice, respectively.

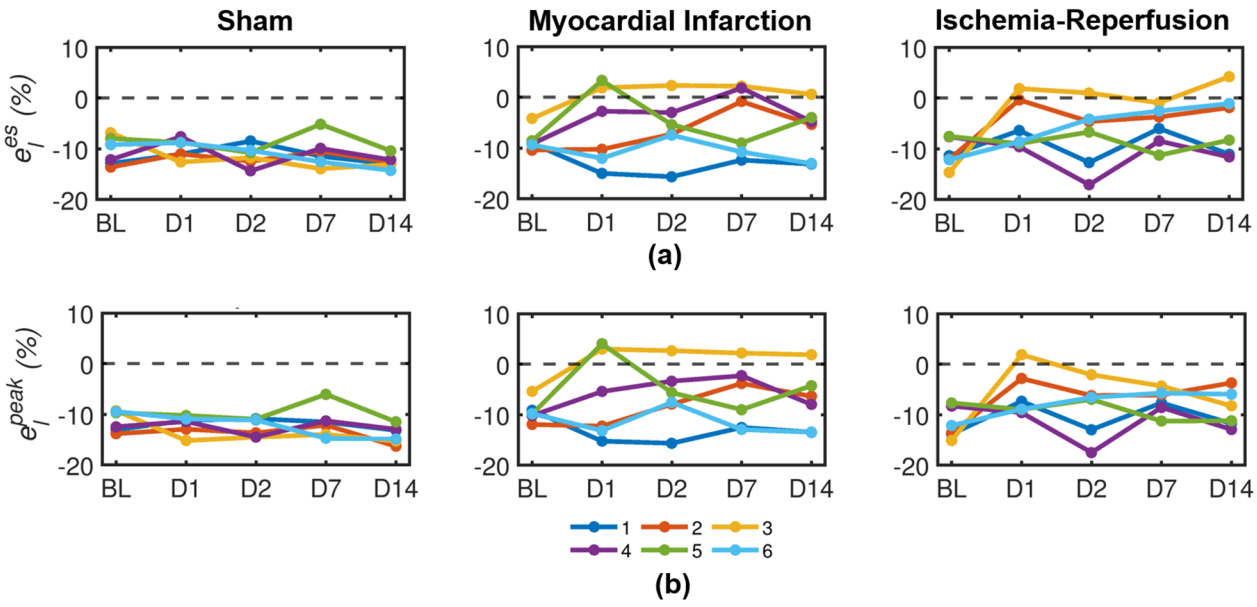

Figure 14.8 Comparison of segmental (a) ES and (b) peak longitudinal strain values over time among sham, MI and IR mice respectively. For each sub-figure, sham, MI and IR results are presented from left to right.

14.3 Cardiac Strain Images Identifies Region of Fibrosis and Correlates with Masson's Trichrome (MT) Stained Digital Histopathology Images

Comparison of day 14th ES radial and longitudinal strain images against MT-stained digital WSIs are shown in Figure 14.9 – Figure 14.11 for sham, MI and IR mice respectively. For each figure, sub-figures (a) – (b) are the ES radial and longitudinal strain images respectively and (c) – (d) denote MT-stained digital WSI, a magnified tissue region marked using a blue rectangular region-of-interest (ROI) in the sub figure (c) and classified WSI using QuPath [28] respectively. For the classified WSI, pink, yellow and gray colors indicated non-collagen tissue, collagen tissue and background regions respectively. Table 14.3 summarizes the comparison between day 14th ES cardiac strain values and collagen content quantified using the MT-strained WSI.

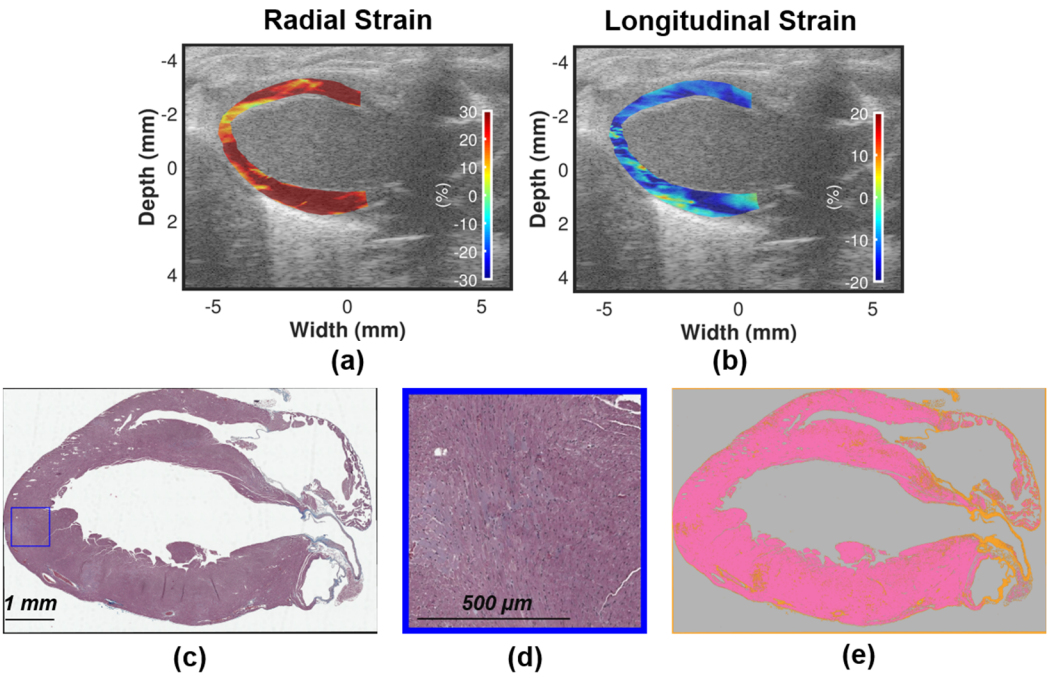

Figure 14.9 Comparison of day 14th *in vivo* cardiac strain images against MT-stained WSI for the sham mouse. (a) radial strain image, (b) longitudinal strain image, (c) digital WSI, (d) a magnified ROI denoted with a blue rectangle in sub-figure (d) and (e) classified WSI with QuPath. WSI = Whole slide image.

Figure 14.9 shows that for the sham mouse, we observed uniform wall thickness with myocardial tissue appearing uniformly dark purple in the classified WSI [Figure 14.9 (e)] being predominantly pink indicating absence of fibrosis [observe the magnified region in Figure 14.9 (d)]. This corroborates the *in vivo* strain images at day 14 [Figure 14.9 (a) – (b)], where uniform wall thickness was observed with high radial and longitudinal strain values represented as uniformly red and blue colors, respectively. This is quantitatively confirmed with only 6.98 % collagen content around the myocardium attributed to the collagen tissue around the blood vessels with ES e_r = 35.09% and e_l = -12.60% [Table 14.3].

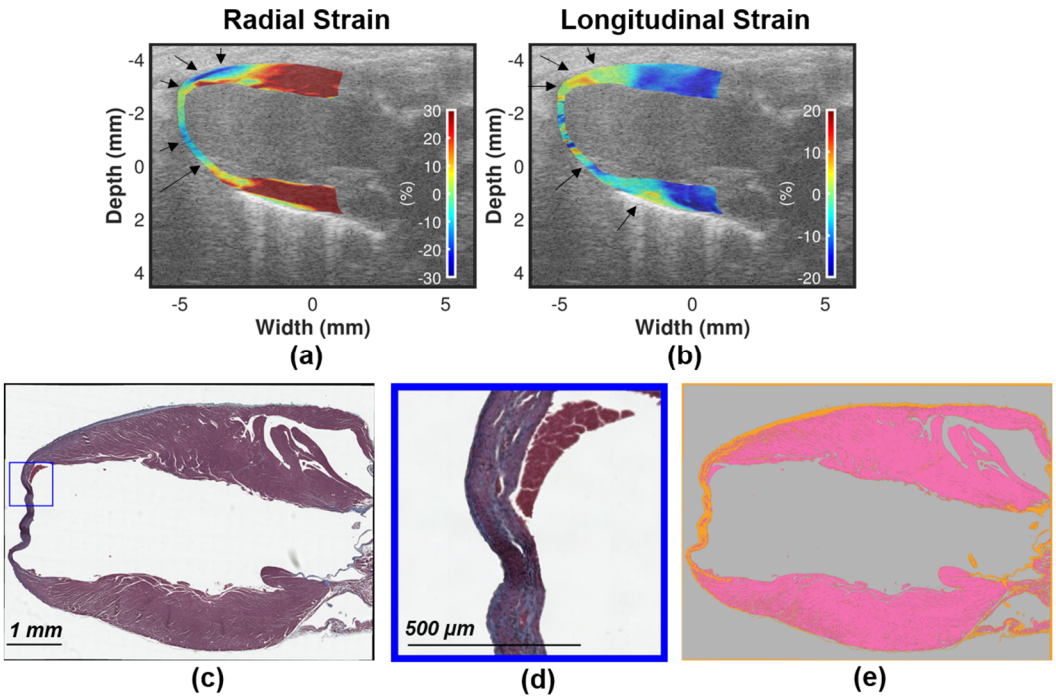

Figure 14.10 Comparison of day 14th *in vivo* cardiac strain images against MT-stained WSI for the myocardial infarction (MI) mouse. (a) radial strain image, (b) longitudinal strain image, (c) digital WSI, (d) a magnified ROI denoted with a blue rectangle in sub-figure (d) and (e) classified WSI with QuPath. WSI = Whole slide image.

For the MI mouse, the presence of an apical infarct is clearly identified by observing wall thinning with infarcted regions [Figure 14.10 (c)] appearing as dark blue [observe the magnified region in Figure 14.10 (d)] and viable regions as dark purple. Consequently, the QuPath machine learning model identified a region of fibrosis in the apical segment represented with yellow in Figure 14.10 (e). ES radial strain image showed excellent agreement in localizing infarcted region [marked with arrows in Figure 14.10 (a)] when compared to classified WSI. Longitudinal strain demonstrated overestimation in infarcted area [marked with arrows in Figure 14.10 (b)] when compared to radial strain image. Quantitative analysis showed higher collagen content in infracted regions with lower ES e_r and e_l strain values [Table 14.3].

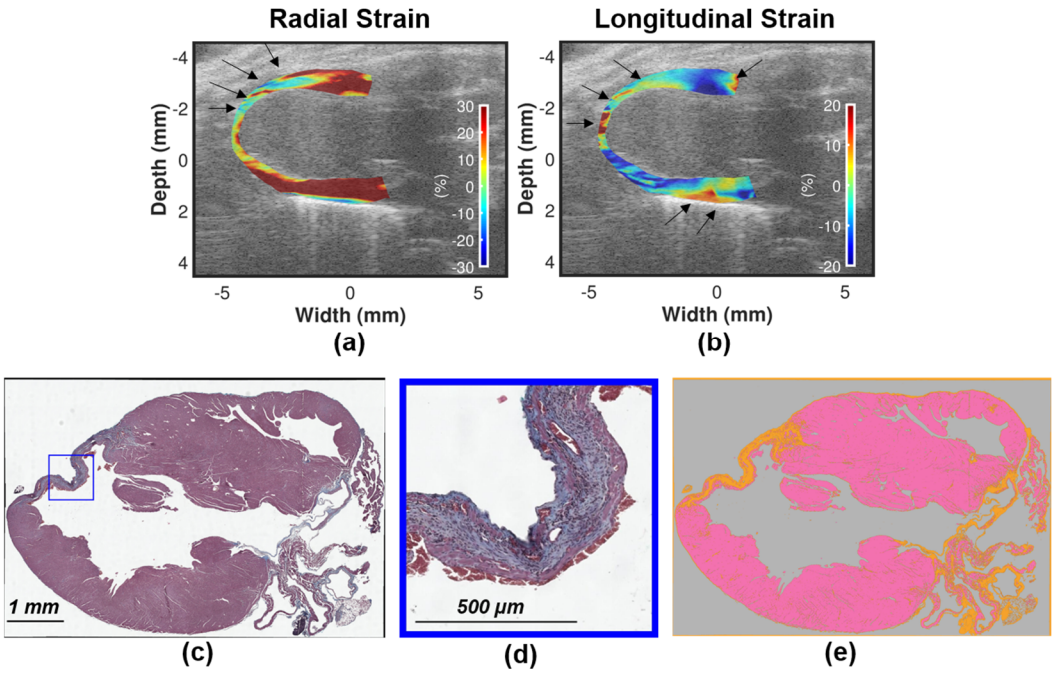

Figure 14.11 Comparison of day 14th *in vivo* cardiac strain images against MT-stained WSI for the ischemia-reperfusion (IR) mouse. (a) radial strain image, (b) longitudinal strain image, (c) digital WSI, (d) a magnified ROI denoted with a blue rectangle in sub-figure (d) and (e) classified WSI with QuPath. WSI = Whole slide image.

Figure 14.11 summarizes the results for comparing CSI findings with MT-stained WSI. Histopathological image analysis results in Figure 14.11 (c) – (d) showed a small region of fibrosis in the apical mid and anterior apex segments. Both *in vivo* radial and longitudinal strain images demonstrated reduced strain values in those segments [Figure 14.11 (a) – (b)] thus showing excellent agreement with the histopathology imaging results. Table 14.3 also reported increase in collagen content in the infarcted regions (76.22%) with corresponding reduction in ES e_r and e_l strain values. Note that, posterior basal segment showed hypokinesis in the longitudinal strain image [Figure 14.11 (b)] even though classified WSI indicate healthy myocardial tissue [Figure 14.11 (e)]. Overall, the results presented in Figure 14.9 – Figure 14.11 and Table 14.3 demonstrate that ABR-CSI was able to detect areas with cardiac fibrosis *in vivo* non-invasively.

Table 14.3 Day 14th ES Strain Values and Collagen Content Comparison*

	ES Radial Strain (%)		ES Longitudinal Strain (%)		Collagen Content (%)	
Mouse	Infarct	Viable	Infarct	Viable	Infarct	Viable
Sham	×	35.09	×	-12.60	×	6.98
MI	-3.23	32.91	-2.09	-8.89	77.37	5.61
IR	4.48	42.39	1.16	-8.09	76.22	4.96

**Infarct and viable regions identified using MT-Stained WSI*

14.4 Discussion on the Experimental Findings and Future Research

In this chapter, we have demonstrated the feasibility of an adaptive Bayesian regularized strain imaging framework for assessment of murine cardiac function *in vivo*. The proposed framework was able to differentiate between cardiac remodeling associated with ischemia-reperfusion injury, myocardial infraction and normal cardiac function in the sham mouse longitudinally over time. Furthermore, the strain variation observed *in vivo* corroborated our findings from *ex vivo* histopathological analysis. Future work will focus on validating the method in a larger cohort of mice and comparison against commercially available speckle tracking echocardiography solutions.

List of References

[1] M. L. Lindsey, R. Bolli, J. M. Canty Jr, X.-J. Du, N. G. Frangogiannis, S. Frantz*, et al.*, "Guidelines for experimental models of myocardial ischemia and infarction," *American Journal of Physiology-Heart and Circulatory Physiology,* vol. 314, pp. H812-H838, 2018.

[2] C. K. Phoon and D. H. Turnbull, "Cardiovascular imaging in mice," *Current protocols in mouse biology,* vol. 6, pp. 15-38, 2016.

[3] M. Bauer, S. Cheng, M. Jain, S. Ngoy, C. Theodoropoulos, A. Trujillo*, et al.*, "Echocardiographic Speckle-Tracking–Based Strain Imaging for Rapid Cardiovascular Phenotyping in Mice," *Circulation research,* p. CIRCRESAHA. 110.239574, 2011.

[4] E. E. Konofagou, J. D'hooge, and J. Ophir, "Myocardial elastography—A feasibility study in vivo," *Ultrasound in medicine & biology,* vol. 28, pp. 475-482, 2002.

[5] T. Varghese, J. Zagzebski, P. Rahko, and C. Breburda, "Ultrasonic imaging of myocardial strain using cardiac elastography," *Ultrasonic imaging,* vol. 25, pp. 1-16, 2003.

[6] W.-N. Lee, "Myocardial elastography: a strain imaging technique for the reliable detection and localization of myocardial ischemia in vivo," COLUMBIA UNIVERSITY, 2010.

[7] J. Luo, K. Fujikura, S. Homma, and E. E. Konofagou, "Myocardial elastography at both high temporal and spatial resolution for the detection of infarcts," *Ultrasound in medicine & biology,* vol. 33, pp. 1206-1223, 2007.

[8] J. Luo and E. E. Konofagou, "High-frame rate, full-view myocardial elastography with automated contour tracking in murine left ventricles in vivo," *IEEE transactions on ultrasonics, ferroelectrics, and frequency control,* vol. 55, pp. 240-248, 2008.

[9] B. Chakraborty, Z. Liu, B. Heyde, J. Luo, and J. D'hooge, "2-D Myocardial Deformation Imaging Based on RF-Based Nonrigid Image Registration," *IEEE transactions on ultrasonics, ferroelectrics, and frequency control,* vol. 65, pp. 1037-1047, 2018.

[10] J. D'hooge, A. Heimdal, F. Jamal, T. Kukulski, B. Bijnens, F. Rademakers*, et al.*, "Regional strain and strain rate measurements by cardiac ultrasound: principles, implementation and limitations," *European Journal of Echocardiography,* vol. 1, pp. 154-170, 2000.

[11] S. Langeland, J. D'hooge, T. Claessens, P. Claus, P. Verdonck, P. Suetens*, et al.*, "RF-based two-dimensional cardiac strain estimation: a validation study in a tissue-mimicking phantom," *IEEE transactions on ultrasonics, ferroelectrics, and frequency control,* vol. 51, pp. 1537-1546, 2004.

[12] A. Bhan, A. Sirker, J. Zhang, A. Protti, N. Catibog, W. Driver*, et al.*, "High-frequency speckle tracking echocardiography in the assessment of left ventricular function and remodeling after murine myocardial infarction," *American Journal of Physiology-Heart and Circulatory Physiology,* vol. 306, pp. H1371-H1383, 2014.

[13] R. Al Mukaddim, N. H. Meshram, C. C. Mitchell, and T. Varghese, "Hierarchical Motion Estimation With Bayesian Regularization in Cardiac Elastography: Simulation and $ In~ Vivo $ Validation," *IEEE transactions on ultrasonics, ferroelectrics, and frequency control,* vol. 66, pp. 1708-1722, 2019.

[14] R. Al Mukaddim and T. Varghese, "Improving Ultrasound Lateral Strain Estimation Accuracy using Log Compression of Regularized Correlation Function," *2020 42nd Annual International Conference of the IEEE Engineering in Medicine and Biology Society (EMBC). IEEE,* 2020.

[15] R. Al Mukaddim, K. Samimi, A. Rodgers, T. A. Hacker, and T. Varghese, "Comparison of cardiac displacements in a murine model of myocardial ischemia using Cardiac Elastography and speckle tracking echocardiography," in *2017 IEEE International Ultrasonics Symposium (IUS)*, 2017, pp. 1-4.

[16] R. Al Mukaddim and T. Varghese, "Cardiac Strain Imaging with Dynamically Skipped Frames: A Simulation Study," in *2020 IEEE International Ultrasonics Symposium (IUS)*, 2020, pp. 1-4.

[17] R. Al Mukaddim, N. H. Meshram, and T. Varghese, "Locally optimized correlation-guided Bayesian adaptive regularization for ultrasound strain imaging," *Physics in Medicine & Biology,* vol. 65, p. 065008, 2020.

[18] H. Shi and T. Varghese, "Two-dimensional multi-level strain estimation for discontinuous tissue," *Physics in medicine and biology,* vol. 52, p. 389, 2007.

[19] H. Chen, H. Shi, and T. Varghese, "Improvement of elastographic displacement estimation using a two-step cross-correlation method," *Ultrasound in medicine & biology,* vol. 33, pp. 48-56, 2007.

[20] M. McCormick, N. Rubert, and T. Varghese, "Bayesian regularization applied to ultrasound strain imaging," *IEEE Transactions on Biomedical Engineering,* vol. 58, pp. 1612-1620, 2011.

[21] C. C. Mitchell, R. Al Mukaddim, A. M. Weichmann, K. W. Eliceiri, M. E. Graham, and T. Varghese, "Carotid Strain Imaging with a Locally Optimized Adaptive Bayesian Regularized Motion Tracking Algorithm," in *2020 IEEE International Ultrasonics Symposium (IUS)*, 2020, pp. 1-4.

[22] N. H. Meshram and T. Varghese, "GPU accelerated multilevel Lagrangian carotid strain imaging," *IEEE transactions on ultrasonics, ferroelectrics, and frequency control,* vol. 65, pp. 1370-1379, 2018.

[23] M. M. McCormick and T. Varghese, "An approach to unbiased subsample interpolation for motion tracking," *Ultrasonic imaging,* vol. 35, pp. 76-89, 2013.

[24] R. Al Mukaddim, N. H. Meshram, C. C. Mitchell, and T. Varghese, "Hierarchical Motion Estimation with Bayesian Regularization in Cardiac Elastography: Simulation and in-vivo Validation," *IEEE transactions on ultrasonics, ferroelectrics, and frequency control,* 2019.

[25] C. Ma and T. Varghese, "Lagrangian displacement tracking using a polar grid between endocardial and epicardial contours for cardiac strain imaging," *Medical physics,* vol. 39, pp. 1779-1792, 2012.

[26] M. L. Lindsey, Z. Kassiri, J. A. Virag, L. E. de Castro Brás, and M. Scherrer-Crosbie, "Guidelines for measuring cardiac physiology in mice," *American Journal of Physiology-Heart and Circulatory Physiology,* vol. 314, pp. H733-H752, 2018.

[27] C. M. Yu, J. Gorcsan, 3rd, G. B. Bleeker, Q. Zhang, M. J. Schalij, M. S. Suffoletto*, et al.*, "Usefulness of tissue Doppler velocity and strain dyssynchrony for predicting left ventricular reverse remodeling response after cardiac resynchronization therapy," *Am J Cardiol,* vol. 100, pp. 1263-70, Oct 15 2007.

[28] P. Bankhead, M. B. Loughrey, J. A. Fernández, Y. Dombrowski, D. G. McArt, P. D. Dunne*, et al.*, "QuPath: Open source software for digital pathology image analysis," *Sci Rep,* vol. 7, p. 16878, Dec 4 2017.

[29] P. P. Sengupta, V. K. Krishnamoorthy, J. Korinek, J. Narula, M. A. Vannan, S. J. Lester*, et al.*, "Left ventricular form and function revisited: applied translational science to cardiovascular ultrasound imaging," *J Am Soc Echocardiogr,* vol. 20, pp. 539-51, May 2007.

[30] S. G. Sathyanarayana, S. T. Acton, and J. A. Hossack, "Closed loop low rank echocardiographic artifact removal," *IEEE Transactions on Ultrasonics, Ferroelectrics, and Frequency Control,* 2020.

[31] F. W. Mauldin, D. Lin, and J. A. Hossack, "The singular value filter: A general filter design strategy for PCA-based signal separation in medical ultrasound imaging," *IEEE transactions on medical imaging,* vol. 30, pp. 1951-1964, 2011.

[32] O. A. Smiseth, H. Torp, A. Opdahl, K. H. Haugaa, and S. Urheim, "Myocardial strain imaging: how useful is it in clinical decision making?," *Eur Heart J,* vol. 37, pp. 1196-207, Apr 14 2016.

[33] Y. Li, C. D. Garson, Y. Xu, P. A. Helm, J. A. Hossack, and B. A. French, "Serial ultrasound evaluation of intramyocardial strain after reperfused myocardial infarction reveals that remote zone dyssynchrony develops in concert with left ventricular remodeling," *Ultrasound Med Biol,* vol. 37, pp. 1073-86, Jul 2011.

Chapter 15

Conclusion and Future Work

15.1 Summary of Contributions

During the course of this dissertation, several image and signal processing algorithms were developed to demonstrate a composite imaging framework for *in vivo* assessment of murine myocardial health non-invasively. The composite imaging framework required experimental design, data collection, and algorithm development for two different imaging modalities – (a) cardiac strain imaging (CSI) using diagnostic ultrasound extracting mechanical properties of cardiac tissue and (b) photoacoustic imaging (PAI) deriving molecular information such as myocardial oxygen saturation. The first part of the dissertation (Chapters 4 – 7) reported on the developed and implemented algorithms for cardiac strain imaging while the second part (Chapters 8 – 13) presented the algorithms and methods developed and implemented for myocardial oxygenation estimation using cardiac PAI. Preliminary results from an *in vivo* longitudinal study focusing on murine models of cardiac ischemia has been summarized in Chapter 14.

A Lagrangian cardiac strain imaging approach with iterative Bayesian regularization was proposed and validated in Chapter 04. Our group previously reported Lagrangian CSI using a multi-level block matching (BM) algorithm for displacement estimation [1, 2]. However, the results were limited to parasternal short axis view data with a requirement of semiautomatic myocardial contour generation for the entire cardiac cycles of interest. In this dissertation, we aimed to develop a more general CSI framework as reported in Chapter 04 which can be adapted for any cardiac imaging view routinely used in clinical and pre-clinical situations. The results from experiments using finite-element-analysis (FEA) model of canine heart deformation and *in vivo*

mouse heart demonstrated significant performance improvement over conventional multi-level BM algorithm previously used. Performance improvement was attributed to error reduction in FEA experiments and resolving physiologically relevant *in vivo* murine cardiac strain images. One caveat of Bayesian CSI (see chapter 04) was that algorithm performance varied as a function of maximum iteration number of Bayesian regularization with a possibility of over-regularization due to incorrect estimate choice resulting in performance degradation. This observation led to the development of an adaptive Bayesian regularization (ABR) algorithm as reported in Chapter 05. The novelty of the ABR approach was the incorporation of information derived from input radio-frequency ultrasound signals into the Bayesian regularization framework to dynamically control regularization. This approach achieved optimal regularization by determining required the maximum iteration number locally per BM location automatically with concurrent estimation quality improvement for both axial and lateral strain tensors, making Bayesian regularization robust for clinical and pre-clinical applications. Additionally, we validated ABR for CSI using both parasternal long axis and short axis view datasets *in vivo* by comparing it against conventional method without regularization thus demonstrating the generalizability of the CSI framework reported in Chapter 04.

We proposed a spatiotemporal Bayesian regularization (STBR) algorithm for CSI in chapter 07 by extending the Bayesian regularization from Chapter 04 into the temporal domain with an underlying assumption of smooth variation in velocity over a short span of time during tissue deformation. Unlike all previous reports on Bayesian strain imaging which utilized information only from its spatial neighbors [3-11], the novelty of STBR algorithm was performing regularization using information from a three-dimensional neighborhood (2-D in space and 1D in time). Two different STBR schemes were investigated using cardiac simulation and *in vivo* data

sets and the results suggested that STBR with simultaneous use of spatiotemporal information (refer to STBR-2 in Chapter 07) provided the best results. Even though no statistical significantly improvement was observed in simulation results with STBR, *in vivo* results demonstrated better performance than spatial Bayesian regularization attributed to smoother strain curves, physiologically accurate end-systole cardiac strain images and higher expected signal-to-noise ($E(\mathrm{SNR}_e|\varepsilon)$) quantified by performing stochastic precision analysis [12]. One caveat was that the temporal regularization parameter was set empirically, a potential drawback which must be addressed before employing STBR for future *in vivo* studies. Furthermore, ABR should be incorporated into STBR to safeguard the algorithm from over-regularization artifact (please refer to Chapter 05 more details).

Dynamic frame skip (DFS) for cardiac strain imaging was investigated in chapter 07. Even though DFS has been routinely used by our group for carotid plaque strain imaging, it has not been formally studied in the context of CSI which motivated this preliminary investigation. Our results from limited initial experiments suggest that DFS can be potentially utilized to enhance cardiac strain imaging quality. However, these results should be interpreted with caution as more detailed parametric studies involving kernel dimension optimization, lateral interpolation factor, iteration number of Bayesian regularization should be done to decide conclusively if there are clear benefits of using DFS over the conventional inter-frame tracking approach for CSI. Additionally, we investigated the use of log compression of regularized correlation function as a simple solution to tackle the over-regularization artifact seen with Bayesian regularization due to incorrect estimate choice for the maximum iteration number in Chapter 07. The results suggest that log compression enabled improved subsample estimation with significant reduction of lateral banding errors due to

over-regularization. However, the experiments were limited to simulated uniform and inclusion phantoms which warrants further analysis using cardiac simulation phantoms and *in vivo* datasets.

As a part of this dissertation, we designed a longitudinal murine study in collaboration with Cardiovascular Physiology Core Facility, Small Animal Imaging and Radiotherapy Facility and Comparative Pathology Lab to validate the developed CSI approaches *in vivo* by collecting high frequency ultrasound radiofrequency (RF) data using Visualsonics Vevo 2100 Imaging system. Based on the experiments done in Chapters 04 – 07, adaptive Bayesian regularized CSI (ABR-CSI) was chosen as the optimal algorithm for the longitudinal study. Some preliminary results from the study were presented in Chapter 14 which demonstrated excellent agreement between *in vivo* findings using CSI and *ex vivo* histopathological image analysis. Note that data collection was done using 47 mice for the entire study which was interrupted and delayed several times due to Covid-19 global pandemic and ultrasound system related issues.

For myocardial perfusion quantification, we first investigated the feasibility of using a commercially available PAI system to study murine myocardial acute ischemia in a longitudinal study involving eight mice. This was one of the earliest comprehensive studies on the use of PAI for ischemia monitoring and detection in murine models. We observed statistically significant reduction in myocardial oxygen saturation (% sO_2) post-ischemia with correlation of findings with echocardiographic measurements quantifying global cardiac function. Even though the findings from Chapter 08 were promising, the employed method suffered from reduced sensitivity in detecting subtle variations of % sO_2 due to the use of high persistence (incoherent averaging of 10 consecutive frames) necessary to generate reasonable % sO_2 estimates to reduce system noise on the Vevo system. For cardiac PAI *in vivo*, this implies the possibility of averaging PA signals from multiple sources (myocardial wall, blood in left ventricular chamber and static tissue) thus

corrupting $\%sO_2$ quantification. This limitation led to the subsequent development of adaptive image processing algorithms reported in Chapters 09 – 13.

In Chapter 09, an adaptive beamforming algorithm termed spatiotemporal coherence factor (STCF) weighted PAI was proposed and validated for suppression of temporally varying incoherent clutter noise seen in cardiac PAI. We used both spatial and temporal information in the aperture domain during beamforming to calculate STCF for weighting delay-and-sum (DAS) and minimum variance (MV) beamformed PA images. The presented results demonstrated noise reduction quantified using contrast ratio (CR), generalized contrast-to-noise ratio (gCNR) and signal-to-noise ratio (SNR) both in simulation and *in vivo* experiments. However, further *in vivo* investigation revealed that STCF weighting may also lead to undesirable signal suppression from the myocardial wall along with sidelobe suppression which motivated to us explore alternative beamforming approaches for PAI leading to the development of photoacoustic sub-aperture processing (PSAP) reported in Chapter 10. Results presented in Chapter 10 showed that PSAP PAI was able to preserve DAS amplitude levels for myocardial wall PA signals and improve target detectability while achieving sidelobe and clutter suppression like coherence based beamformers (e.g., STCF beamformer in Chapter 10). Furthermore, a high resolution PAI beamforming algorithm was presented by combining PSAP with MV in chapter 11.

A spatiotemporal singular value decomposition (ST-SVD) algorithm to enhance cardiac PA signal specificity was presented in Chapter 12. In ST-SVD, basis functions contributing to static tissue, quasi-static clutter and temporal noise artifacts were significantly reduced thereby enhancing low intensity myocardial PAI signals. The novelty of our approach was to utilize the natural deformation of myocardial tissue to achieve PA image enhancement using ST-SVD

processing with automatic myocardial region-of-interest (ROI) generation for quantifying estimated % sO_2 values.

Finally, in Chapter 13, we integrated the methods developed in Chapters 09 – 12 to propose a myocardial oxygen saturation method termed as Oxygenation estimation using Physiological signal gating and Motion Compensation (OPMC). The novelty of OPMC included significant improvement in the spatiotemporal resolution owing to elimination of high persistence and data collection at higher frame rate. Unlike the commercial method investigated in chapter 08, OPMC allowed temporal synchronization of estimated % sO_2 values to different phases of a cardiac cycle such as systole, end-systole, diastole and end-diastole thus enabling studying the temporal progression of myocardial oxygen saturation over a cardiac cycle.

15.2 Future Directions for Cardiac Strain Imaging

Several interesting future avenues can be explored based on the methods developed in this dissertation. One natural future direction is to translate the proposed ABR-CSI from two-dimensional (2-D) ultrasound echocardiography to its three-dimensional (3-D) counterpart resulting in 4-D cardiac strain imaging. One approach for performing 3-D ultrasound echo is to collect several 2-D short axis planes of RF data by translating the ultrasound probe over the entire heart starting from base to apex using a stepper motor with simultaneous acquisition of ECG and respiratory signals. Then, the collected RF data can be spatiotemporally aligned [13] to reconstruct 4D datasets for performing ABR-CSI with 3-D kernels. During this dissertation, an automated 3-D RF data collection protocol as described above was developed for murine cardiac imaging and employed for data collection in a longitudinal study of cardiac disease (myocardial infarction and ischemia-reperfusion injury) involving 15 mice. The collected dataset has laid the foundation for validating the proposed 4-D ABR-CSI algorithm *in vivo*. Alternative approaches for 3-D

ultrasound imaging will be to use a 2-D matrix probe [14] for collecting volumetric ultrasound RF data. This approach might require our lab to acquire a new imaging system capable of data collection with matrix array probes such as the Vantage 256 system (Verasonics, Kirkland, USA).

Machine learning approaches particularly deep learning has become ubiquitous in the field of biomedical imaging with ultrasound imaging being no exception. Deep learning algorithms such as U-Net [15, 16] should be applied and investigated to perform segmentation of cardiac wall at end-diastole (required for displacement accumulation) thus replacing the manual segmentation reported in this dissertation. In addition to the dataset collected during this dissertation, publicly available dataset (e.g., Cardiac Acquisitions for Multi-structure Ultrasound Segmentation (CAMUS) https://www.creatis.insa-lyon.fr/Challenge/camus/) should also be considered for training DL models. Deep learning has also been used for ultrasound elastography in recent years. For example, Tehrani *et al.* [17] demonstrated the use of a pyramidal convolutional neural network for ultrasound strain imaging. However, the reported results were limited to only axial strain images which are typically less noisy due to the presence of phase information in RF data compared to lateral and shear strain imaging results. Similar approaches can be adopted for our CSI framework with proper attention to achieve concurrent improvement in axial, lateral and shear strain tensors. Furthermore, a deep learning model for performing Bayesian regularization optimally can also be developed in future using ABR-CSI results for training.

High frame rate imaging approaches (e.g., diverging wave imaging [18, 19]) should be considered in conjunction with the proposed spatiotemporal Bayesian regularization method to improve the temporal resolution of cardiac strain curves. In our current protocol, anesthesia was titrated to maintain a heart rate of 310 – 340 beats per minutes (bpm) during *in vivo* imaging. However, the limitation of this method is the possibility of suppressing LV systolic function due

to heart rates less than 400 bpm [20]. High frame rate imaging would allow us to address this issue. Finally, ABR-CSI should also be translated into human clinical studies of cardiac ischemia and infarction. This would require adapting the current algorithm to handle RF data collected using phased array transducers.

15.3 Future Directions for Cardiac Photoacoustic Imaging (PAI)

In the immediate future, a fluence compensation technique must be integrated into the proposed OPMC method in chapter 13 and the method should be evaluated *in vivo* for myocardial oxygen saturation estimation in murine models of myocardial infraction and ischemia-reperfusion. We anticipate that the spatiotemporal characteristics of estimates derived with fluence compensated OPMC approach will lead development of novel biomarkers in the investigation of myocardial perfusion using PAI.

In the longer term, several interesting future avenues can be explored based on the beamforming algorithms developed in this dissertation. First, the optimal set of sub-apertures for PSAP PAI was set empirically in this dissertation. However, empirical results suggest that the optimal sub-aperture choice varied with depth which would be a confounding factor for deep tissue imaging with PSAP-PAI. Therefore, an adaptive beamformer with depth-dependent sub-aperture selection should be explored. Second, one caveat of PSAP-PAI is that it may suffer “black region artifact [21]” surrounding a high optically absorbing object. The implication of this artifact is the undesirable suppression of weak PA signals generated from relatively less optically absorbing objects (e.g., vein) if they spatially overlap the sidelobe region of a high optically absorbing object (e.g., artery). Therefore, future research should focus on theoretical understanding of the origins of this artifact which will lead to better approaches to address this issue. Additionally, the sub-aperture selection problem can also be posed as a minimum variance problem following an

approach reported by Stanziola *et al.* [21] and can be investigated in the context of black region artifacts and PSAP-PAI.

Deep learning approaches, such as that proposed by Grohl *et al.* using training models from multi-spectral data per pixel [22] should also be investigated for the OPMC method. This Learned Spectral Decoloring method where a fully connected feed-forward neural network is trained using simulated initial pressure distributions, used deep learning assisted sO_2% quantification *in vivo* for the first time. Key idea was the generation of training datasets that closely resemble phantom and *in vivo* situations. Other reports on sO_2% quantification with DL include the following published work [23, 24]. Even though machine learning assisted sO_2% quantification is very encouraging in simulations, broader validation studies *in vitro* and *in vivo* are required to understand the generalizability of these methods [25]. Therefore, in the context of cardiac PAI, cardiac anatomy derived and co-registered US data and hybrid PAI simulation [26] framework incorporating both relevant optical and acoustic properties (varying probe center frequency, skin layer positions, positioning of vessels, acoustic attenuation, noise corruption) should be used to synthesize application specific training datasets for training a DL model for fluence compensation and myocardial oxygenation.

Even though the image reconstruction and quantification algorithms focused on cardiac PAI as an application, we anticipate these methods can be generalized for other PAI applications such as brachytherapy seed imaging [27, 28], percutaneous radiofrequency ablation needle detection [29] and surgical guidance [30]. Finally, future research should focus on translating these methods from pre-clinical imaging to the clinic on human subjects. Translation of these techniques for clinical imaging would require deep tissue PAI which imposes significant challenge due to optical scattering and attenuation observed *in vivo*. One possible solution would be to utilize a

catheter based light delivery system to provide more localized tissue illumination with detection of generated acoustic waves using an externally placed transducer on the skin surface [31, 32].

List of References

[1] C. Ma and T. Varghese, "Lagrangian displacement tracking using a polar grid between endocardial and epicardial contours for cardiac strain imaging," *Medical physics,* vol. 39, pp. 1779-1792, 2012.

[2] C. Ma, X. Wang, and T. Varghese, "Segmental analysis of cardiac short-axis views using lagrangian radial and circumferential strain," *Ultrasonic imaging,* vol. 38, pp. 363-383, 2016.

[3] R. Al Mukaddim, N. H. Meshram, and T. Varghese, "Locally optimized correlation-guided Bayesian adaptive regularization for ultrasound strain imaging," *Physics in Medicine & Biology,* vol. 65, p. 065008, 2020.

[4] B. Byram, G. E. Trahey, and M. Palmeri, "Bayesian speckle tracking. Part I: An implementable perturbation to the likelihood function for ultrasound displacement estimation," *IEEE transactions on ultrasonics, ferroelectrics, and frequency control,* vol. 60, pp. 132-143, 2012.

[5] B. Byram, G. E. Trahey, and M. Palmeri, "Bayesian speckle tracking. Part II: biased ultrasound displacement estimation," *IEEE transactions on ultrasonics, ferroelectrics, and frequency control,* vol. 60, pp. 144-157, 2012.

[6] D. M. Dumont and B. C. Byram, "Robust tracking of small displacements with a Bayesian estimator," *IEEE transactions on ultrasonics, ferroelectrics, and frequency control,* vol. 63, pp. 20-34, 2015.

[7] M. McCormick, N. Rubert, and T. Varghese, "Bayesian regularization applied to ultrasound strain imaging," *IEEE Transactions on Biomedical Engineering,* vol. 58, pp. 1612-1620, 2011.

[8] C. C. Mitchell, R. Al Mukaddim, A. M. Weichmann, K. W. Eliceiri, M. E. Graham, and T. Varghese, "Carotid Strain Imaging with a Locally Optimized Adaptive Bayesian Regularized Motion Tracking Algorithm," in *2020 IEEE International Ultrasonics Symposium (IUS)*, 2020, pp. 1-4.

[9] R. Al Mukaddim and T. Varghese, "Improving Ultrasound Lateral Strain Estimation Accuracy using Log Compression of Regularized Correlation Function," *2020 42nd Annual International Conference of the IEEE Engineering in Medicine and Biology Society (EMBC). IEEE,* 2020.

[10] R. Al Mukaddim and T. Varghese, "Cardiac Strain Imaging with Dynamically Skipped Frames: A Simulation Study," in *2020 IEEE International Ultrasonics Symposium (IUS)*, 2020, pp. 1-4.

[11] R. Al Mukaddim, A. M. Weichmann, C. C. Mitchell, and T. Varghese, "Ultrasound strain imaging using spatiotemporal Bayesian regularized multi-level block matching method," in *Medical Imaging 2021: Ultrasonic Imaging and Tomography*, 2021, p. 116020R.

[12] E. A. Bunting, J. Provost, and E. E. Konofagou, "Stochastic precision analysis of 2D cardiac strain estimation in vivo," *Physics in Medicine & Biology,* vol. 59, p. 6841, 2014.

[13] A. H. Soepriatna, F. W. Damen, P. P. Vlachos, and C. J. Goergen, "Cardiac and respiratory-gated volumetric murine ultrasound," *Int J Cardiovasc Imaging,* vol. 34, pp. 713-724, May 2018.

[14] C. Papadacci, E. A. Bunting, E. Y. Wan, P. Nauleau, and E. E. Konofagou, "3D Myocardial Elastography In Vivo," *IEEE Trans Med Imaging,* vol. 36, pp. 618-627, Feb 2017.

[15] M. Z. Alom, C. Yakopcic, M. Hasan, T. M. Taha, and V. K. Asari, "Recurrent residual U-Net for medical image segmentation," *Journal of Medical Imaging,* vol. 6, p. 014006, 2019.

[16] O. Ronneberger, P. Fischer, and T. Brox, "U-net: Convolutional networks for biomedical image segmentation," in *International Conference on Medical image computing and computer-assisted intervention*, 2015, pp. 234-241.

[17] A. K. Tehrani and H. Rivaz, "Displacement estimation in ultrasound elastography using pyramidal convolutional neural network," *IEEE transactions on ultrasonics, ferroelectrics, and frequency control,* vol. 67, pp. 2629-2639, 2020.

[18] J. Grondin, V. Sayseng, and E. E. Konofagou, "Cardiac strain imaging with coherent compounding of diverging waves," *IEEE transactions on ultrasonics, ferroelectrics, and frequency control,* vol. 64, pp. 1212-1222, 2017.

[19] V. Sayseng, R. A. Ober, C. S. Grubb, R. A. Weber, and E. Konofagou, "Monitoring Canine Myocardial Infarction Formation and Recovery via Transthoracic Cardiac Strain Imaging," *Ultrasound Med Biol,* vol. 46, pp. 2785-2800, Oct 2020.

[20] M. L. Lindsey, Z. Kassiri, J. A. Virag, L. E. de Castro Brás, and M. Scherrer-Crosbie, "Guidelines for measuring cardiac physiology in mice," *American Journal of Physiology-Heart and Circulatory Physiology,* vol. 314, pp. H733-H752, 2018.

[21] A. Stanziola, "Advanced beamforming for high frame rate ultrasound vascular imaging," 2018.

[22] J. Gröhl, T. Kirchner, T. J. Adler, L. Hacker, N. Holzwarth, A. Hernández-Aguilera*, et al.*, "Learned spectral decoloring enables photoacoustic oximetry," *Scientific reports,* vol. 11, pp. 1-12, 2021.

[23] D. A. Durairaj, S. Agrawal, K. Johnstonbaugh, H. Chen, S. P. K. Karri, and S.-R. Kothapalli, "Unsupervised deep learning approach for photoacoustic spectral unmixing," in *Photons Plus Ultrasound: Imaging and Sensing 2020*, 2020, p. 112403H.

[24] I. Olefir, S. Tzoumas, C. Restivo, P. Mohajerani, L. Xing, and V. Ntziachristos, "Deep Learning-Based Spectral Unmixing for Optoacoustic Imaging of Tissue Oxygen Saturation," *IEEE transactions on medical imaging,* vol. 39, pp. 3643-3654, 2020.

[25] G.-S. Jeng, M.-L. Li, M. Kim, S. J. Yoon, J. J. Pitre, D. S. Li*, et al.*, "Real-time interleaved spectroscopic photoacoustic and ultrasound (PAUS) scanning with simultaneous fluence compensation and motion correction," *Nature communications,* vol. 12, pp. 1-12, 2021.

[26] R. A. Mukaddim and T. Varghese, "Spatiotemporal Coherence Weighting for In Vivo Cardiac Photoacoustic Image Beamformation," *IEEE Trans Ultrason Ferroelectr Freq Control,* vol. 68, pp. 586-598, 2021.

[27] M. A. L. Bell, N. Kuo, D. Y. Song, and E. M. Boctor, "Short-lag spatial coherence beamforming of photoacoustic images for enhanced visualization of prostate brachytherapy seeds," *Biomedical optics express,* vol. 4, pp. 1964-1977, 2013.

[28] D. Allman, A. Reiter, and M. A. L. Bell, "Photoacoustic source detection and reflection artifact removal enabled by deep learning," *IEEE transactions on medical imaging,* vol. 37, pp. 1464-1477, 2018.

[29] K. J. Francis and S. Manohar, "Photoacoustic imaging in percutaneous radiofrequency ablation: device guidance and ablation visualization," *Physics in Medicine & Biology,* vol. 64, p. 184001, 2019.

[30] M. A. Lediju Bell, "Photoacoustic imaging for surgical guidance: Principles, applications, and outlook," *Journal of Applied Physics,* vol. 128, p. 060904, 2020.

[31] M. Li, B. Lan, W. Liu, J. Xia, and J. Yao, "Internal-illumination photoacoustic computed tomography," *J Biomed Opt,* vol. 23, pp. 1-4, Mar 2018.

[32] M. Li, T. Vu, G. Sankin, B. Winship, K. Boydston, R. Terry*, et al.*, "Internal-Illumination Photoacoustic Tomography Enhanced by a Graded-Scattering Fiber Diffuser," *IEEE Trans Med Imaging,* vol. 40, pp. 346-356, Jan 2021.

Appendix A

DAS and DAS_{CF} Performance Optimization for PSAP Comparison

This appendix reports on the parametric studies performed to optimize the performance of DAS and DAS_{CF} algorithms for PSAP comparison reported in **Chapter 10**. Numerical simulations with point targets, diffuse inclusion and microvasculature networks were performed, which are described in detail in **Chapter 10**. For point target simulations, we computed the main-lobe-to-sidelobe (MLSL) ratio (dB) values while diffuse inclusion and microvasculature simulations were quantified using contrast ratio (CR) and generalized contrast-to-ratio (gCNR) [1, 2].

A.1 Experimental findings from DAS beamforming parametric studies

A.1.1 Impact of f-number selection

Figure A.1 , Figure A**.2** and Figure A**.3** summarize the results for point target, inclusion and microvasculature simulations as a function of f-number. Figure A.1 (a) shows that strong sidelobes still persist even with the choice of a higher f-number. Furthermore, no significant variation of main lobe to side lobe (MLSL) ratio was seen for deeper targets due to aperture saturation [black and green curves in Figure A.1 (b)]. For shallower targets, we observe MLSL degradation [red and blue curves Figure A.1 (b)]. Figure A.2 (a) shows similar trends in the inclusion phantom simulation results where no significant qualitative difference was observed for different f-number results except for the slight reduction in sidelobe spread with f-number 2 or higher. Impact of the f-number is more evident at shallow depths due to aperture saturation. Quantitative CR and gCNR evaluation results over 10 independent simulation instances are shown in Figure A.2 (b) – (c). Highest CR and gCNR were achieved with f-number = 1. Similarly, for

microvasculature simulations, only qualitative differences were observed is the slight reduction in sidelobe spread with f-number 2 or higher at shallower depth [observe around 5 mm in Figure A.3 (a)]. Moreover, with f-number = 3 and 4, we observed blurring of structures at shallower depth. Quantitative CR and gCNR evaluation results shown in Figure A.3 (b) – (c) suggest that there might be a slight improvement in CR and gCNR compared to the f-number =1 result. However, the improvement in the results was not sufficient to outperform the results obtained with the PSAP method. Considering results from all three experiments, a f-number = 1 was chosen as default parameter for the PSAP comparison study.

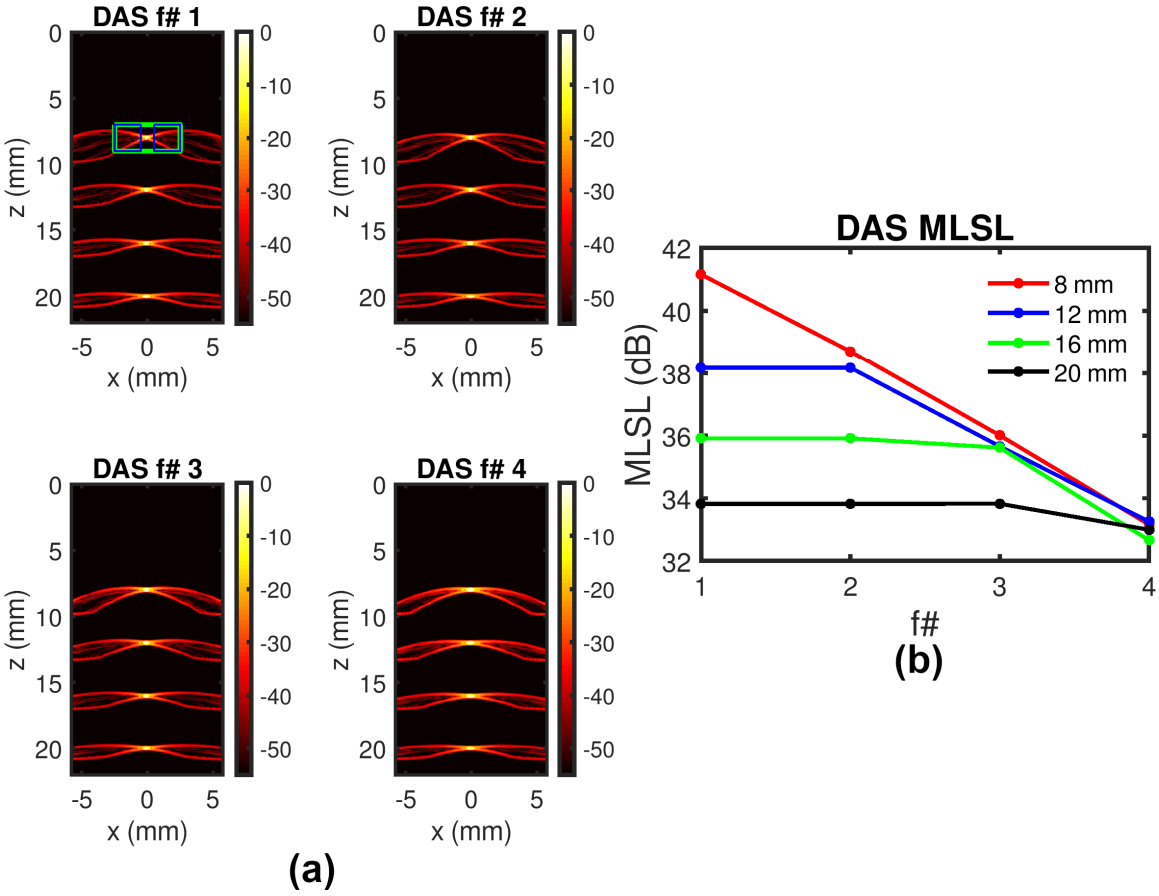

Figure A.1 Point target simulation comparison to obtain a f-number choice. (a) Qualitative results, (b) MLSL variation with f-number.

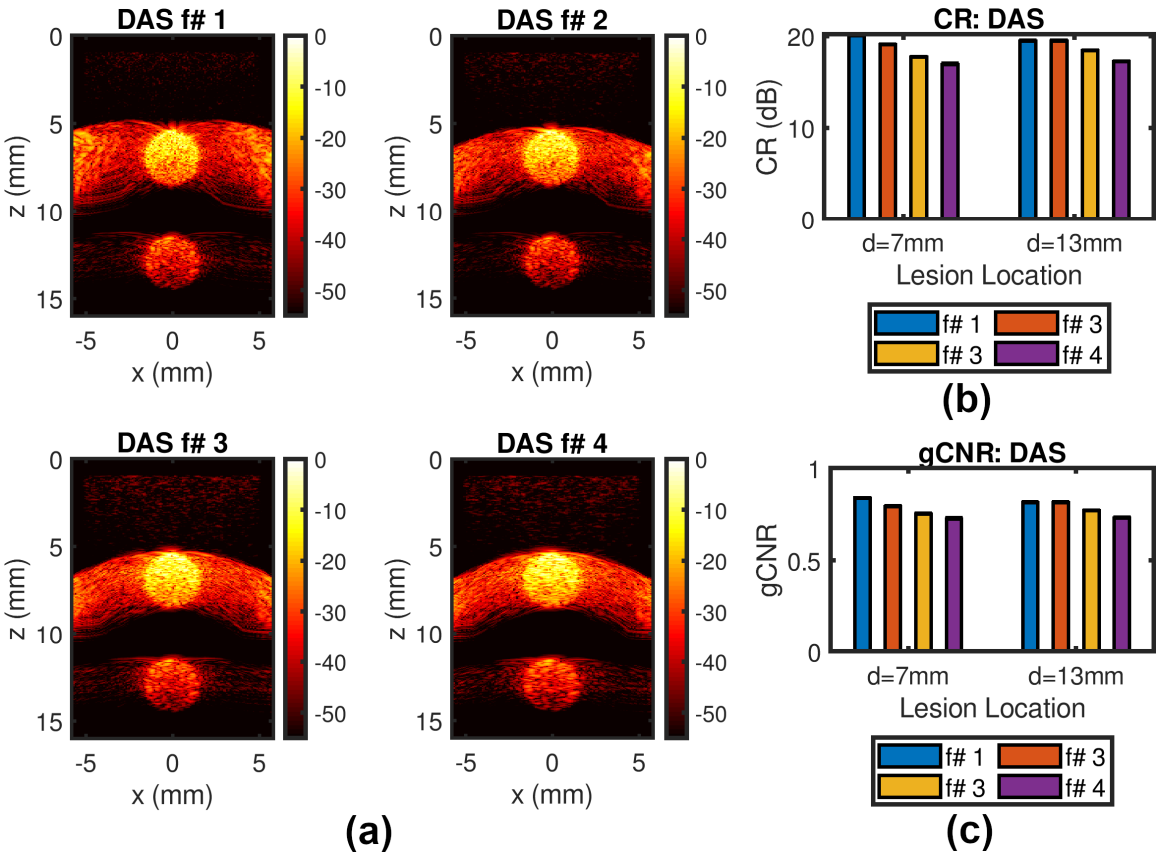

Figure A.2 Diffuse inclusion comparison to obtain f-number value. (a) Qualitative results, (b) and (c) show CR and gCNR variation with f-number, respectively.

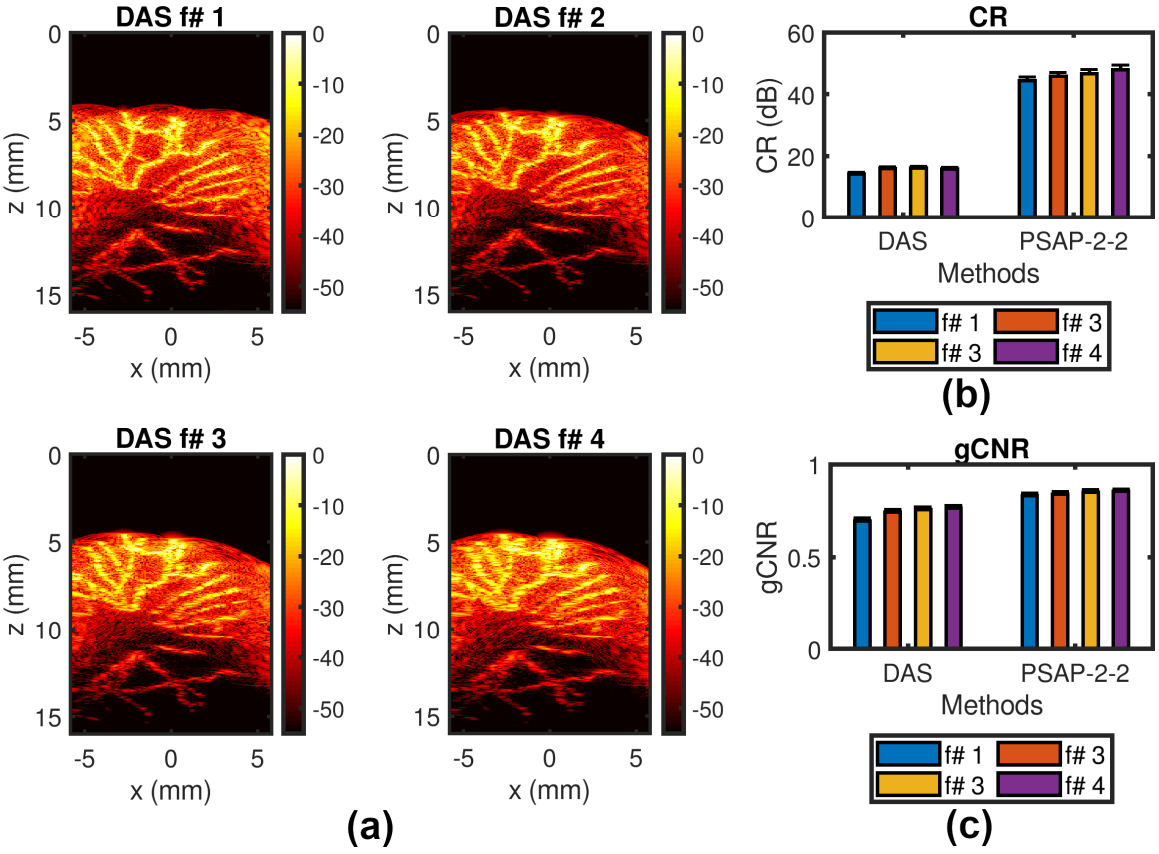

Figure A.3 Microvasculature simulation comparison for the f-number choice. (a) Qualitative results, (b) and (c) show CR and gCNR variation with f-number, respectively.

A.1.2 Impact of Apodization function

Four apodization functions were investigated in this section namely a uniform, Hamming, Blackman and Hann windowing functions respectively. A f-number = 1 was chosen based on the findings from Section A.1.1. Representative DAS beamformed images for the diffuse inclusion simulation phantom as a function of apodization function are shown in Figure A.4. Using Hamming, Blackman and Hann functions, we observed reduction in sidelobe levels when compared to uniform aperture weighting with no significant qualitative differences between each of these methods. Higher CR and gCNR values obtained with Hamming, Blackman and Hann functions when compared to the uniform weighting function corroborates the qualitative

observation [Figure A.5 (a) – (b)]. However, these improvements were not sufficient to outperform the CR and gCNR values obtained using the $PSAP_{NCC}$ (2-2) method as shown in Figure A.5 (c) – (d). Similarly, for the microvasculature simulations, we observed reduction in sidelobe spread and levels with Hamming, Blackman and Hann functions when compared to uniform aperture weighting [Figure A.6 (a)]. Quantitative evaluation results shown in Figure A.6 (a) – (b) also indicate that the improvement in CR and gCNR. However, $PSAP_{NCC}$ (2-2) method results shown in Figure A.6 (c) – (d) had higher CR and gCNR values. The results presented in this section demonstrate that $PSAP_{NCC}$ will perform better than DAS regardless the choice of apodization function.

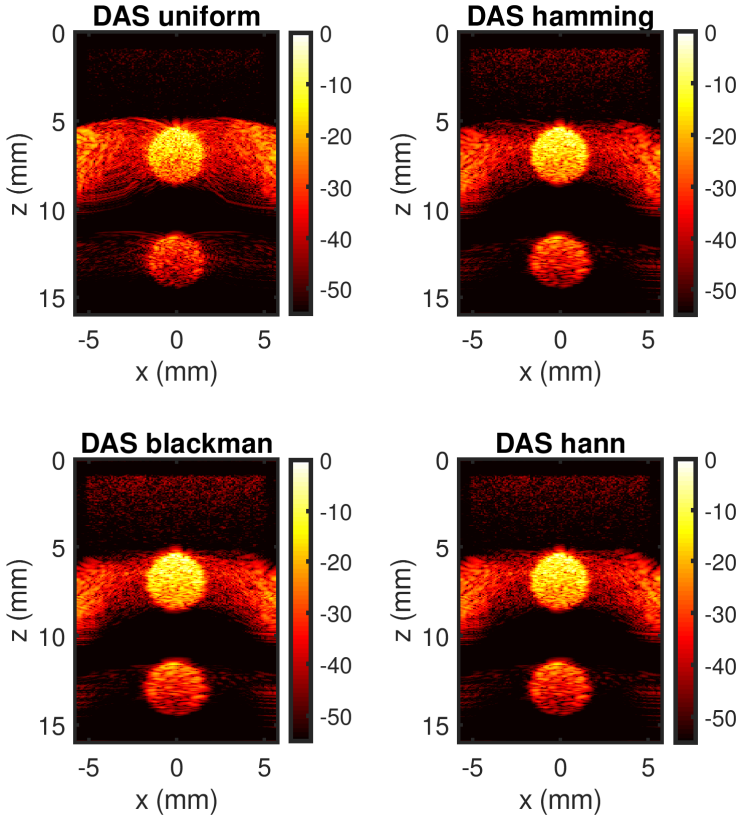

Figure A.4 DAS beamformed images for the diffuse inclusion simulation phantom for different apodization functions.

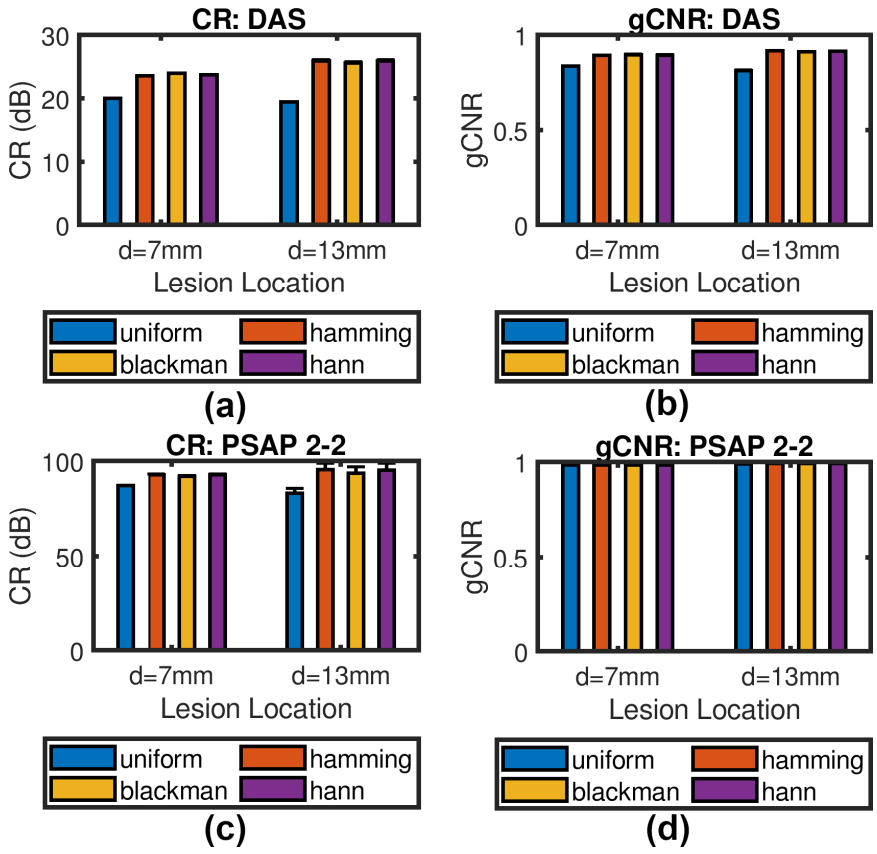

Figure A.5 (a) – (b) CR and gCNR results as a function of apodization function for DAS beamforming. (c) – (d) CR and gCNR results as a function of apodization function for $PSAP_{NCC}$ (2-2) beamforming.

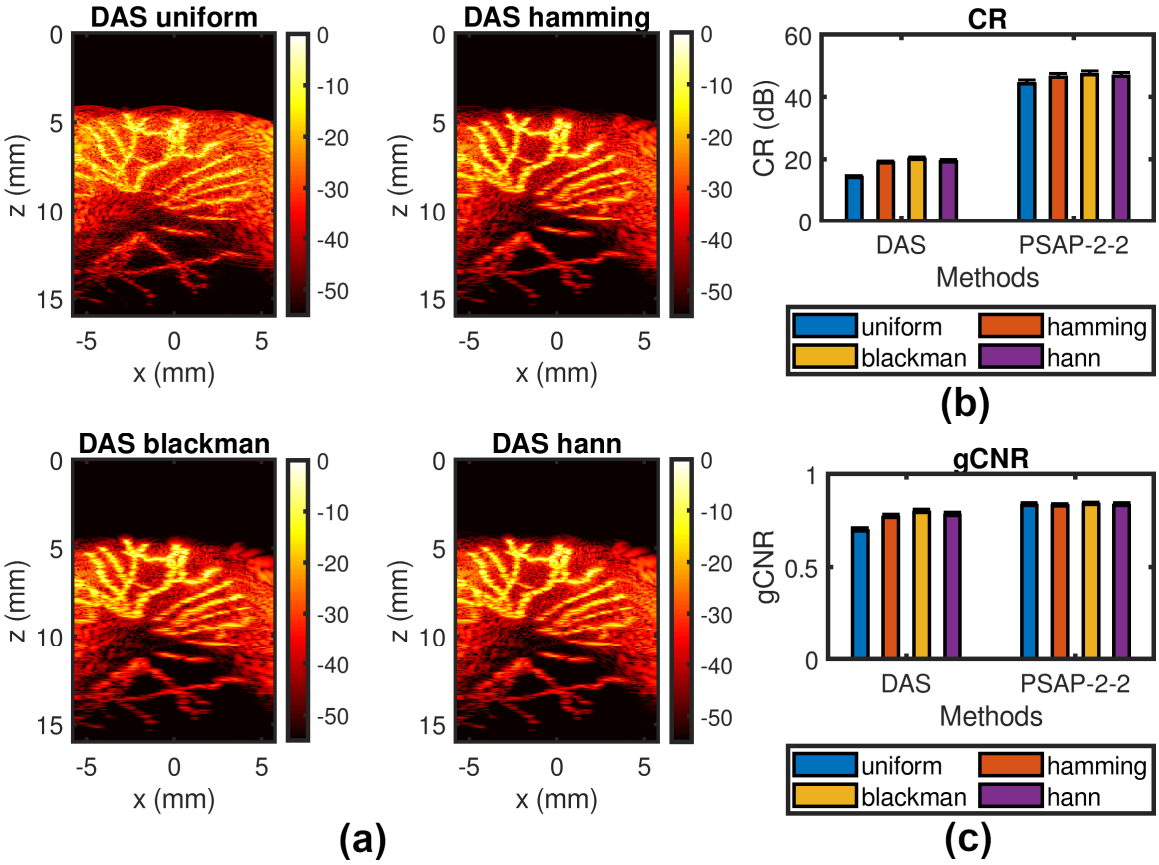

Figure A.6 Microvasculature simulation comparison for the different apodization functions. (a) Qualitative results, (b) and (c) show CR and gCNR variation with apodization function choice, respectively.

A.2 Vertical line artifact reduction for DAS_{CF} beamforming

In **Chapter 10**, we observed few erroneous vertical lines in DAS_{CF} images. To address this issue, a filtered version of coherence factor (F-CF) weighting was investigated in this dissertation. Specifically, we have computed coherence factor (CF) maps using channel data and then, filtered the CF map with a mean kernel of size [1.5λ × 3 A-lines]. The filtered CF map was used to weight the DAS image, denoted as $DAS_{Filtered\ CF}$. Figure A.7 summarizes the comparison results for the diffuse inclusion simulation. Figure A.7 (a) – (d) show DAS_{CF} image, $DAS_{Filtered\ CF}$, CR comparison and gCNR comparison results. A f-number of 1 was used during beamforming. Figure A.7 (a) – (b) show that no significant qualitative difference exists between DAS_{CF} and

$DAS_{Filtered\ CF}$. Furthermore, even with the filtered CF map, we observed significant signal loss within the inclusion, an issue that was resolved with our proposed sub aperture processing scheme (Chapter 10). Quantitative evaluation with CR and gCNR [Figure A.7 (c) – (d)] also demonstrate that no significant differences exist between DAS_{CF} and $DAS_{Filtered\ CF}$. However, with $DAS_{Filtered\ CF}$, we did not observe the vertical line artifact after the Hilbert transform which was present in the DAS_{CF} image.

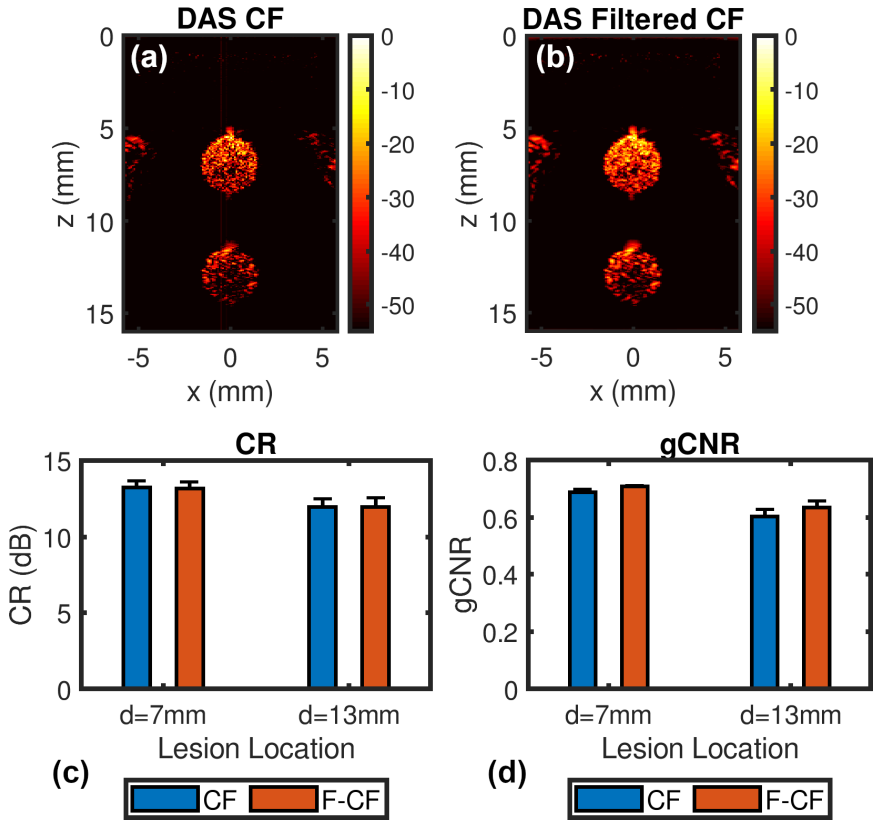

Figure A.7 Diffuse inclusion simulation comparison between conventional CF and filtered CF. (a) DAS_{CF} image, (b) $DAS_{Filtered\ CF}$, (c) CR and (d) gCNR.

Figure A.8 summarizes the comparison results for the microvasculature simulation. Like, the inclusion simulation, we did not observe any significant qualitative differences between DAS_{CF} and $DAS_{Filtered\ CF}$ except elimination of the vertical line artifact. Quantitative evaluation with CR

and gCNR [Figure A.8 (c) – (d)] demonstrate that $DAS_{Filtered\ CF}$ had higher CR and gCNR than DAS_{CF} and $DAS_{Filtered\ CF}$. However, even with the filtered CF map, we observed significant vessel signal loss at depth, an issue that was resolved with our proposed PSAP method (**Chapter 10**).

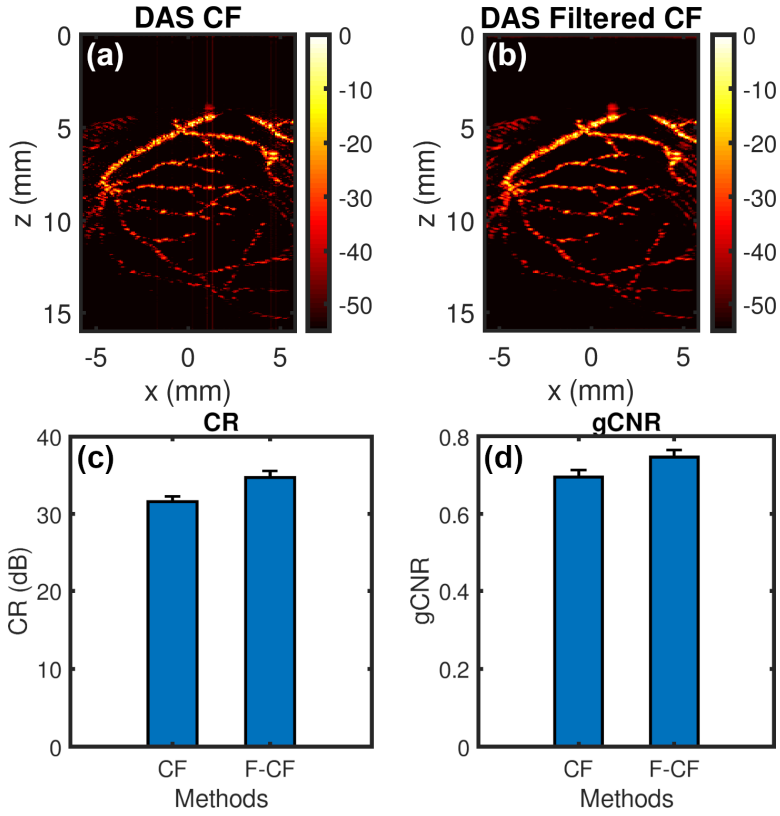

Figure A.8 Microvasculature simulation comparison between conventional CF and filtered CF. (a) DAS_{CF} image, (b) $DAS_{Filtered\ CF}$, (c) CR and (d) gCNR.

List of References

[1] K. M. Kempski, M. T. Graham, M. R. Gubbi, T. Palmer, and M. A. L. Bell, "Application of the generalized contrast-to-noise ratio to assess photoacoustic image quality," *Biomedical Optics Express,* vol. 11, pp. 3684-3698, 2020.

[2] A. Rodriguez-Molares, O. M. H. Rindal, J. D'hooge, S.-E. Måsøy, A. Austeng, M. A. L. Bell*, et al.*, "The generalized contrast-to-noise ratio: a formal definition for lesion detectability," *IEEE Transactions on Ultrasonics, Ferroelectrics, and Frequency Control,* vol. 67, pp. 745-759, 2019.

Appendix B

This appendix reports on a coupled sub-aperture (PSAP) and spatiotemporal singular value decomposition (SVD) processing method to suppress background signals for the results reported in **Chapter 12**. Figure B.1 presents a schematic diagram demonstrating coupled PSAP and SVD processing for background suppression in the DAS SVD processed images. In addition to DAS beamforming with full aperture, beamforming was also done with two non-overlapping sub-apertures having no common elements defined using binary weighting vectors. Here, sub-aperture 1 (S_1) weighting vector was constructed of ones and zeros with an alternating pattern of two elements and sub-aperture 2 (S_2) weighting vector was complimentary of sub-aperture 1. Further details on PSAP can be found here [1]. Both cardiac cycle data reconstructed with S_1 and S_2 were filtered with the proposed spatiotemporal SVD method reported in **Chapter 12**. Then, 3-D (2-D space + 1-D time) weighting matrix (W_{PSAP}) was determined by calculating zero lag normalized cross-correlation (NCC) between each frame of S_1 and S_2 reconstructed cardiac cycle. During NCC calculation, incoherent clutter signals from background have low similarity while myocardial PA signal have high similarity [1]. Therefore, DAS SVD processed images were multiplied with W_{PSAP} to suppress background signals. The resultant images are denoted as PSAP-SVD.

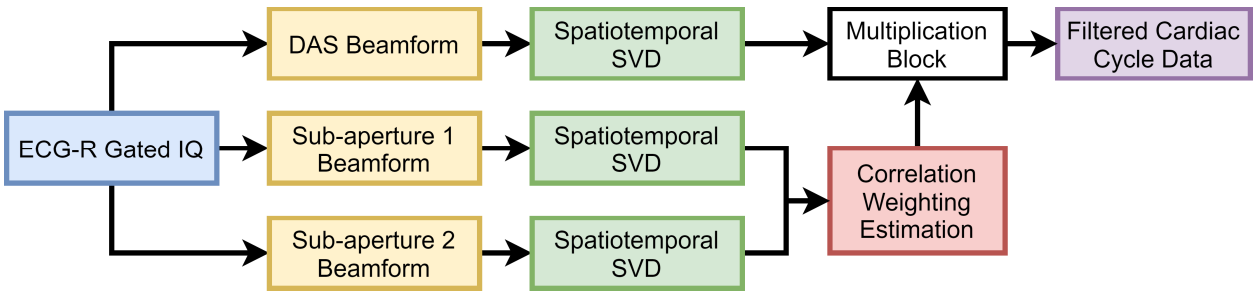

Figure B.1 Schematic diagram demonstrating coupled PSAP and SVD processing

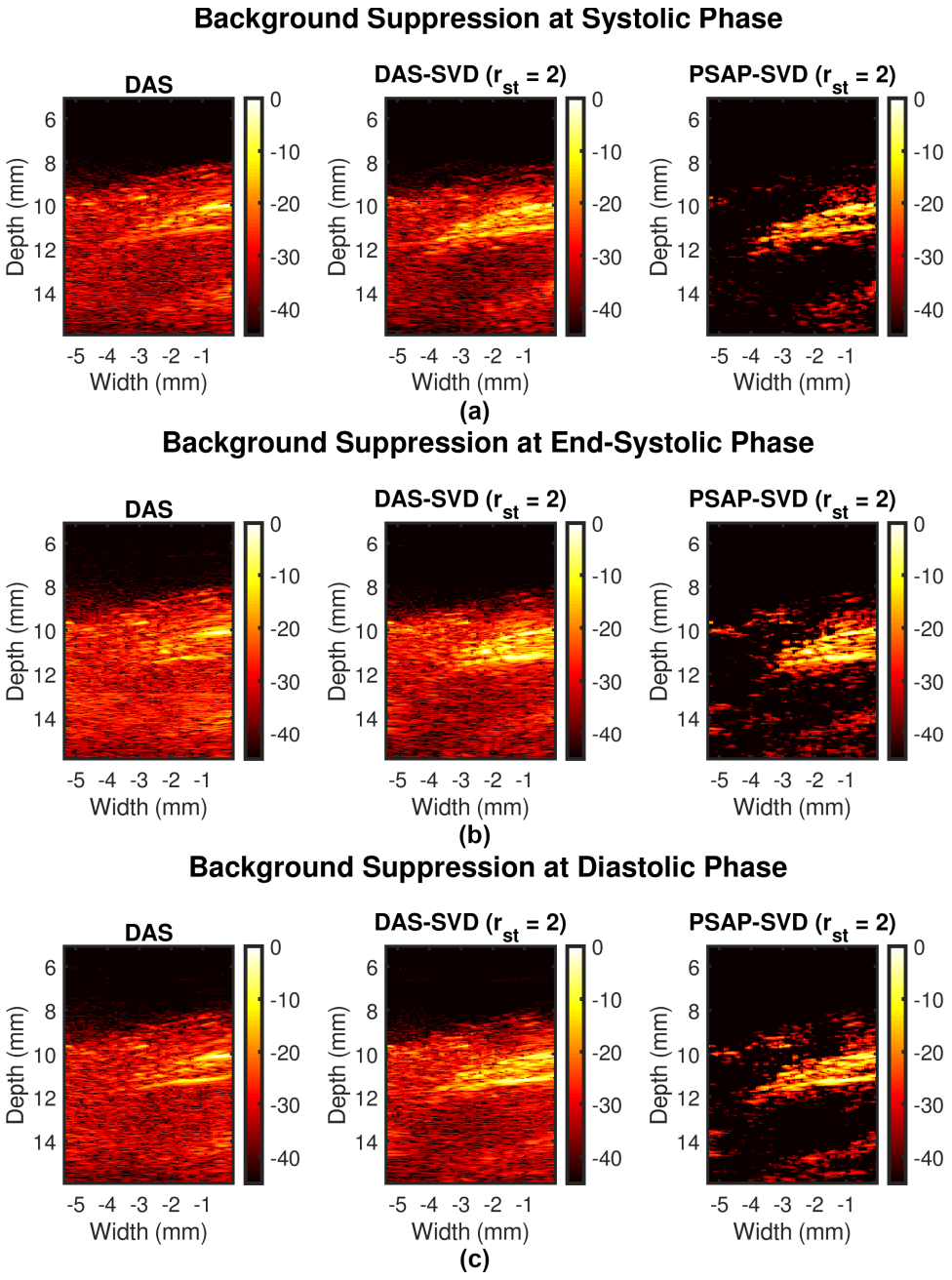

Figure B.2 Representative background suppression results from coupled PSAP and SVD processing. (a) – (c) show results at systolic, end-systolic, and diastolic phase of a cardiac cycle, respectively. Results with DAS, DAS-SVD (r_{st} = 2), and PSAP-SVD (r_{st} = 2) are presented from left to right chronologically for each sub-figure. r_{st} denotes the lower singular value order chosen for thresholding.

Figure B.2 shows representative background suppression results from coupled PSAP and SVD processing. Figure B.2 (a) – (c) show results at systolic, end-systolic, and diastolic phase of a cardiac cycle, respectively. Results with DAS, DAS-SVD ($r_{st} = 2$), and PSAP-SVD ($r_{st} = 2$) are presented from left to right chronologically for each sub-figure. We observe that coupled PSAP and SVD processing achieved simultaneous suppression of background signal and enhancement of myocardial PA signal for all three cases.

List of References

[1] R. Al Mukaddim, R. Ahmed, and T. Varghese, "Sub-aperture Processing Based Adaptive Beamforming for Photoacoustic Imaging," *IEEE Transactions on Ultrasonics, Ferroelectrics, and Frequency Control,* 2021.